*Eur*JIC

European Journal of Inorganic Chemistry
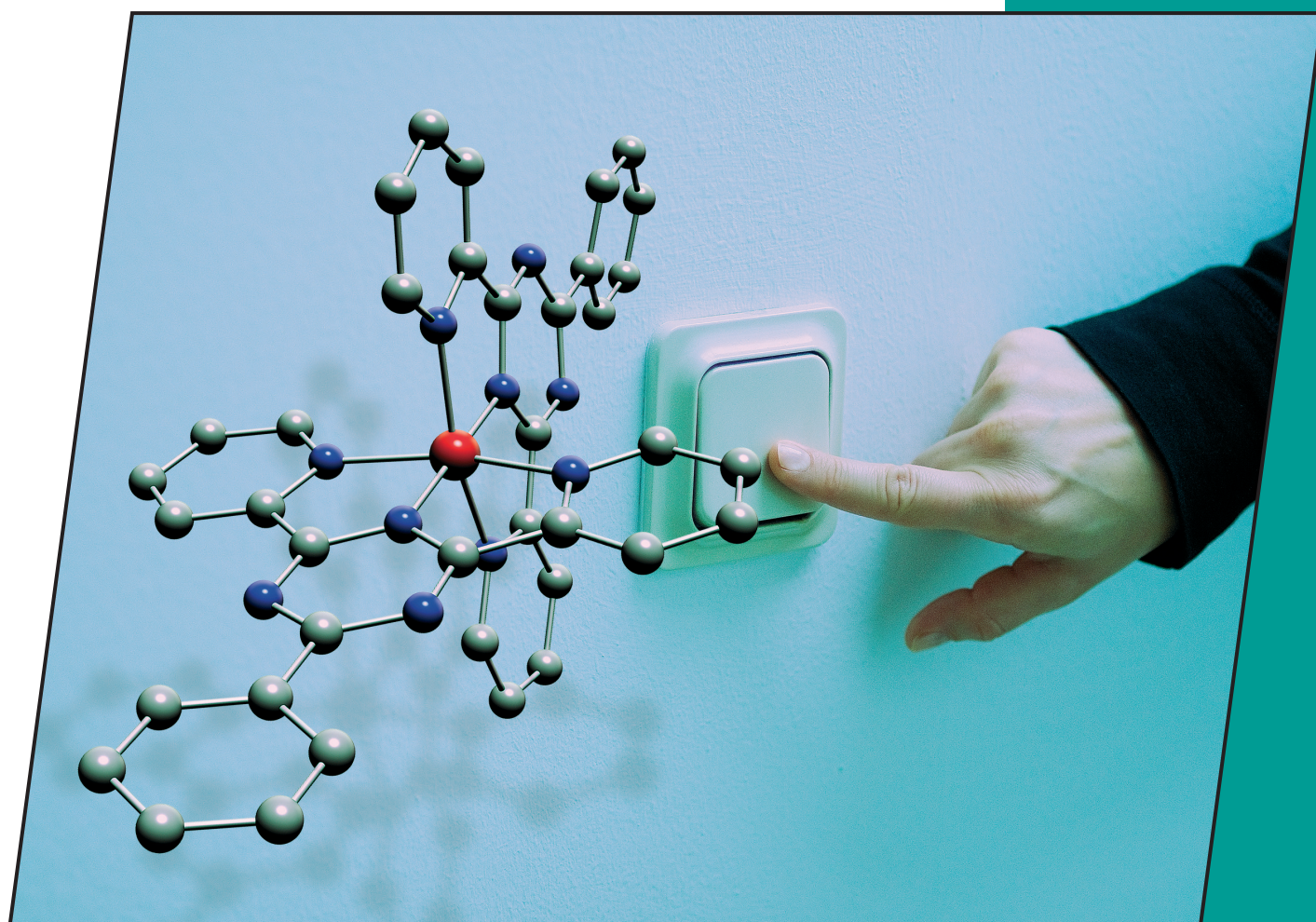
Cover Picture

Gerald Hörner, Andreas Grohmann et al.

On the Spin Behaviour of Iron(II)–Dipyridyltriazine Complexes
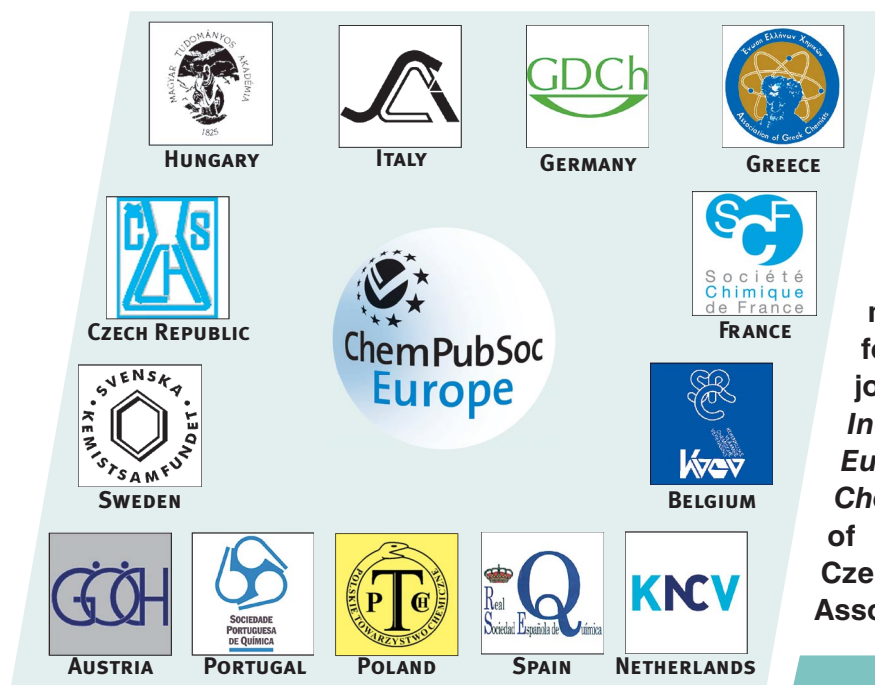
Microreview

Matthias Westerhausen et al.

Subvalent Organometallic Compounds of the Alkaline Earth Metals

A Journal of

ChemPubSoc
Europe

WILEY-VCH

www.eurjic.org

COVER PICTURE

The cover picture shows the crystal structure of an iron(II) complex with a tridentate triazine-based ligand, one of three complexes whose thermal and photonic spin-dynamics are discussed in the article by G. Hörner, A. Grohmann et al. on p. 221ff. While there is a competition between spin crossover and ligand exchange upon thermal excitation in solution, the complexes switch cleanly between their stable low-spin and metastable high-spin forms upon photoexcitation. Artwork: Holger Neumann, Gentura.

COVER PICTURE

The cover picture shows the crystal structure of an iron(II) complex with a tridentate triazine-based ligand, one of three complexes whose thermal and photonic spin-dynamics are discussed in the article by G. Hörner, A. Grohmann et al. on p. 221ff. While there is a competition between spin cross-over and ligand exchange upon thermal excitation in solution, the complexes switch cleanly between their stable low-spin and metastable high-spin forms upon photoexcitation. Artwork: Holger Neumann, Gentura.
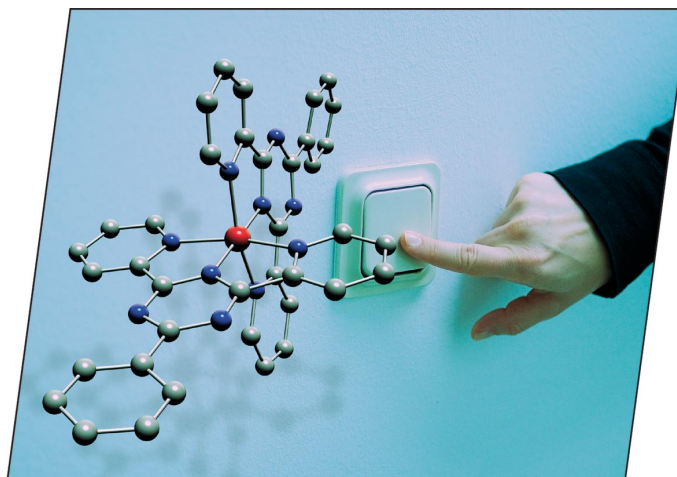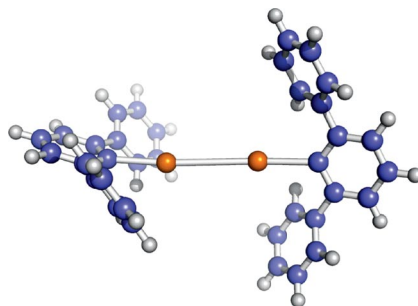
CONTENTS

MICROREVIEW

Subvalent Alkaline Earth Compounds

Subvalent Organometallic Compounds of the Alkaline Earth Metals in Low Oxidation States

Keywords: Main group elements / Metal–metal interactions / Subvalent compounds / Alkaline earth metals / Cluster compounds / Arene ligands / Radical anions

Alkaline earth metals are regarded as redox-inert; only the oxidation state +2 seems to have significance. In the last few years, sophisticated procedures led to the isolation of compounds with low-valent alkaline earth metals, and several concepts of their stabilization are discussed. Metal–metal bond formation (blue: C, grey: H, orange: Ca) is one possibility to obtain subvalent compounds.

SHORT COMMUNICATION

ZnO Colloidal Clusters

Polyol-Mediated Synthesis of Highly Water-Soluble ZnO Colloidal Nanocrystal Clusters

Keywords: Colloids / Crystal growth / Fluorescence / Nanostructures / Zinc
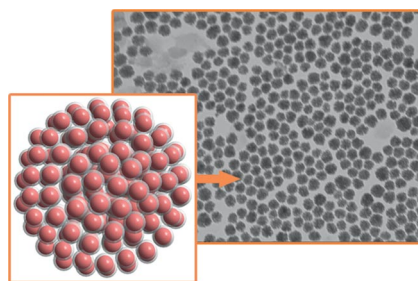
Highly water-soluble ZnO colloidal nanocrystal clusters (CNCs) with tunable size have been prepared successfully by using a high-temperature hydrolysis reaction. The as-prepared ZnO CNCs still exhibited strong UV emission in the photoluminescence (PL) spectrum due to the existence of secondary structures despite a particle size ranging from 60 to ca. 200 nm.

FULL PAPERS

Spin Crossover

Spin Crossover ?

Δ / hν

On the Spin Behaviour of Iron(II)–Dipyridyltriazine Complexes and Their Performance as Thermal and Photonic Spin Switches

Keywords: Iron / Spin crossover / Thermodynamic stability / N ligands / Magnetic properties

Three de novo synthesized iron(II) complexes show markedly diverging thermal and photonic spin behaviour in solution. The substantial thermochromism of the complexes in DMSO is due to a competition between ligand substitution and a thermally induced spin crossover. Efficient photonic low-spin to high-spin switching prevails even in strongly coordinating solvents.

CeO_2 thin films were synthesized on both NiW and $La_2Zr_2O_7$-buffered NiW by a novel, aqueous citric acid based chemical solution deposition (CSD) method. Sufficient thickness was achieved in combination with good texture. The introduction of doping elements allowed us to synthesize dense materials with good morphology.
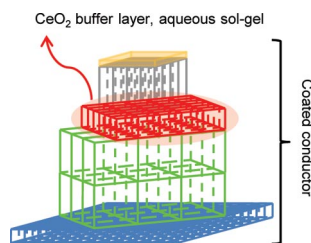
**N. Van de Velde,* D. Van de Vyver,
O. Brunkahl, S. Hoste, E. Bruneel,
I. Van Driessche** **233–241**

CeO_2 Buffer Layers for HTSC by an Aqueous Sol-Gel Method – Chemistry and Microstructure

Keywords: Sol-gel processes / Superconductors / Layered compounds / Cerium oxide / Complex formation

---

Doped ZnS quantum dots were synthesised and subsequently inkjet-printed onto a variety of substrates including inkjet-quality photographic paper, cotton, merino wool, PET film, PEDOT-coated PET film, and silicon wafer. The most successful were inkjet-quality photographic paper and cotton, on which complicated patterns were printed that gave rise to photoluminescence.
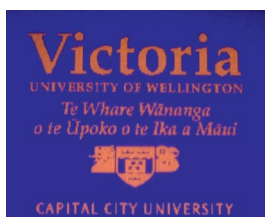
**A. C. Small,* J. H. Johnston,
N. Clark** **242–247**

Inkjet Printing of Water "Soluble" Doped ZnS Quantum Dots

Keywords: Zinc sulfide / Quantum dots / Doping / Imprinting / Inkjet printing / Photophysics / Luminescence / Cellulose / Paper

---

Bisaminopyridinate lanthanoid alkyl complexes may undergo intramolecular methyl group C–H activation. The larger the lanthanide the faster is the decomposition of its parent. In consequence, stable alkyls can only be isolated for the late lanthanoids. Converting them into transient hydrides gives rise to C–H activation products as well.
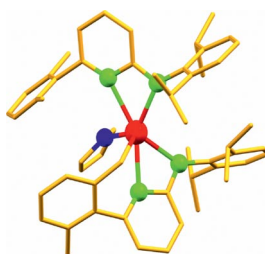
**S. Qayyum, G. G. Skvortsov, G. K. Fukin,
A. A. Trifonov,* W. P. Kretschmer,
C. Döring, R. Kempe*** **248–257**

Intramolecular C–H Bond Activation by Lanthanoid Complexes Bearing a Bulky Aminopyridinato Ligand

Keywords: Lanthanoids / C-H bond activation / N ligands / Aminopyridinato ligands

---

The dimeric barium phosphanide [O(Si-iPr$_2$PH)$_2$Ba(dme)$_2$]$_2$ obtained from the reaction of O(SiiPr$_2$PH$_2$)$_2$ with [Ba{N-(SiMe$_3$)$_2$}$_2$(dme)] accrues with four bridging phosphorus atoms, were as the corresponding Mg, Ca, Sr derivatives show dissent molecular structures.
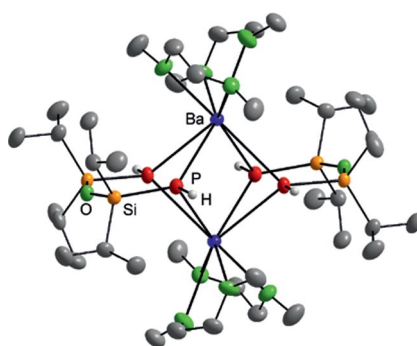
**P. Kopecky, C. von Hänisch,* F. Weigend,
A. Kracke** **258–265**

Observation and Interpretation of Structural Variety in Alkaline Earth Metal Derivatives of Diphosphanyldisiloxane

Keywords: Alkaline earth metals / Phosphorus / Siloxanes / Density functional calculations

---

CONTENTS

Titanium(IV) Complexes

Ethene Polymerization Behavior of MAO-Activated Dichloridotitanium Complexes Bearing Bi- and Tetradentate Salicylaldimine Derivatives

Keywords: Titanium / Polymerization / Homogeneous catalysis / Molecular modeling / N,O ligands
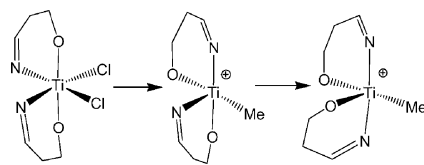
Titanium complexes can undergo changes in geometry during their synthesis. The direction and magnitude of these changes are dependent on both the co-ligands present and the *ortho* substituents of the phenoxy group. According to ab initio calculations the same structural isomerization remains present when the catalytically active species are generated.

Nickelacyclic Carboxylates

Nickelacyclic Carboxylates with Pyridine-Based Ligand Sets − From Mononuclear Complexes to Supramolecular Architectures by Hydrogen Bonding

Keywords: Metallacycles / Nickel / N ligands / Hydrogen bonds / Supramolecular chemistry
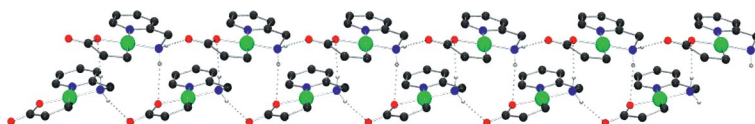
The synthesis, characterization and self-assembly via hydrogen bonding of nickelacyclic carboxylates bearing substituted pyridine ligands is reported.

Nanoscale Photomagnetism

Light-Induced Stored Information in Nanoparticles

Keywords: Spin crossover / Photomagnetism / Nanoparticles / Coordination polymers / Magnetic properties
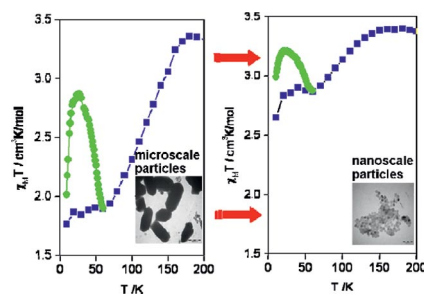
We use reverse micelle techniques to prepare microscale and nanoscale (30−80 nm) particles of the spin-crossover coordination polymer $[Fe(NCS)_2(bpe)_2]$. By comparing the thermal and photoinduced magnetic behaviours of these and that of the original slow-grown macroscale crystals, we show that with particle size reduction, even to the nanoscale, the photoinduced magnetic properties are retained.

Radical Substitution

A Radical Approach to Hydroxylaminotrichlorosilanes: Synthesis, Reactivity, and Crystal Structure of TEMPO-SiCl_3 (TEMPO = 2,2,6,6-Tetramethylpiperidine-*N*-oxyl)

Keywords: Silicon / Radicals / X-ray diffraction / Reaction mechanisms / Computational chemistry
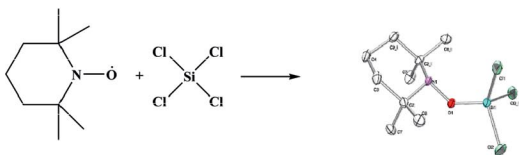
The radical TEMPO reacts with $SiCl_4$ with formation of the primary substitution product TEMPO-SiCl_3 besides several chlorinated and protonated TEMPO derivatives. This set of closely related compounds has been characterized by X-ray crystallography and spectroscopic techniques (IR, NMR). DFT calculations [B3LYP//6-311+G(d)] have been carried out to understand the driving force behind their formation.
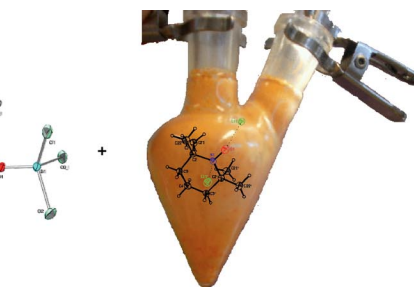
T. J. Mooibroek, E. Bouwman,* M. Lutz, A. L. Spek, E. Drent .... 298−310
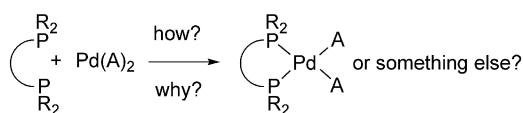
The formation of [Pd(diphosphane)- (anion)₂] complexes was studied by using ¹H- and ³¹P-NMR spectroscopy. It was found that, depending on the ligand struc- ture and the coordinating ability of the anions, the P₂PdA₂ complex is formed in- stantaneously, via some intermediate or not at all.

NMR Spectroscopic Studies of Pal- ladium(II) Complexes of Bidentate Di- phenylphosphane Ligands with Acetate and Tosylate Anions: Complex Formation and Structures

Keywords: Palladium / P ligands / NMR spectroscopy / Complex formation / Anions

P. Bhunia, D. Banerjee, P. Datta, P. Raghavaiah, A. M. Z. Slawin, J. D. Woollins, J. Ribas, C. Sinha* .... 311−321

Copper-Azide-Thioarylazoimidazoles − Structure, Spectra, Redox Properties, Mag- netism and Theoretical Interpretation

Keywords: Copper / Bridging ligands / Structure elucidation / Magnetic proper- ties / Redox chemistry
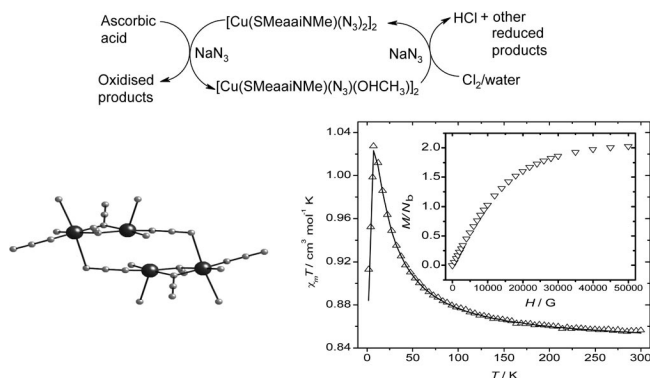
Tetranuclear azido-bridged copper(II) and binuclear methanol-bridged copper(I) com- plexes of 1-alkyl-2-[(o-thioalkyl)phenylazo]- imidazole (SRaaiNR′) are interconvertible: Cu^II is reduced by ascorbic acid, while Cu^I complexes are oxidised by chlorine/water in the presence of an excess amount of NaN₃. The tetranuclear Cu^II complex shows ferro- magnetic and antiferromagnetic interac- tions.

LUMO

HOMO

K. Yu. Monakhov, T. Zessin, G. Linti* .... 322−332

Reduction vs. Metathesis in the Reactions of Bismuth Tribromide with a Bulky Lith- ium Silanide − An Experimental and Theoretical Study

Keywords: Bismuth / Silicon / Lithium / Crystal structure analysis / Density func- tional calculations

The very stable silyl-substituted dibis- muthane is the result of redox conversions via metathesis reactions of bismuth halide BiBr₃ with silyllithium tBuPh₂SiLi(thf)₃ in various ratios.

---

* Author to whom correspondence should be addressed.   🖥 Supporting information on the WWW (see article for access details).

If not otherwise indicated in the article, papers in issue 1 were published online on December 21, 2009

SPOTLIGHTS …

On these pages, we feature a selection of the excellent work that has recently been published in our sister journals. If you are reading these pages on a computer, click on any of the items to read the full article. Otherwise please see the DOIs for easy online access through Wiley InterScience.

Organocatalysis

I. Fleischer, A. Pfaltz*

Enantioselective Michael Addition to α,β-Unsaturated Aldehydes: Combinatorial Catalyst Preparation and Screening, Reaction Optimization, and Mechanistic Studies

Shortcut to chiral catalysts: An efficient combinatorial strategy based on back reaction screening by ESI-MS allows rapid evaluation of organocatalysts for the asymmetric Michael addition to α,β-unsaturated aldehydes (see scheme). An unexpected nonlinear effect has been observed in this reaction, resulting from a double nucleophilic–electrophilic activation mechanism involving two catalyst molecules.
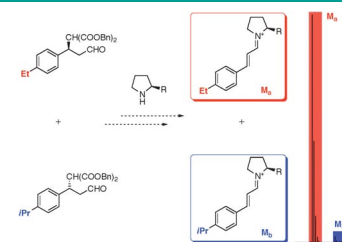
Nanomaterials

J. Sharma, Y. Tai,* T. Imae*

Biomodulation Approach for Gold Nanoparticles: Synthesis of Anisotropic to Luminescent Particles

Fruit salad nanoparticles: A simple biomodulation approach has been developed using extracts of apple (Malus domestica), lemon (Citrus limonia), tomato (Lycopersicon esculentum), and banana peel (Musa cavendish) to generate various nanostructures of gold, for example, spherical, marigold-like, and triangular plates. The synthesis of luminescent gold nanoparticles using fluorescent catabolites of chlorophyll is also demonstrated.
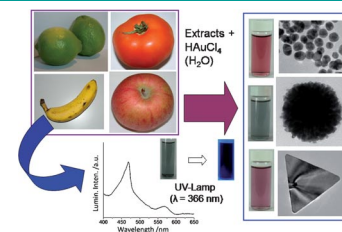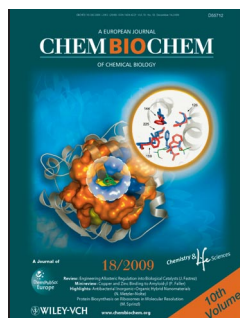
Antibiotics

K. D. Green, W. Chen, J. L. Houghton, M. Fridman,*
S. Garneau-Tsodikova*

Exploring the Substrate Promiscuity of Drug-Modifying Enzymes for the Chemoenzymatic Generation of N-Acylated Aminoglycosides

Creating a synthesis tool: We have developed a chemoenzymatic method for the production of N-acylated aminoglycosides using aminoglycoside acetyltransferases and acyl coenzymes A. The methodology enables rapid production followed by antimicrobial testing of synthetically challenging aminoglycosides.

Nanoswitch

R. Turanský, M. Konôpka, N. L. Doltsinis, I. Štich,* D. Marx

Optical, Mechanical, and Opto-Mechanical Switching of Anchored Dithioazobenzene Bridges

Flip-flop: Mechanical and opto-mechanical switching cycle of a nanoswitch made up of single dithioazobenzene chromophore suspended between two gold tips (see picture). Mechanical switching proceeds on the ground-state S_0 surface while successful optical switching via S_1 state requires mechanical assistance.

ChemPhysChem
DOI: **10.1002/cphc.200900690**

Drug Discovery

J. Tavares, A. Ouaissi, P. Kong Thoo Lin, I. Loureiro, S. Kaur, N. Roy, A. Cordeiro-da-Silva*

Bisnaphthalimidopropyl Derivatives as Inhibitors of *Leishmania* SIR2 Related Protein 1

We have identified a new class of NAD^+-competitive SIR2 inhibitors that preferentially inhibit the *L. infantum* form of sirtuin (LiSIR2RP1). Despite the well-conserved catalytic core domain of SIR2 enzymes, subtle structural differences in the inhibitors can provide selective targeting.

ChemMedChem
DOI: **10.1002/cmdc.200900367**

Organic Chemistry

I. J. S. Fairlamb*

The Phosphine-Catalyzed Wittig Reaction: A New Vista for Olefin Synthesis?

The design of a catalytic manifold for the Wittig reaction is highlighted. Arsenine-, telluride-, and the recently discovered phosphine-catalyzed processes are discussed and placed into context with the related silyl-Reformatsky process. The specific type of phosphine oxide precatalyst employed is compared with an aza-Wittig process and related transformations.

ChemSusChem
DOI: **10.1002/cssc.200900208**

Enzyme Models

L. O. Wiemann, R. Nieguth, M. Eckstein, M. Naumann, O. Thum,* M. B. Ansorge-Schumacher*

Composite Particles of Novozyme 435 and Silicone: Advancing Technical Applicability of Macroporous Enzyme Carriers

Leach out (Si'll be there): The mechanical and leaching stability of enzymes adsorbed on macroporous carriers both benefit from the deposition of silicone on the carrier surface. For silicone-coated Novozyme 435, maximum leaching stability corresponds to the formation of a complete layer of silicone on the outer surface of the carrier at silicone concentrations of 54 % w/w and more (see picture). This layer also aids mechanical stabilization.

ChemCatChem
DOI: **10.1002/cctc.200900199**
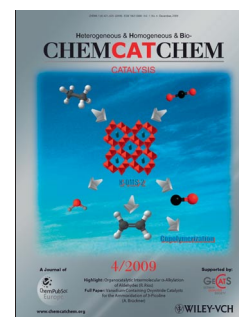
Nanoscale Chirality

A. D'Urso, R. Randazzo, L. Lo Faro, R. Purrello*

Vortexes and Nanoscale Chirality

J-aggregates respond dynamically to vortexes created by stirring. The CD signal inverts with stirring sense and its intensity increases. Prolonged stirring leads to deposition of chiral aggregates on the cuvette wall, the chirality of the deposits depends on the stirring sense. Stirring shifts the equilibrium of a racemic mixture towards the side chosen (and favored) by the stirring sense (see picture, CW = clockwise, CCW = counter clockwise stirring).
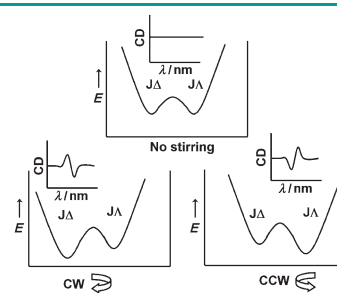
Silver and Gold Cycloisomerization

P. Belmont,* E. Parker

Silver and Gold Catalysis for Cycloisomerization Reactions

In a "golden world", silver-based opportunities for cycloisomerization reactions are also outlined. We offer a quick overview of the usefulness of each metal along with counterion effects. The need of some gold catalysts for activation through silver anion metathesis is also discussed, because it links two coinage metals of increasing interest in the field of organometallic chemistry.

$X = CR^2, NR, O$

$[M] = Ag^I, Au^I, Au^{III}$

Various cyclic products

Subvalent Organometallic Compounds of the Alkaline Earth Metals in Low Oxidation States

Sven Krieck,[a] Lian Yu,[b] Markus Reiher,[b] and Matthias Westerhausen*[a]

Alkaline earth metals (Ae) are regarded as redox-inactive, and their chemistry is dominated by the oxidation state +2. Nevertheless, in recent years several compound classes with alkaline earth metals in low oxidation states were investigated. Various concepts proved to be valid for the stabilization of such compounds and are discussed in this review. In the solid state, subvalency can be achieved by offering a matrix that takes over the excess electrons as, for example, in subnitrides. This fact leads to normal-valent alkaline earth metals with electrons free to move between alkaline-earth-metal-containing cages with or without a metal matrix. Another concept focuses on the synthesis of $[Ae_2]^{2+}$ cations with adequate substituents. The homodinuclear Ae–Ae bonds exhibit binding energies that should allow the synthesis of molecules such as R–Ae–Ae–R. The synthesis of magnesium derivatives succeeded by use of extremely bulky bidentate ligands with a delocalized anionic charge. The heavier alkaline earth metal derivatives are investigated by quantum chemical methods. Another possibility takes advantage of the fact that the first and second ionization potentials of the alkaline earth metals are clearly separated. Therefore, an arene with an extended π-system having an energy level between the two ionization potentials should be able to overtake only one electron, which leads to Ae^+ cations. Sophisticated procedures allowed the synthesis of a calcium(I) derivative, $[(thf)_3Ca(\mu\text{-}\eta^6,\eta^6\text{-}C_6H_3\text{-}1,3,5\text{-}Ph_3)Ca(thf)_3]$, and such structures are investigated by quantum chemical methods also for the other alkaline earth metals.

Contents

1 Introduction: Concepts of Subvalence

A fundamental concept for determining the normal (expected) valency of main group elements (and also of the metals of the scandium and zinc groups) is based on the octet rule and on the number of valence electrons. The elements can obey the octet rule by acceptance of electrons (anion formation, reduction) or by release of electrons (cation formation, oxidation) until the element is isoelectronic to the neighbouring noble gas. On the one hand, this approach explains the formation of anions X^-, X^{2-} and X^{3-} of nonmetals such as halides, chalcogenides and pnictogenides, respectively. On the other hand, the elements of the early groups such as the alkali metals, alkaline earth metals and the earth metals yield cations with noble gas configurations M^+, M^{2+} and M^{3+}, respectively. In these cases, normal (expected) valency would correlate to the number of valence electrons. Thus, BMe_3 and BCl_3 contain an electron-deficient boron atom; however, this element would not be considered to be subvalent. Subvalency would mean that not all valence electrons are used for the bonding situation, which could lead to, for example, B^{2+} and B^+ for ionic salts or R_2B and RB for covalent molecules [usually forming oligomers such as $R_2B–BR_2$ or $(RB)_4$]. In a way, the subvalency of $R_2B–BR_2$ is only a consequence of the way chemists identify the oxidation state (in $R_2B–BR_2$ as well as in BMe_3 the boron atom forms three covalent bonds, achieving an electron sextet, even though the formal oxidation states are +2 and +3, respectively). Even lower oxidation states as, for example, in $B_6H_6^{2-}$ (*closo*-boranates), can lead to a bonding situation where the valence electrons stabilize clusters in a

[a] Institut für Anorganische und Analytische Chemie, Friedrich-Schiller-Universität Jena,
August-Bebel-Str. 2, 07743 Jena, Germany
Fax: +49-3641-948102,
E-mail: m.we@uni-jena.de
[b] Laboratorium für Physikalische Chemie, ETH Zurich
Hönggerberg Campus, Wolfgang-Pauli-Str. 10, 8093 Zurich, Switzerland

way that all bonding MOs are occupied (see, for example, the Wade–Mingos Rules).

The alkali metals can show an oxidation state of either +1 or 0. Both numbers resemble an expected value for the cation and the metal, respectively. Subvalency can result by mixing of an alkali metal with these two oxidation states in one compound. Prominent examples are the suboxides of rubidium and caesium containing oxygen-centred metal octahedrons that are interconnected via common faces to yield Rb_9O_2 and $Cs_{11}O_3$. These compounds can be formulated as $[(Rb_9O_2)^{5+}\cdot 5e]$ and $[(Cs_{11}O_3)^{5+}\cdot 5e]$, the electrons being free to move between the clusters. Additional metal atoms can act as a matrix for these clusters, leading to metal-richer solids such as, for example, Rb_6O, Cs_4O and Cs_7O.[1–6]

This review is limited to subvalent compounds of the alkaline earth metals. Alkaline earth metals are very electropositive metals comparable to alkali metals (similar electronegativities). The heavy alkaline earth metal cations Ae^{n+} are isoelectronic with cations $M^{(n+1)+}$ of the metals of the scandium group. Therefore, we will also include some aspects of subvalent compounds of scandium(II) and scandium(I), which are isoelectronic with calcium(I) and calcium(0). Subvalency can be achieved for alkaline earth metal compounds by several concepts: (i) Non-metal-centred clusters can be embedded in a metal matrix, leading to metal-rich oxides or nitrides. (ii) Monomeric compounds of the type R–Ae are extremely reactive; however, quantum chemical studies and sophisticated experimental procedures offer insight into these systems. (iii) Molecules with Ae–Ae bonds are considered to be subvalent on the basis of the agreement on how to determine the oxidation state in covalent molecules with element–element bonds. (iv) Formation of molecules with monovalent Ae^+ ions is possible by providing an extended π-system whose electron affinity lies energetically between first and second ionization energies that differ significantly.

The scope of this review is the discussion of concepts which are employed in order to prepare and to understand subvalency of strongly electropositive elements such as the

Sven Krieck, born in 1983 in Pößneck/Germany, studied chemistry at the Friedrich-Schiller-University of Jena, Germany. He prepared his diploma thesis at the Institute of Technical and Environmental Chemistry in the working group of Professor Günter Kreisel in the field of electrochemical studies of heterosupramolecular aggregates and obtained his diploma degree in February 2007. Since June 2007 he has been working on his Ph.D. thesis, supported by a Ph.D. grant of the "Verband der Chemischen Industrie VCI/FCI, Germany", at the Institute of Inorganic and Analytical Chemistry at the Friedrich-Schiller-University of Jena, under the supervision of Professor Matthias Westerhausen. The thesis deals with the chemistry of heavy Grignard reagents, organometallic "ate" compounds as well as dispersive s-block metal–arene interactions.

Lian Yu, born in 1974 in Hebei, studied chemistry at Beijing Normal University from 1992 to 1996. After finishing his studies, he worked as a teacher in middle school. Starting in 2002 he studied chemistry at the University of Bonn and joined the group of Professor Markus Reiher in Jena in 2005. In 2006 he moved with the Reiher group to ETH Zurich, where he completed his Ph.D. in May 2009 with a thesis on quantum chemical studies of metal–metal interactions. Since August 2009, he has been working as a postdoc in the group of Professor Suping Peng at the China University of Mining and Technology.

Markus Reiher, born in Paderborn (Westphalia) in 1971, obtained his diploma in chemistry from the University of Bielefeld in 1995 and his Ph.D. in theoretical chemistry from the same university with Professor Juergen Hinze in 1998. He completed his habilitation thesis in theoretical chemistry at the University of Erlangen-Nuremberg in the group of Professor Bernd Artur Hess in September 2002. From October 2003 to March 2005 he worked as a Privatdozent at the University of Bonn and acted as the representative (C4) of the Chair of Theoretical Chemistry at Erlangen (2003/2004) and of the Chair of Theoretical Chemistry at Bonn (2004/2005) during this time. In December 2004 he was offered the position "full professor in theoretical chemistry" at the University of Groningen, but decided to accept a position as Professor for Physical Chemistry at the University of Jena. Since February 2006 he is Professor for Theoretical Chemistry at ETH Zurich (Laboratory of Physical Chemistry). Markus Reiher spent short-time research stays in Tel Aviv (2000), Budapest (2001), Tromsø (2003/2004), Lund (2006) and Singapore (2009). Most of his research focuses on relativistic quantum chemistry, bioinorganic and coordination chemistry, theoretical spectroscopy and the foundations of chemistry.

Matthias Westerhausen, born in 1959 in Nordhorn/Germany, obtained his diploma degree in 1983 from the Philipps-University of Marburg, Germany, and completed his Ph.D. thesis at the University of Stuttgart, Germany, under the supervision of Professor Gerd Becker. His thesis dealt with acyl-substituted phosphanes and arsanes. In 1978/1988, he worked as a postdoctoral fellow with Professor Robert T. Paine at the University of New Mexico in Albuquerque/USA in the field of phosphanylboranes. Back at the University of Stuttgart, he finished his habilitation at the Institute of Inorganic Chemistry in December 1994 and received the venia legendi for Inorganic Chemistry in February 1995. From 1996 to 2004 he was professor at the Ludwig-Maximilians-University of Munich, where he was also vice-rector from 2001 to 2004. He obtained the 1998 teaching excellence award of the state of Bavaria. Since 2004 he has been teaching and conducting research at the Friedrich-Schiller-University of Jena, Germany. His main interests include topics such as the organometallic chemistry of d^0 metals, the phosphanides of d^0 metals, cooperative effects in coordination compounds with very close metal–metal contacts, metal-mediated oxidative C–C coupling reactions as well as proton and electron transfer reactions at biomimetic model systems.

alkaline earth metals, with the main focus on magnesium and calcium. Therefore, a complete coverage of the literature is not intended. For nonmetals, the formation of element–element single and even multiple bonds is the most common way to achieve stable molecules in which the elements are in low oxidation states (e.g. H_2N–NH_2 and HN=NH with N in the oxidation states –2 and –1); however, these molecules would not be considered subvalent, because the octet rule is fulfilled and subvalence is a consequence of the way chemists determine the oxidation state. Electron-deficient elements (boron group) with a weak electropositive character are able to form clusters such as the boranates $[B_6H_{6+n}]^{m-}$ in which all binding MOs are filled (Wade–Mingos Rules). Sophisticated stabilization methods and preparative procedures are mandatory in order to achieve subvalency for the more electropositive metals. Often, subvalency is deduced from the molecular formula, and the bonding situation has to be analyzed in more detail. This is shown for solid subnitrides and suboxides of the alkaline earth metals.

2 Alkaline Earth Metal Subnitrides and Suboxides

Subnitrides of the alkaline earth metals are only known for the heavier ones, calcium, strontium and barium,[3–7] whereas beryllium and magnesium form nitrides of the formula Ae_3N_2. The binary subnitrides Ca_2N,[6,8–10] Sr_2N[6,10,11] and Ba_2N[6,10] can be described as $[(Ae_2N)^+ \cdot e]$ in similarity to the alkali metal suboxides. The structures consist of a cubic close packing of the alkaline earth metal atoms in which all octahedral gaps of every second layer are occupied by nitrogen atoms (*anti*-CdCl$_2$ type). The excess electrons are free to move between these $[Ae_2N]$ layers. Metal-richer subnitrides contain condensed Ba_6N octahedrons interconnected via common faces, as observed for Li-Ba_3N,[12] $NaBa_3N$[13] and Na_5Ba_3N,[14] or even isolated Ba_6N octahedrons, as found in $Na_{16}Ba_6N$.[15] These solids can be prepared from the reaction of nitrogen with barium dissolved in liquid sodium. The free electrons of these compounds are either delocalized between the barium subnitride substructures or overtaken by the alkali metal matrix, leading to the metallic properties of these solids. This description implies that the alkaline earth metals are regarded as normal-valent Ae^{2+}, the excess electrons inducing a negative charge to the alkali metal matrix.

Another group of subnitrides containing alkali and alkaline earth metals is given by the formula $Ba_{14}CaN_6Na_x$ with $x = 7, 8, 14, 17, 21$ and 22 (Figures 1 and 2).[6] These solid phases contain discrete clusters, $[Ba_8CaN_6]$, with Ae^{2+} and N^{3-} ions, and the resulting cages contain six face-sharing $[Ae_6N]$ octahedrons with a central calcium atom embedded in a metallic Ba_6Na_x matrix. Such kinds of phases represent a dispersion of a salt in a metallic environment and can be seen as a salt in a sea of metal.[16] Subnitrides of the alkaline earth metals can also serve as hosts for less electropositive metals such as, for example, in $[Ca_7N_4]M_x$ where M

is Ag, Ga, In or Tl.[17] Edge- and corner-sharing $[Ca_6N]$ octahedrons form the host, and linear M_x metal chains are guests in this framework.
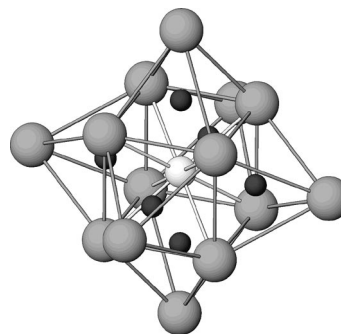
Figure 1. Representation of the $[Ba_{14}CaN_6]$ cluster formed from six $[Ae_6N]$ octahedrons.[6] (Central atom: Ca, black: N, grey: Ba; only Ba–Ba contacts are outlined.) Copyright Wiley-VCH Verlag GmbH & Co. KGaA. Reproduced with permission.

Suboxides are far less common in alkaline earth metal chemistry.[6] The structures also differ significantly from those of alkali metal suboxides and alkaline earth metal subnitrides. Crystalline $[Ba_2ONa]$ contains chains of *trans* edge-sharing $[Ba_4O]$ tetrahedrons that are separated by sodium atoms.[18]

In summary, subnitrides and oxides of the alkaline earth metals, often in combination with alkali metals, show a spatial separation of metallic and ionic bonding. The ionic clusters contain nitrogen-centred $[Ae_6N]$ octahedrons or oxygen-centred $[Ae_4O]$ tetrahedrons, which can be interconnected via common corners, edges or faces to larger units. These ionic moieties are embedded in a metal matrix often consisting of an alkali metal or a mixture of alkali and alkaline earth metals. Subvalence is deduced from the formula by presuming that the nonmetal atoms form anions in agreement with the octet rule (nitride or oxide), the electrons being supplied by the alkaline earth metals. Use of an excess amount of metal and embedding in a metallic matrix lead to subvalency based on the molecular formula.

3 Molecules of the Type (R–Ae)$_n$

For very electropositive metals, such as the alkali and alkaline earth metals, subvalency and low oxidation state are used as synonyms, because the octet rule is not a valid concept for describing ionic compounds. Instead, cations try to attract as many counteranions as possible (depending on the size of the Lewis bases and on the distance between the cation and the donor atoms) to occupy the coordination sphere and to maximize electrostatic attractions. Coordination numbers larger than four are common, for example, in $[(thf)_6Ca]^{2+}$, and subvalency is now directly related to a low oxidation state. According to the octet rule, the release of two electrons leads to expected Ae^{2+} cations, whereas molecules with Ae^+ and Ae^0 are considered as subvalent; never-
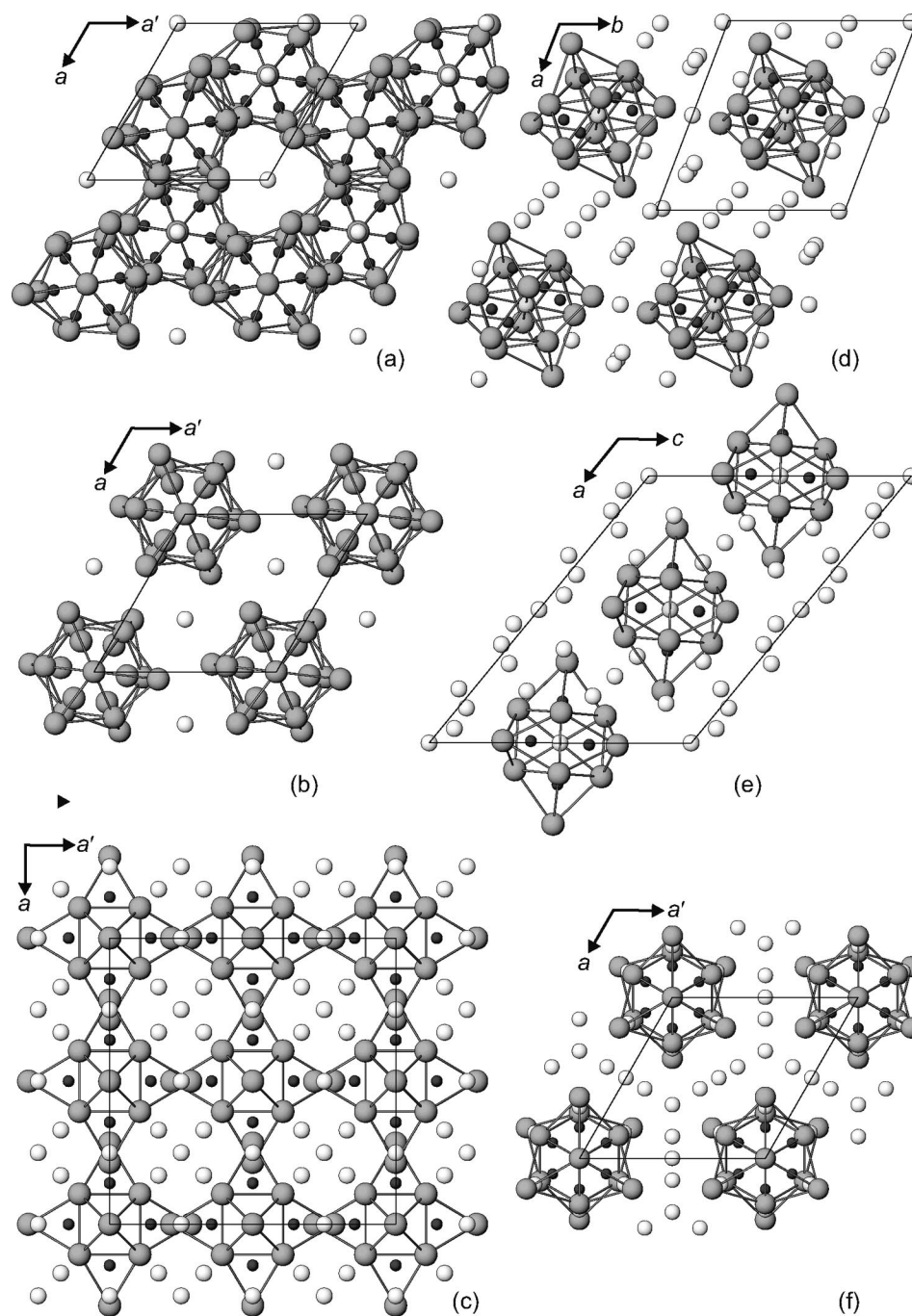
Figure 2. Representation of the $[Ba_{14}CaN_6]Na_x$ clusters: (a) $x = 7$, (b) $x = 8$, (c) $x = 14$, (d) $x = 17$, (e) $x = 21$, (f) $x = 22$.[6] (Central atom: Ca, black: N, grey: Ba, light grey: Na; only Ba–Ba contacts are outlined.) Copyright Wiley-VCH Verlag GmbH & Co. KGaA. Reproduced with permission.

theless, additional neutral coligands can sterically saturate the coordination spheres of these very electropositive metals.

3.1 Molecules R–Ae (*n* = 1)

Low oxidation states at transition metals can be realized in carbonyl complexes. Even anions, carbonyl metallates, can be prepared and isolated with most of these compounds obeying the 18 electron rule. For the s-block elements,

carbonyl complexes are not stable. There are two main reasons for this: On the one hand, there are strong repulsive forces between the electron pair of the carbonyl ligand and the s-electrons of the alkaline earth metals. On the other hand, the reaction of, for example, magnesium with CO to yield MgO and C is exothermic by at least –491 kJ mol^{-1}. Increasing the positive charge on magnesium leads to increasing Mg–C binding energies. For $[Mg(CO)]^+$ and $[Mg(CO)]^{2+}$, values of 41.5 and approximately 200 kJ mol^{-1}, respectively, were determined.[19–21] The reaction of CO

with the less electropositive beryllium in solid argon at 10 K and subsequent sample warming to 30 K leads to the formation of several carbonyl beryllium compounds such as $Be_m(CO)_n$ with $m = 1$ and $n = 2, 3$ as well as those with $m = 2$ and $n = 2, 3, 4$, the primary product [Be(CO)] being unstable.[22]

The interaction of the empty π*-orbital of the carbonyl ligand with filled metal d-orbitals by formation of back-bonding is a well known feature for stabilization of low oxidation states in transition metal complexes. In contrast, in the case of s-block metals, CO is a relatively weakly bonded ligand, because these kinds of metal ions are not able to develop backbonding, and, in addition, the s-electrons interact repulsively with the free valences of the carbonyl group. Stabilization succeeds with harder σ-donor ligands, for example, ammonia. The structure of hexaaminecalcium(0) in [Ca(ND$_3$)$_6$] was determined by using powder neutron diffraction[23] measurements, including lattice constants of [M(NH$_3$)$_6$][24] (M = Ca, Sr, Ba), whereas a contradictory model of distorted ammonia was described by Leclercq.[25]

The major tools for the investigation of monomeric alkaline earth metal(I) compounds R–Ae are quantum chemical methods. Synthesis of such compounds affords highly sophisticated preparative and trapping procedures, because the atomization energies of the metals as well as the metal–metal binding energies have to be invested (Table 1, values taken from ref.[26]). These values foreshadow that the molecules R–Ae should exhibit an enormous reactivity, which makes solution chemistry impossible.

Table 1. Comparison of selected physical data of the alkaline earth metals and the metals of group 12 [EN: Allred–Rochow electronegativities, AE: atomization enthalpy, BE: bond energy of Ae_2^{2+}, $r(M^0)$: radii in metals with coordination number 12, $r(M^{2+})$: radii of hexacoordinate cations M^{2+}].[26]

Metal	EN	AE /kJ mol^{-1}	BE /kJ mol^{-1}	$r(M^0)$ /pm	$r(M^{2+})$ /pm
Be	1.47	324.6	208	111.3	59
Mg	1.23	147.7	129	159.9	86.0
Ca	1.04	178.2	105	197.4	114
Sr	0.99	164.4	84	215.1	132
Ba	0.97	180		224	149
Zn	1.66	130.7	[a]	133.5	88.0
Cd	1.46	112.0	[a]	148.9	109
Hg	1.44	61.3	[a]	162	133

[a] The force constants for [Zn$_2$]$^{2+}$, [Cd$_2$]$^{2+}$ and [Hg$_2$]$^{2+}$ are 0.6, 1.1 and 2.5 N cm^{-1}, respectively.

Mononuclear Me–Ae can be prepared from the gas phase reaction of calcium or strontium metal vapour with HgMe$_2$ yielding the radicals Me–Ca or Me–Sr, respectively.[27] The transmetallation of SnMe$_4$ with Ba vapour allowed the synthesis and characterization of Me–Ba.[28] Additional preparation procedures include the reaction of laser-ablated metal atoms with methane, methyl halides or acetone, which were co-condensed onto a cold noble gas matrix.[29–33] Often, side products such as AeCH$_2$, HAeCH$_3$ and others accompany the formation of Me-Ae.[29,30] An-

other choice is the investigation of supersonic molecular beam samples of alkaline earth metal monomethyl compounds.[34,35]

Selected physical data obtained from high-resolution electronic spectroscopy of Ae–CH$_3$ are summarized in Table 2. The Ae–C bond lengths agree well with data obtained from ab initio calculations.[40,41] These structures allow the calculation of van der Waals radii for alkaline earth metal(I) atoms. The bond dissociation energies (BE) are rather small, with a surprisingly small value for the Mg–C bond. Isoelectronic [Sc–CH$_3$]$^+$ and [Y–CH$_3$]$^+$ show M–C binding energies of more than 200 kJ mol^{-1}, the values of the neutral molecules Sc–CH$_3$ and Y–CH$_3$ lie in the same order of magnitude.[42]

Table 2. Structural data of the ground states of the monomethyl alkaline earth metal compounds, Me–Ae, of Be, Mg, Ca, Sr and Ba obtained from high-resolution electronic spectra.

Metal	r_{vdW}(Ae) /pm[a]	BE /kJ mol^{-1}[b]	Ae–C /pm	C–H /pm	HCH /°
Be		189.9	168.3[c]	109.0[c]	111.5[c,d]
Mg	210.5	85.8	210.2(2)[e]	110.5[e]	108.16(1)[e]
Ca	232.6	109.9	234.9(13)[f]	110(2)[f]	106(3)[f]
			234.8[g]	110.2[g]	105.3[g]
Sr	248.2		248.3 ± 0.5[h]	110[h]	104.7 ± 1.2[h]
			248.7[g]	110.4[g]	105.8[g]
Ba	256.4		256.4 ± 0.7[i]	109[i]	106 ± 3[i]

[a] van der Waals radii calculated from bond lengths of Ae–CH$_3$.[36] [b] Calculated bond dissociation energies of the Ae–C bonds (MP2).[37] [c] Calculated structural data (MP2).[36] [d] Be–C–H angle. [e] Taken from ref.[31] with fixed C–H bond length. [f] Taken from ref.[38] [g] Taken from ref.[32] [h] Taken from ref.[39] with fixed C–H bond length. [i] Taken from ref.[28] with fixed C–H distance.

The reaction of Mg$^+$ and Ca$^+$ with the phenyl radical (yielding normal-valent PhAe$^+$) was also studied with quantum chemical methods. If the unpaired spins on Ae$^+$ and the phenyl radical are opposed, the formation of an Ae–C σ-bond is favoured, leading to closed-shell adducts (singlet state) with Mg–C and Ca–C binding energies of 227.4 and 256.6 kJ mol^{-1}, respectively (B3LYP/6-311+G**). In the case of aligned spins, the π-complex (giving a triplet-state adduct) is lower in energy.[43] The tendency of Ae$^+$ and Ae^{2+} cations to form strong π-complexes with arenes will be discussed in section 4.

Stabilization by coordination of these molecules leads to stable adducts if the coligand is able to overtake an electron to form a radical anion. Thus, the reaction of diphenylmagnesium with 2,2′-bipyridine (bpy) leads to the elimination of a phenyl radical and to the formation of radical [(bpy)-MgPh]$^{\cdot}$ [Equation (1)], which can be understood as an adduct of bpy to Ph–Mg. The chelate base is easily reduced, yielding a radical anion. Kaim investigated a number of bpy complexes and noticed that alkali metal complexes [(bpy)-A]$^{\cdot}$ are mainly ionic, which leads to weak interactions between A$^+$ and bpy$^{\cdot-}$, whereas the covalent character of complexes [(bpy)MPh]$^{\cdot}$ increases in the order Mg < Zn < Be.[44] The reaction of phenylmagnesium bromide with 2,2′-bipyridine in THF in the presence of nickel(II) salts affords black [(bpy)(thf)MgBr].[45]

S. Krieck, L. Yu, M. Reiher, M. Westerhausen

$$(1)$$
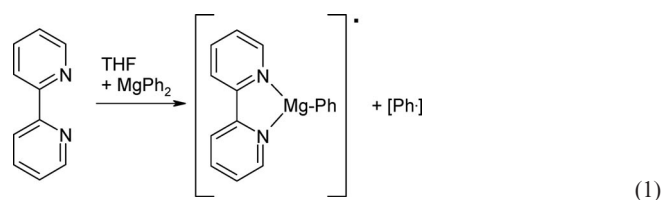
3.2 Small Molecules with Ae–Ae Bonds ($n = 2$)

The $[Ae_2]^{2+}$ cation represents the simplest case of Ae–Ae bond formation; similar cations are well-known for $[Hg_2]^{2+}$ and even for $[(L)_3Zn–Zn(L)_3]^{2+}$, where L is the neutral Lewis base 4-dimethylaminopyridine (dmap).[46] The dinuclear cation with subvalent magnesium is known from several ternary hydrides, such as Mg_4IrH_5 (Mg–Mg 275.4 pm)[47] and Mg_3RuH_3 (Mg–Mg 303.4 pm),[48] and from magnesium boride "MgB_2" (Mg–Mg 308.3 pm) in which the boron atoms form a graphite-like layer structure.[49]

The reaction of magnesium vapour, generated from MgB_2 at 700 °C, with HCl yields MgCl, its dimer and $MgCl_2$, which were condensed with an excess amount of an inert gas (Ar, N_2) on a Cu surface at 10 K. From Raman and IR spectroscopic investigations and from quantum chemical calculations Mg–Cl distances of 223.2 and 221.0 pm were obtained for MgCl and linear ClMg–MgCl (Mg–Mg 276.6 pm,[50] 279.7 pm[51]), respectively. The Mg–Mg binding energy of 197 kJ mol⁻¹ was also supported by ab initio calculations.[50] Even though the disproportionation into $MgCl_2$ and Mg is endothermic by +55.2 kJ mol⁻¹ (which is in agreement with earlier investigations[52]), Mg_2Cl_2 disproportionates spontaneously with formation of magnesium metal and $MgCl_2$ during warm-up of the noble gas matrix.[50] The reason for this disproportionation instability is the atomization energy (see Table 1), which is liberated during metal precipitation.

The reaction of laser-ablated magnesium atoms with hydrogen yields a mixture of magnesium hydrides including MgH, MgH_2, Mg_2H_2, Mg_2H_3 and Mg_2H_4.[53,54] Even the insertion of Mg atoms into MgH_2 to yield H–Mg–Mg–H is exothermic by 12 kJ mol⁻¹.[55] Insertion of magnesium atoms into Grignard reagents Me–Mg–X is also exothermic by 28 kJ mol⁻¹.[56] All these reaction enthalpies have much smaller values than the atomization energy of magnesium, which has to be invested in all reactions.

In Table 3 selected data of alkaline earth metal(I) molecules of the type R–Ae–Ae–R are summarized. The Ae–Ae distances resemble the increasing size of the alkaline earth metal atoms. The bond dissociation energies (BE) decrease from Be to Mg and finally to Ca. Due to the fact that the atomization energy (AE) of calcium is larger than that of magnesium makes it even more difficult to prepare calcium(I)–calcium(I) bonds. In Table 3 parameters of 2,6-$Ph_2H_3C_6$–Ca–Ca–C_6H_3-2,6-Ph_2 are listed. This molecule with a Ca–Ca bond (Figure 3) is more stable by 14.5 kJ mol⁻¹ than the corresponding diaryl calcium and a calcium atom.[60] The tendency of the heavier alkaline earth metals to form rather strong bonds to side-on-bound arenes

(which will be discussed in section 4) leads to other dimers with bridging phenyl substituents. The Ca–Ca bond dissociation energy of H_5C_6–Ca–Ca–C_6H_5 is 190.6 kJ mol⁻¹ (Ca–Ca 386.7 pm); however, the dimer $[Ca(\mu\text{-}\eta^1,\eta^6\text{-}C_6H_5)]_2$ with bridging phenyl groups (Figure 4) is energetically even more favoured by 21.6 kJ mol⁻¹ according to MP2/TZVP calculations as a result of rather strong interactions between the calcium atoms and the phenyl π-systems.[60]

Table 3. Selected parameters of compounds of the type R–Ae–Ae–R based on quantum chemical investigations.

R–Ae–Ae–R	Be	Mg	Ca	Method	Ref.
H–Ae–Ae–H					
Ae–Ae /pm	209.8	288.4	384.7	BP86/TZ2P	[57]
	211.3	288.4	379.7	BP86	[58]
	209.5	286.2	379.4	B3LYP	[58]
Wiberg bond index	0.684	0.586	0.726	B3LYP	[58]
NLMO/NPA bond order	0.898	0.741	0.914	B3LYP	[58]
BE /kJ mol⁻¹	297.7	190.4		G3	[59]
Cl–Ae–Ae–Cl					
Ae–Ae /pm	2.059	278.8	3.714	BP86	[58]
	204.7	277.2	371.7	B3LYP	[58]
		276.6		B3LYP/DZP	[50,51]
Wiberg bond index	0.850	0.818	0.921	B3LYP	[58]
NLMO/NPA bond order	0.920	0.901	0.958	B3LYP	[58]
BE /kJ mol⁻¹		–198.2		B3LYP/DZP	[50,51]
Cp–Ae–Ae–Cp					
Ae–Ae /pm	207.7	280.9	396.1	BP86/TZ2P	[57]
	206.6	278.6	373.4	BP86	[58]
	2.057	277.6	374.0	B3LYP	[58]
		276.3		B3LYP/DZP	[50,51]
Wiberg bond index	0.926	0.912	0.934	B3LYP	[58]
NLMO/NPA bond order	0.996	0.957	0.958	B3LYP	[58]
BE /kJ mol⁻¹		200.6		B3LYP/DZP	[50,51]
$Ph_2H_3C_6$–Ae–Ae–$C_6H_3Ph_2$					
Ae–Ae /pm		283.8	378.3	BP86/RI/TZVP	[60]
BE /kJ mol⁻¹		175.4	115.4	BP86/RI/TZVP	[60]

The structures of the diphenyl dialkaline earth metal(I) compounds H_5C_6–Ae–Ae–C_6H_5 were investigated theoretically. Here we supplement our previous theoretical studies[60] of Ca^I–Ca^I and Mg^I–Mg^I bonds by a systematic comparison comprising also the other alkaline earth metals.[133] BP86/RI/TZVPP structure optimization of these clusters in their singlet states shows that all alkaline earth metals form stable homodinuclear metal–metal bonds (Table 4). The HOMOs of the corresponding metal–metal-bonded complexes as well as the structure of diphenyldibarium(I) are depicted in Figures 5 and 6, respectively.

While the lighter elements beryllium, magnesium and calcium feature linear structures, the homologous strontium and barium derivatives show *trans* bent arrangements, which can be regarded as a characteristic property of these metals {See the literature for detailed discussions of bent structures of molecules with d^0 metals;[61] in particular, concepts of metal d orbital participation and importance of
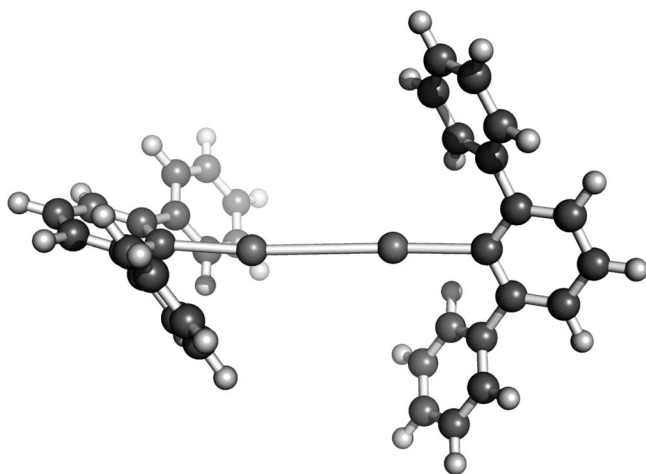
Figure 3. Energetically most favoured calculated structure of steri-cally shielded [2,6-Ph$_2$H$_3$C$_6$–Ca–Ca–C$_6$H$_3$-2,6-Ph$_2$][60] (central atoms: Ca, dark grey: C, light grey: H).
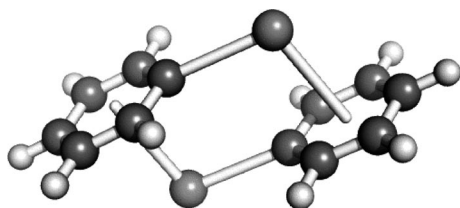
Figure 4. The energetically most favoured isomer of dimeric phen-ylcalcium [Ca(μ-η^1,η^6-Ph)]$_2$ (based on MP2/TZVP calculations)[60] (central atoms: Ca, dark grey: C, light grey: H).

Table 4. Selected parameters of compounds of the type [H$_5$C$_6$–Ae]$_2$ based on quantum chemical investigations (BP86/TZVPP, sin-glet, C$_i$: *ipso*-carbon atom, BE: binding energy of the Ae–Ae bond).[133]

Metal	Ae–Ae /pm	Ae–C$_i$ /pm	Ae–Ae–C$_i$ /°	BE /kJ mol^{-1}
Be	209.5	169.1	177.7	286
Mg	287.0	210.8	178.9	167
Ca	380.6	245.9	179.0	89
Sr	412.1	248.6	138.1	70
Ba	453.7	263.6	116.8	

metal (n – 1)d orbitals vs. np orbitals,[62] and core polariza-tion effects[63] are discussed. A pseudopotential approach like the one used here for strontium and barium describes according to Kaupp et al.[64] linear CaH$_2$ and bent SrH$_2$ as well as BaH$_2$, whereas Gillespie et al.[65] predicted a bent CaH$_2$ molecule. According to ab initio methods CaH$_2$ should be bent with a very small linearization barrier of the molecule,[66] and examinations of relativistic effects led to linear CaH$_2$, whereas SrH$_2$ and BaH$_2$ are bent.[67]}.

The reaction for the general formation of H$_5$C$_6$–Ae–Ae–C$_6$H$_5$ by dimerization of H$_5$C$_6$–Ae [Equation (2)] is very exothermic for the beryllium derivative (–286 kJ mol^{-1}) and less exothermic for Mg–Mg (–167 kJ mol^{-1}) and Ca–Ca bond formation (–89 kJ mol^{-1}). The Sr–Sr binding energy
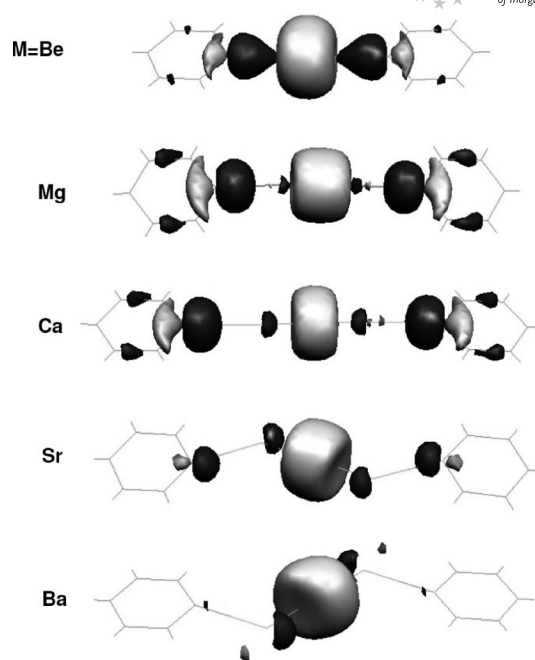
Figure 5. Representation of the highest occupied molecular orbitals (HOMOs) of (H$_5$C$_6$)Ae–Ae(C$_6$H$_5$) with metal–metal σ-bonding in-teractions (BP86/TZVPP, singlet).[133]
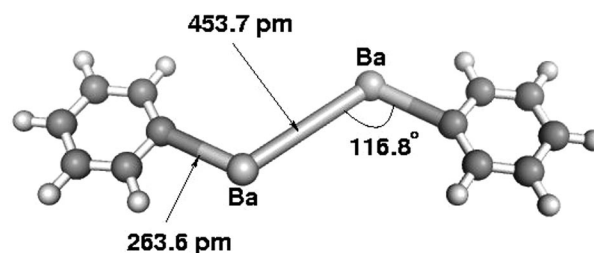
Figure 6. Energetically most favoured calculated structure of [(C$_6$H$_5$)Ba]$_2$ (BP86/RI/TZVPP, singlet).[133]

(–70 kJ mol^{-1}) is almost identical to that of the Ca–Ca bond. Only the dimerization of phenylbarium is an endo-thermic process by +93 kJ mol^{-1}. If, however, the triplet state of diphenyldibarium(I) H$_5$C$_6$–Ba–Ba–C$_6$H$_5$ is consid-ered, this structure turns out to be thermoneutral relative to the two singlet fragments; that is, triplet H$_5$C$_6$–Ba–Ba–C$_6$H$_5$ is more stable than the singlet species by –93 kJ mol^{-1}.

$$2 H_5C_6–Ae \rightarrow H_5C_6–Ae–Ae–C_6H_5 \qquad (2)$$

This picture changes only slightly if we define the forma-tion reaction as an insertion of the corresponding alkaline earth metal Ae in a diphenyl alkaline earth metal(II) com-pound according to Equation (3): Now, the formation of the diberyllium(I) compound H$_5$C$_6$–Be–Be–C$_6$H$_5$ is fav-oured by –137 kJ mol^{-1}, the formation of the homologous magnesium compound only by –25 kJ mol^{-1}, which is sim-ilar to that of the strontium compound (–22 kJ mol^{-1}). Di-phenyldicalcium(I) H$_5$C$_6$–Ca–Ca–C$_6$H$_5$ is more stable than

diphenylcalcium(II) $Ca(C_6H_5)_2$ and Ca by -48 kJ mol^{-1}. The reaction of barium with diphenylbarium is still endothermic by $+118$ kJ mol^{-1}.

$$(H_5C_6–)_2Ae + Ae \rightarrow H_5C_6–Ae–Ae–C_6H_5 \qquad (3)$$

3.3 Stable Molecules R–Ae–Ae–R

The chemical similarities between the elements of group 2 (d^0 metals) and group 12 (d^{10} metals) originate from the oxidation states +2 and the lack of redox activity in common inorganic and organometallic chemistry, because completely filled d shells exhibit neither acceptor nor donor character. Due to this fact, a brief discussion of the chemistry of subvalent metals of the zinc group is included.

For a long time, only salt-like species containing $[Hg_2]^{2+}$ units (e.g. calomel, Hg_2Cl_2) and the rare example of $[Cd_2]^{2+}$ in $Cd_2[AlCl_4]_2$ (Cl–Cd–Cd–Cl stabilized with $AlCl_3$ by formation of the Lewis adduct, $AlCl_4^-$) were known.[26] The surprising synthesis [Equation (4)] of stable decamethyldizincocene [Cp*Zn–ZnCp*] (Cp* = η^5-C_5Me_5) with a Zn–Zn bond by Carmona and co-workers[68] in 2004 renewed the interest in molecular compounds featuring metal–metal bonds between group 12 metals (Figure 7).

A variety of sterically demanding and/or chelating ligands R were employed for kinetic stabilization of the metal–metal bonds in homoleptic R–M–M–R complexes and are presented in Figure 8. Reduction of the nucleophilicity of the carbanionic ligands by extensive delocalization of the negative charge supports the kinetic protection by suppressing the disproportionation process into M^0 and M^{II} compounds (M = Zn). Cp derivatives (R = η^5-C_5Me_5,[68] η^5-C_5Me_4Et[69]), substituted β-diketiminate species (nacnac) {R = [(2,6-iPr$_2C_6H_3$)N(Me)C]$_2$CH[70] (dippnacnac), [{(2,4,6-Me$_3C_6H_2$)N(Me)C}$_2$CH]$^-$[71] (mesnacnac)}, α-diimine ligands {R = 1,2-bis[(diisopropylphenyl)imino]acenaphthene[72] (dpp-bian), [(2,6-iPr$_2C_6H_3$)-N(Me)C]$_2^-$[73]} and diamido ligands (R = Me$_2$Si[N-(2,6-iPr$_2C_6H_3$)]$_2$[74]) are shown.

β-diketiminate (nacnac) **m-terphenyl** **cyclopentadienide**

Aryl = 2,6-iPr$_2C_6H_3$ (**dippnacnac**)
Aryl' = 2,4,6-Me$_3C_6H_2$ (**mesnacnac**)

R = Me (n = 5) (**Cp***)
R = Me (n = 4), Et (n = 1)

$$[Zn(\eta^5\text{-}C_5Me_5)_2] + ZnCl_2 + 2\,KH \xrightarrow[-2\,KCl]{THF,\ 20\,°C} \quad + \ldots \qquad (4)$$

bis(aza) donor **guanidinate**

Aryl = 2,6-iPr$_2C_6H_3$; R = iPr (**priso**)
Aryl = 2,6-iPr$_2C_6H_3$; R = cHex (**giso**)

α-diimine

Aryl = 2,6-iPr$_2C_6H_3$ (**dpp-bian**) R = H; Me
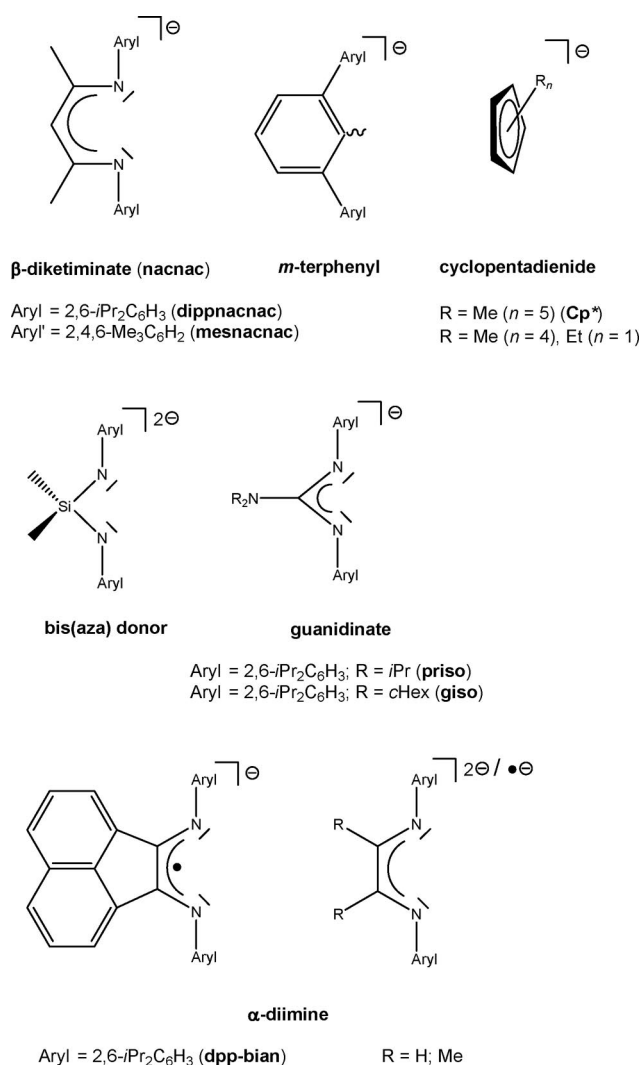
Figure 8. Ligands of structurally characterized complexes containing discrete homodinuclear metal–metal bonds (Aryl = 2,6-iPr$_2C_6H_3$).

Figure 7. Molecular structure of $[(\eta^5\text{-}C_5Me_5)Zn]_2$[68] (dark grey: Zn, light grey: C; H atoms omitted for clarity).

Organometallic homodinuclear complexes of the zinc triad containing M–C bonds were prepared by the Power group for M = Zn, Cd and Hg with m-terphenyl ligands [R = C$_6H_3$-2,6-(C$_6H_3$-2,6-iPr$_2$)$_2$][75,76] shown in Equation (5)

and Figure 9. In addition to the neutral species, anionic complexes of the type $[R–Zn–Zn–R]^{2-}$ with a doubly reduced α-diimine ligand $[(2,6-iPr_2C_6H_3)N(Me)C]_2^{-[77,78]}$ are also characterized. Investigation of the substitution pattern of the N-phenyl ring in the 2,6-position with respect to complex stability indicates that isopropyl groups are essential for the stabilization of the Zn–Zn bond. Less bulky methyl groups in $[(2,6-Me_2C_6H_3)N(Me)C]_2$ and ethyl groups in $[(2,6-Et_2C_6H_3)N(Me)C]_2$ yield mononuclear zinc complexes of the type ZnR_2.[78] Recent studies by the groups of Schulz and Krossing demonstrate another possibility for the stabilization of the dinuclear cation $[Zn_2]^{2+}$ by coordination of the strong Lewis base dmap (4-dimethylaminopyridine) leading to $[(dmap)_3Zn–Zn(dmap)_3]^{2+}$.[46]

$$Ar = C_6H_3\text{-}2,6\text{-}(C_6H_3\text{-}2,6\text{-}iPr_2)_2 \tag{5}$$
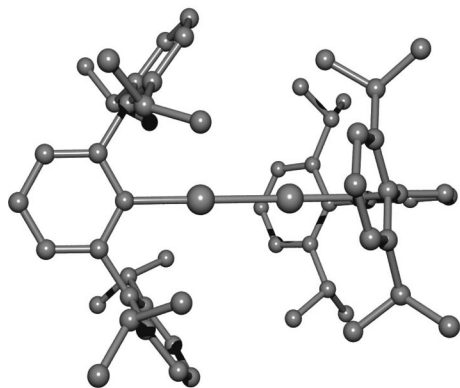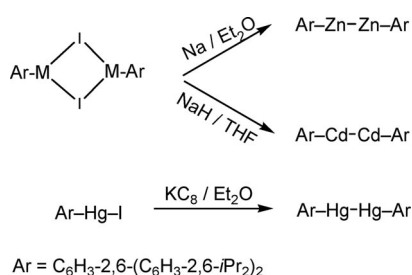
Figure 9. Molecular structure of $[\{C_6H_3\text{-}2,6(C_6H_3\text{-}2,6\text{-}iPr_2)_2\}\text{-}Cd]_2$[76] (central atoms: Cd, grey: C; H atoms omitted for clarity).

These contributions in the chemistry of zinc and cadmium as well as sophisticated synthetic strategies initiated the research on subvalent alkaline earth metal complexes. The breakthrough in the chemistry of monovalent alkaline earth metal chemistry was achieved by Green et al.,[79] who performed the synthesis and full characterization of the first

stable molecular homodinuclear Mg^I compounds.[80] Reduction of the organylmagnesium iodides $[(priso)Mg(\mu-I)_2-Mg(OEt_2)(priso)]$ {priso = 2-diisopropyl-1,3-bis(2,6-diisopropylphenyl)guanidinate} and $[(nacnac)MgI(OEt_2)]$ with an excess amount of potassium in toluene led to colourless $[(priso)Mg]_2$ **A** [Equation (6)] and yellow $[(nacnac)Mg]_2$ **B** [Equation (7)].

$$\text{Aryl} = C_6H_3\text{-}2,6\text{-}iPr_2 \tag{7}$$
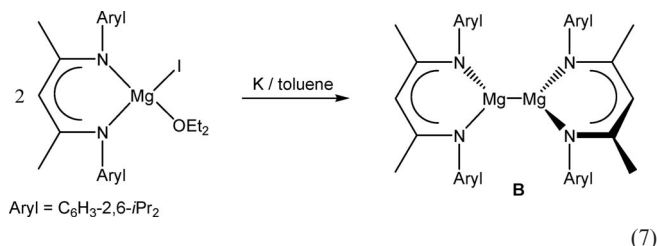
Both compounds **A** and **B** are sensitive toward moisture and air and show an unexpected high thermal capacity, **B** being stable up to 300 °C and sublimeable at 230 °C (10^{-6} Torr). The Mg–Mg distances in **A** and **B** are 285.08(12) and 284.57(8) pm, respectively. These values agree well with calculated metal–metal distances for R–Mg–Mg–R with R = η^5-C_5H_5 (280.9 pm[57]), C_6H_3-2,6-Ph$_2$ (283.8 pm[60]), F (284.1 pm[52]) and H (288.4 pm[57]). In comparison to elemental magnesium (320 pm), the distances are shortened and they are larger than the sum of the covalent radii (272 pm) of the two corresponding atoms.[81] An important feature was the exclusion of bridged hydrides forming a $Mg(\mu-H)_2Mg$ unit and giving Mg^{II} compounds, because a comparable structural fragment was already found in $[(nacnac)Ca(thf)(\mu-H)]_2$[82,83] by Harder and co-workers. The multitude of the observations support the absence of hydride ions: (i) In NMR spectra no hydride species are present. (ii) Compound **B** is isostructural to the zinc complex $[(nacnac)Zn]_2$,[70] and the metallacycles C_3N_2Mg are in a nearly orthogonal orientation to each other, whereas in a hydrido complex a coplanar arrangement was expected. (iii) X-ray diffraction studies reveal no significant residual electron density that would hint at two hydride ions. (iv) High-resolution mass spectra allowed the identification of the molecular ions corresponding to the predicted constitution. Investigation of the bonding situations by NBO analysis suggests a high s-character of the covalent Mg–Mg bond. The bonds between the magnesium atoms and the anionic bidentate aza bases are of largely ionic nature, and for this reason the homodinuclear

$$\text{Aryl} = C_6H_3\text{-}2,6\text{-}iPr_2 \tag{6}$$
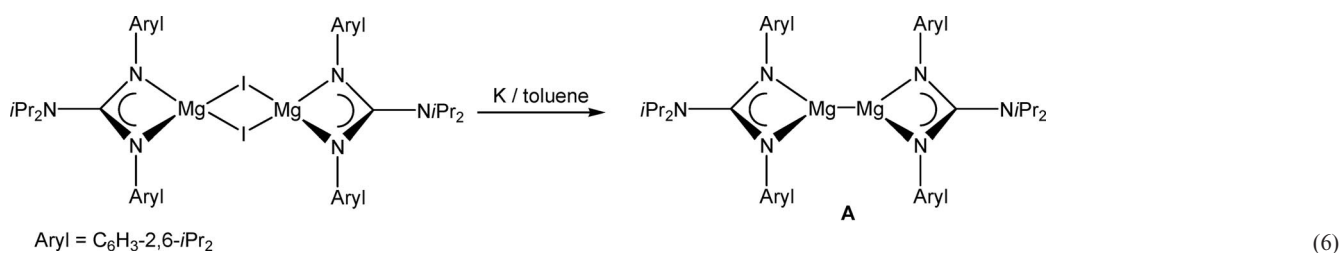
molecules can be regarded as $[Mg_2]^{2+}$ stabilized by anionic units,[79,84] in accordance with the $[Zn_2]^{2+}$ moiety[46] and the R–Mg–Mg–R model systems.[60] Formation of stable Lewis adducts of **B** with redox-inert Lewis bases is shown in Equation (8) and Figure 10.[85]

Aryl = C₆H₃-2,6-iPr₂ → L = THF, dioxane, DMAP, tBuPy

(8)
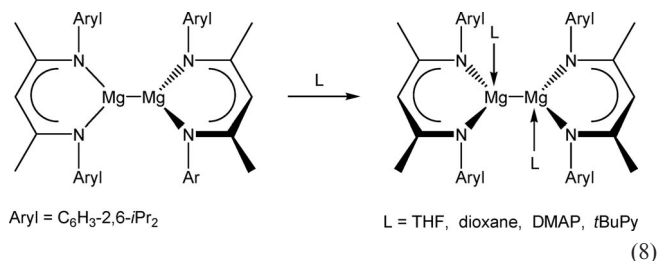
These complexes are surprisingly stable towards disproportionation processes, and under vacuum the ether complexes are regenerated by loss of the weakly coordinated THF or Dx (1,4-dioxane) ligands, respectively. In all cases the Lewis bases are coordinated at both metal centres. In contrast to this observation, bis[organozinc(I)] forms a geminal bis(Lewis base) adduct as found for the addition reaction of $[(\eta^5\text{-Me}_5C_5)Zn]_2$ with dmap, leading to $[(\eta^5\text{-Me}_5C_5)\text{-}Zn\text{–}Zn(\text{dmap})_2(\eta^5\text{-}C_5Me_5)]$.[86] Interestingly **B** shows no tendency to coordinate bidentate chelate ligands such as 1,2-dimethoxyethane (dme), 1,2-bis(dimethylamino)ethane (tmeda) or quinuclidine. Structural investigations of the adducts show the reorientation of the (nacnac)Mg metallacycles from an initial orthogonal orientation to a coplanar orientation to each other. The Mg–Mg distances (Table 5) are elongated by 7.4% in the THF complex and by 12.3% in the dmap complex relative to **B**. The value of the elongation of the metal–metal bond correlates to the strength of the Lewis basicity and its steric demand. The Mg–donor distances are significantly longer in all cases than those observed for tetrahedrally coordinated Mg^{II} ions.

Hydrogenation reactions of **B** with dihydrogen at elevated temperatures (80 °C) or under UV light irradiation do not lead to the formation of the expected μ-hydrido complex $[(\text{nacnac})Mg(\mu\text{-H})]_2$, whereas DFT calculations
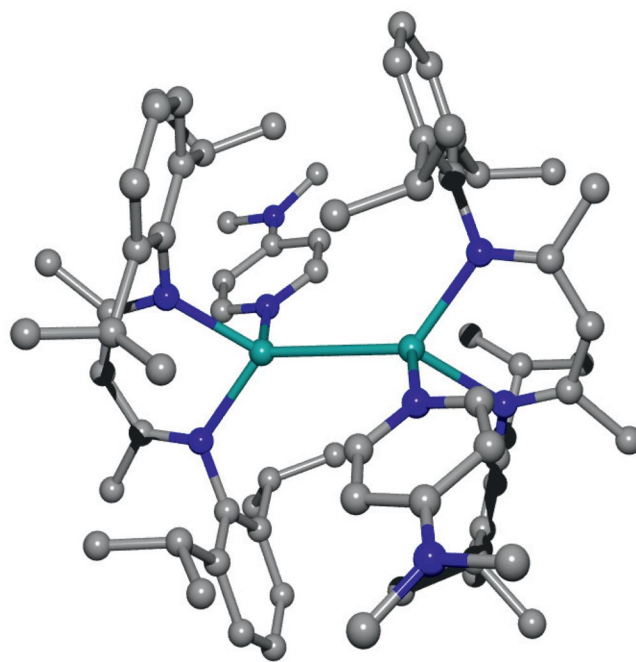
Figure 10. Molecular structure of $[(\text{dmap})(\text{nacnac})Mg]_2$[85] (grey: C, turquoise: Mg, blue: N; H atoms omitted for clarity).

predict that the Mg–Mg bond should undergo hydrogenation reactions to yield hydrido bridges by formation of the thermodynamically more stable product, because the 3c–2e bond in the $\{Mg^{II}(\mu\text{-H})_2Mg^{II}\}$ unit is much stronger than the 2c–2e binding mode in the $Mg^I\text{–}Mg^I$ bond.[87] According to a procedure as employed for the synthesis of $[(\text{nacnac})Ca(\text{thf})(\mu\text{-Bu})]_2$[82,83] by treatment of $[(\text{nacnac})Mg(n\text{Bu})]$ with phenylsilane ($H_5C_6SiH_3$) in hexane, colourless $[(\text{nacnac})Mg(\mu\text{-H})]_2$ was prepared. Treatment with THF led to the Lewis base adduct $[(\text{thf})(\text{nacnac})Mg(\mu\text{-H})]_2$.[85] When THF adducts $[(\text{thf})(\text{nacnac})Mg(\mu\text{-H})]_2$ and **B**(thf) are compared, the latter shows a significantly longer Mg–O(thf) bond, which can be caused by a weaker attraction between the base and the softer Mg^I Lewis acid, whereas Mg^{II} is notably harder. Reduction of unsaturated compounds such

Table 5. Comparison of selected bond lengths and angles of homodinuclear magnesium complexes.

Compound	Mg–Mg /pm	Mg–N(mean) /pm	N–Mg–N /°	Mg–X_donor /pm
[(nacnac)Mg]₂[79]	284.57(8)	206.0	91.78(5)	
[(priso)Mg]₂[79]	285.08(12)	207.36(10)	65.54(5)	
[(α-diimin)Mg]₂²⁻ [90]	293.70(18)	204.7	138.61(8)	
[(thf)(nacnac)Mg]₂[85]	305.60(12)	215.9	87.08(5)	217.33(13)
[(dx)(nacnac)Mg]₂[85]	314.99(18)	215.2	87.79(8)	224.38(18)
[(dmap)(nacnac)Mg]₂[85]	319.62(14)	217.8	86.11(6)	223.53(18)
[(tBuPy)(nacnac)Mg]₂[85]	312.60(15)	216.2	86.30(7)	222.87(18)
[(nacnac)Mg(μ-H)]₂[85]	289.0(2)	206.4	93.14(9)	
[(thf)(nacnac)Mg(μ-H)]₂[85]	303.32(18)	214.3	93.14(9)	209.96(16)
[(η⁵-C₅H₅)Mg]₂[57]	280.9			
[(C₆H₃-2,6-Ph₂)Mg]₂[60]	283.8			
[FMg]₂[52]	284.1			
[HMg]₂[57]	288.4			

as 1-adamantylazide, azobenzene and diisopropylcarbodiimide led to the corresponding hydromagnesiation products. The reactivity is identical to that of the transition metal complex [{HC(tBuCNAr)$_2$}Fe(μ-H)]$_2$.[88]

Notwithstanding the steric protection (like encapsulation in a protecting cage) and kinetic stabilization towards disproportionation of the Mg–Mg bond by several types of strongly coordinating bulky ligands, the two magnesium(I) centres in the homodinuclear unit are able to act as a facile and selective two-center/two-electron reductant. Treatment of **B** with dicyclohexylcarbodiimide (CyNCNCy) led to the formation of an unusual magnesium magnesioamidinate [(nacnac)Mg{(NCy)$_2$C}Mg(nacnac)][79] [Equation (9)], whereas the THF adduct **B**(thf) shows no similar reactivity.[85] This fact underlies that the first step of the reduction is a precoordination of the carbodiimide on a Mg^I centre, which is blocked in **B**(thf) by solvent ligation. Unsaturated substrates such as azobenzene (Ph–N=N–Ph) or 1,3,5,7-cyclooctatetraene (cot) gave the corresponding doubly reduced products, whereas tert-butylisocyanate (tBuNCO) or 1-adamantyl azide (AdN$_3$) led to reductive C–C and N–N coupling reactions (Figure 11).[89] The reaction of **B** with the azide generated an unusual bis(magnesium)hexazenediide complex [Equation (9)], which shows an unexpected thermal stability (Figure 12).

Analogous to the stabilization of Zn–Zn bonds by doubly reduced α-diimine ligands,[77,78] a one-pot synthesis by using a mixture of the ligand and magnesium dichloride with an excess amount of potassium in THF led to the for-
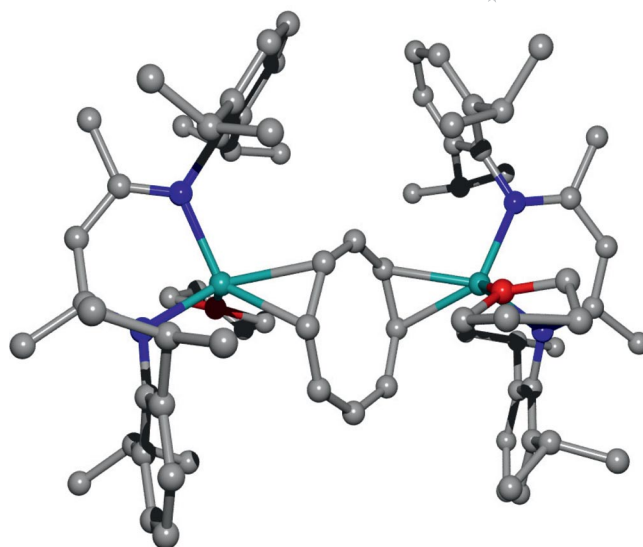
Figure 11. Molecular structure of the bis(magnesium)-μ-η²-cot complex[89] (grey: C, turquoise: Mg, blue: N, red: O; H atoms omitted for clarity).

mation of [(thf)$_3$K{(2,6-iPr$_2$C$_6$H$_3$)N(Me)C}Mg]$_2$ [Equation (10)] by reduction of the initial divalent Mg^{II} to Mg^I.[90] Interestingly, on the one hand, the use of an excess amount of potassium does not lead to the reduction of the [Mg$_2$]$^{2+}$ unit to Mg^0 by formation of the corresponding potassium α-diiminate complex. On the other hand, β-diket-

Aryl = C$_6$H$_3$-2,6-iPr$_2$

Ad = 1-adamantyl

(9)

S. Krieck, L. Yu, M. Reiher, M. Westerhausen

dipp = 2,6-iPr$_2$C$_6$H$_3$
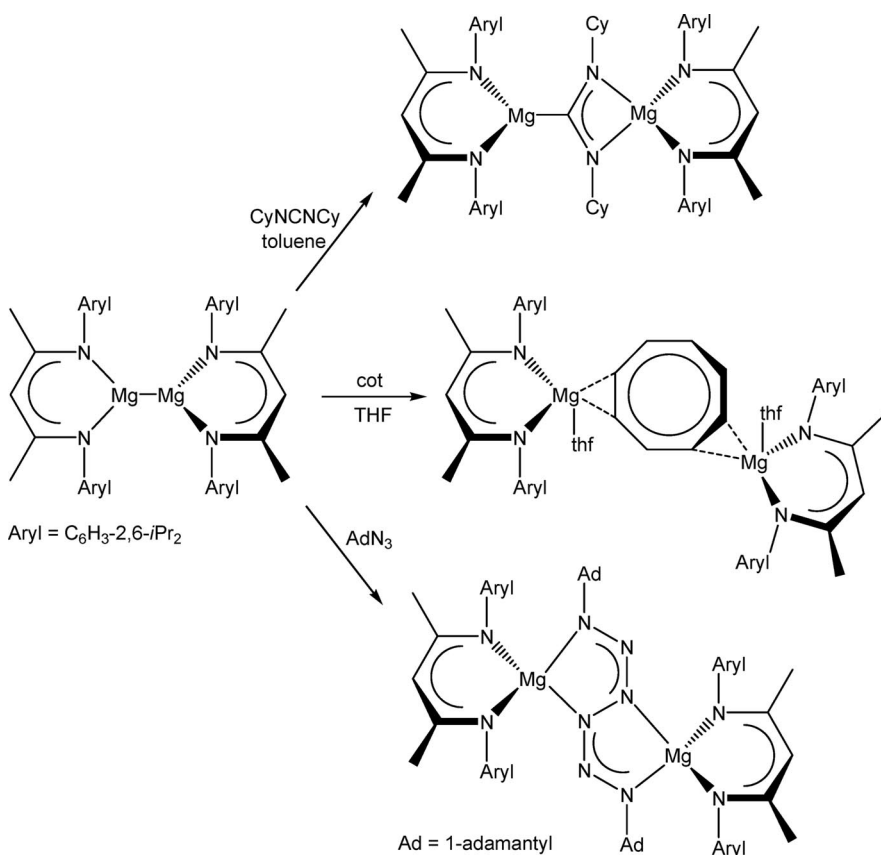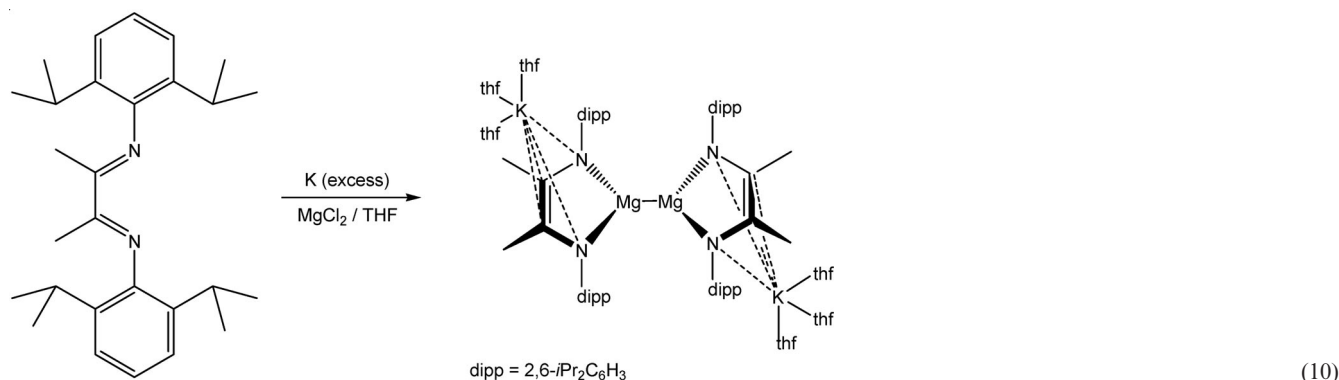
(10)
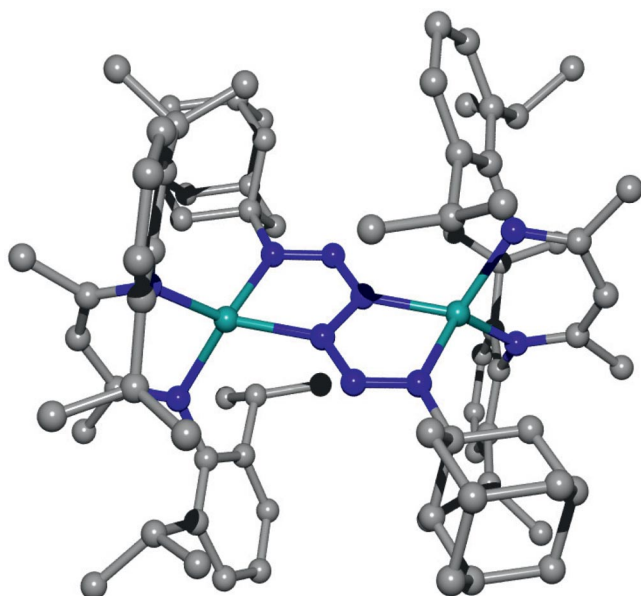
Figure 12. Molecular structure of the bis(magnesium)-μ-η^3-hexa-azadiendiide complex[89] (grey: C, turquoise: Mg, blue: N; H atoms omitted for clarity).

iminate complex **B** forms stable Lewis adducts with THF, whereas a synthesis in THF did not lead to complexation of the Lewis base in the case of the α-diimine ligand. The crystal structure shows a nearly coplanar arrangement of the metallacycles and the Mg–Mg bond [293.70(18) pm] is slightly longer than that in **A** and **B** but shorter than those in the corresponding adducts (Table 4). NBO analysis of the Mg–Mg bond yields 44.8% 3s and 55% 2p character, whereas in **A** 93.2% s character was observed. In the α-diimine complex, a five-membered metallacycle is formed and bridges the gap between the four-membered ring in **A** and the six-membered ring in **B**. A mononuclear Mg^{II} species, [(thf)$_3$Mg{(2,4,6-Me$_3$C$_6$H$_2$)N(Me)C}$_2$], formed by the reduction of the β-diketiminate ligand with magnesium metal.[91]

4 Stabilization of Ae^I Compounds by Extended π-Systems

In an earlier section we have seen that ligands with extended π-systems such as 2,2′-bipyridine are able to accept electrons by forming a radical anion as in the σ complex [(bpy)MgR]. It was also noted earlier that the heavier alkaline earth metals and their cations are in the position to form quite strong interactions to side-on-bound arenes. This kind of interactions attracted much attention when it was found that the graphite intercalation compound CaC$_6$ shows superconductivity at rather high temperatures.[92a–92c,93] Quantum chemical investigations show that significant participation of d states at calcium is essential for understanding the chemical bonding reflecting the tendency of the calcium atoms in CaC$_6$ to behave more as sd metals rather than s or sp metals.[93] In addition, the explanation of the structure of elemental calcium affords occupation of d states.[94]

The wide field of endohedral complexes of alkaline earth metal inclusion in fullerenes (forming fullerides such as, for example, Ae@C$_{60}$, AeC$_{72}$, Ae@C$_{74}$, Ae@C$_{80}$, Ae@C$_{82}$ and Ae@C$_{84}$) will not be discussed in this review, even though only a partial electron transfer from Ae to the fullerene occurs (see, e.g., ref.[95,96]). The interaction of electropositive metals with fullerenes and carbon nanotubes is quite complex, and we will limit this review to investigations of smaller arenes with alkaline earth metals.

4.1 Interaction of Ae^{n+} with Monocyclic Arenes

The alkaline earth metal cations form rather strong bonds with π-systems of arenes, and these interactions reach roughly half the value of an Ae–C σ-bond.[40] The strength of a bond between an alkaline earth metal cation and the π-system of an arene strongly depends on the charge on the metal (Ae^0, Ae$^+$ or Ae^{2+}), on the counteranion in case of cationic metals and on the substitution pattern of the arene.

Bond energies and distances between alkaline earth metals and π-systems of arenes are summarized in Table 6. The interactions of benzene and naphthalene with neutral calcium atoms are weak, thus leading to rather large metal–arene distances. For the complex of calcium with peri-naphthalene, the situation is different: The bond energy is much larger, and the distance between the calcium atom and the arene is much smaller.[97] Whereas the calcium atom remains neutral in complexes with benzene and naphtha-

lene, a charge of +0.98 for calcium was calculated for the perinaphthalene adduct [according to the NBO method based on MP2/6-31G(d,p) calculations] thus forming a subvalent complex. The bond energies between Ae$^+$ and benzene or mesitylene decrease with the size of the metal atom with slightly larger values for the mesitylene complexes. The distances between Ca$^+$ and benzene are much smaller than those calculated for neutral calcium. With increasing charge at the metal atom, the binding energies increase as well, because of an enhanced electrostatic attraction between Ae^{2+} and the arene π-systems. If a second anion is included in these calculations, the binding energies drop to less than half the value. As expected the bond lengths increase if further metal-bound anions are included in the theoretical investigations. Coordination of water molecules to Ae^{2+} also leads to a reduction of the Ae^{2+}–arene binding energies in complexes of the type $[(H_2O)_nAe(\eta^6\text{-}C_6H_6)]^{2+}$.[104] For $[(H_2O)_nMg(\eta^6\text{-}C_6H_6)]^{2+}$ with $n = 1$ a value of 490.9 kJ mol^{-1} was calculated, additional water molecules lead to further reduction of the Mg–benzene binding energies ($n = 2, 3, 4$: 405.5, 309.8 and 228.5 kJ mol^{-1}). For $[(H_2O)_nCa(\eta^6\text{-}C_6H_6)]^{2+}$ comparable trends were calculated (331.1, 273.4, 224.7 and 173.2 kJ mol^{-1} for $n = 1, 2, 3$ and 4, respectively. In all these compounds, the interactions between the alkaline earth metal cation and the arene are mainly ionic, with only small covalent contributions.[105]

Another aspect concerns the binding of benzene in comparison to other Lewis bases. The benzene complexes of the cations Mg$^+$ and Ca$^+$ show binding energies of 129.7 and 111.2 kJ mol^{-1} (Table 4). These values are only slightly lower than the binding energies to rather strong Lewis bases such as ammonia (Mg$^+$: 157.9, Ca$^+$: 134.6 kJ mol^{-1}) and water (Mg$^+$: 131.5, Ca$^+$: 119.9 kJ mol^{-1}). The binding energies to ethyne (Mg$^+$: 75.0, Ca$^+$: 58.1 kJ mol^{-1}) and ethylene (Mg$^+$: 56.2, Ca$^+$: 56.2 kJ mol^{-1}) are calculated to be roughly half the values determined for the benzene complexes.

Kang investigated sandwich complexes of calcium(0) with benzene and borazine ligands.[106] For the exothermic reaction of calcium atoms with two benzene molecules, a reaction enthalpy of –134.1 kJ mol^{-1} was calculated. In this sandwich complex the benzene molecules are coplanar with distances of 226.5 pm between the metal atom and the centres of the arenes. The calcium atom has an atomic charge of +1.592 based on NBO analysis of B3LYP/6-31G(d) calculations. Furthermore, the bonding involves d orbitals at the calcium atom. In the isoelectronic borazine complex of calcium, the planes of the borazine ligands include an angle of 75° with distances to the calcium atom of 219.4 pm, thus forming a bent sandwich structure. The charge on the calcium atom increases to a value of +1.843. In both complexes, the ligands form radical anions with charges –0.796 and –0.922 for the benzene and borazine ligands, respectively.[106]

In the [Ca$_2$(benzene)] complex, the calcium atoms are located at the same side of the ring with a Ca–Ca distance of 346.3 pm and a charge of +0.526 on each metal atom.[98] This bonding leads to a strong C–C bond elongation and to a break-up of the planarity of the C$_6$ ring (dihedral C–

Table 6. Bond energies (BA) and distances between alkaline earth metals and side-on-bound arenes in compounds of the type $[(\eta^6\text{-}arene)Ae]^{n+}$ (X is the centroid of the arene).

Ae^{n+}	Arene	BE /kJ mol^{-1}	Ae–X /pm	Method	Ref.
Ae^0					
Ca	benzene	1.30	500[a]	B3LYP	[97]
Ca	benzene	3.28	378.5	B3LYP	[98]
Ca	naphthalene	0.38	540[a]	B3LYP	[97]
Ca	perinaphthalene	8.00	250[a]	B3LYP	[97]
Ae$^+$					
Mg$^+$	benzene	155.2	232	VTST[b]	[100]
Mg$^+$	benzene	129.7	232.5	B3LYP	[43]
Ca$^+$	benzene	111.2	263.6	B3LYP	[43]
Ca$^+$	mesitylene	135.0		VTST[b]	[100]
Sr$^+$	mesitylene	115.7		VTST[b]	[100]
Ae^{2+}					
Be^{2+}	benzene	995.6	129.0	B3LYP	[101]
Be^{2+}	benzene	895.1	127.7	MP2	[102]
(BeH)$^+$	benzene	361.7	146.5	MP2	[102]
(BeCH$_3$)$^+$	benzene	321.1	149.8	MP2	[102]
(BeCl)$^+$	benzene	365.1	147.8	MP2	[102]
Be^{2+}	mesitylene	1138.0	127.8	B3LYP	[103]
Be^{2+}	aniline	1073.2		B3LYP	[103]
Mg^{2+}	benzene	524.2	194.7	B3LYP	[104]
Mg^{2+}	benzene	454.7	196.0	MP2	[102]
Mg^{2+}	mesitylene	621.3	192.0	B3LYP	[101]
Mg^{2+}	aniline	578.7		B3LYP	[103]
(MgH)$^+$	benzene	198.5	212.9	MP2	[102]
(MgCH$_3$)$^+$	benzene	177.1	215.1	MP2	[102]
(MgCl)$^+$	benzene	232.4	207.2	MP2	[102]
Ca^{2+}	benzene	309.0	247.2	MP2	[102]
Ca^{2+}	aniline	405.2		B3LYP	[103]
(CaH)$^+$	benzene	141.9	261.0	MP2	[102]
(CaCH$_3$)$^+$	benzene	133.1	262.2	MP2	[102]
(CaCl)$^+$	benzene	160.4	255.1	MP2	[102]
SrCl	benzene	151.3		VTST[b]	[100]
SrCl	mesitylene	163.9		VTST[b]	[100]

[a] Estimated from a diagram given in ref.[97] [b] Variational transition state theory VTST; VtSt-derived binding energies show an uncertainty of approximately ±15%.

C=C–C angle of 40.0°). The Ca atoms are bound to the 1,4-positions of the arene, the shortest Ca–C bond lengths being 265.2 pm.[99]

The *normal*-valent alkaline earth metal ions Ae^{2+} are isovalent with the triply charged ions of the scandium group. For this reason, the existence of subvalent compounds of group 3 is an important feature for studies of structure–property relationships between both groups. In the case of scandium Sc^{III} (≈ Ae^{II}), two subvalent forms are known: Sc^{II} (≈ Ae^I) and Sc^I (≈ Ae^0).[107] Co-condensation of scandium vapour in the presence of 1,3,5-tBu$_3$C$_6$H$_3$ led to the formation of substituted bis(η^6-benzene)scandium(0), and, by transformation, involving insertion, of a corresponding scandium(II) compound [Equation (11)].[108] A formally monovalent scandium(I) as a triple decker with [(η^5-arene)-Sc(μ,η^6-arene)Sc(η^5-arene)] arrangement is obtained by co-condensation of scandium vapour with *tert*-butylphosphaethyne under cyclization of the phosphaalkyne.[109]

$$(11)$$
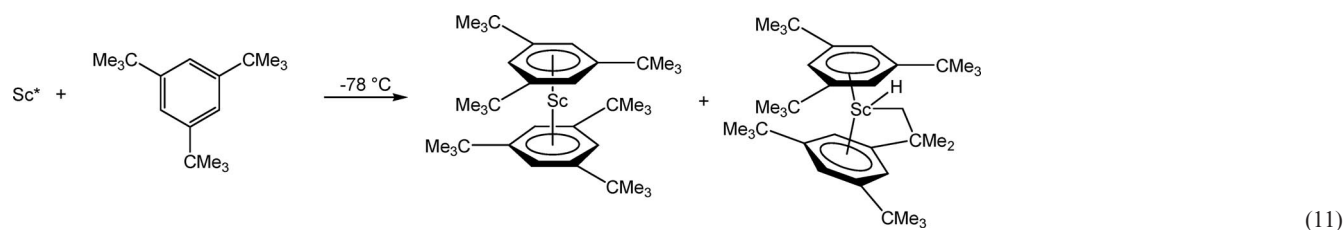
4.2 Inverse Sandwich [(thf)$_3$Ca(μ-η^6,η^6-C$_6$H$_3$Ph$_3$)Ca(thf)$_3$]

Reduction of annulated benzene systems with alkaline earth metals led in all known cases to the formation of divalent metal ions Ae^{2+} and reduced negatively charged arenes. Bogdanović and co-workers[110,111] studied the reduction of anthracene (C$_{14}$H$_{10}$) with alkaline earth metals for activation purposes of the corresponding metals by thermal decomposition (in some cases room temperature is sufficient) of the generated complexes.[112] The direct synthesis of the heavier alkaline earth metals with anthracene in THF yields the corresponding singly or doubly reduced anthracene complexes: [(thf)$_3$Mg(C$_{14}$H$_{10}$)], [(thf)$_4$Ca(C$_{14}$H$_{10}$)], [(thf)$_6$Ca(C$_{14}$H$_{10}$)$_2$], [(thf)$_2$Sr(C$_{14}$H$_{10}$)] and [(thf)Ba-(C$_{14}$H$_{10}$)].[113] Mechanistic studies by Lindow et al. show the localization of the electrons only in the central ring of anthracene.[114] Reduction of biphenyl (C$_{12}$H$_{10}$) in liquid ammonia with calcium generates a doubly reduced biphenyl complex, whereas both electrons are located on one phenyl ring.[114] Similar products were observed by metathesis reactions of bis(lithium)anthracene or bis(lithium)biphenyl, respectively, with anhydrous calcium dibromide.[115] The use of more extended π-systems such as acenaphthene and

guaiazulene[116,117] results in derivatives of calcocene-type structures with Ca–(μ,η^5-arene) interactions. Solvent separated ion couples [(thf)$_6$Ca][C$_{16}$H$_{10}$]$_2$·2C$_{16}$H$_{10}$ form during the reaction of fluoranthene (C$_{16}$H$_{10}$) with potassium and calcium diiodide in THF.[118]

The direct synthesis of activated magnesium (Rieke magnesium) with 1-bromo-2,4,6-triphenylbenzene in THF led to the formation of the expected Grignard reagent [(thf)$_2$-(Br)Mg–C$_6$H$_2$-2,4,6-Ph$_3$] (C), whereas a reaction of an excess amount of activated calcium powder with the bromoarene in THF at –60 °C yields the unexpected product [(thf)$_3$-Ca(μ-η^6,η^6-C$_6$H$_3$Ph$_3$)Ca(thf)$_3$] (E) [Equation (12)].[119] These two reactions show impressively the discrepancy between the reactivity of magnesium and its heavier homologue calcium.[120,121] Solutions of E show pronounced thermochromic and solvatochromic behaviour, and in the solid state E crystallizes as black, strongly opalescent and pyrophoric cubes, which are extremely sensitive toward moisture and air.

An important feature of the characterization of complex E was the verification of the absence of hydride ions or anions other than [1,3,5-C$_6$H$_3$-Ph$_3$]$^{2-}$ by several methods

$$(12)$$
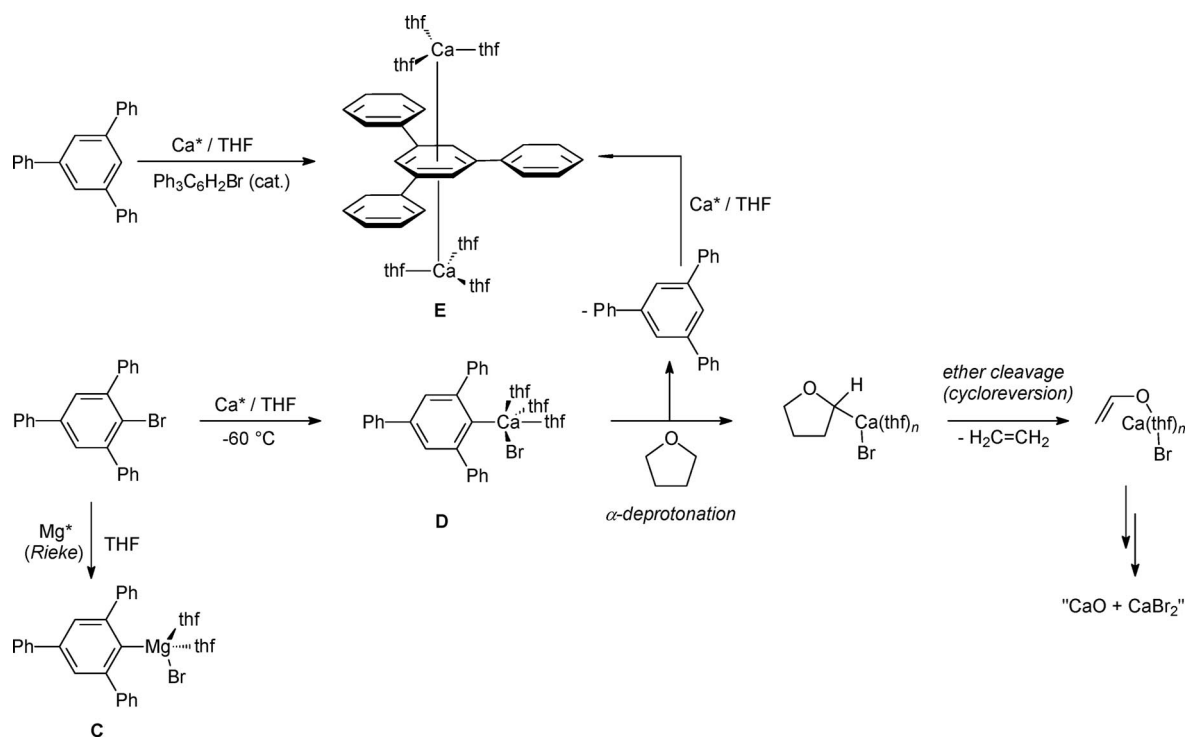
and derivatization reactions for manifestation of the oxidation state of calcium: (i) No hydride ions were detected in ^{1}H NMR spectroscopic experiments (both in solid-state and solution measurements) and neither H_2 nor HD were detected by GC–MS techniques after hydrolysis of crystalline **E** with D_2O or $[D_4]$methanol, respectively. (ii) Vinylate anions (originating from the necessary ether scission reaction) are not detected in NMR spectroscopic experiments; treatment of **E** with chlorotrimethylsilane gave no vinyl trimethylsilyl ether according to GC–MS experiments, whereas a validation of the applied method with [{(thf)-Ca(O–CH=CH$_2$)$_2$}$_4$·CaO·CaI$_2$][122] gave the corresponding derivative. In NMR spectroscopic experiments, vinylate and ethene are detected in stoichiometric amounts in the mother liquor but not in solid state. (iii) The structure determination and elemental analysis confirmed the absence of bromide ions. (iv) Oxide anions can be excluded by X-ray structural analysis, and generally such kind of hard Lewis bases are surrounded by Lewis acids forming oxygen-centred cage compounds.

The central structural element of **E** (Figure 13) consists of a strictly planar doubly reduced triphenylbenzene moiety with two (thf)$_3$Ca^I units located on a C_3-like axis on opposite sides of the arene plane leading to an inverse sandwich arrangement. The distances between Ca–Ca′ [427.9(3) pm], Ca–C [259.2(3) pm] and between the centre of the inner arene and calcium (214 pm) are quite small and smaller than the values calculated for interactions between benzene and Ca$^+$ or Ca^{2+} (see Table 6 and ref.[43]). In comparison to the neutral 1,3,5-triphenylbenzene[123] (tpb) ligand with a propeller-like structure, the C–C bonds in the central arene ring are elongated (146.4 vs. 138.7 pm, tpb) and the ring–ring distances are shortened (143.5 vs. 148.7 pm, tpb). These results are in accordance with the presence of a doubly reduced bridging ligand with pronounced electron delocalization.[119]

EPR spectroscopic investigations suggest a triplet ground state ($S = 1$, two unpaired electrons delocalized over the 1,3,5-triphenylbenezene moiety resulting in an organic π-diradical) and the presence of the high symmetry in **E** both in the solid state as well as in solution. Furthermore, susceptibility measurements and quantum chemical investigations are in agreement with a triplet ground state. The bonding situation of the homodinuclear inverse sandwich **E** could be explained with occupied molecular orbitals delocalized from one Ca centre over the bridging arene to the second calcium centre with notable d-type orbital contribution from the metal atomic orbitals. From each calcium atom, one electron is transferred onto the 1,3,5-triphenylbenzene ligand having acceptor orbitals lying at energy levels between the first and second ionization potential of calcium. Additional population analysis shows a doubly negative charge distribution over the arene plane and localization of positive charge on the calcium fragments, which results in the confirmation of a charge separation such as {Ca$^+$(μ-tpb$^{2–}$)Ca$^+$}.

The use of an excess amount of magnesium metal generates only the typical Grignard compound **C**, and under no
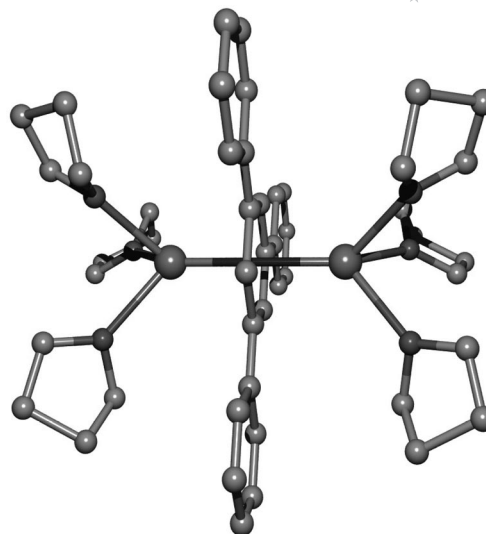
Figure 13. Molecular structure of [(thf)$_3$Ca(μ-η^6,η^6-C$_6$H$_3$Ph$_3$)Ca-(thf)$_3$][119] (central atoms: Ca, light grey: C, dark grey: O; H atoms omitted for clarity).

circumstance was a comparable system like **E** observed, whereas the post-Grignard reagent **D** could not be isolated in a similar way. The enormous reactivity of organocalcium reagents hampers in some cases the discrete isolation of the corresponding arylcalcium halide, but a variety of substituents on the phenyl ring of the halogenoarenes are able to stabilize this type of compounds.[121,124–127] A derivative with the structural motif of **E**, [(thf)$_3$Ca(I)C$_6$H$_3$-2,6-Tol$_2$], is accessible by direct synthesis of I-C$_6$H$_3$-2,6-Tol$_2$ with activated calcium in THF (Figure 14).[128] Treatment of calcium with 1-bromo-2,3,5-triphenylbenzene in THF at strictly low temperatures in a 1:1 stoichiometry yields a pale yellow solution of **E**; upon addition of more than one equivalent of calcium, the solution turns blue immediately. This result suggests that the first step of formation of **E** is the generation of the heavier Grignard reagent **D** by insertion of Ca into the C$_r$–halogen bond, followed by the reduction of the arene system by cleavage of the ether solvent. This assumption is supported by the necessity of the presence of a catalytic amount of 1-bromo-2,4,6-triphenylbenzene for the synthesis of **E** [Equation (12)], because no reaction takes place by treatment of 1,3,5-triphenylbenzene with activated calcium in THF.

Formation of multihapto binding modes as inverse sandwich complexes are known in rare examples for stabilization of low oxidation states of group 13 metals as [M(μ,η^5-C$_5$Me$_5$)M]$^+$ (M = Ga,[129] In;[130,131] note that in both cases the metal ions interact additionally with complex anions) and for an actinide element in the case of a toluene-bridged diuranium(II) complex (μ,η^6-PhMe)[{(tBu)(3,5-C$_6$H$_3$-Me$_2$)-N}$_2$U]$_2$.[132] The bonding situation in the latter one is quite different of that in the inverse calcium(I) sandwich **E**, because strong δ-backbonding from uranium(II) into the formally uncharged arene stabilizes the inverse sandwich structure.
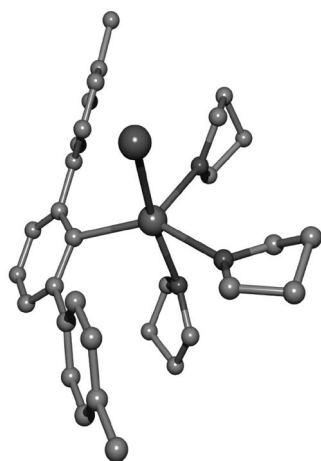
Figure 14. Molecular structure of [(thf)$_3$Ca(I)C$_6$H$_3$-2,6-Tol$_2$][128] (central atom: Ca, light grey: C, small dark grey spheres: O, large dark grey sphere: I; H atoms omitted for clarity).

In the case of the [Mg$_2$]$^{2+}$, [Zn$_2$]$^{2+}$, [Cd$_2$]$^{2+}$ and [Hg$_2$]$^{2+}$ complexes, the corresponding metal contains formal M^I valency, but this subvalency is *only* a consequence of the homodinuclear metal–metal bonding mode and the way to determine the formal oxidation states in multinuclear compounds. The magnesium, zinc, cadmium and mercury species possess sterically shielded diamagnetic divalent homodinuclear metal centres and therefore show binding situations that are fundamentally different from the intrinsically stable paramagnetic calcium(I) inverse sandwich complex without a discrete metal–metal bond. This inverse sandwich complex is characterized by a bifacial multihapto interaction of the calcium atoms with the bridging arene system without a shielding periphery of additional Lewis bases. The subvalent calcium(I) radical species represents a strong reducing agent combined with a rather weak Lewis basicity, which results from pronounced electron delocalization reducing the nucleophilicity. Therefore, these inverse sandwich complexes exhibit no tendency to cleave ethers, which is a common feature in the chemistry of common arylcalcium halides. This observation is in accordance with the stable Lewis base adducts of **B**.

4.3 Quantum Chemical Investigations of [Ae(μ-η^6,η^6-C$_6$H$_3$Ph$_3$)Ae]

Whereas we have studied the inverse sandwich complex with two Ca^I ions in previous work,[119] we may now investigate with B97–D/TZVPP calculations the stability of the lighter and heavier homologous derivatives of this remarkable complex.[133] Structure optimizations show that all compounds (Ae = Mg, Ca, Sr and Ba) are found to form such inverse sandwich structures with the exception of the beryllium derivative. The beryllium system generates no structure like an inverse sandwich complex with a linear Be–Be arrangement comparable to the heavier alkaline earth metals. The inverse magnesium sandwich is presented in Figure 15.
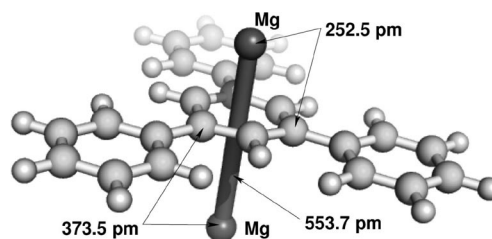
Figure 15. Energetically most favoured calculated structure of the inverse sandwich complex [Mg{μ-η^6,η^6-C$_6$H$_3$Ph$_3$}Mg] (B97–D/TZVPP, triplet).[133]

In analogy to the inverse Ca sandwich complex, all structures are considered in their triplet state. Interestingly, the magnesium derivative possesses an endothermic structure that is 150 kJmol^{-1} higher in electronic energy than two neutral and isolated Mg atoms and an isolated arene ligand. According to our B97–D/TZVPP calculations (Table 7),[133] only the singlet state of the inverse sandwich is energetically favoured by –30 kJmol^{-1} when compared to the isolated metal atoms and the arene (these fragments are, of course, considered in their singlet states). The heavier homologous compounds feature energetically favoured inverse sandwich structures. While the dinuclear calcium complex is –64 kJmol^{-1} more stable than two isolated Ca atoms and the 1,3,5-triphenylbenzene ligand, the strontium homologue is stabilized by only –26 kJmol^{-1}, while the barium system features the largest coordination energy, namely –92 kJmol^{-1}.

Table 7. Selected parameters of compounds of the type [Ae(μ-η^6,η^6-C$_6$H$_3$Ph$_3$)Ae] based on quantum chemical investigations (B97–D/TZVPP, triplet, C carbon atoms of the inner arene ring).[133]

Metal	Ae–Ae /pm	Ae–C /pm
Mg	553.7	252.5/373.5
Ca	432.6	260.1
Sr	492.2	288.7
Ba	506.5	292.7

In order to further evaluate the stability of the inverse sandwich complexes with magnesium and calcium, we may compare these structures with isomeric complexes in which the two metal ions are bound on the same side of the aromatic ligand. For the sake of simplicity, we neglect solvation effects and consider, as before, only the unsolvated generic structures. Although solvation effects can be expected to stabilize the sandwich complexes, their relative stability is likely to be little affected. All complexes are studied in their triplet states (B97–D/TZVPP).[133]

First of all, both metals, magnesium and calcium, form complexes (which are isomeric in their constitution to the inverse sandwich complexes) in which both metal ions are coordinated on the same side of the arene ligand (representation in Figures 16 and 17). With magnesium, however, the inverse sandwich [Mg(μ-η^6,η^6-C$_6$H$_3$Ph$_3$)Mg] is –49.4 kJmol^{-1} more stable than the complex having both

Mg^I ions coordinated on the same side of the ligand. In the case of calcium, the inverse sandwich is less stable by +19.6 kJ mol^{-1}. In view of the size of the error inherent to present-day DFT methods, the two calcium isomers may be considered thermoneutral at this level of approximation. However, the inverse magnesium sandwich complex shows two significantly different magnesium–arene distances. This fact can be interpreted in the sense that we have an arene complex with two differently charged magnesium ions. According to the population analyses, the magnesium atom that is farther away from the bridging arene ligand is also more positively charged in this triplet state.
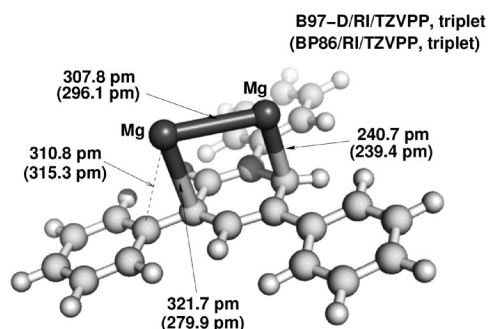
Figure 16. Energetically most favoured calculated structure of the complex [Mg$_2$\{C$_6$H$_3$Ph$_3$\}] (triplet, bond lengths with B97–D/RI/TZVPP and, in parentheses, BP86/RI/TZVPP).[133]
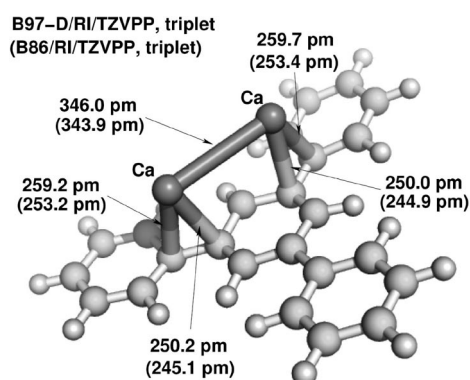
Figure 17. Energetically most favoured calculated structure of the complex [Ca$_2$\{C$_6$H$_3$Ph$_3$\}] (triplet, bond lengths with B97–D/RI/TZVPP and, in parentheses, BP86/RI/TZVPP).[133]

5 Conclusion and Perspective

Compounds with subvalent alkaline earth metals differ strongly from those with subvalent p block elements. The chemistry of low-oxidation-state elements of the p block is rather common, leading to clusters with element–element bonds and cages. For the more electropositive alkaline earth metals Ae, sophisticated methods had to be developed in order to stabilize low-oxidation-state metals such as Ae$^+$.

Solid-state structures such as subnitrides can be regarded as a close packing of the metal atoms with nitrogen atoms in half of the octahedral holes. This arrangement leads to compounds with a formula of [(Ae$_2$N)$^+$·e], which crystallize

in the anti-CdCl$_2$ type. The electrons freely move between the Ae$_2$N layers. These free electrons can also be delocalized within a metallic matrix. A structural variation with the embedment of electron-precise metal nitride cages in a metal matrix also leads to subnitrides such as, for example, solids like [Ba$_8$CaN$_6$]^0·Ba$_6$Na$_x$ with x = 7, 8, 14, 17, 21 and 22.

Monomeric compounds of the type R–Ae are extremely reactive and were investigated in the gaseous phase, in an inert matrix of, for example, a frozen noble gas, or by quantum chemical methods. Their dimers contain the fragment [Ae$_2$]$^{2+}$ with subvalent alkaline earth metal atoms, which is already well-known for [Hg$_2$]$^{2+}$ in calomel. Bidentate aza ligands are able to stabilize [Mg$_2$]$^{2+}$ to yield R–Mg–Mg–R with an unexpected high thermal stability. Quantum chemical investigations show that the Ae–Ae bonds are stable and exhibit rather large binding energies. However, the atomization energies of the alkaline metals are larger than the binding energies and have to be invested during the synthesis of compounds such as R–Ae–Ae–R. The synthesis of these molecules succeeds through the reduction of R–Mg–I with potassium. If the electronegativity difference between the reducing reagent and the alkaline earth metal becomes smaller, the driving force of this reaction diminishes and other pathways have to be developed.

A third concept utilizes the fact that the first and second ionization energies of the alkaline earth metals show significantly different values. If an arene with an extended π*-system with an energy level between these two ionization potentials is offered, it should be possible to form monovalent Ae$^+$ cations. Quantum chemical investigations show that bonds between alkaline earth metal cations (Ae$^+$ and Ae^{2+}) and arenes are of comparable order of magnitude as bonds between these cations and common Lewis bases such as ethers and amines. In [(thf)$_3$Ca(μ-η^6,η^6-C$_6$H$_3$Ph$_3$)Ca-(thf)$_3$] with a triplet ground state, the Ca atoms lie on a C_3 axis on opposite sides of the planar triphenylbenzene ring. According to quantum chemical investigations, also a coordination of [Ae$_2$]$^{2+}$ moieties to an arene yields stable adducts. A transfer of these results to the heavier alkaline earth metals strontium and barium represents a challenging task, because also factors other than the potentials of the π*-orbitals of the arenes play prominent roles, such as solvation effects, which are hard to quantify.

The chemistry of subvalent alkaline earth metals requires sophisticated preparative procedures because of their extreme sensitivity towards moisture and air. Research on the chemistry of these substances is still at the initial stage. However, the use of these compounds as strong reducing reagents can be expected. As an impressive example, azides can be coupled by RMg–MgR to R–N=N–N=N–N=N–R, which is reduced to the dianion at the same time and bound between two Mg^{2+} cations, yielding dinuclear [RMg-(R–N=N–N–N–N=N–R)MgR]. First quantum chemical investigations suggest that hard subvalent alkaline earth metals may be best stabilized as dinuclear [Ae$_2$]$^{2+}$, whereas for the soft alkaline earth metals, extended soft π*-systems might be the best choice for stabilization of Ae$^+$ cations. The strong reducing power also limits the choice of sol-

vents. Due to a rather low nucleophilicity as a consequence of widely delocalized charge, ether cleavage is not a major side reaction. However, the choice of solvents is limited to those which are not easily reduced; it can probably be expected that aromatic solvents such as toluene may react with these compounds. It seems to be challenging to tune this enormous reactivity and to use it for reduction processes. However, it is not hard to predict that many exciting results will emerge in the near future.

Acknowledgments

[1] A. Simon, *Struct. Bonding (Berlin)* **1979**, *36*, 81–127.
[2] T. P. Martin, H.-J. Stolz, G. Ebbinghaus, A. Simon, *J. Chem. Phys.* **1979**, *70*, 1096–1100.
[3] A. Simon, *Pure Appl. Chem.* **1995**, *67*, 311–312.
[4] C. Röhr, *Angew. Chem.* **1996**, *108*, 1289–1291; *Angew. Chem. Int. Ed. Engl.* **1996**, *35*, 1199–1201.
[5] A. Simon, *Coord. Chem. Rev.* **1997**, *163*, 253–270.
[6] A. Simon in *Molecular Clusters of the Main Group Elements* (Eds.: M. Driess, H. Nöth), Wiley-VCH, Weinheim, **2004**, ch. 3.1, pp. 246–266.
[7] E. Horvath-Bordon, R. Riedel, A. Zerr, P. F. McMillan, G. Auffermann, Y. Prots, W. Bronger, R. Kniep, P. Kroll, *Chem. Soc. Rev.* **2006**, *35*, 987–1014.
[8] E. T. Keve, A. C. Skapski, *Inorg. Chem.* **1968**, *7*, 1757–1761.
[9] D. H. Gregory, A. Bowman, C. F. Baker, D. P. Weston, *J. Mater. Chem.* **2000**, *10*, 1635–1641.
[10] U. Steinbrenner, P. Adler, W. Hönle, A. Simon, *J. Phys. Chem. Solids* **1998**, *59*, 1527–1536.
[11] N. E. Brese, M. O'Keeffe, *J. Solid State Chem.* **1990**, *87*, 134–140.
[12] V. Smetana, V. Babizhetskyy, G. V. Vajenine, A. Simon, *J. Solid State Chem.* **2007**, *180*, 1889–1893; erratum: *J. Solid State Chem.* **2007**, *180*, 2990–2994.
[13] P. Rauch, A. Simon, *Angew. Chem.* **1992**, *104*, 1505–1506; *Angew. Chem. Int. Ed. Engl.* **1992**, *31*, 1519–1521.
[14] G. Snyder, A. Simon, *J. Am. Chem. Soc.* **1995**, *117*, 1996–1999.
[15] G. Snyder, A. Simon, *Angew. Chem.* **1994**, *106*, 713–715; *Angew. Chem. Int. Ed. Engl.* **1994**, *33*, 689–691.
[16] U. Steinbrenner, A. Simon, *Angew. Chem.* **1996**, *108*, 595–597; *Angew. Chem. Int. Ed. Engl.* **1996**, *35*, 552–554.
[17] P. Höhn, G. Auffermann, R. Ramlau, H. Rosner, W. Schnelle, R. Kniep, *Angew. Chem.* **2006**, *118*, 6833–6837; *Angew. Chem. Int. Ed.* **2006**, *45*, 6681–6685.
[18] G. V. Vajenine, A. Simon, *Angew. Chem.* **2001**, *113*, 4348–4351; *Angew. Chem. Int. Ed.* **2001**, *40*, 4220–4222.
[19] a) J. F. Liebman, T. Holm, S. W. Slayden in *The Chemistry of Organomagnesium Compounds, Part 1* (Eds.: Z. Rappoport, I. Marek), Wiley, Chichester, **2008**, ch. 2, pp. 101–129; b) A. J. Bridgeman, *Inorg. Chim. Acta* **2001**, *321*, 27–41.
[20] A. Andersen, F. Muntean, D. Walter, C. Rue, P. B. Armentrout, *J. Phys. Chem. A* **2000**, *104*, 692–705.
[21] a) S. Petrie, L. Radom, *Int. J. Mass Spectrom.* **1999**, *192*, 173–183; b) S. Ikuta, *Chem. Phys.* **1985**, *95*, 235–242.
[22] L. Andrews, T. J. Tague, G. P. Kushto, R. D. Davy, *Inorg. Chem.* **1995**, *34*, 2952–2961.
[23] R. B. von Dreele, W. S. Glaunsinger, A. L. Bowman, J. L. Yarnell, *J. Phys. Chem.* **1975**, *79*, 2292–2295.
[24] W. S. Glaunsinger, T. R. White, R. B. von Dreele, D. A. Gordon, R. F. Marzke, A. L. Bowman, J. L. Yarnell, *Nature* **1978**, *271*, 414–417.
[25] P. Damay, F. Leclercq, P. Chieux, *Phys. Rev. B* **1990**, *41*, 9676–9682.
[26] A. F. Holleman, E. Wiberg, N. Wiberg, *Lehrbuch der Anorganischen Chemie*, 102. ed., W. de Gruyter, Berlin, **2007**.
[27] a) A. M. Ellis, E. S. J. Robles, T. A. Miller, *J. Chem. Phys.* **1991**, *94*, 1752–1758; b) C. R. Brazier, P. F. Bernath, *J. Chem. Phys.* **1987**, *86*, 5918–5922.
[28] J. Xin, J. S. Robinson, A. J. Apponi, L. M. Ziurys, *J. Chem. Phys.* **1998**, *108*, 2703–2711.
[29] T. M. Greene, D. V. Lanzisera, L. Andrews, A. J. Downs, *J. Am. Chem. Soc.* **1998**, *120*, 6097–6104.
[30] W. D. Bare, A. Citra, C. Trindle, L. Andrews, *Inorg. Chem.* **2000**, *39*, 1204–1215.
[31] R. Rubino, J. M. Williamson, T. A. Miller, *J. Chem. Phys.* **1995**, *103*, 5964–5969.
[32] P. M. Sheridan, M. J. Dick, J.-G. Wang, P. F. Bernath, *J. Phys. Chem. A* **2005**, *109*, 10547–10553.
[33] M. J. Dick, P. M. Sheridan, J.-G. Wang, P. F. Bernath, *J. Chem. Phys.* **2006**, *124*, 174309/1–174309/7.
[34] T. A. Barckholtz, D. E. Powers, T. A. Miller, B. E. Bursten, *J. Am. Chem. Soc.* **1999**, *121*, 2576–2584.
[35] A. J. Marr, F. Grieman, T. C. Steimle, *J. Chem. Phys.* **1996**, *105*, 3930–3937.
[36] S. S. Batsanov, *THEOCHEM* **1999**, *468*, 151–159.
[37] S. C. Tyerman, G. K. Corbett, A. M. Ellis, T. A. Claxton, *THEOCHEM* **1996**, *364*, 107–119.
[38] C. R. Brazier, P. F. Bernath, *J. Chem. Phys.* **1989**, *91*, 4548–4554.
[39] M. A. Anderson, J. S. Robinson, L. M. Ziurys, *Chem. Phys. Lett.* **1996**, *257*, 471–480.
[40] W.-T. Chan, I. P. Hamilton, *Chem. Phys. Lett.* **1998**, *297*, 217–224.
[41] A. El Hammadi, M. El Mouhtadi, H. Cardy, A. Dargelos, *THEOCHEM* **2003**, *624*, 1–11.
[42] C. W. Bauschlicher, S. R. Langhoff, H. Partridge, L. A. Barnes, *J. Chem. Phys.* **1989**, *91*, 2399–2411.
[43] S. Petrie, *Int. J. Mass Spectrom.* **2003**, *227*, 33–46.
[44] W. Kaim, *Chem. Ber.* **1981**, *114*, 3789–3800.
[45] W. Poppitz, E. Uhlig, *J. Organomet. Chem.* **1983**, *244*, C1–C4.
[46] S. Schulz, D. Schuchmann, I. Krossing, D. Himmel, D. Bläser, R. Boese, *Angew. Chem.* **2009**, *121*, 5859–5862; *Angew. Chem. Int. Ed.* **2009**, *48*, 5748–5751.
[47] F. Bonhomme, K. Yvon, P. Fischer, *J. Alloys Compd.* **1992**, *186*, 309–314.
[48] F. Bonhomme, N. T. Stetson, K. Yvon, P. Fischer, A. W. Hewat, *J. Alloys Compd.* **1993**, *200*, 65–68.
[49] R. B. King, *Polyhedron* **2002**, *21*, 2347–2350.
[50] R. Köppe, P. Henke, H. Schnöckel, *Angew. Chem.* **2008**, *120*, 8868–8872; *Angew. Chem. Int. Ed.* **2008**, *47*, 8740–8744.
[51] T. Pankewitz, W. Klopper, P. Henke, H. Schnöckel, *Eur. J. Inorg. Chem.* **2008**, *31*, 4879–4890.
[52] P. G. Jasien, C. E. Dykstra, *Chem. Phys. Lett.* **1984**, *106*, 276–279.
[53] X. Wang, L. Andrews, *J. Phys. Chem. A* **2004**, *108*, 11511–11520.
[54] T. J. Tague, L. Andrews, *J. Phys. Chem.* **1994**, *98*, 8611–8616.
[55] P. G. Jasien, C. E. Dykstra, *J. Am. Chem. Soc.* **1985**, *107*, 1891–1895.
[56] A. V. Nemukhin, I. A. Topol, F. Weinhold, *Inorg. Chem.* **1995**, *34*, 2980–2983.
[57] A. Velasquez, I. Fernández, G. Frenking, G. Merino, *Organometallics* **2007**, *26*, 4731–4736.
[58] Y. Xie, H. F. Schaefer III, E. D. Jemmis, *Chem. Phys. Lett.* **2005**, *402*, 414–421.
[59] O. Mó, M. Yáñez, M. Eckert-Maksić, Z. B. Maksić, I. Alkorta, J. Elguero, *J. Phys. Chem. A* **2005**, *109*, 4359–4365.

[60] M. Westerhausen, M. Gärtner, R. Fischer, J. Langer, L. Yu, M. Reiher, *Chem. Eur. J.* **2007**, *13*, 6292–6306.

[61] a) R. J. Gillespie, E. A. Robinson, *Angew. Chem.* **1996**, *108*, 539–560; *Angew. Chem. Int. Ed. Engl.* **1996**, *35*, 495–514; b) M. Hargittai, *Chem. Rev.* **2000**, *100*, 2233–2301; c) M. Kaupp, *Angew. Chem.* **2001**, *113*, 3642–3677; *Angew. Chem. Int. Ed.* **2001**, *40*, 3534–3565; d) P. Garcia-Fernandez, I. B. Bersuker, J. E. Boggs, *J. Phys. Chem. A* **2007**, *111*, 10409–10415 and literature cited therein.

[62] a) E. F. Hayes, *J. Phys. Chem.* **1966**, *70*, 3740–3742; b) R. L. DeKock, M. A. Peterson, L. K. Timmer, E. J. Baerends, P. Vernooijs, *Polyhedron* **1990**, *9*, 1919–1934.

[63] M. Guido, G. Gigli, *J. Chem. Phys.* **1976**, *65*, 1397–1402.

[64] M. Kaupp, P. v. R. Schleyer, H. Stoll, H. Preuss, *J. Chem. Phys.* **1991**, *94*, 1360–1366.

[65] R. J. Gillespie, S. Noury, J. Pilmé, B. Silvi, *Inorg. Chem.* **2004**, *43*, 3248–3256.

[66] J. Koput, *J. Phys. Chem. A* **2005**, *109*, 4410–4414.

[67] I. S. Lim, Y. S. Lee, *J. Chem. Phys.* **2007**, *126*, 104307 and literature cited therein.

[68] I. Resa, E. Carmona, E. Gutierrez-Puebla, A. Monge, *Science* **2004**, *305*, 1136–1138.

[69] A. Grirrane, I. Resa, A. Rodriguez, E. Carmona, E. Álvarez, E. Gutierrez-Puebla, A. Monge, A. Galindo, D. del Río, R. A. Andersen, *J. Am. Chem. Soc.* **2007**, *129*, 693–703.

[70] Y. Wang, B. Quillian, P. Wei, H. Wang, X.-J. Yang, Y. Xie, R. B. King, P. v. R. Schleyer, H. F. Schaefer III, G. H. Robinson, *J. Am. Chem. Soc.* **2005**, *127*, 11944–11945.

[71] S. Schulz, D. Schuchmann, U. Westphal, M. Bolte, *Organometallics* **2009**, *28*, 1590–1592.

[72] I. L. Fedushkin, A. A. Skatova, S. Y. Ketkov, O. V. Eremenko, A. V. Piskunov, G. K. Fukin, *Angew. Chem.* **2007**, *119*, 4380–4383; *Angew. Chem. Int. Ed.* **2007**, *46*, 4302–4305.

[73] Y. Liu, S. Li, X.-J. Yang, P. Yang, J. Gao, Y. Xia, B. Wu, *Organometallics* **2009**, *28*, 5270–5272.

[74] Y.-C. Tsai, D.-Y. Lu, Y.-M. Lin, J.-K. Hwang, J.-S. K. Yu, *Chem. Commun.* **2007**, 4125–4127.

[75] Z. Zhu, R. J. Wright, M. M. Olmstead, E. Rivard, M. Brynda, P. P. Power, *Angew. Chem.* **2006**, *118*, 5939–5942; *Angew. Chem. Int. Ed.* **2006**, *45*, 5807–5810.

[76] Z. Zhu, M. Brynda, R. J. Wright, R. C. Fischer, W. A. Merrill, E. Rivard, R. Wolf, J. C. Fettinger, M. M. Olmstead, P. P. Power, *J. Am. Chem. Soc.* **2007**, *129*, 10847–10857.

[77] X.-J. Yang, J. Yu, Y. Liu, Y. Xie, H. F. Schaefer III, Y. Liang, B. Wu, *Chem. Commun.* **2007**, 2363–2365.

[78] J. Yu, X.-J. Yang, Y. Liu, Z. Pu, Q.-S. Li, Y. Xie, H. F. Schaefer, B. Wu, *Organometallics* **2008**, *27*, 5800–5805.

[79] S. P. Green, C. Jones, A. Stasch, *Science* **2007**, *318*, 1754–1757.

[80] M. Westerhausen, *Angew. Chem.* **2008**, *120*, 2215–2217; *Angew. Chem. Int. Ed.* **2008**, *47*, 2185–2187.

[81] J. Emsley, *The Elements*, 2nd ed., Clarendon, Oxford, **1995**.

[82] S. Harder, J. Brettar, *Angew. Chem.* **2006**, *118*, 3554–3558; *Angew. Chem. Int. Ed.* **2006**, *45*, 3474–3478.

[83] J. Spielmann, S. Harder, *Chem. Eur. J.* **2007**, *13*, 8928–8938.

[84] J. Overgaard, C. Jones, A. Stasch, B. B. Iversen, *J. Am. Chem. Soc.* **2009**, *131*, 4208–4209.

[85] S. P. Green, C. Jones, A. Stasch, *Angew. Chem.* **2008**, *120*, 9219–9223; *Angew. Chem. Int. Ed.* **2008**, *47*, 9079–9083.

[86] D. Schuchmann, U. Westphal, S. Schulz, U. Flörke, D. Bläser, R. Boese, *Angew. Chem.* **2009**, *121*, 821–824; *Angew. Chem. Int. Ed.* **2009**, *48*, 807–810.

[87] A. Datta, *J. Phys. Chem. C* **2008**, *112*, 18727–18729.

[88] Y. Yu, A. R. Sadique, J. M. Smith, T. R. Dugan, R. E. Cowley, W. W. Brennessel, C. J. Flaschenriem, E. Bill, T. R. Cundari, P. L. Holland, *J. Am. Chem. Soc.* **2008**, *130*, 6624–6638.

[89] S. J. Bonyhady, S. P. Green, C. Jones, S. Nembenna, A. Stasch, *Angew. Chem.* **2009**, *121*, 3017–3021; *Angew. Chem. Int. Ed.* **2009**, *48*, 2973–2977.

[90] Y. Liu, S. Li, X.-J. Yang, P. Yang, B. Wu, *J. Am. Chem. Soc.* **2009**, *131*, 4210–4211.

[91] Y. Liu, P. Yang, J. Yu, X.-J. Jang, J. D. Zhang, Z. Chen, H. F. Schaefer, B. Wu, *Organometallics* **2008**, *27*, 5830–5835.

[92] a) N. Emery, C. Hérold, M. d'Astuto, V. Garcia, C. Bellin, J. F. Marêché, P. Lagrange, G. Loupias, *Phys. Rev. Lett.* **2005**, *95*, 087003/1–087003/4; b) N. Emery, C. Hérold, P. Lagrange, *J. Solid State Chem.* **2005**, *178*, 2947–2952; c) T. E. Weller, M. Ellerby, S. S. Saxena, R. P. Smith, A. N. T. Skipper, *Nat. Phys.* **2005**, *1*, 39–41.

[93] S. Deng, A. Simon, J. Köhler, *Angew. Chem.* **2008**, *120*, 6805–6808; *Angew. Chem. Int. Ed.* **2008**, *47*, 6703–6706.

[94] S. Deng, A. Simon, J. Köhler, *Solid State Sci.* **2000**, *2*, 31–38.

[95] a) E. Broclawik, A. Eilmes, *J. Chem. Phys.* **1998**, *108*, 3498–3503; b) E. B. Starikov, *Int. J. Quantum Chem.* **1998**, *69*, 201–208.

[96] See also, e.g., K. Prassides (Ed.), *Structure and Bonding Vol. 109: Fullerene-Based Materials* (Series Ed.: D. M. P. Mingos), Springer, Heidelberg, **2004**.

[97] Y. L. Zhao, C. S. Lin, R. Q. Zhang, R. S. Wang, *J. Chem. Phys.* **2005**, *122*, 194322/1–194322/6.

[98] S. L. Sun, C. S. Lin, R. Q. Zhang, C. S. Lee, S. T. Lee, *J. Phys. Chem. B* **2005**, *109*, 12868–12873.

[99] The authors[98] show a presentation (**X**), which, in our opinion, does not seem to characterize the described bonding situation. An extremely large torsion angle C1–C2=C3–C4 and a C2=C3 double bond length of 156 pm are contradictory to the presented formula. Therefore, we suggest depiction **Y**, which would be in accordance with the following calculated findings: short Ca–Ca contact, C2–C3 single bond, C2–C1–C6 and C3–C4–C5 allylic systems.
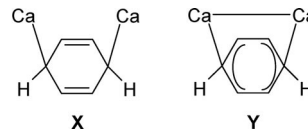
[100] A. Gapeev, R. C. Dunbar, *J. Phys. Chem. A* **2000**, *104*, 4084–4088.

[101] J. Cheng, W. Zhu, Y. Tang, Y. Xu, Z. Li, K. Chen, H. Jiang, *Chem. Phys. Lett.* **2006**, *422*, 455–460.

[102] Y.-H. Cheng, L. Liu, Y. Fu, R. Chen, X.-S. Li, Q.-X. Guo, *J. Phys. Chem. A* **2002**, *106*, 11215–11220.

[103] W. Zhu, X. Tan, J. Shen, X. Luo, F. Cheng, P. C. Mok, R. Ji, K. Chen, H. Jiang, *J. Phys. Chem. A* **2003**, *107*, 2296–2303.

[104] A. S. Reddy, H. Zipse, G. N. Sastry, *J. Phys. Chem. B* **2007**, *111*, 11546–11553.

[105] S. Tsuzuki, T. Uchimaru, M. Mikami, *J. Phys. Chem. A* **2003**, *107*, 10414–10418.

[106] H. S. Kang, *J. Phys. Chem. A* **2005**, *109*, 1458–1467.

[107] M. N. Bochkarev, *Coord. Chem. Rev.* **2004**, *248*, 835–851.

[108] F. G. N. Cloke, K. Khan, R. N. Perutz, *J. Chem. Soc., Chem. Commun.* **1991**, 1372–1373.

[109] P. L. Arnold, F. G. N. Cloke, J. F. Nixon, *Chem. Commun.* **1998**, 797–798.

[110] B. Bogdanović, *Acc. Chem. Res.* **1988**, *21*, 261–267.

[111] L. E. Aleandri, *Active Met.* **1996**, 299–338.

[112] B. Bogdanović, N. Janke, C. Krüger, R. Mynott, K. Schlichte, U. Westeppe, *Angew. Chem.* **1985**, *97*, 972–974; *Angew. Chem. Int. Ed. Engl.* **1985**, *24*, 960–962.

[113] H. Bönnemann, B. Bogdanović, R. Brinkmann, N. Egeler, R. Benn, I. Topalovic, K. Seevogel, *Main Group Met. Chem.* **1990**, *13*, 341–362.

[114] D. F. Lindow, C. N. Cortez, R. G. Harvey, *J. Am. Chem. Soc.* **1972**, *94*, 5406–5412.

[115] H. M. Walborsky, C. Hamdouchi, *J. Org. Chem.* **1993**, *58*, 1187–1193.

[116] I. L. Fedushkin, T. V. Petrovskaya, M. N. Bocharev, S. Dechert, H. Schumann, *Angew. Chem.* **2001**, *113*, 2540–2543; *Angew. Chem. Int. Ed.* **2001**, *40*, 2474–2477.

[117] I. L. Fedushkin, Y. A. Kurskii, V. I. Nevodchikov, M. N. Bocharev, S. Muehle, H. Schumann, *Russ. Chem. Bull. Int. Ed.* **2002**, *51*, 160–169.

[118] I. L. Fedushkin, A. N. Lukoyanov, S. Dechert, H. Schumann, *Eur. J. Inorg. Chem.* **2004**, 2421–2424.

[119] S. Krieck, H. Görls, L. Yu, M. Reiher, M. Westerhausen, *J. Am. Chem. Soc.* **2009**, *131*, 2977–2985.

[120] J. D. Smith, *Angew. Chem.* **2009**, *121*, 6721–6723; *Angew. Chem. Int. Ed.* **2009**, *48*, 6597–6599.

[121] M. Westerhausen, *Z. Anorg. Allg. Chem.* **2009**, *635*, 13–32.

[122] S. Krieck, H. Görls, M. Westerhausen, *J. Organomet. Chem.* **2009**, *694*, 2204–2209.

[123] Y. C. Lin, D. E. Williams, *Acta Crystallogr., Sect. B* **1975**, *31*, 318–320.

[124] R. Fischer, M. Gärtner, H. Görls, M. Reiher, M. Westerhausen, *Angew. Chem.* **2007**, *119*, 1642–1647; *Angew. Chem. Int. Ed.* **2007**, *46*, 1618–1623.

[125] M. Westerhausen, M. Gärtner, R. Fischer, J. Langer, *Angew. Chem.* **2007**, *119*, 1994–2001; *Angew. Chem. Int. Ed.* **2007**, *46*, 1950–1956.

[126] M. Westerhausen, *Coord. Chem. Rev.* **2008**, *252*, 1516–1531.

[127] M. Gärtner, H. Görls, M. Westerhausen, *Synthesis* **2007**, 725–730.

[128] S. Krieck, H. Görls, M. Westerhausen, **2009**, manuscript in preparation.

[129] C. Buchin, C. Gemel, T. Cadenbach, R. Schmid, R. A. Fischer, *Angew. Chem.* **2006**, *118*, 1091–1093; *Angew. Chem. Int. Ed.* **2006**, *45*, 1074–1076. Corrigendum: C. Buchin, C. Gemel, T. Cadenbach, R. Schmid, R. A. Fischer, *Angew. Chem.* **2006**, *118*, 1703; *Angew. Chem. Int. Ed.* **2006**, *45*, 1674.

[130] J. N. Jones, C. L. B. Macdonald, J. D. Gorden, A. H. Cowley, *J. Organomet. Chem.* **2003**, *666*, 3–5.

[131] S. Dagorne, D. A. Atwood, *Chem. Rev.* **2008**, *108*, 4037–4071.

[132] P. L. Diaconescu, P. L. Arnold, T. A. Baker, D. J. Mindiola, C. C. Cummins, *J. Am. Chem. Soc.* **2000**, *122*, 6108–6109.

[133] Computational Methodology: All DFT calculations reported here in addition to our original results from ref.[60] and ref.[119] were performed with the quantum chemical program package Turbomole.[134] For a comparison of various quantum chemical methods, we may refer to our previous work.[119] On the basis of these results, we applied the B97–D[135] and BP86[136,137] density functionals in combination with the resolution-of-the-identity ("RI") density-fitting technique with Ahlrichs' auxiliary basis sets.[138] For the heavy alkaline earth metals, a Stuttgart effective core potential (ECP) has been employed,[139] which also takes care of scalar relativistic effects.[140] Throughout we employed the large TZVPP basis sets based on the TZV core by Schäfer et al. and supplemented by polarization functions by Dunning and co-workers[141,142] (in case of ECPs, the denomination TZVPP refers to reoptimized basis sets by the Karlsruhe group). The molecular structures were visualized with the program Pymol,[143] and we used the program Molekel[144] to visualize the molecular orbitals.

[134] R. Ahlrichs, M. Bär, M. Häser, H. Horn, C. Kölmel, *Chem. Phys. Lett.* **1989**, *162*, 165–169.

[135] S. Grimme, *J. Comput. Chem.* **2004**, *25*, 1463–1473.

[136] A. D. Becke, *Phys. Rev. A* **1988**, *38*, 3098–3100.

[137] J. P. Perdew, *Phys. Rev. B* **1986**, *33*, 8822–8824.

[138] ftp://ftp.chemie.uni-karlsruhe.de/pub/basen.

[139] M. Kaupp, P. v. R. Schleyer, H. Stoll, H. Preuss, *J. Chem. Phys.* **1991**, *94*, 1360–1366.

[140] M. Reiher, A. Wolf, *Relativistic Quantum Chemistry*, Wiley-VCH, Weinheim, **2009**.

[141] A. Schäfer, C. Huber, R. Ahlrichs, *J. Chem. Phys.* **1994**, *100*, 5829–5835.

[142] T. H. Dunning, *J. Chem. Phys.* **1989**, *90*, 1007–1023.

[143] http://pymol.sourceforge.net/.

[144] http://www.cscs.ch/molekel/.

Polyol-Mediated Synthesis of Highly Water-Soluble ZnO Colloidal Nanocrystal Clusters

Chunguang Li,[a] Ying Zhao,[a] Ling Wang,[a] Guanghua Li,[a] Zhan Shi,*[a] and Shouhua Feng[a]

We report on the synthesis of ZnO colloidal nanocrystal clusters with well-tunable particle size and high water solubility by using a high-temperature solution-phase hydrolysis approach. The metal salt hydrolyzed after rapidly injecting a solution of sodium hydroxide in diethylene glycol. Poly-(acrylic acid) served as the capping agent to achieve the superior water solubility without any further surface modification. Strong UV emission in the photoluminescence (PL) spectrum due to the existence of the secondary structures despite a particle size reaching ca. 200 nm, and near absence of oxygen vacancy in the sample as indicated by weak emission in the green region. This important feature makes our highly water-soluble ZnO colloidal nanocrystal clusters a promising candidate for potential applications in optoelectronic and lasing devices.

Introduction

Highly monodisperse colloidal nanocrystals have been intensively pursued as a result of their significance in basic research and practical applications. Recent advances in this research field appear to shift from the traditional preparation of high-quality nanocrystals with well-controlled size or shape to the creation of secondary structures of nanocrystals, either by self-assembly or through direct solution growth.[1–5] This research trend has been evidenced by plenty of interesting works published in the past several years.[6–11] Manipulation of the secondary structures of nanocrystals leads to fine-tuned interactions between the submits and enhances the possibility to tune collective properties eventually. As one of the group II-VI semiconductors, ZnO has attracted increasing attention recently owing to its nontoxicity and chemical stability towards air, especially in its diverse optoelectronic applications. ZnO is a direct-band gap semiconductor with a wide band gap of 3.37 eV and a large exciton binding energy of 60 meV. This strong exciton binding energy can ensure the efficient UV blue emission at room temperature. Many approaches have been developed for the synthesis of ZnO nanostructures with versatile morphologies, typically 1D or branched structures owing to the intrinsic nature of polar hexagonal-phase ZnO.[12–18] Several studies have explored how poly-mer composition and concentration affect precipitation and crystallization. For example, Wegner[19] and Taubert[20] fabricated various ZnO nanostructures in the presence of water-soluble carbohydrates or copolymers and discussed the kinetics and particle formation mechanism. More recently, aggregation of ZnO nanocrystallites involving secondary structures were fabricated in nonpolar solvents or polyol systems.[21,22] Despite the success in ZnO nanostructure synthesis, there are very few approaches capable of producing superior water-soluble ZnO colloids without any further surface modification. In this paper, we describe a polyol-mediated process for the synthesis of highly water-dispersible ZnO colloidal nanocrystal clusters (CNCs) with uniform sizes ranging from about 60 nm to 180 nm, each of which is composed of many single ZnO crystallites approximately 5 nm in size. The strong UV emission and very weak emission in the green region in the photoluminescence (PL) spectrum are a result of the existence of secondary structures. The weak green emission indicates nearly absence of oxygen vacancy in our samples. It is a very important feature and difficult to achieve through other synthetic methodologies.

Results and Discussion

Highly water-soluble ZnO CNCs with various sizes were synthesized by means of high-temperature hydrolysis reaction of Zn^{II} acetate (0.4 mmol) in 16 mL of diethylene glycol solution (DEG, boiling point ca. 244–245 °C) with poly(acrylic acid) (PAA) (6 mmol) as the surfactant. An NaOH/DEG (2.5 mol/L, 2.05 mL) stock solution was in-

[a] State Key Laboratory of Inorganic Synthesis and Preparative Chemistry, College of Chemistry, Jilin University
Qianjin Street 2699, Changchun, Jilin 130012, P. R. China
Fax: +86-431-85168624
E-mail: zshi@mail.jlu.edu.cn

C. Li, Y. Zhao, L. Wang, G. Li, Z. Shi, S. Feng

jected rapidly into the hot mixture, and the temperature dropped to about 200 °C instantly. The reaction solution slowly turned turbid within 2 min and then was further heated at 210 °C under nitrogen protection for 1 h. The products were cooled to room temperature, cleaned three times by precipitation with ethanol followed by centrifugation at 11000 rpm and finally dispersed in distilled water to yield about 89 nm ZnO CNCs (shown in Figure 1a). DEG could easily dissolve a variety of polar inorganic materials owing to its high permittivity ($\varepsilon = 32$).[23] The key point in our synthesis is to use PAA as the surfactant. It shows very strong coordination of carboxylate groups with zinc cations on ZnO surface, and the uncoordinated carboxylate groups on the polymer chains extend into aqueous solution conferring upon the particles a high degree of dispensability in water (Figure 1b). An additional benefit of uncoordinated carboxylate groups is to provide conjunction points for further attachment of other materials. The purpose of introducing NaOH into the hot mixture was to produce water molecules and to increase the alkalinity of the reaction system. Both results favor the hydrolysis of $Zn(OAc)_2$.
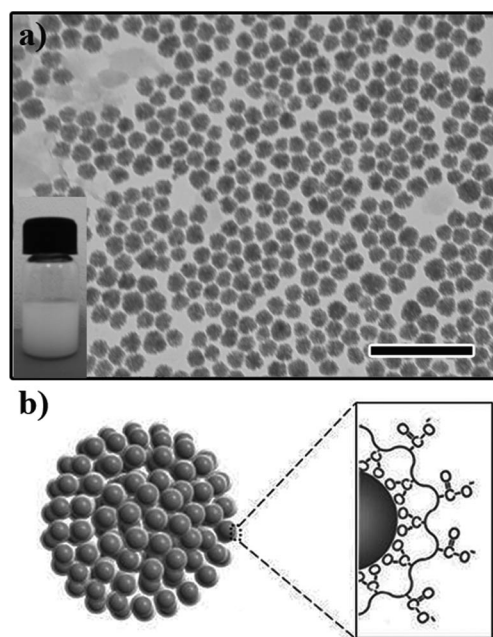
Figure 1. (a) TEM image of ZnO CNCs (inset: photograph of colloidal crystals dispersed in water); (b) schematic illustration of PAA-capped ZnO colloidal nanocrystal clusters. Scale bar: 500 nm.

The size of CNCs can be conveniently tuned from about 60 nm to about 180 nm by simply varying the amount of NaOH without changing other reaction parameters (Figure 2). It has been noticed that more NaOH in the system leads to higher H_2O concentration, and stronger alkalinity could accelerate the hydrolysis reaction and promote the formation of larger-size clusters. As demonstrated in Figure 2a–e, amounts of NaOH/DEG stock solution of 2.0, 2.05, 2.10, 2.15, 2.20 mL lead to CNCs with average sizes of 68 (sample 1), 89 (sample 2), 126 (sample 3), 152 (sample 4) and 180 nm (sample 5), respectively. More NaOH in this

system would result in poor uniformity and wide size distribution. The composition of the as-prepared CNCs was characterized by X-ray diffraction (XRD). The XRD pattern (Figure 2f) indicates that the product has a wurtzite structure (JCPDS 79-2205).
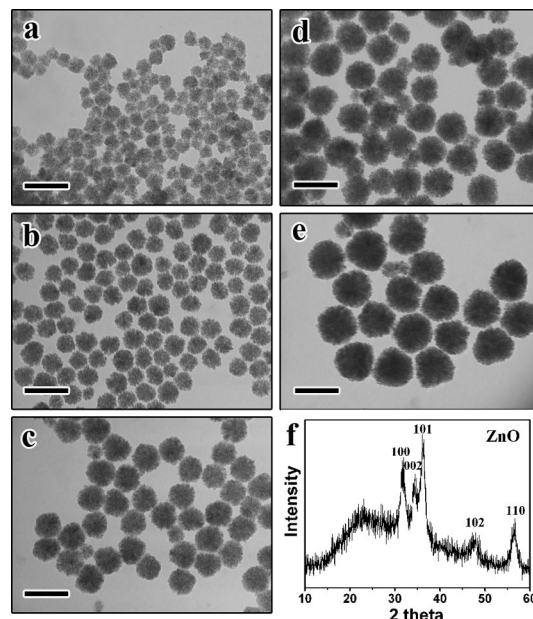
Figure 2. Representative TEM images of ZnO CNCs at the same magnification. Average diameters of the CNCs, obtained by measuring about 100 clusters for each sample, illustrated by sample 1 (a), sample 2 (b), sample 3 (c), sample 4 (d) and sample 5 (e). All scale bars are 200 nm.

The well-documented two-stage growth model may also be fit for the growth of ZnO colloidal nanocrystal clusters, in which the primary ZnO nanocrystals first nucleate in the supersaturated solution, and then under optimized conditions, these nanocrystals spontaneously aggregate into larger flowerlike three-dimensional clusters.[24] Close inspection of the high-magnification TEM image of the 68 nm cluster (Figure 3a) confirms that the monodisperse colloidal sphere consists of many small primary nanocrystals. Its corresponding electron diffraction (ED) pattern is shown in Figure 3b, revealing the single-crystal-like diffraction. The narrow diffraction arcs indicate slight misalignments among the primary nanocrystals. The secondary structure of the cluster can be clearly observed in a typical HRTEM image (Figure 3c). The cluster is composed of many primary nanocrystals with sizes of about 5 nm. Meanwhile, energy-dispersive X-ray (EDX) analysis further confirms the local element composition of the ZnO CNCs (Supporting Information S1).

Fourier transform infrared (FTIR) spectroscopy was performed to characterize the stability of the PAA coating on the surface of ZnO CNCs. The multiple bands between 1200 and 1600 cm^{-1} shown in Figure 4a can be assigned to various vibrational modes of PAA, and the strong adsorption band at ca. 1717 cm^{-1} is characteristic of the C=O
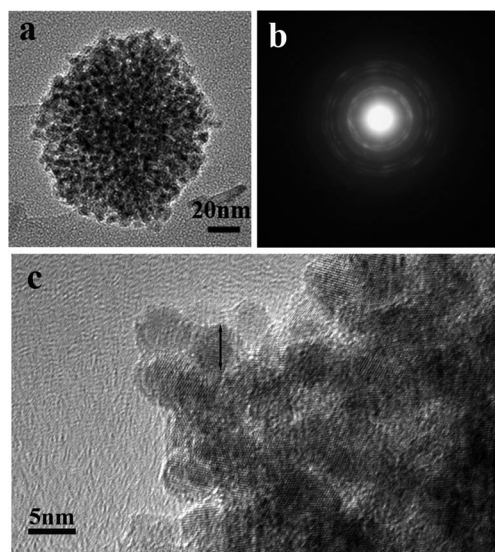
Figure 3. (a) High-magnification TEM image of a single ZnO CNC of sample 1. (b) ED pattern of the cluster. (c) Typical HRTEM image of a cluster of sample 1.

Figure 4. FT-IR spectrum of (a) pure PAA and (b) PAA carboxylate capped ZnO CNC.

stretching mode for protonated carboxylate groups. For comparison, in Figure 4b, the three peaks located at 1455, 1586 and 1415 cm^{-1} can be attributed to the characteristic bands of the carboxylate (COO$^-$) groups, corresponding to the CH$_2$ bending mode, asymmetric and symmetric C–O stretching modes of the COO$^-$ group, respectively.[25,26] A comparison of these two spectra shows clearly that many carboxylate groups remain on the surface of nanocrystals even after excessive washing.

The UV/Vis absorption spectra and the room-temperature PL spectrum of the ZnO CNCs are shown in Figure 5. The onset of absorption is at around 360 nm, somewhat blueshifted from that of bulk ZnO (373 nm). The fact that almost no absorption tail at wavelengths longer than 380 nm could be observed indicates that no colloidal dispersion scattered light exists. The obtained ZnO CNCs show a strong UV emission at around 377 nm, which is attributed to the near band-edge emission coming from the recombination of excitons. The UV emission peak shows a similar profile by changing the excitation wavelength, which is a characteristic feature of bandedge emission. Slight redshift from small ZnO CNCs to large ones was also observed (Supporting Information S2). Weak emissions in the green region, which originate from singly ionized oxygen vacancies and other point defects, are detected (Figure 5).[27] The very weakness of the commonly encountered green emission in the PL spectrum indicates the near absence of oxygen vacancy in our samples. In the previously reported ZnO nanostructures, the UV emission of them is liable to be quenched, and only defect emission in the Vis region is detected. This deficiency hinders progress in the applications of ZnO in optoelectronic and lasing devices. Therefore, our highly water-soluble ZnO CNCs with strong UV emission could be a promising candidate for potential applications in optoelectronic and lasing devices.
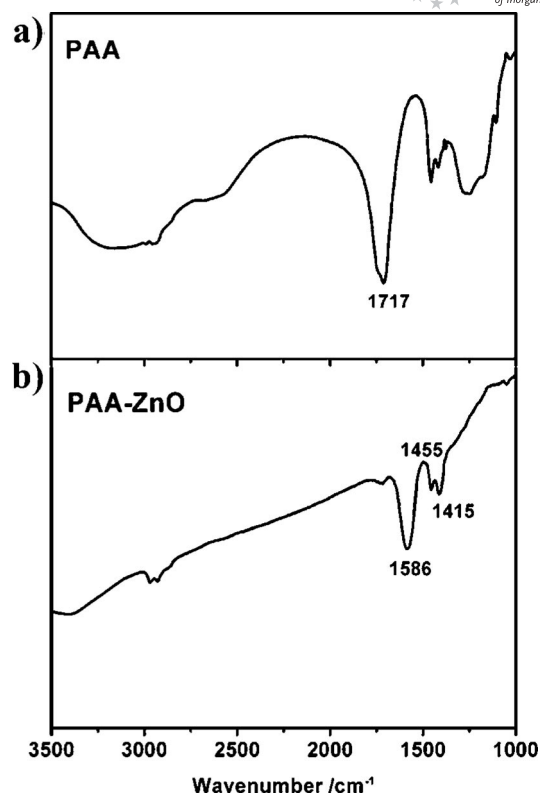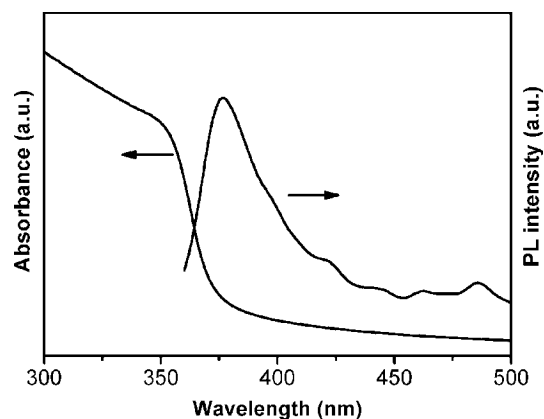
Figure 5. UV/Vis absorption and room-temperature PL spectra (λ = 350 nm) of ZnO CNC (sample 1) dispersed in disionzied water.

Conclusions

We have reported here a polyol-mediated route for the size-controlled production of highly water-soluble ZnO colloidal nanocrystal clusters composed of small primary nanocrystals. The size of the ZnO CNCs can be conveniently tuned from about 60 nm to 180 nm by simply changing the amount of NaOH. The high water solubility is achieved by using PAA as the capping agent. The carboxylate group partially binds to the surface of the CNCs and partially extends into water. The CNCs show strong UV

emission, and very weak defect emission in the Vis region at room temperature, which could possibly be applied for optoelectronic and lasing devices in the future.

Experimental Section

The CNCs were synthesized by means of high-temperature hydrolysis reactions. An NaOH/DEG stock solution was first prepared by dissolving NaOH (50 mmol) in DEG (25 mL); this solution was heated under nitrogen at 120 °C for 1 h, and kept at 70 °C in an oven. In a typical synthesis, Zn^{II} acetate (0.4 mmol), DEG (16 mL) and PAA (6 mmol) were mixed together, the mixture was heated to 210 °C under protective nitrogen. The NaOH/DEG (2.05 mL) stock solution was injected rapidly into the hot mixture, and the temperature dropped to about 200 °C instantly. The reaction solution slowly turned turbid within 2 min and then was further heated at 210 °C for 1 h. The products were cooled to room temperature to yield about 89 nm ZnO CNCs. The amount of NaOH/DEG solution determines the size of CNCs. For instance, amounts of the stock solution of 2.0, 2.05, 2.10, 2.15, 2.20 mL lead to CNCs with average sizes of 68 (sample 1), 89 (sample 2), 126 (sample 3), 152 (sample 4) and 180 nm (sample 5), respectively. The final product was cleaned three times by precipitation with ethanol followed by centrifugation at 11000 rpm and finally dispersion in distilled water. Powder X-ray diffraction (XRD) analysis was performed with a Rigaku D/max-2500 diffractometer with a graphite monochromator by using Cu-K_α radiation operating at 200 mA and 40 kV. XRD data were collected over the range of 10–60° (2θ) with a step interval of 0.02° and a preset time of 1.6 s per step at room temperature. Transmission electron microscopy (TEM), high-resolution transmission eletron microscopic (HRTEM) images and EDX spectra were performed with a JEM-3010 electron microscope equipped with an X-ray energy-dispersive spectroscopy system. IR spectra were acquired with a Bruker IFS 66v/S FTIR spectrometer, whereas UV/Vis absorption spectra and the room-temperature PL spectra of the CNC samples were performed with a UV-2450 spectrophotometer (Shimadzu, Japan) and a Perkin–Elmer LS55 fluorometer.

Supporting Information (see footnote on the first page of this article): EDX, UV/Vis, and PL spectra for samples 1–5.

Acknowledgments

[1]   Y. Yin, A. P. Alivisatos, *Nature* **2005**, *437*, 664–670.
[2]   Z. A. Peng, X. Peng, *J. Am. Chem. Soc.* **2002**, *124*, 3343–3353.
[3]   Y. Sun, Y. Xia, *Science* **2002**, *298*, 2176–2179.
[4]   X. Wang, J. Zhuang, Q. Peng, Y. D. Li, *Nature* **2005**, *437*, 121–124.
[5]   M. P. Pileni, *Nat. Mater.* **2003**, *2*, 145–150.
[6]   A. Narayanaswamy, H. Xu, N. Pradhan, X. Peng, *Angew. Chem.* **2006**, *118*, 5487; *Angew. Chem. Int. Ed.* **2006**, *45*, 5361–5364.
[7]   E. V. Shevchenko, D. V. Talapin, N. A. Kotov, S. O'Brien, C. B. Murray, *Nature* **2006**, *439*, 55–59.
[8]   L. M. Dillenback, G. P. Goodrich, C. D. Keating, *Nano Lett.* **2006**, *6*, 16–23.
[9]   J. Lee, A. O. Govorov, N. A. Kotov, *Angew. Chem.* **2005**, *117*, 7605–7608; *Angew. Chem. Int. Ed.* **2005**, *44*, 7439–7442.
[10] J. E. Halpert, V. J. Porter, J. P. Zimmer, M. G. Bawendi, *J. Am. Chem. Soc.* **2006**, *128*, 12590–12591.
[11] J. P. Ge, Y. X. Hu, M. Biasini, W. P. Beyermann, Y. D. Yin, *Angew. Chem. Int. Ed.* **2007**, *46*, 4342–4345.
[12] a) M. H. Huang, S. Mao, H. Feick, H. Q. Yan, Y. Y. Wu, H. Kind, E. Weberm, R. Russo, P. D. Yang, *Science* **2001**, *292*, 1897–1899; b) Z. L. Wang, J. H. Song, *Science* **2006**, *312*, 242–246.
[13] N. Pinna, G. Garnweitner, M. Antonietti, M. Niederberger, *J. Am. Chem. Soc.* **2005**, *127*, 5608–5612.
[14] a) R. Q. Song, A. W. Xu, B. Deng, Q. Li, G. Y. Chen, *Adv. Funct. Mater.* **2007**, *17*, 296–306; b) Y. Peng, A. W. Xu, B. Deng, M. Antonietti, H. Colfen, *J. Phys. Chem. B* **2006**, *110*, 2988–2993.
[15] a) M. S. Mo, S. H. Lim, Y. W. Mai, R. K. Zheng, S. P. Ringer, *Adv. Mater.* **2008**, *20*, 339–342; b) M. S. Mo, J. C. Yu, L. Z. Zhang, S. K. A. Li, *Adv. Mater.* **2005**, *17*, 756–760.
[16] B. Liu, H. C. Zeng, *J. Am. Chem. Soc.* **2004**, *126*, 16744–16746.
[17] a) B. Liu, H. C. Zeng, *Chem. Mater.* **2007**, *19*, 5824–5826; b) Q. F. Zhang, T. P. Chou, B. Russo, S. A. Jenekhe, G. Z. Cao, *Angew. Chem. Int. Ed.* **2008**, *47*, 2402–2406.
[18] L. Spanhel, *J. Sol-Gel Sci. Technol.* **2006**, *39*, 7–24.
[19] a) J. Norwig, W. H. Meyer, G. Wegner, *Chem. Mater.* **1998**, *10*, 460–463; b) G. Wegner, P. Baum, M. Müller, J. Norwig, K. Landfester, *Macromol. Symp.* **2001**, *175*, 349–355.
[20] a) D. Mumalo-Djokic, W. B. Stern, A. Taubert, *Cryst. Growth Des.* **2008**, *8*, 330–335; b) A. Taubert, G. Wegner, *J. Mater. Chem.* **2002**, *12*, 805–807; c) A. Taubert, G. Glasser, D. Palms, *Langmuir* **2002**, *18*, 4488–4494; d) A. Taubert, C. Ku1bel, D. C. Martin, *J. Phys. Chem. B* **2003**, *107*, 2660–2666.
[21] J. Joo, S. G. Kwon, J. H. Yu, T. Hyeon, *Adv. Mater.* **2005**, *17*, 1873–1877.
[22] X. L. Hu, J. M. Gong, L. Z. Zhang, J. C. Yu, *Adv. Mater.* **2008**, *20*, 4845–4850.
[23] a) C. Feldmann, *Adv. Mater.* **2001**, *13*, 1301–1303; b) C. Feldmann, H. O. Jungk, *Angew. Chem. Int. Ed.* **2001**, *40*, 359–362; c) C. Feldmann, *Adv. Funct. Mater.* **2003**, *13*, 101–107.
[24] S. Libert, V. Gorshkov, D. Goia, E. Matijevi, V. Privman, *Langmuir* **2003**, *19*, 10679–10683.
[25] D. H. Lee, R. A. Condrate, J. S. Reed, *J. Mater. Sci.* **1996**, *31*, 471–478.
[26] H. Li, C. P. Tripp, *Langmuir* **2005**, *21*, 2585–2590.
[27] K. Vanheusden, W. L. Warren, C. H. Seager, D. R. Tallant, J. A. Voigt, B. E. Gnade, *J. Appl. Phys.* **1996**, *79*, 7983–7990.

On the Spin Behaviour of Iron(II)–Dipyridyltriazine Complexes and Their Performance as Thermal and Photonic Spin Switches

Sophie K. Hain,[a] Frank W. Heinemann,[b] Klaus Gieb,[c] Paul Müller,[c] Gerald Hörner,*[d] and Andreas Grohmann*[a]

The temperature-dependent and photodynamic spin behaviour of three iron(II) complexes with different 2,6-dipyridyl-4-phenyltriazine ligands **L1**–**L3** was investigated in the solid state and in solution (DMSO). The ligands differ in the substituent R in the 4-position of the phenyl ring (**L1**: R = H; **L2**: R = OCH_3; **L3**: R = SAc), which allows the electronic properties of the ligands to be finetuned. The magnetic data for the complex $[Fe(\mathbf{L3})_2](BF_4)_2$ in the solid state indicate an incomplete spin transition to the high-spin form upon warming from liquid helium temperature, reaching about 30 % at 400 K. There is circumstantial evidence for paramagnetic contributions compatible with spin transitions, namely, temperature-dependent NMR spectroscopic line shifts and line broadening in solution (DMSO). However, an efficient thermally induced spin crossover in solution is hindered by the substitution lability of the complexes, as has been detected and analyzed in an extended temperature-dependent UV/Vis spectroscopic study. Essentially unaffected by thermally induced substitution lability, the transient dynamics of the iron(II) complexes after nanosecond laser flash excitation of their metal-to-ligand charge-transfer bands provide good evidence for efficient photoinduced spin transitions in solution in all cases. The range of measured lifetimes of the high-spin quintet states is in accord with previously published data. Importantly, in our series of iron(II) complexes, the lifetimes of the high-spin state reflect the electron-donating character of the ligands.

Introduction

Iron(II) complexes of the imine chelators 2,2′-bipyridine (bpy), phenanthroline (phen) or 2,2′:6′,2′′-terpyridine (trpy) and derivatives thereof have been studied in detail to correlate ligand properties with the observed spin behaviour, both in solution and in the solid state.[1,2] Depending on the substitution patterns, the nature of the substituents and modifications of the aromatic system, the resulting $[FeN_6]^{2+}$ complexes can be low spin ($^1A_{1g}/t_{2g}^6$), high spin ($^5T_{2g}/t_{2g}^4e_g^2$) or have a ligand field of intermediate strength enabling thermal spin crossover [Equation (1)]. Iron(II) complexes of the parent ligand 2,2′:6′,2′′-terpyridine are low spin in the solid state, but photoexcitation of the perchlorate salt [in a matrix of the corresponding manga-

nese(II) complex] has been shown to produce a long-lived (at $T < 20$ K) high-spin form.[3] Temperature- or pressure-induced spin crossover in solution is documented for complexes of suitably substituted trpy ligands [Equation (1)].[4]

$$\text{low spin} \xrightleftharpoons{\Delta T \text{ or } h\nu} \text{high spin} \tag{1}$$

We are currently working to derivatize bis(triimine)–iron(II) complexes in such a way as to make them attachable to gold surfaces in order to use their potential bistability in switching devices. In an alternative approach, composites of nanoparticulate titania and iron(II) complexes were reported to act as photoelectrochemical switches with a possible application as chemical logic devices.[5] Whereas the latter approach involves physisorption of the iron(II) complex, our approach uses chemisorption and requires the modification of ligands with suitable anchor groups, such as thiol,[6] thiocyanate[7] or thioacetate.[8] In pyridine-based ligands, the most logical point for appending a linker is the ligand apex, that is, the *para* position of the central ring. Whereas any such derivatization of the trpy ligand is difficult, analogous ligands having a 1,3,5-triazine core may be prepared in a modular fashion, with a potentially wide range of substituents in the 4-position.[9] A study of the effect of structural variations in such ligands on the spin behaviour of their iron(II) complexes has recently been re-

[a] Institut für Chemie, Technische Universität Berlin,
Straße des 17. Juni 135, 10623 Berlin, Germany
Fax: +49-30-314-22935
E-mail: andreas.grohmann@chem.tu-berlin.de
[b] Department Chemie und Pharmazie, Universität Erlangen-Nürnberg,
Egerlandstraße 1, 91058 Erlangen, Germany
[c] Department Physik, Universität Erlangen-Nürnberg,
Erwin-Rommel-Straße 1, 91058 Erlangen, Germany
[d] Faculty of Chemistry, Adam Mickiewicz University of Poznań,
Grunwaldzka 6, 60-780 Poznań, Poland
Fax: +48-61-829-1505
E-mail: hoerner@amu.edu.pl
☐ Supporting information for this article is available on the WWW under http://dx.doi.org/10.1002/ejic.200900588.

ported.[10] Parallel work on ruthenium complexes of such ligands underscored the importance of the ligand-substitution pattern for the excited-state dynamics.[9] It is in this context that we have studied the iron complexes of the three 2,4-dipyridyltriazine ligands **1**, **3** and **4** (Scheme 1), the strongly electron-donating substituents of which, in the 4-position of the phenyl ring, are expected to affect the spin dynamics. We report aspects of ligand and complex synthesis, as well as structural (X-ray diffraction), magnetic (superconducting quantum interference device, or SQUID), electrochemical (cyclic voltammetry) and spectroscopic data (UV/Vis, NMR). Thermal and photonic excitation and possible spin responses of complexes **5–7** (Scheme 2) were investigated in solution by temperature-dependent spectroscopic techniques (UV/Vis and NMR spectroscopy) and nanosecond-resolved transient absorption spectroscopy, respectively. Our results show that, in contrast to iron(II) complexes of terpyridine ligands, which are largely inert towards dissociation, the potential of triazine-based iron(II) complexes for thermal spin switching has to be discussed in terms of their thermodynamic stability.
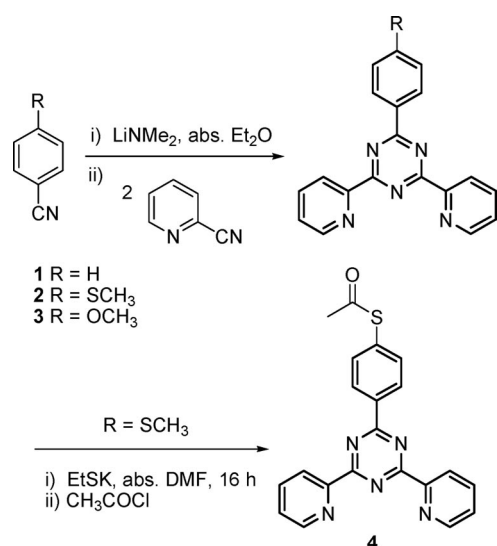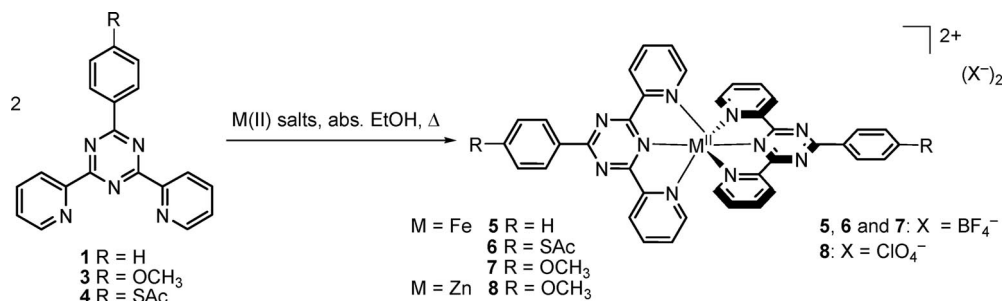
Results and Discussion

Synthesis

Ligands **1–3**, with different substituents in the *para* position of the phenyl ring, were synthesized according to the procedure described by Polson et al.[11] Addition of the respective *p*-substituted benzonitrile to a solution of lithium dimethylamide in anhydrous diethyl ether yields an amidine intermediate, which subsequently reacts with 2-cyanopyridine (2 equiv.) to afford the target ligand, with concomitant loss of lithium dimethylamide.

Thioether **2** was cleaved with potassium ethanethiolate in anhydrous DMF, and the resulting thiolate was treated with acetyl chloride to give ligand **4** in good yield (70% after recrystallization from acetone, Scheme 1).

We prepared three homoleptic iron(II) complexes (i.e., **5–7**) with ligands **1**, **3** and **4**, by treating the respective ligand (2 equiv.) with $Fe(BF_4)_2 \cdot 6H_2O$ in ethanol at reflux (Scheme 2; see the Experimental Section for details). The complexes were obtained as purple solids in moderate yields (typically 60%). Off-white zinc complex **8** (yield 87%) was synthesized as a "diamagnetic" but structurally related reference complex in an analogous manner.

Complexes **5–8** were characterized by elemental analysis, IR spectroscopy, cyclic voltammetry, NMR spectroscopy, SQUID magnetometry and single-crystal X-ray diffraction, as applicable.

X-ray Structure Determination

Single crystals of compounds **5–8** were obtained by slow diffusion of diethyl ether into a solution of the respective complex in acetonitrile at room temperature. All complexes crystallize in the triclinic space group $P\bar{1}$. A summary of selected bond lengths and angles is given in Table 1. The asymmetric unit of the iron(II) complexes contains one complete formula unit in each case, that is, the dicationic iron(II) complex, two tetrafluoroborate (or, in the case of **8**, perchlorate) counterions and one or two acetonitrile solvent molecules. Complex **6** shows disorder (which was resolved) in both thioacetate groups, one phenyl ring, one counterion and two acetonitrile solvent molecules. Resolvable disorder

Scheme 1. Triazine-ring-forming reactions and cleavage of **2**.

Scheme 2. Synthesis of iron complexes **5–7** and of zinc complex **8**.

in complex **8** involves both perchlorate counterions and a third solvent molecule (acetonitrile), which has 50 % site occupancy.

Table 1. Selected bond lengths [Å] and angles [°] for complexes **5**–**8** (standard deviations in parentheses); M = Fe for **5**–**7** and M = Zn for **8**.

	5	6	7	8
M1–N1	1.990(3)	1.998(3)	2.001(3)	2.280(2)
M1–N2	1.864(2)	1.868(3)	1.880(1)	2.048(1)
M1–N3	1.981(2)	1.998(3)	1.999(3)	2.236(1)
M1–N6	1.983(3)	1.995(3)	2.005(2)	2.221(1)
M1–N7	1.870(2)	1.870(3)	1.875(1)	2.045(1)
M1–N8	1.985(3)	2.001(3)	2.005(2)	2.250(1)
C10–C9–C8–N5	1.36(3)	4.23(1)	3.85(3)	1.89(2)
C15–C14–C7–N5	9.44(3)	6.12(4)	11.27(2)	3.11(2)
N7–M1–N2	179.79(1)	178.56(2)	177.64(4)	169.72(5)
N6–M1–N8 ("bite" angle)	160.10(1)	159.33(2)	159.17(2)	149.51(8)

Complexes **5**–**7** have the iron ion in a pseudooctahedral coordination environment, as set up by the two essentially orthogonal tridentate nitrogen ligands [the angles between the best planes containing the two dipyridyltriazine moieties are within the range 1.36(2)–4.23(2)°]. Meridional coordinating ligands of this type give rise to a systematic variation in metal–nitrogen bond lengths, which is reflected by the set of values determined for prototypical complex **5** (Figure 1): Fe–N bonds to the "central" (i.e., triazine) nitrogen atoms are significantly shorter than the bonds connecting the metal and the "lateral" (pyridine) N atoms [average values: 1.87(2) vs. 1.98(3) Å]. The Fe–N bond lengths are typical of iron(II) in the low-spin state. The phenyl rings are twisted by an average of 8.9(3)° with respect to the central triazine rings. This rather small value suggests extensively delocalized π systems within the ligands. The influence of polypyridyl ligand geometries and electronics on the photophysical properties of complexes of such ligands was investigated theoretically.[12] The reported structural data are in accord with those found in related iron(II) complexes.[10]
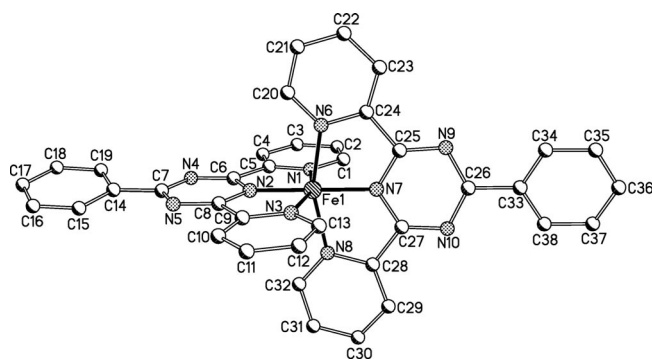
Figure 1. X-ray crystal structure of complex **5**. Hydrogen atoms and the BF_4^- counterions are omitted for clarity. Thermal ellipsoids are at the 50 % probability level.

As expected, compound **8** is isostructural with **5**–**7**. The zinc(II) centre is surrounded by two dipyridyltriazine moieties, which provide a pseudooctahedral coordination envi-

ronment. The apical Zn–N bond lengths are shorter than the basal ones (ca. 2.05 and ca. 2.26 Å, respectively). The Zn–N bond lengths are in the range of 2.05–2.28 Å, similar to the corresponding bond lengths previously reported for related $[ZnN_6]^{2+}$ coordination geometries.[13,14] The "bite" angle N6–Zn1–N8 is somewhat smaller than that in the iron(II) complexes, owing to Zn–N bond lengths that are on average some 10 % greater than their counterparts in the iron complexes.

Magnetic Susceptibility Measurements

The magnetic susceptibilities ($\chi_M T$) of powder samples of complexes **5**–**7** were measured in the temperature range 5–400 K by using a SQUID magnetometer (Figure 2). The magnetization was recorded during warming and cooling for each sample. All samples show reversible magnetization with temperature, with no hysteresis. The molar magnetic susceptibility of **6** increases with the temperature over the whole range: $\chi_M T$ increases from 0.21 cm³ mol⁻¹ K at 21 K, characteristic of low-spin iron(II) ($S = 0$), to 0.99 cm³ mol⁻¹ K at 400 K. At 400 K, the conversion to the high-spin state reaches about 30 %. The sharp decrease in the magnetic susceptibility of compound **6** below 20 K is due to zero-field splitting. By contrast, complexes **5** and **7** are low spin over the whole temperature range (4–400 K). A related iron(II) complex that has a bromophenyl-functionalized triazine ligand was recently reported also to be essentially diamagnetic.[10] In conclusion, greatly diverging spin behaviour of triazine-based iron(II) complexes is observed in the solid state. On the basis of the current data, no correlation of the spin behaviour with the electronic properties of the ligands can be extracted. The subtle geometric and/or electronic effects of the ligands are likely overlaid by crystal-packing effects.
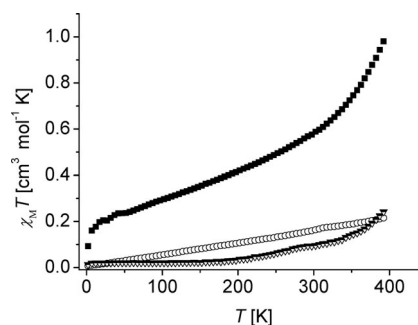
Figure 2. Variable-temperature magnetic behaviour of complexes **5** (circles), **6** (filled squares) and **7** (half-filled triangles).

Electrochemistry

The Fe^II/III redox couples were characterized by cyclic voltammetry in acetonitrile. Metal- and ligand-centred redox potentials are summarized in Table 2, and a representative voltammogram is shown in Figure 3 (for **6** and **7**, see the Supporting Information). Complexes **5**–**7** all show qua-

Table 2. Electrochemical data for complexes 5–8; M = Fe for 5–7 and M = Zn for 8.

Complex	$E_{1/2}$(ox) $M^{II/III[a]}$	$E_{1/2}$(red) triazine[a]			
5	+1.41 (72)[b]	–0.67 (56)	–0.82 (59)	–1.49 (58)	–1.76 (56)
6	+1.21 (64)	–0.86 (55)	–0.99 (62)	–1.70 (73)	–1.91 (77)
7	+1.07 (120)	–1.02 (131)	–1.21 (99)	–1.87 (137)	–2.15 (132)
8	–	–1.06 (50)	–1.28 (irr)	–1.86 (70)	
[Fe(trpy)$_2$]$^{2+}$	+1.17 (60)[c,d]	–1.25 (–61)[d]	–1.40 (–55)[d]		

[a] Potentials are in V versus Fc/Fc$^+$. Solutions of the complexes in CH$_3$CN (c = 1×10^{-3} M, 0.1 M TBABF$_4$). T = 298 K; scan rate = 200 mV s^{-1}. [b] ΔE_P in parentheses [mV]. [c] Measured with a rotating disc platinum electrode (DC). Data taken from ref.[17]; the original value is referenced versus Ag/AgCl and was recalculated versus Fc/Fc$^+$.[18] [d] Slope in parentheses [mV].

sireversible redox waves, as judged on the basis of established criteria (the oxidation/reduction peak separation ranges from 64 to 120 mV; cf. ΔE_P in Table 2).[15] One irreversible and two quasireversible reduction processes are observed for diamagnetic zinc(II) complex **8**.
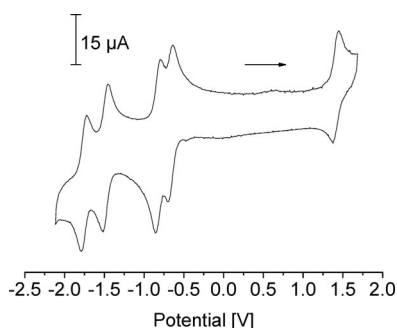
Figure 3. Cyclic voltammogram (scan rate: 200 mV s^{-1}) of **5**; solvent: CH$_3$CN (c = 1×10^{-3} M, 0.1 M TBABF$_4$), T = 298 K.

In the series of iron(II) complexes, the Fe$^{II/III}$ redox potential $E_{1/2}$(ox) shifts to less positive values as the electron-donating character of the R substituent increases, in the order R = H (**5**) >> SAc (**6**) > OMe (**7**). We observed a correlation between the electron-donating properties of the R substituents and the chemical shifts (^{1}H NMR spectra) of the *ortho* H^{16} and H^{18} protons (see the X-ray structure in Figure 1 for the numbering scheme): The most pronounced high-field shifts of these protons are recorded for complex **7**, which has the most strongly electron-donating substituent, with R = OCH$_3$ [$\delta_{H^{16}/H^{18}}$ = 8.10 (**5**), 7.93 (**6**), 7.44 ppm (**7**)]. This trend may be taken to reflect the strength of the donor–acceptor interaction between the iron(II) centre and the ligand, which is attenuated by the R substituent. The R = H substituent in complex **5** stabilizes Fe^{II} due to stronger π back-donation, whereas the methoxy group in complex **7** reduces significantly the π-acceptor character in the ligand, thereby facilitating oxidation of the metal centre, as reflected in a less positive redox potential. Further evidence for the direct influence of the electronic structure of the ligands on the redox properties can be derived from a comparison of dipyridyltriazine complex **5** and the structurally related terpyridine complex [Fe(trpy)$_2$]$^{2+}$. Whereas the oxidation of complex **5** (Fe^{II} → Fe^{III}) is observed at +1.41 V, the same process occurs at a significantly less positive potential (+1.17 V) in the terpyridine-based complex, in accord with the greater π deficiency of triazine relative to pyr-

idine.[16] The ligand-based reduction potentials of complexes **5–7** show similar behaviour.

The cathodic region reveals ligand-based reductions, with two consecutive one-electron reductions per triazine ligand.[19] Within the series of iron(II)–triazine complexes studied in this work, the reduction potentials shift to more negative values in accord with the electron-donating character of the R substituent. Importantly, the ligand reduction potentials of zinc(II) complex **8** appear nearly at the same peak position as in the respective iron(II) complex **7**, which suggests that the nature of the metal ion has only a small effect at best on the relative energies of the ligand-based orbitals.

The cathodic shifts of the first reduction potentials and of the oxidation potentials, for each R substituent, compensate each other in the series of complexes **5–7**. The modulus of the potential difference, $|E_{1/2}$(ox) – $E_{1/2}$(red)$|$, is (2.08 ± 0.01) V in each case. Ideally, this potential difference should be reflected by a photonic energy of 200 kJ mol^{-1} ($\lambda_{MLCT} \approx 597$ nm) necessary to excite the metal-to-ligand charge-transfer (MLCT) band in the UV/Vis spectra.[20] The same potential difference has been reported for related iron(II) complexes that have a bromophenyl- and a tolyl-functionalized triazine ligand, respectively.[10] As became evident (see Figure 4), there is an almost ideal correlation between the electrochemical data and the UV-spectroscopic measurements for complexes **5–7**.

Figure 4. Electronic spectra of solutions of complexes **5** (solid line, c = 1.4×10^{-4} M), **6** (dashed line, c = 1.4×10^{-4} M) and **7** (dash-dotted line, c = 1.9×10^{-4} M) in DMSO at 293 K.

Electronic Spectroscopy

Figure 4 shows the electronic absorption spectra of solutions of **5–7** in DMSO at 293 K. There are no further ab-

sorption bands up to 1200 nm. All complexes have strong absorption bands in the UV region, attributed to ligand-centred $\pi \rightarrow \pi^*$ and $n \ri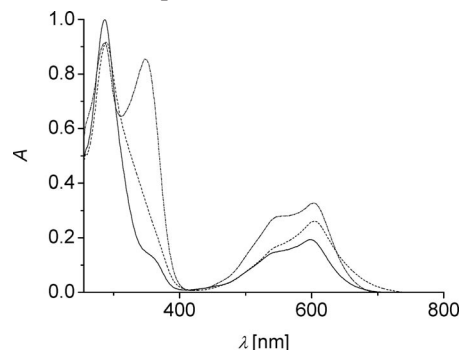ghtarrow \pi^*$ transitions. Complexes **6** and **7**, which have an electron-donating substituent on the phenyl ring, do not show a significant hypsochromic or bathochromic shift in their bands below 320 nm compared with complex **5** (R = H). Complex **7** has a distinctive peak at 349 nm, which is observed only as a broad shoulder in complexes **5** and **6**.

For all three complexes, there are two moderate bands in the visible region, characteristic of metal-to-ligand charge-transfer (^{1}MLCT) transitions. Calculations for iron(II) complexes of bipyridine,[21] although somewhat dated, have shown that the intense absorbance observed in the 500 nm region is due to the charge-transfer transition of an electron from the $3\mathrm{d}\pi$ orbital (primarily metal-localized) to the LUMO of the ligand. In view of the structures of the present ligands, we assume this transition to give rise to the maximum absorbance bands in the 598 to 602 nm region of our UV/Vis spectra. The second MLCT band may be due to a transition to a low-lying, triazine-based LUMO+1 in the ligand.[10] The absorption band maxima and corrected extinction coefficients for the MLCT transitions are listed in Table 3.

Table 3. Spectroscopic data obtained for solutions of **5–8** in DMSO at $T = 293$ K.

Complex	Absorption, λ_{max} [nm] (ε, $M^{-1}\,cm^{-1}$)[a]
5	288, 358 (sh.), 545 (sh.), 598 (15000)
6	289, 549 (sh.), 602 (25000)
7	288, 349, 551 (sh.), 602 (17000)
8	299, 357

[a] Extinction coefficients (ε) obtained from measurements of **5–7** in the presence of a 12-fold molar excess of ligand (see text).

Temperature-Dependent Electronic Spectra

Spin transitions of transition-metal complexes always give rise to pronounced thermochromism, which, in the case of iron(II) complexes, is often accompanied by bleaching of the MLCT absorption bands.[22,23] Accordingly, our complexes show extensive bleaching of the typical MLCT absorption bands in the 500–600 nm spectral range at elevated temperatures but full recovery upon return to the starting temperature (293 K). Solutions of compounds **5–7** in DMSO reversibly cycle between blue at room temperature and almost colourless at 373 K. This is reflected in the temperature-dependent (rising branch) UV/Vis spectra (Figure 5, compound **7** in DMSO; see the Supporting Information for **5** and **6**). Besides the monotonous bleaching of the MLCT transition, heating also causes significant spectral dynamics below 400 nm (intraligand absorptions; Figure 5), which are characterized by well-defined isosbestic points in all cases. The observation of isosbestic points in the UV/Vis spectra of compounds undergoing a reaction is generally considered a necessary feature for processes of

defined stoichiometry. Thus, the spectroscopy discussed so far is compatible with the presence of spin equilibria in solution.[24]
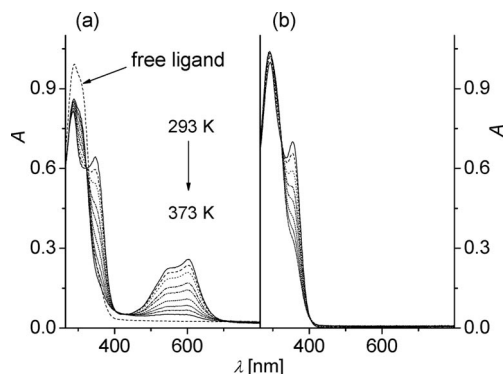
Figure 5. (a) Temperature-dependent UV/Vis spectra of a solution of **7** in DMSO ($c = 1.4 \times 10^{-4}$ M; 10 K intervals between 293 and 373 K); broken line: UV/Vis spectrum of a solution of **3** in DMSO at 293 K. (b) Temperature-dependent UV/Vis spectra of zinc complex **8** ($c = 2.1 \times 10^{-4}$ M; 10 K intervals between 293 and 373 K).

However, several pieces of experimental evidence strongly disfavour this conclusion. A first argument against a causal connection between the observed spectral dynamics of **5–7** and spin-state equilibria is provided by the UV/Vis spectra of zinc analogue **8** of complex **7** (Figure 5, right). Evidently, the appearance and the temperature dependence of the intraligand transitions in the UV/Vis spectra of **8** strongly resemble those of iron(II) complex **7**. In particular, the isosbestic point at 324 nm is observed in both cases. The strong spectral parallel between **7** and **8** favours the possibility of a common molecular origin of the spectral dynamics but, at the same time, precludes spin equilibria, as the zinc complex with its d^{10} electron configuration cannot undergo spin crossover (SCO).

A second argument is provided by considerations concerning the thermodynamics of the thermochromism. Although a rigorous thermodynamic treatment is beyond the scope of this study, the obtained results allow meaningful mechanistic conclusions. On the basis of the assumption that the thermochromism of the complexes is due to the spin equilibrium given by Equation (1), the apparent thermodynamic parameters can be extracted from the temperature dependence of the UV/Vis spectroscopic data. This procedure is demonstrated in Figure 6 for a solution of complex **6** (R = SAc) in DMSO. The apparent equilibrium constants (K_{eq}^{app}) were accessible through an analysis of the MLCT peak absorbances around 600 nm. In particular, due to the spectroscopic silence of the anticipated high-spin species (**Y**) at this wavelength, the absorbance $A(T)$ at the temperature T is a direct measure of the concentration $[[FeL_2]^{2+}](T)$ of original complexes **5–7** {Equations (2) and (3), in which c_0 is the concentration of the regular $[FeL_2]^{2+}$ species}. In an admittedly somewhat simplistic approach, the limiting absorbances A_0 of pure complexes **5–7** were estimated from plots of their temperature dependences (Figure 6a). The relative error of A_0 is estimated to be not smaller than $\pm 5\%$. The reliability of this latter value is cru-

cial for the overall quality of the analysis. The equilibrium constants were then computed from Equation (4). Van't Hoff plots of $\ln K_{eq}^{app}$ versus $1/T$ [Equation (5), in which $\Delta_R H_m$ is the apparent reaction enthalpy, $\Delta_R S_m$ is the apparent reaction entropy and R is the gas constant] were linear in all cases (e.g., for **6** see Figure 6b).

$$[[FeL_2]^{2+}](T) = c_0 \, \frac{A(T)}{A_0(293\,K)} \tag{2}$$

$$[\mathbf{Y}](T) = c_0 - c_0 \, \frac{A(T)}{A_0(293\,K)} = c_0\left(1 - \frac{A(T)}{A_0(293\,K)}\right) \tag{3}$$

$$K_{eq}^{app} = \frac{[\mathbf{Y}](T)}{[[FeL_2]^{2+}](T)} = \frac{A_0(293\,K)}{A(T)} - 1 \tag{4}$$

$$\ln K_{eq}^{app} = -\frac{\Delta_R H_m}{R}\frac{1}{T} + \frac{\Delta_R S_m}{R} \tag{5}$$

Figure 6. (a) Temperature dependence of the peak absorbance of the MLCT band (at 600 nm) of a solution of **6** in DMSO ($c = 1.4 \times 10^{-4}$ M) in the absence (squares) and in the presence of a 12-fold molar excess of ligand **4**; lines have been drawn to guide the eye. (b) Van't Hoff plot of the temperature dependence of the apparent equi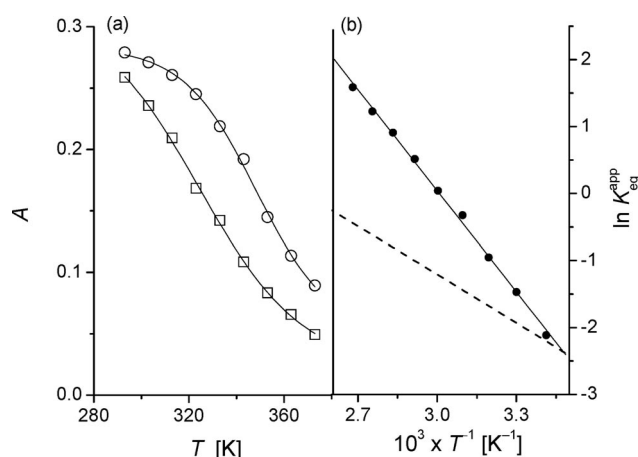librium constants, according to Equation (5) for a solution of complex **6** in DMSO; full line: linear regression of the data according to Equation (5); broken line: Van't Hoff plot of the temperature dependence of a typical SCO equilibrium, computed with $\Delta_R H_m = 20$ kJ mol^{-1} and $\Delta_R S_m = 50$ J mol^{-1} K^{-1}.[25]

From the slopes and the intercepts of the linear fits we derived the apparent reaction enthalpy and the apparent reaction entropy. The obtained thermodynamic parameters allow a discussion of the molecular origin of the observed thermochromism of **5**–**7**. As we will show in the following, the thermodynamic parameters are not in accord with SCO behaviour. In a low-spin (LS) → high-spin (HS) transition, the source of the reaction enthalpy, $\Delta_R H_m$, would be the Fe–N bond-length increase of the order of 0.15–0.20 Å,[26] that is, a reorganization of the inner coordination sphere. Reported values for relevant spin equilibria usually amount

to approximately 20 kJ mol^{-1}.[23,25,27] Our values for the apparent $\Delta_R H_m$ range from 30 to 42 kJ mol^{-1} and are thus not in agreement with typical values of spin equilibria. The same holds for the apparent values of $\Delta_R S_m$, which in our case range from 100 to 125 J mol^{-1} K^{-1}. Generally, the transition from the LS to the HS state is assumed to be driven by the increase in molar entropy, $\Delta_R S_m$, amounting to approximately 50 J mol^{-1} K^{-1}.[28] This deviation from the parameters of established SCO behaviour becomes most evident from a direct graphical comparison, as has been made for complex **6** (see Figure 6b).

A final argument comes from the observed dependence of the peak absorbances of the MLCT absorption bands of **5**–**7** in DMSO at 600 nm on the concentration of the respective free ligand. The addition of an excess amount of ligand to solutions of **5**–**7** in DMSO causes significant increases in the absorbance at 600 nm, which, in turn, points to an increase in the concentration of the absorbing species. A spectroscopic titration of a solution of [Fe(**4**)$_2$](BF$_4$)$_2$ (**6**) in DMSO with stoichiometric portions of the ligand **4** showed saturation behaviour beyond a metal-to-ligand ratio of 1:9, from which we could determine the limiting absorbances A_0 of the MLCT bands. By way of extension, it is reasonable to assume similar behaviour for complexes **5** and **7**, for which no complete titration has been performed. In the latter cases, the absorbances measured at 600 nm in the presence of a 12-fold molar excess of the respective free ligand were taken as measures of the limiting absorbances A_0. Notably, the thus-derived limiting absorbances are in good accord with those extracted graphically from the temperature dependences as shown in Figure 6a. On the basis of these data, the molar absorption coefficients of the MLCT absorption bands could be calculated (see Table 3).

Evidently, an excess amount of free ligands **1**, **3** or **4** shifts the equilibrium between the [FeL$_2$]$^{2+}$ metal complexes **5**–**7** and a species of unknown structure (**Y**) to the side of the complexes. Actually, the thermochromism of **6** is significantly reduced in the presence of a 12-fold molar excess of ligand **4** (Figure 6a, similar results were also obtained for **5** and **7**). No such dependence can be expected for spin-state equilibria. Instead, it is suggested that the observed spectral behaviour is due to dynamic dissociation of ligands in **5**–**7** (and **8**). In agreement with this suggestion, the high-temperature UV/Vis spectra of complexes **5**–**8** clearly resemble the spectrum of the respective free ligand in DMSO (see Figure 5). Accordingly, ESI mass spectra that were obtained for solutions of **5** (R = H) in DMSO that had been heated in the presence of an 11-fold molar excess of ligand **3** reveal the complete thermally induced conversion to the homoleptic complex **7** (R = OMe). In conclusion, solutions of complexes **5**–**8** in DMSO predominantly undergo cleavage with formation of the respective free ligands at elevated temperatures. It becomes clear that the thermodynamic lability of triazine complexes **5**–**7** in DMSO will always obscure the possible observation of spin equilibria in solution. The interpretation of the thermochromism of iron(II) complexes in such cases should be accompanied by an assessment of complex stability.

This conclusion is somewhat at odds with the findings reported for related systems. For instance, substitution lability of iron(II) complexes in strongly coordinating solvents (with a high donor number, like DMSO) is commonly observed for *bidentate* ligands, like bpy,[29] but appears quite exceptional for *tridentate* ligands, like tpy.[30] Examples for the substitution lability of tridentate ligands have been reported by Strauß et al. for a 2,6-bis(benzimidazol-2′-yl)pyridine–iron(II) complex in methanol and DMSO, in which the substitution lability of the ligand compromised the analysis of the SCO behaviour.[31,32]

NMR Spectroscopy

In accord with the above conclusions, most features of the NMR spectra of complexes **5**–**7** suggest that the compounds are diamagnetic. The resonances of the aromatic protons appear in the range $\delta = 7.5$–9.5 ppm at room temperature, typical of a diamagnetic (low-spin) species. The signals of **5**–**7**, and also those of the diamagnetic complex **8**, are substantially broadened at room temperature with respect to those of the free ligand. By way of example, the H^1/H^{13} proton signal of free ligand **1** appears as a resolved ddd-multiplet with a line width of 0.41 Hz, but as a substantially broadened pseudosinglet with a full width at half-maximum (fwhm) of 30.7 Hz (solution in DMSO, room temperature) for iron complex **5** at $\delta = 7.47$ ppm. Similar line broadening, though less pronounced than that observed for **5**–**7**, is observed for diamagnetic zinc(II) complex **8** (fwhm = 7.25 Hz). It is appealing to attribute the line broadening observed for **5**–**8** to the same fluxional/exchange processes that involve decoordination of the ligand,[33,34] as discussed above as the origin of the observed thermochromism of **5**–**7**.

However, some diverging observations made at elevated temperatures for **5**–**7** and **8**, respectively, suggest the presence of two parallel sources for the line broadening. At elevated temperatures, the resonances of the aromatic protons of iron(II) complexes **5**–**7** experience a steadily increasing line broadening, concomitant with significant downfield shifts of the resonances. Both effects are most pronounced for the protons closest to the iron centre, H^1/H^{13} and H^2/H^{12} (e.g., $\Delta\delta_{H^1/H^{13}} = 4$ ppm between 298 and 373 K), but smaller for the protons H^4/H^{10} ($\Delta\delta_{H^4/H^{10}} = 1$ ppm between 298 and 373 K), which are farthest from the coordination site (see the X-ray structure in Figure 1 for the numbering scheme). These findings are in agreement with observations made by Hanan and co-workers for the iron(II) complex of a bromophenyl-functionalized triazine ligand.[19]

In contrast, significant effects of the temperature on the position of the NMR spectroscopic resonances are observed neither for zinc complex **8** nor for respective free ligand **3** at elevated temperatures. In addition, the line widths for complex **8** decrease with increasing temperatures. At 373 K, the coupling fine structure is partly resolved.

In conclusion, both the temperature-promoted downfield shifts in the NMR spectra of iron(II) complexes **5**–**7** and

the observed line broadening at elevated temperatures cannot be associated with the ligand decoordination dynamics, as suggested above on the basis of UV/Vis thermochromism. Instead, the findings point to a paramagnetic contribution (if small) in terms of the spin equilibrium in Equation (1) in addition to the dominant ligand-substitution dynamics. Thus, the suppression of the latter process in the presence of an excess amount of the free ligand, as is evident from the UV/Vis studies (see above), is expected to enhance the contribution of the spin equilibrium. This enhancement is actually observed for complex **5**, for which the temperature dependence of the chemical shifts has been studied in the presence of one additional equivalent of free ligand **1**: The extent of the downfield shift at 373 K is almost doubled by the presence of free ligand; for example, $\Delta\delta_{H^1/H^{13}} = 7.3$ ppm (between 298 and 373 K). Ligand dissociation may, in principle, also be induced by thermal SCO.

Laser Flash Photolysis (LFP) Studies

The experimental evidence presented above disfavours the possibility of efficient thermal spin crossover in solutions of complexes **5**–**7** in DMSO. This is in marked contrast to the results obtained from nanosecond LFP experiments after laser excitation to the ^{1}MLCT state with 532 nm pulses, which are in good accord with photoinduced $LS \rightarrow {}^1MLCT \rightarrow HS \rightarrow LS$ cycles. Interestingly, the different R substituents in the ligand peripheries of **5**–**7** have significant effects on the transient spectral pattern and relaxation dynamics.

Representative transient absorption/bleaching spectra that were recorded 60–400 ns after flashing a dilute solution of **7** (R = OCH$_3$) in DMSO are shown in Figure 7. The spectra are dominated by the bleaching of the strong MLCT absorption band around 600 nm. Very similar behaviour is observed for **5** and **6** (Supporting Information, Figures S7 and S8). In contrast, the respective transient spectra of **5**–**7** differ significantly in the spectral regime of the intraligand absorption bands below 440 nm. Two isosbestic points, with $\Delta A = 0$, are obtained for **7**, whereas only a single isosbestic point at $\lambda > 300$ nm is observed for **5** and **6**. Characteristic data of the transient spectra are summarized in Table 4. The positions of the absorption maxima of the longest-lived excited states of **5**–**7** were taken from their reconstructed absorption spectra. The latter have been obtained from the sum of the lowest-temperature UV/Vis spectrum (summarized in Figure 4) and the transient spectrum of each compound after normalizing the absorbance at 600 nm.

The well-defined isosbestic points in the transient spectra of **5**–**7** suggest processes of well-defined stoichiometry. However, the photoinduced processes that give rise to isosbestic points certainly differ from the thermally induced ones that have been discussed above. This becomes most evident from a comparison of the difference absorption spectrum of **7** (broken line in Figure 7; calculated from the UV/Vis spectra of **7** in DMSO at 293 and 363 K, respectively) with
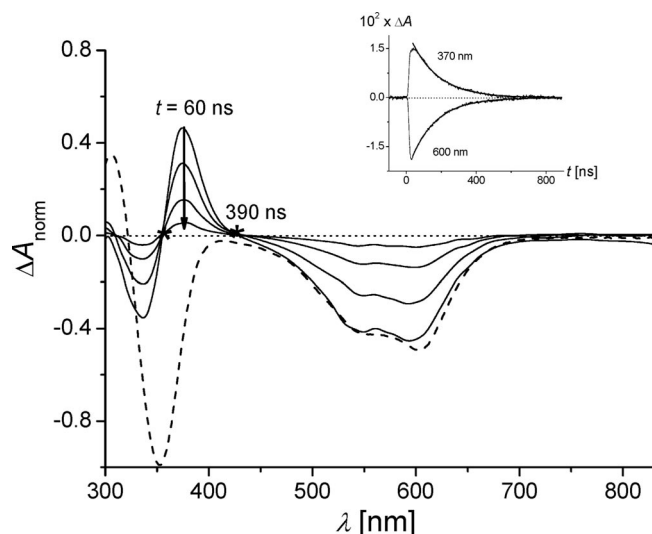
Figure 7. Normalized transient absorption spectra observed after laser flash photolysis of a dilute solution of **7** (2×10^{-5} M) in DMSO at 532 nm (9 ns, 1 mJ per pulse); isosbestic points highlighted by asterisks; broken line: difference absorption spectrum of **7** in DMSO (computed from spectra displayed in Figure 5 for $T = 293$ and 363 K); inset: representative absorption-decay and bleach-recovery profiles, observed at 370 and 600 nm; full lines correspond to first-order fits to the experimental data with time constants of (148 ± 5) ns.

Table 4. Summary of spectroscopic and kinetic results of the LFP experiments.

	λ_{max}[a] [nm]	λ_{iso}[b] [nm]	$\tau_{HS \to LS}$ [ns]
5	<300	336	77 ± 5
6	<300	354	93 ± 5
7	363	354, 428	148 ± 5

[a] Absorption maximum of the longest-lived excited-state species; ± 3 nm. [b] Wavelength of the isosbestic points in the transient absorption spectra; ± 3 nm.

the transient spectra in the region of the intraligand transitions below 440 nm: Whereas thermal activation causes an overall blueshift of the near-UV absorption bands of **5**–**7**, photonic excitation gives rise to a significant redshift of the absorption of **7** (less expressed in the case of **5**–**6**). This suggests that photonic excitation of **5**–**7** is not accompanied by ligand dissociation. Because further evidence comes from the discussion of the decay kinetics, we conclude that the relaxation processes of **5**–**7** on the nanosecond timescale are best discussed in terms of a high-spin/low-spin transition.

What is presumably a high-spin quintet state of **7** has a lifetime of approximately 150 ns in DMSO at room temperature, as indicated by nanosecond laser flash photolysis. Typical time profiles of the transient absorption and of bleach recovery are shown in the inset of Figure 7. Clean decay of all signals to zero-absorption suggests largely reversible processes following the excitation (see inset in Figure 7). Well-defined first-order decays were observed throughout the spectral range from 360 to 700 nm, which could be fitted to monoexponential decay functions with a global de-

cay rate constant of $k_{HS \to LS} = (6.8 \pm 0.2) \times 10^6$ s^{-1}, corresponding to a HS state lifetime of (148 ± 5) ns. Significantly reduced lifetimes of (77 ± 5) and (93 ± 5) ns were observed for complexes **5** and **6**, respectively (Table 4). The lifetime of the high-spin state appears to be correlated with the electron-donating character of the R substituent on the phenyl ring of the ligands: The shortest lifetime is observed for phenyl-substituted complex **5**, whereas the strongly electron-releasing *para*-methoxy substituent in **7** doubles the lifetime. Importantly, the obtained kinetic data compare well with data available in the literature. Iron(II) complexes with polypyridyl ligands consistently yield high spin, that is, quintet-state lifetimes in the range of 40–200 ns at ambient temperatures.[24,35–40]

All the characteristics reported so far are in good agreement with the established picture of a high-spin/low-spin relaxation on the nanosecond timescale. The generation of the high-spin state is well established to proceed on a much shorter timescale and, as such, cannot be observed with nanosecond-time-resolution techniques. The complex relaxation cascade that follows excitation to the charge-transfer manifold involves two spin-inversion processes, that is, intersystem crossings that finally yield the high-spin quintet state. Insights into the subnanosecond relaxation dynamics of the initially populated charge-transfer state are accessible only by picosecond- and femtosecond-resolving optical spectroscopy and X-ray absorption techniques.[41–44] In consequence, on the nanosecond timescale, both the ground-state bleaching and the formation of excited-state absorptions are usually laser-pulse-limited.

Actually, the bleaching of the ground-state absorptions of **5**–**7** around 600 nm was observed with pulse-width-limited (ca. 10 ns) kinetics. However, as can be read from the time profiles obtained below 440 nm (see inset in Figure 7), the formation of the transient absorption maximum at 370 nm appears slightly but significantly delayed with respect to the instant bleaching at 600 nm. At wavelengths below 360 nm, the time profiles of all complexes, although still dominated by the high-spin/low-spin relaxation, receive contributions from a preceding, much faster process (not shown). Finally, significant emission of light was observed for **5**–**7** with an emission maximum wavelength $\lambda_{em} >$ 830 nm. This short-lived but not laser-pulse-limited emission apparently shares the time constants with the fast-decay component in the bleach recovery. Clearly, these findings are in conflict with the common picture of ultrafast MLCT → HS relaxation in iron(II)–polypyridyl complexes and suggest the presence of (at least) one further intermediate on the nanosecond timescale. Further work is underway to clarify the nature of this intermediate.

Conclusions

The following is a quote from a seminal review by Gütlich and Goodwin: "Thermal spin transition is always accompanied by a colour change (thermochromism) which is frequently pronounced and visible".[23] Our study on the

spin behaviour of three homoleptic iron(II) complexes of triazine-based N_3 ligands (which differ in the peripheral substitution pattern) provides a salient example that the reversal of the above statement, that is, taking thermochromism as the sole indicator of a thermal spin transition, is unwarranted because of possible thermal substitution lability of the complexes in strongly coordinating solvents. In particular, the substantial temperature-dependent colour change observed for solutions of complexes **5–7** in DMSO is to be attributed mainly to decoordination of the ligands at elevated temperatures. This behaviour is unusual, as solvent-driven ligand substitution, although well established for bidentate ligands, is usually not observed for tridentate ligands. Apparently, simply exchanging the central pyridine ring of the widely used terpyridine ligand for the electron-poorer triazine unit is sufficient for the resulting iron(II) complex to become substitution-labile. On the other hand, this structural change, at least in part, eases the ligand-field constraints that make terpyridine complexes low spin over the whole range of temperatures. The presence of the high-spin forms of **5–7** at elevated temperatures in solution attests to their intrinsic ability to harbour SCO phenomena. In accordance with this conclusion, partial *thermally induced* spin crossover is observed in the solid state for complex **6**, whereas complexes **5–7** show efficient *photoinduced* SCO even in DMSO at room temperature. Preliminary experiments in acetonitrile and methanol, respectively, indicate that the *photoinduced* SCO behaviour of **5–7** is largely solvent-independent. In contrast, the *thermally induced* ligand substitution appears to be less effective in weaker solvents.

Experimental Section

Materials and Instrumentation: Unless otherwise noted, all reactions were carried out in dried solvents under dry dinitrogen, using standard Schlenk techniques. Compound **1** was synthesized according to a published procedure.[9] All other chemicals were purchased from Aldrich or Acros and used without further purification. IR spectra were measured as KBr disks. Spectroscopic data were obtained using the following instruments: IR spectroscopy: Nicolet Magna System 750; NMR spectroscopy: Bruker ARX 200, ARX 400, ARX 500. The numbering scheme used for the assignment of NMR spectroscopic data is based on that used in the crystal-structure analyses (also see the Supporting Information). Elemental analysis (C, H, N, S) was carried out by combustion analysis using a Thermo Finnigan EAGER 300 (Flash 1112) apparatus; EI: Finnigan MAT95S; ESI: Orbitrap LTQ XL, Thermo Scientific. Solid-state variable-temperature magnetic susceptibility measurements were made using a Quantum Design MPMS-XL5 SQUID magnetometer operating at 0.1 T. Diamagnetic corrections for the sample and the sample holder were applied. UV/Vis spectra were measured with a Varian Cary 50 spectrometer equipped with a UV/Vis quartz immersion probe (light path 1 mm, Hellma), a home-built measuring cell, and an immersion thermometer. Every temperature setting was allowed to equilibrate for 5 min. Cyclic voltammetry was performed using a Princeton Applied Research model 263A potentiostat, platinum reference and counter electrodes, and a glassy carbon working electrode (3 mm diameter). Ionic strengths were adjusted

with tetrabutylammonium tetrafluoroborate (TBABF$_4$; 0.10 M). The measured potentials were referenced to a normal hydrogen electrode (NHE) using ferrocene/ferrocenium as the internal standard (E[Fc/Fc$^+$] = 0.19 V[45]) The setup for laser flash photolysis (LFP) has been described in detail.[46] LFP is based on the 532 nm output of a Nd:YAG laser with a full width at half-maximum of approximately 9 ns and a dose of 5–7 mJ per pulse. Neutral filters were used for attenuation of the laser intensity to a dose of 1 mJ per pulse. The absorbance of the solution of **5** was 0.1 at the excitation wavelength, corresponding to approximately 2×10^{-5} M in dry DMSO. Transient decay and bleach recovery were recorded at individual wavelengths by the step-scan method with a step distance of 5 nm in the range of 300 to 830 nm and obtained as the mean signals of 6 to 16 pulses. Spectral resolution was in the range of ±3 nm. Samples for LFP were rigorously deoxygenated by flushing them with analytical grade nitrogen for 20 min prior to and kept under nitrogen during measurement in a circulating flow system (5×5 mm Suprasil quartz cell). LFP experiments were performed at (295 ± 1) K. DMSO for time-resolved spectroscopy was of analytical grade and used as received.

X-ray Crystallography: Crystal data and details concerning data collection and refinement are given in Table 5. Additional representations of structures have been placed in the Supporting Information. Data collection was performed with a Bruker Nonius KappaCCD diffractometer using graphite-monochromated Mo-K_α radiation with λ = 0.71073 Å. The COLLECT suite[47] was used for data collection and integration. All structures were solved by direct methods and refined by full-matrix least-squares procedures on F^2 using the program SHELXTL NT 6.12.[48] All non-hydrogen atoms were refined anisotropically. Disorder and further structure details: Compound **5** crystallizes with three molecules of acetonitrile per formula unit. In compound **6** one ligand shows disorder in its C_4H_6–SC(O)Me unit. The refinement of two alternative orientations gave a distribution of 69.9(4) and 30.1(4)% for the atoms S1, O1, C14–C21 and S1A, O1A, C14A–C21A, respectively. The second ligand is disordered only in its SC(O)Me unit [56.6(6) and 42.4(6)% for S2, O2, C41, C42, and S2A, O2A, C41A, C42A, respectively]. Both anions are disordered [75.9(6) and 24.1(6)%] for the atoms B1–F14 and B1A–F14A, respectively, and 50.0(8)% for each of the atom series F22–F24 and F22A–F24A. The compound crystallizes with two molecules of acetonitrile per formula unit, which are also disordered. Three orientations could be refined separately for each molecule [49.0(9), 28.5(9), and 22.5(9)% for atoms N100–C122; 51.8(8), 24.4(8), and 23.8(8)% for atoms N200–C222]. SAME, ISOR, and SIMU restraints were used in the refinement of the disorder. Compound **7**: One of the BF$_4^-$ anions is disordered, and two alternative orientations were refined [86.5(5) and 13.5(5)%] for the atoms B2–F24 and B2A–F24A, respectively (same restraints used as for **6**). Compound **8**: Disorder in both ClO$_4^-$ anions: 66(3) and 34(3)% occupation for atoms O12–O14 and O12A–O14A, respectively; 81.8(4) and 18.2(4)% for atoms Cl2, O22–O24 and Cl2A, O22A–F24A, respectively. SIMU restraints were used in this refinement. The compound crystallizes with 2.5 molecules of acetonitrile per formula unit. The half-molecule is disordered and located on a crystallographic inversion centre; its hydrogen atoms were disregarded. All structures: The hydrogen atoms were placed in positions of optimized geometry, and their isotropic displacement parameters were tied to those of the corresponding carrier atoms by a factor of 1.2. CCDC-737477 (for **8**), -737478 (for **6**), -737479 (for **7**) and -737480 (for **5**) contain the supplementary crystallographic data for this paper. These data can be obtained free of charge from the Cambridge Crystallographic Data Centre via www.ccdc.cam.ac.uk/data_request/cif.

Table 5. Crystal data for complexes **5**, **6**, **7** and **8**. The space group is $P\bar{1}$ (triclinic) and the absorption correction was SADABS[a] in all cases.

	5	**6**	**7**	**8**
T [K]	150(2)	150(2)	150(2)	150(2)
Empirical formula	$C_{44}H_{35}B_2F_8FeN_{13}$	$C_{46}H_{36}B_2F_8FeN_{12}O_2S_2$	$C_{44}H_{36}B_2F_8FeN_{12}O_2$	$C_{45}H_{37.5}C_{12}N_{12.5}O_{10}Zn$
Crystal size [mm]	$0.25 \times 0.14 \times 0.12$	$0.32 \times 0.25 \times 0.18$	$0.32 \times 0.26 \times 0.23$	$0.36 \times 0.20 \times 0.14$
Colour	red	purple	purple	yellow
a [Å]	10.789(11)	13.758(2)	11.767(14)	11.3009(7)
b [Å]	11.866(12)	13.857(17)	13.274(15)	15.3135(9)
c [Å]	17.818(13)	14.438(15)	15.735(6)	15.3581(5)
α [°]	73.970(7)	71.899(10)	89.763(7)	62.656(5)
β [°]	89.707(9)	77.272(9)	85.083(6)	80.092(4)
γ [°]	86.269(8)	84.983(13)	66.750(9)	80.597(6)
V [Å³]	2187.5(4)	2551.5(6)	2248.8(4)	2314.8(2)
$\rho_{calcd.}$ [g cm⁻³]	1.481	1.409	1.468	1.506
μ [mm⁻¹]	0.430	0.457	0.422	0.719
Transmission range	0.878–0.950	0.813–0.920	0.854–0.910	0.740–0.900
Scan	ϕ and ω rotations with 1.9° and 190 s per frame	ϕ and ω rotations with 2.0° and 180 s per frame	ϕ and ω rotations with 2.0° and 70 s per frame	ϕ and ω rotations with 2.0° and 80 s per frame
2θ range [°]	3.5–27.1	3.4–26.4	3.3–27.1	6.2–55.0
Measured reflections	50958	64641	81445	68085
Unique reflections	9625	10402	9887	11001
Obsd. reflections[b]	7702	7877	7925	8721
Refined parameters	616	984	672	709
wR_2 (all data)[c]	0.0910	0.1997	0.1081	0.0954
R_1 (observed data)[d]	0.0385	0.0675	0.0401	0.0348
ρ_{fin} (max./min.) [e Å⁻³]	0.579/–0.418	0.959/–0.464	0.582/–0.419	0.458/–0.496
Weighting scheme[e]	$k = 0.0332/l = 1.8513$	$k = 0.0817/l = 6.0537$	$k = 0.0407/l = 2.3177$	$k = 0.0455/l = 1.0369$

[a] *SADABS 2.06*, Bruker AXS, Inc., Madison, WI, U.S.A., **2002**. [b] With $F_o \geq 4\sigma(F)$. [c] $wR2 = \{\Sigma[w(F_o^2 - F_c^2)^2]/\Sigma[w(F_o^2)^2]\}^{1/2}$. [d] $R1 = \Sigma||F_o| - |F_c||/\Sigma|F_o|$ for $F_o \geq 4\sigma(F)$. [e] $w = 1/[\sigma^2(F_o^2) + (kP)^2 + lP]$ and $P = (F_o^2 + 2F_c^2)/3$.

Synthesis of Ligand 2: *n*BuLi (2 M in hexane, 11.4 mL, 22.7 mmol) was added dropwise with stirring to a solution of HNMe₂ (2 M in THF, 11.4 mL, 22.7 mmol) in anhydrous Et₂O (200 mL). The mixture was stirred until a white suspension had formed (20 min), and 4-(methylthio)benzonitrile (3.1 g, 20.6 mmol) was then added as a solid. After stirring at room temperature for 30 min, 2-pyridinecarbonitrile (4.00 mL, 41.4 mmol) was added, producing an olive-green suspension, which was stirred overnight. It was then diluted with H₂O/EtOH (1:1, 200 mL), and the solution was heated to remove Et₂O. Subsequently, the solution was layered with hexane (100 mL), and the beige precipitate thus formed was collected by filtration and washed with hexane (2 × 20 mL). The product was filtered off and dried in vacuo to obtain **2** as a beige powder (10.1 g, 73%). ¹H NMR (400 MHz, CD₃OD): δ = 8.89 (d, J = 8.1 Hz, 2 H, H¹,¹³), 8.79 [mc (= multiplet, centred), 2 H, H⁴,¹⁰], 8.71 (d, ³J = 8.7 Hz, 2 H, H¹⁵,¹⁹), 8.08 (dt, J = 7.7, 7.6, 1.7 Hz, 2 H, H³,¹¹), 7.66 (ddd, ³J = 7.4, 4.8, 1.1 Hz, 2 H, H²,¹²), 7.34 (d, ³J = 8.7 Hz, 2 H, H¹⁶,¹⁸), 3.0 (s, 3 H, H²⁰) ppm. ¹³C NMR (100 MHz, CD₃OD): δ = 174.1 (C, 2 C, C⁶,⁸), 172.1 (C, 1 C, C⁷), 154.1 (C, 2 C, C⁵,⁹), 150.8 (CH, 2 C, C¹,¹³), 147.8 (C, 1 C, C¹⁷), 139.3 (CH, 2 C, C³,¹¹), 132.7 (C, 1 C, C¹⁴), 130.9 (CH, 2 C, C¹⁵,¹⁹), 128.3 (CH, 2 C, C²,¹²), 126.6 (CH, 2 C, C⁴,¹⁰), 126.1 (CH, 2 C, C¹⁶,¹⁸), 14.6 (CH₃, 1 C, C²⁰) ppm. $C_{20}H_{15}N_5S$ (357.43): calcd. C 67.21, H 4.23, N 19.59, S 8.97; found C 67.44, H 4.33, N 19.45, S 8.86. IR (KBr): $\tilde{v}$ = 1565 (m), 1513 (s), 1372 (s), 778 (s), 668 (m) cm⁻¹. MS (EI, 166 °C): m/z (%) = 357 (90) [M]⁺, 310 (5) [M – CH₃S]⁺, 105 (100).

Synthesis of Ligand 3: Prepared according to a procedure closely related to that of ligand **2**. Colourless solid (350 mg, 47%). ¹H NMR (200 MHz, CDCl₃, 25 °C): δ = 8.95 (ddd, J = 4.7, 1.8, 0.9 Hz, 2 H, H¹,¹³), 8.83 (ddd, J = 7.9, 1.1 Hz, 2 H, H⁴,¹⁰), 8.80 (d, ³J = 9.2 Hz, 2 H, H¹⁵,¹⁹), 7.96 (dt, J = 7.9, 7.7, 1.8 Hz, 2 H, H³,¹¹), 7.52 (ddd, J = 7.7, 4.7, 1.1 Hz, 2 H, H²,¹²), 7.07 (d, ³J = 9.2 Hz, 2

H, H¹⁶,¹⁸), 3.93 (s, 3 H, H²⁰) ppm. ¹³C NMR (100 MHz, CD₃OD, 25 °C): δ = 173.7 (C, 2 C, C⁶,⁸), 171.6 (C, 1 C, C⁷), 165.3 (C, 1 C, C¹⁷), 153.9 (C, 2 C, C⁵,⁹), 150.5 (CH, 2 C, C¹,¹³), 139.1 (CH, 2 C, C³,¹¹), 132.4 (CH, 2 C, C¹⁵,¹⁹), 128.6 (C, 1 C, C¹⁴), 128.0 (CH, 2 C, C²,¹²), 126.3 (CH, 2 C, C⁴,¹⁰), 114.9 (CH, 2 C, C¹⁶,¹⁸), 18.4 (CH₃, 1 C, C²⁰) ppm. $C_{20}H_{15}N_5O$ (341.37): calcd. C 70.37, H 4.43, N 20.52, S 8.32; found C 70.14, H 4.17, N 20.18, S 8.37. MS (EI, 166 °C): m/z (%) = 342 (100) [M]⁺, 105 [py – CN]. IR (KBr): $\tilde{v}$ = 1532 (s), 1513 (s), 1265 (w), 1159 (m), 852 (m), 782 (s) cm⁻¹. HRMS (EI): calcd. for $C_{20}H_{15}N_5O$ [M⁺] 341.1276; found 341.1273.

Synthesis of Ligand 4: A solution of potassium ethanethiolate (0.90 g, 9.70 mmol) and **2** (1.40 g, 3.9 mmol) in anhydrous DMF (35.0 mL) was warmed to 130 °C for 16 h. The dark red solution was put on ice, and acetyl chloride (2.80 mL, 38.80 mmol) was added dropwise using a syringe. The resulting beige suspension was stirred at room temperature for 1 h and diluted with CHCl₃ (200 mL). The organic layer was washed with saturated brine (2 × 150 mL), the aqueous phase was extracted with CHCl₃ (8 × 50 mL) and the combined organic phase was washed with saturated aqueous NaHCO₃ (150 mL) and then dried with anhydrous MgSO₄. Removal of the organic phase under reduced pressure gave a solid, which was recrystallized from acetone to afford a beige powder (1.04 g, 70%). ¹H NMR (200 MHz, CDCl₃, 25 °C): δ = 8.94 (ddd, J = 4.7, 1.7, 0.8 Hz, 2 H, H¹,¹³), 8.89 (ddd, J = 7.9, 1.4, 0.9 Hz, 2 H, H⁴,¹⁰), 8.83 (d, ³J = 8.7 Hz, 2 H, H¹⁵,¹⁹), 7.98 (dt, J = 7.9, 7.7, 1.8 Hz, 2 H, H³,¹¹), 7.54 (ddd, J = 7.6, 4.7, 1.2 Hz, 2 H, H²,¹²), 7.66 (d, ³J = 8.7 Hz, 2 H, H¹⁶,¹⁸), 2.45 (s, 3 H, H²¹) ppm. ¹³C NMR (100 MHz, CDCl₃, 25 °C): δ = 192.8 (C, 1 C, C²⁰), 172.1 (C, 2 C, C⁶,⁸), 171.6 (C, 1 C, C⁷), 153.1 (C, 2 C, C⁵,⁹), 150.3 (CH, 2 C, C¹,¹³), 137.1 (CH, 2 C, C³,¹¹), 136.1 (C, 1 C, C¹⁷), 134.2 (CH, 2 C, C¹⁵,¹⁹), 133.5 (C, 1 C, C¹⁴), 129.8 (CH, 2 C, C²,¹²), 126.4 (CH, 2 C, C⁴,¹⁰), 124.9 (CH, 2 C, C¹⁶,¹⁸), 22.7 (CH₃, 1 C, C²¹) ppm.

$C_{21}H_{15}N_5OS$ (385.44): calcd. C 65.44, H 3.92, N 18.17, S 8.32; found C 65.49, H 3.84, N 18.44, S 8.37. MS (EI, 153 °C): m/z (%) = 385 (10) $[M]^+$, 343 (100) $[M + H - SAc]^+$, 105 (55).

General Procedure for the Synthesis of Fe^{II} Complexes 5–7: A solution of $Fe(BF_4)_2 \cdot 6H_2O$ (163.03 mg, 0.48 mmol) in anhydrous ethanol (2.0 mL) was added to a solution of the triazine ligand (0.64 mmol) in anhydrous ethanol (6.0 mL) at room temperature. The purple reaction mixture was heated to reflux for 30 min, during which a purple microcrystalline precipitate was deposited. The product was filtered off and washed with anhydrous ethanol (3×2 mL) and anhydrous diethyl ether (1×3 mL).

Complex 5: Purple solid (261 mg, 58%). ^{1}H NMR (500 MHz, [D$_6$]-DMSO, 25 °C): δ = 9.30 (br. s, 4 H, H$^{4,4',10,10'}$), 9.23 (br. s, 4 H, H$^{15,15',19,19'}$), 8.20 (br. s, 8 H, H$^{11,11',3,3',16,16',18,18'}$), 7.92 (br. s, 6 H, H$^{2,2',12,12',17,17'}$), 7.47 (br. s, 4 H, H$^{1,1',13,13'}$) ppm. ^{13}C NMR (125 MHz, [D$_6$]DMSO, 28 °C): δ = 174.1 (C, 4 C, C$^{6,6',8,8'}$), 172.6 (C, 2 C, C$^{7,7'}$), 156.9 (C, 4 C, C$^{5,5',9,9'}$), 153.2 (CH, 4 C, C$^{2,2',12,12'}$), 140.5 (CH, 2 C, C$^{17,17'}$), 135.4 (CH, 4 C, C$^{3,3',11,11'}$), 135.0 (CH, 4 C, C$^{15,15',19,19'}$), 132.0 (C, 2 C, C$^{14,14'}$), 130.4 (CH, 4 C, C$^{1,1',13,13'}$), 130.1 (CH, 4 C, C$^{4,4',10,10'}$), 128.4 (CH, 4 C, C$^{16,16',18,18'}$) ppm. $C_{38}H_{26}B_2F_8FeN_{10}$ (852.13): calcd. C 53.56, H 3.08, N 16.44; found C 53.30, H 3.19, N 16.62. IR (KBr): ṽ = 3443 (m), 1580 (s), 1560 (m), 1507 (m), 1407 (m), 1360 (s), 1054 (s), 770 (m) cm^{-1}. HRMS (ESI): calcd. for $C_{38}H_{26}FeN_{10}$ $[M]^{2+}$ 339.0840; found 339.0833. MS (ESI): m/z (%) = 339.08 (100) $[M]^{2+}$, 765.17 (13) $[M + BF_4]^+$.

Complex 6: Purple solid (60 mg, 58%). ^{1}H NMR (200 MHz, CD$_3$CN, 25 °C): δ = 9.24 (d, ^3J = 8.4 Hz, 4 H, H$^{15,15',19,19'}$), 9.26–9.14 (br. m, 4 H, H$^{4,4',10,10'}$), 8.13 (br. mc, 4 H, H$^{11,11',3,3'}$), 7.93 (d, ^3J = 8.6 Hz, 4 H, H$^{16,16',18,18'}$), 7.73 (br. mc, 4 H, H$^{2,2',12,12'}$), 7.35 (br. mc, 4 H, H$^{1,1',13,13'}$), 2.54 (s, 6 H, H$^{21,21'}$) ppm. ^{13}C NMR (100 MHz, [D$_6$]DMSO, 25 °C): δ = 192.5 (C, 2 C, C$^{20,20'}$), 173.7 (C, 4 C, C$^{6,6',8,8'}$), 172.0 (C, 2 C, C$^{7,7'}$), 171.1 (C, 2 C, C$^{5,5',9,9'}$), 156.3 (CH, 4 C, C$^{2,2',12,12'}$), 152.7 (C, 2 C, C$^{17,17'}$), 143.3 (C, 2 C, C$^{14,14'}$), 139.9 (CH, 4 C, C$^{3,3',11,11'}$), 133.6 (CH, 4 C, C$^{15,15',19,19'}$), 130.9 (CH, 4 C, C$^{1,1',13,13'}$), 127.7 (CH, 4 C, C$^{4,4',10,10'}$), 127.1 (CH, 4 C, C$^{16,16',18,18'}$), 21.0 (CH$_3$, 2 C, C$^{21,21'}$) ppm. $C_{42}H_{30}B_2F_8FeN_{10}O_2S_2 \cdot 2H_2O$ (1036.37): calcd. C 48.67, H 3.31, N 13.52, S 6.19; found C 48.81, H 3.00, N 13.84, S 5.91. HRMS (ESI): calcd. for $C_{42}H_{30}FeN_{10}O_2S_2$ $[M]^{2+}$ 413.0667; found 413.0663. MS (ESI): m/z (%) = 413.07 (100) $[M]^{2+}$, 913.14 (6) $[M + BF_4]^+$, 845.13 (24) $[M + F]^+$.

Complex 7: Purple solid (247 mg, 62%) ^{1}H NMR (400 MHz, [D$_6$]-DMSO, 25 °C): δ = 9.36 (br. mc, 4 H, H$^{4,4',10,10'}$), 9.16 (d, ^3J = 7.8 Hz, 4 H, H$^{19,19',15,15'}$), 8.51 (br. mc, 4 H, H$^{11,11',3,3'}$), 8.21 (br. mc, 4 H, H$^{2,2',12,12'}$), 7.55 (br. mc, 4 H, H$^{1,1',13,13'}$), 7.44 (d, ^3J = 7.9 Hz, 4 H, H$^{16,16',18,18'}$), 4.05 (s, 6 H, H$^{20,20'}$) ppm. ^{13}C NMR (100 MHz, [D$_6$]DMSO, 25 °C): δ = 172.6 (C, 4 C, C$^{6,6',8,8'}$), 172.0 (C, 2 C, C$^{7,7'}$), 164.7 (C, 4 C, C$^{9,9',5,5'}$), 156.6 (CH, 4 C, C$^{2,2',12,12'}$), 151.6 (C, 2 C, C$^{17,17'}$), 139.6 (CH, 4 C, C$^{3,3',11,11'}$), 132.1 (CH, 8 C, C$^{1,1',13,13',15,15',19,19'}$), 127.8 (CH, 4 C, C$^{4,4',10,10'}$), 126.5 (C, 2 C, C$^{14,14'}$), 114.8 (CH, 4 C, C$^{16,16',18,18'}$), 55.8 (CH$_3$, 2 C, C$^{20,20'}$) ppm. IR (KBr): ṽ = 1577 (vs), 1475 (s), 1407 (vs), 1209 (m), 1177 (vs), 1113 (m), 1055 (vs, BF$_4^-$), 1034 (vs), 779 (vs) cm^{-1}. $C_{40}H_{30}B_2F_8FeN_{10}O_2 \cdot H_2O$ (930.20): calcd. C 51.65, H 3.47, N 15.06; found C 51.31, H 3.79, N 14.86. HRMS (ESI): calcd. for $C_{40}H_{30}FeN_{10}O_2$ $[M]^{2+}$ 369.0938; found 369.0945. MS (ESI): m/z (%) = 369.09 (100) $[M]^{2+}$, 825.19 (6) $[M + BF_4]^+$.

Complex 8: Compound **3** (0.29 mmol, 100 mg) was stirred in ethanol (3 mL) and added to a solution of $Zn(ClO_4)_2 \cdot 6H_2O$ (0.18 mmol, 66 mg) in ethanol (3 mL). After heating to reflux for 45 min, the off-white precipitate was filtered off and washed with ethanol (4×1 mL) and diethyl ether (1×3 mL) to yield **8** as an off-white powder (148 mg, 87%). ^{1}H NMR (400 MHz, [D$_6$]DMSO, 25 °C): δ = 9.20 (m, 4 H, H$^{4,4',10,10'}$), 9.07 (d, ^3J = 8.4 Hz, 4 H, H$^{19,19',15,15'}$), 8.62 (m, 4 H, H$^{3,3',11,11'}$), 8.39 (m, 4 H, H$^{2,2',12,12'}$), 7.75 (m, 4 H, H$^{1,1',13,13'}$), 7.38 (d, ^3J = 8.7 Hz, 4 H, H$^{16,16',18,18'}$), 4.02 (s, 6 H, H$^{20,20'}$) ppm. ^{13}C NMR (100 MHz, [D$_6$]DMSO, 25 °C): δ = 175.1 (C, 4 C, C$^{6,6',8,8'}$), 165.5 (C, 2 C, C$^{7,7'}$), 164.8 (C, 4 C, C$^{9,9',5,5'}$), 149.9 (CH, 4 C, C$^{2,2',12,12'}$), 145.8 (C, 2 C, C$^{17,17'}$), 141.8 (CH, 4 C, C$^{3,3',11,11'}$), 132.9 (CH, 4 C, C$^{15,15',19,19'}$), 130.6 (CH, 4 C, C$^{1,1',13,13'}$), 126.2 (C, 2 C, C$^{14,14'}$), 124.9 (CH, 4 C, C$^{4,4',10,10'}$), 115.2 (CH, 4 C, C$^{16,16',18,18'}$), 56.0 (CH$_3$, 2 C, C$^{20,20'}$) ppm. $C_{40}H_{30}Cl_2N_{10}O_{10}Zn$ (947.92): calcd. C 50.73, H 3.19, N 14.79; found C 50.32, H 3.01, N 14.61. HRMS (ESI): calcd. for $C_{40}H_{30}N_{10}O_2Zn$ $[M]^{2+}$ 373.0917; found 373.0914. MS (ESI): m/z (%) = 373.09 (100) $[M]^{2+}$, 845.13 $[M + ClO_4]^+$.

Supporting Information (see footnote on the first page of this article): Additional crystal structures, cyclic voltammograms and transient spectra.

[1] H. A. Goodwin, *Top. Curr. Chem.* **2004**, *233*, 59.
[2] M. A. Halcrow, *Polyhedron* **2007**, *26*, 3523.
[3] F. Renz, H. Oshio, V. Ksenofontov, M. Waldeck, H. Spiering, P. Gütlich, *Angew. Chem. Int. Ed.* **2000**, *39*, 3699.
[4] E. C. Constable, G. Baum, E. Bill, R. Dyson, R. van Eldik, D. Fenske, S. Kaderli, D. Morris, A. Neubrand, M. Neuburger, D. R. Smith, K. Wieghardt, M. Zehnder, A. D. Zuberbühler, *Chem. Eur. J.* **1999**, *5*, 498.
[5] W. Macyk, G. Stochel, K. Szacilowski, *Chem. Eur. J.* **2007**, *13*, 5676.
[6] C. Shen, M. Haryono, A. Grohmann, M. Buck, T. Weidner, N. Ballav, M. Zharnikov, *Langmuir* **2008**, *24*, 12883.
[7] M. Haryono, F. W. Heinemann, K. Petukhov, K. Gieb, P. Müller, A. Grohmann, *Eur. J. Inorg. Chem.* **2009**, 2136.
[8] Y. Kang, D.-J. Won, S. R. Kim, K. Seo, H.-S. Choi, G. Lee, Z. Noh, T. S. Lee, C. Lee, *Mater. Sci. Eng., C* **2004**, *24*, 43.
[9] M. I. J. Polson, E. A. Medlycott, G. S. Hanan, L. Mikelsons, N. J. Taylor, M. Watanabe, Y. Tanaka, F. Loiseau, R. Passalacqua, S. Campagna, *Chem. Eur. J.* **2004**, *10*, 3640.
[10] E. A. Medlycott, G. S. Hanan, T. S. M. Abedin, L. K. Thompson, *Polyhedron* **2008**, *27*, 493.
[11] M. I. J. Polson, N. J. Taylor, G. S. Hanan, *Chem. Commun.* **2002**, 1356.
[12] N. H. Damrauer, B. T. Weldon, J. K. McCusker, *J. Phys. Chem. A* **1998**, *102*, 3382.
[13] M. A. Harvey, S. Baggio, A. Ibanez, R. Baggio, *Acta Crystallogr., Sect. C: Cryst. Struct. Commun.* **2004**, *60*, m375.
[14] C. Stroh, P. Turek, P. Rabu, R. Ziessel, *Inorg. Chem.* **2001**, *40*, 5334.
[15] J. Heinze, *Angew. Chem.* **1984**, *96*, 823; *Angew. Chem. Int. Ed. Engl.* **1984**, *23*, 831.
[16] I. D. L. Albert, T. J. Marks, M. A. Ratner, *J. Am. Chem. Soc.* **1997**, *119*, 6575.
[17] J. M. Rao, M. C. Hughes, D. J. Macero, *Inorg. Chim. Acta* **1976**, *16*, 231.
[18] K. Izutsu, *Electrochemistry in Nonaqueous Solutions*, Wiley-VCH, Weinheim, **2002**, p. 172.
[19] E. A. Medlycott, K. A. Udachin, G. S. Hanan, *Dalton Trans.* **2007**, 430.

[20] A. B. P. Lever in *Comprehensive Coordination Chemistry II* (Eds.: J. A. McCleverty, T. J. Meyer), Elsevier, Amsterdam, **2003**, p. 251.

[21] I. Hanazaki, S. Nagakura, *Inorg. Chem.* **1969**, *8*, 648.

[22] U. El-Ayaan, F. Murata, Y. Fukuda, *Monatsh. Chem.* **2001**, *132*, 1279.

[23] P. Gütlich, H. A. Goodwin, *Top. Curr. Chem.* **2004**, *233*, 1.

[24] S. Schenker, P. C. Stein, J. A. Wolny, C. Brady, J. J. McGarvey, H. Toftlund, A. Hauser, *Inorg. Chem.* **2001**, *40*, 134.

[25] P. Gütlich, Y. Garcia, H. A. Goodwin, *Chem. Soc. Rev.* **2000**, *29*, 419.

[26] E. König, *Struct. Bonding (Berlin)* **1991**, *76*, 51.

[27] H. Toftlund, J. J. McGarvey, *Top. Curr. Chem.* **2004**, *233*, 151.

[28] A. Bousseksou, G. Molnar, G. Matouzenko, *Eur. J. Inorg. Chem.* **2004**, 4353.

[29] T. G. Spence, T. D. Burns, L. A. Posey, *J. Phys. Chem. A* **1997**, *101*, 139.

[30] T. G. Spence, B. T. Trotter, L. A. Posey, *J. Phys. Chem. A* **1998**, *102*, 7779.

[31] B. Strauss, W. Linert, V. Gutmann, R. F. Jameson, *Monatsh. Chem.* **1992**, *123*, 537.

[32] M. Enamullah, W. Linert, *Thermochim. Acta* **2002**, *388*, 401.

[33] W. Yang, H. Schmider, Q. Wu, Y.-S. Zhang, S. Wang, *Inorg. Chem.* **2000**, *39*, 2397.

[34] K. Kirchner, R. Jedlicka, R. Schmid, *Monatsh. Chem.* **1992**, *123*, 203.

[35] J. K. McCusker, H. Toftlund, A. L. Rheingold, D. N. Hendrickson, *J. Am. Chem. Soc.* **1993**, *115*, 1797.

[36] J. J. McGarvey, I. Lawthers, K. Heremans, H. Toftlund, *J. Chem. Soc., Chem. Commun.* **1984**, 1575.

[37] J. J. McGarvey, I. Lawthers, *J. Chem. Soc., Chem. Commun.* **1982**, 906.

[38] J. K. Beattie, R. A. Binstead, R. J. West, *J. Am. Chem. Soc.* **1978**, *100*, 3044.

[39] E. V. Dose, M. A. Hoselton, N. Sutin, M. F. Tweedle, L. J. Wilson, *J. Am. Chem. Soc.* **1978**, *100*, 1141.

[40] K. A. Reeder, E. V. Dose, L. J. Wilson, *Inorg. Chem.* **1978**, *17*, 1071.

[41] C. Bressler, C. Milne, V. T. Pham, A. El Nahhas, R. M. van der Veen, W. Gawelda, S. Johnson, P. Beaud, D. Grolimund, M. Kaiser, C. N. Borca, G. Ingold, R. Abela, M. Chergui, *Science* **2009**, *323*, 489.

[42] A. L. Smeigh, M. Creelman, R. A. Mathies, J. K. McCusker, *J. Am. Chem. Soc.* **2008**, *130*, 14105.

[43] W. Gawelda, A. Cannizzo, V.-T. Pham, F. van Mourik, C. Bressler, M. Chergui, *J. Am. Chem. Soc.* **2007**, *129*, 8199.

[44] J. E. Monat, J. K. McCusker, *J. Am. Chem. Soc.* **2000**, *122*, 4092.

[45] H.-M. Koepp, H. Wendt, H. Strehlow, *Z. Elektrochem.* **1960**, *64*, 483.

[46] R. Hermann, G. R. Mahalaxmi, T. Jochum, S. Naumov, O. Brede, *J. Phys. Chem. A* **2002**, *106*, 2379.

[47] *COLLECT*, Bruker AXS Inc., Madison WI, USA, **2002**.

[48] *SHELXTL NT 6.12*, Bruker AXS Inc., Madison WI, USA, **2002**.

CeO$_2$ Buffer Layers for HTSC by an Aqueous Sol-Gel Method – Chemistry and Microstructure

Nigel Van de Velde,*[a] David Van de Vyver,[a] Oliver Brunkahl,[b] Serge Hoste,[a] Els Bruneel,[a] and Isabel Van Driessche[a]

During the last decade the focus in superconductivity research has shifted towards the manufacturing of easy-to-handle superconductors, because of their high usability in electronic applications in comparison to bulky ceramics. This article reviews our recent progress made in the buffer-layer architecture of such a coated conductor, focusing on CeO$_2$ thin films prepared by an aqueous sol-gel method and deposited by dip-coating. Starting from water-soluble cerium(III) nitrate precursors, we were able to deposit films showing a very high degree of [002] orientation depending on the film characteristics and synthesis conditions. The formation and stability of the chemical complexes in the solution was studied by potentiometric titrations. The main parameters influencing the texture seem to be the ambient Ar-(5 %)H$_2$ atmosphere and the thickness of the synthesized buffer layers. The microstructure of the thin films deposited on metallic tapes was controlled by the incorporation of doping elements. This research allowed us to achieve a 50 nm thick CeO$_2$ film, showing a very high degree of [002] orientation and exhibiting a low surface roughness. Subsequent YBa$_2$Cu$_3$O$_7$ synthesis by TFA-MOD resulted in promising XRD and J_c measurements. Our easy-to-use, environmentally friendly strategy could contribute to the spreading of the use of coated conductors in everyday applications.

Introduction

YBa$_2$Cu$_3$O$_7$ is regarded as the main material explored towards its superconducting characteristics. Excellent results in terms of critical temperature (T_c) and critical current density (J_c) have been established on single-crystal substrates by various vacuum-deposition techniques such as pulsed laser deposition or chemical vapor deposition. Deposition on SrTiO$_3$ single crystals results in good epitaxial YBa$_2$Cu$_3$O$_7$ growth due to the limited lattice mismatch between SrTiO$_3$ (a = 3.905 Å[1]) and YBa$_2$Cu$_3$O$_7$ (a = 3.818 Å[2]). Restrictions towards several technological applications are found in both the cost of single-crystal substrates and the necessity of energy consuming or material inefficient deposition methods. Such strategies exclude an easy transfer towards continuous production units.

In order to cope with these drawbacks, attention was driven towards a low-cost deposition technique, i.e. chemical solution deposition on more flexible metallic tapes.[3,4] In order to minimize chemical interactions and optimize crystal growth, a buffer layer architecture of sufficient thickness is required to retain the best possible quality superconducting YBa$_2$Cu$_3$O$_7$ thin films. The buffer-layer architecture consists of several thin films, e.g. a combination of CeO$_2$ (a = 5.411 Å[5]) and La$_2$Zr$_2$O$_7$ (a = 10.804 Å[6]) or a single SrTiO$_3$ buffer layer. Recent research into new generation high J_c YBa$_2$Cu$_3$O$_7$-coated conductors shows promising applicability in electrical power and electronic appliances.[7,8] We have explored a multi-layered architecture consisting of both CeO$_2$ and La$_2$Zr$_2$O$_7$. A schematic cross-section of a coated conductor is given in Figure 1.

The synthesis method selected for these innovative materials combines optimal quality and minimal environmental consequences by using mainly water-based compounds and avoiding fluorine containing species. This article reviews the chemistry and texture obtained in the aqueous citrate gel method for synthesizing CeO$_2$ thin films by sol-gel chemistry. Besides the environmental benefits, the main advantage of this aqueous chemical solution deposition (CSD) method is the flexibility during the synthesis, which clears the path towards a continuous production unit on industrial scale. Research towards the incorporation of doping elements in the film can proceed with high precision and without the need for technological adaptations of the process. Specific requirements for a buffer layer consist of a sufficient thickness and smoothness, high crystallinity and epitaxial YBa$_2$Cu$_3$O$_7$ growth.

[a] Department of Inorganic and Physical Chemistry, Ghent University,
    Krijgslaan 281 (S3), 9000 Ghent, Belgium
    Fax: +32-92644983
    E-mail: Nigel.VandeVelde@ugent.be
[b] Zenergy Power GmbH,
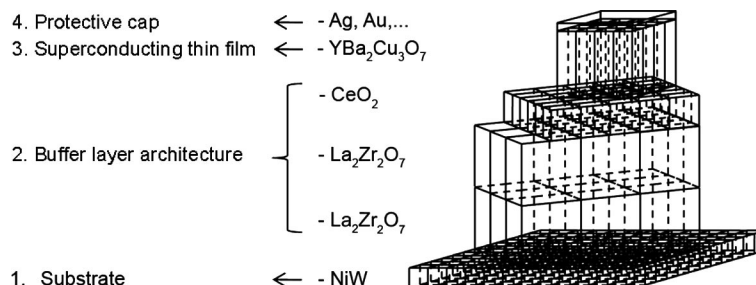   Heisenbergstrasse 16, 53359 Rheinbach, Germany

Figure 1. Coated conductor.

The precursor solutions were prepared by dissolving stable, cost-effective and widely available inorganic salts in an aqueous solution of coordinating ligands. As a result, solvation by water molecules is discouraged and neither extensive hydrolysis nor precipitation is likely to take place, resulting in extremely homogeneous materials. In addition, the sol-gel process involves the development of inorganic networks starting from the formation of a colloidal suspension (sol) and continued by gelation of the sol into a metal-based network in a continuous liquid phase (gel). From a chemical point of view sol-gel chemistry is based on the hydrolysis and condensation of metal complexes.[3,9–13] In the aqueous method described in this work, the metal salts are dissolved in water with formation of unstable metal aqua complexes. Hydrolysis of these species leads to precipitation of metal hydroxides. Thus hydrolysis speed needs to be controlled by adding complexing agents, in this case citric acid (CA), leading to the formation of metal chelates and thus, stabilisation of the precursor solution. Controlling several complex formation parameters, e.g. pH and metal-to-ligand ratio, not only results in an extended stability of the system, but can drive the system towards appropriate 3D-networks as well.

Results and Discussion

Potentiometric Results

In order to obtain homogeneous buffer layers after the sol-gel transition and thermal treatment it is necessary to control and have knowledge of the occurring species in an aqueous metal precursor solution. For this reason a potentiometric analysis has been conducted on an aqueous Ce^{3+}-containing system. The distribution of different complexes present in the precursor solution are determined by the computer program "Superquad" through simulations using the stability constants of the different chemical species present.[13–15] For each of the significant chemical species $M_pL_qH_r$, following expression of the formation constant describes its equilibrium (charges were omitted to improve legibility):

$$\beta_{pgr} = \frac{[M_pL_qH_r]}{[M]^p[L]^q[H]^r}$$

M = metal, with p the number of metal elements linked in one complex structure;

L = ligand, with q the number of ligands surrounding the metals in one complex structure;

H = deprotonation factor of the ligands, with r the number of deprotonations (positive) or dehydroxylations (negative) on every ligand in one complex structure.

Although the thermodynamic definition of a formation constant utilizes activities instead of concentrations, as given above, the quotient of the activity coefficients was assumed to remain constant by performing the experiments in a medium of constant ionic strength by adding potassium nitrate. The stability constants of several aqueous species were calculated by Superquad using a numerical simulation of all experimental titration data by testing a number of chemically acceptable complexation models. These models consist of metal ion-ligand complexes ($M_pL_qH_r$ with $r = 0$), together with some protonated complexes ($r > 0$) and hydroxocomplexes ($r < 0$). After successive attempts the best models were selected according to agreement between observed and calculated data by means of an accurate statistic analysis of the global σ-value for the refinement, by goodness of fit (χ^2) and by the standard deviation of each formation constant as calculated by Superquad. The simulated titration curves and species distribution diagrams for each given set of aqueous species were computed from the equilibrium constants with the program Equil.[16]

Cerium(III) ions will interact with citric acid, forming complexes with this multidentate ligand.[17] Hancock and Martell listed a chemical model for this metal ion, using the protonation constants of citric acid determined by Martell et al.[18] Unfortunately no hydroxo complex species were defined. Therefore a more accurate determination of the stability constants over the whole pH region was necessary for this study. A first series of titrations were performed using Ce^{III} and citric acid in a 1:1, 1:2 and 1:3 molar ratio. The experiments were carried out with an excess of nitric acid. The titration in a 1:1 molar ratio leads to the formation of the insoluble cerium hydroxide, which reveals the formation of M_xL_y ($y > x$) complex species. Further research shows that the potentiometric equilibrium curve for the 1:2 and 1:3 Ce^{III} to citric acid titration possesses a sharp inflection point at $a = 3$ ($a = $ mol OH^-/mol Ligand), matching the formation of the complex species $Ce(CA)_2$. Both curves gave a second inflection at 3.67 (1:2 molar ratio) and 3.44 (1:3
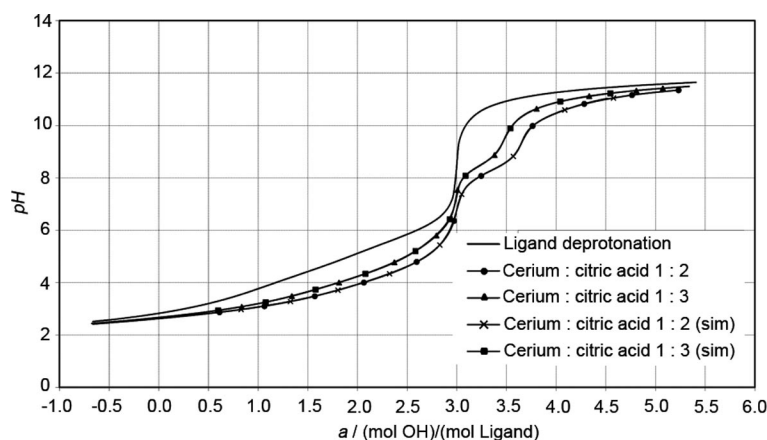
Figure 2. Experimental titration curves in a 1:2 and 1:3 metal/ligand molar ratio, combined with simulated curves formed by the addition of a polynuclear complex 340.
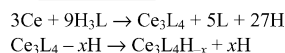
molar ratio). These inflection points could be perfectly simulated by adding polynuclear species to the chemical model. By means of calculations, we were able to identify the polynuclear complex as $M_3L_4H_{-x}$. The theoretical calculation of the *a* value using the polynuclear hydroxo complex $M_3L_4H_{-4}$ perfectly corresponds with the experimental *a* value of the second inflection point found in both the 1:2 and the 1:3 titration. The use of this polynuclear species leads to a perfect fit between the experimental and the simulated curve as shown in Figure 2.

1 to 2 titration

$$3Ce + 6H_3L \rightarrow Ce_3L_4 + 2L + 18H$$
$$Ce_3L_4 - xH \rightarrow Ce_3L_4H_{-x} + xH$$
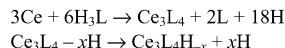
x	1	2	3	4	5	6
a	3.17	3.33	3.50	3.67	3.83	4.00

1 to 3 titration

$$3Ce + 9H_3L \rightarrow Ce_3L_4 + 5L + 27H$$
$$Ce_3L_4 - xH \rightarrow Ce_3L_4H_{-x} + xH$$

| x	1	2	3	4	5	6
a	3.11	3.22	3.33	3.44	3.56	3.67

The confirmation for the presence of the polynuclear species $M_3L_4H_{-4}$ in the solution was given by a second series of titrations in a 2:3 and 3:4 metal-to-ligand molar ratio. The 2:3 titration curve gave rise to a second inflection at a = 3.89, while the 3:4 titration curve lead to an inflection at a = 4.00.

2 to 3 titration

$$3Ce + 4.5H_3L \rightarrow Ce_3L_4 + 0.5L + 13.5H$$
$$Ce_3L_4 - 4H \rightarrow Ce_3L_4H_{-4} + 4H$$
$$a = 3.89$$

3 to 4 titration
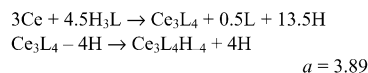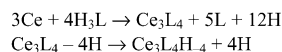
$$3Ce + 4H_3L \rightarrow Ce_3L_4 + 5L + 12H$$
$$Ce_3L_4 - 4H \rightarrow Ce_3L_4H_{-4} + 4H$$
$$a = 4$$

The results of these two supplementary titrations gave extra support to the proposed existence of this polynuclear hydroxo complex. The chemical model was therefore refined

with a series of these polynuclear complexes and the calculations were based on the experimental data of the 1:2 and 1:3 titration. The formation constants of the complex species are given in Table 1.

Table 1. Overall formation constants (β) (Ce^{III} – CA) for the interaction of Ce^{III} with CA (M = Ce^{3+}, CA = citric acid, H = H$^+$, I = 0.10 M KNO$_3$, 25 °C).

Stoichiometry		log β[a]	Stepwise constant K	log K
CA	H			
1	1	5.72	[HCA]/[H][CA]	5.72
1	2	10.10	[H2CA]/[H][HCA]	4.38
1	3	13.05	[H3CA]/[H][H2CA]	2.95

[a] Estimated error = ± 0.02.

It is apparent from the species distribution diagram in Figure 3 that the mononuclear Ce^{III} species begin to form at a pH lower than 3.

It is interesting to note that a protonated metal complex was first found in the theoretically accepted model and was transformed into the ML ("110" in Figure 3) and M_3L_4 ("340" in Figure 3) species. With further increasing pH these complexes gave rise to a Ce^{III} complex of type ML$_2$ ("120" in Figure 3) which is the main species in the pH region between 5 and 8. At higher pH the polynuclear hydroxo complex $M_3L_4H_{-4}$ ("34–4" in Figure 3) is being formed and is the dominating species at higher pH (8.5 < pH < 10.5). At a pH of 7 the main species is the ML$_2$ ("120" in Figure 3) and no hydroxo complex is formed. From potentiometric point of view the main complex at a pH ranging from 6 to 7 exists of a Ce^{III} atom surrounded by two neutral citric acid molecules, which can be seen as the starting material for a three-dimensional network. During the gelation in a thermal oven at 60 °C, water and ammonia will evaporate, which can lead to an increase of the acidity of the solution and as shown in Figure 3 to a higher distribution percentage of the polynuclear species M_3L_4 ("340" in Figure 3). This pH evolution and concurring development of mononuclear into polynuclear species can be
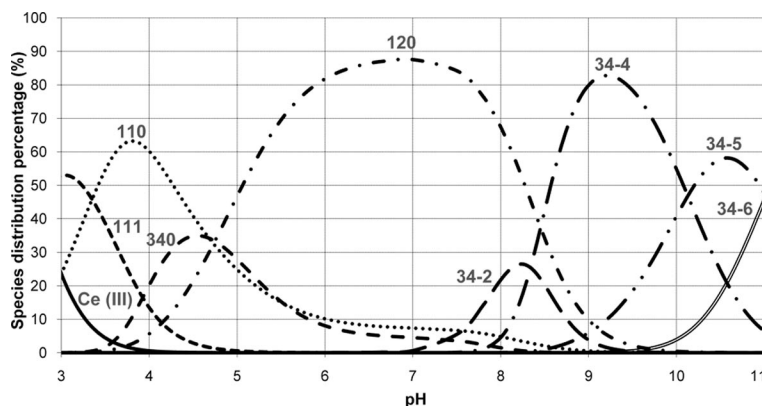
Figure 3. Species distribution diagram showing the species formed as a function of pH when citric acid (3.36×10^{-3} M) and Ce^{III} (1.12×10^{-3} M) are equilibrated at 25 °C and I = 0.10 M (KNO_3).

seen as a direct confirmation for the formation of three-dimensional networks that are known to induce the formation of stable gels.

Experimental proof of a stable sol to gel transition at a metal-to-ligand ratio of 1:3 and a pH between 6 and 7 was found.

Thin-Film Formation

Research towards deposition and synthesis of CeO_2 buffer layers started from previously attained experience, as published before.[19–21] Starting from the thermal process in Figure 4, we mainly focused on the sintering step (at approximately 1050 °C) and its according ambient Ar-(5%)H_2 atmosphere.

A coating starting from the further described precursor solution A (0.2 M – 1.5 cP), resulted in 15 to 20 nm thick CeO_2 films for dip-coating withdrawal speeds up to 170 mm/min. We examined the influence of both sintering time and temperature on the texture (Figure 5) by X-ray diffraction, focusing on both the undesired [111] and preferred [002] orientations.

It is clear that acceptable texture occurs from 1000 °C onwards. There is a sharp increase in [002] crystal growth with time. These films, with thicknesses lower than 20 nm, showed no observable [111] crystal growth. The increase in peak intensities with sintering time could indicate towards
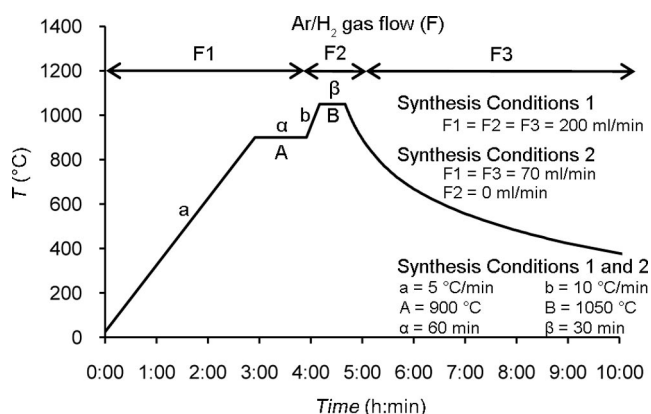
Figure 4. Thermal process.

enlarged crystallite sizes, while the increase of peak intensities with sintering temperature could indicate towards a larger amount of crystalline material. According to these remarks both parameters should be as high as feasible. For films in this order of thickness "synthesis conditions 1" (Figure 4) are very appropriate. The good XRD texture was confirmed by electron backscatter diffraction and pole figures on a sample synthesized at a chosen sintering time of 30 min and a sintering temperature of 1100 °C. These analyses revealed a very high degree of [002] crystal growth (97.9%) with a very small amount of misorientation, as can be seen in Figure 6.

Figure 5. Influence of sintering temperature (left) and time (right) on crystal growth.

Figure 6. EBSD and pole figures.

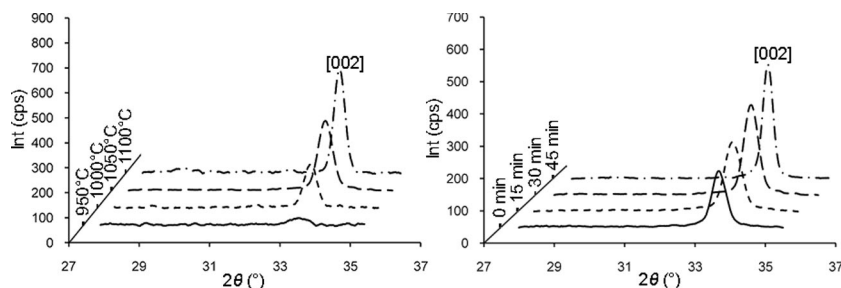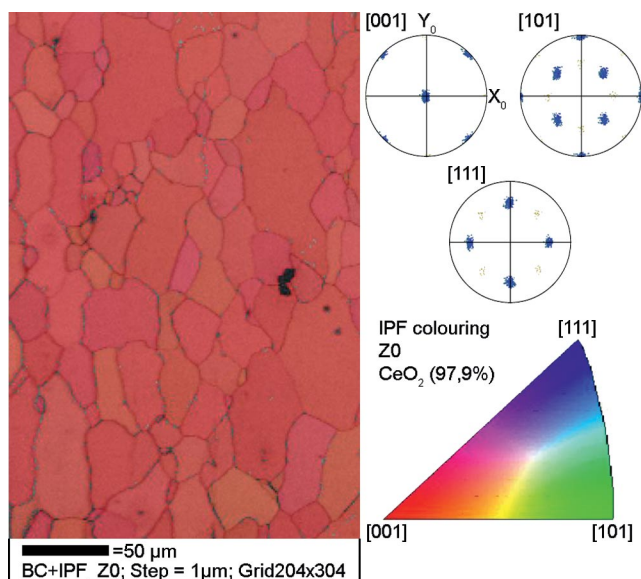FE-SEM images (Figure 7) allowed us to observe smooth surfaces for all experiments using short dwell times, which should be beneficial in the further synthesis of a coated conductor. Therefore a compromise has to be reached for attaining both acceptable XRD texture and surface structures.
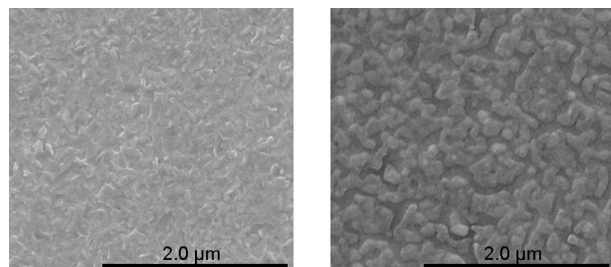

Figure 7. Influence of sintering time on surface morphology (left: 0 min; right: 45 min); sintering temperature: 1050 °C.

As mentioned before, one of the highly desired requirements of a CeO_2 buffer layer in coated conductors is a desired thickness of at least 50 nm, what was not yet accomplished during this stage of the research. Adjusting several parameters occurring in the Landau–Levich equation allows us to control the thickness of thin films. Among these parameters the viscosity of the precursor solution and the dip-coating withdrawal speed are the most straightforward. The use of precursor solution B (0.45 м – 3 cP) resulting in an optimized wettability of our substrates and thicknesses up to several hundredths of nanometer with our dip-coating device. This severe change in film thicknesses in comparison to the previous synthesis however had a huge influence on the achieved texture. Figure 8 shows a heavily decreasing XRD texture with increasing thickness.

There are 2 possible explanations for this observed phenomenon. First of all crystal growth will not reach a 100% growth in the desired [002] direction because of slight differ-
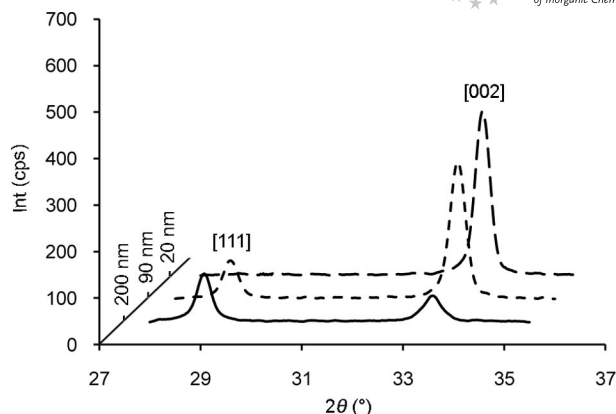

Figure 8. Influence of thickness on the texture; gasflow of ambient Ar/5%-H₂ atmosphere: 70 mL/min.

ences in cell parameters between the substrate and the CeO_2 crystals. Some of the crystals will only show a small difference, while others might be forced to grow in the direction of the more stable [111] orientation, making further [002] crystal growth impossible in subsequent crystal layers.[22] Some material could even remain as an amorphous phase. Every subsequent growing layer of crystals will follow the same trend, which makes it obvious that more and more of the material will develop into the [111] orientation with an increasing number of crystal layers or with increasing thickness.

Another trend that can be seen on the X-ray diffractograms is the behavior of the peak intensities. One would expect the intensity of the [002] orientation to increase, regardless of the further development of the [111] orientation. This opposite trend could be explained by posing either that the material becomes less crystalline with an increasing film thickness or by posing that once a certain thickness is exceeded, the remainder of the material develops into amorphous CeO_2, what could be explained by the crystal growth behavior in the previous paragraph. That makes both the increasing trend in [111] crystal growth and in amorphous material in subsequent crystal layers obvious. At a certain moment the amorphous material might prevent any further growth of crystalline material, resulting in stable peak intensities.

In order to avoid the deteriorating texture of thicker films, the synthesis procedure had to be adapted. Optimizing the flow rate of the ambient Ar-(5%)H₂ atmosphere seemed to be most effective. A first set of experiments examined the difference between low and high flow rates, kept at a constant level during the whole synthesis process. On Figure 9 (left) a remarkably improved texture in case of decreasing flow rates can be seen.

A minimum flow rate of 70 mL/min over longer periods was required in order to avoid substrate oxidation. Therefore a second set of experiments examined the effect of a varying flow rate during the synthesis process (Figure 9 – right). This way a more thorough decrease could proceed during a limited amount of time, i.e. during the relatively short period where crystal growth occurs. During these ex-
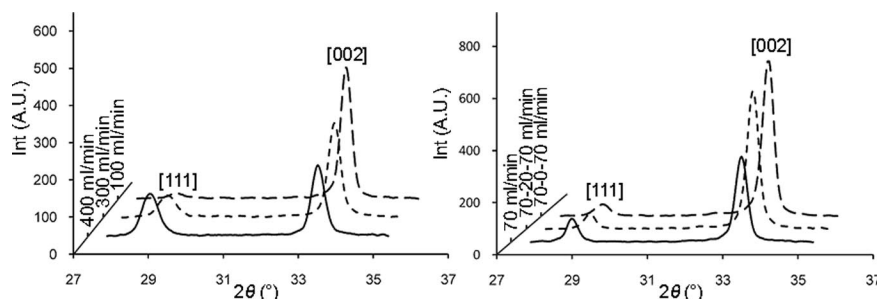
N. Van de Velde et al.

Figure 9. Influence of the ambient gasflow on the texture (left: continuous gasflow; right: varying gasflow); film thickness: 20 nm.

periments other parameters, such as the synthesis temperatures were kept constant. X-ray diffraction on these thicker samples reveals that "synthesis conditions 2" (Figure 4) are very appropriate.

The fact that the diffractograms in Figure 9 (left) show a better [002] to [111] ratio than in Figure 9 (right) is solely caused by a difference in thickness. Coatings used in the first set are approximately 30 nm thick, while those used in the second set are close to 90 nm. Combining the synthesis atmospheres of the second set of experiments with more moderate thicknesses will lead to a more thorough inhibition of the [111] crystal growth. An explanation could be found in the varying oxygen partial pressure between the different synthesizes as there is a variable overpressure inside the furnace in function of the applied Ar-(5%)H$_2$ flowing rate, allowing limited diffusion of oxygen inside the furnace. Earlier research has confirmed a clear influence from oxygen partial pressure on the final texture of CeO$_2$.[23,24] Another possibility to be investigated follows from the stability of the two occurring crystal orientations, with the [002] orientation being the most unstable one in comparison to the [111] orientation. The texture of the substrate benefices [002] crystal growth, while higher temperatures and a more turbulent atmosphere might accelerate the transition towards the most stable orientation. Increasing the thickness will decrease the beneficial [002] growth effect induced by the substrate, which explains the increasing occurrence of the [111] orientation in thicker films.

Our conducted experiments confirmed the possibility to make thick, well-oriented CeO$_2$ buffer layers. We expected, however, that the increasing thickness might cause a degrading microstructure, which was confirmed by secondary electron microscopy in Figure 10 (left).

The appearance of microcracks indicates the existence of stress throughout the material, caused by differences in thermal expansion between the CeO$_2$ material and the substrate or differences in lattice parameters between the CeO$_2$ material and the substrate.

It is clear that the induced stress by thermal expansion increases as the thickness of the films gets higher. In order to decrease the stress, we have focused on the lattice mismatch between the CeO$_2$ (5.411 Å) and the NiW (3.6 Å) material. Attempting to incorporate doping metal elements can create relaxation spots throughout the material.[25] We investigated the effect of four different doping elements (M
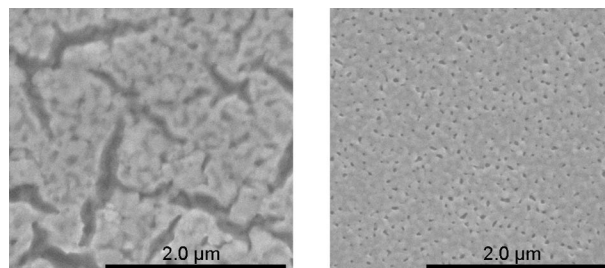

Figure 10. Surface morphology of a 70 nm thick CeO$_2$ film (left: non-doped; right: 5% Yb-doped).

= Co^{2+}, Gd^{3+}, Yb^{3+} and Bi^{3+}) in two different concentrations, i.e. 5 and 10%, on both microstructure and texture of Ce$_{1-x}$M$_x$O$_2$ films. From FE-SEM images the effect of doping on the microstructure seemed beneficial for every combination. Stress can be released whenever a change in cell parameter, positive or negative, occurs. A Typical FE-SEM image is shown in figure10 (right).

Optimal results concerning microstructure were established using the 5% doped solutions. Introducing several doping elements completely inhibited the growth of microcracks in the material for film thicknesses up to at least 80 nm. The observed holes throughout all coatings are most likely caused by a typical redox reaction for metal nitrates and citric acid containing solutions:

18 HNO$_3$(aq.) + 5 (C$_6$H$_8$O$_7$·H$_2$O)(aq.) $\rightarrow$
$$34\ H_2O + 9\ N_2 \uparrow\ + 30\ CO_2 \uparrow$$
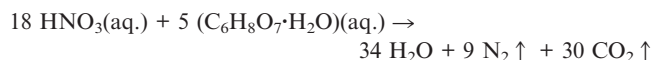
Comparison between the left and right image shows an increasing trend in the number of holes as a function of increasing doping level. Regarding the limited amount of extra NO$_3^-$ – groups introduced, it seems unlikely that this is the only cause of the increasing amount of holes.

Since lattices will be locally deformed due to substitution, an influence on the crystal growth was expected. Based on X-ray diffraction analysis (Figure 11) we found a decrease in [002] to [111] ratio in all cases.

As summarized in Table 2, we examined the influence of both elements with bigger and smaller ionic radii than cerium.[26] On the basis of this experimental setup, we can conclude that there is not a generally acceptable trend towards either optimal dopant concentration or dopant ionic radius. For gadolinium and ytterbium a low concentration seems to be beneficial, while the opposite can be
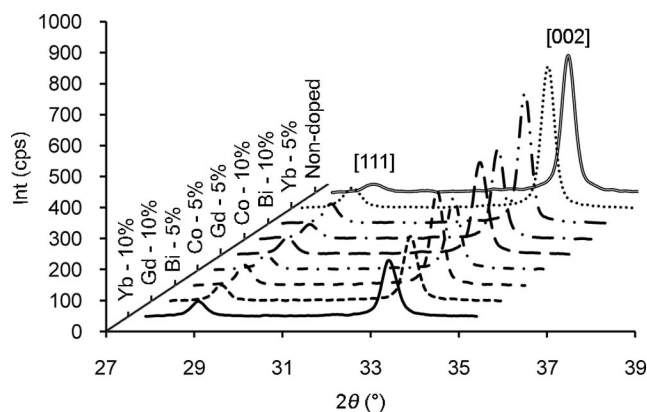
Figure 11. X-ray diffraction analysis; doped vs. non-doped.

concluded in case of cobalt and bismuth. The chemical nature of the elements seems to be less relevant than its physical presence. A local element disorder or lattice deformation seems to suppress epitaxial growth, with development of the more stable [111] orientation as a result.

Table 2. Radii of doping elements in eightfold coordination.

Element	Ionic radius [Å]	Crystal radius [Å]
Co^{2+}	0.90	1.04
Ce^{4+}	0.97	1.11
Yb^{3+}	0.99	1.13
Gd^{3+}	1.05	1.19
Ce^{3+}	1.14	1.28
Bi^{3+}	1.17	1.31

As a coated conductor actually consists of a stacked architecture of subsequent La$_2$Zr$_2$O$_7$ and CeO$_2$ layers, we combined the experiences from previous paragraphs and deposited an undoped CeO$_2$ layer on available NiW-La$_2$Zr$_2$O$_7$ tape, as supplied by Zenergy Power GmbH. The applied synthesis followed the before mentioned "synthesis conditions 2", as shown in Figure 4, while the thicknesses of the La$_2$Zr$_2$O$_7$ and the CeO$_2$ are respectively characterized as 170 and 70 nm. The resulting X-ray diffractogram in Figure 12 reveals an excellent texture with a complete absence of any [111] orientation.
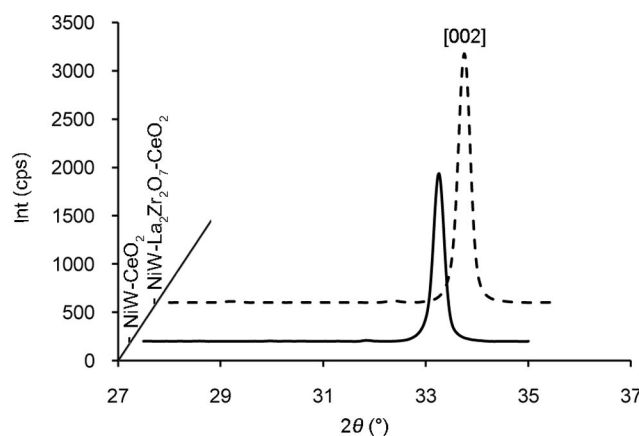
Figure 12. X-ray diffraction of a single (NiW-CeO$_2$) and double (NiW-La$_2$Zr$_2$O$_7$-CeO$_2$) buffer structure.

The underlying buffer layer seems to exhibit a positive influence on the characteristics of the synthesized CeO$_2$ layer. A very substantial gain in intensity between the NiW-La$_2$Zr$_2$O$_7$ film and the NiW-La$_2$Zr$_2$O$_7$-CeO$_2$ film is observed. The improved match in cell parameters between La$_2$Zr$_2$O$_7$ (+/–10.8 Å) and CeO$_2$ (+/–5.41 Å) than between NiW (+/–3.6 Å) and CeO$_2$ will probably be the major factor in the occurring suppression of [111] growth.

A final synthesis of a 500 nm thick YBa$_2$Cu$_3$O$_7$ thin film on top of the previous buffer structure was performed by the TFA-MOD method (Figure 13).[27] X-ray diffraction analysis mainly revealed c-axis growth of the YBCO layer. A minor reflection of the [200] orientation can be seen as well. Also there is no notice of large amounts of barium cerate compounds in the sample, what indicates that the
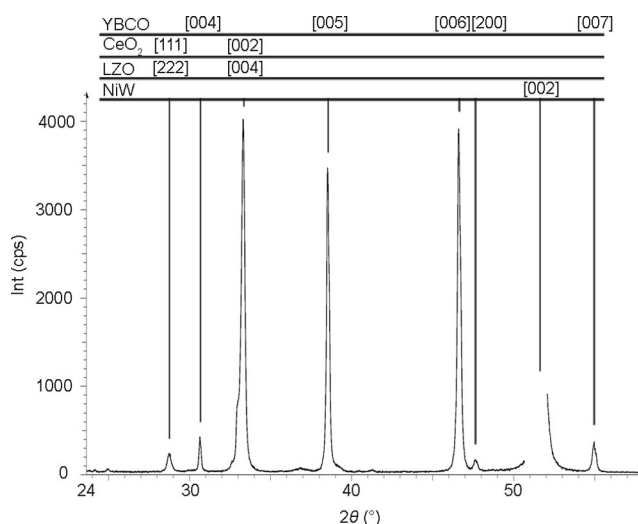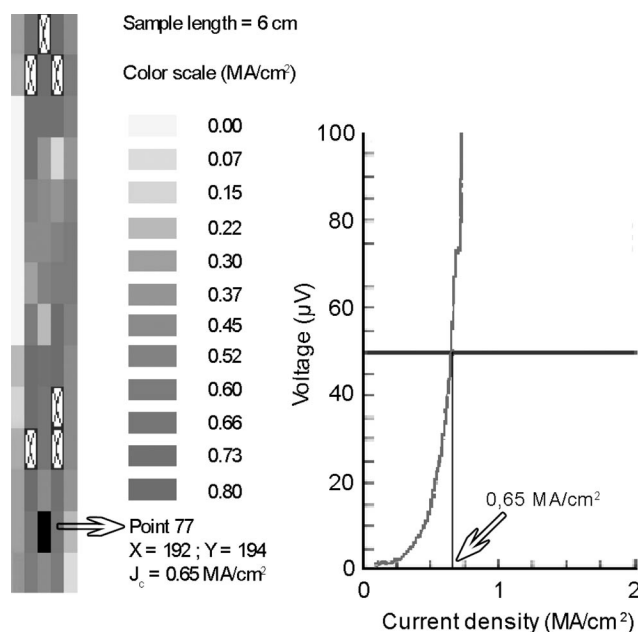

Figure 13. X-ray diffraction of a complete coated conductor structure.

Figure 14. Inductive J_c measurement.

buffer structure exhibits an appropriate surface smoothness for synthesis of a superconducting layer and thus that a slightly porous morphology, as was shown in Figure 10 (right), does not eliminate chances towards successful c-axis growth.

Inductive J_c measurements result in an average J_c value of 0.4 MA/cm², with maxima up to 0.8 MA/cm², for a 500 nm thick $YBa_2Cu_3O_7$ film (Figure 14).

Conclusions

This article reviews both the chemistry of and thin-film synthesis by a cerium-containing citrate gel. Cerium(III) nitrate and citric acid were used as precursors for the examined solution. Sufficiently thick and well-textured CeO_2 buffer layers were synthesized by starting from this aqueous sol-gel system.

A potentiometric study characterized the different chemical species present in the solution. Focusing on the actual buffer layer synthesis, there are several parameters influencing the texture and surface morphology of CeO_2 buffer layers on NiW biaxially textured substrates. Synthesis conditions were optimized for CeO_2 films of varying thickness, where the main focus was drawn towards the sintering period. The microstructure of the resulting buffer layers was optimized by the introduction of several doping elements.

A first attempt in creating a coated conductor was successfully accomplished, resulting in promising superconducting properties.

Experimental Section

Precursor Solution: The chosen metal source was cerium(III) nitrate hexahydrate (99%, Aldrich) dissolved in deionised H_2O in a 0.2 M concentration. Citric acid monohydrate ($\geq$ 98%, Aldrich) was used as complexant (molar ratio of metal-to-ligand: 3). The pH was adjusted to a value of approximately 6 by adding ammonia (25 wt.-%, Chem-Lab), based on theoretical calculations of complex stability, as described in a following section. Subsequent refluxing at 70 °C for 3 h leaded to the formation of the desired complexes and a slight decrease in pH, which was adjusted to 6 by adding extra ammonia. Complexation was supposed to be completed when a stable yellow colour was attained. The yellow-colored stock solution showed a viscosity of approximately 1.5 cP and was indicated as precursor solution A throughout this work. Thicker films were synthesized starting from precursor solution B, which had a higher concentration and viscosity (0.45 M and 3 cP).

Alternatively, a set of experiments was conducted to examine other possible ligands, such as malic acid, acetylacetonate, malonic acid, succinic acid, tartaric acid, a mixture of tri- and diethanolamine and a mixture of EDTA and ethylene glycol. All solutions were prepared using the same procedure and relative quantities as the described $Ce(NO_3)_3$ citrate gel method. In comparison to the alternative systems, the citrate gel method seemed the optimal choice, resulting in both an extended stability of the precursor solution of several months and a possible formation of clear and stable gel structures, a combination which was not accomplished using the alternative complexants.

Gel Formation: Gels were prepared by subjecting 9 mL of stock precursor solution for several hours at 60 °C in order to initiate the condensation reactions towards a gel structure. A set of tests was conducted with different pH values and metal-to-ligand ratios in order to obtain very homogeneous and stable gels, prone to result in buffer layers of optimal quality.

Substrate Preparation: A commonly chosen metal substrate for coated conductors is the biaxially textured Ni-(5%)W tape, fabricated by the RABiTS (Rolling Assisted Biaxially Textured Substrates) process as explained elsewhere.[28] A thorough cleaning was performed before the synthesis of thin films. The cleaning process involved both a thermal and a chemical cleaning.[19] The substrates were heated to 800 °C under ambient Ar-(5%)H_2 atmosphere followed by a chemical cleaning consisting of a degreasing and decontaminating phase, respectively in trichloroethylene, acetone, methanol and water. An etching phase, in a 1:1 mixture of formic acid and hydrogen peroxide, was subsequently applied in order to increase the wettability of the substrate due to deformations of the grain boundaries and smoother surfaces.

Film Synthesis: Thin film depositions were performed by dip-coating, using a computer-controlled dip-coating unit (KSV Instruments) in a clean-room facility (class 100000). Prior to the thermal treatment, the sol-gel transition proceeded in a conventional dry-furnace at 60 °C during 1 h. The high-temperature synthesis was performed in a quartz-tube furnace with controlled atmosphere (Carbolite Furnaces, length: 1 m, inner tube diameter: 6 cm).

Characterization: Characterization of the texture and phase composition was performed by X-ray diffraction (Siemens D5000) and EBSD measurements (JEOL JSM 6400F - EBSD-Camera HKL Nordlys). Structural characterization was carried out using a FE-SEM microscope (FEI Quanta 200F), while spectroscopic ellipsometry (JA Woollam Alpha-SE) allowed us to determine the thickness of the thin films. Thermal analysis (TA Instruments, SDT2960) of the starting products was performed in order to determine the exact water content and purity of the precursors as well as to follow the decomposition process from precursor solution to solid material. J_c measurements were performed by cryoscan mappings (Theva-Tapestar).

Potentiometric Measurements: All reagents for potentiometric analysis were of analytical grade and used as received. Distilled and deionised water (Milli-Q quality, specific conductance < 0.05 µS cm⁻¹) was used for all solutions. Titrisol ampoules were used to obtain carbonate-free potassium hydroxide solutions ($\approx$ 0.2 M). The metal ion stock solution was prepared from metal nitrates, i.e. $Ce(NO_3)_3$, and was standardized by titration with the disodium salt of ethylenediaminetetraacetic acid (EDTA) in the presence of a small amount of the Hg(EDTA) complex using appropriate conditions and electrodes (mercury and calomel).[29] All final solutions for the potentiometric and spectrophotometric titrations were made up to an ionic strength of 0.1 M with KNO_3.

The potentiometric measurements were performed with standard dilute KOH using a Schott® pH-meter and a 5 mL Schott® glass T-burette. The pH-meter was connected with a Schott® H2680 glass electrode and a Schott® B3410 calomel electrode with a second salt bridge filled with 0.1 M KNO_3. Each aqueous system under consideration was measured in a 100 mL jacketed cel thermostatted at 25 °C ± 0.1 °C by a refrigerated circulated water bath. All systems were studied under anaerobic conditions, established by a stream of presaturated nitrogen, obtained by sending the inert gas through a 0.1 M KNO_3 solution. The ionic strength was adjusted to 0.10 M by the addition of KNO_3 as supporting electrolyte. The concentrations of all the experimental ligand solutions were in the

range of 1.0×10^{-3} M. The program Titrate, slightly modified, was used to monitor the titration.[30] The titration data were processed using Gran's method in order to calculate the standard cell potential ($E°$), the dissociation constant of water (K_w), together with the correction terms for changes in the liquid junction potential in strong acid medium, a_j ($-\log[H^+] < 2.5$), and for the non-linear electrode response in a strong alkaline medium, b_j ($-\log[H^+] > 11.5$) as described previously.[31] Experimental runs were performed by adding increments of standard base to a ligand solution containing an excess of HNO$_3$ ($a = $ mol OH$^-$/mol Ligand).

Acknowledgments

[1] H. E. Swanson, R. K. Fuyat, *U. S. Natl. Bur. Stand.* **1954**, *3*, 44.

[2] G. D. Chryssikos, E. I. Kamitsos, J. A. Kapoutsis, A. P. Patsis, V. Psycharis, A. Koufoudakis, C. Mitros, G. Kallias, E. Gamariseale, D. Niarchos, *Physica C* **1995**, *254*, 44–62.

[3] I. Van Driessche, G. Penneman, E. Bruneel, S. Hoste, *Pure Appl. Chem.* **2002**, *74*, 2101–2109.

[4] B. Schoofs, V. Cloet, P. Vermeir, J. Schaubroeck, S. Hoste, I. Van Driessche, *Supercond. Sci. Technol.* **2006**, *19*, 1178–1184.

[5] J. D. McCullough, *J. Am. Chem. Soc.* **1950**, *72*, 1386–1390.

[6] M. Bolech, E. H. P. Cordfunke, F. Janssen, A. Navrotsky, *J. Am. Ceram. Soc.* **1995**, *78*, 2257–2258.

[7] I. Van Driessche, B. Schoofs, G. Penneman, E. Bruneel, S. Hoste, *Measurement 2005*, Proc. **2005**, 339–349.

[8] X. Obradors, T. Puig, A. Pomar, F. Sandiumenge, N. Mestres, M. Coll, A. Cavallaro, N. Roma, J. Gazquez, J. C. Gonzalez, O. Castano, J. Gutierrez, A. Palau, K. Zalamova, S. Morlens, A. Hassini, M. Gibert, S. Ricart, J. M. Moreto, S. Pinol, D. Isfort, J. Bock, *Supercond. Sci. Technol.* **2006**, *19*, S13–S26.

[9] M. S. Bhuiyan, M. Paranthaman, K. Salama, *Supercond. Sci. Technol.* **2006**, *19*, R1–R21.

[10] M. Kakihana, *J. Sol-Gel Sci. Technol.* **1996**, *6*, 7–55.

[11] D. R. Uhlmann, G. Teowee, *J. Sol-Gel Sci. Technol.* **1998**, *13*, 153–162.

[12] J. Livage, M. Henry, C. Sanchez, *Prog. Solid State Chem.* **1988**, *18*, 259–341.

[13] B. Schoofs, D. Van de Vyver, P. Vermeir, J. Schaubroeck, S. Hoste, G. Herman, I. Van Driessche, *J. Mater. Chem.* **2007**, *17*, 1714–1724.

[14] P. Gans, A. Sabatini, A. Vacca, *J. Chem. Soc., Dalton Trans.* **1985**, 1195–1200.

[15] Sabatini, A. Vacca, P. Gans, *Coord. Chem. Rev.* **1992**, *120*, 389–405.

[16] I. Ting-Po, Gh. Nancolla, *Anal. Chem.* **1972**, *44*, 1940.

[17] N. Petrova, D. Todorovsky, S. Angelova, D. Mehandjiev, *J. Alloys Compd.* **2008**, *454*, 491–500.

[18] A. E. Martell, R. M. Smith, *Critical Stability Constants - Other Organic Ligands*, Plenum Press, **1977**.

[19] G. Penneman, I. Van Driessche, E. Bruneel, S. Hoste, *Euro Ceramics VIII*, parts 1–3, **2004**, *264–268*, 501–504.

[20] I. Van Driessche, G. Penneman, C. De Meyer, I. Stambolova, E. Bruneel, S. Hoste, *Euro Ceramics VII*, parts 1–3, **2002**, *206-2*, 479–482.

[21] I. Van Driessche, G. Penneman, J. S. Abell, E. Bruneel, S. Hoste, *Thermec' 2003*, parts 1–5, **2003**, *426-4*, 3517–3522.

[22] Y. Jiang, J. B. Adams, M. van Schilfgaarde, *J. Chem. Phys.* **2005**, 123.

[23] X. Cui, F. A. List, D. M. Kroeger, A. Goyal, D. F. Lee, J. Mathis, E. D. Specht, P. M. Martin, R. Feenstra, D. T. Verebelyi, D. K. Christen, M. Paranthaman, *IEEE Trans. Appl. Supercond.* **1999**, *9*, 1967–1970.

[24] H. G. Lee, Y. M. Lee, H. S. Shin, C. J. Kim, G. W. Hong, *Mater. Sci. Eng., B* **2002**, *90*, 20–24.

[25] M. Mogensen, N. M. Sammes, G. A. Tompsett, *Solid State Ionics* **2000**, *129*, 63–94.

[26] R. D. Shannon, *Acta Crystallogr., Sect. A* **1976**, *32*, 751–767.

[27] M. Falter, W. Haessler, B. Schlobach, B. Holzapfel, *Physica C* **2002**, *372*, 46–49.

[28] T. G. Truchan, F. H. Rountree, M. T. Lanagan, S. M. McClellan, D. J. Miller, K. C. Goretta, M. Tomsic, R. Foley, *IEEE Trans. Appl. Supercond.* **2000**, *10*, 1130–1133.

[29] E. P. Sergeant, in: *Chemical Analysis*, vol. 69 (Eds.: I. M. Kolthoff, P. J. Elving) Wiley, **1984**.

[30] A. P. Arnold, S. A. Daignault, D. L. Rabenstein, *Anal. Chem.* **1985**, *57*, 1112–1116.

[31] G. Gran, *Analyst* **1952**, *77*, 661–671.

FULL PAPER

Inkjet Printing of Water "Soluble" Doped ZnS Quantum Dots

Aaron C. Small,*[a,b] James H. Johnston,[a,b] and Noel Clark[c]

Water-soluble-doped ZnS quantum dots were synthesised and formulated for inkjet printing. The quantum dots were then inkjet-printed onto a variety of substrates, including photo quality inkjet paper, cotton fabric, PET film, and glass. Of these substrates, only inkjet printing of doped ZnS quantum dots on photo-quality inkjet paper and cotton fabric produced a photoluminescent print. The materials were charac- terised using a number of methods, including profilometer measurements, photoluminescence spectroscopy (PL), scan- ning electron microscopy (SEM), transmission electron mi- croscopy (TEM) and viscosity measurements. On excitation with UV light, a photoluminescence emission of approxi- mately 600 nm was observed.

Introduction

In recent years, inkjet printing has become an attractive method for microscale patterning on a variety of surfaces. The main advantages of inkjet printing are its ease of use, the increased number of substrates available for printing, and the fact that it is an additive approach generating little in the way of waste. Inkjet printing has been used in the fabrication of a number of devices, including light-emitting diodes (LED's), solar cells, and field-effect transistors.[1–6]

Zinc sulfide (ZnS) is a well-known semi-conductor material with a band gap of about $E_g = 3.6$ eV which corresponds to the energy range of UV light. ZnS in the form of nanocrystalline particles are referred to as quantum dots. When the ZnS quantum-dot lattice is doped with transition-metal ions and excited by UV light, it exhibits photoluminescence in the visible region with the colour depending on the nature and level of the transition-metal-ion dopant. ZnS quantum dots doped with Mn^{2+} ions exhibit a red-orange colour at a wavelength of about 600 nm and when doped with Cu^{2+} ions they exhibit a green-blue colour at a wavelength of about 530 nm, when excited by UV light. In ambient light they are invisible. The dopants act as recombination centres for the excited electron-hole pairs, resulting in strong and characteristic photoluminescence.[7] The size of the quantum dots does have an effect on the fluorescence quantum yield (Ø) of the doped quantum dots, given by:

$$\phi = \frac{1}{1 + \beta D^2}$$

Where D is the diameter of the quantum dot and β is the ratio of the non-radiative and radiative decay lifetimes.[8] This shows that the smaller the particle size, the larger the fluorescence or photoluminescence yield. Doped ZnS quantum dots are typically up to about 10 nm in size.

A stable colloid of doped ZnS quantum dots is colourless as the particles are too small to scatter light in the visible region but exhibits the sharply defined characteristic photoluminescence colour in the visible region due to the particular transition metal ion dopant, when viewed under UV light. Colloid stability is usually achieved by the use of capping agents that coat the individual quantum-dot nanocrystals and prevent agglomeration. The ability to form stable colloids of photoluminescent quantum dots opens up the exciting possibility for their use as photoluminescent inks in security documents and labels in both single colour and full colour characters and images, and also in novel flexible photoluminescent displays and advertising.

This paper presents the results of a study where Mn^{2+}- and Cu^{2+}-doped ZnS quantum dots have been formulated into an ink-jet ink and images printed onto paper using a 2811 Dimatix Materials printer. A number of methods have been made to inkjet print quantum-dot suspensions,[2] however, we believe this is the first report of the inkjet printing of doped ZnS quantum dots on cellulosic materials.

Methods

Mn^{2+}- and Cu^{2+}-doped ZnS quantum dots were synthesised using a chemical precipitation method.[9] All reagents used were AR grade and double distilled water was used for all solutions.

[a] School of Chemical and Physical Sciences, Victoria University of Wellington,
 P. O. Box 600, Wellington, New Zealand
[b] The MacDiarmid Institute for Advanced Materials and Nano- technology,
 P. O. Box 600, Wellington, New Zealand
[c] CSIRO Materials Science and Engineering,
 Private Bag 10, Clayton South VIC 3169, Australia

In a typical synthesis of Mn^{2+}-doped ZnS, 10 cm^3 of 1.0 M $ZnCl_2$, 10 cm^3 of 0.01 M $MnCl_2$ and 10 cm^3 of 0.5 M sodium citrate solution were mixed and stirred for 10 min. From a burette, 10 cm^3 of 1 M Na_2S solution was added dropwise. A white precipitate of ZnS:Mn^{2+} quantum dots was formed and the resulting suspension was centrifuged and washed with distilled water and redispersed in 40 cm^3 of distilled water to provide a colloidal suspension. Several experiments were conducted using different concentrations of Mn^{2+} ranging from 1–10 mol-% to determine the optimum photoluminescence yield.[9]

Similarly, in a typical synthesis of Cu^{2+}-doped ZnS quantum dots, 10 cm^3 of 1.0 M $ZnCl_2$, 10 cm^3 of 0.01 M $Cu(CH_3COO)_2$, 10 cm^3 of 0.5 M sodium citrate and 10 cm^3 of 0.5 M sodium thiosulfate solution were mixed and stirred for 10 min. The procedure was then the same as that for Mn^{2+}-doped ZnS quantum dots and a colloidal suspension was similarly formed. The dopant concentrations were adjusted from 0.2–1 mol-% to determine the optimum photoluminescence yield.[9]

The photoluminescent spectra of the doped ZnS quantum-dot colloids were measured with a Perkin–Elmer LS-55 Photoluminescence Spectrometer using an excitation wavelength of 335 nm and over a range of 300–800 nm with a filter to remove the excitation line from the emission spectra.

The quantum-dot colloids were incorporated into an ink-jet formulation and ink-jet-printed onto paper and textile substrates using a 2811Dimatix Materials digital printer. The requirements for the ink-jet formulation that needed to be matched as close as possible are shown in Table 1.

Table 1. Summary of fluid properties for inkjet printing.

Property	Value
Viscosity	10–12 centipoise at 60 °C
Surface tension	28–33 dynes at 60 °C
Low volatility	boiling points < 100 °C
Density	specific gravity > 1 g cm^{-1}
Filtration	filtered to 0.2 μm

In order to approximately match these requirements and to ensure stability of the ink formulation, mercaptosuccinic acid (MSA) in a mole ratio of MSA/Zn = 8:1 for Mn^{2+}-doped ZnS and 4:1 for Cu^{2+}-doped ZnS was used. At 60 °C, a viscosity value of 4.1 centipoise was obtained, slightly below that of the specified printer requirements. The boiling point of the "ink" was approximately 100 °C and the specific gravity was 1.09 g cm^{-3}. Surface tension was not measured. A 1.5-cm^3 DMC-11610 (10 picolitre nominal drop volume) cartridge was used and the solution printed with a 15 micron drop spacing and 30 °C reservoir temperature. These settings gave an acceptable balance between print uniformity and edge resolution on most substrates. Substrates were taped down onto the platen using masking tape. The number of "passes" of the printhead over the substrate was set at 1, 2 or 3.

Results and Discussion

The printing of doped ZnS quantum-dot "inks" on variety of substrates was attempted. These include photographic-quality inkjet paper, photocopy paper, cotton fabric, PET film, ITO-coated PET film, silicon wafer and wool.

The photoluminescence spectrum of Mn^{2+}-doped ZnS is shown in Figure 1. A photoluminescence peak is observable in the visible range at about 600 nm which gives rise to the red-orange colour. This is due to the presence of Mn^{2+} in the host ZnS lattice which produces localised energy levels ($^4T_1$–$^6A_1$). Incident UV light with energy greater than the band gap promotes an electron from the valence band to the conduction band. This then decays back to the valance band via a pathway involving a transition from the intermediate $^4T_1$ to the $^6A_1$ energy levels and hence the emission of light in the visible region (red-orange colour).[8] The emission at about 400 nm is due to S^{2-} vacancies in the ZnS lattice.[10]
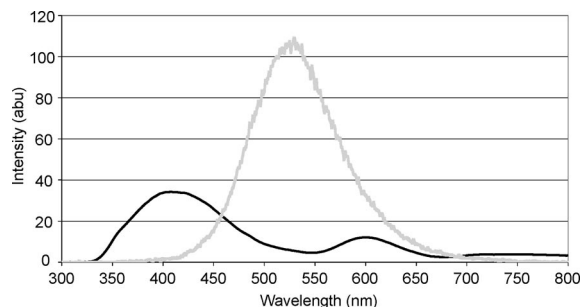

Figure 1. Photoluminescence emission spectrum of ZnS:Mn^{2+} and ZnS:Cu^{2+} quantum dots (λ^{Ex} = 335 nm).

A similar mechanism takes place for Cu^{2+}-doped ZnS (Figure 1) where the transition is between the ^2E–$^2T_2$ energy levels and the emission occurs at about 530 nm giving rise to the blue-green colour.[11] The emission from the S^{2-} vacancies is not observable in this case as there are fewer S^{2-} ions available due to the use of $S_2O_3^{2-}$ in the reaction.

The photoluminescence emission spectrum of MSA-capped ZnS:Mn^{2+} quantum dots is shown in Figure 2. The large peak at approximately 600 nm is present, as in uncapped ZnS:Mn^{2+}. An interesting point to note is that the peak at 600 nm is larger than that of uncapped ZnS:Mn^{2+} quantum dots (Figure 1), indicating that the MSA cap has actually improved the luminescence of the quantum dots. A possible reason for this is that the capping agent has reduced the number of surface defects present on the material. This would mean that there is a greater chance of a photogenerated electron-hole pair recombining at a luminescent centre, rather than at the site of a defect, which leads to an increase in photoluminescence efficiency.

The photoluminescence spectrum of MSA-capped ZnS:Cu^{2+} quantum dots is also shown in Figure 2. The characteristic emission at approximately 530 nm is visible, although unlike the MSA-capped ZnS:Mn^{2+} variety, the capping agent does not seem to increase the luminescence of the material.
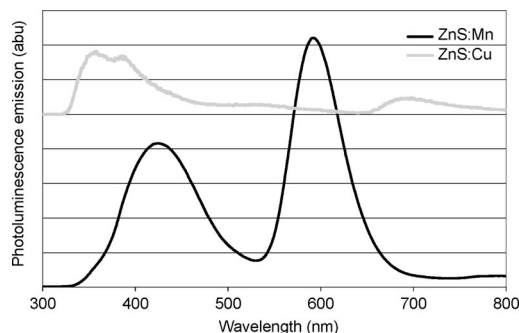
Figure 2. Photoluminescence emission spectrum of MSA-capped ZnS:Mn^{2+} and ZnS:Cu^{2+} quantum dots (λ^{Ex} = 335 nm).

Figure 4. IR spectrum of MSA (below) and MSA-capped ZnS:Mn^{2+} (above).

The photoluminescence emission spectrum for MSA-capped ZnS:Cu^{2+} quantum dots is also markedly different to that of the precursor ZnS:Cu^{2+} quantum dots (Figure 1), whereas the photoluminescence emission spectra of MSA-capped ZnS:Mn^{2+} quantum dots and the precursor ZnS:Mn^{2+} quantum dots are very similar – the only difference being the increase in relative peak heights of the $^4T_1$–$^6A_1$ emission (ca. 600 nm) and the S^{2-} vacancy emission (ca. 430 nm).

Figure 3 shows the surface of the ZnS quantum dots capped with MSA. The stabilising agent is presumably bound through interaction between the sulfur groups on the surface of the quantum dot, and the thiol group of the MSA.[12] MSA is not a large molecule, and stabilisation must therefore occur electrostatically, rather than sterically.
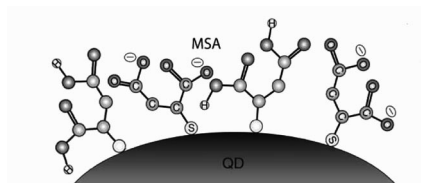

Figure 3. Schematic showing the binding of MSA to the ZnS quantum-dot surface.

The IR spectra of both MSA and MSA-capped ZnS:Mn^{2+} are shown in Figure 4. On comparison between the two spectra, their difference is clear. Therefore, it can be deduced that a change in bonding is occurring. This is most likely associated with the thiol group present in the MSA, as the thiol stretch at approximately 2550–2600 cm^{-1} has diminished on bonding to the ZnS:Mn^{2+} quantum dots. The spectra also differ in both the area of a disulfide stretch (400–550 cm^{-1}) and in the fingerprint region (400–1000 cm^{-1}), further indication that a change in bonding has occurred. In particular, the disulfide area is broadened, which suggests the vibrations of the MSA molecules have been changed considerably due to bonding of the MSA with the ZnS:Mn^{2+} quantum dots through the S.
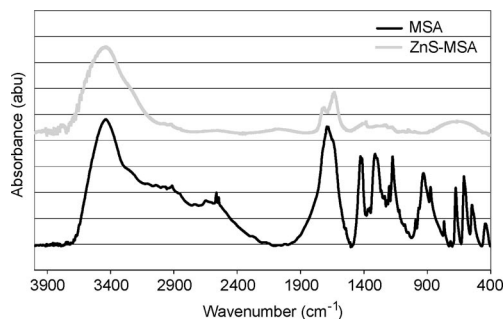
On printing these quantum-dot "inks" onto the various substrates, the characteristic luminescence peaks (ca. 600 nm for ZnS:Mn^{2+} and ca. 530 nm for ZnS:Cu^{2+}) are observed, indicating the substrate has not altered the chemistry of the quantum dots. The photoluminescence emission spectrum for ZnS:Mn^{2+} quantum dots inkjet-printed onto photographic-quality inkjet paper are shown in Figure 5, which shows the photoluminescence emission spectrum for one and two layers of ZnS:Mn^{2+} quantum dots. The greater peak height at 600 nm is indicative of the increased brightness arising from the printing of two layers (as observed visually in the photograph shown in Figure 10).
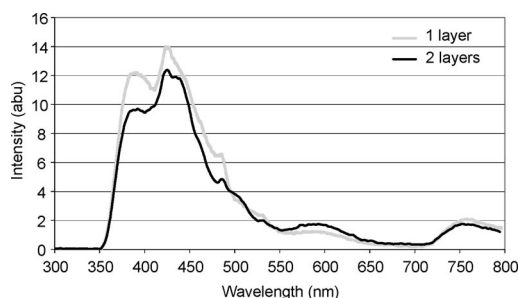

Figure 5. Photoluminescence emission spectrum for ZnS:Mn^{2+} quantum dots printed onto photographic-quality inkjet paper (λ^{Ex} = 335 nm).

The photoluminescence emission spectrum of two layers of ZnS:Mn^{2+} quantum dots inkjet-printed onto cotton fabric is shown in Figure 6. Again, the characteristic emission at approximately 600 nm can be seen, indicating that the cotton has not changed the chemistry of the quantum dots.

Merino wool was also used as a substrate for inkjet printing ZnS:Mn^{2+} quantum dots onto. Figure 6 shows the photoluminescence emission spectrum of two layers of ZnS:Mn^{2+} quantum dots inkjet-printed onto merino wool fabric. Again the characteristic emission at approximately 600 nm can be seen, along with the emission arising from the S^{2-} vacancy and the luminescence characteristics of the wool substrate – different from those of cotton fabric, and photographic-quality inkjet paper (already shown in Figure 5).
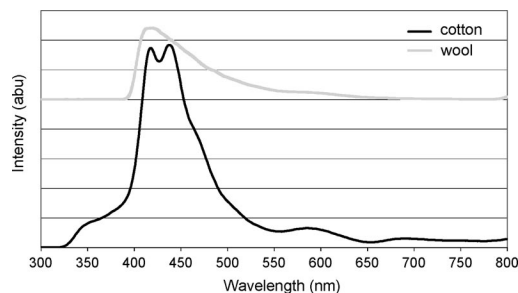
Figure 6. Photoluminescence emission spectrum for two layers of ZnS:Mn^{2+} quantum dots printed onto cotton fabric and merino wool (λ^{Ex} = 335 nm).

The photoluminescence emission spectrum of ZnS:Cu^{2+} quantum dots inkjet-printed onto photographic-quality inkjet paper is shown in Figure 7. Although the characteristic emission at approximately 530 nm can be seen visually in Figure 11, it seems to be masked in the photoluminescence spectrum by the luminescence of the inkjet-paper substrate of photographic quality.
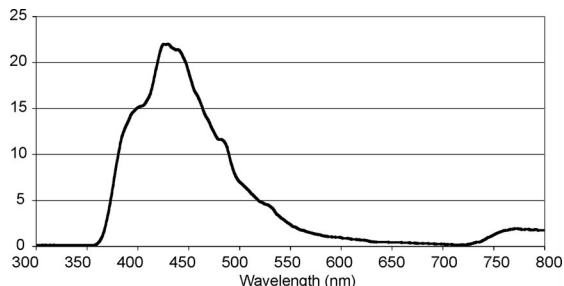

Figure 7. Photoluminescence emission spectrum for two layers of ZnS:Cu^{2+} quantum dots printed on photographic-quality inkjet paper (λ^{Ex} = 330 nm).

The images in Figure 8 show first pieces of photographic paper printed with a strip of ZnS:Mn^{2+} quantum dots. On the left is the photographic paper under normal light, while on the right, is the same sheet of paper under UV light conditions. The above success was followed by the successful printing of detailed images, as shown by the photographs in Figures 9 and 10 of a printed circuit-board template and the Victoria University of Wellington logo.
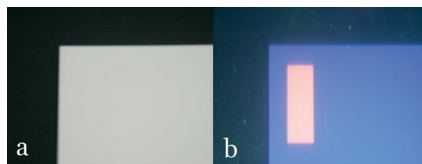

Figure 8. Photographic-quality inkjet paper with a strip of ZnS:Mn^{2+} quantum dots printed on the surface. Under normal light conditions (a), and under UV light conditions (b).

Several parameters of the printer may be adjusted to improve the print quality and brightness, and include drop spacing and the number of layers printed. A lower drop spacing gives more "ink" per unit area (or a higher "ink" loading), and would result in an increase in print quality and brightness. At a drop spacing of 10 µm, however, the
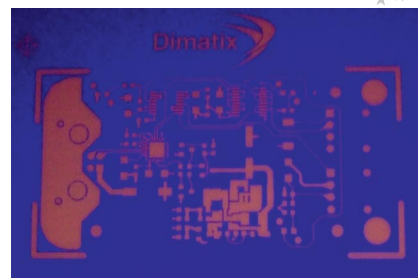

Figure 9. A detailed inkjet-printed image of a printed circuit board template on photo quality inkjet paper using ZnS:Mn^{2+} quantum dots.

Figure 10. Comparison between images printed using 1 layer (a) and 2 layers (b) of ZnS:Mn^{2+} quantum dots.

substrate (photographic-quality inkjet paper) could not absorb all the "ink", resulting in smearing of the print. Therefore, a drop spacing of 15 µm was used throughout this study. Another way to increase brightness is by changing the number of passes made (or layers printed) by the printhead over the substrate. In this study, the number of passes was set at either 1, 2 or 3, in order to obtain the best print. Figure 10 shows the difference between 1 and 2 layers. The image printed with 2 layers of ZnS:Mn^{2+} quantum dots is noticeably brighter. On printing three layers, however, the print began to smear, and the printing cycle was cancelled in order to maintain the cleanliness of the printhead.

ZnS:Cu^{2+} quantum dots were also inkjet-printed onto photographic-quality inkjet paper. The copper-doped variety was unstable in the MSA surfactant, however, and as a result the ZnS:Cu^{2+} quantum-dot "ink" had to be prepared only a few hours before printing in order to obtain a stable and printable "ink" containing no solids. Once formulated, however, the ZnS:Cu^{2+} quantum dots posed no problems during the inkjet printing process. Figure 11 shows

Figure 11. A detailed inkjet-printed image of the Victoria University of Wellington logo on photographic-quality inkjet paper using ZnS:Cu^{2+} quantum dots (a), and on cotton fabric using ZnS:Mn^{2+} quantum dots (b).

ZnS:Cu^{2+} quantum dots inkjet-printed on photographic-quality inkjet paper and illuminated with UV light, giving a green luminescence.

Cotton fabric also performed well in print tests, although whiteners present in the cotton fabric produced a blue-coloured background, making it difficult to photograph the emission under UV light. An image of ZnS:Mn^{2+} quantum dots printed on cotton fabric is shown in Figure 11.

Other substrates did not perform as well during the print tests as the photographic-quality inkjet paper. Patterns printed on PET film, PEDOT-coated PET film and silicon wafer were unable to be seen under UV illumination, even though the pattern was visible to the naked eye under normal light conditions, and is confirmed to be present by contact profilometer measurements (Figure 14).

For silicon, this lack of photoluminescence is probably due to the fact that silicon is a semiconductor. At 1.1 eV, the band energy of silicon is lower than that of ZnS. Hence, when an electron-hole pair is generated by the absorption of a photon of light, the charge carrier is conducted away from the luminescent centres in the doped ZnS lattice, and the electron-hole pair cannot recombine to produce luminescence. Instead it relaxes back to the ground state through a non-radiative transition, with no photoluminescence. As the surface of PEDOT-coated PET is also a conductor due to PEDOT, the same effect could be occurring in PEDOT-coated PET as well.

PET film on its own is not a conductor, however so a possibility is that the substrates are quenching the photoluminescence emission through functional groups present near the surface, such as the C=O groups that are present in PET. Silicon Wafer, PET and PEDOT-coated PET are "flat" surfaces also, and perhaps an interesting phenomenon is occurring whereby light is reflected away from the surface, and in the process interfering with the visibility of the quantum dots luminescent properties. Photocopy paper is only a filled paper with a rough absorbent surface, and its poor performance in printing tests can be attributed to the "spreading" of the quantum-dot "ink" throughout the fibre matrix as it comes into contact with the paper structure.

Cross-sectional SEM images of two layers of ZnS:Mn^{2+} quantum dots inkjet-printed onto photographic-quality inkjet paper are shown in Figure 12 at different magnifications. The print pattern is visible as a series of lines on the surface of the photographic-quality inkjet paper that comprise part of the "V" in the Victoria University of Wellington logo. The cross section shows the structure of the paper, containing the pulp fibres sandwiched between two layers of a coating, most likely polyethylene. The receptor layer of the silicon ink sits on the surface of the paper, and is itself isolated from the paper. At higher magnifications, the uniform structure of the paper is even more apparent, and there is no evidence of any migration of the ZnS:Mn^{2+} quantum dots in the z-direction – important for print quality. The only evidence of the ZnS:Mn^{2+} quantum-dot "ink" can be seen at the highest magnification, whereby the "ink" can be seen as a thin bright line on the surface of the ink receptor layer. These results suggest that the quantum dots remained printed on the surface and have not penetrated the substrate in the z-direction, giving rise to the maximum luminescence.

Transmission-electron microscopy was used to assess the particle size of the ZnS:Mn^{2+} quantum dots. From the TEM image shown in Figure 13, spherical particles approximately 40–80 nm in diameter can be seen. Although, there is a distinct lack of any visible crystal lattice fringes in these images (probably due to the presence of the MSA capping layer interfering with imaging), the quantum dots are still crystalline, as in order to produce a photoluminescence emission, the dopant must be included in a lattice.
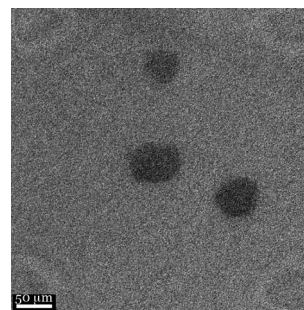

Figure 13. TEM image of MSA-capped ZnS:Mn^{2+} quantum dots.

Contact Profilometer measurements of one layer of ZnS:Mn^{2+} quantum dots printed on a silicon wafer are shown in Figure 14. Due to the contact angle of the droplets on the hydrophobic surface, the droplets have remained as isolated droplets, rather than merging to form a con-
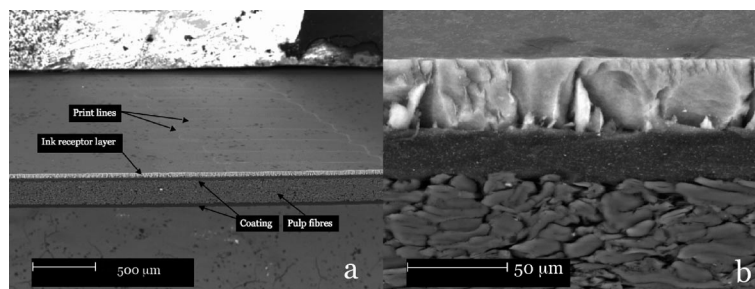

Figure 12. Cross sectional SEM images of photographic-quality inkjet paper printed with two layers of ZnS:Mn^{2+} quantum dots. Note: no evidence of z-migration in high magnification image (b).
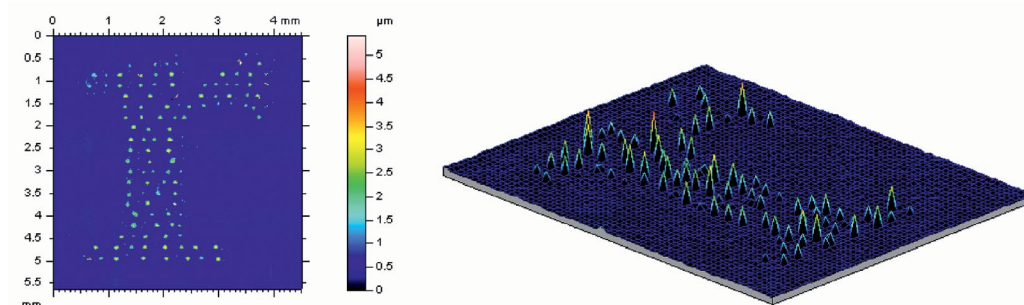
Figure 14. 2D and 3D images of contact profilometer measurements of the letter "r" in the Victoria University of Wellington logo, printed by with ZnS:Mn^{2+} quantum dots.

tinuous film. As a result, the droplets appear as a series of individual peaks, ranging in height from 0.5–4 µm. The drop spacing of 15 µm can also be seen from the images.

Conclusions

Doped ZnS quantum-dot inks were successfully formulated and inkjet-printed onto various substrates, including photographic-quality inkjet paper, photocopy paper, cotton fabric, PET film, ITO-coated PET film, silicon wafer and wool.

A number of surfactants were tested initially in order to "solubilise" doped ZnS quantum dots for inkjet printing. The most satisfactory of these was mercaptosuccinic acid (MSA), and stable MSA-capped ZnS:Mn^{2+} quantum dots were obtained. MSA-capped ZnS:Cu^{2+} quantum dots were unstable as the sodium thiosulfate used to complex Cu^{2+} ions during synthesis was reduced to elemental sulfur by the MSA, destroying any photoluminescence as a consequence.

The fluid properties of the quantum-dot "ink" were sufficiently close to those specified by the manufacturer of the inkjet printer, and the quantum-dot "ink" was successfully printed.

Best results were obtained by using photographic-quality inkjet paper or cotton fabric. One, two, or three passes were made over the substrate by the printhead (number of layers printed). For photographic-quality inkjet paper, the optimum number of passes was found to be two, before the capacity of the substrate was exceeded and the print was smudged. For cotton fabric, this was found to be three. Best results were also obtained for all substrates with a drop spacing of 15 µm and a reservoir temperature of 30 °C.

The doped ZnS quantum-dot "inks" and the printed substrates were characterised by a number of techniques in-cluding Contact Profilometer measurements, PL Spectroscopy, SEM and TEM.

The photoluminescent qualities of the precursor-doped ZnS quantum dots were retained when "solubilised" ZnS quantum dots were obtained. The substrates exhibited photoluminescence emission at approximately 600 nm and 530 nm, when printed with MSA-capped ZnS:Mn^{2+} and MSA-capped ZnS:Cu^{2+} quantum dots, respectively.

Such materials have potential application in the upcoming "smart" packaging industry for advertising and as security papers. As doped ZnS is also an electroluminescent material, this work represents the early stages of a printable electroluminescent display based on cellulose substrates.

[1] E. Tekin, P. J. Smith, S. Hoeppener, A. M. J. van den Berg, A. S. Susha, A. L. Rogach, J. Feldmann, U. S. Schubert, *Adv. Funct. Mater.* **2007**, *17*, 23.
[2] S. H. Eom, S. Senthilarasu, P. Uthirakumar, S. C. Yoon, J. Lim, C. Lee, H. S. Lim, J. Lee, S. Lee, *Org. Electron.* **2009**, *10*, 536.
[3] S. Gamerith, A. Klug, H. Scheiber, U. Scherf, E. Moderegger, E. J. W. List, *Adv. Funct. Mater.* **2007**, *17*, 3111.
[4] M. Wu, Z. Gong, A. J. C. Kuehne, A. L. Kanibolotsky, Y. J. Chen, I. F. Perepichka, A. R. Mackintosh, E. Gu, P. J. Skabara, R. A. Pethrick, M. D. Dawson, *Optics. Express.* **2009**, *17*, 16436.
[5] H. M. Haverinen, R. A. Myllya, G. E. Jabbour, *Appl. Phys. Lett.* **2009**, *94*, 073108.
[6] V. Wood, J. Panzar, J. Chen, M. S. Bradley, J. E. Halpert, M. G. Bawendi, V. Bulovic, *Adv. Mater.* **2009**, *21*, 2151.
[7] D. R. Vij, *Luminescence of Solids*, Plenum Press, New York, **1998**.
[8] R. N. Bhargava, D. Gallagher, *Phys. Rev. Lett.* **1994**, *72*, 416.
[9] A. C. Small, J. H. Johnston, *Curr. Appl. Phys.* **2008**, *8*, 512.
[10] K. Sooklal, B. S. Cullum, S. M. Angel, C. J. Murphy, *J. Phys. Chem.* **1996**, *100*, 4551.
[11] L. Sun, C. Liu, C. Liao, C. Yan, *Solid State Commun.* **1999**, *111*, 483.
[12] W. R. Algar, U. J. Krull, *ChemPhysChem* **2007**, *8*, 561.

FULL PAPER

Intramolecular C–H Bond Activation by Lanthanoid Complexes Bearing a Bulky Aminopyridinato Ligand

Sadaf Qayyum,[a] Grigorii G. Skvortsov,[b] Georgii K. Fukin,[b] Alexander A. Trifonov,*[b] Winfried P. Kretschmer,[a] Christian Döring,[a] and Rhett Kempe*[a]

The present work is aimed towards the synthesis of C–H activation products of various group 3 and lanthanoid metals bearing a bulky aminopyridinato ligand, (2,6-diisopropylphenyl)[6-(2,6-dimethylphenyl)pyridin-2-yl]amine (**1**, Ap′H). Deprotonation of **1** using KH leads to polymeric [Ap′K]$_n$ (**2**), which undergoes clean salt metathesis reaction with MX$_3$ [M = Sc, Nd and Sm, and X = Cl or M = La and X = Br] forming mono thf adducts [Ap′$_2$ScCl(thf)] (**3**), [Ap′$_2$LaBr(thf)] (**4**), [Ap′$_2$NdCl(thf)] (**5**), and [Ap′$_2$SmCl(thf)] (**6**). However, reacting **2** with LuCl$_3$ leads to mono- as well as bis(aminopyridinato)lutetium complexes [Ap′LuCl$_2$(thf)$_2$] (**7**) and [Ap′$_2$LuCl(thf)] (**8**), respectively, while the analogous reaction with LaCl$_3$ at 50 °C produces the tris(aminopyridinato)lanthanum complex [Ap′$_3$La] (**9**). For the selective synthesis of **8** in good yield amine elimination route was adopted. X-ray diffraction studies revealed a distorted octahedral coordination for the bis(aminopyridinato) complexes **3**, **4** and **6**, despite the differences in their ionic radii. Alkylation of the bis(aminopyridinato) monohalide complexes

with equimolar amounts of LiCH$_2$SiMe$_3$ in hexane allowed the isolation of the corresponding alkyl derivatives. For the smaller metals like Sc and Lu affording [Ap′$_2$ScCH$_2$SiMe$_3$(thf)] (**10**) and [Ap′$_2$LuCH$_2$SiMe$_3$(thf)] (**11**), respectively. However, lanthanoids with large ionic radii such as La and Nd resulted in the formation of methyl group C–H bond activation products [Ap′(Ap′$_{-H}$)La(thf)$_2$] (**12**) and [Ap′(Ap′$_{-H}$)Nd(thf)] (**13**), respectively. Most likely an alkyl species was formed which then undergoes intramolecular C–H activation and C–H activation runs fast with regard to the rate of alkyl complex formation. The alkylation of **6** (Sm) with LiCH$_2$SiMe$_3$ did not give a clear product. The reaction of **11** with PhSiH$_3$ (Ph = phenyl) led via intramolecular C–H bond activation to [Ap′(Ap′$_{-H}$)Lu(thf)] (**14**). In this case most likely a hydride species was formed which then undergoes rapid C–H activation. The alkyl complex **10** (Sc) did not react with PhSiH$_3$. The molecular structures of **11**, **12** and **13** have been confirmed by X-ray crystal structure analysis.

Introduction

The activation of C–H bonds and in particular the activation of the C–H bonds of inert alkyls by transition metal and lanthanoid complexes is a reaction of general interest due to its relevance for the functionalization of organic molecules.[1] The chemistry of lanthanoid metals is characterized by their high electrophilicity, their tendency to high coordination numbers and their unique feature of varying the sizes of the rare earth atom[2] with a nearly identical coordination chemical behavior. Complexes of these metals are strong Lewis acids which may attack the electron density of C–H bonds, thus forming agostic[3] interactions and activate C–H bonds. Watson has even shown that methane,

itself, could be activated by lanthanocene complexes such as (Cp*)$_2$LuCH$_3$ (Cp* = pentamethylcyclopentadienyl).[4] Consequently, intermolecular alkyl group C–H activation of spectator ligands of lanthanoid complexes has been observed for a variety of ligands, for instance, for methyl groups of the Cp* ligand.[5] Similar alkyl group C–H activation reactions have been described for non-metallocene lanthanoid complexes.[6]

Aminopyridinato ligands[7] have been used successfully for the stabilization of early transition metals and lanthanoids and we started recently a research program to investigate the reactivity of metal complexes coordinated by very bulky aminopyridinates.[8] In the course of these studies we observed that alkyl and hydrido yttrium complexes supported by the aminopyridinato ligand Ap′ {Ap′H = (2,6-diisopropylphenyl)[6-(2,6-dimethylphenyl)pyridin-2-yl]amine, Figure 1} undergo methyl group C–H activation of one of the methyl groups of the 2,6-dimethylphenly moiety of the Ap′ ligand.[8i]

The alkyl complex [Ap′$_2$YCH$_2$SiMe$_3$] undergoes this C–H activation rather slowly and the corresponding hydride does it more than 500 times faster.

[a] Lehrstuhl Anorganische Chemie II, Universität Bayreuth, 95440 Bayreuth, Germany
Fax: +49-921552157
E-mail: kempe@uni-bayreuth.de
[b] G. A. Razuvaev Institute of Organometallic Chemistry of the Russian Academy of Sciences,
Tropinina 49, GSP-445, 603950 Nizhny Novgorod, Russian Federation
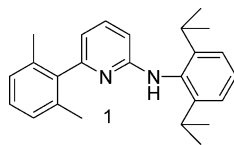E-mail: trif@iomc.ras.ru

Figure 1. Used aminopyridine.

Since yttrium mimics the size of the late lanthanoids quite well we became interested in how this ligand metallation proceeds for early lanthanoids as well as for Lu and Sc. Herein we report on synthesis and characterization of lanthanoid monohalide complexes stabilized by bulky Ap′ ligands, their alkylation with $LiCH_2SiMe_3$ which leads – depending on the size of the lanthanoid ion – to C–H activation products or to (rather) stable alkyl complexes (Scheme 1).
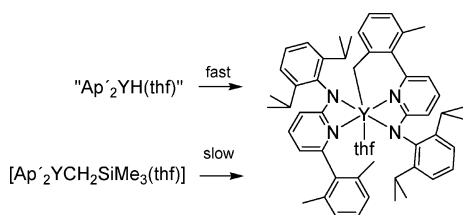
Scheme 1. Ligand metallation (methyl group C–H activation) reaction of Ap′$_2$Y-alkyl and -hydride complexes.

Results and Discussion

Polymeric **2** was prepared according to the literature reported procedure.[8a] Two equivalents of **2** were treated with MX_3 [M = Sc, Nd, and Sm, and X = Cl or M = La and X = Br] in a salt metathesis reaction to afford the corresponding bis(aminopyridinato) complexes [Ap′$_2$ScCl(thf)] (**3**), [Ap′$_2$LaBr(thf)] (**4**), [Ap′$_2$NdCl(thf)][8b] (**5**), and [Ap′$_2$SmCl(thf)] (**6**) in good yields (Scheme 2).

M = Sc, X = Cl (**3**) M = Nd, X = Cl (**5**)
M = La, X = Br (**4**) M = Sm, X = Cl (**6**)
M = Lu, X = Cl (**8**)
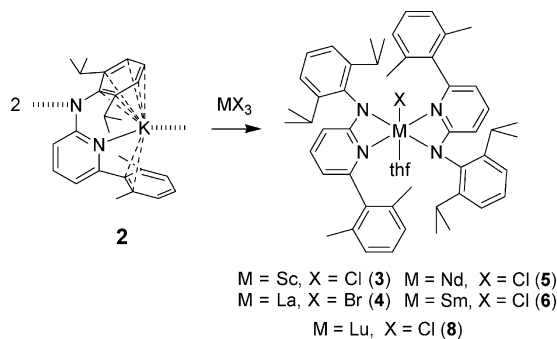
Scheme 2. Synthesis of bis(aminopyridinato) halide complexes.

However, in case of Lu both mono- as well as bis(aminopyridinato)lutetium complexes [Ap′LuCl$_2$(thf)$_2$] (**7**) and [Ap′$_2$LuCl(thf)] (**8**) were observed, respectively. Due to the poor solubility of **8** in hexane **7** can be separated easily in 24% yield if extracted with hexane. Residue **8** was extracted with toluene in a yield of 20%. Due to the poor yield of **8** we became interested in using an amine elimination route.

Compound **8** was synthesized in (90%) yield by reacting four equivalents of **1** with [(R$_2$N)$_2$LuCl(thf)]$_2$ where R = diisopropyl (Scheme 3).
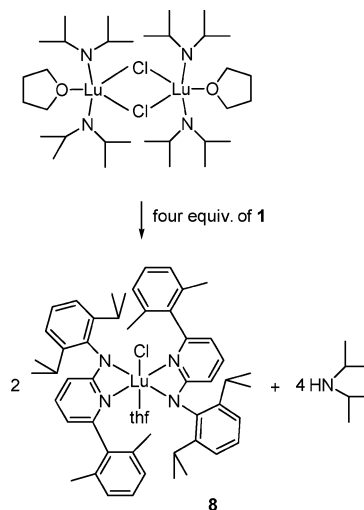
Scheme 3. Amine elimination synthesis of **8**.

The thf ligand is labile and a thf-free derivative of compound **3** was isolated after work up in toluene. However, crystals suitable for X-ray analysis were grown from concentrated toluene solution after adding a few drops of thf which coordinates to the vacant site of the metal centre. Compound **4** is isolated as yellow crystalline material from hexane in moderate yield. Compound **6** and **8** were isolated as yellow crystals by slow diffusion of hexane or toluene into a saturated thf solution of these complexes. This series of compounds is a rare example of lanthanoid complexes with the same ligand environment for which the same coordination number is observed despite their different ionic radii. The coordination of the bis(aminopyridinato)lanthanoid halide complexes is best described as a distorted octahedron arising from the two bidentate aminopyridinates, the chloro/bromo as well the thf ligand, as shown in Figures 2, 3, 4, and 5. Crystallographic details of all structures are listed in Tables 1 and 2. It has been observed that in all cases the aminopyridinato ligands induce distortion from the ideal octahedral symmetry. N$_{pyridine}$–M–N$_{amido}$ angles of 60.21, 52.98, 55.16 and 57.7° in **3**, **4**, **6** and **8**, respectively, were observed and are comparable to previously published **5** [54.5°].[8b] The longer M–N$_{pyridine}$ bond lengths compared to M–N$_{amido}$ bond length is indicative of the localization of the anionic function of the ligand at the amido N-atoms.[9]

The compound **7** is dimeric in solid state and the coordination around each Lu can be best described as distorted pentagonal bipyramid (Figure 6). The two chloro ligands, the pair of nitrogen atoms and one thf ligand form the pentagonal (equatorial) plane and the remaining chloro and thf ligands occupy the axial positions of the polyhedron. The distortion is caused by the small N–Lu–N angle of 56.5(2)° due to the strained binding mode of the ligand. It leads to a situation in which all other angles in the pentagonal plane are over 72°. The N1–Lu–Cl2 and O2–Lu–Cl2 cis angles
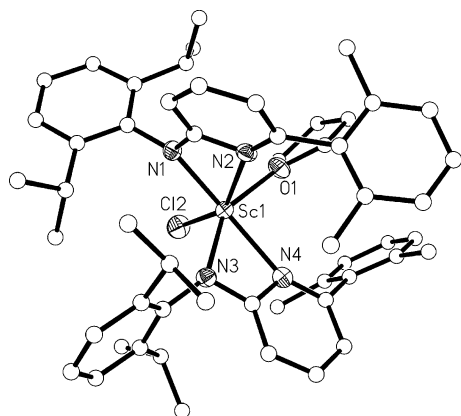
Figure 2. Molecular structure of **3**; selected bond lengths [Å] and angles [°]: N1–Sc1 2.109(5), N2–Sc1 2.403(6), N3–Sc1 2.151(6), N4–Sc1 2.314(5), O1–Sc1 2.190(5) Cl2–Sc1 2.365(2); N1–Sc1–N3 105.9(2), N1–Sc1–O1 101.61(19), N3–Sc1–O1 149.00(18), N1–Sc1–N4 160.4(2), N3–Sc1–N4 60.57(19), O1–Sc1–N4 89.09(19), N1–Sc1–Cl2 92.25(16), N3–Sc1–Cl2 101.97(16), O1–Sc1–Cl2 90.88(15), N4–Sc1–Cl2 104.05(16), N1–Sc1–N2 59.85(19), N3–Sc1–N2 94.0(2), O1–Sc1–N2 87.57(19), N4–Sc1–N2 104.89(19), Cl2–Sc1–N2 150.99(14).

Figure 4. Molecular structure of **6**; selected bond lengths [Å] and angles [°]: N1–Sm1 2.334(2), N2–Sm1 2.572(2), N3–Sm1 2.352(2), N4–Sm1 2.519(2), O1–Sm1 2.4064(18), Cl1–Sm1 2.5681(6); N1–Sm1–N4 156.85(7), N1–Sm1–O1 103.58(7), N4–Sm1–O1 89.57(7), N1–Sm1–N3 107.83(7), N4–Sm1–N3 55.63(7), O1–Sm1–N3 144.80(7), N1–Sm1–N2 54.69(6), N4–Sm1–N2 107.57(6), O1–Sm1–N2 88.88(6), N3–Sm1–N2 96.43(7), N1–Sm1–Cl1 89.50(5), N4–Sm1–Cl1 109.53(5), O1–Sm1–Cl1 90.98(5), N3–Sm1–Cl1 104.61(5), N2–Sm1–Cl1 142.90(5).
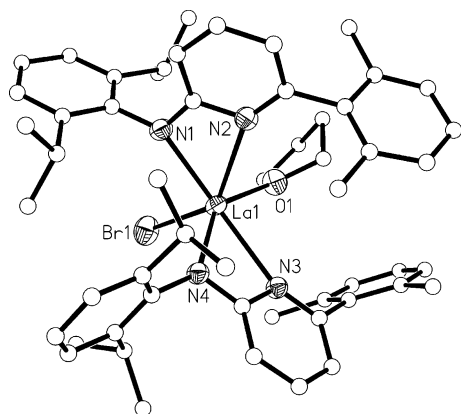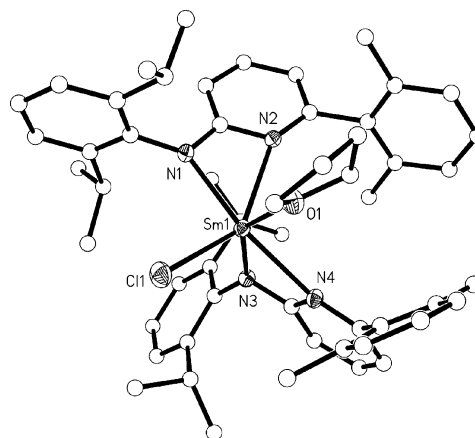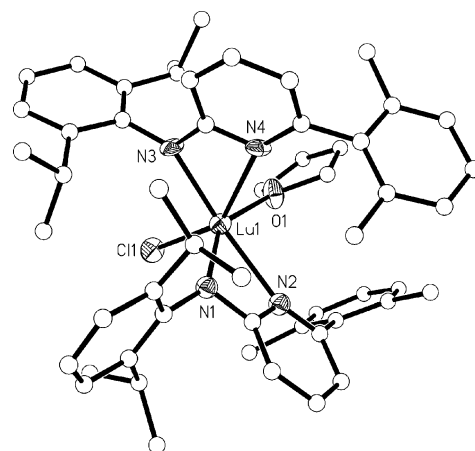

Figure 3. Molecular structure of **4**; selected bond lengths [Å] and angles [°]: N1–La1 2.418(3), N2–La1 2.650(4), N3–La1 2.639(3), N4–La1 2.433(3), O1–La1 2.525(3), Br1–La1 2.8625(6); N1–La1–N4 104.46(11), N1–La1–O1 110.29(11), N4–La1–O1 144.13(11), N1–La1–N3 151.20(11), N4–La1–N3 53.04(11), O1–La1–N3 91.22(10), N1–La1–N2 52.92(12), N4–La1–N2 102.77(11), O1–La1–N2 91.42(10), N3–La1–N2 109.73(11), N1–La1–Br1 89.59(9), N4–La1–Br1 103.33(8), O1–La1–Br1 85.80(7), N3–La1–Br1 111.59(8), N2–La1–Br1 138.63(8).

Figure 5. Molecular structure of **8**; selected bond lengths [Å] and angles [°]: [A°] and angles [°]: N1–Lu1 2.248(7), N2–Lu1–2.422(8), N3–Lu1 2.246(8), N4–Lu1 2.462(10), O1–Lu1 2.297(6), Cl1–Lu1 2.479(3); N1–Lu1–N4 95.0(3), N1–Lu1–O1 147.8(3), N4–Lu1–O1 88.5(4), N1–Lu1–N3 105.8(3), N4–Lu1–N3 56.7(3), O1–Lu1–N3 102.8(3), N1–Lu1–N2 58.7(2), N4–Lu1–N2 107.1(3), O1–Lu1–N2 89.7(3), N3–Lu1–N2 158.6(3), N1–Lu1–Cl1 102.8(3), N4–Lu1–Cl1 146.8(19), O1–Lu1–Cl1 90.9(2), N3–Lu1–Cl1 91.3(2), N2–Lu1–Cl1 106.1(2).

are 77.13(18) and 72.66(15)°. The N2–Lu–O2 angle is the widest [81.5(2)°] of all. The O1$_{ax}$–Lu–O2$_{eq}$ and Cl$_{ax}$–Lu–O2$_{eq}$ angles are 80.63(18) and 90.05(14)°, respectively.

Although structurally very similar, complexes **3** and **4** demonstrated different dynamic behaviour in solution. We essentially attribute this to the different radii of the lanthanoid ions. In **3** the signals of the two methyl groups are well separated as two sharp peaks at room temperature. At 330 K a very slow exchange between two methyl groups is observed. The exchange becomes faster at 350 K but the signals still remain inequivalent. The ^{1}H NMR spectrum of compound **4** at room temperature consists of one broad signal corresponding to methyl group. The cooling of the

[D$_8$]toluene solution to 273 K afforded the splitting of the above signal into two broad resonances. Further cooling resulted first in sharpening of these signals (253 K) and then again into the broadening and splitting of each of them to a new pair of signals (233 K). Most likely, two dynamic processes are present, first the exchange of the positions of the two Ap ligand and secondly the freezing out of the rotation of the 2,6-dimethylphenyl substituent Figure 7.

Reacting two equivalents of **2** with LaCl$_3$ in thf at 65 °C without stirring it at room temperature leads to a homoleptic complex, [Ap′$_3$La] (**9**) in overall yield of 37%

Table 1. Details of the X-ray crystal structure analyses.

	3	4 · 1/2(C_6H_{14})	6
Crystal system	triclinic	triclinic	triclinic
Space group	$P\bar{1}$	$P\bar{1}$	$P\bar{1}$
a [Å]	12.6930(11)	12.2880(7)	12.8440(7)
b [Å]	14.030(12)	12.3570(7)	13.9910(8)
c [Å]	14.1790(12)	19.3060(11)	14.2110(8)
α [°]	73.880(10)	99.975(5)	104.986(4)
β [°]	79.920(10)	90.309(5)	99.473(4)
γ [°]	88.820(5)	113.791	90.957(4)
V [Å^3]	2391.2(4)	2632.8(3)	2428.5(2)
Crystal size [mm]	0.22 × 0.17 × 0.15	0.21 × 0.20 × 0.19	0.49 × 0.36 × 0.22
ρ_{calcd} [g cm^{-3}]	1.205	1.322	1.330
μ [mm^{-1}] (Mo-K_α)	0.252	1.611	1.305
T [K]	191(2)	191(2)	133(2)
θ range [°]	1.55 to 25.69	1.82 to 24.69	1.51 to 25.75
Number of reflections unique	3681	6434	8251
Number of reflections obsd. [$I > 2\sigma(I)$]	22008	28979	31719
Number of parameters	550	562	562
wR_2 (all data)	0.222	0.080	0.071
R value [$I > 2\sigma(I)$]	0.087	0.042	0.027

Table 2. Details of the X-ray crystal structure analyses.

	7	8	9
Crystal system	monoclinic	triclinic	monoclinic
Space group	$P2_1/n$	$P\bar{1}$	$P2_1/n$
a [Å]	10.222(5)	12.7414(9)	13.7710(4)
b [Å]	18.663(5)	13.9751(13)	22.5550(8)
c [Å]	17.437(5)	14.1997(10)	20.1650(7)
α [°]		105.467(7)	
β [°]	93.047(5)	99.750(7)	91.11(3)
γ [°]		90.090(7)	
V [Å^3]	3322(2)	2898.8(3)	6262.2(4)
Crystal size [mm]	0.17 × 0.08 × 0.07	0.23 × 0.20 × 0.18	0.59 × 0.50 × 0.35
ρ_{calcd} [g cm^{-3}]	1.495	1.381	1.285
μ [mm^{-1}] (Mo-K_α)	0.71	2.155	0.73
T [K]	193(2)	133(2)	191(2)
θ range [°]	1.60 to 26.15	1.51 to 25.70	1. 35 to 25.7
Number of reflections obsd. [$I > 2\sigma(I)$]	2790	4437	10335
Number of reflections	6538	6249	81811
Number of parameters	361	544	881
wR_2 (all data)	0.064	0.139	0.076
R value [$I > 2\sigma(I)$]	0.033	0.057	0.030

(Scheme 4). Crystals of **9** suitable for X-ray analysis (crystallographic details are listed in Table 2) were grown by slow condensation of hexane into a saturated thf solution of **9**. The coordination around La can best be described as distorted trigonal prism as shown in Figure 8. The slightly elongated La–$N_{pyridine}$ bond length in **9** (2.745 Å, averaged value) indicates some steric overcrowding. The averaged La–pyridine distance is 2.703 (47 values taken from the CSD version 5.30).

As we have previously shown for yttrium[8i] that such bis-(aminopyridinato)lanthanoid halide complexes can be successfully alkylated using LiCH$_2$SiMe$_3$. The reaction of these alkyls with PhSiH$_3$ to form the intramolecular C–H bond activation products is fast compared to the slow decomposition of the parent alkyls (Scheme 1). In order to investigate the role of the size of the used metal to form such intramolecular C–H bond activation products we extended our

studies to various other lanthanoids. We observed that **3** and **8** comprised of smaller lanthanoids like Sc and Lu can be alkylated successfully by reacting them with one equivalent of LiCH$_2$SiMe$_3$ in hexane to give the corresponding alkyl complexes [Ap′$_2$ScCH$_2$SiMe$_3$] (**10**) and [Ap′$_2$LuCH$_2$-SiMe$_3$(thf)] (**11**) in good yields of 62% and 86%, respectively (Scheme 5).

In the ^{1}H NMR spectrum of complex **10** we observed a singlet at $\delta = 0.13$ ppm for the protons of the –SiMe$_3$ group and a broad singlet at $\delta = 0.22$ ppm for the methylene protons. In the ^{13}C NMR we observed a sharp signal for the –SiMe$_3$ group at $\delta = 3.62$ ppm, however a signal for methylene carbon could not be observed since the carbon signals of scandium alkyls are usually broad due to the 7/2 spin of Sc. Complex **10** is quite stable in solution and doesn′t show any detectable decomposition when its C$_6$D$_6$ solution was monitored for several weeks. Compound **11** (Figure 9) was
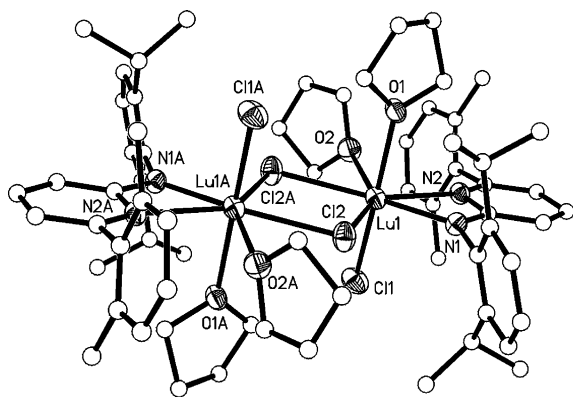
Figure 6. Molecular structure of **7**; selected bond lengths [Å] and angles [°]: Lu1–N1 2.283(5), Lu1–O1 2.341(5), Lu1–O2 2.375(5), Lu1–N2 2.474(6), Lu1–Cl1 2.516(2), Lu1–Cl2 2.675(2), Lu1–Cl2 2.718(2), 3.556; N1–Lu1–O1 86.21(17), O1–Lu1–O2 80.63(18), N1–Lu1–N2 56.5(2), O1–Lu1–N2 85.93(17), O2–Lu1–N2 81.5(2), N1–Lu1–Cl1 98.79(12), O1–Lu1–Cl1 170.23(13), O2–Lu1–Cl1 90.05(14), N2–Lu1–Cl1 89.83(14), N1–Lu1–Cl2 77.13(18), O1–Lu1–Cl2 94.14(12), O2–Lu1–Cl2 144.41(14), Cl1–Lu1–Cl2 95.16(7), O1–Lu1–Cl2 85.57(12), O2–Lu1–Cl2 72.66(15), N2–Lu1–Cl2 153.81(14), Cl1–Lu1–Cl2 94.48(7), Cl2–Lu1–Cl2 71.85(7).
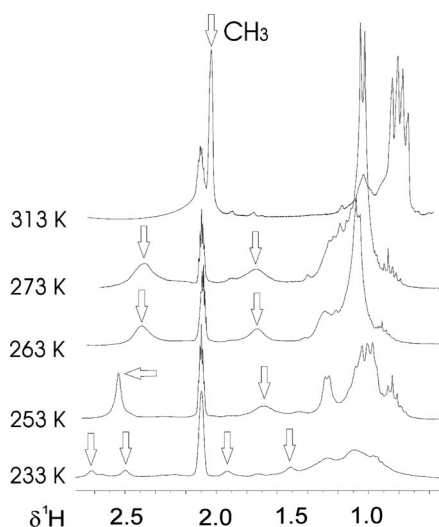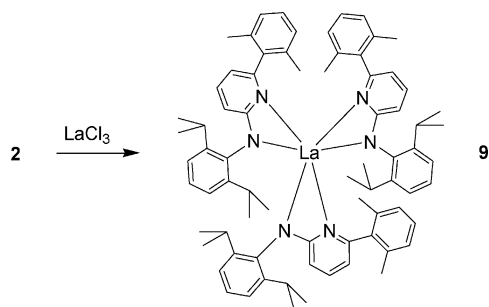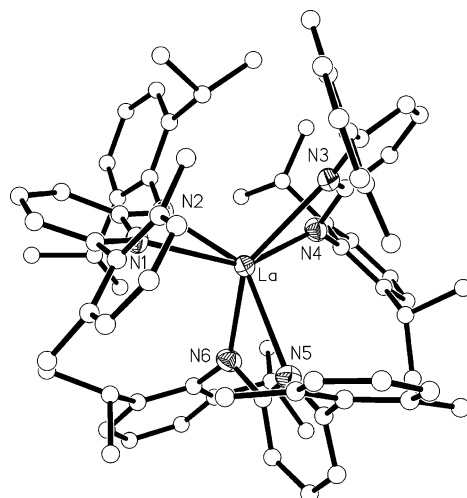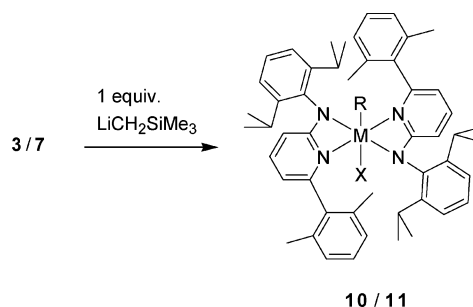

Figure 8. Molecular structure of **9**; selected bond lengths [Å] and angles [°]: N1–La 2.7249(17), N2–La 2.4446(18), N3–La 2.7302(17), N4–La 2.4478(19), N5–La 2.7815(17), N6–La 2.4365(18), N4–La–N2 96.75(6), N4–La–N6 98.69(6), N2–La–N6 100.64(6), N4–La–N1 144.11(6), N2–La–N1 52.31(6), N6–La–N1 104.22(6) N4–La–N3 52.24(5), N2–La–N3 103.74(6), N6–La–N3 143.72(6), N1–La–N3 111.92(5), N4–La–N5 105.61(6), N2–La–N5 146.32(6), N6–La–N5 51.84(6), N1–La–N5 110.25(5), N3–La–N5 109.84(5).

Figure 7. Variable-temperature ^{1}H NMR of **4** in C_7D_8.

Scheme 5. Synthesis of **10** and **11** [**10**: M = (Sc, X = no thf); **11**: M = (Lu, X = thf), (R = CH_2SiMe_3)].

Scheme 4. Synthesis of tris(aminopyridinato)lanthanum complex **9**.

crystallized by slow cooling of its concentrated hexane solution when layered with thf to –20 °C. X-ray analysis show one thf molecule per molecule of [Ap′$_2$LuCH$_2$SiMe$_3$(thf)]

in the crystal. The structure refinement data are listed in Table 3. The coordination sphere of the lutetium atom is set up by four nitrogen atoms of two aminopyridinato ligands, one carbon atom of the alkyl group and one oxygen atom of the thf molecule resulting in the coordination number of six. The Lu–C bond length of 2.323(14) Å is slightly shorter than the values reported for related anilido phosphinimino (2.370 Å), 4,4′,4′′-tri-*tert*-butyl-2,2′:6′,2′′-terpyridine (2.378 Å) and β-ketoiminato (2.402 Å) ligand complexes.[10]

In the ^{1}H NMR spectrum of complex **11** the hydrogen atoms of the methylene group attached to the lutetium atom appear as a broad singlet at δ = –0.65 ppm whereas in the ^{13}C NMR the appropriate carbon appears at δ = 47.8 ppm. Similarly in the ^{1}H NMR spectrum the nine protons of the SiMe$_3$ group appear as a singlet at δ = 0.15 ppm. It is noteworthy that the signal sets corresponding to the aminopyridinate fragments in the ^{1}H NMR spectrum of **11** is quite different from its parent chloro complex **7**. In the latter pro-
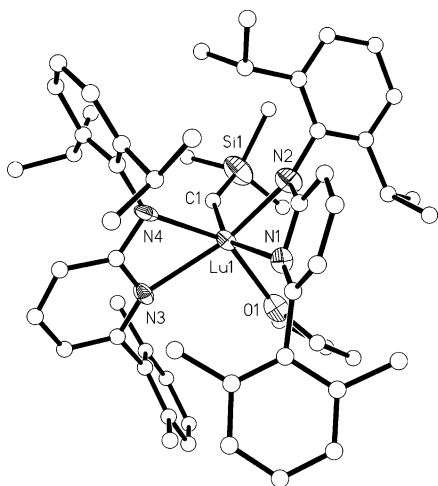
Figure 9. Molecular structure of **11**; selected bond lengths [Å] and angles [°]: N1–Lu1 2.536(9), N2–Lu1 2.242(9), N3–Lu1 2.426(9), N4–Lu1 2.310(10), O1–Lu1 2.294(9), C1–Lu1 2.323(14); N1–Lu1–N4 94.1(3), N1–Lu1–O1 84.3(3), N4–Lu1–O1 148.2(3), N1–Lu1–N3 108.3(3), N4–Lu1–N3 56.8(3), O1–Lu1–N3 93.5(3), N1–Lu1–N2 58.2(3), N4–Lu1–N2 101.3(3), O1–Lu1–N2 104.6(3), N3–Lu1–N2 155.3(3), N1–Lu1–C1 154.2(4), N4–Lu1–C1 100.1(4), Si1–Lu1–C1 149.8(7), O1–Lu1–C1 94.4(4), N3–Lu1–C1 97.5(4), N2–Lu1–C1 97.7(4).

tons of the methyl substituents appear as a singlet at $\delta = 2.90$ ppm whereas the same group of protons in **11** gives two individual singlets at $\delta = 1.46$ and 2.46 ppm. This different behavior can be explained in terms of the steric bulk of the alkyl group introduced that slows down the ligand exchange process due to increased hindrance to rotation. Complex **11** does not coordinate thf during the course of the reaction and results in the thf adduct if a few drops of thf are added during crystallization process. Compound **11** can be stored in solid state without decomposition at –20 °C while in solution it decomposes quite slowly at room temperature compared to its yttrium analogue eliminating SiMe₄.[8i]

In contrast to Sc and Lu the alkylation of the chloro complexes **4** and **5** comprised of the larger lanthanoids La and Nd with one equivalent of LiCH₂SiMe₃ did not yield the desired alkyl complexes and led directly to the intramolecular C–H bond activated products [Ap′(Ap₋H′)La(thf)] (**12**) and [Ap′(Ap₋H′)Nd(thf)] (**13**), in good yields of 61 % and 63 %, respectively (Scheme 6).
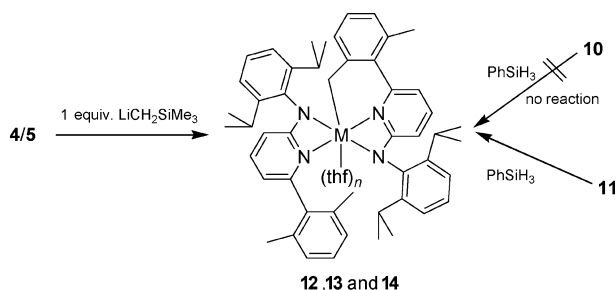
Scheme 6. Synthesis of C–H activation products [**12**: M = La, $n = 2$; **13**: M = Nd, $n = 1$; **14**: M = Lu, $n = 1$].

Orange crystals of **12** were grown by slow cooling of a concentrated thf/hexane (1:2) solution to –20 °C whereas brown crystals of **13** suitable for X-ray analysis were grown from a mixture of thf/pentane (1:10) at low temperature. The molecular structures of **12** and **13** are depicted in Figures 10 and 11, respectively. In **12** one extra thf coordinates to the La compared to the parent **4** increasing the coordination number to seven. Complex **13** shows strongly distorted octahedral coordination. The bond lengths of 2.601(4) and 2.519 (10) Å in **12** and **13**, respectively, between the corresponding metal (lanthanum/neodymium) and the "benzylic" carbon are elongated as expected compared to previously reported Y–C bond [2.420(11) Å].[8i] In comparison to the averaged bond length of La–C bonds which is 2.797 Å (averaged from 48 La⋯methyl distances, CSD version 5.30) and the corresponding Nd distance 2.649 Å (average of 55 distances, CSD version 5.30) the Ln–C bond lengths in **12** and **13** are a little shorter. Unlike the

Table 3. Details of the X-ray crystal structure analyses.

	11 · C₄H₈O	**12**	**13**
Crystal system	triclinic	monoclinic	monoclinic
Space group	P1̄	P2₁/c	P2(1)
a [Å]	12.5940(10)	12.2350(5)	9.7600(6)
b [Å]	12.6940(13)	23.4280(11)	20.8890(12)
c [Å]	18.972(2)	18.6550(8)	12.2070(7)
α [°]	75.789(8)		
β [°]	89.453(5)	103.847(3)	107.083(4)
γ [°]	83.858(7)		
V [Å³]	2922.9(5)	5191.9(4)	2378.9(2)
Crystal size [mm]	0.14 × 0.11 × 0.06	0.28 × 0.25 × 0.23	0.15 × 0.15 × 0.11
ρ_{calcd} [g cm⁻³]	1.274	1.276	1.299
μ [mm⁻¹] (Mo-K_α)	1.753	0.87	1.13
T [K]	133(2)	133(2)	173(2)
θ range [°]	1.63 to 25.7	1.42 to 25.6	1.75 to 25.7
Number of reflections obsd. [$I > 2\sigma(I)$]	5084	6999	6044
Number of reflections	9976	61178	25156
Number of parameters	638	588	522
wR_2 (all data)	0.154	0.087	0.110
R value [$I > 2\sigma(I)$]	0.071	0.038	0.062

chloro compounds **4** and **5**, in complexes **12** and **13** one aminopyridinato ligand is bidentate, while the second one becomes tridentate due to metallation of the methyl group of one of the $Me_2C_6H_3$ fragments and formation of the new M–C σ-bond. The interesting features of **12** and **13** are the different ways of coordination of the aminopyridinato ligands. We have observed in the chloro complexes that both of the ligands have amidopyridine binding modes. The type of coordination of the bidentate Ap′ ligand is similar to that observed in chloro complexes: one short M–N bond with amido nitrogen atom [La1–N1 2.489(3) and Nd1–N4 2.416(6)] Å and one long with the nitrogen atom of pyridine fragment [La1–N2 2.700(7) and Nd1–N3 2.556(8) Å]. In the tridentate Ap$_{-H}$′ ligand formation of the M–C bond influences dramatically the bonding situation: the covalent bond between metal and amido nitrogen atom [La1–N4 2.565(3) and Nd1–N1 2.499(7) Å] becomes longer than the coordination bond between metal and pyridine nitrogen atom [La1–N3 2.528(3) and Nd1–N2 2.448(7) Å] which means a switch from the amidopyridine to the aminopyridinato form is observed.[9]
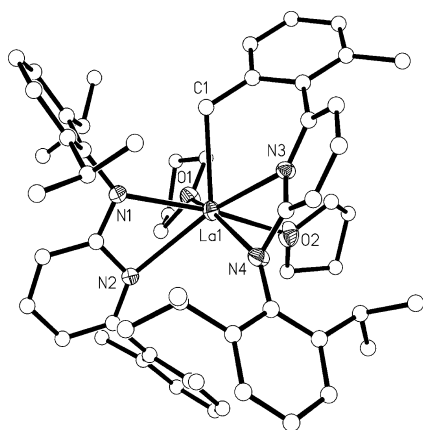

Figure 10. Molecular structure of **12**; selected bond lengths [Å] and angles [°]: N1–La1 2.489(3), N2–La1 2.700(3), N3–La1 2.528(3), N4–La1 2.565(3), O1–La1 2.554(2), O2–La1 2.609(2), C1–La1 2.601(4); La–C1–C2 117.4(2), N1–La1–N4 107.81(9), N1–La1–O1 90.44(9), N4–La1–O1 155.45(9), N1–La1–N3 119.46(9), N4–La1–N3 52.97(8), O1–La1–N3 131.32(8), N1–La1–N2 51.83(9), N4–La1–N2 99.29(8), O1–La1–N2 78.87(8), N3–La1–N2 149.74(8), N1–La1–C1 70.5(3), N4–La1–C1 112.37(10), O1–La1–C1 87.36(10), N3–La1–C1 66.43(10), N2–La1–C1 125.78(10), N1–La1–O2 159.17(9), N4–La1–O2 88.91(9), O2–La1–N3 80.39(11), O2–La1–N2 114.44(8), O1–La1–C1 117.7(3), O1–La1–O2 70.21(8), C1–La1–O2 109.18(10).

We observe a broad singlet at δ = 1.35 ppm for the La–CH_2 protons in the ^{1}H NMR spectrum that coincides with the signal of coordinated thf. However the respective signals were observed as a singlet at δ = 68.9 ppm in the ^{13}C NMR spectrum. In case of **13** the paramagnetic nature of the complex excludes the observations of this resonance.

We know from our previous studies that such C–H activated products are accessible if the parent alkyl is reacted with equimolar amount of $PhSiH_3$ therefore for smaller scandium and lutetium the σ-bond metathesis reactions of alkyl complexes **10** and **11** with phenylsilane were employed
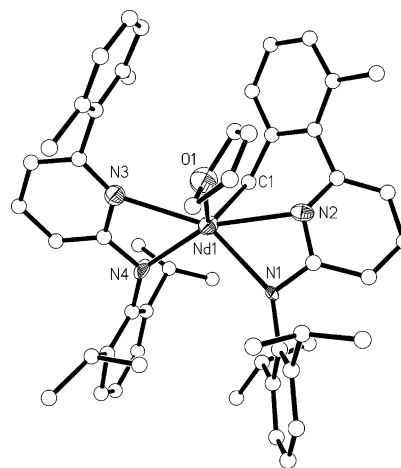

Figure 11. Molecular structure of **13**; selected bond lengths [Å] and angles [°]: N1–Nd1 2.499(7), N2–Nd1 2.448(7), N3–Nd1 2.556(8), N4–Nd1 2.416(6), O1–Nd1 2.462(6), C1–Nd1 2.519(10); N1–Nd1–N4 107.8(2), N1–Nd1–O1 91.3(2), N4–Nd1–O1 127.8(2), N1–Nd1–N3 147.6(2), N4–Nd1–N3 54.4(2), O1–Nd1–N3 83.7(2), N1–Nd1–N2 53.8(2), N4–Nd1–N2 148.9(2), O1–Nd1–N2 81.0(2), N3–Nd1–N2 154.1(2), N1–Nd1–C1 107.9(3), N4–Nd1–C1 99.8(3), O1–Nd1–C1 120.2(3), N3–Nd1–C1 102.3(3), N2–Nd1–C1 68.6(3).

as a synthetic approach to bis(aminopyridinato)lanthanoid hydrides or intramolecular C–H bond activation products. We observed that **10** was quite inert towards phenylsilane and did not undergo any observable change when the reaction was monitored by ^{1}H NMR spectroscopy. However stirring of **11** in toluene with phenylsilane for three days at room temperature and then cooling to –20 °C allowed the isolation of complex [Ap′(Ap$_{-H}$′)Lu(thf)] (**14**) in 60% yield (Scheme 6).

In order to understand the role of the size of the used lanthanoid we studied the formation of complex **14** on NMR scale in [D$_6$]benzene at 296 K in the presence of phenylsilane. We observed that for lutetium the rate of formation of the C–H activation product is about twenty times slower than for the comparatively larger yttrium based on half-times.[8i] The ^{1}H NMR spectrum did not indicate the presence of a hydride specie in the reaction mixture.

Conclusions

Several conclusions can be made from this study. The bulky aminopyridinato ligand Ap′ affords isostructural bis-aminopyridinate monohalide complexes from La to Sc despite of the large difference in the ionic radii of the metals. The corresponding alkyl complexes, synthesized via salt metathesis starting from the monohalides, can be unstable and can undergo intramolecular methyl group C–H activation depending on the size of the lanthanoids used. For larger lanthanoids the rate of decomposition of the parent alkyl at room temperature is fast and precludes the isolation of these alkyls. Gradual decrease of the metal size enables the isolation of stable alkyl complexes which may undergo intramolecular C–H activation via a transient hydride species

at reasonable rates at room temperature. C–H activation of 2,6-dimethylphenyl moieties can be avoided by using 2,6-dichlorophenyl instead.[11]

Experimental Section

General Procedures: All reactions and manipulations with air-sensitive compounds were performed under dry argon, using standard Schlenk and glovebox techniques. Non halogenated solvents were distilled from sodium benzophenone ketyl and halogenated solvents from P_2O_5. Deuterated solvents were obtained from Cambridge Isotope Laboratories and were degassed, dried and distilled prior to use. All chemicals were purchased from commercial vendors and used without further purification. Compound [Ap′$_2$NdCl(thf)] (**5**) was prepared according to previously published procedure.[8b] NMR spectra were obtained using either a Bruker ARX 250 or Varian Inova Unity 400 spectrometer. Chemical shifts are reported in ppm relative to the deuterated solvent; an atom numbering scheme for signal assignments is given in Scheme 7. X-ray crystal structure analyses were performed by using a STOE-IPDS I or II equipped with an Oxford Cryostream low-temperature unit. Structure solution and refinement were accomplished using SIR97,[12] SHELXL-9[13] and WinGX.[14] Crystallographic details are summarized in Tables 1, 2 and 3. Elemental analyses were carried out by means of a Vario elementar EL III or Leco CHN-932 elemental analyser.
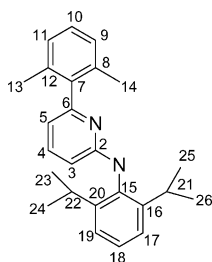
Scheme 7. Numbering scheme for NMR labelling.

Synthesis of Lanthanoid Complexes

Synthesis of 3: thf (40 mL) was added to ScCl$_3$ (0.302 g, 2.00 mmol) and **2** (1.586 g, 4.00 mmol) in a Schlenk flask. The resulting bright yellow coloured reaction mixture was stirred overnight. The solvent was evaporated under vacuum and the product was extracted with toluene (30 mL). Toluene was fully evaporated and the resulting product was washed with hexane; yield (0.9 g, 52%). Crystals suitable for X-ray analysis were grown by adding a few drops of thf to a concentrated toluene solution. C$_{54}$H$_{66}$ClN$_4$OSc (867.5): calcd. for thf coordinated crystals C 74.76, H 7.67, N 6.46; found. C 74.26, H 8.01, N 6.46. ^{1}H NMR (250 MHz, C$_6$D$_6$): δ = 0.81–1.26 [m, 24 H, H^{23,24,25,26}], 1.47 [s, 6 H, H^{13,14}], 2.34 [s, 6 H, H^{13,14}], 3.28 [sept, 4 H, H^{21,22}], 5.60 [d, J = 8.4 Hz, 2 H, H^3], 5.68 [d, J = 7.2 Hz, 2 H, H^5], 6.67 [dd, 2 H, H^4], 7.02–7.18 [m, 12 H, H^{9,10,11,17,18,19}] ppm. ^{13}C NMR (C$_6$D$_6$): δ = 19.2 [C^{13,14}], 24.7 [C^{23,24,25,26}], 29.9 [C^{13,14}], 104.8 [C$^{3/5}$], 110.6 [C$^{3/5}$], 124.1 [C^{17,19}], 124.4 [C^{9,11}], 129.2 [C^{10,18}], 135.7 [C^{8,12}], 137.3 [C^7], 141.6 [C^{16,20}], 144.0 [C^4], 144.5 [C^{15}], 156.1 [C^6], 168.7 [C^2] ppm.

Synthesis of 4: thf (40 mL) was added to LaBr$_3$ (0.757 g, 2.00 mmol) and **2** (1.58 g, 4.00 mmol) in a Schlenk flask. The resulting bright yellow colour reaction mixture was stirred overnight. The solvent was removed under vacuum and the product was extracted with hexane (30 mL). The filtrate was concentrated to af-

ford bright yellow crystals suitable for X-ray analysis after 48 h at room temperature; yield (1.066 g, 53%). C$_{54}$H$_{66}$BrLaN$_4$O (1005.94): calcd. C 64.47, H 6.61, N 5.57; found C 64.60, H 7.07, N 5.10. ^{1}H NMR (250 MHz, C$_6$D$_6$, 298 K): δ = 0.96–1.39 [m, 28 H, (4 H, β-CH$_2$, thf), 24 H, H^{23,24,25,26}], 2.12 [br., s, 12 H, H^{13,14}], 3.32 [br., s, 4 H, α-CH$_2$, thf], 3.45 [sept, 4 H, H^{21,22}], 5.57 [d, 2 H, J = 8.5 Hz, H^3], 5.75 [d, 2 H, J = 7.0 Hz, H^5], 6.70 [dd, 2 H, H^4], 6.88–7.21 [m, 12 H, H^{9,10,11,17,18,19}] ppm. ^{13}C NMR (C$_6$D$_6$, 298 K): δ = 20.6 [C^{13,14}], 25.0 [C^{23,24,25,26}], 25.3 [β-CH$_2$, thf], 28.7 [C^{21,22}], 70.1 [α-CH$_2$, thf], 107.7 [C$^{3/5}$], 109.8 [C$^{3/5}$], 124.2 [C^{17,19}], 124.9 [C^{9,11}], 127.8 [C^{10,18}], 136.3 [C^{8,12}], 139.5 [C^7], 140.3 [C^4], 144.0 [C^{16,20}], 144.8 [C^{15}], 155.8 [C^6], 170.4 [C^2] ppm.

Synthesis of 6: A solution of **2** (0.34 g, 0.86 mmol) in thf (30 mL) was added to a suspension of SmCl$_3$ (0.11 g, 0.43 mmol) in thf (5 mL) and the reaction mixture was stirred for 7 h at 50 °C. After cooling to the room temperature thf was evaporated in vacuo and the remaining residue was extracted with toluene (30 mL). The extracts were filtered and the solvent was removed under vacuum and the resulting yellow solid was redissolved in thf. Slow condensation of hexane into concentrated thf solution afforded complex **6** as yellow crystals. The crystals were washed with cold hexane and dried in vacuo at room temperature; yield (0.33 g, 81%). C$_{54}$H$_{66}$ClN$_4$OSm (972.94): calcd. C 66.66, H 6.84, N 5.76; found C 66.11, H 6.88, N 5.64.

Synthesis of 7 and 8: thf (40 mL) was added to LuCl$_3$ (0.562 g, 2.00 mmol) and **2**, (1.58 g, 4.00 mmol) in a Schlenk flask. The resulting yellow colour reaction mixture was stirred overnight. The solvent was removed under vacuum and hexane (30 mL) was added. The yellow reaction mixture was filtered and on standing at room temperature for 48 h, yellow crystals (suitable for X-ray analysis) of the title compound **7** were formed; yield (0.37 g, 24%). C$_{66}$H$_{90}$Cl$_4$Lu$_2$N$_4$O$_4$ (1495.19): calcd. C 53.02, H 6.07, N 3.75; found C 52.85, H 5.96, N 3.74. ^{1}H NMR (250 MHz, C$_6$D$_6$, 298 K): δ = 0.50–1.09 [br. m, 24 H, 24 H, H^{23,24,25,26}], 1.22 [br. s, 16 H, (4 H, β-CH$_2$, thf) H^{13,14}], 2.40 [br. s, 12 H, H^{13,14}], 3.76 [br. s, 16 H, α-CH$_2$, thf], 4.09 [sept, 4 H, H^{21,22}], 5.82 [br. d, 4 H, H$^{3/5}$], 6.87–7.25 [m, 14 H, H^{4,9,10,11,17,18,19}] ppm. ^{13}C NMR (C$_6$D$_6$, 298 K): δ = 23.83 [C^{13,14}], 24.88 [C^{23,24,25,26}], 25.2 and 25.4 [β-CH$_2$, thf], 28.7 [C^{21,22}], 71.9 [α-CH$_2$, thf], 106.7 [C$^{3/5}$], 107.5 [C$^{3/5}$], 124.1 [C^{17,19}], 125.2 [C^{9,11}], 127.4 [C^{10,18}], 128.2 [C^{8,12}], 139.9 [C^7], 140.8 [C^4], 143.1 [C^{16,20}], 145.8 [C^{15}], 155.1 [C^6], 168.1 [C^2] ppm.

Toluene (30 mL) was added to the residue of the reaction. The mixture was filtered and the filtrate was concentrated. A few drops of thf were added to afford bright yellow crystals of **8** suitable for X-ray analysis after 24 h at room temperature; yield (0.200 g, 20%). C$_{54}$H$_{66}$ClLuN$_4$O (997.55): calcd. C 65.02, H 6.67, N 5.62; found C 64.15, H 6.80, N 5.33. ^{1}H NMR (400 MHz, C$_7$D$_8$, 298 K): δ = 0.88–1.11 [m, 28 H, (4 H, β-CH$_2$, thf), 24 H, H^{23,24,25,26}], 2.92 [s, 12 H, H^{13,14}], 3.28–3.59 [br., sept, 8 H, (4 H, α-CH$_2$, thf, 4 H, H^{21,22})], 5.79 [br. d, 4 H, H$^{3/5}$], 6.74–7.19 [m, 14 H, H^{4,9,10,11,17,18,19}] ppm. ^{13}C NMR (C$_7$D$_8$, 298 K): δ = 20.4 [C^{13,14}], 21.3 [C^{23,24,25,26}], 23.8 and 24.9 [β-CH$_2$, thf], 28.1 [C^{21,22}], 72.7 [α-CH$_2$, thf], 104.2 [C$^{3/5}$], 109.9 [C$^{3/5}$], 124.2 [C^{17,19}], 125.2 [C^{9,11}], 129.2 [C^{10,18}], 135.9 [C^{8,12}], 139.5 [C^7], 141.3 [C^4], 144.3 [C^{16,20}], 148.0 [C^{15}], 156.4 [C^6], 157.4 [C^2] ppm.

Selective Synthesis of 8: {[(R$_2$N)$_2$LuCl (thf)]$_2$} (R = diisopropyl; 0.539 g, 1.11 mmol) and **1** (0.800 g, 2.23 mmol) were loaded together into a Schlenk flask in glove box. Toluene (40 mL) was added to the yellow reaction mixture. The mixture was stirred overnight. Toluene was fully removed in vacuo to yield **8**. The product was washed with hexane; yield (1.00 g, 90%).

Synthesis of 9: A solution of **2** (0.49 g, 1.24 mmol) in thf (30 mL) of was added to a suspension of LaCl$_3$ (0.152 g, 0.61 mmol) in thf (5 mL) and the reaction mixture was stirred for 20 h at 65 °C. After cooling to the room temperature thf was evaporated in vacuo and the remaining residue was extracted with toluene (30 mL). The solvent was removed under vacuum and the resulting solid residue was redissolved in thf. Slow condensation of hexane into concentrated thf solution afforded complex **9** as brown crystals. The crystals were washed with cold hexane and dried in vacuo at room temperature; yield (0.12 g, 32%). C$_{75}$H$_{87}$LaN$_6$ (1211.44): calcd. C 74.36, H 7.24, N 6.94; found C 73.81, H 7.42, N 7.10. ^{1}H NMR (250 MHz, C$_6$D$_6$, 298 K): δ = 0.57–1.16 [br. m, 36 H, H^{23,24,25,26}], 1.59 [br. s, 6 H, H^{13,14}], 2.24 [br. s, 6 H, H^{13,14}], 2.34 [br. s, 6 H, H^{13,14}], 2.83 [sept, J = 6.7 Hz, 2 H, H^{21,22}], 3.33 [sept, J = 6.7 Hz, 4 H, H^{21,22}], 5.57 [d, J = 8.7 Hz, 3 H, H^3], 5.78 [d, J = 7.0 Hz, 3 H, H^5], 6.61 [dd, J = 8.7, J = 7.1 Hz, 3 H, H^4], 6.82–7.23 [m,18 H, H^{9,10,11,17,18,19}] ppm. ^{13}C NMR (C$_6$D$_6$, 298 K): δ = 20.5 [C^{13,14}], 24.7, 26.5, 26.7 [C^{23,24,25,26}]; 28.8, 29.1 [C^{21,22}], 109.0 [C$^{3/5}$], 112.0 [C$^{3/5}$], 124.5 [C^{17,19}], 125.0 [C^{9,11}], 125.3 [C^{10,18}], 138.1 [C^{8,12}], 140.9 [C^7], 144.0 [C^4], 145.7 [C^{16,20}], 145.9 [C^{15}], 156.0 [C^6], 171.0 [C^2] ppm.

Synthesis of 10: LiCH$_2$SiMe$_3$ (0.105 g, 1.11 mmol) in hexane (30 mL) was added to a stirred suspension of **3** (0.886 g, 1.11 mmol) in hexane and the reaction mixture was stirred for 24 h. The mixture was filtered and volume of the filtrate was reduced under vacuum. A light yellow crystalline material deposited at –25 °C after standing overnight; yield (0.572 g, 62%). C$_{54}$H$_{69}$N$_4$ScSi (847.19): calcd. C 76.56, H 8.21, N 6.61; found C 77.25, H 7.82, N 6.72. ^{1}H NMR (250 MHz, C$_6$D$_6$, 298 K): δ = 0.13 [s, 9 H, CH$_2$Si(CH$_3$)$_3$], 0.22 [s, 2 H, CH$_2$Si(CH$_3$)$_3$], 0.81–1.27 [m, 24 H, H^{23,24,25,26}], 1.45 [s, 6 H, H^{13,14}], 2.18 [s, 6 H, H^{13,14}], 3.18–3.44 [sept, 4 H, H^{21,22}], 5.62 [br., dd, 4 H, H$^{3/5}$], 6.65 [br., dd, 2 H, H^4], 7.01–7.37 [m, 12 H, H^{9,10,11,17,18,19}] ppm. ^{13}C NMR (C$_6$D$_6$, 298 K): δ = 3.62 [Si(CH$_3$)$_3$], 21.26 [C^{13,14}], 23.66 [C^{13,14}], 24.7 and 24.8 [C^{23,24,25,26}], 25.1 and 25.4 [C^{21,22}], 29.2 [C^{21,22}], 105.5 [C$^{3/5}$], 110.4 [C$^{3/5}$], 124.4 [C^{17,19}], 125.9 [C^{9,11}], 128.4 [C^{10,18}], 136.3 [C^{8,12}], 139.4 [C^7], 142.8 [C^{16,20}], 144.1 [C^4], 144.1 [C^{15}], 144.5 [C^6], 169.2 [C^2] ppm. (CH$_2$ signal could not be observed).

Synthesis of 11: LiCH$_2$SiMe$_3$ (0.094 g, 1.00 mmol) in hexane (30 mL) was added to a stirred suspension of **8** (1.0 g, 1.00 mmol) in hexane and the reaction mixture was stirred for 24 h. The mixture was filtered and yellow crystals of **11** suitable for X-ray analysis were obtained by slow cooling of the concentrated mixture thf/hexane (1:5). The crystals were dried under vacuum for two hours for elemental analysis; yield (0.900 g, 86%). C$_{58}$H$_{77}$LuN$_4$OSi (1049.31): calcd. C 66.39, H 7.40, N 5.34; found C 66.73, H 7.29, N 5.71. ^{1}H NMR (250 MHz, C$_6$D$_6$, 298 K): δ = –0.65 [s, 2 H, CH$_2$Si(CH$_3$)$_3$], 0.15 [s, 9 H, CH$_2$Si(CH$_3$)$_3$], 0.92–1.22 [m, 24 H, H^{23,24,25,26}], 1.40 [br. s, 4 H, -CH$_2$, thf], 1.46 [s, 6 H, H^{13,14}], 2.16 [s, 6 H, H^{13,14}], 3.29 [sept, J = 6.8 Hz, 4 H, H^{21,22}], 3.59 [thf, 4 H, β-CH$_2$], 5.62 [d, J = 8.4 Hz, 2 H, H$^{3/5}$], 5.67 [d, J = 6.9 Hz, 2 H, H$^{3/5}$], 6.70 [br., H^4, J = 7.9 Hz, 2 H, dd], 6.96–7.22 [m, 12 H, H^{9,10,11,17,18,19}] ppm. ^{13}C NMR (C$_6$D$_6$, 298 K): δ = 4.34 [Si(CH$_3$)$_3$], 19.5 [C^{13,14}], 21.1 [C^{13,14}], 24.1[C^{23,24,25,26}], 24.7[C^{23,24,25,26}] 25.0[C^{23,24,25,26}] 25.7 [β-CH$_2$, thf], 28.0 [C^{21,22}], 29.3 [C^{21,22}], 47.8[CH$_2$], 68.4 [β-CH$_2$, thf], 106.3 [C$^{3/5}$], 109.8 [C$^{3/5}$], 124.1 [C^{17,19}], 124.4 [C^{17,19}], 125.4 [C^{9,11}], 127.8 [C^{9,11}],128.5 [C^{10,18}], 135.7 [C^{8,12}], 136.2 [C^{8,12}], 139.4 [C^7], 140.8 [C^4], 144.1 [C^{15}], 144.2 [C^{16,20}], 156.0 [C^6], 168.0 [C^2] ppm.

Synthesis of 12: A toluene solution of LiCH$_2$SiMe$_3$ (0.043 g, 0.46 mmol) in (30 mL) was added to a suspension of **4** (0.46 g, 0.46 mmol) in toluene (5 mL) and then reaction mixture was stirred

for 30 min at room temperature and for 1 h at 50 °C. After cooling to room temperature the mixture was filtered and toluene was removed in vacuo. The solid residue was dissolved in thf/hexane mixture ($\approx$ 1:2). Slow cooling of the concentrated solution of complex **12** to –20 °C afforded brown crystals of **12**. The crystals were separated from the mother liquor by decantation, washed with cold hexane and dried in vacuo at room temperature (30 min); yield (0.28 g, 61%). C$_{58}$H$_{73}$LaN$_4$O$_2$ (997.1): calcd. C 69.86, H 7.38, N 5.62; found C 69.73, H 7.81, N 5.66. ^{1}H NMR (400 MHz, C$_6$D$_6$, 25 °C): δ = 1.03, 1.21, 1.27 [d, J = 6.8 Hz, 24 H, H,^{23,24,25,26}], 1.35 [br. s together, 10 H, β-CH$_2$, thf, CH$_2$La], 2.27, 2.42 [s, 9 H, H^{13,14}], 3.33 [br. s, 2 H, H^{21,22}], 3.48 [m, 2 H, H^{21,22}], 3.51 [br. s, 8 H, α-CH$_2$, thf], 5.79, 5.81 [d, J = 8.4 Hz, 2 H, H^3], 5.94, 6.46 [d, J = 7.2 Hz, 2 H, H^5], 6.56–7.35 [m, 14 H, H^{4,9,10,11,17,18,19}] ppm. ^{13}C NMR (100 MHz, C$_6$D$_6$, 25 °C): δ = 20.4, 22.4 [C^{13,14}], 24.1, 25.1 [C^{23,24,25,26}], 25.2 [β-CH$_2$, thf], 28.4, 28.5 [C^{21,22}], 68.8[α-CH$_2$, thf], 68.9 [s, CH$_2$], 106.4, 108.4 [C^3], 108.0, 109.0 [C^5], 118.2, 122.8, 123.6, 123.8, 124.0, 127.4, 127.5, 127.6, 128.1 [C^{9,10,11,17,18,19}], 138.4, 139.3 [C^4], 134.3, 136.0, 141.7, 143.2, 143.6, 146.4, 147.1, 153.1 [C^{7,8,12,15,16,20}], 153.7, 155.8 [C^6], 166.7, 170.4 [C^2] ppm.

Synthesis of 13: A solution of LiCH$_2$SiMe$_3$ (0.045 g, 0.48 mmol) in (30 mL) hexane was added to a suspension of **5** (0.464 g, 0.48 mmol) in hexane (20 mL) and the reaction mixture was stirred for 1 h. The mixture was filtered and hexane was removed in vacuo. The solid residue was dissolved in a thf/pentane mixture ($\approx$ 1:10). Slow cooling of the concentrated solution of complex **13** to –20 °C afforded brown crystals of **13**. The crystals were separated from the mother liquor by decantation, washed with cold hexane and dried in vacuo at room temperature; yield (0.29 g, 63%). C$_{54}$H$_{65}$N$_4$NdO (930.36): calcd. C 69.71, H 7.04, N 6.02; found C 69.05, H 7.44, N 6.04.

Synthesis of 14: A solution of PhSiH$_3$ (0.061 g, 0.57 mmol) in toluene solution (3 mL) was added to a solution of **11** (0.600 g, 0.57 mmol) in toluene (30 mL) at room temperature and the reaction mixture was stirred for 72 h. The solution was concentrated to small volume and cooled to –25 °C affording yellow crystalline material; yield (0.319 g, 60%). C$_{54}$H$_{65}$LuN$_4$O (961.09): calcd. C 67.48, H 6.82, N 5.83; found C 67.28, H 7.20, N 5.99. ^{1}H NMR (400 MHz, C$_7$D$_8$, 298 K): δ = 0.80–1.58 [m, together 32 H, H^{23,24,25,26}, β-CH$_2$, thf, CH$_2$Lu],1.78–2.33 [m,together 9 H, H^{13,14}], 3.19–3.45 [br., sept, 8 H, (4 H, α-CH$_2$, thf) (4 H, H^{21,22})], 5.64 [m, 4 H, H$^{3/5}$], 6.63–7.27 [m,14 H, H^{4,9,10,11,17,18,19}] ppm. ^{13}C NMR (C$_7$D$_8$, 298 K): δ = 20.3, 20.5 [C^{13,14}], 23.0, 25.0 [C^{23,24,25,26}], 25.2 [β-CH$_2$, thf], 28.1,28.6 [C^{21,22}], 68.6 [α-CH$_2$, thf], 72.1 [s,CH$_2$], 103.7, 108.8 [C$^{3/5}$], 110.1, 114.5 [C$^{3/5}$], 124.2, 124.3, 124.8, 125.0, 127.5, 127.7, 128.5, 129.7 [C^{9,10,11,17,18,19}], 134.7, 135.2 [C^4], 135.9, 136.0, 138.9, 139.5, 140.8, 141.8, 144.4 [C^{7,8,12,15,16,20}], 148.0, 156.3 [C^6], 159.3, 159.9 [C^2] ppm.

CCDC-740977 (for **7**), -740978 (for **4**), -740979 (for **13**), -740980 (for **11**), -740981 (for **3**), -740982 (for **9**), -740983 (for **6**), -740984 (for **12**) and -741180 (for **8**) contain the supplementary Crystallographic details for this paper. These data can be obtained free of charge from The Cambridge Crystallographic Data centre via: www.ccdc.cam.ac.uk/conts/retrieving.html.

Acknowledgments

these ligands please see: G. Glatz, S. Demeshko, G. Motz, R. Kempe, *Eur. J. Inorg. Chem.* **2009**, 1385–1392.

[1] For selected reviews please see: a) A. E. Shilov, G. B. Shul'pin, *Chem. Rev.* **1997**, *97*, 2879–2932; b) C. Jia, T. Kitamura, Y. Fujiwara, *Acc. Chem. Res.* **2001**, *34*, 633–639; c) K. Godula, D. Sames, *Science* **2006**, *312*, 67–72; d) F. Kakiuchi, T. Kochi, *Synthesis* **2008**, *19*, 3013–3039.

[2] R. D. Shannon, *Acta Crystallogr., Sect. A* **1976**, *32*, 751–767.

[3] a) M. Brookhart, M. L. H. Green, *J. Organomet. Chem.* **1983**, *250*, 395–408; b) W. J. Evans, L. A. Hughes, T. P. Hanusa, *J. Am. Chem. Soc.* **1984**, *106*, 4270–4272; c) W. J. Evans, L. A. Hughes, T. P. Hanusa, *Organometallics* **1986**, *5*, 1285–1291; d) P. B. Hitchcock, J. A. K. Howard, M. F. Lappert, S. Prashar, *J. Organomet. Chem.* **1992**, *437*, 177–189.

[4] a) P. L. Watson, *J. Chem. Soc., Chem. Commun.* **1983**, 276–277; b) P. L. Watson, G. B. Parshall, *Acc. Chem. Res.* **1985**, *18*, 51–56; c) P. L. Watson, *J. Am. Chem. Soc.* **1983**, *105*, 6491–6493; d) N. Barros, O. Eisenstein, L. Maron, *Dalton Trans.* **2006**, 3052–3057.

[5] a) K. H. den Haan, J. H. Teuben, *J. Chem. Soc., Chem. Commun.* **1986**, 682–683; b) M. E. Thompson, S. M. Baxter, A. R. Bulls, B. J. Burger, M. C. Nolan, B. D. Santarsiero, W. P. Schaefer, J. E. Bercaw, *J. Am. Chem. Soc.* **1987**, *109*, 203–219; c) K. H. den Haan, Y. Wiestra, J. H. Teuben, *Organometallics* **1987**, *6*, 2053–2060; d) W. J. Evans, T. A. Ulibarri, J. W. Ziller, *Organometallics* **1991**, *10*, 134–142; e) M. Booij, A. Meetsma, J. H. Teuben, *Organometallics* **1991**, *10*, 3246–3552; f) M. Booij, B. J. Deelman, R. D. Duchateau, J. Postma, A. Meetsma, J. H. Teuben, *Organometallics* **1993**, *12*, 3531–3540; g) W. J. Evans, J. M. Perotti, J. W. Ziller, *Inorg. Chem.* **2005**, *44*, 5820–5825; h) W. J. Evans, J. M. Perotti, J. W. Ziller, *J. Am. Chem. Soc.* **2005**, *127*, 3894–3909; i) W. J. Evans, T. M. Champagne, J. W. Ziller, *J. Am. Chem. Soc.* **2006**, *128*, 14270–14271.

[6] For selected examples please see: a) M. D. Fryzuk, T. S. Haddad, S. J. Rettig, *Organometallics* **1991**, *10*, 2026–2036; b) Y. Mu, W. E. Piers, D. C. Mac Quarrie, M. J. Zaworotko, V. G. Young, *Organometallics* **1996**, *15*, 2720–2726; c) R. Duchateau, T. Tuinstra, E. A. C. Brussee, A. Meetsma, P. T. van Duijnen, J. H. Teuben, *Organometallics* **1997**, *16*, 3511–3522; d) D. J. H. Emslie, W. E. Piers, M. Parvez, R. McDonald, *Organometallics* **2002**, *21*, 4226–4240; e) D. J. H. Emslie, W. E. Piers, M. Parvez, *Dalton Trans.* **2003**, 2615–2620; f) L. K. Knight, W. E. Piers, P. Fleurat-Lessard, P. Masood, R. McDonald, *Organometallics* **2004**, *23*, 2087–2094; g) L. K. Knight, W. E. Piers, R. McDonald, *Organometallics* **2006**, *25*, 3289–3292; h) M. Zimmermann, F. Estler, E. Herdtweck, W. K. Törnroos, R. Anwander, *Organometallics* **2007**, *26*, 6029–6041.

[7] For reviews please see: R. Kempe, *Eur. J. Inorg. Chem.* **2003**, 791–803 and R. Kempe, H. Noss, T. Irrgang, *J. Organomet. Chem.* **2002**, *647*, 12–20; and for the general applicability of

[8] a) N. M. Scott, T. Schareina, O. Tok, R. Kempe, *Eur. J. Inorg. Chem.* **2004**, 3297–3304; b) N. M. Scott, R. Kempe, *Eur. J. Inorg. Chem.* **2005**, 1319–1324; c) W. P. Kretschmer, A. Meetsma, B. Hessen, T. Schmalz, S. Qayyum, R. Kempe, *Chem. Eur. J.* **2006**, *12*, 8969–8978; d) W. P. Kretschmer, A. Meetsma, B. Hessen, N. M. Scott, S. Qayyum, R. Kempe, *Z. Anorg. Allg. Chem.* **2006**, *632*, 1936–1938; e) S. M. Guillaume, M. Schappacher, N. M. Scott, R. Kempe, *J. Polym. Sci., Part A: Polym. Chem.* **2007**, *45*, 3611–3619; f) A. M. Dietel, O. Tok, R. Kempe, *Eur. J. Inorg. Chem.* **2007**, 4583–4586; g) R. Kempe, *Chem. Eur. J.* **2007**, *13*, 2764–2773; h) W. P. Kretschmer, B. Hessen, A. Noor, N. M. Scott, R. Kempe, *J. Organomet. Chem.* **2007**, *692*, 4569–4579; i) G. G. Skvortsov, G. K. Fukin, A. A. Trifonov, A. Noor, C. Döring, R. Kempe, *Organometallics* **2007**, *26*, 5770–5773; j) A. Noor, R. Kempe, *Eur. J. Inorg. Chem.* **2008**, 2377–2381; k) A. Noor, W. P. Kretschmer, G. Glatz, A. Meetsma, R. Kempe, *Eur. J. Inorg. Chem.* **2008**, 5088–5098; l) D. M. Lyubov, C. Döring, G. K. Fukin, A. V. Cherkasov, A. S. Shavyrin, R. Kempe, A. A. Trifonov, *Organometallics* **2008**, *27*, 2905–2907; m) A. Noor, F. R. Wagner, R. Kempe, *Angew. Chem. Int. Ed.* **2008**, *47*, 7246–7249; n) S. Qayyum, K. Haberland, C. M. Forsyth, P. C. Junk, G. B. Deacon, R. Kempe, *Eur. J. Inorg. Chem.* **2008**, 557–562; o) C. Döring, R. Kempe, *Eur. J. Inorg. Chem.* **2009**, 412–418; p) A. Noor, G. Glatz, R. Müller, M. Kaupp, S. Demeshko, R. Kempe, *Nature Chem.* **2009**, *1*, 322–325; q) A. Noor, G. Glatz, R. Müller, M. Kaupp, S. Demeshko, R. Kempe, *Z. Anorg. Allg. Chem.* **2009**, *635*, 1149–1152; r) S. Qayyum, A. Noor, G. Glatz, R. Kempe, *Z. Anorg. Allg. Chem.* **2009**, 635, in press; s) C. Döring, W. P. Kretschmer, T. Bauer, R. Kempe, *Eur. J. Inorg. Chem.* **2009**, accepted.

[9] S. Deeken, G. Motz, R. Kempe, *Z. Anorg. Allg. Chem.* **2007**, *633*, 320–325.

[10] a) B. Liu, D. Cui, J. Ma, X. Chen, X. Jing, *Chem. Eur. J.* **2007**, *13*, 834–845; b) C. J. Kimberly, L. S. Brian, P. J. Hay, J. C. Gordon, J. L. Kiplinger, *J. Am. Chem. Soc.* **2006**, *128*, 6322–6323; c) M. Wie, S. Li, D. Cui, B. Huang, *J. Organomet. Chem.* **2002**, *692*, 3823–3834.

[11] R. R. Schrock, P. J. Bonitatebus Jr., Y. Schrodi, *Organometallics* **2001**, *20*, 1056–1058.

[12] A. Altomare, M. C. Burla, M. Camalli, G. L. Cascarano, C. Giacovazzo, A. Guagliardi, A. G. G. Moliterni, G. Polidori, R. Spagna, *J. Appl. Crystallogr.* **1999**, *32*, 115–119.

[13] G. M. Sheldrick, *SHELX-97*, Program for Crystal Structure Analysis (rel. 97–2), Institut für Anorganische Chemie der Universität Göttingen, Germany, **1998**.

[14] L. J. Farrugia, *J. Appl. Crystallogr.* **1999**, *32*, 837–838.

FULL PAPER

Observation and Interpretation of Structural Variety in Alkaline Earth Metal Derivatives of Diphosphanyldisiloxane

Peter Kopecky,[a] Carsten von Hänisch,*[a,b] Florian Weigend,[b,c] and Andreas Kracke[a]

Alkaline earth metal derivatives of the diphosphanyldisiloxane $O(SiiPr_2PH_2)_2$ (**1**) were obtained by reactions of **1** with $MgBu_2$ and $M\{N(SiMe_3)_2\}_2$ (M = Ca, Sr, Ba), respectively. The metal complexes formed were characterised by elemental analysis, NMR spectroscopy, and IR spectroscopy as well as by single-crystal structure analysis. The solid-state structures depend on the metal ion involved. The magnesium derivative crystallizes from thf as a trimer and exhibits a six-membered Mg_3P_3 ring. In contrast, the Ca und Sr derivatives show a dimeric structure via formation of M_2P_2 rings (M = Ca, Sr). Eventually, the Ba derivative forms a dimeric structure with an octahedral P_4Ba_2 moiety. Quantum chemical investigations indicate that the structural variety is a consequence of accessibility and spatial extent of the d-orbitals of the alkaline earth metal atoms.

Introduction

Phosphanides of the heavy alkaline earth metals have been investigated for nearly 15 years.[1] A simple approach to synthesize these compounds is the metathesis reaction of alkaline earth metal silazanides with primary or secondary phosphanes. In this manner, one obtains alkaline earth metal phoshanides with a variety of structures depending on the substituent as well as the solvent used. For example in donor solvents such as thf and with sterically demanding substituents, one can isolate colourless solids with monomer structures (Type **I**).[2] In some cases, equilibria are established in solution between the monomer and dimeric species which contain two or three bridging phosphorus atoms (see types **II** and **III** in Figure 1).[1–3] Hartree–Fock calculations for $[M(PH_2)_2]_2$ show that bicyclic structures (Type **III**) are favoured for M = Ca or Sr, whereas for Ba, the tricyclic structure seems to be the most stable form (Type **IV**).[1,4] According to the best of our knowledge, only the monomeric (**I**) as well as the dimeric, double (**II**) and threefold (**III**) bridged structures were isolated in solid state, whereas a type **IV** structure was not reported up to date.

As we could show in previous work, the conjunction of primary silylphosphanes via oxygen atoms between the silyl groups, in other words the use of diphosphanylsiloxanes has a considerable influence on the structure and on the degree of oligomerisation of metal derivatives of such phosphanes.
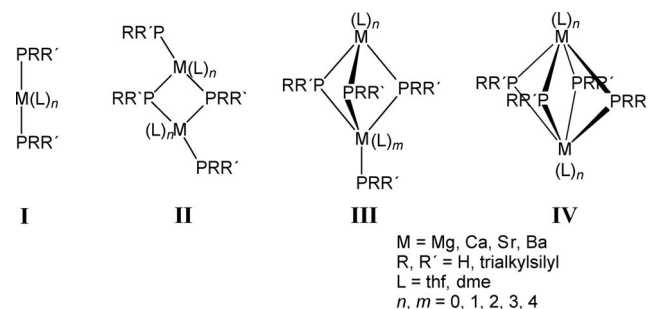

Figure 1. Molecular structures of the alkaline earth metal phosphanides $[(L)_nM(PRR')_2]_x$ (x = 1, 2).

For example, the reaction of 1,1,3,3-tetraisopropyl-1,3-diphosphanyldisiloxane (**1**) with $AlEt_3$ or $GaEt_3$ yields sixteen-membered rings, where as aluminium or gallium phosphanides usually show four or six-membered ring structures.[5]

In this work we report on reactions of alkaline earth metal silazanides $M\{N(SiMe_3)_2\}_2$ (M = Ca, Sr, Ba), as well as $MgBu_2$, with **1**. We have succeeded in isolating compounds which have not been previously observed, but which were theoretically predicted structural motifs. The reasons for the preference of different structure types for different alkaline earth metals have been investigated by quantum chemical calculations.

[a] Institut für Anorganische Chemie, KIT, Campus Süd, Kaiserstr. 12, 76131 Karlsruhe, Germany
[b] Institut für Nanotechnologie, KIT, Campus Nord, P. O. Box 3640, 76021 Karlsruhe, Germany
Fax: +49-7247-826372
E-mail: carsten.vonhaenisch@int.fzk.de
[c] Institut für Physikalische Chemie, KIT, Campus Süd, Kaiserstraße12, 76131 Karlsruhe, Germany

Synthesis and Characterisation

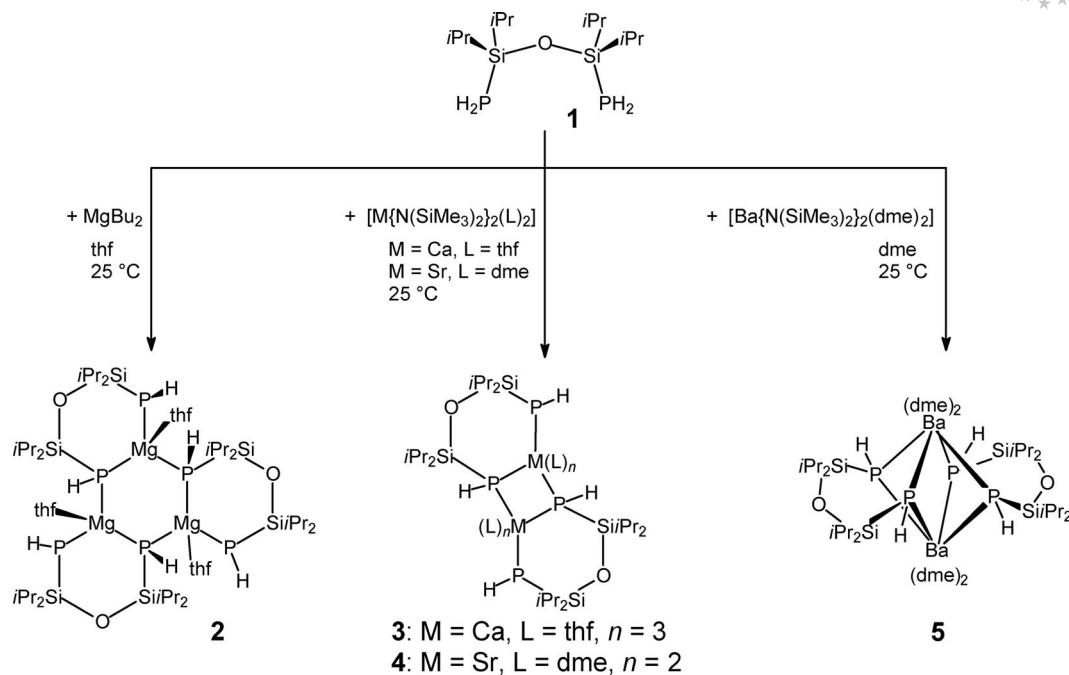The reactions of **1** with $MgBu_2$ or the silazanides of calcium, strontium and barium, respectively, lead to the polycyclic products **2**, **3**, **4** und **5** as shown in Figure 2.

Figure 2. Synthesis of the compounds **2–5**.

The trimeric compound **2** crystallizes in the triclinic space group $P\bar{1}$ (Figure 3). The dianionic $[O(iPr_2SiPH)_2]^{2-}$ entities act as bidentate ligands, coordinating each to magnesium to form six-membered rings. In addition, one of the phosphorus atoms of these rings binds to another Mg atom of a vicinal MgP_2Si_2O ring, so that a central, six-membered Mg_3P_3 ring is formed. Due to the coordination of one thf molecule to each magnesium atom, the latter achieves a co-ordination number four. These three thf ligands show a *cis, trans,trans* orientation. The Mg_3P_3 ring is slight folded towards a boat conformation, the three MgP_2Si_2O rings are slightly twisted. Within these MgP_2Si_2O rings the two PH groups are in a *trans* position to each other. The Mg–P distances are between 255.7 and 259.3 pm within the six-membered Mg_3P_3 ring, while the remaining three external Mg–P-bonds are slightly shorter with values between 249.5 and 250.9 pm. This can be traced back to the different coor-dination numbers of the phosphorus atoms (four in the in-ner ring and three outside the inner ring). Similar bond lengths could also be found in other magnesium phosphan-ides; for example for the bicyclic species $[Mg_3\{P(SiMe_3)_2\}_6]$ the distances are between 245 and 262 pm.[6] Compound **2** is not soluble in non- or weakly polar solvents (e.g. hexane, benzene or ethyl ether) but is soluble in thf. The ^{31}P NMR spectrum of **2** in $[D_8]$thf shows only one doublet at $\delta = -320.5$ ppm, which is maybe the result of the formation of solvated monomers in thf or of dynamic behaviour in solu-tion. Monomeric complexes were obtained from the reac-tions of $MgBu_2$ with **1** in the presence of the bidentate li-gands tmeda or dme. From this reactions, the products $[O(SiiPr_2PH)_2Mg(tmeda)]$ (**2a**) and $[O(SiiPr_2)_2Mg(dme)_2]$ (**2b**) were isolated. **2a** shows a strongly twisted ring with a

trans orientation of the PH groups, whereas compound **2b** exhibits a almost planar ring with the PH groups in *cis* configuration (see Figure 4).

Figure 3. Molecular structure of **2**, thermal ellipsoids represent a 50% probability level, hydrogen of the organic groups are not shown. Selected atom distances/pm and angles/°: Mg1–P1 257.1(2), Mg1–P2 249.5(2), Mg1–P3 255.7(2), Mg2–P3 256.1(2), Mg2–P4 250.0(2), Mg2–P5 259.3(2), Mg3–P1 258.2(2), Mg3–P5 257.7(2), Mg3–P6 250.9(2), Si–P 221.1(2) – 224.6(2); Mg1–P1–Mg3 127.76(5), Mg1–P3–Mg2 128.98(5), Mg2–P5–Mg3 131.02(5), P–Mg–P 99.45(5) – 123.44(6).

The reaction of calcium silazanide with **1** follows a sim-ilar path as described for the reaction with $MgBu_2$. One observes a twofold deprotonation of the diphosphanyldisil-

Figure 4. Molecular structure of the compounds 2a (left) und 2b (right), thermal ellipsoids represent a 50% probability level, hydrogen of the organic groups are not shown.

oxane, and the solid compound [Ca(thf)$_3${O(SiiPr$_2$PH)$_2$}]$_2$ (**3**) forms, and in contrast to compound **2**, contains dimers with a central planar four-membered Ca$_2$P$_2$ ring. Compound **3** crystallizes in the space group $P\bar{1}$ with two noncoordinated thf molecules per unit cell. As in **2**, the [O(iPr$_2$SiPH)$_2$]$^{2-}$ unit acts as a bidentate ligand and builds a six-membered almost planar OSi$_2$P$_2$Ca ring with the P–H protons in a *cis* configuration (Figure 5). The distorted octahedral sphere of the calcium atom is completed by three neutral thf molecules and by one phosphorus atom of the second ring. The phosphorus atom, and one oxygen atom of a thf ligand lie in the plane of the planar four-membered ring. Two other oxygen atoms of thf ligands occupy the apical positions of the octahedron with an O–Ca–O angle of 165.0°. The bonds between the calcium and the phosphorus atoms in the six-membered ring are between 293.7 and 296.6 pm long. The distance of the two monomeric units to each other amounts to 300.9 pm. Westerhau-

sen et al. synthesized a Ca$_2$P$_2$ ring compound [(Me$_3$Si)$_2$-NCa(dme)(μ-PHSiiPr$_3$)]$_2$, with similar Ca–P bond lengths of 300.0 and 300.5 pm.[2c]

The [D$_8$]toluene solution of **3** shows a ^{31}P NMR spectrum with only one multiplet signal of higher order at δ = –253 ppm. A monomer in solution can be excluded due to the fact, that the multiplet in the ^{31}P NMR is definitely not the AA′ part of an AA′XX′ sin system (max. ten lines). In fact the spectrum indicates dynamic behaviour which leads to four equivalent PH groups (AA′A′′A′′′XX′X′′X′′′ spin system), see Figure 6. Similar behaviour has been observed for several phosphanides of strontium and barium.[2e,7] Low-temperature NMR experiments at –50 °C show no significant change in the spectra. Accordingly, the ^{29}Si{^{1}H} NMR spectrum shows also only one signal at δ = 19.6 ppm. The ^{1}H NMR spectrum of **3** shows, in addition to the signals of the isopropyl groups, a multiplet at –0.05 ppm, which corresponds to the protons which are bonded to the phosphorus atoms (XX′X′′X′′′ part).
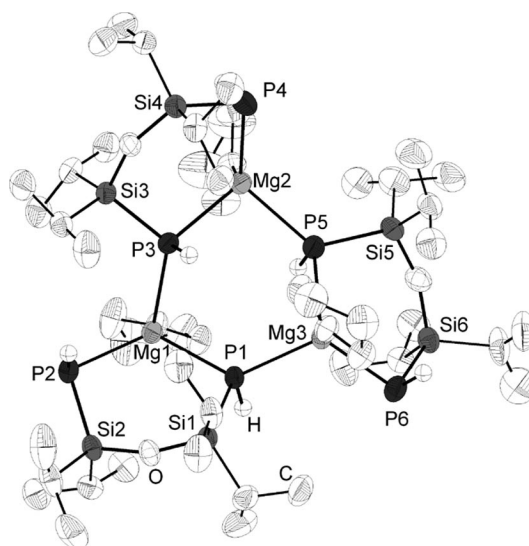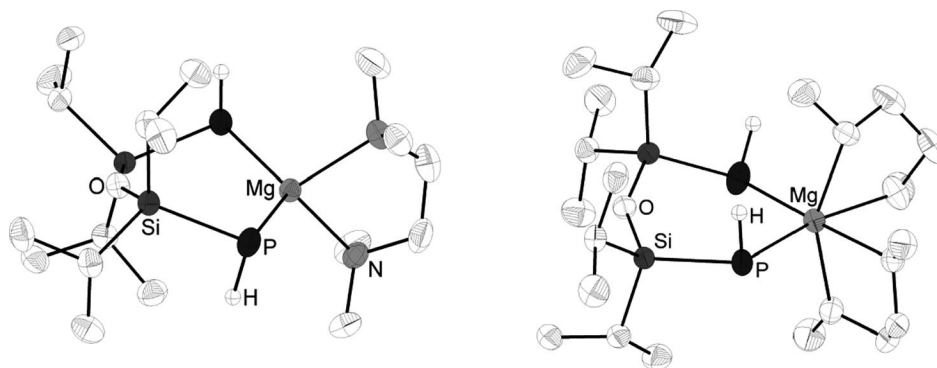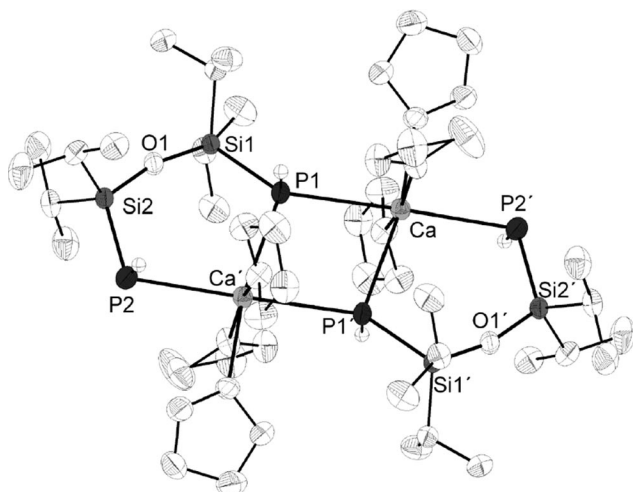

Figure 5. Molecular structure of **3**, thermal ellipsoids represent a 50% probability level, hydrogen atoms are not shown. Selected atom distances/pm and angles/°: P1–Ca 301.9(1), P2′–Ca 294.8(1), P1′–Ca 295.9(1), Si1–P1 221.1(1), Si2–P2 219.6(1), Ca–O 239.5(2) – 241.3(2); Si1–P1–Ca 144.41(4), Si1–P1–Ca′ 103.47(3), Ca1–P1–Ca1′ 103.47(3), Si2–P2–Ca′ 109.90(4), O–Ca–O 164.96(7), 79.84(8), 85.45(8), P2–Ca′–P1 102.52(3), P2–Ca′–P1′ 178.03(3), P1–Ca1–P1′ 76.53(3).
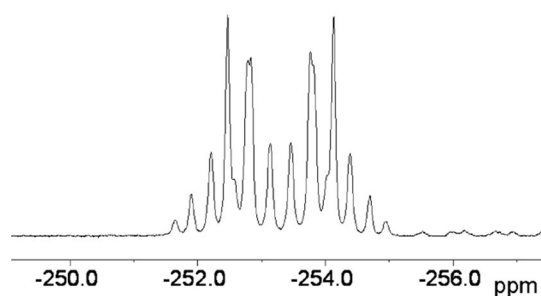
Figure 6. ^{31}P NMR spectrum of compound 3 in [D$_8$]toluene.

The reactions of strontium or barium silazanide with diphosphanylsiloxane **1** are fast, and the products can be obtained in good yields up to 85%. In thf after only 10 min, fine and colourless precipitates appear, which are insoluble, even at temperatures up to 60 °C. Single crystals, suitable for X-ray structure analyses, were grown from dme. The compound **4**, see Figure 7, crystallizes in the monoclinic space group $P2_1/n$. The molecular structure is similar to that of **3**, but the strontium atom is in a distorted, pentagonal bipyramidal coordination sphere as a consequence of

the coordination of two dme molecules. The bidentate [O(iPr₂SiPH)₂]²⁻ ligand occupies an apical and a basal position. The four remaining basal positions are occupied by the oxygen atoms of the two dme molecules, the second apical position of the pyramid is occupied by a third phosphorus atom due to the dimerisation. The Sr–P bonds within the OSi₂P₂Sr rings range between 309.8 and 314.9 pm. The Sr–P bond lengths between these rings amount to 316.7 pm. So in **4** the Sr–P bonds are slightly longer than in other known strontium phosphanides (300.6 to 308.9 pm), such as [Sr{P(SiMe₃)₂}₂(thf)₄] and [Sr{P(SiMe₂iPr)₂}₂(thp)₄] (thp = tetrahydropyran), in which the metal atoms show a coordination number of only six.[2b,2e]

Figure 7. Molecular structure of **4**, thermal ellipsoids represent a 50% probability level, hydrogen atoms of the organic groups are not shown. Selected atom distances/pm and angles/°: P1–Sr1 309.8(1), P2–Sr1 314.9(1), P2′–Sr1 316.7(1), Si1–P1 219.8(1), Si2–P2 221.1(1), Sr–O 264.1(2)–269.3(2); Si1–P1–Sr1 106.08(3), Si2–P2–Sr1′ 143.80(3), Si2–P2–Sr1 108.54(3), Sr1–P2–Sr1′ 105.27(3), P2–Sr1–P1 101.28(3), P1–Sr1–P2′ 176.01(2), P2–Sr1–P2′ 74.73(3).

The NMR spectra of compound **4** are similar to the NMR spectra of compound **3**; the PH-groups are observed in the ¹H NMR spectrum at $\delta = -0.07$ ppm, and the ³¹P NMR spectrum shows a multiplet at $\delta = -250.3$ ppm.

From the reaction of barium silazanide with **1**, compound **5** was isolated as colourless crystals (Figure 8). It crystallises in the monoclinic space group $P2_1/n$. In contrast to the calcium and strontium compounds which dimerize by formation of M₂P₂ rings, compound **5** exists as a binuclear species with all four phosphorus atoms of the [O(Si-iPr₂PH)]²⁻ ligands in bridging positions. This leads to a central Ba₂P₄ octahedron with barium in the apical and phosphorus in the basal positions. The coordination sphere of each barium atom is completed by two dme molecules each, giving a coordination number of eight. This structural motif (Type **IV** in Figure 1) has not been observed before, although ab initio SCF calculation predicted this molecular structure as the energetically most favoured isomer for bar-

ium hydrides and barium phosphanides.[1,4] The Ba–P bonds in **5** are on average 331.5 pm long, this corresponds to values which are known for other barium phosphanides.
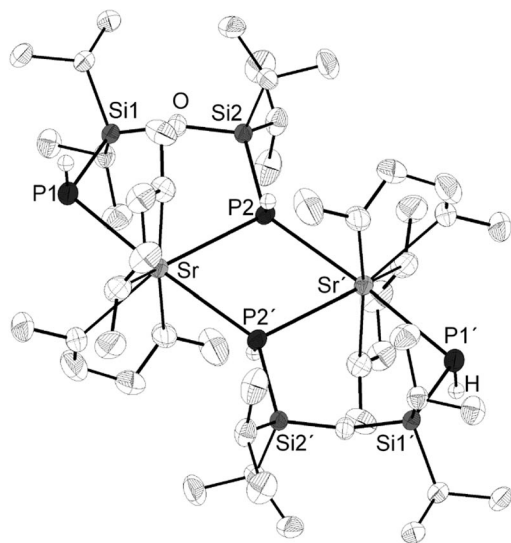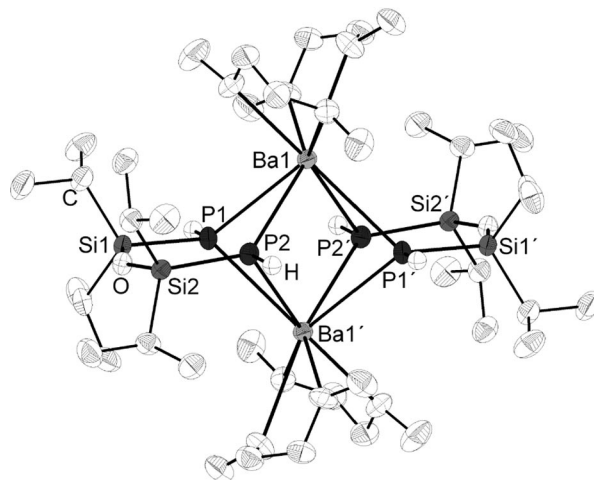

Figure 8. Molecular structure of **5**. Thermal ellipsoids represent a 50% probability level, hydrogen atoms of the organic groups are not shown. Selected atom distances/pm and angles/°: Ba1–P1 330.2(1), Ba1–P1′ 330.0(1), Ba1–P2 333.4(1), Ba1–P2′ 332.1.(1), Si1–P1 220.5(1), Si2–P2 220.9(1), Ba–O 277.7(2)–295.2(2); P1–Ba1–P1′ 101.23(2), P1–Ba1–P2 61.31(2), P1–Ba1–P2′ 71.41(2), P1′–Ba1–P2′ 61.47(3), P1′–Ba1–P2 71.28(3), P2–Ba1–P2′ 101.99(2), P1–Ba1–P1′ 101.23(2), Ba1–P1–Ba1′ 78.77(2), Ba1–P2–Ba1′ 78.01(2), Si1–O–Si2 144.33(1).

The ³¹P NMR spectrum of the compound **5** shows a broad doublet with a coupling constant of approximately 180 Hz at $\delta = -220$ ppm, which is shifted about 30 ppm to lower field compared to the calcium and strontium compounds **3** and **4**. The ¹H NMR spectrum shows the typical signals for isopropyl groups and dme molecules as well as the expected doublet for the PH groups at $\delta = 0.07$ ppm ($J \approx 180$ Hz).

Quantum Chemical Investigations

Quantum chemical calculations with TURBOMOLE[8] were carried out in order to rationalize the correlation of preferred topology and type of the alkaline earth metal ion, in particular the preference of the ring-type topology for Sr and the octahedral topology for Ba. Both the Sr and the Ba compound were calculated in both topologies including the four dme molecules in each case. Structure parameters were optimized by means of density functional (BP-86[9]) theory, DFT, with def2-SV(P)[10] basis sets for C and H and def2-TZVP[9] bases for the other elements. The RI-J approximation was employed with the respective auxiliary basis sets.[11] For Ba (Sr) effective core potentials were used, which cover the inner 46(28) electrons.[12] As a check for DFT we also did Hartree–Fock and MP2 calculations (with the same basis and for the structure parameters obtained with DFT). Calculated energy differences between octahedral and ring structures for the Sr and the Ba compound

P. Kopecky, C. von Hänisch, F. Weigend, A. Kracke

are presented in Table 1. We note that for both Sr and Ba, at all levels of theory, the octahedral structure is predicted to be more stable than the ring structure. This is not in line with the experiment, where for Sr the latter is preferred. On the other hand, all methods indicate a more pronounced preference (by ca. 30 kJ/mol) of the octahedral structure for Ba than for Sr, so at least the trend is reflected correctly. Moreover for DFT and HF, the preference of the octahedral structure in the case of strontium is only a few kJ/mol, which is less than the accuracy of these methods. We note, that these results are in line with the results of previous studies carried out at a lower level of theory.[4] Here, we rationalize these trends and we discuss, why for Mg a monomeric complex has been formed with dme as donor solvent (compound **2b**).

Table 1. Calculated energy differences, ΔE, between octahedral and ring structure for M = Sr, Ba in kJ/mol. Positive values indicate a preference of the octahedral structure.

Method	ΔE(Sr)	ΔE (Ba)
DFT	7	36
HF	2	35
MP2	43	79

At first glance, the compounds presented here might be described in an ionic way: repulsive forces between the two M^{2+} ions and also between the two $[O(iPr_2SiPH)_2]^{2-}$ units which are overcompensated by attractive forces between the M^{2+} ions and the $[O(iPr_2SiPH)_2]^{2-}$ units. On the other hand, it has been known for many years, that for the 6s elements in particular, the 5d orbitals (which are unoccupied in the atomic ground state) play an important role[13] and cause unusual bond situations.[14,15]

Analysis of the high-lying occupied molecular orbitals (HOMOs) shows that a purely ionic description is not adequate. To show this, we first calculated the MOs of the $[O(iPr_2SiPH)_2]_2^{4-}$ framework and then investigated the interaction of the M^{2+} orbitals with the MOs of the framework. In Figure 9, the four HOMOs of the $[O(iPr_2SiPH)_2]_2^{4-}$ framework are plotted, for octahedral as well as for ring-topology. They were obtained from the optimized structures for the Ba compound by removal of Ba^{2+}. The conductor-like screening model, COSMO,[16] was used to compensate for the negative charge and to obtain negative energies for occupied orbitals. As is evident from Figure 9, the four HOMOs are (linear combinations of) p-orbitals at the P atoms, which are perpendicular to the plane spanned by the respective P atom and its bond partners (Si and H, see also Figures 7 and 8). In the case of the ring structure (left part), they are parallel to the plane spanned by the four P atoms, for the octahedral structure (right part) they are perpendicular to this plane. This is a consequence from the fact that the H atoms are perpendicular to this plane in the first case, but in plane in the second case.

The HOMOs of the entire system are plotted in Figure 10 for the ring compound and in Figure 11 for the octahedral compound for M = Ba (for M = Sr they have very similar shape). All orbitals can be regarded as combinations
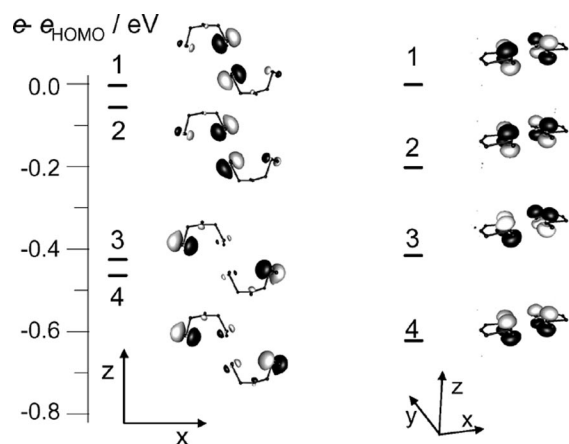
Figure 9. Energy and shape of the four HOMOs of the $[O(iPr_2SiPH)_2]_2^{4-}$ framework being part of the in ring-type topology, left-hand side (see also Figure 7), and being part of the octahedral topology, right-hand side (see also Figure 8). Contour plots are drawn at 0.04 (electrons/bohr^3)$^{1/2}$.

of the HOMOs of the $[O(iPr_2SiPH)_2]_2^{4-}$ frameworks and mainly the d-, but also the s- and p orbitals of the metal ion, in this way forming a (polarized) covalent bond. The contributions of s- p- and d orbitals of the metal centre were calculated by a Mulliken population analysis and are also shown in Figures 10 and 11. Obviously, for both the octahedral and ring structures a necessary precondition is the easy availability of (unoccupied) d-orbitals. So, these structure types are favourable only for Ca, Sr or Ba, but not for Mg (or Li).[17] Indeed, the corresponding Mg compound shows a completely different structure (see above).

Figure 10. Energy (scale on the left in eV) and shape of the four HOMOs of $M_2[O(iPr_2SiPH)_2]_2$ (M = Sr, Ba) in ring-type topology. The numbers at the left-hand side refer to the MO labels in Figure 9. The diagrams on the right-hand side show the contributions of s- p- and d orbitals of each Sr/Ba centre (Mulliken population analysis). For all diagrams the maximum value of the abscissa is 0.1 electrons. Contour plots (middle) are drawn at 0.02 (electrons/bohr^3)$^{1/2}$. Non-relevant C and H atoms as well as solvent molecules are omitted in the plot for clarity.

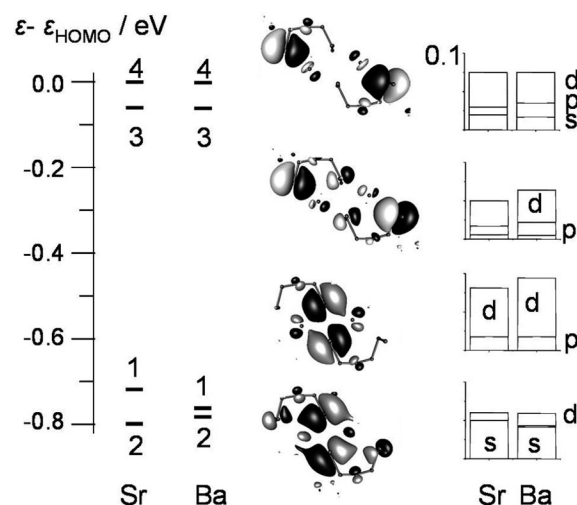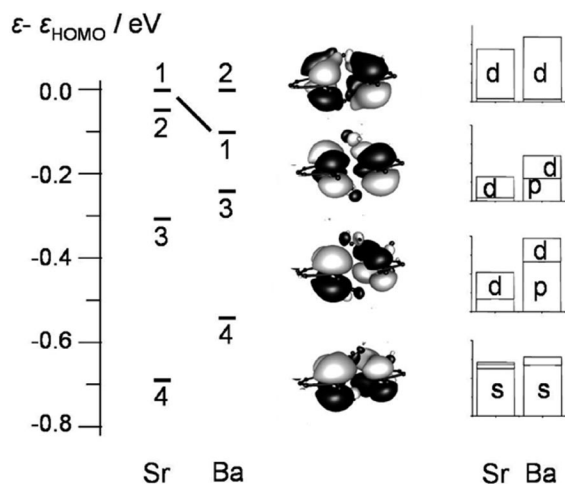Figure 11. Energy (scale on the left in eV) and shape of the four HOMOs of $M_2[O(iPr_2SiPH)_2]_2$ (M = Sr, Ba) in octahedral topology. For details see Figure 9.

In order to rationalize the more pronounced preference of the octahedral structure for Ba we take a closer look at the MOs shown in Figures 10 and 11. For the ring structure, Figure 10, the contributions from the metal ion are largest for the two highest occupied MOs of the respective anionic fragment, left-hand side of Figure 9: the HOMO of the anionic fragment is stabilized mainly by the d_{xz} orbital of the metal ion, the HOMO-1 by the d_{z^2} and the s orbital. Note that for this topology the relevant orbitals of the anionic framework and the metal centres are in the same plane, so significant overlap of orbitals of the metal atoms and the P atoms of the anionic fragment is feasible even for comparably large distances between the two M centres. For the octahedral compound, Figure 11, effects are largest for the HOMO of the anionic fragment, which is stabilized by the d_{xy} orbital of the metal ion. For Ba this effect is large enough to cause a change in the energetic sequence of the two HOMOs, for Sr this is not the case. For all HOMOs, contributions from the metal centre are higher for M = Ba than for M = Sr. The main reason probably is, that reasonable overlap of orbitals between metal ions and the anionic framework results in comparably short M–M distances (Ba: 424 pm, Sr: 401 pm), which on the other hand leads to larger Coulomb repulsion between the metal ions. This situation is favourable rather for larger ions (Ba) than for smaller (Sr or Ca), as for the former significant orbital overlap is possible also for comparatively larger M–M distances.

Conclusions

Alkaline earth metal derivatives of primary phosphanes show versatile structural chemistry. We have described derivatives of the diphosphanylsiloxane $O(SiiPr_2PH_2)_2$ with the metals Mg, Ca, Sr and Ba. Three principal molecular structural motifs were observed even for identical donor solvents and elemental formulas (compound **2b**, **4** and **5**). The Ba_2P_4-octahedron (compound **5**), which was theoretic-

ally predicted several year ago, was observed for the first time. Detailed quantum chemical investigations show, that the structural variety mainly is a consequence of the energetic and spatial properties of the d-orbitals of the metal atoms (which are unoccupied in their atomic ground state). Structure types **II** and **IV** (as well as **III**) thus can be realized only by Ca, Sr, Ba. Structure type **IV** is preferred rather for larger alkaline earth metals, as due to relative orientation of metal atom orbitals and orbitals of the respective $[O(iPr_2SiPH)_2]_2^{4-}$ frameworks a concurrence between overlap of these orbitals and Coulomb repulsion of the positively charged metal centres emerges.

Experimental Section

General: All operations were carried out under an oxygen and water-free nitrogen atmosphere by using standard Schlenk techniques. Solvents were rigorously dried and distilled under nitrogen by standard methods. All air and moisture sensitive substances were stored and handled in a glove-box under argon atmosphere. The starting compounds $[M\{N(SiMe_3)_2\}_2(thf)_2]$ (M = Ca, Ba), $[Sr\{N(SiMe_3)_2\}_2(dme)]^{[18]}$ and $O(SiiPr_2PH_2)_2^{[5]}$ were prepared by reported methods. The metals calcium and strontium (99.9%), were purchased at Sigma–Aldrich. Barium was purchased at Alfa Aesar in form of bars (99.7%). NMR spectra were recorded on a Bruker DPX Avance 300. The structural analyses were carried out with appropriate single crystals on an automatic diffractometer. The structures were solved and refined with SHELLXTL and Xstep32[19] (Table 2). The vibrational spectra were gathered with a Perkin–Elmer GX spectrometer and the microanalyses were made with the model "elementar vario MICRO CUBE".

[Mg{(P(H)SiiPr_2)$_2$O}(thf)]$_3$ (2): To a solution of 350 µL (1.0 mmol) of **1** in 10 mL thf 1.0 mL of a 1.0 M solution of $MgBu_2$ in hexane was added dropwise. The resulting solution was stirred for 62 h at ambient temperature and afterwards all volatile contents were removed under reduced pressure. The residue was solved in 3 mL toluene and the solution was stored at –35 °C. Over two days colourless crystals of **2** were formed with a yield of 53%. $C_{48}H_{114}Mg_3O_6P_6Si_6$ ($M = 1214.70$ g/mol): calcd. C 47.46, H 9.46; found C 47.57, H 9.29. ^1H NMR ($[D_8]thf$): $\delta = -1.35$ (d, $^2J_{P,H} = 153$ Hz, 2 H, PH), 0.91 (sept, $^3J(H,H) = 7.2$ Hz, 4 H, C$H(CH_3)_2$), 1.04 [d, $^3J(H,H) = 7.2$ Hz, 12 H, CH(C$H_3)_2$], 1.06 [d, $^3J(H,H) = 7.2$ Hz, 12 H, CH(C$H_3)_2$], 1.80 (m, thf), 3.65 (m, thf) ppm. ^{13}C NMR ($[D_8]thf$): $\delta = 17.6$ [d, $^2J(P,C) = 11.3$ Hz, $CH(CH_3)_2$], 18.0 [br. s, CH(CH$_3)_2$], 25.4 (s, thf), 67.2 (s, thf) ppm. ^{31}P NMR ($[D_8]$-thf): $\delta = -320.5$ (d, $^1J_{P,H} = 153$, PH, Si satellites: $^1J_{P,Si} = 57.5$ Hz) ppm. IR (KBr): $\tilde{v} = 3161$ (w), 2941 (vs), 2888 (vs), 2862 (vs), 2616 (w), 2560 (w), 2286 (s), 2263 (s), 1462 (vs), 1382 (s), 1362 (m), 1345 (w), 1260 (m), 1236 (m), 1159 (w), 1035 (vs), 987 (vs), 918 (s), 881 (vs), 808 (w), 674 (m), 591 (vs), 495 (s), 461 (m), 421 (m) cm^{-1}.

[Ca{(P(H)SiiPr_2)$_2$O}(thf)$_3$]$_2$ (3): 260 mg (0.5 mmol) of [Ca{N-(SiMe$_3)_2\}_2$(thf)$_2$] were dissolved In 4 mL thf. Subsequently 175 µL (0.5 mmol) of **1** were added. After 12 h stirring at room temperature the obtained solution was stored at –32 °C. During two days colourless crystals of **3** were formed with a yield of 56.8%. $C_{48}H_{106}Ca_2O_8P_4Si_4$ ($M = 1127.76$ g/mol): calcd. C 51.12, H 9.47; found C 50.91, H 9.35. ^1H NMR ($[D_8]$toluene): $\delta = -0.05$ (m, 4 H, PH), 1.29 [sept, $^3J(H,H) = 7.2$ Hz, 8 H, C$H(CH_3)_2$], 1.46 [d, $^3J(H,H) = 7.2$ Hz, 24 H, CH(C$H_3)_2$], 1.47 [d, $^3J(H,H) = 7.2$ Hz, 24 H, CH(C$H_3)_2$], 1.59 (m, 24 H, thf), 3.90 (m, 24 H, thf) ppm. $^{13}C\{^1H\}$

Table 2. Crystallographic data of **2**–**5**.[19]

Compound	2	2a	2b
Formula	$C_{48}H_{114}Mg_3O_6P_6Si_6$	$C_{18}H_{46}MgN_2OP_2Si_2$	$C_{20}H_{50}MgO_5P_2Si_2$
Space group	$P\bar{1}$	$P2_1/n$	$P\bar{1}$
Formula units	2	4	2
Temperature	180 K	180 K	190 K
Lattice constants	a = 1217.8(2) pm	a = 1016.3(2) pm	a = 1098.0(2) pm
	b = 1390.6(3) pm	b = 1464.8(3) pm	b = 1108.9(2) pm
	c = 2211.6(4) pm	c = 1913.3(4) pm	c = 1242.1(3) pm
	α = 100.52(3)°	α = 90°	α = 96.76(3)°
	β = 97.72(3)°	β = 104.51°	β = 91.33(3)°
	γ = 98.31(3)°	γ = 90°	γ = 93.33(3)°
Volume	3593.9(12) Å^3	2757.5(9) Å^3	1498.7(5) Å^3
density	1.115 g/cm^3	1.082 g/cm^3	1.137 g/cm^3
2Θ range	3–46°	3.5–52	3–47°
Reflections measured	18790	14624	7641
Independent reflections	9510 (R_{int} = 0.0327)	5149 (R_{int} = 0.0256)	4214 (R_{int} = 0.0248)
Ind. reflections with $F_o > 4\sigma(F_o)$	8057	4747	3391
Parameter	644	241	279
μ(Mo-K_α)	0.313 mm^{-1}	0.277 mm^{-1}	0.271 mm^{-1}
$R1$	0.0443	0.0348	0.0312
$wR2$ (all data)	0.1295	0.0960	0.0778
Residual electron density	0.782 e/Å^3	0.729 e/Å^3	0.277 e/Å^3

Compound	3	4	5
Formula	$C_{48}H_{108}Ca_2O_8P_4Si_4 \cdot 2\ C_4H_8O$	$C_{40}H_{100}O_{10}P_4Si_4Sr_2$	$C_{40}H_{100}Ba_2O_{10}P_4Si_4$
Space group	$P\bar{1}$	$P2_1/n$	$P2_1/n$
Formula units	1	2	2
Temperature	190 K	190 K	180 K
Lattice constants	a = 1211.6(2) pm	a = 1527.0(3) pm	a = 1301.0(3) pm
	b = 1240.2(3) pm	b = 1202.0(2) pm	b = 1379.7(3) pm
	c = 1395.0(3) pm	c = 1698.6(3) pm	c = 1777.3(4) pm
	α = 77.10(3)°	α = 90°	γ = 90°
	β = 69.35(3)°	β = 101.96(3)°	β = 102.94(3)°
	γ = 70.86(3)°	α = 90°	γ = 90°
Volume	1839.2(6) Å^3	3050.1(11) Å^3	3109.2(11) Å^3
density	1.147 g/cm^3	1.255 g/cm^3	1.337 g/cm^3
2Θ range	3.5–51°	3.5–51°	4–51°
Reflections measured	12810	20710	10732
Independent reflections	6500 (R_{int} = 0.0502)	5761 (R_{int} = 0.0412)	5306 (R_{int} = 0.0342)
Ind. reflections with $F_o > 4\sigma(F_o)$	5202	5113	4257
Parameter	318	271	279
μ(Mo-K_α)	0.354 mm^{-1}	1.975 mm^{-1}	1.481 mm^{-1}
$R1$	0.0560	0.0326	0.0263
$wR2$ (all data)	0.1689	0.1043	0.0524
Residual electron density	0.734 e/Å^3	0.493 e/Å^3	0.294 e/Å^3

NMR ([D$_8$]toluene): δ = 18.2 [s, CH(CH$_3$)$_2$], 19.2 [s, CH(CH_3)$_2$], 19.6 [s, CH(CH_3)$_2$], 25.1 (s, thf), 69.5 (s, thf) ppm. ^{29}Si[^{1}H] NMR ([D$_8$]toluene): δ = 19.6 (br) ppm. ^{31}P{^{1}H} NMR ([D$_8$]toluene): δ = –253.1 (s) ppm. IR (KBr): $\tilde{v}$ = 2944 (vs), 2894 (m), 2867 (vs), 2300 (m), 1462 (s), 1083 (vs), 1053 (vs), 987 (s), 882 (s) cm^{-1}.

[Sr{(P(H)Si*i*Pr$_2$)$_2$O}(dme)$_2$]$_2$ (4): 294 mg (0.5 mmol) [Sr{N-(SiMe$_3$)$_2$}$_2$·(dme)$_2$] were dissolved In 4 mL dme. Subsequently 175 µL (0.5 mmol) of **1** were added. After 18 h stirring at room temperature the obtained solution was stored at –32 °C. During two days colourless crystals of **4** were formed with a yield of 65.2%. $C_{40}H_{100}O_{10}P_4Si_4Sr_2$ (M = 1152.71 g/mol): calcd. C 41.68, H 8.74; found C 41.52, H 8.54. ^{1}H NMR ([D$_8$]toluene): δ = –0.07 (m, 4 H, PH), 1.34 [sept, ^3J(H,H) = 7.2 Hz, 8 H, CH(CH$_3$)$_2$], 1.50 [d, ^3J(H,H) = 7.2 Hz, 24 H, CH(CH_3)$_2$], 1.5 [d, ^3J(H,H) = 7.2 Hz, 24 H, CH(CH_3)$_2$], 3.10 (s, 16 H, dme-CH$_2$), 3.38 (s, 24 H, dme-CH$_3$) ppm. ^{13}C{^{1}H} NMR ([D$_8$]toluene): δ = 18.45 [s, CH(CH$_3$)$_2$], 19.60 [s, CH(CH_3)$_2$], 19.64 [s, CH(CH_3)$_2$], 59.73 (s, dme), 70.44 (s, dme) ppm. ^{29}Si[^{1}H] NMR ([D$_8$]toluene): δ = 19.6 (br) ppm. ^{31}P{^{1}H}

NMR ([D$_8$]toluene): δ = –250.4 (s) ppm. IR (KBr): $\tilde{v}$ = 2946 (vs), 2898 (s), 2868 (vs), 2303 (m), 1464 (vs), 1386 (m), 1083 (vs), 1053 (vs), 987 (s), 883 (vs), 696 (s), 598 (m), 470 (m) cm^{-1}.

[Ba{(P(H)Si*i*Pr$_2$)$_2$O}(dme)$_2$]$_2$ (5): 602 mg (0.5 mmol) of [Ba{N(SiMe$_3$)$_2$}$_2$(thf)$_2$] were dissolved In 10 mL dme. Subsequently 175 µL (0.5 mmol) of **1** were added. After 1.5 h stirring at room temperature fine colourless needles precipitated. This suspension was stirred for 16 h and afterwards the precipitate was recrystallized warming the suspension up to 40 °C and slowly cooling to 5 °C. **5** was obtained as colourless crystals with a yield of 85%. $C_{40}H_{100}Ba_2O_{10}P_4Si_4$ (M = 1252.15 g/mol): calcd. C 38.37, H 8.05; found C 38.32, H 7.74. ^{1}H NMR ([D$_8$]toluene): δ = 0.07 [br. d, ^1J(P,H) = 178 Hz, 4 H, PH], 1.00 [m, 8 H, CH(CH$_3$)$_2$], 1.48 [m, 48 H, CH(CH_3)$_2$], 3.15 (s, 3.23 (s, dme) ppm. ^{31}P NMR ([D$_8$]toluene): δ = –220.1 [br. d, ^1J(P,H) = 178 Hz, PH] ppm. IR (KBr): $\tilde{v}$ = 2944 (vs), 2891 (s), 2866 (vs), 2299 (m), 1463 (s), 1385 (m), 1365 (w), 1260 (w), 1240 (w), 1160 (w), 1082 (vs), 1051 (vs), 990 (s), 919 (w), 882 (s), 808 (m), 680 (m), 644 (m), 604 (m), 497 (m) cm^{-1}.

Acknowledgments

[1] a) M. Driess, R. E. Mulvey, M. Westerhausen, in: *Molecular Clusters of the Main Group Elements* (Eds.: M. Driess, H. Nöth), Wiley-VCH, Weinheim, **2004**, p. 391–424; b) M. Westerhausen, *Coord. Chem. Rev.* **1998**, *176*, 157–210.

[2] a) M. Gärtner, H. Görls, M. Westerhausen, *Z. Anorg. Allg. Chem.* **2007**, *633*, 2025–2031; b) M. Westerhausen, M. H. Digeser, H. Nöth, J. Knizek, *Z. Anorg. Allg. Chem.* **1998**, *624*, 215–220; c) M. Westerhausen, R. Löw, W. Schwarz, *J. Organomet. Chem.* **1996**, *513*, 213–229; d) M. Westerhausen, A. Pfitzner, *J. Organomet. Chem.* **1995**, *487*, 187–195; e) M. Westerhausen, *J. Organomet. Chem.* **1994**, *479*, 141–151.

[3] M. Westerhausen, M. H. Digeser, M. Krofta, N. Wiberg, H. Nöth, J. Knizek, W. Ponikwar, T. Seifert, *Eur. J. Inorg. Chem.* **1999**, 743–750.

[4] M. Kaupp, P. von Ragué Schleyer, *J. Am. Chem. Soc.* **1993**, *115*, 11202–11208.

[5] C. von Hänisch, S. Stahl, *Angew. Chem.* **2006**, *118*, 2360–2363; *Angew. Chem. Int. Ed.* **2006**, *45*, 2302–2305.

[6] M. Westerhausen, M. H. Digeser, B. Wieneke, H. Nöth, J. Knizek, *Eur. J. Inorg. Chem.* **1998**, 517–521.

[7] M. Westerhausen, M. Hartmann, W. Schwarz, *Inorg. Chem.* **1996**, *35*, 2421–2426.

[8] *TURBOMOLE* Version 5.10 (c), TURBOMOLE GmbH, **2008**. TURBOMOLE is a development of the University of Karlsruhe and Forschungszentrum Karlsruhe, **1989**–**2007**, TURBOMOLE GmbH since **2007**.

[9] A. D. Becke, *Phys. Rev. A* **1988**, *38*, 3098–3100; J. P. Perdew, *Phys. Rev. B* **1996**, *33*, 8822–8824.

[10] F. Weigend, R. Ahlrichs, *Phys. Chem. Chem. Phys.* **2005**, *7*, 3297–3305.

[11] F. Weigend, *Phys. Chem. Chem. Phys.* **2006**, *8*, 1057–1065.

[12] M. Kaupp, P. v. R. Schleyer, H. Stoll, H. Preuss, *J. Chem. Phys.* **1991**, *94*, 1360–1366.

[13] P. Pyykkö, J. C. Snijders, E. J. Baerends, *Chem. Phys. Lett.* **1981**, *83*, 432–437.

[14] L. Gagliardi, *J. Am. Chem. Soc.* **2002**, *124*, 8757–8761.

[15] L. Gagliardi, P. Pyykkö, *Theor. Chem. Acc.* **2003**, *110*, 205–210.

[16] A. Klamt, G. Schüürmann, *J. Chem. Soc. Perkin Trans. 2* **1993**, *2*, 799–805.

[17] C. von Hänisch, S. Stahl, *J. Organomet. Chem.* **2007**, *692*, 2780–2783.

[18] a) M. Westerhausen, *Inorg. Chem.* **1991**, *30*, 96–101; b) D. C. Bradley, M. B. Hursthouse, A. A. Ibrahim, K. M. A. Malik, M. Motevalli, R. Möseler, H. Powell, J. D. Runnacles, A. C. Sullivan, *Polyhedron* **1990**, *9*, 2959–2964.

[19] *STOE-IPDS2* (Mo-K_α radiation, λ = 0.71073 Å). The structure was resolved by direct methods and refined against F^2 by the full-matrix least-squares technique (Ba, Sr, Ca, Mg, C, O, Si, P refined anisotropically, H atoms at the phosphorus atoms refined isotropically, all other H atoms calculated at ideal positions). CCDC-741883 (for **2**), -741884 (for **2a**), -741885 (for **2b**), -741886 (for **3**), -741887 (for **4**), -741888 (for **5**) contain the supplementary crystallographic data for this paper. These data can be obtained free of charge from The Cambridge Crystallographic Data Centre via www.ccdc.cam.ac.uk/data_request/cif.

Ethene Polymerization Behavior of MAO-Activated Dichloridotitanium Complexes Bearing Bi- and Tetradentate Salicylaldimine Derivatives

**Antti Pärssinen,[a] Tommi Luhtanen,[b] Tapani Pakkanen,[b] Markku Leskelä,[a] and Timo Repo*[a]**

New chiral bridged tetradentate $(N_2O_2)Ti^{IV}Cl_2$-type complexes bearing dimethylbiphenyl (**1-Ti–3-Ti**) and previously published binaphthyl-bridged (**4-Ti**) complex were synthesized with high yields. This was achieved by treating the corresponding Schiff-base ligand (H_2L) precursors with $Ti(NMe_2)_4$, followed by conversion of these diamido complexes to $LTiCl_2$ derivatives by the addition of excess of Me_3-SiCl. A series of unbridged titanium complexes **5-Ti–8-Ti** with similar substituents at the phenoxy group were studied and their polymerization properties, after methylaluminoxane (MAO) activation, compared with the above bridged complexes. It was found that the catalysts bearing chiral tetradentate biaryl-bridged salicylaldimine ligands produce multimodal polyethylene (PE) with low activity [below 10 $kg_{PE}/(mol_{Ti}h\,bar)$] while their unbridged analogues provide activities that are 10–1000 times greater under similar reaction conditions. The reasons for this dramatic difference in polymerization activities are discussed based on the stabilities of the different cationic species configurations.

Introduction

Group 4 metal-based bis(salicylaldiminato) dichlorido complexes are known for their high activities in ethene polymerisation upon activation with MAO.[1] In highly active titanium and zirconium complexes fluorinated-[1] or alkylphenyl[2] groups at the imine nitrogen and *t*Bu or cumyl substituents at the 3-position adjacent to the phenoxy oxygen are distinctive features. These highly active catalysts polymerize ethene with narrow polydispersity values typical for single-site catalysts. However, considerable number of bis(salicylaldiminato)Ti catalysts have low polymerization activities and tend to give multimodal polyethylene. According to our previous results, various active species in polymerization is linked to simultaneous presence of different structural isomers of catalysts.[3]

As shown before, substituents on the salicylaldiminato ligands have an effect on the geometry of the dichlorido complexes. Three different octahedral configurations have been determined by X-ray structure analysis.[4,5] In these solid-state structures, the imine nitrogen atoms as well as the phenoxy oxygens have either *cis*, *ciscis* or *trans* orientation towards each other while the chlorides adopt a *cis* orientation (Scheme 1).
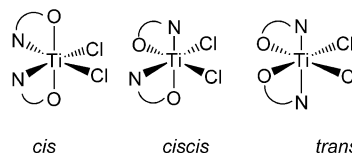
Scheme 1. Octahedral configurations for bis(salicylaldiminato)-$TiCl_2$ complexes wherein chlorides occupy *cis* orientation. R can be any aromatic or aliphatic substituent. *cis* (*cis*-N, *trans*-O and *cis*-Cl, C_2 symmetry), *ciscis* (*cis*-N, *cis*-O and *cis*-Cl, C_1 symmetry) and *trans* (*trans*-N, *cis*-O and *cis*-Cl, C_2 symmetry) abbreviations are related to the orientation of imine nitrogen atoms in the complexes.

In solution, the dichloride complexes can have mixture of different coordination geometries and their relative ratios are dependent upon salicylaldiminato ligand substituents.[2,6,7]

Besides of substituents in salicylaldiminato ligands also co-ligands have an influence for the coordination geometries of the complexes and their relative ratios. This phenomenon is clearly observable when converting bis(salicyl-aldiminato)Ti amido complexes to corresponding chloride analogues.[2,7] According to the recent calculation results the coordination geometries can further change when dichloride complexes are activated with MAO. The relative stabilization energies of the cationic Ti isomers do not necessarily follow the same pattern as their corresponding neutral chloride analogues.[2] The change in geometry subsequent to activation and the magnitude of the change is dependent upon the ligand substituents as well as the applied reaction conditions. As a consequence solid-state structures of dichlorido complexes cannot be used to predict their po-

[a] Department of Chemistry, Laboratory of Inorganic Chemistry,
P. O. Box 55, 00014 University of Helsinki, Finland
Fax: +358-9-19150198
E-mail: timo.repo@helsinki.fi
[b] Department of Chemistry, University of Joensuu,
P. O. Box 111, 80101 Joensuu, Finland

lymerization behavior. In fact, our previous results have demonstrated that the most active bis(salicylaldiminato) catalysts bearing alkyl[2] and aromatic[3] imino substituents are those complexes which tend to change the relative orientation of their imine nitrogen atoms from *cis* to *trans* upon activation (Scheme 2).

cis   *ciscis*   *trans*
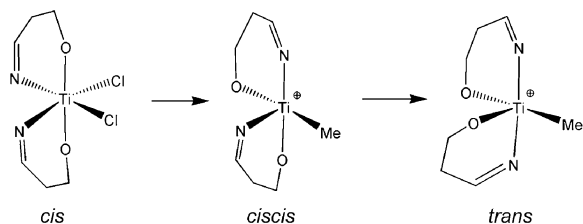
Scheme 2. Schematic representation of the plausible *cis* to *trans* change in complex configuration during the activation procedure. *cis* and *trans* abbreviations are related to the orientation of imine nitrogen atoms in complexes.

To further attest the benefit of the *cis* to *trans* change on catalytic activity, a series of biphenyl bridged (**1-Ti**–**3-Ti**, Scheme 3), binaphthyl bridged (**4-Ti**, Scheme 4) and unbridged Ti complexes (**5-Ti**–**8-Ti**, see Schemes 5 and 6) were studied to compare their polymerization properties after MAO activation. The bridging in **1-Ti**–**4-Ti** prevents any possible *cis* to *trans* isomerisation of the imino nitrogen atoms.
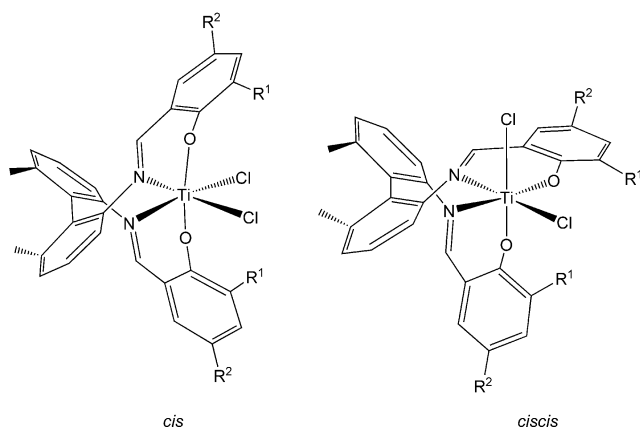
cis   *ciscis*

Scheme 3. The dimethylbiphenyl bridged titanium dichloride complexes (**1-Ti**–**3-Ti**) possess the *cis* or *ciscis* configuration or their combinations at room temp. in solution. **1-Ti** ($R^1 = R^2 = H$, *cis* and *ciscis* configurations in ratio of 1:4), **2-Ti** ($R^1 = tert$-butyl, $R^2 = H$, *ciscis* configuration) and **3-Ti** ($R^1 = R^2 = $ cumyl, *cis* configuration).

The basic salen-type ligands, having an ethylene linkage between the imino nitrogen atoms, favour planar coordination with Group 4 metals which results in the chlorides being forced to adopt a *trans* ($\approx 180°$) orientation. These types of conformers are known to have low activities in α-olefin polymerisation.[8]

Therefore our interest was drawn towards the study of chiral tetradentate biaryl-iminophenolate ligand systems wherein the rigid biaryl bridge forces both the chlorides and
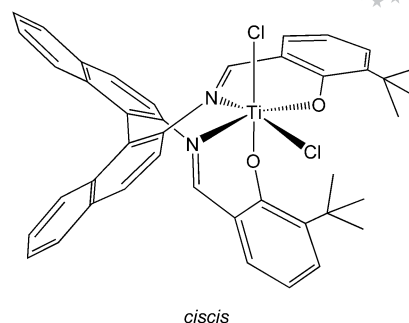
ciscis

Scheme 4. The binaphthyl-bridged titanium dichloride complex **4-Ti** possesses the *ciscis* configuration in solution.
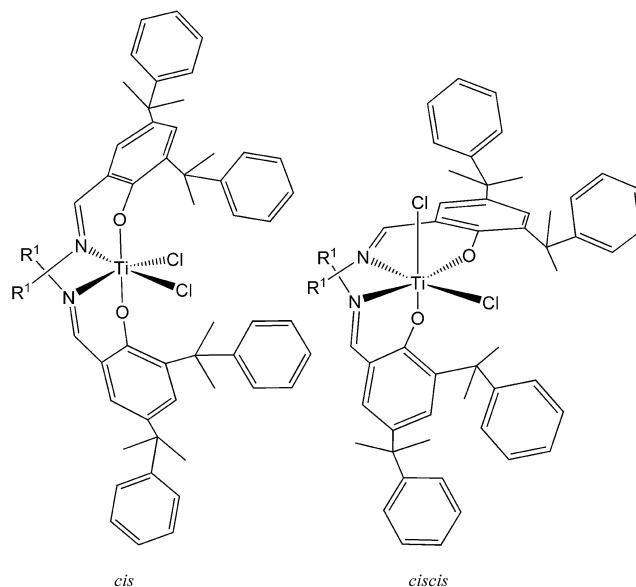
cis   *ciscis*

Scheme 5. In solution the unbridged complex **5-Ti** ($R^1 = CH_2CH_2Ph$) possesses both the *cis* and the *ciscis* configurations in ratio of 1:2 while complex **6-Ti** ($R^1 = Ph$) possesses *ciscis* configuration.

7-Ti   **8-Ti**
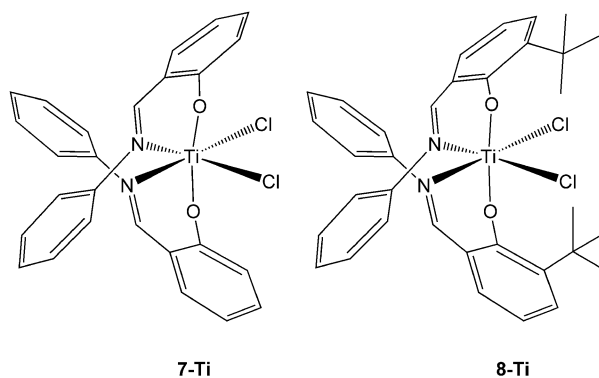
Scheme 6. Schematic presentation of complexes **7-Ti** and **8-Ti**.

imino nitrogen atoms to occupy *cis* coordination sites in C_1 and C_2-symmetric complexes.[7,9,10] Intriguingly, despite of the attractive octahedral symmetry and similar substitution pattern with the most active bis(salicylaldiminato) catalysts

those with tetradentate ligands have only low activity in polymerization. It is also worth to notice, that in *ciscis*-type complexes the Ti–O, Ti–N, and Ti–Cl bond lengths and even O–Ti–O and Cl–Ti–Cl bond angles for bidentate and tetradentate phenoxy-iminotitanium(IV) complexes are very close to each other and therefore do not explain the dramatic difference in catalytic activity in ethene polymerization.[5,9]

Results and Discussion

Preparation of Ligands and Complexes

As shown previously with *N*-(salicylidene)anilines,[2] the Schiff base condensation reaction occurs efficiently when carried out in toluene solution in round-bottomed flask at temperature above 100 °C. By this method three 6,6′-dimethylbiphenyl (**1–3**) and previously published binaphthyl-bridged ligand precursors (**4**) (Scheme 7) as well as 2-phenylethyl-*N*-(3,5-dicumylsalicylaldimine) (**5**) and phenyl-*N*-(3,5-dicumylsalicylaldimine) (**6**) (Scheme 8) were obtained with very high yields from their corresponding salicylaldehydes and amines.
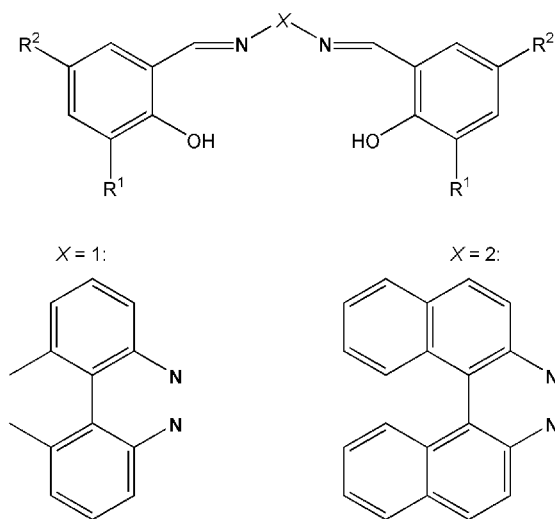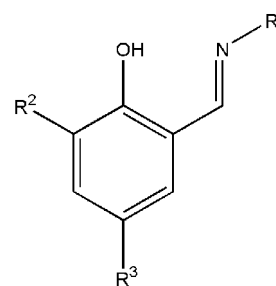

Scheme 7. Schematic representation of the biaryl-bridged salicylaldimine ligand precursors **1–4**. **1**: *X* = 1, R¹ = R² = H; **2**: *X* = 1, R¹ = *tert*-butyl, R² = H; **3**: *X* = 1, R¹ = R² = CMe₂Ph; **4**: X = 2, R¹ = *tert*-butyl, R² = H.

Direct metallation of the ligand precursors with Ti(NMe₂)₄, followed by chlorination of the formed bis(dimethyl)amido titanium complexes using an excess of chlorotrimethylsilane, proved to be a highly selective and simple method of synthesis for complexes (**1-Ti**–**3-Ti**) bearing the 6,6′-dimethylbiphenyl moiety and for complex **4-Ti** with a binaphthyl bridge between the salicylaldimine moieties (see Schemes 3 and 4).[9] However, this method was not directly suitable for the synthesis of complex **5-Ti** (Scheme 5) as the chlorination procedure resulted in the formation of an amino salt which could not been completely removed under vacuum and lead to a 5–6% deficit in the carbon proportion. However, the amino salt was nearly completely re-

Scheme 8. Schematic representation of the bidentate ligand precursors **5–8**. **5**: R¹ = CH₂CH₂Ph, R² = R³ = CMe₂Ph; **6**: R¹ = Ph, R² = R³ = CMe₂Ph; **7**: R¹ = Ph, R² = R³ = H; **8**: R¹ = Ph, R² = *tert*-butyl, R³ = H.

moved by the addition of a slight excess of triethylamine which led to the pure complex being obtained with 90% yield.[4]

Attempts to prepare complex **6-Ti** by direct metallation were not successful. Although treatment of compound **6** with Ti(NMe₂)₄ resulted in formation of the desired titanium amido complex intermediate, the chlorination procedure was unselective. After chlorination, substantial amounts of amido signals (NMe₂) including an additional sharp signal at 8.5 ppm were detected by ¹H NMR spectroscopy. The peak at 8.5 ppm indicates the presence of non coordinating imine. Therefore, the preparation of complex **6-Ti** required the use of the traditional route via lithium salt followed by complexation with TiCl₄. By heating the lithium salt together with TiCl₄ at 85 °C for two days the complex was obtained with nearly quantitative yield. Complex **6-Ti** was discovered to be very sensitive and hence all NMR samples were prepared in a glovebox under argon atmosphere. Even traces of moisture can lead to the detachment of the phenoxy imine ligand, as testified by the appearance of two new sharp resonances at δ = 8.52 ppm and 8.62 ppm in ¹H NMR indicating the presence of uncoordinated imines.

Configurations of Amido and Chlorido Complexes

The amido derivative of complex **1-Ti** possesses indistinguishable imino and amido proton signals in its ¹H-NMR spectrum possibly caused by presence of *cis* and *ciscis* isomers and hindered rotation of ligands. When the NMe₂ ligands of **1-Ti** are replaced by chlorides, three slightly broad imine proton signals appears, a singlet from the *cis* isomer together with two separate singlets from the *ciscis* isomer, the ratio being 1:4. In order to gain insight into the possible fluxional behaviour of **1-Ti** in its dichloride form, dynamic ¹H NMR (C₆D₆) measurements were carried out. The results of this study revealed that both of the isomers seem to be stable even at 67 °C as no changes in ratio or in the positions of the imine signals were observed.[7]

For complex **2-Ti** which bears a *tert*-butyl group at the phenoxy moiety, both the amido and dichloro derivatives adopt the *ciscis* geometry while both the amido and dichloro derivatives of cumyl-substituted complex **3-Ti**

adopt the *cis* geometry exclusively. In the case of the amido derivative of complex **4-Ti**, one sharp singlet from the imino protons (δ = 7.82 ppm) is observed indicating the presence of the *cis* isomer. Upon subsequent chlorination two sharp resonances is observed indicating conversion of the complex from *cis* to the *ciscis* isomeric form.[9] A similar phenomenon was previously observed by Scott et al. for a comparable, 6,6′-dimethylbiphenyl-bridged bis(3,5-di-*tert*-butylsalicylaldimino)TiCl$_2$ complex.[7]

As for the bridged complex **4-Ti**, the unbridged complexes are prone to configurational changes upon chlorination. The amido derivative of complex **6-Ti** revealed a sharp singlet in ^{1}H NMR indicating a possible C_2-symmetric *cis* configuration while the corresponding dichlorido complex adopts a C_1-symmetric *ciscis* structure resolved from its HSQC spectra (Scheme 5).

Due to overlapping signals arising from different isomers, the ^{1}H-NMR spectrum of amido derivative **5-Ti** was ambiguous. The configuration of the corresponding dichloride complex was resolved using ^{13}C-NMR revealing three imino signals arising from *cis* and *ciscis* isomers in the estimated ratio of 1:2 (see Supporting Information). It can be concluded that the geometries of studied complexes can vary and their configurations are dependent upon the substituents at the phenoxy *ortho* position as well as on the anionic monodentate co-ligands present (Cl and NMe$_2$).

Ethene Polymerization

The bridged Ti complexes **1-Ti**–**4-Ti** were activated with an excess of methylaluminoxane (MAO) (Al/Ti ratio 2000) and used in ethene polymerisation. The structure of precatalysts of **2-Ti**/MAO and **4-Ti**/MAO are similar, the only difference being the chiral backbone (see Schemes 3 and 4). In fact, this structural difference has only a minor influence on polymerisation behavior. Regardless of the applied polymerisation temperature and monomer pressure, polymerisation activities of both **2-Ti**/MAO and **4-Ti**/MAO were very low [1–6 kg$_{PE}$/(mol$_{Ti}$ h bar)] and they produced, in general, PE with unimodal but slightly broadened distribution curves (Table 1). Interestingly, at certain polymerisation conditions (6 bar, 40 °C) both catalysts exhibited bimodal behavior, particularly **2-Ti**/MAO which produced PE with two clearly distinguishable distribution curves. The highest molar mass polymers were achieved either at low temperatures or low pressures (Table 1).

Catalyst **1-Ti**/MAO, although missing *ortho tert*-butyl groups and therefore having reduced steric bulkiness around the active center, has comparable activity with **2-Ti**/MAO and **4-Ti**/MAO[10] (Table 1). The major difference between these three catalysts is that **1-Ti**/MAO tends to form bimodal PE at all polymerization conditions. Curiously, **1-Ti**/MAO produced clearly unimodal PE at 4 bar and 60 °C. Catalyst **3-Ti**/MAO, bearing sterically bulky cumyl substituents, differs from the other bridged catalysts in that it has slightly increased activity [10–20 kg$_{PE}$/(mol$_{Ti}$ h bar)] and the ability to produce trimodal PE under

Table 1. Ethene polymerisation results with complexes (1-Ti–6-Ti). Reaction conditions: runs 1–20 [Al]/[Ti] = 2000, time 40 min; run 21 [Al]/[Ti] = 2000, time 141 s; runs 22–24 [Al]/[Ti] = 5000, time 500 s; run 25 [Al]/[Ti] = 5000, time 134 s; run 26 [Al]/[Ti] = 5000, time 200 s; run 27 [Al]/[Ti] = 5000, time 300 s.

Run	Complex	Yield [g]	Cat. [μmol]	$T^{[a]}$ [°C]	$p^{[b]}$ [bar]	Act.[c]	M_w [kg/mol]	M_w/M_n
1	**1-Ti**	0.48	20	60	4	9	930	3.9
2	**1-Ti**	0.24	20	40	6	4	620	3.9
3	**1-Ti**	0.40	20	60	6	5	900	6.5
4	**1-Ti**	0.72	20	80	6	9	320	5.2
5	**1-Ti**	0.75	20	60	8	7	560	12.8
6	**2-Ti**	0.21	20	60	4	4	1020	3.6
7	**2-Ti**	0.08	20	40	6	1	580	9.2
8	**2-Ti**	0.08	20	60	6	1	970	3.6
9	**2-Ti**	0.08	20	80	6	1	490	3.3
10	**2-Ti**	0.32	20	60	8	3	180	2.3
11	**3-Ti**	0.64	20	60	4	12	1060/30/3	1.5[d]
12	**3-Ti**	0.80	20	40	6	10	1090/34/1	1.5[d]
13	**3-Ti**	1.76	20	60	6	22	1040/34/3	1.5[d]
14	**3-Ti**	0.96	20	80	6	12	1250/32/1	1.5[d]
15	**3-Ti**	1.60	20	60	8	15	890/30/3	1.5[d]
16	**4-Ti**	0.21	20	60	4	4	570	3.9
17	**4-Ti**	0.40	20	40	6	5	600	7.6
18	**4-Ti**	0.40	20	60	6	5	360	3.7
19	**4-Ti**	0.08	20	80	6	1	330	3.7
20	**4-Ti**	0.64	20	60	8	6	390	2.2
21	**5-Ti**	7.30		60	4	6210	110	2.1
22	**5-Ti**	2.63	2	40	4	2360	120	2.1
23	**5-Ti**	5.17	2	60	4	4650	110	2
24	**5-Ti**	3.46	2	80	4	3110	110	1.9
25	**6-Ti**	6.70	2	60	4	22500	370	2
26	**6-Ti**	1.86	2	60	2	8370	380	2.1
27	**6-Ti**	1.55	2	40	4	4650	380	2
28	**6-Ti**	0.54	2	80	4	2460	635	3.3
29	**7-Ti**[8]	–	20	80	5	143	520	3.5
30	**8-Ti**[14]	3.14	5	75	0.1	380000	44[e]	≈ 2

[a] Polymerisation temperature. [b] Monomer pressure. [c] Activity in (kg PE)/(mol$_{Ti}$ h bar). [d] PDI values were between 1–2. Exact values can't be given due to overlapping of molecular mass areas. [e] Molecular mass value is given as a viscosity average molecular mass M_v.

all polymerisation conditions (Figure 1). For example, the molecular mass distribution curve (MMD) of PE at 80 °C consists of three separate, almost equal molecular mass areas with each having narrow PDI values (1.5–2.0). The molecular mass of the polymer in the high M_w-region is close to 1000 kg/mol. In the middle region the molecular mass is around 30 kg/mol while in the low region it is only few kg/mol. The relative sizes of these molecular mass areas are dependent on the polymerisation temperatures. At 60 °C the MMD curve consists mostly of high and average M_w areas while at 40 °C the average M_w area is favored. It is worth noting that **3-Ti**/MAO produces comparable trimodal PE to a similarly substituted unbridged bis(salicylaldiminato) zirconium catalyst, although the latter is more active.[6] This phenomenon is discussed in more detail in the following section.

For the bridged Ti complexes **1-Ti**–**4-Ti**/MAO, ethene consumption during 40 min polymerization reactions is stable. Thus, the observed average low activities and various modalities of PE cannot be explained by deactivation of the catalyst during the polymerisation. Based on the low

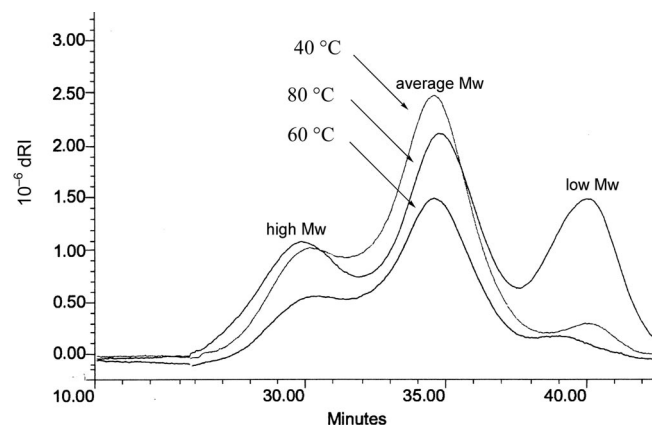A. Pärssinen, T. Luhtanen, T. Pakkanen, M. Leskelä, T. Repo

Figure 1. Molecular mass distribution curve of trimodal PE polymerized with MAO activated complex **3-Ti** at different temperatures.

polymerisation activities recorded for the series of bridged catalysts, it can be summarized that neither the *cis* nor *ciscis* geometry provides a Ti-center of high activity. Alternative explanation for low activity was presented by e.g. Scott et al. who proposed that during complex activation process one of the imino groups is replaced with amido one.[7]

In order to identify the influence of bridging on catalytic properties, a series of unbridged complexes were chosen for study under similar polymerization conditions. This series included a new non-bridged complex (**5-Ti/MAO**) and the previously reported **6-Ti/MAO**,[11] **7-Ti/MAO**[3,4] and **8-Ti/MAO**[12] (see Scheme 5 and 6). This series of unbridged complexes covers the same range of *o*-substitution patterns as present in the series of bridged complexes studied above. These selected unbridged complexes also have *cis* and/or *ciscis* orientation of their imine nitrogen atoms in the dichloro form as was the case for the bridged complexes.

Catalyst **5-Ti/MAO** bearing a cumyl substituent in the *o*-position and an ethylphenyl group at imino nitrogen had high catalytic activity 6,000 $kg_{PE}/(mol_{Ti}\,h\,bar)$ at 60 °C and 4 bar ethylene (Table 1). This catalyst also had appreciable thermal stability as is evident from its activity at 80 °C which was 70 % of that achieved at 60 °C. The polymerization properties of the catalyst resemble those typical for single center catalysts e.g. metallocenes. Typical polydispersity values were 2 and the obtained molecular masses were 100 kg/mol. At 80 °C traces of high M_w PE were obtained.

At 60 °C and 4 bar ethylene, the activity of **6-Ti/MAO** (having a phenyl group at imino nitrogen) is remarkably high over very short polymerization times. During a short two minute polymerization run, the activity was over 20,000 $kg_{PE}/(mol_{Ti}\,h\,bar)$; however after three minutes the activity decreased to 8,000 $kg_{PE}/(mol_{Ti}\,h\,bar)$ which is close to the literature reported values.[13] **5-Ti/MAO** and **6-Ti/MAO** produce PE with narrow PDI values indicating the presence of one active catalytic centre.

At the highest temperature studied (80 °C) the activity of **6-Ti/MAO** was clearly reduced and PE with broad PDI was obtained. Accordingly, **6-Ti/MAO** appears to have lower thermal stability than **5-Ti/MAO**.

Under similar polymerization conditions the previously published **7-Ti/MAO** having a phenyl group at imino nitrogen and H at *ortho*-position has low activity and produces PE with a slightly broadened PDI of 3.5.[3] Conversely, very high activities have been reported for **8-Ti/MAO** bearing *ortho tert*-butyl groups and a phenyl group at imino nitrogen. **8-Ti/MAO** produces PE with narrow PDI (≈ 2)[11] (Scheme 6).

Correlation between Complex Structure and Polymerisation Behaviour

In order to find a correlation between the structure of the bridged and the unbridged complexes **1-Ti**–**8-Ti** and their polymerisation properties, all complexes were subjected to ab initio calculations. Unfortunately the ab initio calculations failed with complexes **3-Ti**, **5-Ti** and **6-Ti** due to their large and freely rotating cumyl groups. Despite this setback, the data-set produced from the remaining complexes provides an interesting insight into the polymerisation behaviour of these catalysts.

The calculations concerning relative stabilisation energies of the bridged dichlorido complexes **1-Ti**, **2-Ti** and **4-Ti** are in accordance with the experimental results. In these complexes the relative stabilisation energies of *cis* and *ciscis* conformers are very close to each other (Table 2). Therefore, depending on the conditions it follows that both conformers may be present in solution. Similarly, when activated, both isomers of the cationic species have the same stability. Thus under certain polymerisation conditions, bimodal PE or unimodal with slightly broadened distribution curves is expected.

Table 2. The relative stabilisation energies (E_{Rel} = kJ/mol) for different isomeric structures of dichloro as well as cationic derivatives of **1-Ti**, **2-Ti**, **4-Ti**, **7-Ti** and **8-Ti** $E_{Rel}(Cl_2)$ and $E_{Rel}(Ti^+)$, respectively. In these calculations, the *cis* isomer has been chosen as a point of reference for the bridged and the *trans* isomer for the non-bridged complexes. For the complexes **1-Ti**–**4-Ti** stability energies of *trans* isomers were left out of table due to high values (<+200 kj/mol). $E_{Rel}(Ti^+)$ stands for the methylated cationic form of the titanium dichloride complex (Scheme 2).

Complex	$E_{Rel}(Cl_2)$	$E_{Rel}(Ti^+)$
1-Ti_*cis*	0.9	0.0
1-Ti_*ciscis*	0	0.0
2-Ti_*cis*	0	0.0
2-Ti_*ciscis*	0.1	0.0
4-Ti_*cis*	1.6	0.0
4-Ti_*ciscis*	0	0.0
7-Ti_*cis*	−21	0.0
7-Ti_*ciscis*	−8	0.0
7-Ti_*trans*	0	0.0
8-Ti_*cis*	2.6	26.4
8-Ti_*ciscis*	0.0	5.4
8-Ti_*trans*	18.8	0.0

In our earlier studies with a series of non-bridged bis-(phenoxyimine)titanium catalysts, we found that the highest activities in ethene polymerisation are achieved with com-

plexes which are, according to calculations, prone to adopt the *trans* orientation of the imino nitrogen atoms upon activation.[2,3] This orientation brings the imine substituents into the frontal position and thus steric shielding of the active centre increases. As shown below, this appears to be crucial for catalytic activity.

The bridged **1-Ti** and unbridged **7-Ti** have otherwise similar ligand environments, both of which consist of unsubstituted phenoxy and imino phenyl groups. However, the polymerisation activity of the unbridged complex is ten times higher. Ab initio calculations concerning the cationic **7-Ti** revealed that all three isomers (*cis*, *ciscis* and *trans*) have similar stabilisation energies and so are equally likely to be present. This decreases the fraction of the highly active *trans* isomer present and hence the increase in activity is limited to ten-fold only.[3] The presence of various isomers of the active species is also reflected in the relatively broad PDI ($\approx$ 3.5).

Both the bridged **2-Ti** and unbridged **8-Ti** have *ortho tert*-butyl substituents that in the case of latter one has been shown previously to increase the catalytic activity of these types of complexes.[12] This *tert*-butyl substituent effect is not evident in the case of the bridged **2-Ti** as its activity shows no further increase from that of **1-Ti**. Conversely, however, the unbridged **8-Ti** has an activity superior than that of **7-Ti** (Table 1) which demonstrates that the *tert*-butyl substituent effect is operational for the unbridged type complexes.

These findings were once again supported by the calculations which showed that the *trans* geometry is clearly favoured for the cationic form of **8-Ti** which explains it high activity. This isomeric form cannot exist for **2-Ti** due to bridging which results in this complex having low activity which is not enhanced by the presence of *tert*-butyl substituents. As the *trans* form of the cationic **8-Ti** is preferable, only one active centre is present in polymerization and unimodal PE with very high activity is observed.[12] The difference between the bridged and the unbridged catalysts in polymerisation activity is 10,000-fold.

The cumyl-substituted, bridged **3-Ti** and unbridged **6-Ti** complexes make up the third catalytic pair studied. The unbridged **6-Ti** polymerizes ethene with high activity [8000 kg PE/(mol$_{Ti}$ h bar)] and produces unimodal PE (PDI = 2.0). **3-Ti** has the highest activity in the series of the bridged complexes [up to 20 kg PE/(mol$_{Ti}$ h bar)] and produces trimodal PE. It must be noted, however, that the activity of the bridged **3-Ti** is 400 times lower than the activity of the unbridged **6-Ti**.

Since the existence of the *trans* geometry in **3-Ti** is prevented by bridging, possible *cis* and *ciscis* conformers leads to catalytic species with low activities. As **6-Ti** is highly active and produce PE with unimodal, narrow PDI it can be concluded that the *trans* geometry of the catalytically active **6-Ti** is prevalent. It is worth to notice that the unbridged **6-Ti** was prone to changes in the coordination geometry when amido ligands are changed to chlorines.

The observation that the cumyl-substituted, bridged **3-Ti** produce trimodal PE is interesting. As the third isomer

(*trans*) is missing in **3-Ti**, the explanation for the trimodality can arise from interaction of the bulky cumyl substituents with the cationic metal center. In our previous studies concerning bis(salicylaldiminato) catalysts bearing bulky benzyl substituents, which are sterically quite similar to the corresponding cumyl ones used herein, we observed that increased proximity of these substituents to the active site results in dramatic decreases in polymerization activity and leads to the formation of multimodal PE.[2] The freely rotating aromatic ring may form a temporary steric blockade preventing polymer chain growth and hence causing the formation of low molecular mass PE.

Conclusions

Titanium complexes can undergo changes in geometry during their synthesis. The direction and magnitude of these changes are dependent on both the co-ligands present and the *ortho* substituents of the phenoxy group. According to ab initio calculations the same structural isomerization remains present when the catalytically active species are generated. This finding underlines the fact that the isomeric form present in the solid-state structure of such dichlorido complexes is not necessarily the same isomer that is responsible for catalytic activity in ethene polymerization.

After MAO activation, the differences in catalytic activities between non-bridged bis(salicylaldiminato)TiCl$_2$ and their bridged, chiral tetradentate analogues are at best 10,000-fold, the former being more active. As demonstrated in this study using the series of catalysts, this significant difference in catalytic activity arises from the bridging itself rather than the *ortho* ligand substituents. We previously reported that structural isomerisation can be a significant factor in the generation of active species with high catalytic activity. These observations are now further supported by the obtained results.

The bridged complexes **1-Ti**, **2-Ti** and **4-Ti** have two possible structural isomers (*cis* and *ciscis*), which based on ab initio calculations, have similar stabilization energies. As shown, neither of these two isomers is capable of providing high polymerization activity. This finding helps to answer the question of why titanium dichlorido complexes bearing tetradentate biaryl-bridged salicylaldimine ligands have low activity in ethene polymerizations after MAO activation. Additionally, the relatively equal stabilization energies of the two isomers lead to the generation of polymers with bimodal distribution. Bridging in these complexes prevent the presence of the *trans* isomer, which appears to be the most active isomeric form. For example, according to the calculations the cation of non-bridged **8-Ti** prefers the *trans* isomer. The consequence of this is a 10,000 fold increase in activity from its bridged analogue **2-Ti**, which as a result of its constricted isomeric freedom exists in its *cis* and/or *ciscis* forms only. *trans* orientation of the imine nitrogen atoms brings the imine substituents into the frontal position and thus steric shielding of the active centre increases. This appears to be crucial for catalytic activity.

Experimental Section

General: All manipulations of air- and water-sensitive compounds were carried out under dry argon using standard Schlenk techniques. HPLC-grade toluene was dried and purified by refluxing over sodium followed by distillation under argon. Benzophenone was used to detect the absence of water. Toluene was stored over sodium under argon. Salicylaldehyde (Fluka), 3-*tert*-butylsalicylaldehyde (Aldrich), 2,4-bis(α,α′-dimethylbenzyl)phenol (Aldrich), 2,2′-diamino-6,6′-dimethylbiphenyl (MCAT), 2,2′-diaminobinaphthyl (Aldrich), chlorotrimethylsilane (98%) (Aldrich) and tetrakis(dimethylamino)titanium (Aldrich) were used as received, methylaluminoxane (MAO, 30 wt.-% solution in toluene) was purchased from Borealis Polymers Oy. ^{1}H and ^{13}C NMR spectra were collected on a Varian Gemini 2000 (200 MHz). Chemical shifts are referenced with respect to CHCl$_3$. For the complexes **1-Ti**–**6-Ti** complete list of ^{13}C resonances are presented in ESI. Dynamic NMR measurements were carried out with a Varian spectrometer (500 MHz), deuterated benzene was used as solvent, the temperature scan area was from 27–67 °C. Mass spectra (EI) were acquired by JEOL-SX102. DSC measurements (melting point) were performed on a Perkin–Elmer DSC-2, calibrated with indium (temperature scanning 20 °C/min). The scan area was from 25–232 °C. Mass average molecular weights (M_w), number average molecular weights (M_n) and molecular weight distribution (MWD, M_w/M_n) of the polyethylene samples were determined by GPC (Waters Alliance GPCV 2000, high temperature gel chromatographic device). GPC had HMW7, 2*HMWGE and HMW2 Waters Styrogel columns. Measurements were carried out in 1,2,4-trichlrobentzene (TCB) at 160 °C relative to polystyrene (PS) standards. 2,6-Di-*tert*-butyl-4-methylphenol was used as a stabilizer. For the earlier published but differently synthesized ligand precursors (1,4) and complexes (4-Ti) only selected experimental information was included. All the synthezied ligand precursors and complexes precipitated out of solution as yellow powder and as dark red powder respectively.

Synthesis of Ligand Precursors 1–6

2,2′-Bis[(2-hydroxybenzylidene)amino]-6,6′-dimethyl-1,1′-biphenyl (1):[14] A 50 mL round-bottomed flask was charged with salicylaldehyde (1.00 mL, 9.42 mmol) and 2,2′-diamino-6,6′-dimethylbiphenyl (1.0 g, 4.71 mmol) The reactants were dissolved in 20 mL of toluene and heated at 110 °C for overnight. The raw product (yellow powder) was recrystallized from 2-propanol (yield 1.94 g, 98%). ^{1}H NMR (200 MHz, CDCl$_3$, 29 °C): δ_H = 12.33 (s, 2 H, 2×OH), 8.54 (s, 2 H, 2×NCH), 7.45–6.68 (m, 14 H, aromatic), 2.09 (s, 6 H, 2×CH$_3$) ppm.

2,2′-Bis[(3-*tert*-butyl-2-hydroxybenzylidene)amino]-6,6′-dimethyl-1,1′-biphenyl (2) was prepared by a similar method as described for **1**. 3-*tert*-Butylsalicylaldehyde (1.61 mL, 9.42 mmol) and 2,2′-diamino-6,6′-dimethylbiphenyl (1.0 g, 4.71 mmol) were used (yield 2.25 g, 90%, yellow powder). C$_{36}$H$_{40}$N$_2$O$_2$ (532.7): calcd. C 81.17, H 7.57, N 5.26; found C 81.30, H 7.28, N 5.52. ^{1}H NMR (200 MHz, CDCl$_3$, 29 °C): δ_H = 13.11 (s, 2 H, 2×OH), 8.46 (s, 2 H, 2×NCH), 7.40–6.74 (m, 12 H, Ar), 2.10 (s, 6 H, 2×CH$_3$), 1.33 (s, 18 H, CH$_3$) ppm. ^{13}C{^{1}H} NMR (50.3 MHz, CDCl$_3$, 29 °C): δ_C = 162.1 (CN), 160.8 (CO), 146.9, 137.4, 130.5, 130.0, 128.6, 119.2, 117.9, 115.4 (Ar), 35.0 (CMe$_3$), 29.4 (CH$_3$), 20.0 (Ar-CH$_3$) ppm. MS (EI), *m/z*: 532–534 [with appropriate isotope ratio for (C$_{36}$H$_{40}$N$_2$O$_2$$^+$)].

2,2′-Bis{[3,5-bis(α,α′-dimethylbenzyl)-2-hydroxybenzylidene]amino}-6,6′-dimethyl-1,1′-biphenyl (3) was prepared by a similar method as described above for **1**. 3,5-Bis(α,α′-dimethylbenzyl)salicylalde-

hydes[15] (0.5 g, 1.40 mmol) and 2,2′-diamino-6,6′-dimethylbiphenyl (0.15 g, 0.70 mmol) were used. The product was recrystallized from 2-propanol (yield 0.56 g, 90%). C$_{64}$H$_{64}$N$_2$O$_2$ (893.2): calcd. C 86.06, H 7.22, N 3.14; found C 85.87, H 7.12, N 2.62. ^{1}H NMR (200 MHz, CDCl$_3$, 29 °C): δ_H = 12.51 (s, 2 H, 2×OH), 8.09 (s, 2 H, 2×NCH), 7.33–6.96 (m, 6 H, Ar), 6.83 and 6.79 (both s, each 1 H, Ar) 1.91 (s, 6 H, 2×Ar-CH$_3$), 1.69 (s, 12 H, 4×CH$_3$), 1.55 and 1.52 (12 H, 4×CH$_3$) ppm. MS (EI), *m/z*: 892–894 [with appropriate isotope ratio for (C$_{64}$H$_{64}$N$_2$O$_2$$^+$)].

2,2′-Bis[(3-*tert*-butyl-2-hydroxybenzylidene)amino]-1,1′-binaphthyl (4):[9] Preparation by a similar method as described above for **1**, starting from 3-*tert*-butylsalicylaldehyde (1.61 mL, 9.42 mmol) and 2,2′-diaminobinaphthyl (1.34 g, 4.71 mmol) (yield 2.78 g, 98%). ^{1}H NMR (200 MHz, CDCl$_3$, 29 °C): δ_H = 12.94 (s, 2 H, 2×OH), 8.62 (s, 2 H, 2×NCH), 8.08 (d, 2 H, Ar), 7.98 (d, 2 H, Ar), 7.63–7.18 (m, 10 H, Ar), 7.03 (d, 2 H, Ar), 6.70 (t, 2 H, Ar), 1.22 (s, 18 H, 6×CH$_3$) ppm.

1-{[3,5-Bis(α,α′-dimethylbenzyl)-2-hydroxybenzylidene]amino}-2-phenylethane (5): Preparation by a similar method as described above for **1**, starting from 2-phenylethylamine (0.2 mL, 1.59 mmol) and 3,5-bis(α,α′-dimethylbenzyl)salicylaldehyde (0.57 g, 1.59 mmol). C$_{33}$H$_{35}$NO (461.6): calcd. C 85.86, H 7.64, N 3.03; found C 85.79, H 7.85, N 2.84. ^{1}H NMR (200 MHz, CDCl$_3$, 29 °C): δ_H = 13.44 (s, 1 H, OH), 8.15 (s, 1 H, CNH), 7.35–7.14 (m, 16 H, Ar-H), 6.97, 6.96 (d, 1 H, Ar-H), 3.68 (t, 2 H, NCH$_2$), 2.88 (t, 2 H, Ar-CH$_2$), 1.70 and 1.68 (both s, each 6 H, CH$_3$) ppm. ^{13}C{^{1}H} NMR (50.3 MHz, CDCl$_3$, 29 °C): δ_C = 165.8 (CN), 158.0 (CO), 151.0, 150.9, 139.6, 139.5, 136.3, 129.0, 129.0, 128.6, 128.2, 128.0, 126.9, 126.5, 125.8, 125.2, 118.1, 61.2 (NCH$_2$), 42.6 (CMe$_2$), 42.3 (CMe$_2$), 37.7 (Ar-CH$_2$), 31.1 (CH$_3$), 29.6 (CH$_3$) ppm. MS (EI), *m/z*: 461 with appropriate isotope ratio for (C$_{33}$H$_{35}$NO$^+$).

{[3,5-Bis(α,α′-dimethylbenzyl)-2-hydroxybenzylidene]amino}benzene (6): Preparation by a similar method as described above for **1**, starting from aniline (0.254 mL, 2.79 mmol) and 3,5-bis(α,α′-dimethylbenzyl)salicylaldehyde (0.57 g, 2.79 mmol) (yield 80%, 0.96 g). C$_{31}$H$_{31}$NO (433.6): calcd. C 85.87, H 7.21, N 3.23; found C 85.87, H 7.22, N 3.24. ^{1}H NMR (200 MHz, CDCl$_3$, 29 °C): δ_H = 13.33 (s, 1 H, OH), 8.53 (s, 1 H, CNH), 7.47–7.16 (m, 17 H, H-Ar), 1.78 and 1.74 (both s, each 6 H, 2×CH$_3$) ppm. ^{13}C{^{1}H} NMR (50.3 MHz, CDCl$_3$, 29 °C): δ_C = 163.5 (CN), 158.0 (CO), 150.7, 148.8, 140.3, 136.6, 130.0, 129.4, 129.0, 128.3, 128.1, 126.9, 126.7, 125.9, 125.8, 125.4, 121.3, 118.7, 42.7 (CMe$_2$), 42.4 (CMe$_2$), 31.1 (CH$_3$), 29.6 (CH$_3$) ppm. MS (EI), *m/z*: 433 with appropriate isotope ratio for (C$_{31}$H$_{31}$NO$^+$).

Synthesis of Ti Complexes

1-Ti: Compound **1** (0.79 g, 1.88 mmol) was poured into precooled toluene (60 mL) solution of Ti(NMe$_2$)$_4$ (0.44 mL, 1.88 mmol). The reaction mixture was warmed to ambient temperature and stirred overnight. Quantitative formation of complex LTi(NMe$_2$)$_2$ was observed. The reaction was continued by decreasing the amount of solution to 20 mL followed by addition of trimethylsilyl chloride (5 mL, 20 mmol) at room temperature. Reaction mixture was stirred overnight followed by removal of solvent and side products at 70 °C in vacuo (yield 0.99 g, 98%): C$_{28}$H$_{22}$Cl$_2$N$_2$O$_2$Ti (537.3): calcd. C 62.60, H 4.13, N 5.21; found C 62.16, H 4.35, N 5.28. ^{1}H NMR [200 MHz, CDCl$_3$, 29 °C, mixture of two isomers in solution, 25% C_2 isomer (*cis*)]: δ_H = 8.49 (s, 2 H, NCH, *cis*), 8.34 and 8.20 (both s, each 1 H, NCH, *ciscis*), 7.59–6.63 (m, 14 H, aromatic), 2.17 (s, 3 H, CH$_3$), 1.99 (s, 3 H, CH$_3$) ppm. ^{13}C{^{1}H} NMR (50.3 MHz, CDCl$_3$, 29 °C): δ_C = 167.1, 166.8, 165.5 (CN), 164.2, 164.0, 163.7 (CO), 151.5, 150.3, 150.0, 137.5–116.6 (m, Ar), 20.2,

20.0, 19.96 (Ar-CH$_3$) ppm. MS (EI) *m/z*: 537–539 with appropriate isotope ratio for (C$_{28}$H$_{22}$Cl$_2$N$_2$O$_2$Ti$^+$).

2-Ti was prepared by a similar method as described below for **1-Ti**. Compound **2** (1.0 g, 1.87 mmol) and Ti(NMe$_2$)$_4$ (0.44 mL, 1.87 mmol) were used (yield 1.19 g, 98%). C$_{36}$H$_{38}$Cl$_2$N$_2$O$_2$Ti (649.5): calcd. C 66.57, H 5.90, N 4.31; found C 66.59, H 5.77, N 4.10. ^{1}H NMR (CDCl$_3$): δ = 8.34 (s, 1 H, NCH), 8.17 (s, 1 H, NCH), 7.68–6.88 (m, 10 H, Ar), 6.56–6.52 (2 H, Ar), 2.16 (s, 3 H, CH$_3$), 1.98 (s, 3 H, CH$_3$), 1.52 (s, 9 H, CH$_3$), 1.39 (s, 9 H, CH$_3$) ppm. ^{13}C\{^{1}H\} NMR (50.3 MHz, CDCl$_3$, 29 °C): δ_C = 167.3 (CNH), 165.9 (CNH), 163.4 (CO), 163.2 (CO), 151.6, 150.3, 138.1–121.8 (m, Ar), 35.8, 35.3, 35.2 (CMe$_3$), 29.9, 29.7 (CCH$_3$), 20.1, 20.0 (Ar-CH$_3$) ppm. MS (EI) *m/z*: 649–651 with appropriate isotope ratio for (C$_{36}$H$_{38}$ N$_2$O$_2$Ti$^+$).

3-Ti was prepared by a similar method as described above for **1-Ti**. Compound **3** (0.84 g, 0.94 mmol) and Ti(NMe$_2$)$_4$ (0.22 mL, 0.94 mmol) were used. Pure complex **3-Ti** with traces of amino salt was obtained (yield 0.93 g, 98%): C$_{64}$H$_{62}$Cl$_2$N$_2$O$_2$Ti (1010.0): calcd. C 76.11, H 6.19, N 2.77; found C 75.63, H 6.91, N 3.27. ^{1}H NMR (200 MHz, CDCl$_3$, 29 °C): δ_H = 7.86 (s, 2 H, 2×NCH), 7.55–6.61 (m, 28 H, Ar), 4.99 (s, 1 H, Ar), 4.95 (s, 1 H, Ar), 2.08 (s, 6 H, 2×Ar-CH$_3$), 1.85 (s, 3 H, CH$_3$), 1.72 and 1.71 (both s, each 3 H, 2×CH$_3$), 1.65 (s, 6 H, 2×CH$_3$), 1.62 (s, 3 H, CH$_3$), 1.50 (s, 3 H, CH$_3$), 1.34 (s, 3 H, CH$_3$) ppm. ^{13}C\{^{1}H\} NMR (50.3 MHz, CDCl$_3$, 29 °C): δ_C = 167.5 (CNH), 165.4 (CNH), 160.9 (CO), 160.8 (CO), 151.4, 150.6, 150.3, 150.3, 149.7, 143.6, 143.4, 138.1–121.7 (m, Ar), 42.9, 41.8, 33.2, 32.0, 31.1, 31.0, 30.8, 27.1, 21.7, 20.1, 19.9 ppm. MS (EI) *m/z*: 1010–1012 with appropriate isotope ratio for (C$_{64}$H$_{62}$Cl$_2$N$_2$O$_2$Ti$^+$).

4-Ti[9] was prepared by a similar method as described above for **1-Ti**. Compound **4** (1.14 g, 1.88 mmol) and Ti(NMe$_2$)$_4$ (0.44 mL, 1.88 mmol) were used (yield 0.99 g, 98%). ^{1}H NMR (200 MHz, CDCl$_3$, 29 °C): δ_H = 8.42 (s, 1 H, NCH), 8.16 (s, 1 H, NCH), 8.05–6.88 (m, 16 H, Ar), 6.80 (t, 2 H, Ar), 1.54 (s, 9 H, 3×CH$_3$), 1.42 (s, 9 H, 3×CH$_3$) ppm.

5-Ti: Compound **5** (0.83 g, 1.88 mmol) was poured into precooled toluene (60 mL) solution of Ti(NMe$_2$)$_4$ (0.44 mL, 1.88 mmol). The reaction mixture was warmed to ambient temperature and stirred overnight. The reaction was continued by decreasing the amount of solution to 20 mL followed by addition of trimethylsilyl chloride (5 mL, 20 mmol) at room temperature. Reaction mixture was stirred overnight followed by removal of solvent and side products at 70 °C in vacuo. The purification process was continued by solvating chlorinated complex to 40 mL of toluene and dry triethylamine (0.39 mL, 2.8 mmol) followed by several hours of stirring. Thereafter the formed amino salt was allowed to precipitate and removed from the main solution. Solvent and residual triethylamine were removed at 70 °C in vacuo and pure complex with traces of amino salt was obtained (1.20 g, 90%). C$_{66}$H$_{68}$Cl$_2$N$_2$O$_2$Ti (1040.0): calcd. C 76.22, H 6.59, N 2.69; found C 75.62, H 5.86, N 2.67. ^{1}H NMR [20 MHz, CDCl$_3$, 29 °C, mixture of two isomers in solution, 33% *C$_2$* isomer (*cis*)]: δ_H = 7.78–6.68 (m, Ar-H), 6.60–6.30 (m, Ar-H), 3.80–2.70 (m, CH$_2$), 2.17–1.27 (m, CH$_3$ region) ppm. ^{13}C\{^{1}H\} NMR (50.3 MHz, CDCl$_3$, 29 °C): δ_C = 168.3 (CNH), 165.9 (CNH), 164.4 (CNH), 159.6 (CO), 159.5 (CO), 159.4 (CO), 150.5 (Ar), 150.1–125.4 (m, Ar), 124.3, 124.2, 123.2, 65.0 (NCH$_2$), 60.8 (NCH$_2$), 59.6 (NCH$_2$), 43.0–41.8 (m, CCH$_3$ and Ar-CH$_2$), 33.5–26.0 (m, CH$_3$) ppm. MS (EI) *m/z*: 1040 with appropriate isotope ratio for (C$_{66}$H$_{70}$Cl$_2$ N$_2$O$_2$Ti$^+$).

6-Ti: *n*-Butyllithium (1.6 M in hexanes, 1.31 mL, 2.1 mmol) was added dropwise to a solution of ligand precursor **6** (0.86 g, 2.0 mmol) in toluene (40 mL) at –78 °C. The solution was warmed

to room temperature and stirred for 2 h and then added dropwise via cannula to a solution of TiCl$_4$ (0.11 mL, 1.00 mmol) in toluene (20 mL) at –78 °C. The resulting solution was warmed up to 85 °C and stirred under nitrogen for 48 h. The reaction mixture was filtered through Celite followed by removal of the solvent in vacuo. The complex was pure as such (99%, 0.98 g). C$_{62}$H$_{60}$Cl$_2$N$_2$O$_2$Ti (983.9): calcd. C 75.68, H 6.15, N 2.85; found C 75.71, H 6.69, N 2.60. ^{1}H NMR (200 MHz, CDCl$_3$, 29 °C): δ_H = 7.68 and 7.34 (s, 2 H, 2×NCH), 7.85–6.20 (m, 34 H, Ar-H), 2.16–1.25 (m, 24 H, 8×CH$_3$) ppm. ^{13}C\{^{1}H\} NMR (50.3 MHz, CDCl$_3$, 29 °C): δ_C = 169.0 (CNH), 165.6 (CNH), 160.4 (CO), 159.5 (CO), 155.6, 151.3, 150.2, 149.3, 149.2, 144.2, 144.1, 137.1, 136.8, 133.5, 132.1, 131.8, 131.7, 129.4–121.2, (m, Ar), 43.0, 42.8, 42.0 (m, CCH$_3$), 32.7–26.5 (m, CMe) ppm. MS (EI) *m/z*: 982 with appropriate isotope ratio for (C$_{62}$H$_{60}$Cl$_2$ N$_2$O$_2$Ti$^+$).

Polymerization Experiments

Polymerizations were performed in a 1.0 L Büchi stainless steel autoclave equipped with Julabo ATS-3 and Lauda RK 20 temperature controlling units. Toluene (200 mL) and the co-catalyst (MAO) were introduced to the argon-purged autoclave reactor. Once the polymerization temperature was reached, the reactor was charged with ethylene to the appropriate pressure. Polymerizations were initiated by injecting 20 mL of the catalyst precursor solution (2–20 μmol solution in toluene) into the reactor. Mechanical stirring was applied at a speed of 800 r.p.m. During the polymerizations the partial pressure of ethylene and the temperature were maintained constant. Ethylene consumption was measured using a calibrated mass flow meter and monitored together with the autoclave temperature and pressure. The polymerization reaction was terminated by pouring the contents of the reactor into methanol, which was then acidified with a small amount of concentrated hydrochloride acid. The solid polyethylene was collected by filtration, washed with methanol and dried overnight at 70 °C.

Theoretical Calculations

Geometry optimizations were performed at the HF/3-21G* level, which has been shown to provide reliable structures for Group 4 transition metal complexes, especially for titanium based complexes.[16,17] Based on earlier studies, neither increasing the size of the basis set nor inclusion of electron correlation at the MP2 level has a significant influence on the geometries; however, these would certainly increase calculation times. Single point MP2 calculations were performed to confirm the relative stabilization order of conformations of the studied titanium complexes. For single point calculations, the basis set 6-31G* for C, H, O and N and a generated basis set of equal level for Ti were used. The stabilizations orders produced by both methods were generally in good agreement with each other. Geometry minima were confirmed by frequency calculations. All calculations were carried out by the Gaussian 03 program package.

Supporting Information (see also the footnote on the first page of this article): selected ^{1}H and ^{13}C NMR spectra of the titanium complexes **1-Ti** to **6-Ti**, dynamic NMR spectrum of **1-Ti**, HSQC spectrum of **6-Ti**, all of the ^{13}C NMR resonances of the titanium complexes **1-Ti** to **3-Ti**, **5-Ti** and **6-Ti** and ^{1}H NMR resonances of the complexes **5-Ti** and **6-Ti**.

Acknowledgments

A. Pärssinen, T. Luhtanen, T. Pakkanen, M. Leskelä, T. Repo

[1] a) H. Makio, T. Fujita *Acc. Chem. Res.* **2009**, DOI: 10.1021/ar900030a; b) H. Makio, N. Kashiwa, T. Fujita, *Adv. Synth. Catal.* **2002**, *344*, 477–493.

[2] A. Pärssinen, T. Luhtanen, M. Klinga, T. Pakkanen, M. Leskelä, T. Repo, *Organometallics* **2007**, *26*, 3690–3698.

[3] A. Pärssinen, T. Luhtanen, M. Klinga, T. Pakkanen, M. Leskelä, T. Repo, *Eur. J. Inorg. Chem.* **2005**, *11*, 2100–2109.

[4] J. Strauch, T. H. Warren, G. Erker, R. Frölich, P. Saarenketo, *Inorg. Chim. Acta* **2000**, *300–302*, 810–821.

[5] A. Cherian, E. Lobkovsky, G. Coates, *Macromolecules* **2005**, *38*, 6259–6268.

[6] Y. Tohi, H. Makio, S. Matsui, M. Onda, T. Fujita, *Macromolecules* **2003**, *36*, 523–525.

[7] P. Woodman, N. Alcock, I. Munslow, C. Sanders, P. Scott, *J. Chem. Soc., Dalton Trans.* **2000**, *19*, 3340–3346.

[8] a) T. Repo, M. Klinga, P. Pietikäinen, M. Leskelä, A.-M. Uusitalo, T. Pakkanen, K. Hakala, P. Aaltonen, B. Löfgren, *Macromolecules* **1997**, *30*, 171–175; b) M. Wang, H. Zhu, K. Jin, D. Dai, L. Sun, *J. Catal.* **2003**, *220*, 392–398; c) H. Zhu, M. Wang, C. Ma, B. Li, C. Chen, L. Sun, *J. Organomet. Chem.* **2005**, *690*, 3929–3936; d) I. Kim, Y. Ha, Z. Sun, F. Dan, C.-S. Ha, U. Lee, *Macromol. Rapid Commun.* **2004**, *25*, 1319–1323.

[9] A. Soriente, M. De Rosa, M. Lamberti, C. Tedesco, A. Scettri, C. Pellecchia, *J. Mol. Catal. A* **2005**, *235*, 253–259.

[10] M. Strianese, M. Lamberti, M. Mazzeo, C. Tedesco, C. Pellecchia, *J. Mol. Catal. A* **2006**, *258*, 284–291.

[11] T. Fujita, Y. Tohi, M. Mitani, S. Matsui, J. Saito, M. Nitabaru, K. Sugi, H. Makio, T. Tsutsui, *Eur. Pat. Appl.* **1998**, EP 874005 A1 19981028.

[12] S. Matsui, Y. Tohi, M. Mitani, J. Saito, H. Makio, H. Tanaka, M. Nitabaru, T. Nakano, T. Fujita, *Chem. Lett.* **1999**, *10*, 1065–1066.

[13] M. Mitani, J. Mohri, Y. Yoshida, J. Saito, S. Ishii, K. Tsuru, S. Matsui, R. Furuyama, T. Nakano, H. Tanaka, S.-i. Kojoh, T. Matsugi, N. Kashiwa, T. Fujita, *J. Am. Chem. Soc.* **2002**, *124*, 3327–3336.

[14] H. Musso, W. Steckelberg, *Justus Liebigs Ann. Chem.* **1966**, *693*, 187–196.

[15] S. Matsui, M. Mitani, J. Saito, Y. Tohi, H. Makio, N. Matsukawa, Y. Takagi, K. Tsuru, M. Nitabaru, T. Nakano, H. Tanaka, N. Kashiwa, T. Fujita, *J. Am. Chem. Soc.* **2001**, *123*, 6847–6856.

[16] M. J. Frisch, G. W. Trucks, H. B. Schlegel, G. E. Scuseria, M. A. Robb, J. R. Cheeseman, J. A. Montgomery Jr, T. Vreven, K. N. Kudin, J. C. Burant, J. M. Millam, S. S. Iyengar, J. Tomasi, V. Barone, B. Mennucci, M. Cossi, G. Calmani, N. Rega, G. A. Petersson, H. Nakatsuji, M. Hada, M. Ehara, K. Toyota, R. Fukuda, J. Hasegawa, M. Ishida, T. Nakajima, Y. Honda, O. Kitao, H. Nakai, M. Klene, X. Li, J. E. Knox, H. P. Hratchian, J. B. Cross, C. Adamo, J. Jaramillo, R. Gomperts, R. E. Stratmann, O. Yazyev, A. J. Austin, R. Cammi, C. Pomelli, J. W. Ochterski, P. Y. Ayala, K. Morokuma, G. A. Voth, P. Salvador, J. J. Dannenberg, V. G. Zakrzewski, S. Dapprich, A. D. Daniels, M. C. Strain, O. Farkas, D. K. Malick, A. D. Rabuck, K. Raghavachari, J. B. Foresman, J. V. Ortiz, Q. Cui, A. G. Baboul, S. Clifford, J. Cioslowski, B. B. Stefanov, G. Liu, A. Liashenko, P. Piskorz, I. Komaromi, R. L. Martin, D. J. Fox, T. Keith, M. A. Al-Laham, C. Y. Peng, A. Nanayakkara, M. Challacombe, P. M. W. Gill, B. Johnson, W. Chen, M. W. Wong, C. Gonzalez, J. A. Pople, Gaussian Inc., Pittsburgh PA, **2003**.

[17] a) M. Linnolahti, T. A. Pakkanen, *Macromolecules* **2000**, *33*, 9205–9214; b) M. Linnolahti, P. Hirva, T. A. Pakkanen, *J. Comput. Chem.* **2001**, *22*, 51–64.

Nickelacyclic Carboxylates with Pyridine-Based Ligand Sets – From Mononuclear Complexes to Supramolecular Architectures by Hydrogen Bonding

Jens Langer,*[a] Dirk Walther,[a] Astrid Malassa,[a] Matthias Westerhausen,[a] and Helmar Görls[a]

In Memoriam Professor Egon Uhlig

A series of nickelacyclic carboxylates of the general formula $[Ni(CH_2CH_2COO)(L_2)]$ with p-substituted pyridine ligands (**2**: L = 4-picoline; **3**: L = 4-MeO_2C-C_4H_4N; **4**: 4-Me_2N-C_4H_4N) was synthesized and characterized by NMR spectroscopy. A correlation between the shift of the CH_2 groups of the nickelacycle in the ^1H NMR spectra and basicity of the used pyridine ligand was observed. Furthermore, amino-substituted pyridine derivatives were used in ligand-ex-change reactions leading to supramolecular assemblies via H-bond formation between the amino function and the carboxylate group. Depending on the ligand used, discrete dimers [**5**: L_2 = (*t*Bu)(Me)_2Si-aminomethylpyridine], chains [**6**: L_2 = 2-(aminomethyl)pyridine] or layers (**7**: L = 4-H_2N-C_4H_4N) were observed. The molecular structures of all new compounds **2–7** were determined by X-ray measurement.

Introduction

Saturated nickelacyclic carboxylates are a well-known group of compounds which have been synthesized by different synthetic approaches,[1–3] among them the oxidative addition of cyclic anhydrides to zero-valent nickel compounds followed by decarbonylation as developed by Uhlig and co-workers.[4] Particularly interesting is their preparation by oxidative coupling of CO_2 and simple alkenes at the nickel centre,[5–7] which can be considered as the initial step of so far not realized catalytic reactions using CO_2 as a C1 building block.[8,9] Some of those complexes are valuable starting compounds in organic synthesis, for example for the preparation of carboxylic acids or their derivatives.[10–12] Furthermore, some nickelacycles can be used as precursors for oligo-nuclear coordination compounds of nickel.[13]

We recently reported the preparation of pyridine-stabilized nickelacyclic carboxylates, which proved to be useful starting compounds for ligand-exchange reactions.[14] By utilizing these complexes it was possible to greatly enhance the ligand pool available for stabilizing nickelacyclic carboxylates. Besides N-heterocyclic carbenes[15] and 1,2-diiminoethane derivatives,[16] monodentate phosphane li-

gands can be introduced in nickelacyclic carboxylates, resulting in the ligand-driven self-assembly to oligomeric derivatives by formation of Ni–O–C=O–Ni or Ni–O–Ni bridges.[17]

These interesting results encouraged us to undertake further investigations in the field of supramolecular organometallic chemistry.[18] Although the construction of supramolecular aggregates from well-defined monomeric organometallic compounds is generally a challenging goal, no further investigations with nickelacyclic carboxylates have been reported so far. Modern supramolecular chemistry knows of many connectivities between monomers, among them dative bonds, π-interactions, secondary bonds or hydrogen bonds. The last-mentioned seemed to be a suitable tool to generate supramolecular aggregates using nickelacyclic carboxylates, since there are different alcohol adducts known.[16,17,19] In addition, the introduction of hydrogen-bond donors into the neutral ligand may enhance the reactivity and selectivity of such nickelacycles in organic synthesis via substrate recognition and pre-coordination.

In this paper, we describe the preparation and characterization of new monomeric nickelacyclic carboxylates containing different pyridine derivatives as neutral ligands. From these discrete molecules different supramolecular assemblies can be derived, if NH functionalities are introduced into the ligands. Depending on the ligand used, 1- or 2-dimensional hydrogen-bond networks are found.

[a] Institute of Inorganic and Analytical Chemistry,
Friedrich-Schiller-University Jena,
Am Steiger 3, Haus 4, 07743 Jena, Germany
E-mail: j.langer@uni-jena.de

Results and Discussion

Synthesis of Monomeric Nickelacyclic Carboxylates

Similar to the recently reported synthesis of [Ni(C₂H₄-COO)(py)₂][14] it is possible to derive the corresponding 4-picoline complex by evaporating a solution of [Ni(C₂H₄-COO)(tmeda)] (1)[20] in 4-picoline to dryness. The remaining residue was identified as [Ni(C₂H₄COO)(4-Me-py)₂] (2) by NMR measurement and elemental analysis. Additionally, the molecular structure was determined by X-ray diffraction (Figure 1). This simple strategy failed to yield the desired derivatives, if less basic pyridine derivatives were applied to this reaction.
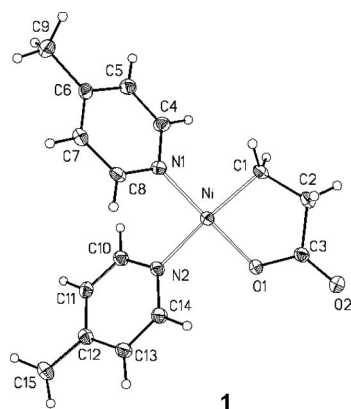

Figure 1. Molecular structure of 2. Selected bond lengths [Å] and angles [°]: Ni–C(1) 1.915(3), Ni–O(1) 1.860(3), Ni–N(1) 1.895(3), Ni–N(2) 1.992(3), N(1)–Ni–N(2) 92.49(12), C(1)–Ni–O(1) 85.68(13), N(2)–Ni–O(1) 89.96(11), C(1)–Ni–N(1) 92.46(14).

For instance, isonicotinic acid methyl ester was not capable of replacing tmeda, even if used as solvent. Only crystals of [Ni(C₂H₄COO)(tmeda)]·4-MeO₂C-py (Figure 2) were obtained from the reaction mixture. In order to isolate the desired compound it was necessary to employ [Ni(C₂H₄-COO)(py)₂] as the starting compound underlining its superiority in ligand-exchange reactions (Scheme 1).
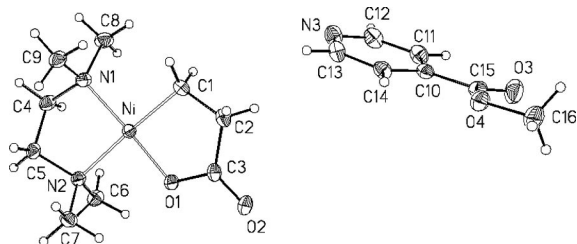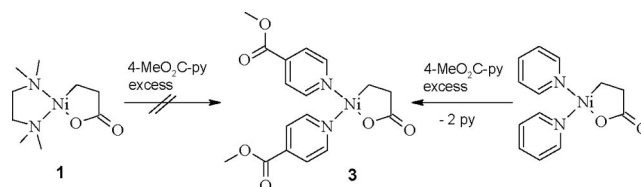

Figure 2. Molecular structure of 1·4-CH₃O₂C-py. Selected bond lengths [Å] and angles [°]: Ni–C(1) 1.9220(17), Ni–O(1) 1.8553(12), Ni–N(1) 1.9565(15), Ni–N(2) 2.0246(14), N(1)–Ni–N(2) 87.63(6), C(1)–Ni–O(1) 87.08(7), N(2)–Ni–O(1) 89.76(5), C(1)–Ni–N(1) 95.52(7).

The molecular structure of [Ni(C₂H₄COO)(4-MeO₂C-py)₂] (3) was determined by X-ray diffraction (Figure 3). In order to elucidate the influence of the basicity of the used

Scheme 1. Formation of 3.

pyridine derivative on measurable values like bond angles, bond lengths or NMR shifts, a nickelacyclic carboxylate with 4-Me₂N-py (4) was also prepared and its molecular structure was determined by X-ray diffraction experiments as well (Figure 5). When compared to the molecular structures of 2, 3 and [Ni(C₂H₄COO)(py)₂], almost no changes in bond lengths were found. Although the Ni–O1 bond is elongated from 1.852(4) Å in 3, containing the least-basic pyridine ligand, to 1.867(2) Å in 4 with the most basic one, this does not seem to be a general trend since the observed values of 1.8655(13) Å of [Ni(C₂H₄COO)(py)₂] and 1.860(3) Å of 2 do not fit into the scheme.
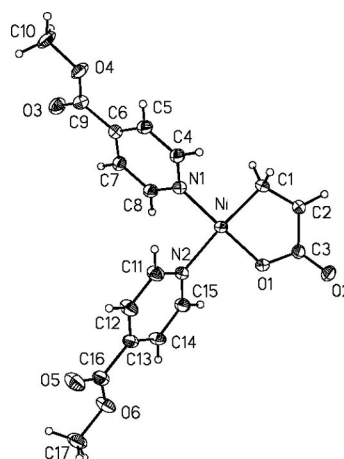

Figure 3. Molecular structure of 3 (cocrystallized THF omitted). Selected bond lengths [Å] and angles [°]: Ni–N1 1.873(4), Ni–N2 1.998(5), Ni–C1 1.926(6), Ni–O1 1.852(4), C1–C2 1.522(8), C2–C3 1.513(8), C3–O1 1.302(7), C3–O2 1.220(7), N1–Ni–N2 92.43(19), N1–Ni–C1 92.3(2), N2–Ni–O1 89.03(18), C1–Ni–O1 86.5(2).

While there is no distinct correlation between the basicity of the pyridine derivatives used and structural features of the corresponding nickelacyclic carboxylates, such a correlation was found for the ¹H NMR shift of the CH₂ groups of the nickelalactones. The pK_a values of the corresponding pyridinium ions in water were taken as values for the basicity of the pyridine derivatives.[21] Although those values are not correct for DMF as solvent, the order and the differences between the ligands should be similar.

As shown in Figure 4, an increase of the pK_a value of the ligand leads to a high-field shift of both CH₂ groups within the nickelalactone moiety. As expected, this shift is stronger for the Ni-CH₂ group. A similar influence of the ligand to the ¹³C NMR signals should be expected, but even

though nickelacyclic carboxylates with more basic ligands tend to have lower values for δ(Ni-C), no rigid correlation to pK_a values was found.
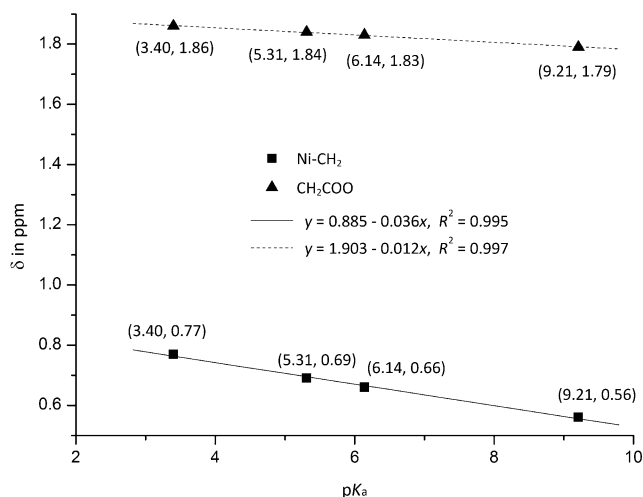

Figure 4. Linear correlation of the ligand basicity (pK_a values of the corresponding pyridinium ions were used) and the ^{1}H NMR shift of the CH_2 groups of the resulting complexes.

Supramolecular Structures Derived from Nickelacyclic Carboxylates

The carboxylate functionality of nickelalactones is a potential H-bond acceptor as proven by the isolation and structural characterization of several alcohol adducts.[16,17,19] Depending on the neutral ligands used, the endocyclic as well as the exocyclic oxygen was involved in hydrogen-bond formation. In order to obtain more complex supramolecular structures, H-bond donor groups (–NH or –OH) should be introduced into the neutral ligand. Chelating ligands were used in initial experiments to enhance the stability of the nickelacyclic carboxylates formed. A group of ligands, which meets these requirements, are 2-aminomethylpyridines which can form a rigid five-membered chelate ring at metal centres and bear additional NH functionalities to form H-bridges.

The nickelacycle **5** with *N*-[(*t*Bu)(Me)$_2$Si-aminomethyl]-pyridine as chelating ligand was prepared by ligand exchange starting with [Ni(C$_2$H$_4$COO)(py)$_2$] and was characterized by NMR measurements. From a solution in THF green crystals were obtained and the solid-state structure of **5** was determined by X-ray measurements (Figure 5). Figure 6 shows that the compound [Ni{(*t*Bu)(Me)$_2$Si-ampy}-(C$_2$H$_4$COO)] (**5**) is a typical nickelacyclic carboxylate with a nickel centre in an essentially square-planar environment. The nitrogen donor atom of the pyridine ring is in *trans* position to the oxygen atom of the carboxylate group, and the coordinated amine nitrogen atom is in *trans* position to the carbon atom. Compound **5** shows planar chirality and in the crystal a racemic mixture of enantiomers is found.

Each enantiomer forms a dimeric unit with its opposite by hydrogen bonding between the NH group of the ligand and the *endocyclic* oxygen of the carboxylate group.
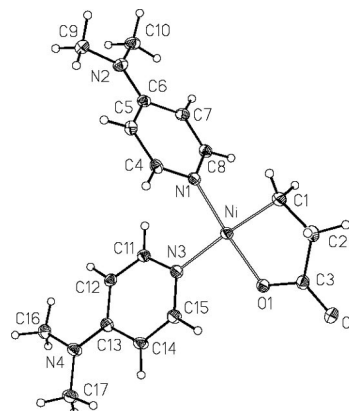

Figure 5. Molecular structure of **4** (cocrystallized DMF omitted). Selected bond lengths [Å] and angles [°]: Ni–N1 1.890(2), Ni–N3 2.012(2), Ni–C1 1.920(3), Ni–O1 1.867(2), C1–C2 1.529(4), C2–C3 1.509(4), C3–O1 1.299(4), C3–O2 1.234(4), N1–Ni–N3 93.56(10), N1–Ni–C1 90.22(12), N3–Ni–O1 89.81(9), C1–Ni–O1 86.37(11).
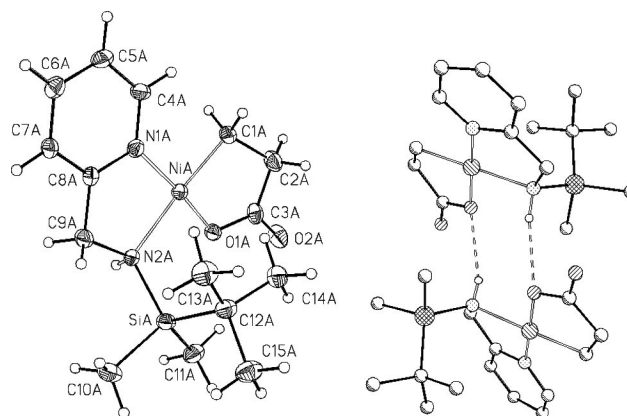

Figure 6. Molecular structure of **5** (left) and dimeric unit (right); (cocrystallized THF is omitted for clarity). Selected bond lengths [Å] and angles [°]: NiA–N1A 1.889(3), NiA–N2A 2.027(3), NiA–C1A 1.921(4), NiA–O1A 1.859(2), C1A–C2A 1.519(6), C2A–C3A 1.512(6), C3A–O1A 1.298(5), C3A–O2A 1.224(5), SiA–N2A 1.797(4), N1A–NiA–N3A 86.43(13), N1A–NiA–C1A 96.80(16), N2A–NiA–O1A 90.88(12), C1A–NiA–O1A 86.13(14).

A larger hydrogen-bond system was found when the unsubstituted 2-aminomethylpyridine (ampy) was applied to ligand-exchange reactions. In this case the corresponding compound [Ni(ampy)(C$_2$H$_4$COO)] (**6**) is insoluble in common aprotic solvents and was characterized by single-crystal X-ray diffraction and elemental analysis (Figure 7).

Compared with its silylated analogue, **6** shows some differences in its molecular as well as crystal structure. While the complex is still square planar, the ligand arrangement around the nickel centre has changed. The nitrogen atom of the pyridine ring is now found in *trans* position to the coordinated carbon atom while the amine nitrogen occupies the position *trans* to the oxygen atom. This change could be the result of the different basicity of the amine nitrogen
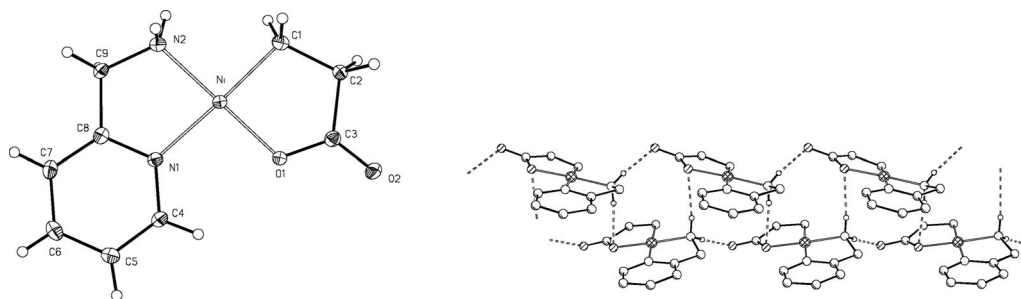
Figure 7. Molecular structure of **6** (top) and formed double chain (bottom). Selected bond lengths [Å] and angles [°]: Ni–N1 1.961(2), Ni–N2 1.990(2), Ni–C1 1.910(3), Ni–O1 1.8635(16), C1–C2 1.520(4), C2–C3 1.523(3), C3–O1 1.301(3), C3–O2 1.231(3), N1–Ni–N2 84.85(9), N2–Ni–C1 92.51(10), N1–Ni–O1 94.90(7), C1–Ni–O1 87.69(9).

in ampy and its silylated form. Another driving force for this structural change may be the formation of a different supramolecular architecture as was found for **6**. Instead of discrete dimers a chain is formed in which the molecules are linked by a hydrogen bridge between the *exocyclic* oxygen of the carboxylate function and the NH$_2$ group. In solid state another short contact between the *endocyclic* oxygen and a NH$_2$ group of a neighbouring chain is found leading to double chains in the crystal.

The larger number of potential H-bond donors results in this case in an increase of dimensionality of the formed network. In order to further enhance the ratio of H-bond donors to H-bond acceptors it is necessary to introduce a second NH$_2$ group into the neutral ligands. Since the Ni–C bond has proven to be stable against NH functionalities so far, the simplest way to do this is to switch back to monodentate pyridine ligands as described above.

By using 4-H$_2$N-py as ligand the compound [Ni(C$_2$H$_4$-COO)(4-H$_2$N-py)$_2$] **7** was prepared by addition of two equivalents of the ligand to a solution of [Ni(C$_2$H$_4$-COO)(py)$_2$] in DMF. The resulting green precipitate was identified by NMR measurements as **7**. Initial attempts to obtain crystals from DMF failed but recrystallization from a DMF/THF mixture resulted in suitable crystals for X-ray measurement. The determined molecular structure is similar to those of compounds **2**–**4** (Figure 8). However, compound **7** forms a 2-dimensional hydrogen-bond network in the crystal.

As shown in Figure 8 the smallest subunit found within this hydrogen-bond network is a dimer, which is connected via H-bonds between the exocyclic oxygen of the carboxylate group and the NH$_2$ group of the ligand in *cis* position to the carboxylate function of the neighbouring molecule. These dimers form folded double chains in the crystal as can be seen in Figure 9.

In a next step a layer is formed by connecting the double chains in a stair-like orientation by hydrogen bonding (Figure 10). Above and below the layer DMF molecules are attached by H-bonds between the remaining unused NH functions and the carbonyl function of DMF. There is no bonding between different layers. The rest of the space is filled with cocrystallized THF. Overall, a discreet sequence of solvent layers and layers of the organometallic compound is found in the crystal.
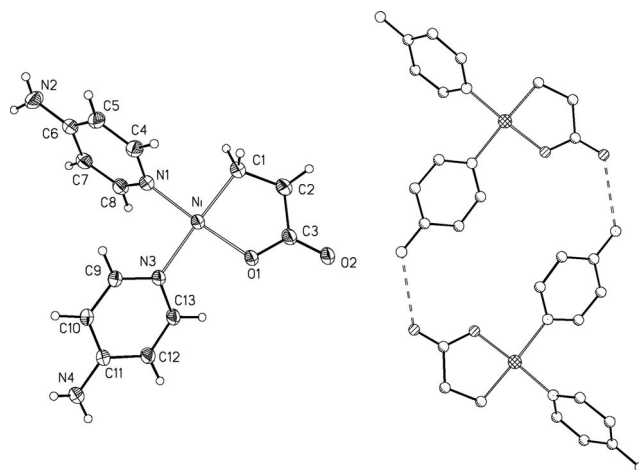
Figure 8. Molecular structure of **7** (cocrystallized THF and DMF omitted) (left); dimeric unit (right). Selected bond lengths [Å] and angles [°]: Ni–N1 1.885(3), Ni–N3 1.999(3), Ni–C1 1.915(3), Ni–O1 1.882(2), C1–C2 1.505(5), C2–C3 1.504(5), C3–O1 1.281(4), C3–O2 1.244(4), N1–Ni–N3 92.57(10), N1–Ni–C1 90.15(13), N3–Ni–O1 90.86(9), C1–Ni–O1 86.42(12).

Figure 9. Hydrogen-bond network of **7**, double chain (top); view along *b*-axis (bottom).

In the above-described H-bond network the more basic endocyclic oxygen is not used as the H-bond acceptor at all. Compared to alcohol adducts of nickelacyclic carboxylates,

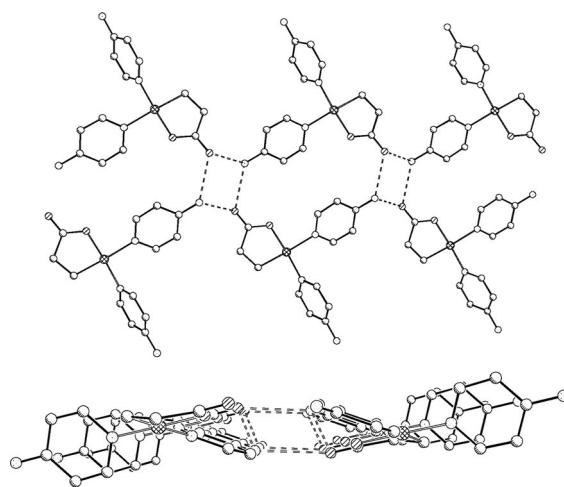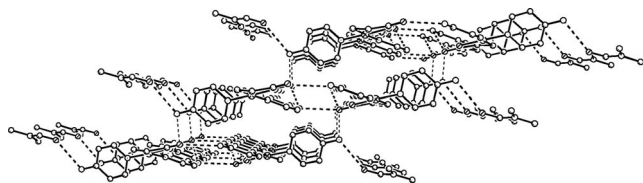Figure 10. Hydrogen-bond network of **7** (layer, view along *b*-axis).

where increased steric pressure of the ligand in *cis* position of the carboxylate function seems to prevent H-bond formation to the endocyclic oxygen (the H-bond is established to the exocyclic oxygen instead), in the case of **7** the formation of an extensive network seems to be the driving force. The exclusive formation of hydrogen bonds towards the exocyclic oxygen atom of the carboxylate function also results in detectable changes of the bond lengths when compared to **4**.

The Ni–O1 bond in **7** is lengthened to 1.882(2) Å [**4**: 1.867(2) Å]. In addition the value observed for the O2–C3 bond length of 1.244(4) Å is also slightly enhanced [**4**: 1.234(4) Å] while the O1–C3 bond of 1.281(4) Å tends to be shorter than in **4** [1.299(3) Å]. All together these changes can be interpreted as an increased contribution of the resonance structure **B** (see Scheme 2) to the real bonding situation.
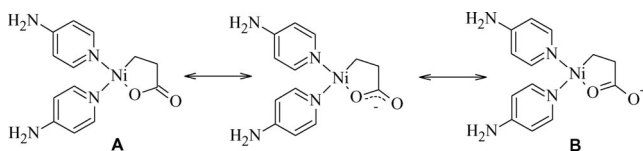
Scheme 2. Resonance structures of **7**.

Conclusions

The systematic variation of the ligand basicity as investigated here using *para*-substituted pyridine derivatives, did not lead to systematic differences of bond angles and lengths of the synthesized nickelacyclic carboxylates. However, a correlation with the chemical shift of the CH_2 groups of those compounds was observed. The introduction of NH groups into the ligands resulted in the formation of different supramolecular aggregates (dimers, double chains or layers), depending on the ligand geometry and the ratio of hydrogen-bond donors to hydrogen-bond acceptors. As expected the increase of this ratio by incorporation of further NH functions led to a higher dimensionality of the formed network. In the case of **7** containing two 4-amino pyridine ligands a 3-dimensional network should be expected, but by use of DMF, a competitive H-bond acceptor was introduced into the system resulting in a layered structure. Since nickelacyclic carboxylates can be easily thermally activated for further reactions these compounds are interesting starting materials for the synthesis of new coordination compounds of nickel(II). Depending on the ligand used, β-hydride elimination or reductive decoupling of the nickela-

cycle are possible initial steps of such a thermally activated reaction.[16] The combination of pre-organization by hydrogen bonding and fine tuning of the stability and reactivity of the nickelacycle by variation of the ligand set offers an interesting approach towards new oligo- and polynuclear nickel compounds via thermally induced solid-state reactions. Additionally, these amino-substituted nickelacyclic carboxylates should allow pre-coordination of organic substrates containing hydrogen-bond acceptors like carbonyl functions and therefore may offer enhanced reactivity or selectivity of such organonickel compounds in organic synthesis.

Experimental Section

General Remarks: Infrared spectra were recorded with a Perkin–Elmer 2000 FT-IR. ^{1}H NMR spectra were recorded with a Bruker 400 MHz/200 MHz spectrophotometer.

All manipulations were carried out using modified Schlenk techniques under argon. Prior to use, THF, benzene and diethyl ether were dried with potassium hydroxide and distilled from sodium/benzophenone. DMF, 4-picoline and isonicotinic acid methyl ester were dried with CaH_2.

Caution: DMF may decompose explosively when heated with strong bases. Do not heat DMF over CaH_2!

[(tmeda)Ni(C_2H_4COO)] and [(py)$_2$Ni(C_2H_4COO)] were prepared according to literature procedures.[20,14] [(*t*Bu)(Me)$_2$Si-aminomethyl]pyridine was prepared in analogy to a known procedure but further purified by distillation in a vacuum to remove residual LiCl.[22]

4-(Dimethylamino)pyridine and 4-aminopyridine were purchased from Aldrich and used without further purification.

[Ni(C_2H_4COO)(4-Me-py)$_2$] (2): Green [Ni(C_2H_4COO)(tmeda)] (0.23 g, 0.93 mmol) was suspended in 4-picoline (5 mL) and stirred for 15 min. Afterwards the reaction mixture was evaporated to dryness in vacuo. The formed crude product was recrystallized from 4-picoline. The saturated solution was cooled from room temp. to –20 °C resulting in the formation of green crystals of **2** suitable for X-ray measurements. The product was isolated by filtration and dried in vacuo; yield 0.16 g (54%). $C_{15}H_{18}N_2NiO_2$ (317.0): calcd. C 56.83, H 5.72, N 8.84; found C 56.54, H 5.88, N 9.03. ^{1}H NMR (200 MHz, [D$_7$]DMF, 25 °C): $\delta = 0.66$ [t, $^3J_{H,H} = 7.5$ Hz, 2 H, Ni-CH_2], 1.83 (t, $^3J_{H,H} = 7.5$ Hz, 2 H, CH_2-COO), 2.33 (s, 6 H, CH_3), 7.26 (m, 4 H, CH py), 8.24 (br., 2 H, CH py), 8.79 (br., 2 H, CH py) ppm. $^{13}C\{^1H\}$ NMR (50 MHz, [D$_7$]DMF): $\delta = 1.7$ (br., Ni-CH_2), 20.81 (CH_3), 20.9 (CH_3), 38.3 (CH_2-COO), 126.0 (*m*-CH, py), 126.7 (*m*-CH, py), 150.0 (o-CH, py), 150.1 (*o*-CH, py), 152.1 (*p*-C, py), 187.0 (COO) ppm. IR (Nujol): $\tilde{v}$(C=O) = 1617 cm^{-1} (s).

[Ni(C_2H_4COO)(4-MeO$_2$C-py)$_2$] (3): Green [Ni(C_2H_4COO)(py)$_2$] (0.64 g, 2.21 mmol) was dissolved in isonicotinic acid methyl ester (6 mL). The uncoordinated pyridine formed was removed by distillation in vacuo. The resulting red solution was filtered, layered with diethyl ether (10 mL) and stored at –20 °C for 2 days. Afterwards the formed microcrystalline precipitate was isolated by filtration, washed with diethyl ether (3 mL) and dried in vacuo; yield 0.65 g (54%) red **3**·4-CH$_3$OOC-py. $C_{24}H_{27}N_3NiO_8$ (544.2): calcd. C 52.97, H 5.00, N 7.72; found C 52.59, H 4.65, N 7.67. ^{1}H NMR (200 MHz, [D$_7$]DMF, 25 °C): $\delta = 0.77$ (t, $^3J_{H,H} = 7.6$ Hz, 2 H, Ni-CH_2), 1.86 (t, $^3J_{H,H} = 7.6$ Hz, 2 H, CH_2-COO), 3.95 (s, 9 H, 3 × O-

CH$_3$), 7.82 (m, 2 H, 2×m-CH py), 7.90 (br., 4 H, m-CH py), 8.81 (br., 4 H, o-CH py), 9.21 (m, 2 H, o-CH py) ppm. ^{13}C{^{1}H} NMR (50 MHz, [D$_7$]DMF): δ = 3.7 (Ni-CH$_2$), 38.2 (CH_2-COO), 53.1 (2×CH$_3$-O), 53.4 (CH$_3$-O), 123.7 (br., 4×CH), 124.3 (2×CH), 138.0 (3×i-C-COO-), 151.4 (br., 4×CH), 153.7 (2×CH), 165.0 (COO), 165.9 (br., 2×COO), 186.2 (Ni-OOC) ppm. IR (Nujol): $\tilde{\nu}$(C=O$_{Ester}$) = 1735 cm^{-1} (vs), ν(C=O$_{Ni-OCO}$) = 1643 cm^{-1} (vs).

Crystals of **3**·THF suitable for X-ray diffraction experiments were obtained from a saturated solution in THF at –20 °C.

[Ni(C$_2$H$_4$COO)(4-Me$_2$N-py)$_2$] (4): 4-(Dimethylamino)pyridine (0.60 g, 4.91 mmol) was added to a stirred suspension of green [Ni(C$_2$H$_4$COO)(py)$_2$] (0.71 g, 2.46 mmol) in THF (20 mL). The resulting reaction mixture was stirred for 30 min. Afterwards the formed product was isolated by filtration, washed with THF (5 mL) and dried in vacuo; yield 0.92 g (92%) green **4**·0.5THF. ^{1}H NMR (200 MHz, [D$_7$]DMF, 25 °C): δ = 0.56 (t, $^3J_{H,H}$ = 7.4 Hz, 2 H, Ni-CH$_2$), 1.79 (br., 4 H, CH$_2$-COO + CH$_2$ THF), 3.02 (s, 12 H, 4×CH$_3$), 3.62 (br., 2 H, O-CH$_2$ THF), 6.4–6.7 (br., 2 H, m-CH py), 6.61 (d, J = 6.2 Hz, 2 H, m-CH py), 7.63 (br., 2 H, o-CH py), 8.27 (d, J = 6.2 Hz, 2 H, o-CH py) ppm. ^{13}C{^{1}H} NMR (50 MHz, [D$_7$]DMF): δ = 1.6 (br., Ni-CH$_2$), 26.0 (CH$_2$ THF), 38.2 (CH_2COO), 39.0 (4×CH$_3$), 67.9 (O-CH$_2$ THF), 107.2 (br., 2×m-CH py), 108.2 (2×m-CH py), 149.4 (br., 2×o-CH py), 151.1 (2×o-CH py), 154.7 (i-C py), 155.1 (i-C py), 187.1 (COO) ppm. IR (Nujol): $\tilde{\nu}$(C=O) = 1626 cm^{-1} (vs). Crystals of **4**·DMF suitable for X-ray diffraction experiments were obtained by cooling a saturated solution of **4**·0.5THF in DMF from room temp. to 5 °C.

[Ni{(tBu)(Me)$_2$Si-ampy}(C$_2$H$_4$COO)] (5): N-[(Dimethyl-$tert$-butylsilyl)aminomethyl]pyridine (0.16 g, 0.72 mmol) was added to a stirred suspension of green [Ni(C$_2$H$_4$COO)(py)$_2$] (0.20 g, 0.69 mmol) in THF (8 mL). The resulting reaction mixture was stirred for 1 h. Afterwards the microcrystalline solid formed was isolated by filtration, washed with diethyl ether (5 mL) and dried

in vacuo; yield 0.15 g (51%) green **5**·THF. ^{13}C{^{1}H} NMR (50 MHz, [D$_8$]THF): δ = –4.0 (br., 2 C, Si-CH$_3$), 2.4 (s, 1 C, Ni-CH$_2$), 19.4 (s, 1 C, Si-C), 27.3 (s, 3 C, CH$_3$), 36.7 (s, 1 C, CH_2COO), 49.7 (s, 1 C, CH$_2$-N), 121.7 (s, 1 C, CH py), 123.8 (s, 1 C, CH py), 137.2 (s, 1 C, CH py), 148.5 (s, 1 C, CH py), 167.7 (s, 1 C, C py), 186.4 (s, 1 C, COO) ppm.

Crystals of **5**·THF suitable for X-ray diffraction experiments were obtained by cooling a saturated solution in THF from room temp. to –20 °C.

[Ni(C$_2$H$_4$COO)(ampy)](6): (Aminomethyl)pyridine was added to a stirred solution of green [Ni(C$_2$H$_4$COO)(py)$_2$] (0.16 g, 0.55 mmol) in DMF (5 mL) resulting in almost immediate precipitation of a green microcrystalline solid. The reaction mixture was stirred for an additional 30 min. Afterwards the solid was isolated by filtration, washed with THF (5 mL) and dried in vacuo; yield 0.12 g (91%). C$_9$H$_{12}$N$_2$NiO$_2$ (238.9): calcd. C 45.25, H 5.06, N 11.73; found C 45.14, H 4.92, N 11.77.

Crystals of **6** suitable for X-ray diffraction experiments were obtained directly from the reaction mixture.

[Ni(C$_2$H$_4$COO)(4-NH$_2$-py)$_2$] (7): 4-Aminopyridine (0.39 g, 4.14 mmol) was added to a stirred solution of green [Ni(C$_2$H$_4$-COO)(py)$_2$] (0.59 g, 2.04 mmol) in DMF (20 mL). The resulting solution was stirred for 30 min. Afterwards the reaction mixture was evaporated to dryness; yield quantitative (crude product, contains a small amount of uncoordinated 4-aminopyridine). ^{1}H NMR (200 MHz, [D$_7$]DMF, 25 °C): δ = 0.49 (br., 2 H, Ni-CH$_2$), 1.75 (br., 2 H, CH$_2$-COO), 6.45–6.63 (m, 8 H, CH py + NH$_2$), 7.47 (br., 2 H, CH py), 8.10 (br., 2 H, CH py) ppm. ^{13}C{^{1}H} NMR (50 MHz, [D$_7$]DMF): δ = 8.4 (Ni-CH$_2$), 38.2 (CH$_2$-COO), 110.5 (4×m-CH, py), 151.6 (4×o-CH, py), 156.0 (2×i-C, py), 194.4 (COO) ppm. IR (Nujol): $\tilde{\nu}$(NH$_2$) = 3340 cm^{-1} (m) + 3200 cm^{-1} (m); ν(C=O) = 1619 cm^{-1} (s).

Table 1. Crystal data and refinement details for the X-ray structure determinations.

Compound	**1**·C$_7$H$_7$NO$_2$	**2**	**3**	**4**	**5**	**6**	**7**
Formula	C$_9$H$_{20}$N$_2$NiO$_2$·C$_7$H$_7$NO$_2$	C$_{15}$H$_{18}$N$_2$NiO$_2$	C$_{17}$H$_{18}$N$_2$NiO$_6$·C$_4$H$_8$O	C$_{17}$H$_{24}$N$_4$NiO$_2$·C$_3$H$_7$NO	C$_{15}$H$_{26}$N$_2$NiO$_2$Si·C$_4$H$_8$O	C$_9$H$_{12}$N$_2$NiO$_2$	C$_{13}$H$_{16}$N$_4$NiO$_2$·C$_4$H$_8$O·C$_3$H$_7$NO
Fw [g mol^{-1}]	384.12	317.02	477.15	448.21	425.28	238.92	464.21
T [K]	–90(2)	–90(2)	–90(2)	–90(2)	–90(2)	–90(2)	–90(2)
Crystal system	monoclinic	monoclinic	triclinic	triclinic	triclinic	monoclinic	triclinic
Space group	$P2_1/n$	$P2_1/c$	$P\bar{1}$	$P\bar{1}$	$P\bar{1}$	$P2_1/c$	$P\bar{1}$
a [Å]	13.6990(4)	6.7981(2)	7.5858(6)	9.3138(3)	10.5065(7)	9.7809(5)	9.2506(2)
b [Å]	8.0903(3)	10.0785(4)	11.3934(7)	9.6236(3)	11.1870(5)	13.5576(9)	10.6596(3)
c [Å]	17.0800(5)	21.2740(8)	13.3860(9)	13.1854(4)	19.8033(9)	7.2050(7)	13.5731(4)
α [°]	90	90	107.720(4)	110.967(1)	94.435(4)	90	103.161(1)
β [°]	106.251(2)	93.629(3)	93.365(3)	96.150(1)	95.870(4)	103.861(4)	106.167(1)
γ [°]	90	90	90.591(3)	97.137(1)	111.675(4)	90	108.491(1)
V [Å^3]	1817.33(10)	1454.66(9)	1099.65(13)	1080.28(5)	2134.9(2)	927.60(12)	1143.40(5)
Z	4	4	2	2	4	4	2
ρ [g cm^{-3}]	1.404	1.448	1.441	1.378	1.323	1.711	1.348
μ [mm^{-1}]	10.92	13.36	9.27	9.28	9.85	20.63	8.83
Measured data	7832	5911	7269	7530	14383	6310	8211
Data with $I > 2\sigma(I)$	3474	2338	3569	3842	5268	1707	4145
Unique data (R_{int})	4142/0.0230	3297/0.0483	4798/0.0626	4893/0.0289	9401/0.0600	2110/0.0368	5181/0.0216
wR_2 (all data, on F^2)[a]	0.0852	0.1146	0.2666	0.1147	0.1539	0.0834	0.1591
R_1 [$I > 2\sigma(I)$][a]	0.0309	0.0440	0.0947	0.0425	0.0614	0.0334	0.0554
S[b]	1.011	0.937	1.064	0.871	1.014	1.027	1.016
Resid. dens. [e Å^{-3}]	0.522/–0.343	0.325/–0.325	0.686/–0.767	0.309/–0.388	0.624/–0.580	0.337/–0.494	0.647/–0.688
Absorption corr.	none	none	none	none	none	none	none
CCDC number	745120	745121	745122	745123	745124	745125	745126

[a] Definition of the R indices: $R_1 = (\Sigma||F_o| - |F_c||)/\Sigma|F_o|$; $wR_2 = \{\Sigma[w(F_o^2 - F_c^2)^2]/\Sigma[w(F_o^2)^2]\}^{1/2}$ with $w^{-1} = \sigma^2(F_o^2) + (aP)^2 + bP$; $P = [2F_c^2 + \max(F_o^2)]/3$. [b] $s = \{\Sigma[w(F_o^2 - F_c^2)^2]/(N_o - N_p)\}^{1/2}$.

Suitable crystals for X-ray diffraction experiments were obtained by cooling a saturated solution of **7** in a mixture of DMF and THF from room temperature to –20 °C.

X-Ray Crystallographic Study: The intensity data for the compounds were collected with a Nonius Kappa CCD diffractometer using graphite-monochromated Mo-K_α radiation. Data were corrected for Lorentz and polarization effects but not for absorption effects.[23,24] The structures were solved by direct methods (SHELXS[25]) and refined by full-matrix least-squares techniques against $F_o{}^2$ (SHELXL-97[26]). All hydrogen atoms for **6** and the hydrogen atoms for the amine-groups of **5** and **7** were located by difference Fourier synthesis and refined isotropically. All other hydrogen atoms were included at calculated positions with fixed thermal parameters. All nondisordered, non-hydrogen atoms were refined anisotropically.[26] Crystallographic data as well as structure solution and refinement details are summarized in Table 1. XP (SIEMENS Analytical X-ray Instruments, Inc.) was used for structure representations.

CCDC-745120 to -745126 (for assignments to compounds see Table 1) contains the supplementary crystallographic data for this paper. These data can be obtained free of charge from The Cambridge Crystallographic Data Centre via www.ccdc.cam.ac.uk/data_request/cif.

Acknowledgments

[1] T. Yamamoto, K. Igarashi, S. Komiya, A. Yamamoto, *J. Am. Chem. Soc.* **1980**, *102*, 7448.

[2] R. Fischer, D. Walther, G. Bräunlich, B. Undeutsch, H. Bandmann, *J. Organomet. Chem.* **1992**, *427*, 395.

[3] K. Sano, T. Yamamoto, A. Yamamoto, *Chem. Lett.* **1983**, 115.

[4] E. Uhlig, G. Fehske, B. Nestler, *Z. Anorg. Allg. Chem.* **1980**, *465*, 141–146.

[5] H. Hoberg, D. Schaefer, *J. Organomet. Chem.* **1983**, *251*, C51–C52.

[6] H. Hoberg, D. Schaefer, G. Burkhart, C. Krüger, M. J. Romão, *J. Organomet. Chem.* **1984**, *266*, 203–224.

[7] H. Hoberg, Y. Peres, C. Krüger, Y.-H. Tsay, *Angew. Chem.* **1987**, *99*, 799–800.

[8] I. Papai, G. Schubert, I. Mayer, G. Besenyei, M. Aresta, *Organometallics* **2004**, *23*, 5252.

[9] D. C. Graham, C. Mitchell, M. I. Bruce, G. F. Metha, J. H. Bowie, M. A. Buntine, *Organometallics* **2007**, *26*, 6784–6792.

[10] R. Fischer, D. Walther, G. Bräunlich, B. Undeutsch, W. Ludwig, *J. Organomet. Chem.* **1992**, *427*, 395–407.

[11] A. M. Castaño, A. M. Echavarren, *Organometallics* **1994**, *13*, 2262–2268.

[12] R. Fischer, B. Schönecker, D. Walther, *Synthesis* **1993**, 1267–1270.

[13] J. Langer, H. Görls, G. Gillies, D. Walther, *Z. Anorg. Allg. Chem.* **2005**, *631*, 2719–2726.

[14] J. Langer, R. Fischer, H. Görls, D. Walther, *J. Organomet. Chem.* **2004**, *689*, 2952.

[15] J. Langer, D. Walther, H. Görls, *J. Organomet. Chem.* **2006**, *691*, 4874–4881.

[16] R. Fischer, J. Langer, H. Görls, A. Malassa, D. Walther, G. Vaughan, *Chem. Commun.* **2006**, 2510–2512.

[17] J. Langer, R. Fischer, H. Görls, D. Walter, *Organometallics* **2005**, *24*, 272–279.

[18] For reviews see: a) I. Haiduk, F. T. Edelmann, *Supramolecular Organometallic Chemistry*, Wiley-VCH, Weinheim, **1999**; b) B. Moulton, M. J. Zaworotko, *Chem. Rev.* **2001**, *101*, 1629–1658; c) J. L. Atwood, J. W. Steed (Eds.), *Encyclopedia of Supramolecular Chemistry*, Dekker, New York, **2004**.

[19] B. Hipler, M. Döring, C. Dubs, H. Görls, T. Hübler, E. Uhlig, *Z. Anorg. Allg. Chem.* **1998**, *624*, 1329–1335.

[20] R. Fischer, B. Nestler, H. Schütz, *Z. Anorg. Allg. Chem.* **1989**, *577*, 111–114.

[21] E. Chrystiuk, A. Williams, *J. Am. Chem. Soc.* **1987**, *109*, 3040–3046.

[22] M. Westerhausen, T. Bollwein, N. Makropoulos, T. M. Rotter, T. Haberender, M. Suter, H. Nöth, *Eur. J. Inorg. Chem.* **2001**, 851–857.

[23] *COLLECT*, Data Collection Software; Nonius BV, Delft, The Netherlands, **1998**.

[24] Z. Otwinowski, W. Minor, *Processing of X-ray Diffraction Data Collected in Oscillation Mode*, in: *Methods in Enzymology*, vol. 276, *Macromolecular Crystallography*, part A (Eds.: C. W. Carter, R. M. Sweet), Academic Press, New York, **1997**, pp. 307–326.

[25] G. M. Sheldrick, *Acta Crystallogr., Sect. A* **1990**, *46*, 467–473.

[26] G. M. Sheldrick, *SHELXL-97* (rel. 97-2), University of Göttingen, Germany, **1997**.

Light-Induced Stored Information in Nanoparticles

Suzanne M. Neville,[a] Céline Etrillard,[a] Saket Asthana,[a] and Jean-François Létard*[a]

We investigate here the consequence on light-induced and thermally induced spin-crossover (SCO) properties with particle size reduction from the macroscopic to microscale to nanoscale domains. Three samples with distinct particle sizes of the SCO coordination polymer [Fe(NCS)$_2$(bpe)$_2$] [bpe = 1,2-bis(4′-pyridyl)ethane] have been prepared by water-in-oil reverse micelle methods. Comparison of the magnetic properties with particle size reduction of these and the original macroscale slow-grown crystals revealed that the spin transition becomes more gradual, more incomplete and concomitantly the transition temperature ($T_{1/2}$) decreases – much

like what is observed in metal dilution studies. Importantly, here, in the first photoinduced magnetic studies on a nanoparticle SCO system, we see that even on the nanoscale photoconversion of the low spin species to a metastable high-spin state is possible. Furthermore, particle size reduction appears to have little effect on the temperature at which the stored photomagnetic information is erased. These results highlight that light-induced SCO properties are governed by direct metal coordination environment (i.e., on the molecular scale), whereas, thermally induced magnetic properties rely more on crystal packing and ligand field effects.

Introduction

The ability to control the physical properties (i.e., superparamagnetism, spin crossover, photomagnetism and luminescence) of advanced materials on the molecular level is an important goal for the eventual realization of functional devices.[1–3] Materials that show magnetic switching, such as spin crossover (SCO) where multiple electronic states can be accessed through variation in external stimuli such as temperature, pressure and light, have been identified as a viable class of materials for incorporation into such devices (i.e., information storage, sensing or display devices) − in particular, when they show properties that can be accessed at room temperature.[2,4] The current challenge in this field is to control the cluster size towards the levels required for the achievement of nanoscale devices, whilst retaining the magnetic/cooperative properties.[2] To this end, it has recently been demonstrated that monodispersed nanoscale particles of SCO coordination polymers[5–10] can be fabricated by exploiting the established micelle techniques utilized for Prussian Blue analogues[11] (i.e., the "bottom-up" approach). This is an important step for emerging nanoscale technologies, as the alternate approach for miniaturizing particle size through mechanical processing into smaller particles (i.e., the "top-down" approach) results in gradual, diminished or even nonexistent SCO characteristics.[12,13] Although in an alternate top-down approach, micrometer-

and nanometer-sized patterns of SCO materials have been successfully achieved through a combination of lift-off and multilayer steps.[14]

With regard to the bottom-up approach, classically this has been achieved by well-established step-by-step combination of reactants and, indeed, has resulted in many mononuclear, dinuclear and polynuclear materials with interesting magnetic properties − including those features required for potential integration into devices (i.e., room-temperature transitions, hysteresis loops).[15] More recently, with the identified requirement for control of particle size, the elaboration of nanoparticles of SCO materials by reverse micelle techniques was developed by Létard et al.[5,7,10] In this way, through variation of the reaction conditions, such as oil/water ratio and reactant concentration, the size of the particles can be tailored/controlled. Overall at this stage, in this and further reports by other groups, it appears that with particle size reduction the spin transition nature becomes more gradual, the hysteresis loop size is diminished and the transition temperature decreases, but importantly, the SCO nature is retained in the nanoscale domain.[5–10] These trends were nicely depicted in a recent systematic study of a series of six different particle-sized analogues of [Fe(NH$_2$trz)$_3$]Br$_2$·nH$_2$O (covering macro- to nanometer), highlighting the possibility to tune the size of a hysteresis loop to that required for application through particle size control.[5,10]

A further question concerns the effect on the photomagnetic response upon particle size reduction, as photocontrol of magnetic properties at the molecular scale opens new perspectives in information storage.[16] The photomagnetic effect on the molecular scale is an extremely active field of

[a] Laboratoire des Sciences Moléculaires, ICMCB (CNRS UPR 9048), Université Bordeaux I,
33608 Pessac, France
Fax: +33-5-40002649
E-mail: letard@icmcb-bordeaux.cnrs.fr

research in regards to magnetically ordering systems such as Prussian Blue analogues[1,3] but has yet to be investigated for SCO coordination materials. Of particular interest is that for bulk SCO materials: whereas thermally induced magnetic properties are largely governed by solid-state communicative effects, light-induced properties are influenced more by the direct metal coordination environment. Thus, with particle size reduction to the nanoscale, whereby the metal coordination environment is unchanged, it should still be possible to observe a photomagnetic response. Furthermore, taking into consideration the well-established relationship at the macroscopic scale between the light-induced excited spin state trapping effect (LIESST) and the transition temperature ($T_{1/2}$), that is, T(LIESST) = T_0 – $0.3(T_{1/2})$, whereby T(LIESST) is defined as the temperature at which the light-induced stored information is erased[17,18] and T_0 is a parameter related fundamentally to the rigidity of the metal coordination environment,[17–19] w might expect that at the nanoscopic scale any change in $T_{1/2}$ will effect the T(LIESST) value.

Thus, here we examine the consequence of particle size reduction on the thermal and light-induced magnetic properties of the SCO coordination polymer [Fe(NCS)$_2$(bpe)$_2$]· n(solvent) [bpe = 1,2-bis(4′-pyridyl)ethane], which has previously been reported to exhibit both light-induced and thermally induced SCO when macroscale slow-grown crystals are prepared.[20] Here, using water-in-oil reverse micelle techniques three further samples with analogous structures have been prepared such that the microscopic to nanoscale particle size domains are encompassed, as evidenced by transmission electron microscopy. The occurrence of thermal spin transition and LIESST effects have been examined through both optical and susceptibility measurements. This is the first such study on the particle size reduction effect on LIESST activity.

Results and Discussion

Synthesis and Physical Characterization

The water-in-oil emulsion method has been shown to be effective for the formation of nanoparticles of a number of polymeric materials.[1,5,11] By this method, the resultant particle volume is defined by the size of the water droplet within the emulsion. The most effective way to control the water droplet size is to vary the relative ratio of water-to-oil, such that smaller droplets are formed when the amount of oil is increased.[10] To precisely control the particle size in this study, the reactant concentration was kept constant (0.05 M) and only the mass of the nonionic polyoxyethylenic surfactant Ifralan D0205 was varied (25, 78 and 85%). In other reports of nanoparticle preparation, different sized particles were obtained through varying the solution metal concentration,[8,9] and we found that the strategy of keeping the concentration constant and varying the oil/water ratio allowed the size to be varied more precisely.

Commonly, the water-in-oil emulsion method utilized for polymer formation consists of the preparation of two sepa-

rate emulsions (i.e., one containing the metal salt and one containing the ligand), and their subsequent combining results in contents exchange between the two emulsions with eventual formation of the polymer.[7] Here, the bpe ligand is only slightly soluble in aqueous media and thus a slightly modified procedure was used, whereby an emulsion of the metal salt [i.e., Fe(BF$_4$)$_2$·6H$_2$O + KNCS] was prepared and the bpe ligand was directly added as a powder. This results in the bpe being incorporated into the water droplets over time. Upon addition of the bpe ligand to the metal salt emulsion a striking colour change is observed from clear to bright yellow as the coordination polymer is formed.[20] It was noted that with particle size reduction the resultant product showed a less-intense yellow colour − such particle-size-dependent hypochromic effects have been observed previously for nanoparticles of Cu(AOT)$_2$ and more recently for [Fe(NH$_2$trz)$_3$]Br$_2$·nH$_2$O.[10,21]

Comparison of the powder X-ray diffraction patterns of the previously reported analogue [Fe(NCS)$_2$(bpe)$_2$]· 3(acetone), prepared as large crystals by slow diffusion techniques,[20] and the materials prepared here by the water-in-oil emulsion technique, revealed the same overall coordination polymer is formed by both methods (Figure 1). As the framework topologies are the same, with the change in solvation between the two differently prepared materials we expect only subtle variation in the powder diffraction patterns, in particular at high angle, related to the position of the solvent within the pores. Furthermore, with the reduction in particle size the peaks become broader as expected, because the number of coherent domains decreases within individual particles (Figure 1). Interestingly, attempts to synthesize a macroscopic powder in water, but in the absence of Ifralan D0205 [i.e., through direct addition of bpe to a solution of Fe(NCS)$_2$ in water] resulted only in the formation of the previously reported material [Fe(NCS)$_2$-(bpe)$_2$], consisting of linear chains − this material does not undergo a spin transition.[22]
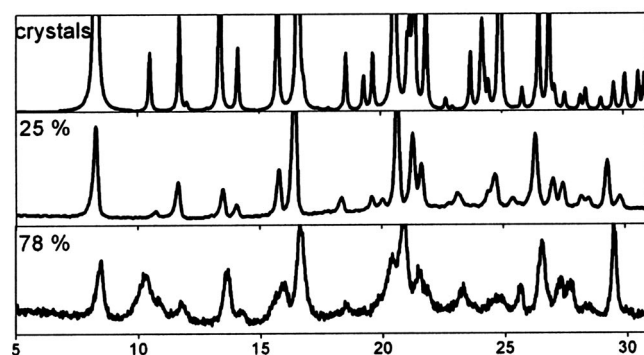

Figure 1. Powder X-ray diffraction comparison of [Fe(NCS)$_2$(bpe)]· 3(acetone), [Fe(NCS)$_2$(bpe)$_2$]_25% and _78% confirming the overall structural topology.

The particle size of each material was measured by using transmission electron microscopy (TEM). For [Fe(NCS)$_2$-(bpe)$_2$]_25%, rod-like crystallites within the macroscopic range were observed (1–4 μm, Figure 2). For [Fe(NCS)$_2$-

S. M. Neville, C. Etrillard, S. Asthana, J.-F. Létard

(bpe)$_2$]_78% rod-like yellow crystals were also observed but with the reduced size towards the nanoscale (0.5–1.5 µm). For [Fe(NCS)$_2$(bpe)$_2$]_85%, spherical particles in the nanoscale range (30–80 nm, Figure 2) were observed. Thermogravimetric analysis revealed a weight loss of 18% at room temperature under a constant flow of argon, with no further weight loss with heating until 150 °C when decomposition begins. The weight loss at room temperature is consistent with the loss of surface and pore solvent (here, likely a mixture of water and diethyl ether) and agrees with that previously reported for [Fe(NCS)$_2$(bpe)$_2$]·3(acetone).[20]
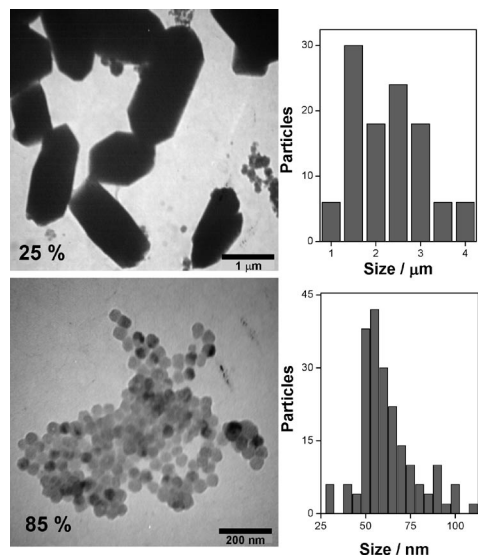

Figure 2. Representative TEM images of [Fe(NCS)$_2$(bpe)$_2$]_25% (1–4 µm) and Fe(NCS)$_2$(bpe)$_2$_85% (30–80 nm) including size distribution histograms.

Thermally induced and Light-Induced Magnetic Properties

Magnetic susceptibility measurements on each of the particle sizes were carried out and revealed gradual one-step spin transitions for each. Figure 3 compares the magnetic susceptibility versus temperature data of the original bulk slow-grown crystals and the three micellar produced materials. The most noticeable variation is that the micellar grown materials do not display the two-step nature observed in the macroscale crystalline material. Additionally, at high temperature, with cooling the onset temperature of the spin transition from high spin (HS) → low spin (LS) is shifted to lower temperatures with smaller particle size (ca. 180, 160 and 150 K, respectively). With further cooling, the $\chi_M T$ values decrease gradually for the three micellar-grown materials until 60 K, such that the $\chi_M T$ values at this temperature (1.9, 2.6 and 2.8 cm^3 K mol^{-1}, respectively) indicate 55, 70 and 78% retention of the HS state, for [Fe(NCS)$_2$(bpe)$_2$]_25%, [Fe(NCS)$_2$(bpe)$_2$]_78% and [Fe(NCS)$_2$(bpe)$_2$]_85%. The original material, [Fe(NCS)$_2$(bpe)$_2$]_bulk, shows less than 10% retention of HS character at low temperature. For each sample below 10 K a further small decrease in the $\chi_M T$ values is observed, which is attributed to

zero-field splitting effects of the HS species. Thus, overall we find that the transition temperature, $T_{1/2}$, shifts systematically with particle size reduction ($T_{1/2}$ = [Fe(NCS)$_2$(bpe)$_2$]_25%: 120 K, [Fe(NCS)$_2$(bpe)$_2$]_78%: 110 K, [Fe(NCS)$_2$(bpe)$_2$]_85%: 90 K). The $T_{1/2}$ values were calculated as the minimum of the $\delta(\chi_M T)/\delta T$ curve. The magnetic properties for each sample are summarized in Table 1.
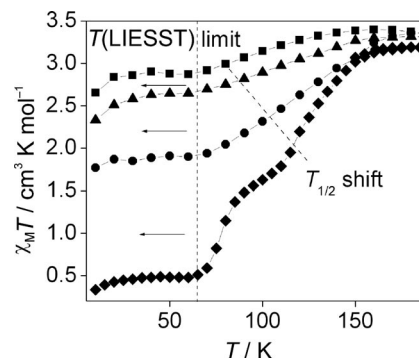

Figure 3. Plot of $\chi_M T$ vs. temperature for [Fe(NCS)$_2$(bpe)$_2$]_bulk (♦, $T_{1/2}$ = 80/133 K) [Fe(NCS)$_2$(bpe)$_2$]_25% (●, $T_{1/2}$ = 120 K), [Fe(NCS)$_2$(bpe)$_2$]_78% (▲, $T_{1/2}$ = 110 K), [Fe(NCS)$_2$(bpe)$_2$]_85% (■, $T_{1/2}$ = 90 K).

Table 1. Summary of physical and magnetic characteristics of [Fe(NCS)$_2$(bpe)$_2$].

	Particle size	HS residual [%]	SCO range [K]	$T_{1/2}$ [K]	T(LIESST) [K]
bulk	0.2–0.4 mm	<10	165–60	80/133	52
25%	1–3 µm	55	180–60	120	52
78%	0.5–1.5 µm	70	160–60	110	50
85%	30–80 nm	78	150–60	90	50

The changes at the sample surface associated with a transition from HS to LS states were monitored for the micro- and nanoscale materials by optical reflectivity measurements over the temperature range 280–10 K. Data were collected for each sample both over the entire spectral range 500–900 nm and at single wavelengths (550 and 830 nm). Figure 4 shows a comparison of the reflectivity signal versus temperature recorded at 530 nm for each, which corresponds to the d–d transition of the LS state. In other words, along the thermal HS → LS transition, the d–d absorption band of the LS state is increased, and consequently, the reflectivity signal recorded at 530 nm is decreased. The response at the surface of the samples match well with that observed by thermally induced magnetic susceptibility such that the onset temperature from HS to LS is decreased with particle size reduction and the minimum LS state is attained at 60 K for each.

For the entire optical reflectivity measurements, the samples were kept under constant irradiation with white light such that the changes at low temperature associated with a photoinduced response could be monitored. For each sample, below 60 K the signal intensity increases, which is indicative of a light-induced spin conversion from LS to a metastable HS state (Figure 4). The intensity for each particle size relative to the full HS state (ca. 200 K) is indicative
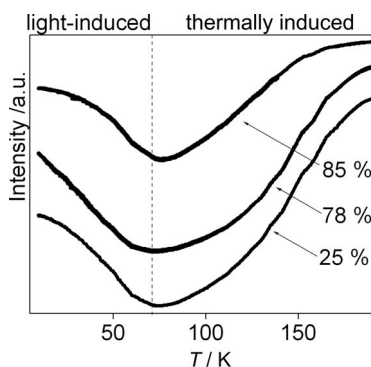
Figure 4. Optical reflectivity signal vs. temperature at 550 nm for [Fe(NCS)$_2$(bpe)$_2$]_25%, [Fe(NCS)$_2$(bpe)$_2$]_78% and [Fe(NCS)$_2$-(bpe)$_2$]_85%, showing the variation over the thermally induced and light-induced regions.

of nonquantitative LIESST activity even at the surface of the sample − as was reported for the original bulk material.[20]

Subsequently, light-induced magnetic susceptibility measurements of each sample were carried out and revealed that at 10 K with irradiation (λ = 530.2 nm) a light-induced excitation of the LS state to a metastable HS state is observed, irrespective of the size of the particles (Figure 5). Whatever our efforts of tuning the wavelength and increasing the intensity, and as observed from optical reflectivity measurements (where even at the surface only partial conversion was obtained), a nonquantitative conversion was observed. For each sample, when the photostationary limit was reached, that is, typically after one hour, the light was switched off and the magnetic response was recorded by increasing the temperature at 3 K min^{-1}, following the procedure for comparing T(LIESST) temperatures in the already existing database.[17–19] A comparison of the light-induced magnetic behaviours of the original bulk material and the micellar prepared materials are in Figure 5 (note: the LIESST plot of [Fe(NCS)$_2$(bpe)$_2$]_78% has been omitted from this figure for clarity; however, the results are sum-

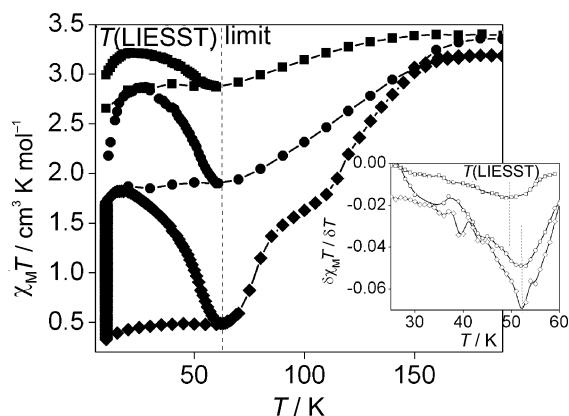Figure 5. Plot of $\chi_M T$ vs. temperature for the thermally induced and light-induced SCO of [Fe(NCS)$_2$(bpe)$_2$]_bulk (macroscale particles, ♦), [Fe(NCS)$_2$(bpe)$_2$]_25% (microscale particles, ●) and [Fe(NCS)$_2$(bpe)$_2$]_85% (nanoscale particles, ■). Inset: Plot of $\delta\chi_M T/\delta T$ vs. T indicating the T(LIESST) values (Table 1).

marized in Table 1). In the absence of irradiation, for each material, between 10 and 25 K an increase in the $\chi_M T$ values is observed and reflects the zero-field splitting within the spin quintet HS state observed for the thermally induced SCO. Over the range 25–60 K the $\chi_M T$ values for each gradually decrease to equal that of the thermally induced spin transition at the same temperature. The temperature at which the light-induced stored information is erased, defined as the T(LIESST) value (inset Figure 5), are approximately equivalent for each of the particle sizes (i.e., [Fe(NCS)$_2$(bpe)$_2$]_bulk: 52 K, [Fe(NCS)$_2$(bpe)$_2$]_25%: 52 K, [Fe(NCS)$_2$(bpe)$_2$]_78%: 50 K and [Fe(NCS)$_2$(bpe)$_2$]_85%: 50 K, Figure 5 insets). The T(LIESST) values were calculated as the minimum of the $\delta(\chi_M T)/\delta T$ curve.

Discussion

Being the first such investigation on the effect of particle size reduction on the light-induced magnetic properties of a SCO coordination polymer, our aim here was not to answer the many questions that are evident about nanoparticle chemical and physical behaviour but more importantly to see if the photomagnetic SCO effect can be translated from the macroscopic to the microscopic to the nanoscale domains. Furthermore, with the new-found ability to control particle size of SCO coordination polymers comes the possibility to increase our understanding of the relationship between light-induced and thermally induced magnetic properties towards achieving the higher T(LIESST) values required for device implementation.[2]

Firstly, in regard to the thermally induced magnetic behaviour with particle size reduction observed here, we see that: (1) the two-step nature of the spin transition is lost, (2) the spin transition becomes more gradual, (3) the residual HS fraction increases systematically and (4) the transition temperature ($T_{1/2}$) decreases (Table 1). With particle size reduction, from a physical perspective it is obvious that surface chemistry has greater importance as the surface area to volume ratio is increased dramatically, that is, by a factor of 20 over the micro- to nanometer scales observed here. Thus, with a greater relative surface area there is increased potential for defects to be introduced, for example, as the outer coordination environments may not be complete or contain bound solvents. Such defects are known to result in more gradual SCO natures as well as resulting in increased HS residual fractions at low temperature, as commonly observed in past reports on the effect of grinding SCO materials into finer particles and for metal dilution studies.[13,23] Indeed, a more gradual SCO nature has also been observed in nanoparticle preparations of the polymeric system Fe(pyrazine){Pt(CN)$_4$} and in this report it was suggested that this is caused by the peripheral iron(II) sites not undergoing SCO.[1,8] These effects would also contribute to the observed loss of two-step nature.

Furthermore, we would like to note that each of the trends we observe here are remarkably similar to that observed previously in metal dilution studies on SCO materi-

als, potentially indicating that with particle size reduction the samples are effectively being diluted in respect to the thermal spin transition properties (however many more such studies would need to be made before this can be confirmed).[23–25] In Figure 6 we show purely for comparative purposes the results of a previously reported metal dilution study on the material [Fe$_x$Mn$_{1-x}$(bpp)$_2$](NCSe)$_2$ [bpp = 2,6-bis(pyrazol-3-yl)pyridine] to highlight the similarities with the current micellar preparation study. Of particular note is the more gradual spin transition, greater residual HS fraction and decreased transition temperatures with increasing SCO metal dilution.[24] Indeed, as thermally induced SCO properties are known to be largely controlled by thermodynamics and the degree of cooperative interactions available, with particle size reduction it is obvious that surface chemistry has greater importance as the surface area to volume ratio is increased dramatically. With a greater relative surface area there is increased potential for defects to be introduced, for example, as the outer coordination environments may not be complete or contain bound solvents. Consequently, with the particle size reduction the potential SCO sites available to propagate are decreased significantly and the spin transition may effectively become "diluted".
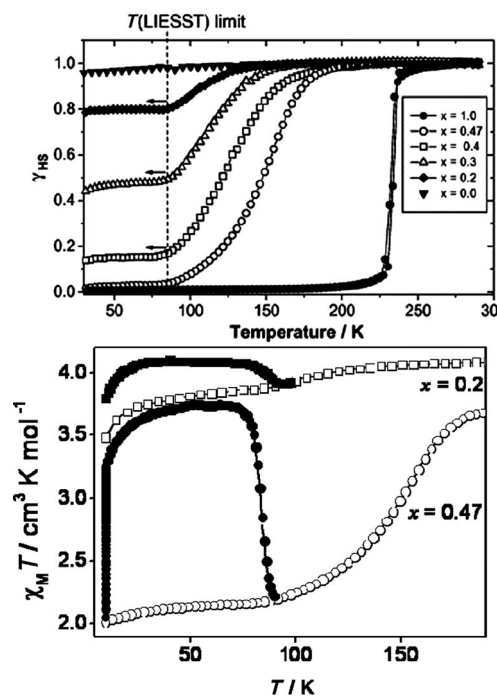

Figure 6. Representative example of a metal dilution study for comparison to particle size reduction in [Fe(NCS)$_2$(bpe)$_2$]. Top: HS fraction vs. T for [Fe$_x$Mn$_{1-x}$(bpp)$_2$](NCSe)$_2$ showing a T(LIESST) limit. Bottom: $\chi_M T$ vs. T for $x = 0.47$ (o) and $x = 0.2$ (□) showing the variation over the thermal (open symbol) and light-induced (closed symbol) regions.[24]

Concerning now the photomagnetic properties of our series of miniaturized particles, overall, we observed that quantitatively the degree of conversion from the LS to metastable HS state in the presence of irradiation is not affected by the particle size. Additionally, we see that tem-

perature at which the metastable state is retained with particle size variation, that is, the T(LIESST) value (Table 1), is largely unaffected by the particle size. We note again that as with the thermally induced SCO properties discussed above, the photomagnetic properties observed here mimic that observed in metal dilution studies. This is highlighted in the example in Figure 6 where the degree of photosaturation at low temperature and the T(LIESST) values remain unchanged upon SCO metal dilution. Indeed, because photomagnetic properties are thought to be largely governed on the molecular scale,[17,18,24] with particle size reduction where the local geometry of the SCO centres are unaltered we could expect little change to the photomagnetic properties. If this is indeed true, after further studies on other materials, this property would prove useful for the use of photomagnetically active nanoparticles in working devices − as opposed to thermal magnetically active nanoparticles where the key SCO features, such as hysteresis, have been seen to diminish with miniaturization.

Additionally, looking at the relationship established for bulk materials between the transition temperature ($T_{1/2}$) and the temperature at which the light-induced information is erased [T(LIESST) = $T_0 - 0.3(T_{1/2})$],[17] with particle size reduction, as the metal coordination sphere is not being modified, we can see that the T(LIESST) values should remain essentially unchanged, and if anything increase minimally with any decrease observed in $T_{1/2}$ character (Table 1). Here, the $T_{1/2}$ is seen to decrease with particle size reduction but with no apparent effect on the T(LIESST) values, and this indicates that the molecular environment on the SCO centre plays the largest role in the photomagnetic behaviour.

With respect to the systematic increase in paramagnetic residual species at low temperatures with particle miniaturization it appears that there is a limiting temperature at which the thermal transition is inhibited. Interestingly, this temperature is approximately the same for each of the particle sizes and corresponds to the T(LIESST) limit. Moreover, we can again note that such an effect has been observed for metal dilution studies (Figures 3 and 6). Let us recall that the existence of the LIESST effect at low temperatures indicates that the potential energy surface displays two minima, corresponding to the LS and HS states, separated by activation energy. With the approach of the thermodynamically stable HS region (i.e., $T_{1/2}$) towards the metastable HS region [i.e., T(LIESST)] the HS state becomes infinitely long owing to the activation barrier that slows down the HS → LS process (i.e., less kinetically favourable).[24] Thus, with the combined reduction of $T_{1/2}$ values and more gradual nature observed with particle size reduction, higher residual fractions are seen overall with particle size reduction. Along this line, it suggests that for photomagnetic (and indeed thermally induced) SCO properties to be observed on very small particle sizes there must be a large gap between $T_{1/2}$ and T(LIESST) for the macroscale material to restrict the $T_{1/2}$ becoming lower than T(LIESST) upon miniaturisation, hence resulting in a total HS state and no photomagnetic properties.

Conclusions

Overall, at this time it is a complicated matter to have a clear view of the global effect of particle size reduction on both the thermal and photoinduced magnetic properties due to the very small number of reports in this field. At this stage we can suggest, firstly, that for each family there may be one critical size lower limit where we will first observe the influence of surface defects, that is, through increased residual HS fractions. Secondly, for each system one must also consider the effect of merging $T_{1/2}$ and T(LIESST), which also results in HS residual fractions in some materials. Indeed, in a given material it is possible that a combination of both of these factors may synergistically affect the HS residual fraction to some degree. Thus, many more such studies will need to be carried out to have a more clear view of the relative importance of these factors to a given material with particle size reduction.

One of the most important aspects of this study is regarding the retention of the light-induced magnetic effect from the macro- to micro- to nanoscales (ca. 30–80 nm particles), opening new perspectives in photoinduced information storage on the nanoscale. In this study, we confirm that the thermally induced and light-induced SCO processes are governed by different factors, as globally, the thermally induced transition temperature is systematically lowered with particle size reduction but the photoinduced limiting temperature is not affected. Thus, whereas the thermal SCO regime is governed by solid-state cooperative interactions (which decrease with particle size miniaturization), the photoinduced SCO properties are governed on the molecular scale (which are unaffected by particle size reduction). Importantly, this highlights that for the future of nanoscale SCO materials in active devices, exploiting photoinduced properties may be more feasible, as the important magnetic features are retained at this level.

Experimental Section

Synthesis: Three samples of $Fe(NCS)_2(bpe)_2$ were prepared by the general method of water-in-oil emulsions, whereby the particle size was controlled by varying the weight percent ratio of oil/water over the range 25–85% ([Fe(NCS)$_2$(bpe)$_2$]_25%, [Fe(NCS)$_2$(bpe)$_2$]_78% and [Fe(NCS)$_2$(bpe)$_2$]_85%).

General Procedure for the Preparation of the Fe(NCS)$_2$(bpe)$_2$ Samples: A solution of $Fe(BF_4)_2\cdot6H_2O$ (0.0674 g, 0.2 mmol) and KNCS (0.0388 g, 0.4 mmol) in water (4 mL) plus a small amount of ascorbic acid was prepared [overall concentration based on iron(II) was 0.05 M]. Then, Ifralan D0205 [1.4 (25%), 14.8 (78%) and 23.6 g (85%)] was added, and the emulsion was stirred for 5 min. The bpe ligand (0.0736 g, 0.4 mmol) was then directly added as a powder, and the resulting bright-yellow emulsion was stirred for 15 min. The powder was then removed from the surfactant environment through a series of washing, centrifuging and decanting steps with diethyl ether (4×) and a small amount of ethanol for the first washing. [Fe(NCS)$_2$(bpe)$_2$]_25% yield: 100 mg (92%). IR (KBr): ṽ = 2050.3 (s), 1610.9 (s), 1559.7 (m), 1499.6 (m), 1422.7 (m), 1223.6 (m), 1013.5 (m), 827.3 (w), 521.5 (m) cm^{-1}. Fe(NCS)$_2$(bpe)$_2$_78% yield: 82 mg (85%). IR (KBr): ṽ = 2051.1 (s), 1611.4 (s), 1559.5 (m), 1499.8 (m), 1423.1 (m), 1223.8 (m), 1014.2 (m), 827.9 (w), 521.4 (m) cm^{-1}. Fe(NCS)$_2$(bpe)$_2$_85% yield: 55 mg (51%), IR (KBr): ṽ = 2051.1 (s), 1611.3 (s), 1559.7 (m), 1499.4 (m), 1422.9 (m), 1223.9 (m), 1014.0 (m), 827.5 (w), 521.5 (m) cm^{-1}.

Physical Measurements

Transmission Electron Microscopy (TEM) Analysis: The size and morphology of each sample was investigated by using a JEOL, JEM-2000FX (resolution 2–3 nm) equipped with an electronic gun (a filament of monocrystalline LaB_6), magnetic lenses and a system of electron detectors under a vacuum of 10^{-7} mbar for the detector CDD to 10^{-10} mbar for the source electrons. Samples were prepared on copper grids by dispersion in ethanol.

Thermogravimetric Analysis (TGA): Measurements were carried out with a TAG 24 device whereby the sample was kept at room temperature under a constant flow of argon until the weight loss stabilized. The sample was then heated at a rate of 2 K min^{-1} up to 250 °C. The sample was then maintained at this temperature for 2 h before returning to room temperature.

Powder X-ray Diffraction: Patterns were recorded by using a Panalytical X′pert diffractometer (Cu-K_α radiation and X′Celerator detector) within the range 2θ = 6–80° by using 60 s exposures with a 0.02° step size.

Optical Reflectivity: Reflectivity was investigated on all samples by using a home-built set-up coupled with a SM240 spectrometer (Opton Laser International), which allows both the reflectivity spectra to be collected in the 450–950 nm range at a given temperature and the temperature dependence of the signal at a selected wavelength (±2.5 nm) between 5 and 290 K to be followed. Samples were irradiated with light over the entire temperature range of measurement. The diffuse reflected signal was calibrated by using activated charcoal (Merck) as a black standard and barium sulfate ($BaSO_4$, DIN50533, Merck) as a white standard. The source of the white light consisted of a halogen lamp emitting between 350–2400 nm. This analysis was performed directly on a thin layer of a powdered sample without any dispersion in a matrix.

Thermally Induced and Light-Induced Magnetic Susceptibility: Thermal magnetic susceptibility data on bulk samples (5–10 mg) were collected by using a MPMS-55 Quantum Design SQUID magnetometer operating at 1 T over the temperature range 290 to 10 to 290 K. Photomagnetic characterization of each material was performed by using a Kr$^+$ laser coupled through an optical fibre into the cavity of the MPMS-55 Quantum Design SQUID magnetometer operating at 2 T. Samples were prepared as a thin layer (≈0.1 mg) to promote maximal penetration of the irradiated light. Sample weights were obtained by comparing their thermal SCO behaviour with a larger, accurately weighed sample.[17] Samples were first slow-cooled to 10 K to ensure that trapping of HS species at low temperatures did not occur and irradiated at λ = 530.2 nm at 6 mW cm^{-2} until photosaturation was reached. In the absence of irradiation, the temperature was then increased in 1 K steps to 100 K to determine the T(LIESST) values, and at 3 K steps over the range 100 to 290 to 10 K to follow the thermal SCO. The extreme of the $\delta\chi_M T/\delta T$ vs. T plot gave the T(LIESST) values, defined as the temperature for which the light-induced HS information is erased.[17]

Acknowledgments

[1] L. Catala, F. Volatron, D. Brinzei, T. Mallah, *Inorg. Chem.* **2009**, *48*, 3360.

[2] J.-F. Létard, P. Guionneau, L. Goux-Capes, *Top. Curr. Chem.* **2004**, *235*, 221.

[3] W. Lin, W. J. Rieter, K. M. L. Taylor, *Angew. Chem. Int. Ed.* **2009**, *48*, 650; A. M. Spokoyny, D. Kim, A. Sumrein, C. A. Mirkin, *Chem. Soc. Rev.* **2009**, *38*, 1218–1227.

[4] O. Kahn, *Acc. Chem. Res.* **2000**, *33*, 647; O. Kahn, C. J. Martinez, *Science* **1998**, *279*, 44; P. Gütlich, Y. Garcia, T. Woike, *Coord. Chem. Rev.* **2001**, *219–221*, 839.

[5] J. F. Létard, N. Daro, O. Nguyen, Patent FR 0512476, **2005**; J. F. Létard, N. Daro, O. Nguyen, Patent WO 2007/065996, **2007**; J. F. Létard, N. Daro, O. Nguyen, US 2008/0311401, **2008**.

[6] E. Coronado, J. R. Galán-Mascarós, M. Monrabal-Capilla, J. García-Martínez, P. Pardo-Ibáñez, *Adv. Mater.* **2007**, *19*, 1359.

[7] T. Forestier, S. Mornet, N. Daro, T. Nishihara, S.-I. Mouri, K. Tanaka, O. Fouché, E. Freysz, J.-F. Létard, *Chem. Commun.* **2008**, 4327.

[8] F. Volatron, L. Catala, E. Rivière, A. Gloter, O. Stéphan, T. Mallah, *Inorg. Chem.* **2008**, *47*, 6584; I. Boldog, A. B. Gaspar, V. Martínez, P. Pardo-Ibañez, V. Ksenofontov, A. Bhattacharjee, P. Gütlich, J. A. Real, *Angew. Chem. Int. Ed.* **2008**, *47*, 6433.

[9] J. Larionova, L. Salmon, Y. Guari, A. Tokarev, K. Molvinger, G. Molnár, A. Bousseksou, *Angew. Chem. Int. Ed.* **2008**, *47*, 8236.

[10] T. Forestier, A. Kaiba, S. Pechev, P. Guionneau, N. Daro, E. Freysz, J.-F. Létard, *Chem. Eur. J.* **2009**, *15*, 6122.

[11] S. Vaucher, M. Li, S. Mann, *Angew. Chem. Int. Ed.* **2000**, *39*, 826.

[12] P. Guionneau, M. Marchivie, G. Bravic, J.-F. Létard, D. C. Chasseau, *Top. Curr. Chem.* **2004**, *234*, 97; E. W. Müller, H. Spiering, P. Gütlich, *Chem. Phys. Lett.* **1982**, *93*, 567; N. Tsuchiya, A. Tsukamoto, T. Ohshita, T. Isobe, M. Senna, N. Yoshioka, H. Inoue, *Solid State Sci.* **2001**, *3*, 705.

[13] M. S. Haddad, W. D. Federer, M. W. Lynch, D. N. Hendrickson, *J. Am. Chem. Soc.* **1980**, *102*, 1468.

[14] G. Molnár, S. Cobo, J. A. Real, F. Carcenac, E. Daran, C. Vieu, A. Bousseksou, *Adv. Mater.* **2007**, *19*, 2163.

[15] See, for examples: *Topics in Current Chemistry Vols. 233–235: Spin Crossover in Transition Metal Compounds I–III*, **2004**, Springer, New York; J. A. Real, A. B. Gaspar, M. C. Muñoz, P. Gütlich, V. Ksenofontov, H. Spiering, *Top. Curr. Chem.* **2004**, *233*, 167–193; J. J. A. Kolnaar, G. van Dijk, H. Kooijman, A. L. Spek, V. G. Ksenofontov, P. Gütlich, J. Haasnoot, J. Reedijk, *Inorg. Chem.* **1997**, *36*, 2433; M. Ruben, E. Breuning, J.-M. Lehn, V. Ksenofonotv, F. Renz, P. Gütlich, G. B. M. Vaughan, *Chem. Eur. J.* **2003**, *9*, 4422; M. Nihei, M. Ui, M. Yokota, A. Maeda, H. Kishida, H. Okamoto, H. Oshio, *Angew. Chem. Int. Ed.* **2005**, *40*, 6484–6487; M. B. Duriska, S. M. Neville, B. Moubaraki, J. D. Cashion, G. J. Halder, K. W. Chapman, C. Baldé, J.-F. Létard, K. S. Murray, *Angew. Chem. Int. Ed.* **2009**, *48*, 2549–2552.

[16] S. Decurtins, P. Gütlich, C. P. Kölher, H. Spiering, A. Hauser, *Chem. Phys. Lett.* **1984**, *105*, 1; A. Hauser, *Chem. Phys. Lett.* **1986**, *124*, 543; P. Gütlich, A. Hauser, H. Spiering, *Angew. Chem. Int. Ed. Engl.* **1994**, *33*, 2024.

[17] J. F. Létard, *J. Mater. Chem.* **2006**, *16*, 2550.

[18] J. F. Létard, P. Guionneau, O. Nguyen, J. S. Costa, S. Marcén, G. Chastanet, M. Marchivie, L. Goux-Capes, *Chem. Eur. J.* **2005**, *11*, 4582.

[19] C. Carbonera, J. S. Costa, V. A. Money, J. Elhaïk, J. A. Howard, M. A. Halcrow, J. F. Létard, *Dalton Trans.* **2006**, 3058; J.-F. Létard, L. Capes, G. Chastanet, N. Moliner, S. Létard, J. A. Real, O. Kahn, *Chem. Phys. Lett.* **1999**, *313*, 115; S. Marcén, L. Lecren, L. Capes, H. A. Goodwin, J.-F. Létard, *Chem. Phys. Lett.* **2002**, *358*, 87; V. A. Money, J. S. Costa, S. Marcén, G. Chastanet, J. Elhaïk, M. A. Halcrow, J. A. Howard, J.-F. Létard, *Chem. Phys. Lett.* **2004**, *391*, 273.

[20] G. J. Halder, K. W. Chapman, S. M. Neville, B. Moubaraki, K. S. Murray, J.-F. Létard, C. J. Kepert, *J. Am. Chem. Soc.* **2008**, *130*, 17552.

[21] M. P. Pileni, *Langmuir* **1997**, *13*, 632.

[22] M. L. Hernández, M. G. Barandika, M. K. Urtiaga, R. Cortés, L. Lezama, M. I. Arriortua, T. Rojo, *J. Chem. Soc., Dalton Trans.* **1999**, 1401.

[23] C. Baldé, C. Desplanches, M. Grunert, Y. Wei, P. Gütlich, J.-F. Létard, *Eur. J. Inorg. Chem.* **2008**, 5382–5389.

[24] C. Baldé, C. Desplanches, P. Gütlich, E. Freysz, J.-F. Létard, *Inorg. Chim. Acta* **2008**, *361*, 3529.

[25] M. Sorai, J. Ensling, P. Gütlich, *Chem. Phys.* **1976**, *18*, 199; H. Spiering, E. Meissner, H. Köppen, E. W. Müller, P. Gütlich, *Chem. Phys.* **1982**, *68*, 65.

A Radical Approach to Hydroxylaminotrichlorosilanes: Synthesis, Reactivity, and Crystal Structure of TEMPO-SiCl₃ (TEMPO = 2,2,6,6-Tetramethylpiperidine-N-oxyl)

Spirk Stefan,[a] Ferdinand Belaj,[a] Tobias Madl,[b] and Rudolf Pietschnig*[a]

Keywords: Silicon / Radicals / X-ray diffraction / Reaction mechanisms / Computational chemistry

The reaction of the nitroxy radical 2,2,6,6-tetramethylpiperidine-N-oxyl (TEMPO) with $SiCl_4$ has been investigated in detail. One silicon-containing product, TEMPO-SiCl₃ (**1**), could be isolated in crystalline form, and its crystal structure was determined. The structural parameters have been compared with the related hydroxylaminotrichlorosilane known from the literature and with DFT calculations. According to the calculations, the formation of **1** follows an S_N2 mechanism, which is thermodynamically favored over an S_N1 pathway. Upon hydrolysis, **1** decomposes and yields several TEMPO-containing species. These were all characterized crystallographically.

Introduction

2,2,6,6-Tetramethylpiperidine-N-oxyl (TEMPO), a stable organic nitroxy radical,[1] and its derivatives have been used for numerous purposes over the past decades.[2–8] In recent years, the unpaired electron situated at the oxygen atom was used to perform spin labeling of biomolecules such as peptides or proteins to gain structural information of, for example, the surface topology of the protein, which can be obtained by the determination of pseudocontact shifts (PCS).[9]

We became interested in the relaxation enhancement properties of TEMPO because of its high solubility in a wide variety of organic solvents as well as its volatility, which facilitates the separation of the enhancer and sample after the NMR spectroscopic measurement. Recently, we described a study involving TEMPO as a relaxation enhancer in ^{29}Si NMR spectroscopy, which takes advantage of these favorable properties.[10] Although we found that TEMPO is a good alternative to other known relaxation enhancers in ^{29}Si NMR spectroscopy, we also realized that very sensitive compounds may react with TEMPO. For organosilicon compounds, it is known from literature that silylenes[11–14] and H-silanes[2,3,5,6] are oxidized in the presence of TEMPO under certain conditions. It is also known that hypervalent silicon–porphyrin complexes can react with TEMPO upon irradiation with UV light.[8] By contrast, the most reactive compound used in our relaxation-enhancement studies was $SiCl_4$, and it seemed that this compound also reacts slowly with TEMPO at higher concentrations. To clarify this observation, we performed a detailed investigation of the reactivity of $SiCl_4$ with TEMPO, the results of which are presented in this manuscript.

Results and Discussion

In the course of the previously mentioned investigation of TEMPO as relaxation enhancer in ^{29}Si NMR spectroscopy, we observed that the red NMR spectroscopic samples containing TEMPO and $SiCl_4$ decolorize after standing for some days. We assumed the formation of TEMPO-containing chlorosilanes with formation of thermodynamically favored silicon–oxygen bonds owing to a lack of steric protection at the silicon center. Unfortunately, the high $SiCl_4$/TEMPO ratio in these measurements did not allow a characterization of the TEMPO-containing silanes by ^{29}Si NMR spectroscopy because of the low concentration of these compounds in the presence of a large excess amount of $SiCl_4$. To avoid this problem, we performed the reaction on a larger scale with equimolar concentrations of TEMPO and $SiCl_4$.

The reaction of both components was followed by ^{29}Si NMR spectroscopy. Initially only the resonance of unreacted $SiCl_4$ could be observed. Whereas in our relaxation studies the highest TEMPO concentration used was 0.26 mol/L and no significant line broadening or signal shifting was observed, the much higher TEMPO concentration of the upscaled reaction (3.52 mol/L) resulted in a low-field shift of more than 2 ppm for the $SiCl_4$ signal. In addition, the high concentration of TEMPO also caused significant line broadening $[\nu(SiCl_4)_{1/2} = 25\,Hz]$ in the ^{29}Si NMR spectrum. In contrast, the "silicon grease" signal at $\delta = -21.8$ ppm, which may be used as an internal refer-

[a] Department of Chemistry, University of Graz,
Schubertstrasse 1, 8010 Graz, Austria
E-mail: rudolf.pietschnig@uni-graz.at
[b] Department of Chemistry, University of Technology Munich,
Lichtenbergstrasse 4, 85747 Garching, Germany
⌨ Supporting information for this article is available on the WWW under http://dx.doi.org/10.1002/ejic.200900969.

ence, showed a narrow line ($v_{1/2}$ = 1.5 Hz) and was nearly unaffected by high TEMPO concentrations, thereby indicating no interactions with the TEMPO molecule.

After some hours, an additional signal at –30.6 ppm could be observed in the ^{29}Si NMR spectra that can be assigned to trichlorosilane **1**. An indication that TEMPO is consumed during the formation of **1** stems from the signal of SiCl$_4$, which gets sharper again with reduced line shifting. After 72 h, the chemical shift and the half-line widths reached their starting values before TEMPO addition. Along with the slightly yellow color of the solution, this indicates that all TEMPO has been consumed. After removal of the volatiles and sublimation under a stationary vacuum, colorless crystals of **1** suitable for X-ray diffraction purposes were obtained (Figure 1).
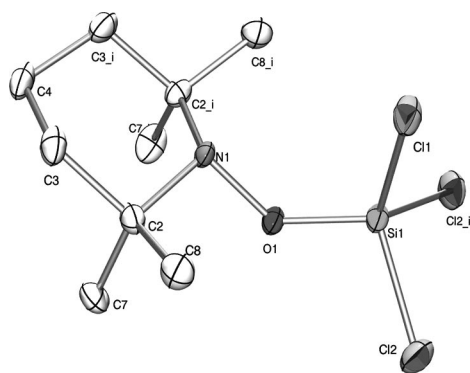
Figure 1. Crystal structure of **1** showing the atomic numbering scheme. Hydrogen atoms are omitted for clarity. Ellipsoids are drawn at the 50% probability level.

For the characteristic N–O–SiCl$_3$ functionality in **1**, the Si–O and N–O bond lengths are 1.619(1) and 1.485(2) Å, respectively, and the Si–Cl bond lengths vary between 2.016(1) and 2.028(1) Å. The geometric parameters of **1** can be compared with the only structurally characterized hydroxylaminotrichlorosilane in the literature, that is, *N*,*N*-dimethylhydroxylaminotrichlorosilane (**2**).[15] Generally, the bond lengths for both compounds are very similar (Table 1); however, the angles involving silicon show significant differences. Whereas the geometry at the silicon atom in **1** can be described as tetrahedral with O–Si–Cl angles of 109.2(1)° (Cl2, Cl2′) and 114.3(1)°, the geometry in **2** is more distorted with values ranging from 104.2(1)° to 113.5(1)°. Perhaps the most significant difference concerns the Si–O–N angle, which is 119.5(1)° for **1** and therefore much larger than that in **2** [103.4(1)°], thus leading to a smaller distance between the silicon and the geminal nitrogen atom of 2.441 Å for the latter. This short distance is smaller than the Bartell's radii[16,17] of silicon and nitrogen (2.69 Å) and indicates a weak interaction between the silicon and nitrogen atoms in the case of **2**. By contrast, this Si···N distance is 2.683(1) Å for **1**, which suggests no such interaction for this compound. DFT calculations [B3LYP//6-311+g(d)] on **1** that describe a single molecule in the gas phase yield similar values (Si···N: 2.748 Å; Si–O–N: 124.3°).

The difference between the calculated and experimental values of the Si–O–N angle may be a consequence of the shallow vibrational potential of the Si–O–N fragment, which is comparable to the situation present in siloxanes.

Table 1. Comparison of bond lengths [Å] and angles [°] of **1** and **2**.

	1 (X-ray)	**1** B3LYP/6-311+g*	**2** (X-ray) ref.[15]
Si–O	1.619(1)	1.638	1.618(2)
Si–Cl1	2.016(1)	2.048	2.018(1)
Si–Cl2	2.028(1)	2.056	2.015(1)
Si–Cl3	2.028(1)	2.056	2.013(1)
N–O	1.485(2)	1.469	1.491(2)
N–C1	1.495(1)	1.500	1.462(4)
N–C2	1.495(1)	1.500	1.455(4)
Si–O–N	119.5(1)	124.3	103.4(1)
O–Si–Cl1	114.3(1)	113.9	104.2(1)
O–Si–Cl2	109.2(1)	108.7	113.5(1)
O–Si–Cl3	109.2(1)	108.7	113.3(1)
O–N–C1	106.1(1)	106.9	104.2(2)
O–N–C2	106.1(1)	106.9	104.5(2)

A further aspect of the crystal structure of **1** is the fact that the Si–Cl bond lying in the N–O–Si–Cl plane is slightly shorter [Si–Cl1: 2.016(1) Å] than the two other ones [2.028(1) Å]. Again this trend is reproduced by the DFT calculations (Table 1). A possible explanation is negative hyperconjugation through an n(O) → σ*(Si–Cl2) interaction as observed in related cases.[18–20]

As mentioned initially, the formation of **1** proceeds from the reaction of TEMPO with SiCl$_4$. In principle, the replacement of a chlorine radical from SiCl$_4$ may occur by TEMPO accompanied by the liberation of elemental chlorine. However, we found evidence that besides **1** a further product is formed that contains no silicon at all. This byproduct was identified as TEMPO$^+$Cl$^-$ (**3**). It was possible to isolate **3** in crystalline form and its crystal structure was determined (Figure 2).
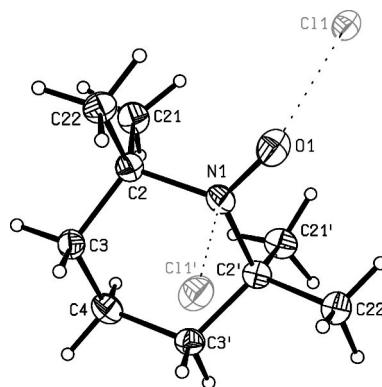

Figure 2. Molecular structure of **3**. Ellipsoids are drawn at the 50% probability level.

The N–O bond has a length of 1.237(3) Å and is much shorter than that in TEMPO but is longer than that in the two other known corresponding oxopiperidinium compounds in which perchlorate (1.194 Å) and 2,3,4,5-tetra-

fluoro-6,6,7,7-quinodimethanate (DQM) (1.195 Å) act as counteranions.[21,22] The nitrogen atom shows a pyramidalization of about 10° out of the C2–O1–C2′ plane, which is very unusual for N–O doubly bonded systems. By contrast, in the other above-mentioned oxopiperidinium compounds near planarity around the N–O bond is observed with deviations of 0.73° (ClO$_4^-$) and 3.56° (DQM) from the least-squares plane C2–O1–C2′. TEMPO$^+$Cl$^-$ has been described in the literature before, but no crystal structure has been reported yet. It can be prepared directly from TEMPO and Cl$_2$ and has been employed as an oxidation reagent in organic synthesis.[23–26]

Mechanism of Formation

Although the formation of **1** (Scheme 1) proceeds cleanly, we were interested in gaining insight into the mechanism of its formation. The obvious alternatives are that the reaction of TEMPO with tetrachlorosilane follows either an S$_N$1 or an S$_N$2 pathway. The S$_N$1 pathway would lead to the formation of TEMPO$^+$Cl$^-$ (**3**), and the ·SiCl$_3$ radical, which then can react with a second equivalent of TEMPO to give **1** (Scheme 2). By contrast, pentavalent silicon species **4** would be involved if the reaction proceeds along an S$_N$2 pathway. Intermediate **4** would then be able to eliminate a chlorine radical with formation of **1**. The chlorine radicals may react further with TEMPO directly (formation of **3**) or recombine to elemental chlorine in the closed reaction vessel (Scheme 3). Although silicon compounds with pentavalent coordination geometry at silicon can be quite stable, intermediate **4** could not be isolated or observed spectroscopically.
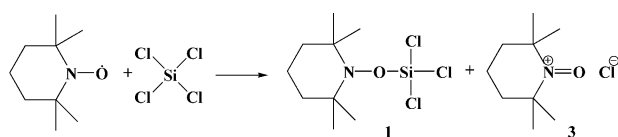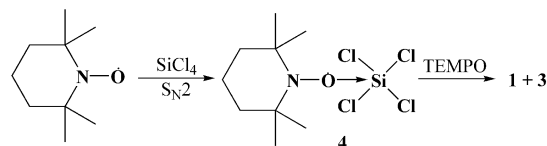

Scheme 1. Formation of **1**.

Quantum chemical calculations were performed to assess the relative energies of the intermediates involved in both mechanisms. At the B3LYP/6-311+g* level of theory, the S$_N$1 reaction that leads to the trichlorosilyl radical and **3** is
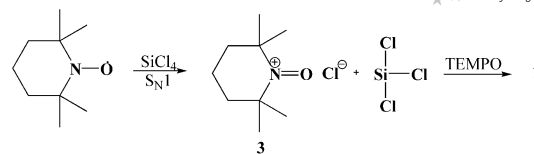
Scheme 2. Reaction of TEMPO with SiCl$_4$ following an S$_N$1 pathway.

Scheme 3. Reaction of TEMPO with SiCl$_4$ following an S$_N$2 pathway.

about 69.4 kcal/mol higher in energy than TEMPO and SiCl$_4$ (Figure 3). In contrast, the formation of adduct **4** is only 14.9 kcal/mol higher in energy than the starting materials. Although the transition states and the corresponding activation energies have not been calculated so far, the S$_N$1 mechanism seems to be quite unlikely because of the high energy difference of about 54 kcal/mol between the initial intermediates of the S$_N$1 and S$_N$2 pathways in the reaction cascade.

By just looking at the product side, the final product **1** plus a chlorine radical is 30 kcal/mol higher in energy than the starting materials. This energy is reduced to 6.2 kcal/mol by recombination of the chlorine radicals to Cl$_2$. The reaction energy is further decreased when the reaction of Cl$_2$ with additional TEMPO is admitted but is still endothermic by 4.2 kcal/mol with respect to the starting materials (2TEMPO + SiCl$_4$).

Room-temperature corrections to ΔG^{298K} lead to an even higher preference for the starting materials with energy differences of 13.5 kcal/mol and 18.0 kcal/mol, respectively (Figure 1).

The corresponding equilibrium constants (K) of 1.4×10^{-10} and 6.3×10^{-14} illustrate that TEMPO + SiCl$_4$ is the thermodynamically favored side of the equilibrium, which is also the grounds for the suitability of TEMPO as a relaxation enhancer. In turn, however, the equilibrium
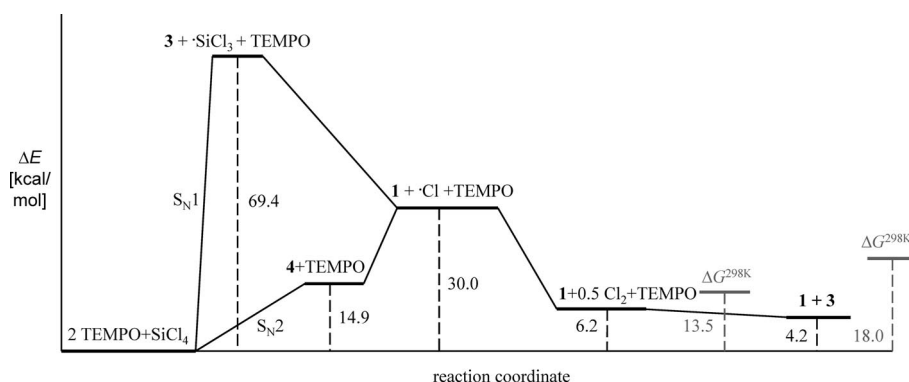

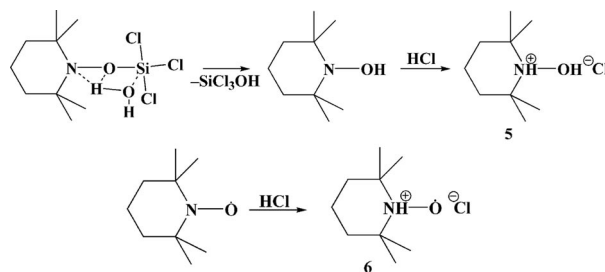Figure 3. Relative energies [B3LYP//6-311+g(d)] of intermediates in the formation of **1**.

may be shifted by high $SiCl_4$ concentrations, higher temperature, and solvents in which ionic **3** is insoluble. Furthermore, the lattice energy of **3** is not included in the calculations and can be expected to favor the product side even further. It seems that the formation of byproduct **3** is one of the relevant driving forces in the preparation of **1** (Figure 3).

Scheme 4. Hydrolytic decomposition of **1**.

Stability

When exposed to ambient atmosphere, **1** decomposes by reacting with traces of water, which leads to undefined silicon-containing products and eventually silica. Nevertheless, some TEMPO-containing species could be isolated, and recrystallization from dichloromethane yielded single crystals suitable for diffraction experiments. Initially, it seemed that the isolated crystals had the same identity as **3** as indicated by very similar cell constants after unit-cell determination. Nevertheless, it turned out that different compounds were obtained, namely, TEMPOH·HCl (**5**) and TEMPO·HCl (**6**).

These compounds are presumably formed by hydrolysis of **1** concomitant with the formation of HCl. This may proceed through a pentavalent transition state (Scheme 4) stabilized by the formation of hydrogen bonds, which is more likely than hydrolysis of the silicon–chlorine bonds, and which should then lead to a cleavage of the Si–O(N) fragment. A similar mechanism was described by Waymouth et al. when hydrolyzing TEMPO-containing titanium chloride derivatives.[27] Although compounds **5** and **6** have been reported based on proton NMR and IR spectroscopy, no crystal structures are available for these compounds.[24,28]

Compounds **3**, **5**, and **6** crystallize in the orthorhombic space system and are members of the space group $Cmc2_1$. For a comparison of the tiny differences of the cell constants see Table 3. For the underlying set of compounds it is very illustrative to see the increase in the N–O bond length, which is dependent on the number of hydrogen atoms present at the N–O fragment. Radical **6**, for instance,

shows a N–O bond length of 1.358(4) Å, whereas in **5** the N–O bond length was found to be 1.427(2) Å, which is in the range of N–O single bonds.[29]

As summarized in Table 2, the experimental values for the N–O bond length of TEMPO and compounds **1**, **3**, **5**, and **6** in the solid state correspond well with calculated ones for the gas phase at the DFT B3LYP//6-311+G(d) level of theory. The changing character of the N–O unit in these compounds is also reflected by the ν(NO) band in the IR spectra.

The experimental values are in good agreement with calculated ones. Correction factors range from 1.08 for **5** to 1.16 for TEMPO. A survey of the ν(NO) stretching frequencies of **1**, **3**, **5**, and **6** is included in Table 2.

These compounds show some other interesting features besides their N–O unit. In **6** the hydrogen atom is located at the nitrogen atom, which forms a hydrogen bond to a symmetry-related chlorine atom Cl1′ ($1 - x$, $1 - y$, $z + \frac{1}{2}$) with D–A distances of 3.197(3) Å and a DHA angle of 172.2°, thereby indicating a strong interaction according to Steiner.[30] In **5**, in which two hydrogen atoms are present, one is bonded to the oxygen atom and the other one is located at the nitrogen atom, thereby forming hydrogen bonds to Cl1 and Cl1′ ($1 - x$, $1 - y$, $z - \frac{1}{2}$). The D···A distances are 3.022(1) (D=O) and 3.130(1) Å (D=N) with DHA angles of 156.1 and 175.6°, which indicates here, too, the presence of strong hydrogen bonds that result in the formation a hydrogen-bonded network (Figure 4). The oxy-

Table 2. Stretch frequencies and relevant structural features of the N–O unit in TEMPO and its derivatives **1**, **3**, **5**, and **6**.

	Unit	TEMPO	TEMPO-SiCl₃ 1	TEMPO⁺Cl⁻ 3	TEMPOH·HCl 5	TEMPO·HCl 6
ν(NO)	cm⁻¹	1467	1068	1614	1031	1020
ν(NO) (calcd.)[a]	cm⁻¹	1268	959	1465	959	927
ν(exp)/ν(calcd.)	–	1.16	1.11	1.10	1.08	1.10
N1–O1	Å	1.296(3)	1.485(2)	1.237(3)	1.424(2)	1.358(4)
N1–O1 (calcd.)[a]	Å	1.280	1.469	1.231	1.416	1.367
N1–C2	Å	1.498(2)	1.495(1)	1.531(2)	1.545(1)	1.533(3)
O1···Cl1	Å	–	–	3.187(2)	3.022(1)	3.036(3)
N1···Cl1[b]	Å	–	–	3.297(2)	3.130(1)	3.197(3)
N1–O1···Cl1	°	–	–	114.3(2)	126.9(1)	122.4(2)
O1···Cl1···N1[c]	°	–	–	117.5(5)	118.5(1)	118.8(1)
O1–N1···Cl1[b]	°	–	–	86.4(1)	100.7(1)	94.9(2)
O1–N1–C2 (=a_1)	°	115.6(2)	106.1(1)	117.1(1)	111.8(1)	114.5(1)
C2–N1–C2[b] (=a_2)	°	125.1(2)	119.1(1)	123.3(1)	119.9(1)	121.5(2)
$\Sigma(2\,a_1 + a_2)$	°	356.3	331.3	357.5	343.5	350.5

[a] Calculated at the B3LYP//6-311+G(d) level of theory. [b] Symmetry transformations used to generate equivalent atoms: $1 - x$, $1 - y$, $z - \frac{1}{2}$. [c] Symmetry transformations used to generate equivalent atoms: $1 - x$, $1 - y$, $z + \frac{1}{2}$.

gen–chlorine distances of these compounds are significantly shorter (3.022 and 3.036 Å) than those of **3**, which reflects the ionic nature of this TEMPO derivative. Similarly the nitrogen–chlorine distances are shorter in **5** and **6** than in **3**. There are some parameters that seem to be surprisingly similar for all compounds, for example, the angle O1–Cl1–N1′ ($1 - x$, $1 - y$, $z + ½$) with values ranging from 117.5 in **3** to 118.8° in **6**, or the N1–C2 bond length with values ranging from 1.531(2) to 1.545(1) Å.
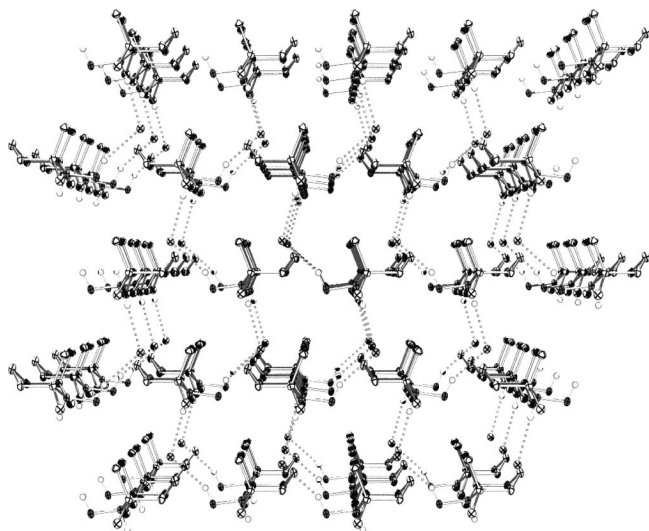

Figure 4. Hydrogen-bonded network in **5**.

It makes sense to compare the geometric parameters obtained for the various TEMPO derivatives mentioned above to TEMPO itself. In the literature, several crystallographic studies of TEMPO have been reported; however, all of them exhibit very poor R values and/or disorder. The N–O bond lengths found in these studies are 1.269, 1.270, and 1.295 Å.[31–33] In the course of our investigations we have been able to obtain crystals of TEMPO by sublimation with excellent quality for X-ray diffraction. The structure could be solved and refined with an R_1 value of 3.8% and no disordered atoms. The N–O bond length in this crystal structure has been determined to be 1.296(3) Å, which is just between the range of N–O double bonds (ca. 1.20 Å) and single bonds (ca. 1.45 Å). A survey of all relevant geometric parameters of the TEMPO-containing compounds investigated by us can be found in Table 2.

In an inert argon atmosphere, **1** also decomposes slowly. Over several weeks we monitored its slow decomposition by ^{29}Si NMR spectroscopy in solution. Over the course of the reaction, molecules of **1** exchanged TEMPO units, which may generate the disubstituted derivative **7** in addition to SiCl$_4$ (Scheme 5).

Multiply substituted products from TEMPO and SiCl$_4$ can also be obtained directly by increasing the relative amount of TEMPO. The resulting orange solid was investigated by solid-state magic angle spinning (MAS) ^{29}Si NMR spectroscopy to avoid additional reactions with the solvent. Besides **1**, which resonates at $\delta = -30.8$ ppm, several other signals were observed that can be assigned to (TEMPO)$_2$-
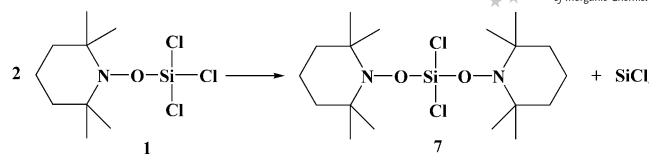
Scheme 5. Nonhydrolytic decomposition of **1** with formation of **7**.

SiCl$_2$ ($\delta = -57.8$ ppm), (TEMPO)$_3$SiCl ($\delta = -70.4$ ppm), and (TEMPO)$_4$Si ($\delta = -96.8$ ppm) based on gauge-including atomic orbital (GIAO) shift calculations [B3LYP//6-311+g(d)] and their characteristic SiO$_n$Cl$_m$ ($n + m = 4$) substitution pattern. In addition, minor amounts of hydrolysis and condensation products ($\delta = -46$ and -84 ppm) are detected as a consequence of short exposure to air during the sample transfer into the rotor. However, it was not possible to isolate these compounds in a pure form. A further investigation by means of mass spectrometry, for example, was not successful and showed only the presence of the TEMPO moiety at $m/z = 156$. In addition, it seems worth noting that according to the solid-state NMR spectroscopic data some silicon tetrachloride is still present in the solid ($\delta = -18.6$ ppm) despite thorough evacuation of the solid to remove unreacted SiCl$_4$. It seems possible that also in the solid state a decomposition as in solution (Scheme 5) may slowly take place that regenerates SiCl$_4$.

Conclusion

We have shown that the reaction between TEMPO and SiCl$_4$, for which the free reaction enthalpy is >0 at room temperature, may nevertheless take place at high concentrations in organic solvents owing to the insolubility of the inherent byproduct TEMPO$^+$Cl$^-$ (**3**). The primary reaction product is TEMPO-SiCl$_3$ (**1**), which is formed via pentacoordinate intermediate **4** rather than by direct radical abstraction according to our results. Compound **1** slowly undergoes substituent scrambling with formation of (TEMPO)$_2$SiCl$_2$ (**7**). In the presence of air and moisture hydrolysis takes place, which results in the formation of protonated compounds like TEMPOH·HCl (**5**) and TEMPO·HCl (**6**).

All compounds involved in the formation of **1** and its decomposition have been characterized by single-crystal X-ray diffraction and show a continuous transition between N–O double and single bonds, which is accurately reproduced by DFT calculations and IR stretch frequencies.

Compound **1** is only the second example of a structurally characterized molecule with an N–O–SiCl$_3$ functionality, which differs from the previously published *N*,*N*-dimethyl-hydroxylaminotrichlorosilane not only structurally but also by the completely different synthetic access.

The crystal structure of TEMPO itself also has been reinvestigated, and a satisfying structure solution ($R_1 = 3.8\%$) could be obtained. At 1.296(3) Å, the N–O bond length is at the higher end of the range reported before (1.269–1.295 Å).

In summary, TEMPO shows a unique reactivity towards SiCl$_4$ through formal radical exchange reactions that follow an associative pathway. It is clear that this chemistry can be extended also to other main-group halides, which will be explored in the future.

Experimental Section

General: All manipulations were carried out under strict exclusion of moisture and air in an inert argon atmosphere. C$_6$D$_6$ was dried with potassium and distilled prior to use. Tetrachlorosilane was purchased from Sigma and distilled prior to use. TEMPO (99%) was obtained from Sigma and used without further purification. ^{1}H, ^{13}C, and ^{29}Si NMR spectra were recorded with a Bruker Avance III at a Larmor frequency of 300 MHz for ^{1}H using TMS as reference and C$_6$D$_6$ as solvent. Solid-state ^{29}Si NMR spectra were recorded at a frequency of 500 MHz and at a rotation frequency of 15 kHz. DFT calculations were performed using the program Gaussian 03[34] at the high-performance computing center of the University of Graz. Mass spectra were recorded with an Agilent 5975C using a direct insertion of the sample into the ionization source. Voltage was set to 70 eV using a starting temperature of 50 °C, followed by subsequent heating to 350 °C (20 °C/min).

Synthesis of 1: TEMPO (0.55 g, 3.5 mmol) was placed in a 5 mL Schlenk tube and was dissolved in C$_6$D$_6$ (1 mL). SiCl$_4$ (0.60 g, 3.5 mmol) was added slowly with a syringe. The solution decolorized after some hours and was stirred for 72 h (longer stirring leads to byproducts as can be followed by ^{29}Si NMR spectroscopy). Then all volatiles were removed in vacuo (1 mbar) and the residue was subjected to sublimation. After approximately 3 h, very moisture-sensitive, colorless crystals suitable for X-ray diffraction purposes were obtained in 23% yield based on TEMPO, which could be identified as **1**. M.p. 101–103 °C (dec.). ^{1}H NMR (300 MHz, C$_6$D$_6$, TMS, 298 K): δ = 1.43 (s, 6 H, CH$_3$), 1.65 (s, 6 H, CH$_3$), 1.80–1.89 [m, ^{3}J(H$_{ax}$,H$_{ax}$) = 13.1 Hz, 2 H, CH$_2$], 2.01–2.11 [m, ^{3}J(H$_{ax}$,H$_{ax}$) = 13.1 Hz, 4 H, CH$_2$] ppm. ^{13}C NMR (75.435 MHz, C$_6$D$_6$, TMS, 298 K): δ = 17.96 (CH$_2$), 21.37 (CH$_3$), 27.70 (CH$_3$), 41.05 (CH$_2$), 62.44 (C$_q$) ppm. ^{29}Si NMR (59.602 MHz, C$_6$D$_6$, TMS, 298 K): δ = –30.6 ppm. MS (EI, 70 eV): m/z (%) = 156 (15) [M$^+$ – OSiCl$_3$], 141 (100) [M$^+$ – OSiCl$_3$–CH$_3$], 126 (12), 69 (73) [C$_4$H$_7$N$^+$], 55 (50) [C$_3$H$_5$N$^+$]. C$_9$H$_{18}$Cl$_3$NOSi (290.68): calcd. C 37.19, H 6.24; found C 37.77, H 6.81.

Isolation of 3

Method A: The sublimation residue obtained in the synthesis of **1** was recrystallized from dry CH$_2$Cl$_2$ at room temperature. By this route, however, only a few crystals were obtained.

Method B: Similar to the synthesis of **1** described above, SiCl$_4$ (6.0 g, 35 mmol) was added slowly with a syringe to TEMPO (0.55 g, 3.5 mmol). Due to the insolubility of TEMPO$^+$Cl$^-$ in SiCl$_4$, **3** precipitated as an orange-yellow solid and was collected by filtration. Isolated yield: 0.25 g (1.4 mmol, 82% based on TEMPO).

Synthesis of 5: Compound **5** was obtained in small amounts in the hydrolysis of **1**. Alternatively, **5** was obtained according to the following procedure. 2-Propanol (10 mL) containing 10% water was added to a solution of **1** (0.10 g, 0.3 mmol) dissolved in C$_6$D$_6$ (2 mL). The formation of a white precipitate (SiO$_2$) immediately occurred, and this precipitate was filtered off. The resulting red-brown solution was allowed to stir for one day, and after standing for seven days, white crystals of **5** were obtained. Yield: 51 mg (77%). ^{1}H NMR (CDCl$_3$, 300 MHz, 300 K): δ = 1.33 (s, 6 H, CH$_3$),

1.61 (s, 6 H, CH$_3$), 1.67–1.76 [m, ^{3}J(H$_{ax}$,H$_{ax}$) = 13.9 Hz, 4 H, CH$_2$], 2.23–2.33 [m, ^{3}J(H$_{ax}$,H$_{ax}$) = 13.9 Hz, 2 H, CH$_2$], 11.33 (s, 1 H, HCl) ppm; NH not visible. ^{13}C NMR (CDCl$_3$, 300 MHz, 300 K): δ = 16.26 (CH$_2$), 20.60 (CH$_3$), 28.46 (CH$_3$), 36.67 (CH$_2$), 68.79 (C$_q$) ppm. MS (EI, 70 eV): m/z (%) = 157 (12) [M$^+$ – HCl], 142 (100) [M$^+$ – HCl – CH$_3$], 69 (25) [C$_4$H$_7$N$^+$], 36/38 (5) [HCl].

Spectroscopic Data for 6: Compound **6** was obtained in small amounts in the hydrolysis of **1**. Alternatively, **6** was obtained according to a published procedure.[28] ^{1}H NMR (CDCl$_3$, 300 MHz, 300 K): δ = 1.40 (s, 6 H, CH$_3$), 1.65 (s, 6 H, CH$_3$), 1.76–1.86 [m, ^{3}J(H$_{ax}$,H$_{ax}$) = 15.6 Hz, 4 H, CH$_2$], 2.16–2.25 [m, ^{3}J(H$_{ax}$,H$_{ax}$) = 15.6 Hz, 2 H, CH$_2$], 11.15 (s, 1 H, HCl) ppm. ^{13}C NMR (CDCl$_3$, 300 MHz, 300 K): δ = 15.65 (CH$_2$), 20.06 (CH$_3$), 27.89 (CH$_3$), 36.06 (CH$_2$), 68.25 (C$_q$) ppm. MS (EI, 70 eV): m/z (%) = 156 (30) [M$^+$ – HCl], 141 (20) [M$^+$ – HCl – CH$_3$], 69 (100) [C$_4$H$_7$N$^+$], 36/38 (35) [HCl].

^{13}C NMR Spectroscopic Data for 7: The assignments made for **7** are based on intensity ratios obtained from ^{29}Si NMR spectra, in which the ratio of **7** to **1** is 1:3, which corresponds to a ratio of 2:3 in the ^{13}C NMR spectra. ^{13}C NMR (75.435 MHz, C$_6$D$_6$, TMS, 298 K): δ = 16.74 (CH$_2$), 20.38 (CH$_3$), 28.32 (CH$_3$), 36.57 (CH$_2$), 68.70 (C$_q$) ppm.

Crystallographic Section

Details of the data acquisition for the single-crystal X-ray diffraction experiments of TEMPO, TEMPOCl (**3**), TEMPO·HCl (**5**), TEMPOH·HCl (**6**), and TEMPOSiCl$_3$ (**1**) are summarized in Table 3.

Structure Solution and Refinement for TEMPO: A total of 815 reflections were collected (Θ_{max} = 30.0°), from which 704 were unique (R_{int} = 0.0291), with 594 having $I > 2\sigma(I)$. The structure was solved by direct methods (SHELXS-97)[35] and refined by full-matrix least-squares techniques against F^2 (SHELXL-97).[36] The non-hydrogen atoms were refined with anisotropic displacement parameters without any constraints. The H atoms of the CH$_2$ groups were refined with common isotropic displacement parameters for the H atoms of the same group and idealized geometry with approximately tetrahedral angles and C–H bond lengths of 0.99 Å. The H atoms of the methyl groups were refined with common isotropic displacement parameters for the H atoms of the same group and idealized geometry with tetrahedral angles, thereby enabling rotation around the X–C bond, and C–H bond lengths of 0.98 Å. Due to the absence of heavier elements, the absolute structure of the chiral molecules could not be determined reliably. For 61 parameters final R indices of $R1$ = 0.0387 and wR_2 = 0.0977 (GOF = 1.052) were obtained. The largest peak in a difference Fourier map was 0.199 e/Å^3.

Structure Solution and Refinement for TEMPO-SiCl$_3$ (1): A total of 2818 reflections were collected (Θ_{max} = 30.0°), from which 2077 were unique (R_{int} = 0.0203), with 1825 having $I > 2\sigma(I)$. The structure was solved by direct methods (SHELXS-97)[35] and refined by full-matrix least-squares techniques against F^2 (SHELXL-97).[36] The non-hydrogen atoms were refined with anisotropic displacement parameters without any constraints. The H atoms of the CH$_2$ groups were refined with common isotropic displacement parameters for the H atoms of the same group and idealized geometry with approximately tetrahedral angles and C–H bond lengths of 0.99 Å. The H atoms of the methyl groups were refined with common isotropic displacement parameters for the H atoms of the same group and idealized geometry with tetrahedral angles, enabling rotation around the X–C bond, and C–H bond lengths of 0.98 Å. For 82 parameters final R indices of $R1$ = 0.0281 and wR_2

Table 3. Crystallographic details for TEMPO, **1**, **3**, **5**, and **6**.[a]

Identification code	TEMPO	TEMPO$^+$Cl$^-$ 3	TEMPO·HCl 5	TEMPOH·HCl 6	TEMPO-SiCl$_3$ 1
Empirical formula	C$_9$H$_{18}$NO	C$_9$H$_{18}$ClNO	C$_9$H$_{19}$ClNO	C$_9$H$_{20}$ClNO	C$_9$H$_{18}$Cl$_3$NOSi
M_r [g/mol]	156.24	191.69	192.70	193.71	290.68
Crystal description	block, red	needle, orange	needle, yellow	block, yellow	block, colorless
Crystal size[34]	0.32 × 0.26 × 0.24	0.34 × 0.30 × 0.28	0.35 × 0.08 × 0.07	0.30 × 0.24 × 0.24	0.35 × 0.30 × 0.22
Crystal system	monoclinic	orthorhombic	orthorhombic	orthorhombic	orthorhombic
Space group	Cm	$Cmc2_1$	$Cmc2_1$	$Cmc2_1$	$Pnma$
a [Å]	6.399(3)	9.4010(5)	9.4948(8)	9.5361(2)	11.5717(16)
b [Å]	14.243(4)	11.3012(6)	11.2351(9)	11.1841(3)	12.6397(16)
c [Å]	5.757(2)	9.9064(5)	9.8937(8)	9.9748(2)	9.3742(12)
α [°]	90	90	90	90	90
β [°]	117.04(3)	90	90	90	90
γ [°]	90	90	90	90	90
V [Å^3]	467.3(3)	1052.48(10)	1055.41(15)	1063.84(4)	1371.1(3)
Z	2	4	4	4	4
$D_{calcd.}$ [Mg/m^3]	1.110	1.210	1.213	1.209	1.408
$F(000)$	174	416	420	424	608
μ [mm^{-1}]	0.071	0.321	0.320	0.318	0.733
Unit cell determination [°]	5.83 < Θ < 18.30	2.82 < Θ < 25.93	2.81 < Θ < 25.93	2.8 < Θ < 30.0	17.91 < Θ < 19.75
T [K]	95	100	100	100	95
Diffractometer	Stoe	Bruker APEX-II CCD	Bruker APEX-II CCD	Bruker APEX-II CCD	Stoe
Scan type	ω–θ scans	ϕ and ω scans	ϕ and ω scans	ϕ and ω scans	ω scans
θ range for data collection [°]	2.86 to 30.00	2.82 to 26.02	2.81 to 26.00	2.81 to 30.00	2.71 to 30.00
Index ranges	–8 ≤ h ≤ 8,	–11 ≤ h ≤ 11,	–9 ≤ h ≤ 11,	–13 ≤ h ≤ 12,	–16 ≤ h ≤ 16,
	–20 ≤ k ≤ 13,	–13 ≤ k ≤ 13,	–13 ≤ k ≤ 12,	–14 ≤ k ≤ 15,	–5 ≤ k ≤ 17,
	–3 ≤ l ≤ 8	–10 ≤ l ≤ 11	–11 ≤ l ≤ 11	–13 ≤ l ≤ 14	–2 ≤ l ≤ 13
Reflections collected/unique	815/704	4066/1015	3892/1019	6716/1505	2818/2077
Significant unique reflections [$I > 2\sigma(I)$]	594	996	1004	1489	1825
R(int), R(sigma)	0.0291, 0.0584	0.0182, 0.0166	0.0209, 0.0195	0.0369, 0.0255	0.0203, 0.0397
Completeness to Θ = 26.0° [%]	99.6	98.6	98.8	99.2	99.7
Data/parameters/restraints	704/61/2	1015/67/1	1019/68/1	1505/69/1	2077/82/0
Goodness-of-fit on F^2	1.052	1.175	1.093	1.143	1.074
Final R indices [$I > 2\sigma(I)$]	$R1$ = 0.0387, wR_2 = 0.0889	$R1$ = 0.0277, wR_2 = 0.0715	$R1$ = 0.0352, wR_2 = 0.0840	$R1$ = 0.0235, wR_2 = 0.0648	$R1$ = 0.0281, wR_2 = 0.0628
R indices (all data)	$R1$ = 0.0529, wR_2 = 0.0977	$R1$ = 0.0286, wR_2 = 0.0719	$R1$ = 0.0355, wR_2 = 0.0842	$R1$ = 0.0238, wR_2 = 0.0650	$R1$ = 0.0353, wR_2 = 0.0658
Largest difference peak and hole [e/Å^3]	0.199 and –0.180	0.303 and –0.121	0.877 and –0.290	0.548 and –0.111	0.301 and –0.260

[a] For all compounds, Mo-K_α radiation (λ = 0.71073 Å) with a graphite monochromator was used and the refinement method was full-matrix least-squares on F^2.

= 0.0658 (GOF = 1.074) were obtained. The largest peak in a difference Fourier map was 0.301 e/Å^3.

Structure Solution and Refinement for TEMPOCl (3): A total of 4066 reflections were collected (Θ_{max} = 26.0°), from which 1015 were unique (R_{int} = 0.0182), with 996 having $I > 2\sigma(I)$. The structure was solved by direct methods (SHELXS-97)[35] and refined by full-matrix least-squares techniques against F^2 (SHELXL-97).[36] The non-hydrogen atoms were refined with anisotropic displacement parameters without any constraints. The H atoms of the CH$_2$ groups were refined with common isotropic displacement parameters for the H atoms of the same group and idealized geometry with approximately tetrahedral angles and C–H bond lengths of 0.99 Å. The H atoms of the methyl groups were refined with common isotropic displacement parameters for the H atoms of the same group and idealized geometry with tetrahedral angles, thereby enabling rotation around the X–C bond, and C–H bond lengths of 0.98 Å. The absolute configuration was established by anomalous dispersion effects in diffraction measurements on the crystal. For 67 parameters final R indices of $R1$ = 0.0277 and wR_2 = 0.0719 (GOF = 1.175) were obtained. The largest peak in a difference Fourier map was 0.303 e/Å^3.

Structure Solution and Refinement for TEMPO·HCl (5): A total of 3892 reflections were collected (Θ_{max} = 26.0°), from which 1019 were unique (R_{int} = 0.0209), with 1004 having $I > 2\sigma(I)$. The structure was solved by direct methods (SHELXS-97)[35] and refined by full-matrix least-squares techniques against F^2 (SHELXL-97).[36] The non-hydrogen atoms were refined with anisotropic displacement parameters without any constraints. The H atom of the N–H group was refined with an individual isotropic displacement parameter, and all X–N–H angles equal at a N–H distance of 0.93 Å. The H atoms of the CH$_2$ groups were refined with common isotropic displacement parameters for the H atoms of the same group and idealized geometry with approximately tetrahedral angles and C–H bond lengths of 0.99 Å. The H atoms of the methyl groups were refined with common isotropic displacement parameters for the H atoms of the same group and idealized geometry with tetrahedral angles, thereby enabling rotation around the X–C bond, and C–H bond lengths of 0.98 Å. The absolute configuration was established by anomalous dispersion effects in diffraction measurements on the crystal. For 68 parameters final R indices of $R1$ = 0.0352 and wR_2 = 0.0842 (GOF = 1.093) were obtained. The largest peak in a difference Fourier map was 0.877 e/Å^3.

Structure Solution and Refinement for TEMPOH·HCl (6): A total of 6716 reflections were collected (Θ_{max} = 30.0°), from which 1505 were unique (R_{int} = 0.0369), with 1489 having $I > 2\sigma(I)$. The structure was solved by direct methods (SHELXS-97)[35] and refined by full-matrix least-squares techniques against F^2 (SHELXL-97).[36] The non-hydrogen atoms were refined with anisotropic displacement parameters without any constraints. The H atom of the O–H group was refined with an individual isotropic displacement parameter, and a tetrahedral angle X–O–H at an O–H distance of 0.84 Å. The H atom of the N–H group was refined with an individual isotropic displacement parameter, and all X–N–H angles equal at a N–H distance of 0.93 Å. The H atoms of the CH_2 groups were refined with common isotropic displacement parameters for the H atoms of the same group and idealized geometry with approximately tetrahedral angles and C–H bond lengths of 0.99 Å. The H atoms of the methyl groups were refined with common isotropic displacement parameters for the H atoms of the same group and idealized geometry with tetrahedral angles, thereby enabling rotation around the X–C bond, and C–H bond lengths of 0.98 Å. The absolute configuration was established by anomalous dispersion effects in diffraction measurements on the crystal. For 69 parameters final R indices of $R1$ = 0.0235 and wR_2 = 0.0650 (GOF = 1.143) were obtained. The largest peak in a difference Fourier map was 0.548 e/Å^3.

CCDC-737221 (TEMPO), -737331 (**1**), -737222 (**3**), -737223 (**5**), and -737224 (**6**) contain the supplementary crystallographic data for this paper. These data can be obtained free of charge from The Cambridge Crystallographic Data Centre via www.ccdc.cam.ac.uk/data_request/cif.

Computational Details: Quantum chemical calculations were carried out using the Gaussian 03 suite of programs[34] employing a 6-311+G(d) basis set[37–40] on the DFT(B3LYP) level.[41,42] All reported geometries have been optimized starting from C_1 symmetry on the B3LYP level. Stationary points were confirmed as minima on the potential surface by second-derivative calculations. The reported ΔG_f values of TEMPO and compounds **1**, **3**, **5**, and **6** have been calculated at the DFT level using a 6-311+G(d) basis set and were corrected for 298.15 K and 1 bar.

Supporting Information (see footnote on the first page of this article): Output summaries for TEMPO and compounds **1**, **3**, **5**, and **6**, including complete data of harmonic vibrational frequencies at the B3LYP level [6-311+G(d) basis set], optimized geometries, and total energies (E, in hartree).

Acknowledgments

[1] O. L. Lebedev, S. N. Kazarnovskii, *Zhur. Obshch. Khim.* **1960**, *30*, 1631–1635.

[2] C. Chatgilialoglu, C. Ferreri, D. Vecchi, M. Lucarini, G. F. Pedulli, *J. Organomet. Chem.* **1997**, *545/546*, 475–481.

[3] C. Chatgilialoglu, A. Guerrini, M. Lucarini, G. Pedulli, P. Carrozza, G. Da Roit, V. Borzatta, V. Lucchini, *Organometallics* **1998**, *17*, 2169–2176.

[4] C. J. Hawker, *Acc. Chem. Res.* **1997**, *30*, 373–382.

[5] M. Lucarini, E. Marchesi, G. F. Pedulli, C. Chatgilialoglu, *J. Org. Chem.* **1998**, *63*, 1687–1693.

[6] J. L. Pitters, P. G. Piva, X. Tong, R. A. Wolkow, *Nano Lett.* **2003**, *3*, 1431–1435.

[7] A. Studer, *Angew. Chem. Int. Ed.* **2000**, *39*, 1108–1111.

[8] J.-Y. Zheng, K. Konishi, T. Aida, *J. Am. Chem. Soc.* **1998**, *120*, 9838–9843.

[9] G. Pintacuda, M. John, X.-C. Su, G. Otting, *Acc. Chem. Res.* **2007**, *40*, 206–212.

[10] S. Spirk, T. Madl, R. Pietschnig, *Organometallics* **2008**, *27*, 500–502.

[11] A. Naka, N. J. Hill, R. West, *Organometallics* **2004**, *23*, 6330–6332.

[12] B. Tumanskii, P. Pine, Y. Apeloig, N. J. Hill, R. West, *J. Am. Chem. Soc.* **2004**, *126*, 7786–7787.

[13] T. Iwamoto, H. Masuda, S. Ishida, C. Kabuto, M. Kira, *J. Am. Chem. Soc.* **2003**, *125*, 9300–9301.

[14] T. Iwamoto, H. Masuda, S. Ishida, C. Kabuto, M. Kira, *J. Organomet. Chem.* **2004**, *689*, 1337–1341.

[15] U. Losehand, N. W. Mitzel, D. W. H. Rankin, *J. Chem. Soc., Dalton Trans.* **1999**, *24*, 4291–4297.

[16] L. S. Bartell, *J. Chem. Phys.* **1960**, *32*, 827–831.

[17] C. Glidewell, *Inorg. Chim. Acta* **1975**, *12*, 219–227.

[18] A. E. Reed, P. v. R. Schleyer, *J. Am. Chem. Soc.* **1990**, *112*, 1434–1445.

[19] P. v. R. Schleyer, A. J. Kos, *Tetrahedron* **1983**, *39*, 1141–1150.

[20] M. Bender, E. Niecke, M. Nieger, R. Pietschnig, *Eur. J. Inorg. Chem.* **2006**, 380–384.

[21] S. Nakatsuji, A. Takai, K. Nishikawa, Y. Morimoto, N. Yasuoka, K. Suzuki, T. Enoki, H. Anzai, *J. Mater. Chem.* **1999**, *9*, 1747–1754.

[22] L. O. Atovmyan, V. A. Golubev, N. I. Golovina, G. A. Klitskaya, *Zh. Strukt. Khim.* **1975**, *16*, 92–97.

[23] V. A. Golubev, E. G. Rozantaev, M. B. Neiman, *Bull. Acad. Sci. USSR (Engl. Transl.)* **1965**, *11*, 1898–1904.

[24] V. A. Golubev, R. I. Zhdanov, E. G. Rozantaev, *Bull. Acad. Sci. USSR (Engl. Transl.)* **1970**, 186–187.

[25] D. H. Hunter, D. H. R. Barton, W. J. Motherwell, *Tetrahedron Lett.* **1984**, *25*, 603–606.

[26] D. H. Hunter, J. S. Racok, A. W. Rey, Y. Z. Ponce, *J. Org. Chem.* **1988**, *53*, 1278–1281.

[27] K.-W. Huang, R. M. Waymouth, *Dalton Trans.* **2004**, 354–356.

[28] M. C. Krishna, W. DeGraff, O. H. Hankovszky, C. P. Sár, T. Kálai, J. Jekö, A. Russo, J. B. Mitchell, K. Hideg, *J. Med. Chem.* **1998**, *41*, 3477–3492.

[29] *International Tables for Crystallography Vol. C* (Ed.: A. J. C. Wilson), Kluwer Academic Publishers, Dordrecht/Boston/London, **1992**.

[30] T. Steiner, *Angew. Chem. Int. Ed.* **2002**, *41*, 48–76.

[31] D. Bordeaux, J. Lajzerowicz-Bonneteau, R. Briere, H. Lemaire, A. Rassat, *Org. Magn. Reson.* **1973**, *5*, 47–52.

[32] A. Capiomont, J. Lajzerowicz, J.-F. Legrand, C. Zeyen, *Acta Crystallogr., Sect. B: Struct. Crystallogr. Cryst. Chem.* **1981**, *37*, 1557–1560.

[33] A. Capiomont, J. Lajzerowicz-Bonneteau, *Acta Crystallogr., Sect. B: Struct. Crystallogr. Cryst. Chem.* **1974**, *30*, 2160–2166.

[34] M. J. Frisch, G. W. Trucks, H. B. Schlegel, G. E. Scuseria, M. A. Robb, J. R. Cheeseman, J. A. Montgomery Jr., T. Vreven, K. N. Kudin, J. C. Burant, J. M. Millam, S. S. Iyengar, J. Tomasi, V. Barone, B. Mennucci, M. Cossi, G. Scalmani, N. Rega, G. A. Petersson, H. Nakatsuji, M. Hada, M. Ehara, K. Toyota, R. Fukuda, J. Hasegawa, M. Ishida, T. Nakajima, Y. Honda, O. Kitao, H. Nakai, M. Klene, X. Li, J. E. Knox, H. P. Hratchian, J. B. Cross, C. Adamo, J. Jaramillo, R. Gomperts, R. E. Stratmann, O. Yazyev, A. J. Austin, R. Cammi, C. Pomelli, J. W. Ochterski, P. Y. Ayala, K. Morokuma, G. A. Voth, P. Salvador, J. J. Dannenberg, V. G. Zakrzewski, S. Dapprich, A. D. Daniels, M. C. Strain, O. Farkas, D. K. Malick, A. D. Rabuck, K. Raghavachari, J. B. Foresman, J. V. Ortiz, Q. Cui, A. G. Baboul, S. Clifford, J. Cioslowski, B. B. Stefanov, G. Liu, A. Liashenko, P. Piskorz, I. Komaromi, R. L. Martin, D. J. Fox, T. Keith, M. A. Al-Laham, C. Y. Peng, A. Nanayakkara, M. Challacombe, P. M. W. Gill, B. Johnson, W. Chen, M. W.

Wong, C. Gonzalez, J. A. Pople, *Gaussian 03*, Revision B.04, Gaussian, Inc., Pittsburgh, PA, **2003**.

[35] G. M. Sheldrick, *SHELXS-97, Program for the Solution of Crystal Structures*, University of Göttingen, Germany, **1997**.

[36] G. M. Sheldrick, *SHELXL-97, Program for the Refinement of Crystal Structures*, University of Göttingen, Germany, **1997**.

[37] K. Raghavachari, J. A. Pople, E. S. Replogle, M. Head-Gordon, *J. Phys. Chem.* **1990**, *94*, 5579–5586.

[38] M. J. S. Dewar, C. H. Reynolds, *J. Comput. Chem.* **1986**, *7*, 140–143.

[39] A. D. McLean, G. S. Chandler, *J. Chem. Phys.* **1980**, *72*, 5639–5648.

[40] R. Krishnan, J. S. Binkley, R. Seeger, J. A. Pople, *J. Chem. Phys.* **1980**, *72*, 650–654.

[41] C. Lee, W. Yang, R. G. Parr, *Phys. Rev. B* **1988**, *37*, 785–789.

[42] A. D. Becke, *J. Chem. Phys.* **1993**, *98*, 5648–5652.

NMR Spectroscopic Studies of Palladium(II) Complexes of Bidentate Diphenylphosphane Ligands with Acetate and Tosylate Anions: Complex Formation and Structures

Tiddo J. Mooibroek,[a] Elisabeth Bouwman,*[a] Martin Lutz,[b] Anthony L. Spek,[b] and Eite Drent[a]

The synthetic pathways towards Pd[II] complexes of functionalized bidentate diphenylphosphane ligands of the type [Pd(ligand)(anion)$_2$] and [Pd(ligand)$_2$](anion)$_2$ have been investigated. Eighteen different ligands have been used in combination with strongly (acetate, OAc⁻) or weakly (tosylate, OTs⁻) coordinating anions. The solid-state structure of some representative complexes was determined with X-ray crystallography. It is shown that the solid-state structures are fully retained in solution. The formation of [Pd(ligand)-(anion)$_2$]-type complexes was studied in detail by ¹H- and ³¹P-NMR spectroscopy. Depending on the ligand structure, the complex is formed instantaneously, via a polynuclear intermediate or is not formed at all. Complex formation is demonstrated to depend on the length and rigidity of the ligand backbone and on the steric bulk at the *ortho* position of the phenyl rings on phosphorus. It was also found that the coordinating ability of the anions can alter the structure of the kinetic and/or thermodynamic product.

Introduction

For some decades, Pd[II]-diphosphane catalytic systems have enjoyed much attention, both from academia and industry. Especially the copolymerization of CO and ethene has been widely studied[1,2] and applied [Carilon®(Shell) and Ketonex® (BP)] using such catalytic systems. A reaction, in which these palladium catalysts are relatively poorly studied, is the carbonylation of nitroaromatic molecules to aromatic isocyanates.[4–9] For this reaction most endeavours involve catalysts of the type [Pd[II](1,10-phenanthroline)$_2$](anion)$_2$,[5–19] and only few involve catalysts of the type P$_2$Pd[II].[5,17,20,21] Because there is no fundamental reason why N$_2$Pd[II] complexes should perform better than P$_2$Pd[II] complexes, we are studying these palladium-phosphane complexes in the carbonylation of nitrobenzene. In many catalytic studies the catalyst is often formed in situ by mixing a palladium(II) salt with a diphosphane ligand in methanol, assuming that the desired [Pd(diphosphane)-(anion)$_2$]-type complexes are actually formed. However, complex formation is not always a trivial process. For example, for the copolymerization of CO and ethene it has been reported that the catalytic performance of in situ formed catalysts may be inferior to that of the preformed catalysts.[23]

It has also been reported that when [Pd(OAc)$_2$] and an equimolar amount of dppe [1,2-bis(diphenylphosphanyl)-ethane] are dissolved in CD$_3$OD, initially the catalytically inactive complex [Pd(dppe)$_2$](OAc)$_2$ is formed; only after standing for about 24 h, the catalytically active species [Pd(dppe)(OAc)$_2$] is obtained.[3]

To the best of our knowledge, there is no simple way to predict the exact kinetic pathway by which a certain ligand will or will not form the desired [Pd(diphosphane)-(anion)$_2$]-type complex. We therefore set out to determine the influence of the bridging groups and substituents in chelating diphosphane ligands (see Table 1) on the kinetics and the result of complex formation. Furthermore, the role of the anion in the complex formation process was investigated by using acetate (strongly coordinating) and tosylate (weakly coordinating) anions. Prior to this, however, the synthesis of this type of complexes is reported, followed by their structural characteristics in the solid phase and in solution.

Results and Discussion

Complex Synthesis

Starting from crystalline [Pd$_3$(OAc)$_6$],[24] four solvents were employed in the complex synthesis. In order of increasing polarity these are: CHCl$_3$, CH$_2$Cl$_2$, (CH$_3$)$_2$CO and
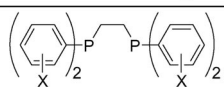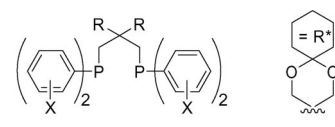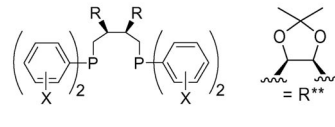
[a] Leiden Institute of Chemistry, Gorlaeus Laboratories, University of Leiden,
P. O. Box 9502, 2300 RA Leiden, The Netherlands
Fax: +31-71-527-4671
E-mail: bouwman@chem.leidenuniv.nl
[b] Bijvoet Center for Biomolecular Research, Crystal and Structural Chemistry, Utrecht University,
Padualaan 8, 3584 CH Utrecht, The Netherlands

Table 1. Schematic representation of the ligands used in this study. The inset figures show the general structures.

Code	X	R	Schematic drawing
L1	H		
L2	o-MeO		
L3	o-EtO		
L4	H	H	
L5	H	CH$_3$	
L6	o-Me	H	
L7	o-MeO	H	
L8	o-EtO	H	
L9	p-MeO	H	
L10	o-MeO	CH$_3$	
L11	o-MeO	CH$_2$CH$_3$	
L12	o-EtO	CH$_2$CH$_3$	
L13	o-MeO	R*	
L14	H	H	
L15	o-MeO	H	
L16	o-EtO	H	
L17	p-MeO	H	
L18	H	R**	
L19	o-MeO	R**	

CH$_3$OH. The methods by which the desired complexes can successfully be obtained are summarized schematically in Figure 1. However, some difficulties were encountered in the synthesis and isolation of these complexes. Dry and degassed solvents must be used as too much water generally hampered the isolation due to the formation of an oil and partial oxidation of the ligand. Furthermore, the flasks were wrapped in foil; the absence of light in most cases prevented plating of Pd^0. The choice of the solvent appeared to be most important. CHCl$_3$ must be avoided since severe plating was usually observed when working with this solvent. CH$_2$Cl$_2$ and (CH$_3$)$_2$CO were best suited for the synthesis of the monochelate [Pd(ligand)(anion)$_2$]-type complexes. Methanol is the only solvent in which the bischelate [Pd(ligand)$_2$](OAc)$_2$-type complexes can be synthesized; the other solvents are not polar enough to sufficiently dissociate the OAc$^-$ anions. The bischelate complexes [Pd(ligand)$_2$]-(OTs)$_2$ can be prepared in all four solvents.

Not all complexes form instantaneously. Indeed, in some cases the desired complex is formed only after several hours (Δt, see complex formation studies for details). Therefore, depending on the ligand, the reaction mixture should stand for an appropriate amount of time (usually overnight), as otherwise a mixture of species may be isolated.

Once the monochelate or bischelate complex had been formed with the acetate anions, addition of two equivalents of p-toluenesulfonic acid resulted in the quantitative replacement of the anions in any of the solvents, as evidenced by the appearance of a peak around 1.0 ppm for acetic acid.

The 1,4-butyl-bridged ligands present a special case. When applying the procedure of Mul and co-workers,[3] the unsubstituted ligand L14 yielded the monochelate complex. This was not the case for L15 and L16. When a solution of Pd(OAc)$_2$ was added to L15, a clear yellow solution was
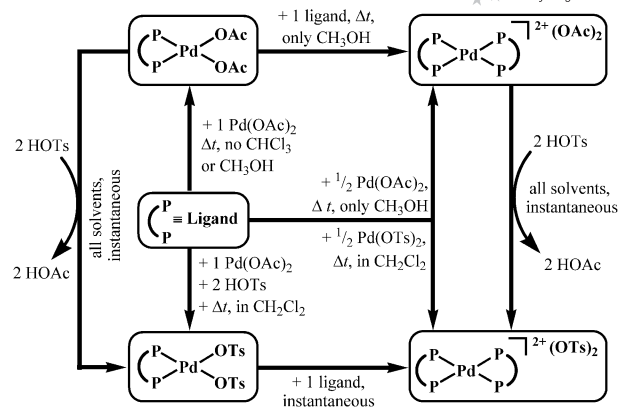

Figure 1. Schematic overview of the synthetic methods to form the monochelate complex [Pd(ligand)(anion)$_2$] or the bischelate complex [Pd(ligand)$_2$](anion)$_2$ with acetate or tosylate anions.

formed immediately. However, after standing for two minutes, a yellow precipitate formed, which turned red-brown over time. The isolated solid proved to be insoluble in a vast variety of different solvents, indicating that this solid is a coordination polymer. When a solution of Pd(OAc)$_2$ was added to L16, a mixture of species was formed (several ^{31}P resonances), which did not change over time. No attempts were made to further characterize these compounds.

Not all complexes were isolated and fully characterized; some were only detected in situ during the NMR spectroscopic studies. Nevertheless, for convenience, in Table S1 (Supporting Information) the proton and phosphorus resonances of all the palladium complexes that could be measured are summarized. The monochelate complexes are indicated as **MxA** or **MxT** with ligand **Lx** and coordinating acetate or tosylate anions, respectively, whereas the bischelate complexes are indicated as **BxA** or **BxT** with ligand **Lx** and non-coordinating acetate or tosylate anions.

Complex Structures in the Solid State

Light yellow transparent single crystals of the compounds [Pd(**L2**)(OAc)$_2$] (**M2A**), [Pd(**L7**)(OAc)$_2$] (**M7A**), [Pd(**L10**)(OAc)$_2$] (**M10A**), [Pd(**L13**)(OAc)$_2$] (**M13A**), and [Pd(**L10**)$_2$](OTs)$_2$ (**B10T**) were obtained using the solvent diffusion technique. The crystal structures were determined by X-ray diffraction; crystallographic data and details of the structure refinement are given in Table 4. Perspective views of the molecular structures of **M10A** and **B10T** in the crystal are shown in Figure 2. Because the global structures of the monochelate complexes are very similar, projections of the complexes **M2A**, **M7A** and **M13A** can be found in the Supporting Information. Selected bond lengths, angles and torsion angles are listed in Table 2.

Complexes **M2A** and **B10T** are located on twofold rotation axes, respectively, running through the palladium centre and the central carbon atom(s) of the ligand backbone. Hence, **M2A** has only one unique phosphorus atom, and **B10T** only two. The palladium centres in the complexes **M2A**, **M7A**, **M10A**, **M13A**, and **B10T** are in distorted
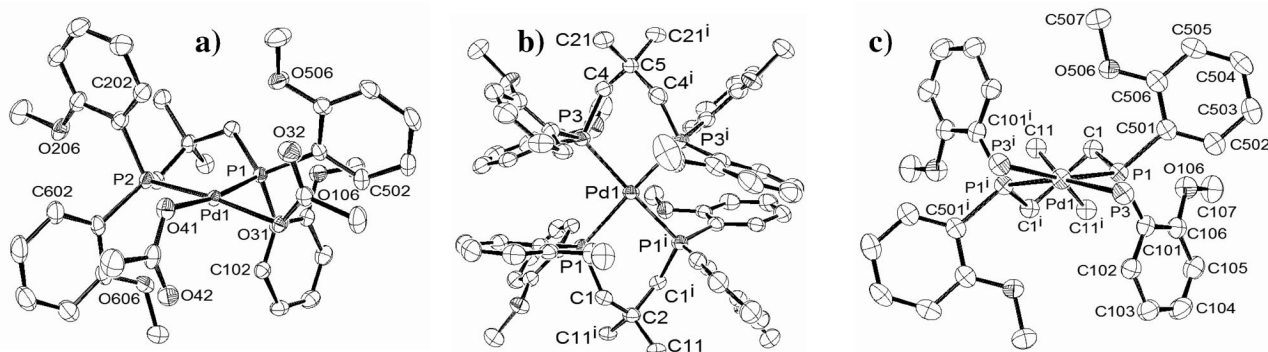
Figure 2. Displacement ellipsoid plots (50% probability level) of (a) [Pd(**L10**)(OAc)$_2$] (front view), (b) cation of [Pd(**L10**)$_2$](OTs)$_2$ (top view), (c) cation of [Pd(**L10**)$_2$](OTs)$_2$ (front view along the twofold axis, one ligand omitted, except for the phosphorus atoms). Hydrogen atoms, uncoordinated anions and uncoordinated solvent molecules are omitted for clarity. Symmetry operation i: 1 – x, y, 0.5 – z.

square-planar geometries with *cis*-P$_2$O$_2$ donor sets for the monochelate complexes and a P$_4$ donor set for the bischelate complex. The Pd–P and Pd–O distances can be considered as normal.[25] Although the acetate anions are coordinated in a monodentate fashion, they may be considered pseudo-chelating with their second O-atom at distances to Pd ranging between 2.8067(19) (**M7A**) and 3.1771(16) (**M10A**) Å, and Pd–O–C angles ranging between 67.53(18)° (**M13A**) and 75.65(14)° (**M10A**). The magnitude of the distortion from the ideal square-planar geometry varies considerably. The dihedral angle between the P–Pd–P and X–Pd–X (X = P or O) planes range from 1.56(7)° in **M2A**, to 7.22(8)–10.46(6)° in **M7A**, **M10A**, and **M13A**, and is 19.78(5)° in the bischelate complex **B10T**. The large tetrahedral distortion in **B10T** is due to the presence of large steric bulk of two ligands around the palladium centre; there are no other intermolecular or intramolecular contacts responsible for this distortion. The ligand bite angles also vary considerably. The ethylene-bridged ligand **L2** in **M2A** has a bite angle of 85.98(3)°, whereas the propylene-bridged ligand **L7** in **M7A** has a bite-angle of 95.497(19)°. This angle is slightly compressed by the addition of steric bulk to the backbone, resulting in 90.62(2)° in **M10A** and 92.22(3)° in **M13A**. In the bischelate complex **B10T**, the angle is compressed even further to a mere 85.69(4)°. The six-membered PdP$_2$C$_2$ coordination rings in **M10A**, **M13A**, and **B10T** have a twist-boat and in **M7A** a screw-boat conformation, while the five-membered PdP$_2$C ring in **M2A** has a half-chair conformation.

It is possible to distinguish the two aryl rings on each phosphorus atom as oriented either axially (for the NMR spectroscopic discussion denoted as rings 100, 200, 300, and 400) or equatorially (rings 500, 600, 700, and 800) with respect to the chelate ring of the bidentate ligand (see for example rings 100 and 500 in Figure 2, a and c). The axial phenyl rings are held in place by Pd···H interactions between its *ortho* proton and the filled palladium d$_{z^2}$ orbital. Similar interactions have been reported for related nickel and palladium complexes.[26,27] These interactions have been described as anagostic,[28] and are characterized by a Pd–P–C–C torsion angle close to 0°. The Pd···H distances

[between 2.71 (**M13A**) and 3.06 Å (**B10T**)], and the Pd–P–C–C torsion angles [between 1.38(18)° (**M10A**) and 11.5(3)° (**M13A**)] of the observed anagostic interactions, can be considered as normal.[28] Furthermore, relatively strong intramolecular C–H···π interactions between the *ortho* protons of the equatorial rings (H502, H602, H702) and one π-bond of the axial rings (C101/C106, C201/C206, C301/C306) are observed.[29] The various H···C distances, ranging between 2.527 (for **M10A**) and 2.817 (for **M7A**) Å, are well within the sum of the van der Waals radii of H and C (2.90 Å).

The structures of the complexes [Pd(**L1**)OAc$_2$],[30] [Pd(**L2**)Cl$_2$] and [Pd(**L7**)Cl$_2$],[31] as well as of the analogous nickel(II) complexes [Ni(**L2**)I$_2$][26] and [Ni(**L7**)Cl$_2$][32] have been published; the reported distances, angles and Pd···H or Ni···H interactions are comparable to those described above.

Complex Structure in Solution

As typical examples, the ^{1}H NMR spectra of the monochelate complexes **M13A** and **M13T** are shown in parts a and c of Figure 3, respectively [in (CD$_3$)$_2$CO]. In the solid-state structures, the two phenyl rings on each phosphorus atom are distinct with respect to their orientation to the plane of coordination and have been labelled as axial or equatorial. In solution at room temperature, however, only one set of resonances is observed, as is shown in Figure 3a for **M13A**. The observation that the two phenyl rings appear to be equivalent in solution is due to dynamic flipping of the backbone.[26] When this flipping is frozen at low temperature, the axial and equatorial protons become inequivalent; two sets of proton resonances are observed in ^{1}H NMR spectra (Figure 3, b). The proton resonances of the axial phenyl rings are relatively deshielded due to the Pd···H interactions, whereas the proton resonances of the equatorial phenyl rings are shielded due to the H···Cπ interactions.

For the monochelate complex **M13T** with the weakly-coordinating OTs$^-$ anions (Figure 3, c) a different phenomenon is observed upon cooling; the peaks are not split, but broadened (Figure 3, d). It suggests that the weakly-coordi-

Table 2. Selected interatomic distances, angles, and other relevant geometric data for complexes **M2A**, **M7A**, **M10A**, **M13A**, and **B10T**.

Complex:	M2A[a]	M7A	M10A	M13A	B10T[a]	
(pseudo) coordination (Å)						
Pd^1–P^1	2.2177(6)	2.2223(6)	2.2366(6)	2.2341(8)	2.4091(8)	
Pd^1–P^2		2.2273(5)	2.2305(5)	2.2254(8)		
Pd^1–P^3					2.3938(9)	
Pd^1–O^{31}	2.0984(14)	2.1112(14)	2.0891(13)	2.047(2)		
Pd^1–O^{41}		2.0946 (13)	2.0936(15)	2.064(2)		
Pd^1–O^{32}	2.9169(17)	2.8662(19)	3.1771(16)	3.099(2)		
Pd^1–O^{42}		2.8067(19)	3.0718(16)	3.153(2)		
Anagostic interactions [Å][b]						
Pd^1···H^{102}	2.75	2.72	2.87	2.82	3.03	
Pd^1···H^{202}		2.69	2.75	2.71		
Pd^1···H^{302}					3.06	
C–H···π interactions [Å][b]						
H^{502}···C^{101}	2.57	2.70	2.53	2.59	2.66	
H^{502}···C^{106}	2.77	2.82	2.53	2.72	2.63	
H$^{602/702}$···C$^{201/301}$		2.61	2.55	2.54	2.67	
H$^{602/702}$···C$^{206/306}$		2.59	2.66	2.68	2.82	
Angles [°]						
P^3–Pd^1–P$^{3'}$					86.04(3)	
P^1–Pd^1–P^3					95.71(3)	
P^1–Pd^1–P$^{3'}$					166.56(3)	
P^1–Pd^1–P$^{2/1'}$	85.98(3)	95.497(19)	90.62(2)	92.22(3)	85.69(4)	
O^{31}–Pd^1–O$^{41/31'}$	92.22(8)	87.03(5)	92.20(6)	94.97(9)		
P^1–Pd^1–O^{41}	90.91(5)	90.78(4)	90.38(4)	87.00(6)		
P^2–Pd^1–O^{42}		87.14(4)	87.70(4)	86.24(6)		
P^1–Pd^1–O$^{41/31'}$	176.69(4)	174.80(4)	170.96(4)	172.80(6)		
P^2–Pd^1–O^{31}		171.72(4)	174.09(4)	176.36(6)		
Pd^1–O^{31}–C^{31}	111.28(14)	108.29(13)	121.81(13)	117.90(18)		
Pd^1–O^{41}–C^{41}		107.86(12)	117.96(14)	120.6(2)		
Pd^1–O^{32}–C^{31}	73.80(14)	74.79(14)	68.60(12)	67.53(18)		
Pd^1–O^{42}–C^{41}		75.65(14)	70.89(13)	68.40(18)		
Dihedral angles between the PdP$_2$ and the PdX$_2$ planes (°)						
PdP$_2$–PdX$_2$ (dihedral)	1.56(7), X = O	7.22(8), X = O	10.46(6), X = O	7.63(9), X = O	19.78(5), X = P	
Cremer–Pople ring puckering parameters for the PdP$_2$C$_2$ and PdP$_2$C rings[c]						
					Ring 1	Ring 2
Q$_2$ [Å]	0.492(2)	0.5247(19)	0.8588(17)	0.812(2)	0.906(3)	0.898(3)
Q$_3$ [Å]		0.3266(19)	–0.0369(16)	0.051(2)	0.000(2)	0.000(3)
θ [°]		58.09(18)	92.46(11)	86.42(14)	90.00(13)	90.00(19)
ϕ_2 [°]	270.00(12)	156.4(2)	266.99(11)	82.57(16)	270.00(14)	270.00(14)
Torsion angles (°)						
Pd^1–P^1–C^{101}–C^{102}	–7.1(2)	–4.95(18)	–1.38(18)	11.5(3)	6.1(3)	
Pd^1–P^2–C^{201}–C^{202}		–5.67(19)	–1.8(2)	8.3(3)		
Pd^1–P^3–C^{301}–C^{302}					13.0(3)	
Pd^1–P^1–C^{501}–C^{502}	102.30(18)	–104.51(18)	105.15(18)	–113.0(3)	120.0(3)	
Pd^1–P^2–C^{601}–C^{602}		–102.44(17)	104.54(17)	–108.1(3)		
Pd^1–P^3–C^{701}–C^{702}					101.7(3)	

[a] Coordination rings are located on twofold axis. [b] Hydrogen atoms were introduced in calculated positions based on a C–H distance of 0.95 Å. [c] Cremer–Pople ring puckering parameters for the PdP$_2$C$_2$ and PdP$_2$C rings.[22]

nating OTs$^-$ anions are displaced with solvent molecules; the Pd^{II} ion is in a [Pd(ligand)(solvent)$_2$]$^{2+}$ coordination sphere and even at low temperatures the coordinated solvent ligands are quickly exchanged with other solvent molecules, thus decreasing the steric hindrance for the flipping of the backbone. Further cooling should result in a complete splitting into two sets of protons. In contrast, the presence of relatively strongly coordinating OAc$^-$ anions in **M13A** makes the overall complex more rigid at lower temperature, thereby hindering the dynamic flipping of the backbone. In the case of the crowded [Pd(ligand)$_2$](anion)$_2$ complexes, two sets of proton resonances are observed at all temperatures. Their spectra resemble the one shown in Figure 3, b.
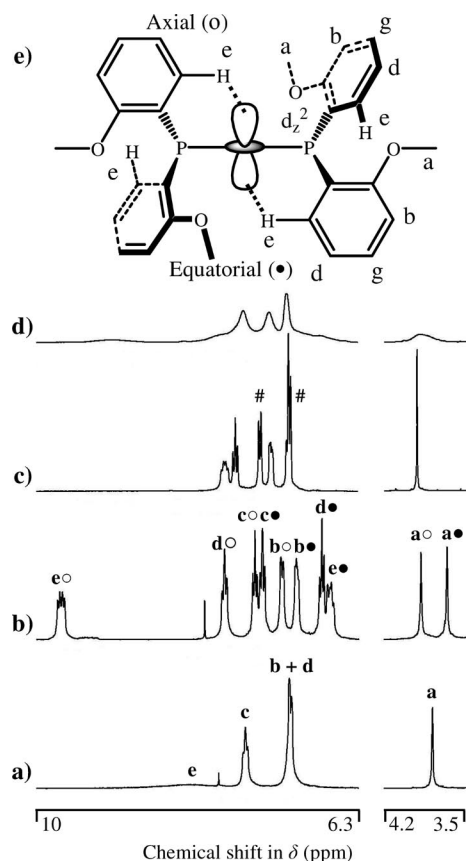
T. J. Mooibroek, E. Bouwman, M. Lutz, A. L. Spek, E. Drent

Figure 3. ^1H NMR spectra of monochelate complexes in $(CD_3)_2$-CO: a) **M13A** at 23 °C; b) **M13A** at –60 °C; c) **M13T** at 23 °C; d) **M13T** at –60 °C; e) schematic view of the interactions and labelling of the H atoms. The symbol ● indicates that the resonance belongs to an equatorially aligned ring, o indicates that the resonance belongs to an axially aligned ring, and # indicates a resonance from a tosylate anion.

Complex Formation Studies

NMR spectroscopic studies were performed to explore the kinetics of formation of the palladium complexes of different types of ligands in more detail. Using $Pd(OAc)_2$, the complex formation was studied in the deuterated solvents CD_2Cl_2, $(CD_3)_2CO$, and CD_3OD. When using $Pd(OTs)_2$ the only suitable solvent is a mixture of $(CD_3)_2CO$ in CD_2Cl_2 (17% v/v); $Pd(OTs)_2$ is immediately reduced in CD_3OD, HOTs and $Pd(OTs)_2$ are insoluble in pure CD_2Cl_2, and most $[Pd(ligand)_2](OTs)_2$-type complexes are insoluble in $(CD_3)_2CO$. An overview of the results of selected complex formation studies is presented in Table 3. During these studies a variety of complexes were observed in situ, but were not isolated. Nonetheless, an overview of the ^1H- and ^{31}P-NMR spectroscopic data of all the detected complexes is given in Table S1.

Ethylene-Bridged Ligands

Use of the ethylene-bridged ligands **L1**–**L3** directly results in the formation of the monochelate complex [Pd(ligand)(OAc)₂] when the reaction is performed in $(CD_3)_2CO$

or CD_2Cl_2 (Entries 1–3). In CD_3OD however, as reported by Mul and co-workers,[3] **L1** initially forms the bischelate complex (δ_P = 58.7 ppm) as the kinetic product, which converts to the thermodynamically more stable monochelate complex (δ_P = 63.7 ppm) over time (k' = 0.44 h^{-1}). In the case of the sterically more demanding ligands **L2** (*o*-MeO) and **L3** (*o*-EtO), in CD_3OD the monochelate complex is formed directly as the major species (≈ 70%). The other product is the bischelate complex (≈ 30%). The composition of this mixture did not change over time (eight hours), nor upon addition of another 0.2 equiv. of $Pd(OAc)_2$. This indicates that the *o*-MeO moieties on the ligand shield the palladium in the bischelate complex from OAc⁻ coordination. It thus appears that ethylene-bridged ligands directly form the monochelate complex, except in a relatively polar solvent. Only then the OAc⁻ anions may dissociate from Pd^{II} to allow a second ligand to coordinate, thus forming the bischelate complex. Indeed, it has been reported that by employing the weakly coordinating OTs⁻ anions, the bischelate complex is formed exclusively.[3]

Propylene-Bridged Ligands

For the ligands with an unsubstituted propylene backbone (Entries 4 and 6–9) different behaviour is observed when starting from $Pd(OAc)_2$. In the case of **L4** (dppp), the monochelate complex is formed immediately in all solvents. However, the *ortho*-methoxy analogue of this ligand (**L7**) forms the monochelate complex via an intermediate species, as is illustrated in Figure 4 (in CD_2Cl_2).

This intermediate is not the usual bischelate complex, since the characteristic resonances of the axial and equatorial (*ortho*) protons are not observed. In the NMR spectra of this intermediate, no free ligand ^{31}P resonance is observed at –37 ppm, and several resonances are observed for the *ortho*-methoxy protons (3.3–3.9 ppm). The resonances around 1.8 and 0.6 ppm are indicative of different types of OAc⁻ anions. These observations suggest the formation of a polynuclear species, which could be either a polymeric compound $[Pd(L7)(OAc)_2]_n$ in which the ligand is monodentate and bridging, or a dinuclear complex $[\{Pd(L7)-(OAc)\}_2L7](OAc)_2$. The intermediate species could be isolated, but we were unable to detect a mass higher than that of the monochelate complex using ESI mass spectroscopy.

To investigate whether the difference in behaviour of the ligands **L4** and **L7** is due to steric or electronic reasons, a series with increased steric bulk on the *ortho* position was studied; **L4** (H), **L6** (Me), **L7** (MeO), and **L8** (EtO). The same type of intermediate is observed for the ligands **L6**–**L8** in $(CD_3)_2CO$; the conversion to the monochelate complex follows approximate first-order kinetics (see Figure 5). An increase in steric bulk results in a lower $p \rightarrow m$ conversion rate, with k' = 1.03, 0.49, and 0.25 h^{-1} for **L6**, **L7**, and **L8**, respectively. Apparently, in the proposed intermediate polynuclear species, the larger steric "*ortho*-bulk" of the ligand shields the palladium d_{z^2} orbital (see also Figure 3, e) for the approach of a phosphane (in the case of [Pd(L)-

Table 3. Overview of complex formation studies, monitored by ^{1}H and ^{31}P NMR spectroscopy.[a]

	Ligand (L)				Pd(OAc)$_2$			Pd(OTs)$_2$
Entry	Schematic drawing	R	X	Code	CD$_3$OD	(CD$_3$)$_2$CO	CD$_2$Cl$_2$	CD$_2$Cl$_2$[b]
1			H	L1	b→m (0.44)	m	m	(b in CD$_3$OD)[3]
2			o-MeO	L2	m + b	m	m	
3			o-EtO	L3	m + b	m	m	
4		H	H	L4	m	m	m	b→m (6.23)
5		CH$_3$	H	L5	m	m	m	
6		H	o-Me	L6	i	p→m (1.03)	m	
7		H	o-MeO	L7	p→m (0.07)[b]	p→m (0.49)	p→m (0.53)	b→m (0.01)[c]
8		H	o-EtO	L8	i	p→m (0.25)	p→m (1.00)	
9		H	p-MeO	L9	m	m	m	
10		CH$_3$	o-MeO	L10	m	m	m	
11		C$_2$H$_5$	o-MeO	L11	m	m	m	
12		C$_2$H$_5$	o-EtO	L12	m	m	m	
13		R*	o-MeO	L13	i	m	m	
14		H	H	L14			p→m (1.07)	m
15		H	o-MeO	L15	i	i	p→x (1.26)	
16		H	o-EtO	L16	i	i	p→x (0.58)	
17		H	p-MeO	L17			p→m (1.15)	
18		R**	H	L18			m	
19		R**	o-MeO	L19			m	

[a] [Pd(OAc)$_2$] or [Ligand] = 16 mM. The values between parentheses represent a reaction constant (k' in h^{-1}, see Exp. Sect.) for the observed conversion. m = monochelate complex; b = bischelate complex; p = polynuclear complex; x = unidentified complex(es); i = ligand or complex is insoluble. See text for further explanation. [b] 17% (v/v) of (CD$_3$)$_3$CO in CD$_2$Cl$_2$ was actually used due to solubility problems. [c] The complex formation was accompanied by plating over time.
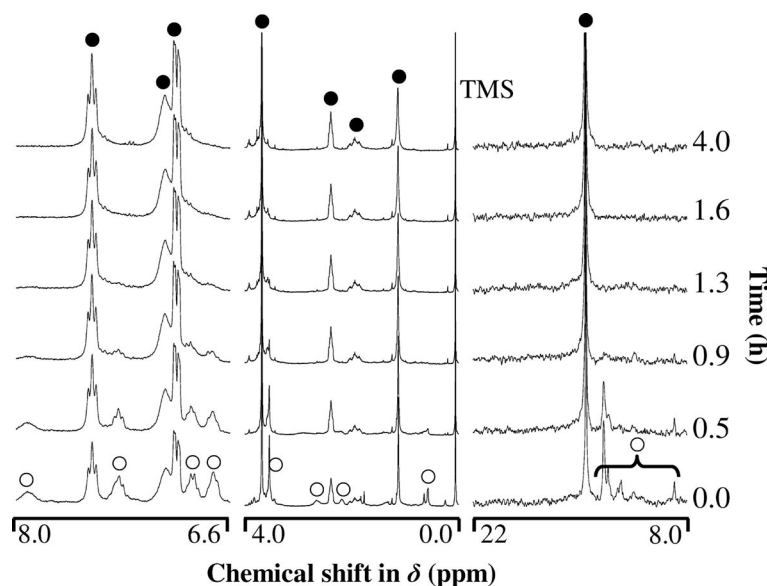
Figure 4. Complex-forming study followed by ^{1}H and ^{31}P NMR spectroscopy; [Pd(OAc)$_2$] in CD$_2$Cl$_2$ added to L7. ● resonance of the (thermodynamic) monochelate complex; ○ resonance of the (kinetic) intermediate.

(OAc)$_2$]$_n$) or an acetate anion (in the case of [{Pd(L)(OAc)}$_2$L](OAc)$_2$). This is illustrated in Figure 6. To confirm that the effect is purely based on steric grounds the experiment was repeated with L9 (p-MeO, Entry 9). This ligand indeed showed the immediate formation of the monochelate complex in all three solvents.

Interestingly, when the propylene backbone is more rigid by the gem-dialkyl substitution of the central carbon atom in the bridge (L10 – L13, Entries 10–13), no intermediate species is observed. In these cases the monochelate complex is immediately formed, even for ligand L12, which comprises the larger o-EtO substituent on the phenyl rings. This
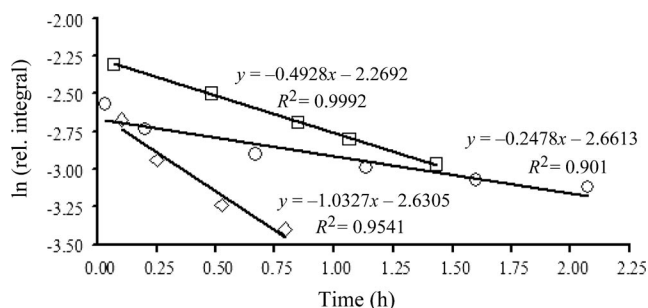
Figure 5. Effect of the steric bulk on monochelate complex formation with propylene-bridged ligands in acetone; plot of ln(rel. integral) vs. time (h), at 23 °C with linear trend lines. ◇ **L6** at δ = 8.1 ppm; ◯ **L7** at δ = 7.4 ppm; ☐ **L8** at δ = 7.3 ppm.
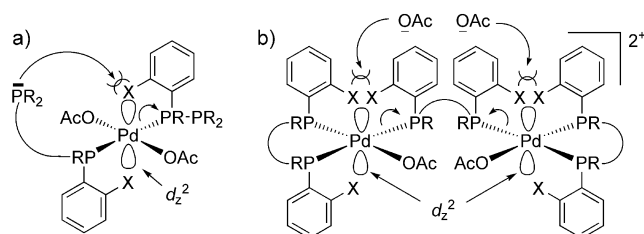

Figure 6. Illustration of the ligand-induced steric hampering that retards the formation of [Pd(**L**)(OAc)$_2$]-type complexes. The steric bulk of the *ortho*-moieties (X) of the ligand shields the palladium d_{z^2} orbital from ligand approach in [Pd(**L**)(OAc)$_2$]$_n$ (a), or from acetate coordination in [{Pd(**L**)(OAc)}$_2$**L**](OAc)$_2$ (b).

observation is attributed to the so-called "Thorpe–Ingold" effect;[33,34] due to the presence of the two substituents on the central carbon atom in the backbone, the two phosphorus atoms are pre-oriented and more likely to form a chelate on palladium. In line with this, **L5** also forms the monochelate complex immediately.

Butylene-Bridged Ligands

With the butylene-bridged ligands **L14** and **L17** (*o*-H and *p*-MeO, Entries 14 and 17) the monochelate complex is formed only via an intermediate species; several ^{31}P resonances around 12 ppm disappear over the time. The approximate first-order reaction constants of these conversions are of the same magnitude (in CD$_2$Cl$_2$ k' = 1.07 and 1.15 h^{-1} for **L14** and **L17**, respectively). This difference in behaviour between the unsubstituted C3- and C4-bridged ligands is ascribed to the increased flexibility of the butylene backbone. This renders the ligand a weaker chelate thus favouring the initial formation of a polynuclear species. In agreement with this hypothesis, using a ligand with a more rigid backbone (**L18**, Entry 18) the monochelate complex is formed immediately.

A different thermodynamic species is observed when steric bulk is added to the *ortho* position in the flexible butylene-bridged ligands (**L15** and **L16**). This is exemplified for ligand **L15** in Figure 7. The kinetic product is rather similar to those formed for the *o*-H (**L14**) and *p*-MeO (**L17**) analogues. A number of resonances is observed in the ^{31}P NMR spectrum around 11 ppm, and in the ^{1}H NMR spectrum around 3.75 ppm for the methoxy group. Especially the aromatic resonance around 7.9 ppm is very characteristic for this type of intermediate. However, for **L15** and **L16** the nature of the thermodynamic product is unclear; it is most certainly not the desired monochelate complex, or the bischelate complex. The rate of conversion again depends on the size of the steric bulk; k' = 1.26 (**L15**; *o*-MeO) and 0.58 (**L16**; *o*-EtO). Because **L17** (*p*-MeO) eventually forms the monochelate complex, the formation of the unidentified species is ascribed to steric influences. When the backbone is made more rigid (**L19**), the monochelate complex is formed immediately and none of the other species were detected.
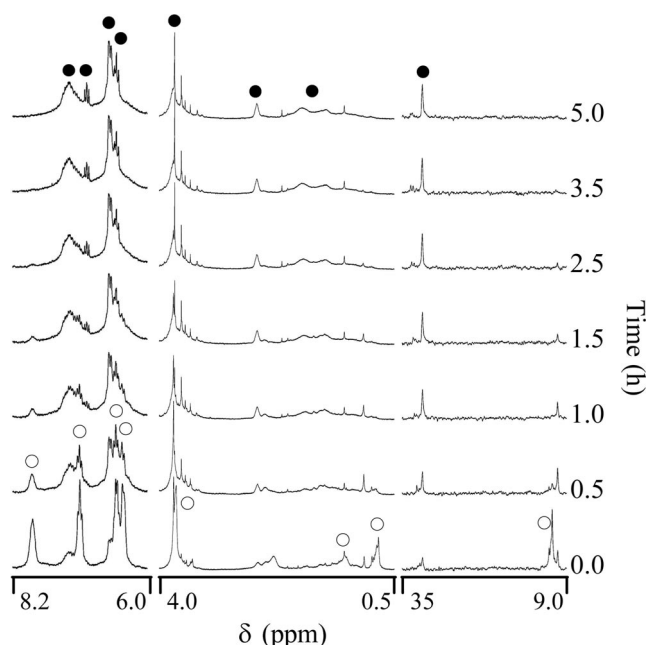

Figure 7. Complex formation for **L15** monitored by ^{1}H- and ^{31}P NMR spectroscopy; [Pd(OAc)$_2$] in CD$_2$Cl$_2$ added to **L15**. ● resonance of thermodynamic product; ◯ resonance of the kinetic intermediate.

The Role of the Coordinating Strength of the Anions

Not only the steric bulk and (the rigidity of) the ligand backbone are important for the course and rate of the complex formation. The coordination strength of the anions was also found to be an important factor. For **L1** (ethylene backbone) it is known that when employing the weakly coordinating CF$_3$C(O)O$^-$ anions in CD$_3$OD, the bischelate complex is both the kinetic and thermodynamic species.[3]

For the propylene-bridged ligands, it was found that the more polar the solvent, the more dissociated the OAc$^-$ anions become, and hence the slower the conversion to the monochelate complex. This is most prominently reflected in the series performed with **L7** (*o*-MeO). As can be seen from Entry 7 in Table 4, the monochelate complex is

Table 4. Details of the X-ray crystal structure determinations.

	[Pd(**L2**)(OAc)$_2$]	[Pd(**L7**)(OAc)$_2$]	[Pd(**L10**)(OAc)$_2$]	[Pd(**L13**)(OAc)$_2$]	[Pd(**L10**)$_2$](OTs)$_2$
Empirical formula	C$_{34}$H$_{38}$O$_8$P$_2$Pd·2CHCl$_3$	C$_{35}$H$_{40}$O$_8$P$_2$Pd·H$_2$O	C$_{37}$H$_{44}$O$_8$P$_2$Pd·3H$_2$O	C$_{43}$H$_{52}$O$_{10}$P$_2$Pd	[C$_{66}$H$_{76}$O$_8$P$_4$Pd] (C$_7$H$_7$O$_3$S)$_2$ + disordered solvent
Fw	981.72	775.03	839.11	897.19	1569.92[a]
Crystal colour	colourless	yellow	colourless	yellow	yellow
Crystal size [mm]^3	0.21×0.15×0.12	0.24×0.18×0.15	0.30×0.12×0.08	0.66×0.12×0.12	0.30×0.12×0.12
Crystal system	monoclinic	monoclinic	monoclinic	monoclinic	monoclinic
Space group	C2/c (no. 15)	P2$_1$/c (no. 14)	P2$_1$/c (no. 14)	P2$_1$/c (no. 14)	C2/c (no. 15)
a [Å]	21.3571(2)	13.9845(3)	13.7552(1)	10.8518(4)	26.4819(3)
b [Å]	11.0576(1)	16.2664(4)	14.2919(1)	26.8681(11)	14.1198(2)
c [Å]	19.5445(2)	20.0199(3)	20.0689(2)	15.5000(7)	24.7120(3)
β [°]	116.1887(4)	130.991(2)	96.4044(4)	113.881(3)	118.1165(6)
V [Å^3]	4141.78(7)	3437.47(16)	3920.68(6)	4132.4(3)	8149.85(18)
Z	4	4	4	4	4
$d_{calcd.}$ [g/cm^3]	1.574	1.498	1.422	1.442	1.279
μ [mm^{-1}]	0.961	0.687	0.612	0.584	0.417
(sin θ/λ)$_{max}$ [Å^{-1}]	0.65	0.65	0.65	0.65	0.60
Refl. (meas./unique)	33907/4746	58871/7906	55912/8984	136182/9451	37289/7346
Abs. corr.	multi-scan	multi-scan	multi-scan	multi-scan	multi-scan
Abs. corr. range	0.85–0.89	0.75–0.90	0.92–0.96	0.60–0.93	0.74–0.96
Param./restraints	270/66	438/0	470/0	511/0	464/0
R1/wR2 [$I > 2\sigma(I)$]	0.0299/0.0731	0.0257/0.0579	0.0314/0.0722	0.0409/0.0745	0.0463/0.1129
R1/wR2 [all refl.]	0.0436/0.0793	0.0400/0.0637	0.0470/0.0797	0.0676/0.0856	0.0685/0.1222
S	1.100	1.044	1.067	1.152	1.031
$\Delta\rho_{min./max.}$ [e Å^{-1}]	–0.54/0.51	–0.43/0.60	–0.68/0.84	–0.71/0.57	–0.59/0.95

[a] Derived values do not contain the contribution of the disordered solvent.

formed slightly faster in CD$_2$Cl$_2$ (*k'* = 0.53) than in (CD$_3$)$_2$-CO (*k'* = 0.49), and only very slowly in CD$_3$OD (*k'* = 0.07). Similar trends were observed with ligands **L6** and **L8** (Entries 6 and 8). That these observations are due to the coordinating ability of the anions is confirmed by employing weakly-coordinating OTs$^-$ anions. Instead of a polynuclear species, **L7** now forms the bischelate complex as kinetic product (Entry 7). Evidently, OTs$^-$ anions are highly dissociated (even in the relatively apolar CD$_2$Cl$_2$) to allow the formation of a cationic species with a P$_4$ donor set. The conversion to the monochelate complex is extremely slow (*k'* = 0.01 h^{-1}), because the *o*-MeO moieties shield the palladium d_{z^2} orbitals from anion coordination (see Figure 6). Evidently, OTs$^-$ anions coordinate so weakly that they can hardly overcome this steric repulsion induced by the *o*-MeO moieties. When working with **L4** (*o*-H, Entry 4), the bischelate complex was also formed as intermediate. However, due to the smaller *ortho*-bulk the conversion to the monochelate complex proceeds very rapidly (*k'* = 6.23 h^{-1}).

The coordinating ability of the anions also influences the course of the complex formation with butylene-bridged ligands. As can be seen in Entry 14 (**L14**, *o*-H), when employing OTs$^-$ anions the monochelate complex is formed immediately, whereas with OAc$^-$ anions it proceeds via some intermediate. This can be rationalized as follows. When OAc$^-$ anions are used, the monochelate complex (P$_2$O$_2$ donor set) is formed via a PO$_3$ donor set. This is due to the strongly-coordinating nature of the OAc$^-$ anions (perhaps in a bridging manner). When the anions are weakly coordinating (OTs$^-$) the P$_2$O$_2$ donor set is formed immediately. That the ligand **L14** does not form the bischelate complex (e.g., a P$_4$ donor set like its propylene-bridged analogue **L4**) is ascribed to its larger bite-angle (*β* ≈ 99°

vs. 94°).[35] This imposes a steric constraint on the adjacent coordination sites,[36,37] thus disfavouring bischelate complex formation.

Conclusions

A variety of palladium complexes with substituted bidentate diphenylphosphane ligands has been synthesized using straightforward synthetic procedures. More specifically, monochelate and bischelate complexes with strongly (OAc$^-$) or weakly (OTs$^-$) coordinating anions have been obtained, and structures of representative complexes have been described. By using variable-temperature NMR spectroscopic studies, it was shown that the solid-state structure of this type of complexes is fully retained in solution.

It was shown that three ligand-dependent factors play a crucial role in the formation of [Pd(ligand)(anion)$_2$]-type complexes: the length of the bridge between the phosphorus donors, the steric bulk at the *ortho* position of the phenyl rings, and the rigidity of the backbone. The coordinating ability of the anions was also found to be an important factor in the complex forming process.

Depending on these factors, the desired [Pd(ligand)(-anion)$_2$] complex is formed instantaneously, via some intermediate, or not at all. Notably, when making the ligand bridge more rigid, the desired [Pd(ligand)(anion)$_2$] complex is formed directly in all cases studied.

It is thus concluded that it is important to realize that the formation of [Pd(ligand)(anion)$_2$]-type complexes is not always instantaneous or successful. Thus, when performing catalytic reactions with in situ formed complexes, one should make sure that the desired complex will actually

form. We hope to have provided a significant contribution to the fundamental understanding of whether the desired catalyst will indeed be formed.

Experimental Section

Materials: Solvents and chemicals were commercially available as A.R. grade and used as received, unless stated otherwise. The ligand and complex syntheses were performed under argon and the purifications were commonly performed in air, unless stated otherwise. A schematic overview of the ligands used in this study is presented in Table 1. The ligands **L1**, **L4**, **L14**, and **L17** are commercially available and were used as received. The ligands **L5**, **L15**, and **L16** have been synthesized according to literature procedures.[38–41] The other ligands were obtained as a gift from Shell International Chemicals B.V., where they were prepared according to literature procedures.[42–50] All ligand molecular data are summarized in Table S1.

Physical Methods

Common Analytical Techniques: ^{1}H- and ^{31}P{^{1}H}-NMR spectra were recorded using a DPX Bruker instrument operating at 300 or 400 MHz. Chemical shifts are reported in δ (parts per million); the proton resonances are given relative to the solvent peak [CD$_3$OD = 3.33 ppm, (CH$_3$)$_2$SO = 2.50 ppm, (CH$_3$)$_2$CO = 2.06 ppm, CDCl$_3$ = 7.26 ppm, CD$_2$Cl$_2$ = 5.30 ppm] or tetramethylsilane (TMS, 0 ppm). The phosphorus resonances are given relative to the external standard H$_3$PO$_4$ (85%, 0 ppm). C, H, and N analyses were carried out using an automatic Perkin–Elmer 2400 Series II CHNS/O microanalyzer. ESI Mass Spectroscopy was carried out using a Finnigan Aqua Mass Spectrometer equipped with an electrospray ionization (ESI) source. Sample solutions (10 µL of a 1 mg/mL solution) were introduced in the ESI source by using a Dionex ASI-100 automated sampler injector and an eluent running at 0.2 mL/min.

X-ray Crystal Structure Determinations: X-ray intensities were measured with a Nonius KappaCCD diffractometer with rotating anode (graphite monochromator, λ = 0.71073 Å) at a temperature of 150(2) K. Data were integrated with the HKL2000[51] ([Pd(**L2**)(OAc)$_2$], [Pd(**L10**)(OAc)$_2$], [Pd(**L10**)](OTs)$_2$) or Eval-CCD[52] ([Pd(**L7**)(OAc)$_2$], [Pd(**L13**)(OAc)$_2$]) software. The structures were solved with Direct Methods using the programs SIR-97[53] ([Pd(**L2**)(OAc)$_2$], [Pd(**L10**)](OTs)$_2$) and SHELXS-97[54] ([Pd(**L10**)(OAc)$_2$]) or with automated Patterson Methods using the program DIRDIF-99[55] ([Pd(**L7**)(OAc)$_2$], [Pd(**L13**)(OAc)$_2$]). The structures were refined with SHELXL-97.[54] Non-hydrogen atoms were refined with anisotropic displacement parameters. Hydrogen atoms were located in difference-Fourier maps ([Pd(**L2**)(OAc)$_2$], [Pd(**L10**)(OAc)$_2$]) or introduced in calculated positions ([Pd(**L7**)(OAc)$_2$], [Pd(**L13**)(OAc)$_2$], [Pd(**L10**)$_2$](OTs)$_2$) and refined with a riding model. Drawings, structure calculations and checking for higher symmetry were performed with the PLATON software.[56] Further experimental details are given in Table 4.

CCDC-748839 (for [Pd(**L2**)(OAc)$_2$]), -748840 (for [Pd(**L7**)(OAc)$_2$]), -748841 (for [Pd(**L10**)(OAc)$_2$]), -748842 (for [Pd(**L13**)(OAc)$_2$]), -748843 (for [Pd(**L10**)$_2$](OTs)$_2$) contain the supplementary crystallographic data for this paper. These data can be obtained free of charge from The Cambridge Crystallographic Data Centre via www.ccdc.cam.ac.uk/data_request/cif.

[Pd(**L2**)(OAc)$_2$]: The CHCl$_3$ solvent molecule was refined with a disorder model. [Pd(**L7**)(OAc)$_2$]: Hydrogen atoms of the water molecule were refined freely with isotropic displacement parameters. [Pd(**L10**)(OAc)$_2$]: Hydrogen atoms of the water molecules were kept fixed at the positions located in difference Fourier maps. The methyl groups of the acetate ligands were refined with two conformations, respectively. [Pd(**L10**)$_2$](OTs)$_2$: The crystal structure contains solvent accessible voids (1046 Å^3/unit cell) filled with disordered solvent molecules. Their contribution to the structure factors was secured by back-Fourier transformation using the SQUEEZE routine of the program PLATON[56] resulting in 307 e$^-$/unit cell.

NMR Spectroscopic Complex Formation Studies

Preparation of the Samples, Using Pd(OAc)$_2$: The ligand (12.8 µmol) was weighed into an NMR tube and put under argon. In another tube, Pd(OAc)$_2$ (3.59 mg, 16 µmol) was dissolved in 1 mL of solvent under argon. Of this solution, (0.8 mL, 12.8 µmol of Pd) was added to the ligand using a 1-mL syringe, which was dry and flushed with argon. The thus obtained mixture (16 mM) was thoroughly mixed using a vortex mixer until a clear solution was obtained. When no clear solution was obtained within ten minutes of mixing, the sample was considered to be insoluble and was discarded.

Preparation of the Samples, Using Pd(OTs)$_2$: The ligand (12.8 µmol) was weighed into an NMR tube and put under argon. In another tube, Pd(OAc)$_2$ (3.59 mg, 16 µmol) and HOTs (5.51 mg, 32 µmol) were dissolved in 1 mL of (CD$_3$)$_2$CO in CD$_2$Cl$_2$ (17% v/v), under argon. Of this solution, 0.8 mL (12.8 µmol of Pd) was added to the ligand using a 1-mL syringe, which was dry and flushed with argon. The thus obtained mixture (16 mM) was thoroughly mixed using a vortex mixer until a clear solution was obtained. When no clear solution was obtained within ten minutes of mixing, the sample was considered to be insoluble and was discarded.

NMR Kinetic Measurements: The clear solutions were monitored with ^{1}H- and ^{31}P{^{1}H}-NMR spectroscopy, over a period of about four to fourteen hours. All measurements of the same experiment (e.g., a specific complex formation study) were recorded with an identical number of free inductive decays (FIDs). For a typical proton measurement, the number of FIDs was 16. For the phosphorus NMR spectra the number of FIDs was typically 40.

Data Analysis: For the data analysis of the complex formation studies, the integral of an isolated aromatic resonance of the intermediate species was taken relative to the total integral of all aromatic protons. The natural logarithm of this number was plotted against time, which always resulted in a hyperbolically shaped curve. Of the initial linear part, the best fit was calculated with the least-squares method. These are the graphs that are given in this paper. The slopes of these linear functions reflect the (presumed first order) reaction constant (k'), not in absolute, but in relative sense. This was done because the exact nature of the disappearing species is (in most cases) unknown.

Low-Temperature NMR Spectroscopic Experiments: Some of the obtained complexes were characterized by ^{1}H and ^{31}P{^{1}H} NMR spectroscopy, both at room temperature (20 °C) and at low temperature (–60 °C). This was typically done by monitoring the ^{1}H and ^{31}P NMR resonances of a 16 mM solution during cooling at 20, 0, –20, –40, and –60 °C. Before a spectrum at a specific temperature was recorded, it was ensured that the cooling apparatus was stable with an error of about 1 °C. When this was achieved, a waiting period of about ten minutes was applied to ensure that the sample had acquired the temperature as indicated by the cooling apparatus.

General Synthetic Methods for the Synthesis of the Complexes

Method A. For [Pd(L)(OAc)$_2$]: A solution of Pd(OAc)$_2$ (74 mM) in CH$_2$Cl$_2$ was prepared and filtered. A 25-mL round-bottomed flask filled with argon was charged with 10 mL of this solution and a magnetic stirring rod. To the stirred solution, 0.74 mmol of the solid ligand was added and the reaction mixture was stirred overnight (wrapped in aluminium foil), where after the solvent volume was reduced to about 5 mL. The complex was precipitated with Et$_2$O/*n*-hexane, collected by filtration through a glass frit (P4), washed with Et$_2$O/*n*-hexane and dried in vacuo.

Method B. For [Pd(L)(OTs)$_2$]: A solution of Pd(OAc)$_2$ (74 mM) in CH$_2$Cl$_2$ was prepared and filtered. A 25-mL round-bottomed flask filled with argon was charged with 10 mL of this solution and a magnetic stirring rod. To the stirred solution, 0.74 mmol of the solid ligand was added and the reaction mixture was stirred overnight (wrapped in aluminium foil). Then, *para*-toluenesulfonic acid (1.5 mmol, 0.26 g) was added and the solvent volume was reduced to about 5 mL. The complex was precipitated with Et$_2$O/*n*-hexane, collected by filtration through a glass frit (P4), washed with Et$_2$O/*n*-hexane and dried in vacuo.

Method C. For [Pd(L)$_2$](OAc)$_2$: A 25-mL round-bottomed flask filled with argon was charged with 15 mL MeOH, 1 mmol of the ligand, and a stirring rod. The resulting suspension was stirred, and 2 mL of a filtered Pd(OAc)$_2$ solution (0.25 M in CH$_2$Cl$_2$) was added. After overnight stirring (wrapped in aluminium foil), the solvent volume was reduced to about 5 mL. The complex was precipitated with Et$_2$O/*n*-hexane, collected by filtration through a glass frit (P4), washed with Et$_2$O/*n*-hexane and dried in vacuo.

Method D. For [Pd(L)$_2$](OTs)$_2$: A 25-mL round-bottomed flask filled with argon was charged with 15 mL MeOH, 1 mmol of the ligand, and a stirring rod. In another round-bottomed flask, 2 mmol (0.35 g) of *para*-toluenesulfonic acid was added to 4 mL of a 0.25 M solution of Pd(OAc)$_2$ in CH$_2$Cl$_2$. From this solution, 2 mL were added to the ligand/MeOH suspension. After overnight stirring (wrapped in aluminium foil), the solvent volume was reduced to about 5 mL. The complex was precipitated with Et$_2$O/*n*-hexane, collected by filtration through a glass frit (P4), washed with Et$_2$O/*n*-hexane and dried in vacuo.

Complexes

[Pd(L1)(OAc)$_2$] (M1A): This compound was prepared following method A. The product was obtained as a yellow powder, with an isolated yield of 97% (447 mg). The compound was recrystallized by layering a solution of the complex in dichloromethane with diethyl ether. ^{1}H NMR (300 MHz, CH$_3$OH): δ = 7.80 (q, 8 H, *m*-Ph-*H*), 7.52 (m, 4 H, *p*-Ph-*H*), 7.45 (t, 8 H, *o*-Ph-*H*), 2.50 (m, 4 H, PC*H*$_2$), 1.49 (s, 6 H, OC(O)C*H*$_3$) ppm. ^{31}P NMR (300 MHz, CH$_3$OH): δ = 63.66 ppm. [Pd(L1)(OAc)$_2$]: C$_{30}$H$_{30}$O$_4$P$_2$Pd (622.92) ·0.75CH$_2$Cl$_2$: calcd. C 53.79, H 4.62; found C 53.58, H 4.65. ESI Mass Spectroscopy, *m/z* found (calcd.): [M – OAc]$^+$ = 562.66 (563.05).

[Pd(L1)(OTs)$_2$] (M1T): This compound was prepared following method B. The product was obtained as a yellow powder, with an isolated yield of 89% (558 mg). The compound was recrystallized by layering a solution of the complex in dichloromethane with *n*-hexane. ^{1}H NMR [300 MHz, OC(CH$_3$)$_2$]: δ = 7.95 (q, 8 H, *m*-Ph-*H*), 7.76 (m, 4 H, *p*-Ph-*H*), 7.63 (m, 8 H, *o*-Ph-*H*), 7.51 (d, 4 H, *o*-OTs-*H*), 7.11 (d, 4 H, *m*-OTs-*H*), 3.08 (m, 4 H, PC*H*$_2$), 2.32 (s, 6 H, *p*-OTs-C*H*$_3$) ppm. ^{31}P NMR [300 MHz, OC(CH$_3$)$_2$]: δ = 74.26 ppm. Elemental analyses for [Pd(L1)(OTs)$_2$]. C$_{40}$H$_{38}$O$_6$P$_2$PdS$_2$ (847.22)·0.5CH$_2$Cl$_2$·0.25C$_6$H$_{14}$: calcd. C 54.24, H

5.08, S 5.88; found C 54.24, H 5.00, S 5.91. ESI Mass Spectroscopy, *m/z* found (calcd.): [M – OTs]$^+$ = 674.70 (675.05).

[Pd(L1)$_2$](OTs)$_2$ (B1T): This compound was prepared following method D. The product was obtained as a yellow powder, with an isolated yield of 92% (573 mg). The compound was recrystallized by layering a solution of the complex in dichloromethane with *n*-hexane. ^{1}H NMR (300 MHz, CHCl$_3$): δ = 8.08 (d, 4 H, *o*-OTs-*H*), 7.46 (m, 20 H, *m*-Ph-*H*, *m*-OTs-*H*), 7.26 (m, 20 H, *o*-Ph-*H*, *p*-Ph-*H*), 3.16 (m, 8 H, PC*H*$_2$), 2.39 (s, 6 H, *p*-OTs-C*H*$_3$) ppm. ^{31}P NMR (300 MHz, CHCl$_3$): δ = 56.74 ppm. Elemental analyses for [Pd-(L1)$_2$](OTs)$_2$. C$_{66}$H$_{62}$O$_6$P$_4$PdS$_2$ (1245.64)·2CH$_2$Cl$_2$·C$_6$H$_{14}$: calcd. C 59.19, H 5.37, S 4.05; found C 59.26, H 5.25, S 3.94. ESI Mass Spectroscopy, *m/z* found (calcd.): [M – OTs]$^+$ = 1072.73 (1073.19).

[Pd(L2)(OAc)$_2$] (M2A): This compound was prepared following method A. The product was obtained as a yellow powder, with an isolated yield of 81% (445 mg). Single crystals suitable for X-ray crystallography were obtained by layering a solution of the complex in dichloromethane with *n*-hexane. ^{1}H NMR (300 MHz, CDCl$_3$): δ = 8.04 (q, 4 H, *o*-Ph-*H*), 7.50 (t, 4 H, *p*-Ph-*H*), 7.04 (t, 4 H, OC=C-*H*), 6.92 (q, 4 H, *m*-Ph-*H*), 3.72 (s, 12 H, OC*H*$_3$), 2.63 (d, 4 H, PC*H*$_2$), 1.36 [s, 6 H, OC(O)C*H*$_3$] ppm. ^{31}P NMR (300 MHz, CDCl$_3$): δ = 60.91 ppm. Elemental analyses for [Pd(L2)(OAc)$_2$], C$_{34}$H$_{38}$O$_8$P$_2$Pd (743.03)·0.3H$_2$O: calcd. C 54.52, H 5.20; found C 54.99, H 5.65. ESI Mass Spectroscopy, *m/z* found (calcd.): [M – OAc]$^+$ = 682.75 (683.98).

[Pd(L2)(OTs)$_2$] (M2T): This compound was prepared following method B. The product was obtained as a yellow powder, with an isolated yield of 68% (487 mg). The compound was recrystallized by layering a solution of the complex in dichloromethane with diethyl ether. ^{1}H NMR [300 MHz, OC(CH$_3$)$_2$]: δ = 7.65 (m, 4 H, *p*-Ph-*H*, *o*-Ph-*H*), 7.50 (d, 4 H, *o*-OTs-*H*), 7.24 (t, 4 H, OC=C-*H*), 7.09 (m, 8 H, *m*-Ph-*H*, *m*-OTs-*H*), 3.80 (s, 12 H, OC*H*$_3$), 3.05 (m, 4 H, PC*H*$_2$), 2.29 (s, 6 H, *p*-OTs-C*H*$_3$) ppm. ^{31}P NMR [300 MHz, OC(CH$_3$)$_2$]: δ = 57.50 ppm. Elemental analyses for [Pd(L2)(OTs)$_2$], C$_{44}$H$_{46}$O$_{10}$P$_2$PdS$_2$ (967.33)·1CH$_2$Cl$_2$·0.25O(C$_2$H$_3$)$_2$: calcd. C 51.60, H 4.75, S 2.97; found C 51.67, H 4.64, S 2.82. ESI Mass Spectroscopy, *m/z* found (calcd.): [M – OTs]$^+$ = 794.77 (796.13).

[Pd(L2)$_2$](OAc)$_2$ (B2A): This compound was prepared following method C. The product was obtained as a yellow powder, with an isolated yield of 73% (460 mg). The compound was recrystallized by layering a solution of the complex in dichloromethane with diethyl ether. ^{1}H NMR (300 MHz, CDCl$_3$): δ = 8.14 [br., 4 H, *o*-Ph-*H*(ax)], 7.80 [t, 4 H, *p*-Ph-*H*(ax)], 7.54 [m, 4 H, *m*-Ph-*H*(ax)], 7.35 [m, 4 H, *m*-Ph-*H*(eq)], 7.11 [d, 4 H, OC=C-*H*(ax)], 6.88 [d, 4 H, OC=C-*H*(eq)], 6.46 [t, 4 H, *p*-Ph-*H*(eq)], 5.88 [br., 4 H, *o*-Ph-*H*(eq)], 3.68 [s, 12 H, OC*H*$_3$(ax)], 3.59 [s, 12 H, OC*H*$_3$(eq)], 3.20 (m, 8 H, PC*H*$_2$), 2.02 [s, 6 H, OC(O)C*H*$_3$] ppm. ^{31}P NMR (300 MHz, CDCl$_3$): δ = 55.83 ppm. Elemental analyses for [Pd(L2)$_2$]-(OAc)$_2$, C$_{64}$H$_{70}$O$_{12}$P$_4$Pd (1261.55)·1O(C$_2$H$_3$)$_2$·3H$_2$O: calcd. C 52.63, H 5.70; found C 52.35, H 5.93. ESI Mass Spectroscopy, *m/z* found (calcd.): [M – 2OAc]$^{2+}$ = 571.72 (571.73).

[Pd(L2)$_2$](OTs)$_2$ (B2T): This compound was prepared following method D. The product was obtained as a yellow powder, with an isolated yield of 30% (223 mg). The compound was recrystallized by layering a solution of the complex in dichloromethane with diethyl ether. ^{1}H NMR (300 MHz, CDCl$_3$): δ = 8.08 [br., 4 H, *o*-Ph-*H*(ax)], 7.89 (d, 4 H, *o*-OTs-*H*), 7.81 [t, 4 H, *p*-Ph-*H*(ax)], 7.50 [t, 4 H, *m*-Ph-*H*(ax)], 7.26 [t, 4 H, *m*-Ph-*H*(eq)], 7.12 (d, 4 H, *m*-OTs-*H*), 6.97 [d, 4 H, OC=C-*H*(ax)], 6.82 [d, 4 H, OC=C-*H*(eq)], 6.56 [t, 4 H, *p*-Ph-*H*(eq)], 5.84 [br., 4 H, *o*-Ph-*H*(eq)], 3.67 [s, 12 H, OC*H*$_3$(ax)], 3.52 [s, 12 H, OC*H*$_3$(eq)], 3.03 (m, 8 H, PC*H*$_2$), 2.33 (s, 6 H, *p*-OTs-C*H*$_3$) ppm. ^{31}P NMR (300 MHz, CDCl$_3$): δ =

55.95 ppm. Elemental analyses for [Pd($\mathbf{L2}$)$_2$](OTs)$_2$, $C_{74}H_{78}O_{14}P_4PdS_2$ (1485.85)·2CH$_2$Cl$_2$·2O(C$_2$H$_3$)$_2$: calcd. C 55.93, H 5.70, S 3.63; found C 56.04, H 5.88, S 3.80. ESI Mass Spectroscopy, m/z found (calcd.): [M − OTs]$^+$ = 1072.73 (1073.19).

[Pd($\mathbf{L4}$)(OAc)$_2$] (M4A): This compound was prepared following method A. The product was obtained as a yellow powder, with an isolated yield of 93% (438 mg). The compound was recrystallized by layering a solution of the complex in dichloromethane with diethyl ether. ^{1}H NMR (300 MHz, CHCl$_3$): δ = 7.72 (m, 8 H, m-Ph-H), 7.34 (m, 12 H, o-Ph-H, p-Ph-H), 2.51 (m, 4 H, PCH_2), 2.15 (m, 2 H, PCH$_2$CH_2), 1.34 [s, 6 H, OC(O)CH_3] ppm. ^{31}P NMR (300 MHz, CHCl$_3$): δ = 9.74 ppm. Elemental analyses for [Pd($\mathbf{L4}$)(OAc)$_2$], $C_{31}H_{32}O_4P_2Pd$ (636.95)·0.5CH$_2$Cl$_2$·0.5O(C$_2$H$_3$)$_2$: calcd. C 56.16, H 5.35; found C 56.64, H 5.33. ESI Mass Spectroscopy, m/z found (calcd.): [M − OAc]$^+$ = 576.65 (577.91).

[Pd($\mathbf{L4}$)(OTs)$_2$] (M4T): This compound was prepared following method B. The product was obtained as a yellow powder, with an isolated yield of 78% (497 mg). The compound was recrystallized by layering a solution of the complex in dichloromethane with diethyl ether. ^{1}H NMR (300 MHz, CHCl$_3$): δ = 7.67 (q, 8 H, o-Ph-H), 7.41 (m, 8 H, p-Ph-H, o-OTs-H), 7.26 (t, 8 H, m-Ph-H), 6.86 (d, 4 H, m-OTs-H), 2.83 (m, 4 H, PCH_2), 2.25 (m, 2 H, PCH$_2$CH_2), 2.31 (s, 6 H, p-OTs-CH_3) ppm. ^{31}P NMR (300 MHz, CHCl$_3$): δ = 15.88 ppm. Elemental analyses for [Pd($\mathbf{L4}$)(OTs)$_2$], $C_{41}H_{40}O_6P_2PdS_2$ (861.25)·1.3H$_2$O: calcd. C 55.63, H 4.86, S 5.15; found C 55.73, H 4.79, S 5.51. ESI Mass Spectroscopy, m/z found (calcd.): [M − OTs]$^+$ = 688.71 (689.07).

[Pd($\mathbf{L5}$)(OAc)$_2$] (M5A): This compound was prepared following method A. The product was obtained as a yellow powder, with an isolated yield of 96% (472 mg). The compound was recrystallized by layering a solution of the complex in dichloromethane with diethyl ether. ^{1}H NMR (300 MHz, CHCl$_3$): δ = 7.90 (m, 8 H, o-Ph-H), 7.44 (m, 12 H, m-Ph-H, p-Ph-H), 2.29 (d, 4 H, PCH_2), 0.91 (s, 6 H, CCH_3), 1.44 [s, 6 H, OC(O)CH_3] ppm. ^{31}P NMR (300 MHz, CHCl$_3$): δ = 16.35 ppm. Elemental analyses for [Pd($\mathbf{L5}$)(OAc)$_2$], $C_{33}H_{36}O_4P_2Pd$ (665.00)·0.25CH$_2$Cl$_2$·0.5O(C$_2$H$_3$)$_2$: calcd. C 58.62, H 5.65; found C 58.66, H 5.57. ESI Mass Spectroscopy, m/z found (calcd.): [M − OAc]$^+$ = 604.77 (605.10).

[Pd($\mathbf{L5}$)(OTs)$_2$] (M5T): This compound was prepared following method B. The product was obtained as a yellow powder, with an isolated yield of 83% (546 mg). The compound was recrystallized by layering a solution of the complex in dichloromethane with diethyl ether. ^{1}H NMR (300 MHz, CH$_3$OH): δ = 7.88 (d, 4 H, o-OTs-H), 7.58 (br., 8 H, o-Ph-H), 7.29 (m, 16 H, m-Ph-H, p-Ph-H, m-OTs-H), 2.59 (br., 4 H, PCH_2), 2.38 (s, 6 H, p-OTs-CH_3), 0.26 (s, 6 H, CCH_3) ppm. ^{31}P NMR (300 MHz, CH$_3$OH): δ = 6.72 ppm. Elemental analyses for [Pd($\mathbf{L5}$)(OTs)$_2$], $C_{43}H_{44}O_6P_2PdS_2$ (889.30)·CH$_2$Cl$_2$·1.25O(C$_2$H$_5$)$_2$: calcd. C 55.29, H 5.30, S 4.52; found C 55.37, H 5.19, S 4.69. ESI Mass Spectroscopy, m/z found (calcd.): [M − OTs]$^+$ = 688.71 (689.07).

[Pd($\mathbf{L5}$)$_2$](OTs)$_2$ (B5T): This compound was prepared following method D. The product was obtained as a yellow powder, with an isolated yield of 92% (612 mg). The compound was recrystallized by layering a solution of the complex in dichloromethane with diethyl ether. ^{1}H NMR (300 MHz, CH$_3$OH): δ = 8.00 (d, 4 H, o-OTs-H), 7.60 (br., 16 H, o-Ph-H), 7.26 (m, 28 H, m-Ph-H, p-Ph-H, m-OTs-H), 2.62 (br., 8 H, PCH_2), 2.38 (s, 6 H, p-OTs-CH_3), 0.26 (s, 12 H, CCH_3) ppm. ^{31}P NMR (300 MHz, CH$_3$OH): δ = 5.63 ppm. Elemental analyses for [Pd($\mathbf{L5}$)$_2$](OTs)$_2$, $C_{72}H_{74}O_6P_4PdS_2$ (1329.80)·1.25CH$_2$Cl$_2$·O(C$_2$H$_3$)$_2$: calcd. C 63.83, H 6.00, S 4.33; found C 63.73, H 6.24, S 4.62. ESI Mass Spectroscopy, m/z found (calcd.): [M − OTs]$^+$ = 1156.91 (1157.28).

[Pd($\mathbf{L7}$)(OAc)$_2$] (M7A): This compound was prepared following method A. The product was obtained as a yellow powder, with an isolated yield of 87% (487 mg). Single crystals suitable for X-ray crystallography were obtained by layering of n-hexane with a solution of the complex in dichloromethane. ^{1}H NMR (300 MHz, CDCl$_3$): δ = 8.25 (br., 4 H, o-Ph-H), 7.50 (t, 4 H, p-Ph-H), 7.08 (br., 4 H, m-Ph-H), 6.94 (d, 4 H, OC=C-H), 3.76 (s, 12 H, OCH_3), 2.44 (m, 4 H, PCH_2), 1.95 (m, 2 H, PCH$_2$CH_2), 1.26 [s, 6 H, OC(O)CH_3] ppm. ^{31}P NMR (300 MHz, CDCl3): δ = 14.50 ppm. Elemental analyses for [Pd($\mathbf{L7}$)(OAc)$_2$], $C_{35}H_{40}O_8P_2Pd$ (757.05)·CH$_2$Cl$_2$: calcd. C 54.35, H 6.08; found C 54.18, H 6.21. ESI Mass Spectroscopy, m/z found (calcd.): [M − OAc]$^+$ = 698.62 (698.01).

[Pd($\mathbf{L7}$)$_2$](OAc)$_2$ (B7A): This compound was prepared following method C. The product was obtained as a yellow powder, with an isolated yield of 94% (606 mg). The compound was recrystallized by layering a solution of the complex in dichloromethane with diethyl ether. ^{1}H NMR (300 MHz, CH$_3$OH): δ = 8.59 [br., 4 H, o-Ph-H(ax)], 7.74 [t, 4 H, m-Ph-H(ax)], 7.46 [t, 4 H, p-Ph-H(ax)], 7.30 [t, 4 H, p-Ph-H(eq)], 7.05 [m, 8 H, OC=C-H(ax, eq.)], 6.61 [t, 4 H, m-Ph-H(eq)], 5.91 [br., 4 H, o-Ph-H(eq)], 4.23 [s, 12 H, OCH_3(ax)], 3.42 [s, 12 H, OCH_3(eq)], 2.90 [m, 4 H, PCH_2(ax)], 2.38 [m, 4 H, PCH_2(eq)], 1.95 (m, 2 H, PCH$_2$CH_2), 1.87 [s, 6 H, OC(O)CH_3] ppm. ^{31}P NMR (300 MHz, CH$_3$OH): δ = 5.56 ppm. Elemental analyses for [Pd($\mathbf{L7}$)$_2$](OAc)$_2$, $C_{66}H_{74}O_{12}P_4Pd$ (1289.60)·CH$_2$Cl$_2$: calcd. C 55.96, H 6.58; found C 55.91, H 6.58. ESI Mass Spectroscopy, m/z found (calcd.): [M − 2 OAc]$^{2+}$ = 584.83 (585.15).

[Pd($\mathbf{L7}$)$_2$](OTs)$_2$ (B7T): This compound was prepared following method D. The product was obtained as a yellow powder, with an isolated yield of 72% (545 mg). The compound was recrystallized by layering a solution of the complex in dichloromethane with diethyl ether. ^{1}H NMR (300 MHz, CHCl$_3$): δ = 8.51 [br., 4 H, o-Ph-H(ax)], 7.96 (d, 4 H, o-OTs-H), 7.73 [t, 4 H, m-Ph-H(ax)], 7.64 [t, 4 H, p-Ph-H(ax)], 7.20 [m, 8 H, p-Ph-H(eq), m-OTs-H], 6.99 [d, 4 H, OC=C-H(ax)], 6.83 [d, 4 H, OC=C-H(eq)], 6.47 [t, 4 H, m-Ph-H(eq)], 5.82 [br., 4 H, o-Ph-H(eq)], 4.33 [s, 12 H, OCH_3(ax)], 3.38 [s, 12 H, OCH_3(eq)], 2.85 [m, 4 H, PCH_2(ax)], 2.36 (s, 6 H, p-OTs-CH_3), 2.25 [m, 4 H, PCH_2(eq)], 1.52 (br., 4 H, PCH$_2$CH_2) ppm. ^{31}P NMR (300 MHz, CHCl$_3$): δ = 4.81 ppm. Elemental analyses for [Pd($\mathbf{L7}$)$_2$](OTs)$_2$, $C_{76}H_{82}O_{14}P_4PdS_2$ (1513.90)·0.25CH$_2$Cl$_2$·0.25O(C$_2$H$_3$)$_2$: calcd. C 59.72, H 5.52, S 3.96; found C 59.48, H 5.87, S 3.96. ESI Mass Spectroscopy, m/z found (calcd.): [M − OTs]$^+$ = 1340.53 (1341.30).

[Pd($\mathbf{L10}$)(OAc)$_2$] (M10A): This compound was prepared following method A. The product was obtained as a yellow powder, with an isolated yield of 96% (558 mg). Single crystals suitable for X-ray crystallography were obtained by layering of n-hexane with a solution of the complex in dichloromethane. ^{1}H NMR (300 MHz, CDCl$_3$): δ = 8.15 (br., 4 H, o-Ph-H), 7.51 (t, 4 H, m-Ph-H), 7.07 (m, 4 H, p-Ph-H), 6.92 (d, 4 H, OC=C-H), 3.86 (s, 12 H, OCH_3), 2.58 (d, 4 H, PCH_2), 1.20 [s, 6 H, OC(O)CH_3], 0.33 (s, 6 H, CCH_3) ppm. ^{31}P NMR (300 MHz, CDCl3): δ = 20.84 ppm. Elemental analyses for [Pd($\mathbf{L10}$)(OAc)$_2$], $C_{37}H_{44}O_8P_2Pd$ (785.11)·CH$_2$Cl$_2$·0.7C$_6$H$_{12}$: calcd. C 54.51, H 6.01; found C 54.39, H 5.96. ESI Mass Spectroscopy, m/z found (calcd.): [M −OAc]$^+$ = 724.77 (726.06).

[Pd($\mathbf{L10}$)$_2$](OAc)$_2$ (B10A): This compound was prepared following method C. The product was obtained as a yellow powder, with an isolated yield of 97% (653 mg). The compound was recrystallized by layering a solution of the complex in dichloromethane with diethyl ether. ^{1}H NMR (300 MHz, CH$_3$OH): δ = 8.36 [br., 4 H, o-Ph-H(ax)], 7.64 [t, 4 H, m-Ph-H(ax)], 7.30 [m, 8 H, p-Ph-H(ax), p-Ph-H(eq)], 7.11 [d, 4 H, OC=C-H(ax)], 6.92 [d, 4 H, OC=C-H(eq)], 6.70 [t, 4 H, m-Ph-H(eq)], 6.48 [br., 4 H, o-Ph-H(eq)], 4.26 [s, 12

H, OCH_3(ax)], 3.41 [s, 12 H, OCH_3(eq)], 2.78 [d, 4 H, PCH_2(ax)], 2.44 [d, 4 H, PCH_2(eq)], 1.88 [s, 6 H, OC(O)CH_3], 0.22 (s, 12 H, CCH_3) ppm. ^{31}P NMR (300 MHz, CH$_3$OH): δ = 10.88 ppm. Elemental analyses for [Pd(**L10**)$_2$](OAc)$_2$, C$_{70}$H$_{82}$O$_{12}$P$_4$Pd (1345.71)·2.5CH$_2$Cl$_2$·2.5O(C$_2$H$_3$)$_2$: calcd. C 57.28, H 6.44; found C 56.97, H 6.90. ESI Mass Spectroscopy, *m*/*z* found (calcd.): [M – 2OAc]$^{2+}$ = 613.43 (613.18).

[Pd(L10)$_2$](OTs)$_2$ (B10T): This compound was prepared following method D. The product was obtained as a yellow powder, with an isolated yield of 89% (699 mg). Single crystals suitable for X-ray crystallography were obtained by layering of hexane with a solution of the complex in acetone. ^{1}H NMR (300 MHz, CDCl$_3$): δ = 8.29 [br., 4 H, *o*-Ph-*H*(ax)], 7.95 (d, 4 H, *o*-OTs-*H*), 7.56 [m, 8 H, *p*-Ph-*H*(ax), *m*-Ph-*H*(ax)], 7.16 [m, 8 H, *p*-Ph-*H*(eq), *m*-OTs-*H*], 7.07 [d, 4 H, OC=C-*H*(ax)], 6.68 [d, 4 H, OC=C-*H*(eq)], 6.53 [t, 4 H, *m*-Ph-*H*(eq)], 6.34 [br., 4 H, *o*-Ph-*H*(eq)], 4.38 [s, 12 H, OCH_3(ax)], 3.38 [s, 12 H, OCH_3(eq)], 2.70 [d, 4 H, PCH_2(ax)], 2.36 (s, 6 H, *p*-OTs-CH_3), 2.30 [d, 4 H, PCH_2(eq)], 0.12 (s, 12 H, CCH_3) ppm. ^{31}P NMR (300 MHz, CDCl$_3$): δ = 10.10 ppm. Elemental analyses for [Pd(**L10**)$_2$](OTs)$_2$, C$_{80}$H$_{90}$O$_{14}$P$_4$PdS$_2$ (1570.01)·0.25CH$_2$Cl$_2$·0.5C$_6$H$_{14}$: calcd. C 58.87, H 5.79, S 3.92; found C 58.40, H 5.99, S 3.51. ESI Mass Spectroscopy, *m*/*z* found (calcd.): [M – OTs]$^+$ = 1396.47 (1396.37).

[Pd(L13)(OAc)$_2$] (M13A): This compound was prepared following method A. The product was obtained as a yellow powder, with an isolated yield of 94% (624 mg). Single crystals suitable for X-ray crystallography were obtained by layering of *n*-hexane with a solution of the complex in acetone. ^{1}H NMR (300 MHz, CDCl$_3$): δ = 8.50 (br., 4 H, *o*-Ph-*H*), 7.52 (br., 4 H, *m*-Ph-*H*), 7.08 (br., 4 H, *p*-Ph-*H*), 6.94 (d, 4 H, OC=C-*H*), 3.88 (s, 12 H, OCH_3), 3.09 (s, 4 H, CCH_2O), 2.68 (s, 4 H, PCH_2), 1.57 (m, 4 H, OCCH_2), 1.37 (m, 6 H, OCCH$_2$CH_2, OCCH$_2$CH$_2$CH_2), 1.21 [s, 6 H, OC(O)CH_3] ppm. ^{31}P NMR (300 MHz, CDCl$_3$): δ = 18.05 ppm. Elemental analyses for [Pd(**L13**)(OAc)$_2$], C$_{43}$H$_{52}$O$_{10}$P$_2$Pd (897.23): calcd. C 57.56, H 5.84; found C 57.00, H 6.16. ESI Mass Spectroscopy, *m*/*z* found (calcd.): [M – OAc]$^+$ = 836.82 (838.19).

[Pd(L13)$_2$](OAc)$_2$ (B13A): This compound was prepared following method C. The product was obtained as a yellow powder, with an isolated yield of 70% (550 mg). The compound was recrystallized by layering a solution of the complex in dichloromethane with *n*-hexane. ^{1}H NMR (300 MHz, CH$_3$OH): δ = 8.35 [br., 4 H, *o*-Ph-*H*(ax)], 7.34 [t, 4 H, *p*-Ph-*H*(ax)], 7.29 [t, 4 H, *p*-Ph-*H*(eq)], 7.14 [d, 4 H, OC=C-*H*(ax)], 6.97 [d, 4 H, OC=C-*H*(eq)], 6.78 [t, 4 H, *m*-Ph-*H*(ax)], 6.72 [t, 4 H, *m*-Ph-*H*(eq)], 6.48 [br., 4 H, *o*-Ph-*H*(eq)], 4.30 [s, 12 H, OCH_3(ax)], 3.42 [s, 12 H, OCH_3(eq)], 2.88 [d, 4 H, PCH_2(ax)], 2.56 [m, 12 H, PCH_2(eq), CCH_2O], 1.88 [s, 6 H, OC(O)CH_3], 1.37 (m, 8 H, OCCH_2), 1.23 (m, 12 H, OCCH$_2$CH_2, OCCH$_2$CH$_2$CH2) ppm. ^{31}P NMR (300 MHz, CH$_3$OH): δ = 8.82 ppm. Elemental analyses for [Pd(**L13**)$_2$](OAc)$_2$, C$_{82}$H$_{98}$O$_{16}$P$_4$Pd (1569.96)·0.5CH$_2$Cl$_2$·0.5C$_6$H$_{14}$: calcd. C 62.03, H 6.45; found C 62.00, H 6.46. ESI Mass Spectroscopy, *m*/*z* found (calcd.): [M – 2 OAc]$^{2+}$ = 725.15 (725.23).

[Pd(L13)$_2$](OTs)$_2$ (B13T): This compound was prepared following method D. The product was obtained as a yellow powder, with an isolated yield of 63% (565 mg). The compound was recrystallized by layering a solution of the complex in dichloromethane with *n*-hexane. ^{1}H NMR (300 MHz, CHCl$_3$): δ = 8.28 [br., 4 H, *o*-Ph-*H*(ax)], 8.00 (d, 4 H, *o*-OTs-*H*), 7.60 [m, 8 H, *p*-Ph-*H*(ax), *m*-Ph-*H*(ax)], 7.17 [m, 20 H, OC=C-*H*(ax), *p*-Ph-*H*(eq), *m*-OTs-*H*], 6.74 [d, 4 H, OC=C-*H*(eq)], 6.54 [t, 4 H, *m*-Ph-*H*(eq)], 6.34 [br., 4 H, *o*-Ph-*H*(eq)], 4.44 [s, 12 H, OCH_3(ax)], 3.40 [s, 12 H, OCH_3(eq)], 2.73 [d, 4 H, PCH_2(ax)], 2.44 [m, 18 H, PCH_2(eq), CCH_2O, *p*-OTs-CH_3],

1.42 (br., 8 H, OCCH_2), 1.23 (br., 12 H, OCCH$_2$CH_2, OCCH$_2$CH$_2$CH_2) ppm. ^{31}P NMR (300 MHz, CHCl$_3$): δ = 8.03 ppm. Elemental analyses for [Pd(**L13**)$_2$](OTs)$_2$, C$_{92}$H$_{106}$O$_{18}$P$_4$PdS$_2$ (1794.26)·0.33CH$_2$Cl$_2$: calcd. C 60.84, H 5.90, S 3.50; found C 60.84, H 5.90, S 3.02. ESI Mass Spectroscopy, *m*/*z* found (calcd.): [M – 2 OTs]$^{2+}$ = 726.50 (725.94).

[Pd(L14)(OAc)$_2$] (M14A): This compound was prepared following method A. The product was obtained as a yellow powder, with an isolated yield of 96% (463 mg). The compound was recrystallized by layering a solution of the complex in dichloromethane with diethyl ether. ^{1}H NMR (300 MHz, CH$_3$OH): δ = 7.63 (q, 8 H, *o*-Ph-*H*), 7.47 (t, 4 H, *p*-Ph-*H*), 7.34 (t, 8 H, *m*-Ph-*H*), 2.44 (br., 4 H, PCH_2), 1.93 (m, 4 H, PCH$_2$CH_2), 1.32 [s, 6 H, OC(O)CH_3] ppm. ^{31}P NMR (300 MHz, CH$_3$OH): δ = 28.56 ppm. Elemental analyses for [Pd(**L14**)(OAc)$_2$], C$_{32}$H$_{34}$O$_4$P$_2$Pd (650.98)·1.5CH$_2$Cl$_2$: calcd. C 51.69, H 4.79; found C 51.88, H 4.93. ESI Mass Spectroscopy, *m*/*z* found (calcd.): [M – OAc]$^+$ = 590.73 (591.08).

[Pd(L14)(OTs)$_2$] (M14T): This compound was prepared following method B. The product was obtained as a yellow powder, with an isolated yield of 92% (596 mg). The compound was recrystallized by layering a solution of the complex in dichloromethane with diethyl ether. ^{1}H NMR (300 MHz, CHCl$_3$): δ = 7.70 (t, 8 H, *p*-Ph-*H*), 7.54 (t, 8 H, *m*-Ph-*H*), 7.40 (m, 8 H, *o*-Ph-*H*, *o*-OTs-*H*), 6.93 (d, 4 H, *m*-OTs-*H*), 2.58 (br., 4 H, PCH_2), 2.31 (s, 6 H, *p*-OTs-CH_3), 2.15 (m, 4 H, PCH$_2$CH_2) ppm. ^{31}P NMR (300 MHz, CHCl$_3$): δ = 32.80 ppm. Elemental analyses for [Pd(**L14**)(OTs)$_2$], C$_{42}$H$_{42}$O$_6$P$_2$PdS$_2$ (875.28)·1.25CH$_2$Cl$_2$·1.25O(C$_2$H$_3$)$_2$: calcd. C 54.08, H 5.13, S 5.02; found C 54.22, H 5.00, S 5.13. ESI Mass Spectroscopy, *m*/*z* found (calcd.): [M – OTs]$^+$ = 702.62 (703.08).

Supporting Information (see also the footnote on the first page of this article): ^{1}H and ^{31}P NMR data, ESI-MS and elemental analysis for the ligands and palladium complexes (Table S1); lists of hydrogen-bond interactions in **M7A** and **M10A** (Tables S2 and S3); perspective views of **M2A**, **M7A** and **M13A** (Figures S1–S5).

Acknowledgments

[1] E. Drent, P. H. M. Budzelaar, *Chem. Rev.* **1996**, *96*, 663–681.
[2] C. Bianchini, A. Meli, *Coord. Chem. Rev.* **2002**, *225*, 35–66.
[3] A. Marson, A. B. van Oort, W. P. Mul, *Eur. J. Inorg. Chem.* **2002**, 3028–3031.
[4] F. Paul, *Coord. Chem. Rev.* **2000**, *203*, 269–323.
[5] E. Drent, P. W. N. M. van Leeuwen, European patent number 0.086.281.A1, **1982**.
[6] E. Drent, European patent number 0.231.045.A2, **1987**.
[7] F. Ragaini, C. Cognolato, M. Gasperini, S. Cenini, *Angew. Chem. Int. Ed.* **2003**, *42*, 2886–2889.
[8] E. Drent, *Pure Appl. Chem.* **1990**, *62*, 661–669.
[9] P. Wehman, L. Borst, P. C. J. Kamer, P. W. N. M. van Leeuwen, *J. Mol. Catal. A* **1996**, *112*, 23–36.
[10] E. Drent, European patent number 224292, **1987**.

[11] A. Bontempi, E. Alessio, G. Chanos, G. Mestroni, *J. Mol. Catal.* **1987**, *42*, 67–80.

[12] S. Cenini, F. Ragaini, M. Pizzotti, F. Porta, G. Mestroni, E. Alessio, *J. Mol. Catal.* **1991**, *64*, 179–190.

[13] R. Santi, A. M. Romano, F. Panella, G. Mestroni, A. Sessanti, A. S. o Santi, *J. Mol. Catal. A* **1999**, *144*, 41–45.

[14] P. Leconte, F. Metz, A. Mortreux, J. A. Osborn, F. Paul, F. Petit, A. Pillot, *J. Chem. Soc., Chem. Commun.* **1990**, 1616–1617.

[15] P. Wehman, V. E. Kaasjager, W. G. J. de Lange, F. Hartl, P. C. J. Kamer, P. W. N. M. van Leeuwen, J. Fraanje, K. Goubitz, *Organometallics* **1995**, *14*, 3751–3761.

[16] P. Wehman, G. C. Dol, E. R. Moorman, P. C. J. Kamer, P. W. N. M. van Leeuwen, J. Fraanje, K. Goubitz, *Organometallics* **1994**, *13*, 4856–4869.

[17] P. Wehman, Ph. D. Thesis, University of Amsterdam (UVA) **1995**.

[18] F. Ragaini, M. Gasperini, S. Cenini, *Adv. Synth. Catal.* **2004**, *346*, 63–71.

[19] F. Ragaini, *Dalton Trans.* **2009**, 6251–6266.

[20] J. H. Grate, D. R. Hamm, D. H. Valentine, United States patent number 4.603.216, **1986**.

[21] P. Wehman, R. E. Rulke, V. E. Kaasjager, P. C. J. Kamer, H. Kooijman, A. L. Spek, C. J. Elsevier, K. Vrieze, P. W. N. M. van Leeuwen, *J. Chem. Soc., Chem. Commun.* **1995**, 331–332.

[22] D. Cremer, J. A. Pople, *J. Am. Chem. Soc.* **1975**, *97*, 1354–1358.

[23] C. Bianchini, A. Meli, W. Oberhauser, *Dalton Trans.* **2003**, 2627–2635.

[24] F. A. Cotton, S. Han, *Rev. Chim. Miner.* **1983**, *20*, 496–503.

[25] A. G. Orpen, L. Brammer, F. H. Allen, O. Kennard, D. G. Watson, R. Taylor, *J. Chem. Soc., Dalton Trans.* **1989**, S1.

[26] I. M. Angulo, E. Bouwman, M. Lutz, W. P. Mul, A. L. Spek, *Inorg. Chem.* **2001**, *40*, 2073–2082.

[27] C. Bianchini, A. Meli, W. Oberhauser, A. M. Segarra, C. Claver, E. J. G. Suarez, *J. Mol. Catal. A* **2007**, *265*, 292–305.

[28] M. Brookhart, M. L. H. Green, G. Parkin, *Proc. Natl. Acad. Sci. USA* **2007**, *104*, 6908–6914.

[29] J. F. Malone, C. M. Murray, M. H. Charlton, R. Docherty, A. J. Lavery, *J. Chem. Soc. Faraday Trans.* **1997**, *93*, 3429–3436.

[30] C. Bianchini, H. M. Lee, A. Meli, W. Oberhauser, M. Peruzzini, F. Vizza, *Organometallics* **2002**, *21*, 16–33.

[31] C. Bianchini, P. Bruggeller, C. Claver, G. Czermak, A. Dumfort, A. Meli, W. Oberhauser, E. J. G. Suarez, *Dalton Trans.* **2006**, 2964–2973.

[32] I. M. Angulo, E. Bouwman, R. van Gorkum, S. M. Lok, M. Lutz, A. L. Spek, *J. Mol. Catal. A* **2003**, *202*, 97–106.

[33] M. E. Jung, *J. Am. Chem. Soc.* **1991**, *113*, 224–232.

[34] P. v. R. Schleyer, *J. Am. Chem. Soc.* **1961**, *83*, 1368–1373.

[35] T. Hayashi, M. Konishi, Y. Kobori, M. Kumada, T. Higuchi, K. Hirotsu, *J. Am. Chem. Soc.* **1984**, *106*, 158–163.

[36] R. J. van Haaren, K. Goubitz, J. Fraanje, G. P. F. van Strijkdonk, H. Oevering, B. Coussens, J. N. H. Reek, P. C. J. Kamer, P. W. N. M. van Leeuwen, *Inorg. Chem.* **2001**, *40*, 3363–3372.

[37] A. G. Avent, R. B. Bedford, P. A. Chaloner, S. Z. Dewa, P. B. Hitckcock, *J. Chem. Soc., Dalton Trans.* **1996**, 4633–4638.

[38] L. Brandsma, H. D. Verkruijsse, *Synth. Commun.* **1990**, *20*, 2273–2274.

[39] P. H. M. Budzelaar, J. A. van Doorn, N. Meijboom, *Recl. Trav. Chim. Pays-Bas-J. Roy. Neth. Chem. Soc.* **1991**, *110*, 420–432.

[40] J. A. van Doorn, PhD Thesis, University of Amsterdam **1991**.

[41] W. Hewertson, H. R. Watson, *J. Chem. Soc.* **1962**, 1490–1494.

[42] F. Bickelhaupt, United States Patent Number 4874897, **1989**.

[43] W. Eilenberg, European Patent Number 364046, **1991**.

[44] J. A. van Doorn, United States Patent Number 4994592, **1991**.

[45] R. van Ginkel, United States Patent Number 6548708, **2003**.

[46] E. Drent, United States Patent Number 5091587, **1992**.

[47] C. F. Hobbs, United States Patent Number 4120901, **1987**.

[48] P. W. Clark, B. J. Mulraney, *J. Organomet. Chem.* **1981**, *217*, 51–59.

[49] J. M. Brown, B. A. Murrer, *Tetrahedron Lett.* **1980**, *21*, 581–584.

[50] R. L. Wife, A. B. van Oort, J. A. van Doorn, P. W. N. M. van Leeuwen, *Synthesis* **1983**, 71–73.

[51] Z. Otwinowski, W. Minor, *Methods in Enzymology*, vol. 276 (Eds.: C. W. Carter, R. M. Sweet), Acedemic Press, **1997**, pp. 307–326.

[52] A. J. M. Duisenberg, L. M. J. Kroon-Batenburg, A. M. M. Schreurs, *J. Appl. Chem.* **2003**, *36*, 220–229.

[53] A. Altomare, M. C. Burla, M. Camalli, G. L. Cascarano, C. Giacovazzo, A. Guagliardi, A. G. G. Moliterni, G. Polidori, R. Spagna, *J. Appl. Crystallogr.* **1999**, *32*, 115–119.

[54] G. M. Sheldrick, *Acta Crystallogr., Sect. A* **2008**, *64*, 112.

[55] P. T. Beurskens, G. Admiral, G. Beurskens, W. P. Bosman, S. Garcia-Granda, R. O. Gould, J. M. M. Smith, C. Smykalla, *The DIRDIF97 program system: Technical report of the Crystallography Laboratory; University of Nijmegen, The Netherlands* **1997**.

[56] A. L. Spek, *J. Appl. Crystallogr.* **2003**, *36*, 7–13.

Copper-Azide-Thioarylazoimidazoles – Structure, Spectra, Redox Properties, Magnetism and Theoretical Interpretation

Prasenjit Bhunia,[a] Debasis Banerjee,[a] Papia Datta,[a] Pallepogu. Raghavaiah,[b] Alexandra M. Z. Slawin,[c] John D. Woollins,[c] Joan Ribas,[d] and Chittaranjan Sinha*[a]

Azido-copper(II) and -copper(I) complexes of 1-alkyl-2-[(o-thioalkyl)phenylazo]imidazole (SRaaiNR′) have been prepared and studied. Complex **2** [Cu(SRaaiNR′)($\mu_{1,1}$-N$_3$)(N$_3$)]$_2$ dimerises via end-to-end ($\mu_{1,3}$)-N$_3$ to form a tetrameric structure. Azido-copper(I) complexes of the ligands are obtained as MeOH-bridged dimers, [Cu(SRaaiNR′)(N$_3$)(μ-OHMe)]$_2$ (**3**). The electronic spectra suggest that a small reorganisation energy (0.08 eV) is associated with the change in electronic

configuration, structure and oxidation state from Cu^{II} to Cu^I. Redox interconversion, Cu^{II} $\leftrightarrow$ Cu^I, [Cu(SMeaaiNMe)(μ-N$_3$)-(N$_3$)]$_2$ (**2a**) $\leftrightarrow$ [Cu(SMeaaiNMe)(N$_3$)(μ-OHCH$_3$)]$_2$ (**3a**), has been performed in one case. The tetranuclear complex shows ferromagnetic and antiferromagnetic interactions. The spectra, redox chemistry and magnetism are explained by DFT studies.

Introduction

Structure and electronic configuration are interrelated properties in transition metal chemistry.[1–4] The structural change associated with Cu^{II}/Cu^I reorganisation effects is utilised by biochemical systems in copper-containing metalloenzymes.[4–9] Cu(II)- and Cu(I)-diimine complexes (diimine function, –N=C–C=N–) have attracted much research interest in the field of redox chemistry, photochemistry and photophysics, supramolecular chemistry, bioinorganic and medicinal chemistry, magnetic materials etc., inspiring us to design new ligands isoelectronic to diimine. We have previously reported 2-(arylazo)imidazoles[10–13] with the azoimine (–N=N–C=N–) chelating functional group, which is π-acidic and stabilises low-valent metal oxidation states. 1-Alkyl-2-(arylazo)imidazole successfully stabilises the Cu^I state.[11,12] 1-Alkyl-2-[(o-thioalkyl)phenylazo]imidazoles (SRaaiNR′) are ligands with N(imidazole) (N), N(azo) (N′) and S(thioether) donor centres. The reaction of CuCl$_2$ with SRaaiNR′ gives a pentacoordinate square pyramidal Cu(SRaaiNR′)Cl$_2$ compound.[13] In this work, we have selected azide (N$_3^-$) as counterion, because

of its ability to generate bridging systems with Cu^{II}/Cu^I.[14–16] Azide may serve as an end-on ($\mu_{1,1}$) and an end-to-end ($\mu_{1,3}$) bridging agent. In general the end-on coordination mode is associated with ferromagnetic coupling, whereas end-to-end bridging leads to antiferromagnetic interactions.[15] In this work, we report copper(I) complexes of SRaaiNR′ and ternary complexes of Cu^{II}/Cu^I, SRaaiNR′ and azide (N$_3^-$). The complexes have been characterised by spectroscopic and electrochemical techniques. as well as X-ray diffraction studies. One of the azide-bridging Cu^{II}-SRaaiNR′ complexes has been used to examine magnetic coupling at variable temperature, and it shows strong ferromagnetic (J_1 = 13.35 cm^{-1}) and weak antiferromagnetic (J_2 = –0.55 cm^{-1}) interaction. Redox interconversion has been studied in one case. DFT and TD-DFT computations have been performed on optimised geometries of selected molecules to define electronic structure, spectra, magnetism and redox properties of the complexes both in the gas phase and in solution.

Results and Discussion

1-Alkyl-2-[(o-thioalkyl)phenylazo]imidazoles (SRaaiNR′) have three potential donor centres N(imidazole), N(azo) and S(thioether).[13] They were synthesised by coupling o-(thioalkyl)phenyldiazonium ions with imidazole in aqueous sodium carbonate and purified by solvent extraction and chromatography. The alkylation was carried out by adding alkyl iodide (MeI, EtI) in dry THF solution to the corresponding 2-[o-(thioalkyl)phenylazo]imidazole in the presence of sodium hydride.

[a] Inorganic Chemistry Section, Department of Chemistry, Jadavpur University,
Kolkata 700032, India
Fax: +91-033-2413-7121
E-mail: c_r_sinha@yahoo.com
[b] Department of Chemistry, Hyderabad Central University,
Hyderabad 500046, India
[c] Department of Chemistry, University of St Andrews,
St Andrews, Fife KY16 9ST, UK
[d] Departament de Química Inorgànica, Universitat de Barcelona,
Diagonal 6487, 08028 Barcelona, Spain
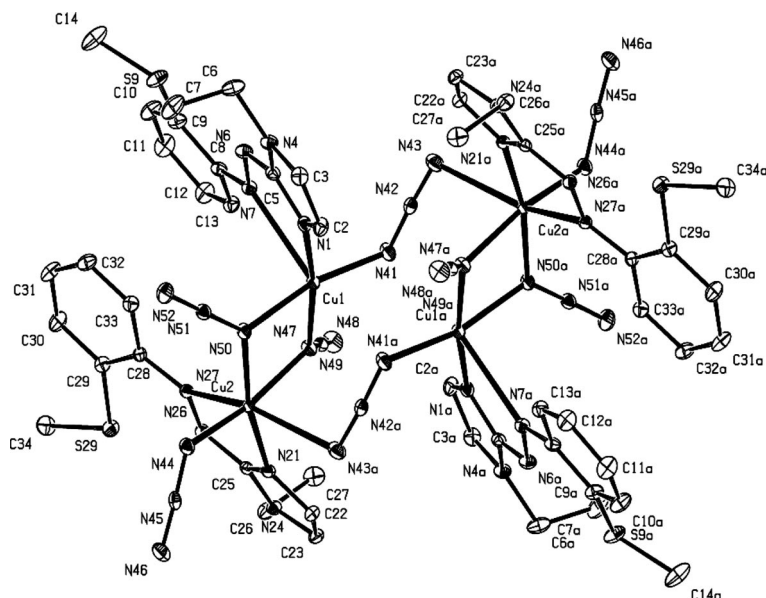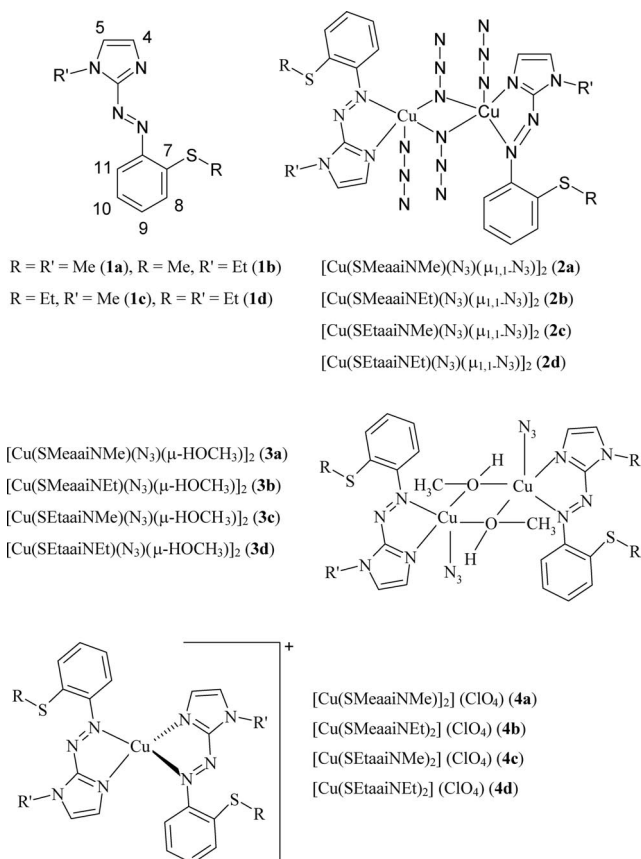☐ Supporting information for this article is available on the WWW under http://dx.doi.org/10.1002/ejic.200900648.

Figure 1. Molecular structure of [Cu(SMeaaiNEt)(μ-N$_3$)(N$_3$)]$_2$ (**2b**) with atom numbering scheme (symmetry codes: –x + 1, –y + 2, –z + 1) (35% ellipsoids shown).

A methanol solution of Cu(ClO$_4$)$_2$·6H$_2$O and the appropriate ligand SRaaiNR′ in a 1:1 mol ratio were treated with aqueous solutions of NaN$_3$ (2.5 equiv.). Slow evaporation of the solution gave block-shaped brown crystals. The complexes were characterised by microanalytical, spectroscopic, redox and magnetic (bulk and EPR) measurements. The X-ray structure determination in one case shows that **2** has a tetranuclear structure (see the discussion of crystal structure and Figure 1). The complexes are soluble in methanol, ethanol, chloroform, dichloromethane and acetonitrile but insoluble in hydrocarbons (hexane, benzene, toluene). They are nonconducting. Their magnetic moments at room temperature (1.6–1.7 B.M.) are lower than those for typical S = ½ (Cu^{II}) compounds.

The Cu^I complexes (Scheme 1) were synthesised by adding SRaaiNR′ (**1**) to a well-stirred solution of NaN$_3$ and [Cu(MeCN)$_4$](ClO$_4$) in methanol under dry nitrogen. Brown crystalline compounds separated on slow evaporation of the solvent. The complexes were characterised by C, H, N analyses and spectroscopic data as [Cu-(SRaaiNR′)(N$_3$)(μ-OHCH$_3$)]$_2$ (**3**). Structural confirmation has been carried out in one case by single-crystal X-ray crystallography. [Cu(SRaaiNR′)$_2$](ClO$_4$) (**4**) were synthesised by refluxing mixtures of [Cu(MeCN)$_4$](ClO$_4$) and SRaaiNR′ in dry MeOH under dry nitrogen. The complexes are fairly soluble in CH$_3$CN, CHCl$_3$, CH$_2$Cl$_2$ and are insoluble in hydrocarbons. The molar conductance measurement shows that complexes **2** and **3** are nonconducting and **4** exhibits 1:1 electrolytic conductivity.

The X-ray structure (Figure 1) reveals that complex **2b** has a neutral tetranuclear copper(II) centre comprising a dimer of dinuclear copper(II) subunits. Selected bond lengths and angles are given in Table 1. The ligand, SMeaai-NEt, is a bidentate N(imidazole) (N), N(azo) (N′) chelator; –S–Me (thioether) remains free and away from the

R = R′ = Me (**1a**), R = Me, R′ = Et (**1b**)
R = Et, R′ = Me (**1c**), R = R′ = Et (**1d**)

[Cu(SMeaaiNMe)(N$_3$)(μ$_{1,1}$-N$_3$)]$_2$ (**2a**)
[Cu(SMeaaiNEt)(N$_3$)(μ$_{1,1}$-N$_3$)]$_2$ (**2b**)
[Cu(SEtaaiNMe)(N$_3$)(μ$_{1,1}$-N$_3$)]$_2$ (**2c**)
[Cu(SEtaaiNEt)(N$_3$)(μ$_{1,1}$-N$_3$)]$_2$ (**2d**)

[Cu(SMeaaiNMe)(N$_3$)(μ-HOCH$_3$)]$_2$ (**3a**)
[Cu(SMeaaiNEt)(N$_3$)(μ-HOCH$_3$)]$_2$ (**3b**)
[Cu(SEtaaiNMe)(N$_3$)(μ-HOCH$_3$)]$_2$ (**3c**)
[Cu(SEtaaiNEt)(N$_3$)(μ-HOCH$_3$)]$_2$ (**3d**)

[Cu(SMeaaiNMe)$_2$] (ClO$_4$) (**4a**)
[Cu(SMeaaiNEt)$_2$] (ClO$_4$) (**4b**)
[Cu(SEtaaiNMe)$_2$] (ClO$_4$) (**4c**)
[Cu(SEtaaiNEt)$_2$] (ClO$_4$) (**4d**)

Scheme 1.

metal centre. There are two crystallographically unique copper(II) environments: one of them is square-based pyramidal CuN$_5$, and the second is a distorted octahedral CuN$_6$-type environment. The two unique copper atoms are linked

by two $\mu_{1,1}$-azides, whilst dimerisation of the dinuclear motif is accomplished through $\mu_{1,3}$-N_3 groups. There are two different N-donor centres of SMeaaiNEt: N(imidazole) [N1, N21 or N1a, N21a] and N(azo) [N7, N27 or N7a, N27a]. The Cu–N distances of these two types of N centres differ significantly by approximately 0.07 Å {Cu–N(azo) [Cu1–N7, 2.6277(16); Cu2–N27, 2.5837(18) Å] and Cu–N(imidazole) [Cu1–N1, 1.9610(16); Cu2–N21, 1.9788(16) Å]}. The stronger binding of N(imidazole) to Cu^{II} may be due to the comparable hardness of Cu^{II} and N(imidazole). This is also observed in copper-containing biomolecules.[17] The N=N distance [N6–N7/N26–N27] is 1.278(2) Å, which is slightly elongated relative to the free ligand value,[18] implies some degree of charge delocalisation, d(Cu)→π*(azo).[11–13]

Table 1. Bond lengths and bond angles of **2b** and **3b**.

2b

Bond lengths /Å		Bond angles /°	
Cu1–N1	1.9610(16)	N1–Cu1–N41	98.02(7)
Cu1–N41	1.9633(17)	N1–Cu1–N47	169.52(7)
Cu1–N47	1.9936(16)	N41–Cu1–N47	92.43(7)
Cu1–N50	2.0120(17)	N1–Cu1–N50	91.89(7)
Cu1–N7	2.628(4)	N41–Cu1–N50	167.41(7)
Cu2–N44	1.9536(17)	N47–Cu1–N50	77.65(7)
Cu2–N21	1.9788(16)	N44–Cu2–N21	100.98(7)
Cu2–N50	1.9987(16)	N44–Cu2–N50	91.17(7)
Cu2–N47	2.0392(17)	N21–Cu2–N50	167.57(7)
Cu2–N27	2.584(3)	N44–Cu2–N47	168.04(7)
N6–N7	1.278(2)	N21–Cu2–N47	90.97(6)
N26–N27	1.278(2)	N50–Cu2–N47	76.91(7)
N41–N42	1.203(2)	N1–Cu1–N7	70.41(6)
N42–N43	1.153(2)	N21–Cu2–N27	70.86(7)
N44–N45	1.205(2)	Cu1–N47–Cu2	101.47(7)
N45–N46	1.158(2)	Cu1–N50–Cu2	102.25(7)
N47–N48	1.215(2)	N43–N42–N41	176.3(2)
N48–N49	1.145(2)	N49–N48–N47	179.1(2)
N50–N51	1.210(2)	Cu1–N50–Cu2	102.25(7)
N51–N52	1.143(2)	Cu1–N47–Cu2	101.47(7)
Cu2a–N43	2.732(3)	N50–Cu1–N47	77.65(7)
Cu1a–N41a	1.963(4)	N50–Cu2–N47	76.91(7)

3b

Bond lengths /Å		Bond angles /°	
Cu1–N1	1.987(3)	N1–Cu1–N4	71.69(13)
Cu1–N4	2.468(4)	N5–Cu1–N1	93.97(16)
Cu1–N5	1.964(4)	N5–Cu1–N4	89.43(17)
Cu1–O1	1.938(3)	O1–Cu1–O1a*	76.18(13)
Cu1–O1a*	1.939(3)	O1–Cu1–N5	93.40(15)
N3–N4	1.268(5)	O1–Cu1–N5	167.13(16)
N5–N6	1.179(6)	O1–Cu1–N1	171.76(13)
N6–N7	1.156(6)	O1a*–Cu1–N1	96.02(13)
Cu1–Cu1a*	3.0516(11)	O1–Cu1–N4	112.07(13)
		O1–Cu1–N4	101.41(13)
		O1a*–Cu1–Cu1	38.10(8)
		O1a*–Cu1a*–Cu1	38.08(8)
		N7–N6–N5	177.5(5)
		Cu1–O1–Cu1a*	103.82(13)

*Symmetry: –x + 1, –y + 2, –z + 1

The single-crystal X-ray structure of [Cu(SMeaaiNEt)(N₃)(μ-OHCH₃)]₂ (**3b**) is shown in Figure 2. Selected bond lengths and angles are given in Table 1. The copper(I) centre exhibits a distorted tetrahedral CuN₃O coordination sphere bridged by OHCH₃ and two N centres from chelat-

ing ligand. The ligand, SMeaaiNEt, has three eligible donor centres: N(imidazole), N(azo) and S(thioether); in this case, it acts as an N(imidazole), N(azo) bidentate chelating agent. The chelate angle [Cu–N=N–C=N (N–N)] is 71.69(3)°, which is comparable to the reported data.[11,12] The deviation of the angle from the ideal 90° for a regular structure is a result of steric requirements of the chelated ligands. The Cu–N(azo) bond length [Cu1–N4, 2.468(4) Å] is longer than the Cu–N(imidazole) distance [Cu1–N1, 1.987(3) Å]. The N=N bond length [N3–N4, 1.268(4) Å] is greater than that of the free ligand value [1.252(1) Å][18] but is shorter than that in the Cu^{II} analogue (Table 1, Figure 1), perhaps as a consequence of better dπ(Cu)→π*(azo) charge overlap[12,19,20] in this compound than in **2b**. CH₃OH acts as bridging molecule through the O centre, and thus a dimer is formed. The Cu1–O1 distance is 1.939(3) Å. The Cu1···Cu1A distance is too long (3.052 Å) to consider any metal–metal interaction. In the dinuclear motif, the bridging unit Cu₂O₂ is a distorted four-armed plane of mean deviation of approximately 0.02 Å. The bridge angle is Cu1–O1–Cu1A, 103.82(13)° and the remaining angle is O1–Cu1–O1A, 76.18(13)°. The chelate and bridge planes are inclined at an angle of 78.39(16)°.
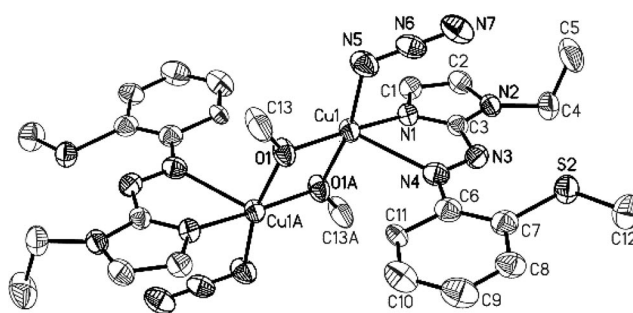
Figure 2. Thermal ellipsoidal plot with atom labelling scheme of [Cu(SMeaaiNEt)(N₃)(μ-OHCH₃)]₂ (**3b**) (30% probability). Atoms with label A are generated by symmetry.

Infrared spectra of complexes **2** exhibit ν(N=N) and ν(C=N) at 1410–1430 and 1580–1595 cm⁻¹, respectively, and these values are redshifted by 10–25 cm⁻¹ relative to those of the free ligands. This supports coordination of N(azo) and N(imine) to Cu^{II}. The most significant observation is the appearance of a strong doublet at 2090–2105 and 2065–2085 cm⁻¹. These correspond to bridging ν$_{asym}$-(N₃).[15,16,21]

In complexes **3**, ν(N₃) appears as a single sharp stretch at 2035–2045 cm⁻¹. The ν(N=N) and ν(C=N) appear at 1410–1415 and 1580–1590 cm⁻¹, respectively. The stretching frequency of N=N in [Cu(SRaaiNR′)(N₃)(μ-OHCH₃)]₂ (**3**) appears at a lower value than that for Cu^{II} complexes, [Cu(S-RaaiNR′)(μ-N₃)(N₃)]₂ (**2**) (Δν = 5–10 cm⁻¹), and this effect has been attributed to better dπ(Cu)-π*(azo of ligand) back bonding in copper(I) complexes[11–13,19] than in copper(II) complexes (also supported by N=N bond length data, vide supra). In [Cu(SRaaiNR′)₂](ClO₄) (**4**), ν(N=N) and ν(C=N) appear at 1390–1400 and 1560–1575 cm⁻¹, respec-

Table 2. FTIR[a] and UV/Vis spectra[b] of the complexes in CH_3CN.

Compound	UV/Vis spectra λ_{max} /nm ($10^{-3} \times \varepsilon$ /dm^{3}mol^{-1}cm^{-1})	IR spectra /cm^{-1} $\nu(N_3^-)$	$\nu(ClO_4^-)$	$\nu(C=N)$	$\nu(N=N)$
2a	725(0.37), 410(27.01), 362(38.11), 265(11.03)	2092, 2065		1581	1423
2b	759(0.12), 413(9.57), 367(13.73), 269(9.31)	2102, 2071		1587	1420
2c	728(0.15), 416(18.31), 364(21.05), 263(9.23)	2090, 2068		1585	1426
2d	726(0.48), 403(20.10), 367(26.34), 268(14.12)	2098, 2069		1590	1443
3a	711(0.18), 434(13.96), 369(13.59), 251(8.41)	2040		1589	1421
3b	715(0.16), 428(12.24), 368(13.27), 259(8.77)	2035		1586	1429
3c	737(0.18), 436(10.45), 371(12.71), 254(7.93)	2043		1590	1455
3d	735(0.18), 434(13.57), 373(12.71), 253(8.19)	2040		1576	1446
4a	762(0.45), 415 (16.54), 359(22.19), 262(15.74)		1094	1591	1429
4b	756(0.41), 410 (14.66), 358(21.47), 260(14.52)		1089	1587	1428
4c	752(0.47), 419 (14.14), 362(21.30), 260(14.15)		1089	1585	1423
4d	765(0.38), 419 (20.11), 352(26.24), 257(15.13)		1090	1590	1428

[a] In KBr disk. [b] In MeCN solution.

tively. The $\nu(ClO_4)$ frequency appears as a high intense sharp band at 1085–1090 cm^{-1} with a weak signal at 625 cm^{-1}. Some interesting IR data are given in Table 2.

The electronic spectra of **2** exhibit multiple highly intense transitions ($\varepsilon \approx 10^4$ M^{-1}cm^{-1}) in the visible region, 400–445 nm, along with a broad weak band at 725–760 nm. In the free ligand SRaaiNR′, the intraligand charge transitions, n–π* and π–π*, appear at 370–380 and 250–260 nm, respectively. Some of the transitions are new (Table 2, Figure 3) in the complexes: these are characteristic of copper(II) azoheterocycles[16,19,22] and are the MLCT transitions involving dπ(Cu)→π*(arylazoheterocycle). By comparing them with values for copper(II)-1-alkyl-2-(arylazo)-imidazoles,[11–13,16] copper(II)-2-(arylazo)pyridine,[19] copper(II)-pyridylthioazophenolates[22] and other pyridylthioethers,[23] we can assign the transitions at approximately 410 nm to the MLCT [dπ(Cu)→π*(azoimidazole)] band, and the absorption at approximately 740 nm is undoubtedly a d–d transition.[24] The visible ranges of the spectra of copper(I) complexes (**3**, **4**) show similar metal-to-ligand charge-transfer (MLCT) transitions at 710–765 nm and 410–

435 nm (Figure 3), which are characteristic features of Cu^I complexes when bonded with conjugated organic chromophores.[14–16]

EPR Spectra

Solid state EPR spectra of **2** at room temperature (298 K) are weakly resolved. Copper(I) complexes **3** and **4** are EPR silent. The hyperfine splitting in the EPR spectra of **2** is poor. The resolution is better at 77 K in MeCN solution (Figure 4). The complexes show the expected four-line (^{63}Cu, I = 3/2) EPR spectra and are anisotropic at higher magnetic field, exhibiting axial spectra having g_{II} values varying from 2.188 to 2.226 and A_{II} in a range from 140×10^{-4} to 165×10^{-4} cm^{-1}. The results are in general agreement with the electronic spectra, which also suggest the existence of distorted geometry. From the observed g-tensor values of the Cu^{II} complexes, it is clear that $g_\parallel > g_\perp > 2.0023$, which agrees with the ground state configuration of d$_{x^2-y^2}$, giving $^2B_{1g}$.

Figure 4. EPR spectrum of [Cu(SEtaaiNEt)(μ-N$_3$)(N$_3$)]$_2$ (**2d**) in MeCN at 77 K.

The stereochemistry of [Cu(SRaaiNR′)(N$_3$)(μ-OH-CH$_3$)]$_2$ (**3**) and [Cu(SRaaiNR′)$_2$](ClO$_4$) (**4**) was studied by ^{1}H NMR spectroscopy. The aromatic and imidazole protons are shifted downfield on coordination of SRaaiNR′ to

Figure 3. UV/Vis spectra of **2b** (—) and **3b** (- - -) in DMF at 298 K.

Table 3. ^{1}H NMR spectroscopic data of [Cu(SRaaiNR′)]$_2$(ClO$_4$) (**4**) and [Cu(SRaaiNR′)(N$_3$)(μ-OH CH$_3$)]$_2$ (**3a**) in CDCl$_3$ at room temperature.

Compound	δ /ppm (J /Hz)										
	4-H[b][a]	5-H[b]	8H[d]	9, 10-H[m]	11-H[d]	N1-CH$_3$[s]	N1-CH$_2$[q]	N1-CH$_2$CH$_3$[t]	S-CH$_3$[s]	S-CH$_2$[q]	S-(CH$_2$)CH$_3$[t]
3a	7.34	7.22	7.45 (7.0)	7.57	7.84 (7.5)	4.28				2.72	
3b	7.38	7.24	7.50 (7.0)	7.55	7.87 (7.5)		4.48 (9.0)	1.68 (8.0)	2.68		
3c	7.36	7.20	7.40 (7.0)	7.60	7.85 (7.5)	4.31				3.36 (7.5)	1.52 (8.0)
3d	7.30	7.30	7.45 (7.0)	7.56	7.88 (7.5)		4.40 (9.0)	1.62 (8.0)		3.40 (7.5)	1.57 (8.0)
4a	7.28	7.27	7.44 (7.0)	7.53	7.86 (8.0)	4.22			2.70		
4b	7.27	7.24	7.46 (7.5)	7.53	7.84 (8.0)		4.74 (9.0)	1.78 (8.0)	2.72		
4c	7.31	7.25	7.43 (7.5)	7.54	7.89 (7.5)	4.24				3.42 (9.0)	1.56 (8.0)
4d	7.30	7.28	7.47 (7.5)	7.56	7.83 (7.5)		4.72 (9.0)	1.75 (8.0)		3.40 (9.0)	1.57 (8.0)

[a] [b] Broad singlet; [d] doublet; [m] multiplet; [s] singlet; [t] triplet; [q] quartet.

Cu[I] relative to the free ligand data[11,12] (Table 3). This implies significant bonding interaction of the metal ion with the ligand. Imidazole protons (4- and 5-H) and aryl protons (8–11-H) suffer approximately 0.10 to 0.15 ppm downfield shift. The S–R and N1-R′ do not shift significantly, which implies a non-coordinated –S–R centre. Ligands SRaaiNR′ are capable of showing a tridentate $N,N′,S$ donor system. However, ^{1}H NMR spectroscopic data reflect no coordination of –S–R to Cu[I], thus these ligands serve as bidentate $N,N′$ chelators.

The magnetic properties of complex **2b** are shown in Figure 5 as a $\chi_M T$ vs. T plot (χ_M is the molar magnetic susceptibility for two Cu[II] ions). The value of $\chi_M T$ at 300 K is 0.86 cm[3]mol^{−1}K, a typical value for two copper(II) ions with $g > 2.00$, as expected. On lowering the temperature, there is a rapid increase in $\chi_M T$ to 1.03 cm[3]mol^{−1}K at 5 K and then a decrease to 0.91 cm[3]mol^{−1}K at 2 K. These features indicate noticeable intramolecular ferromagnetic coupling with the presence of weak intermolecular antiferromagnetic interactions, always present at very low temperature.

The plot of the reduced magnetisation at 2 K is included in Figure 5. The M/N μ$_B$ value at saturation (5 T) is 2.00, in agreement with the presence of two electrons in the ground state.

Complex **2b** is a tetranuclear entity, constituted by dimerisation of two Cu$_2$ "dinuclear entities". In the "dinuclear entity" each Cu[II] is linked by two azido ligands in an end-on (μ$_{1,1}$-N$_3$) coordination mode. Furthermore, one of the terminal azido ligands of each dinuclear unit links the neighbouring dinuclear entity by means a long apical Cu–N(azido) bond. (Figure 1). The resulting tetranuclear entity, together with the two different magnetic pathways (J_1 and J_2) are depicted in Scheme 2.

For calculating the values of J_1 and J_2 two approaches have been carried out. First, we have considered the Cu$_2$ "dinuclear entity" by applying the Bleaney–Bowers formula,[25] with the Hamiltonian $H = -J_1 \Sigma S_i S_j$, and introduc-
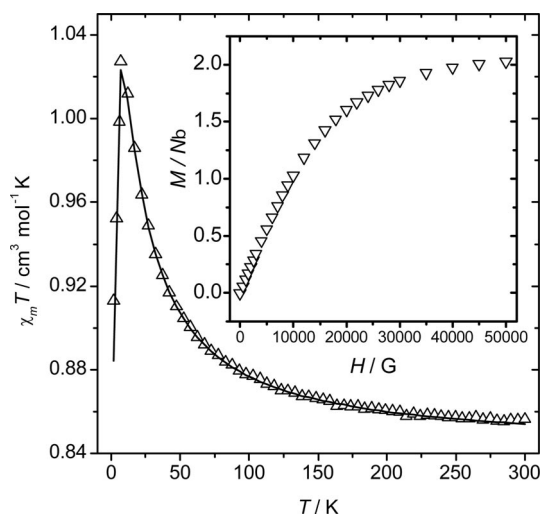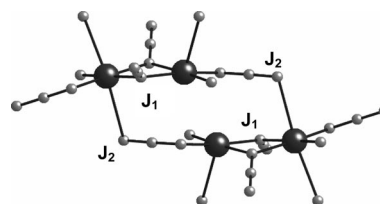

Figure 5. Plot of the susceptibility data, $\chi_M T$ vs. T, for **2b**, assuming a dinuclear entity. The solid line represents the best fit using the J_2 parameter with the mean field approach (see text for explanation). Inset: plot of the reduced magnetisation M/N μ$_B$ vs. H data at 2 K.

Scheme 2.

ing a J_2 parameter through the mean-field approach for calculating the intermolecular interactions.[26,27] This approach is valid because of the long apical Cu–N(azido) distance, which allows to assume a very weak magnetic coupling. The best-fit parameters were: $J_1 = 13.35 \pm 0.5$ cm[−1], $g =$

2.12 ± 0.002, $J_2 = -0.55 \pm 0.01$ cm^{-1} and $R = 4.0 \times 10^{-5}$ {R is the agreement factor defined as $\Sigma_i[(\chi_m T)_{obs} - (\chi_m T)_{calc}]^2/\Sigma_i[(\chi_m T)_{obs}]^2$}.

The second approach consists of considering the tetranuclear complex as an isolated entity. The corresponding fit can be made by applying the corresponding formula for the model indicated in Scheme 2 or, more easily, by working with the Clumag program,[28] using the same Hamiltonian and with the coupling values shown in Scheme 2. Both models are exact, and thus the results are identical and independent of the method. The best-fit parameters are: $J_1 = 11.25 \pm 0.5$ cm^{-1}, $J_2 = -0.85 \pm 0.02$ cm^{-1}, $g = 2.12 \pm 0.01$ and $R = 3.7 \times 10^{-3}$ {R is the agreement factor defined as $\Sigma_i[(\chi_m T)_{obs} - (\chi_m T)_{calc}]^2/\Sigma_i[(\chi_m T)_{obs}]^2$}.

By applying two different methods, we have obtained very similar results, as expected: J_1 is medium and positive (ferromagnetic) and J_2 is weak and negative (antiferromagnetic).

All experimentally reported complexes,[29] as well as theoretical studies,[30] have demonstrated that almost all dinuclear complexes with double azido ligand bridges in the $\mu_{1,1}$ coordination mode create ferromagnetic coupling. All data seem to indicate that the main parameter is the M–N–M angle (N referring to the N$_3$ bridging ligand). For Cu^{II}, when this angle is extraordinarily large, for example greater than 108°, the magnetic coupling becomes antiferromagnetic.[31] In fact, almost all complexes have a Cu–N–Cu angle between 96° and 104°, thus being ferromagnetic. Many other structural factors may influence the J value, such as the Cu–N distance and the Cu–N$_3$–Cu torsion angle.[32] A clear dependence of the exchange coupling constant on the Cu–N distance has been found, the ferromagnetic coupling decreasing as the Cu–N distance increases.[30] The J_1 value found for complex **2b** is rather small compared to those reported in the literature.[30] The three most important factors are: the Cu–N–Cu angles [Cu1–N50–Cu2 102.25(7)° and Cu1–N47–Cu2 101.47(7)°], the Cu–N distances (these are rather long, from 1.994 to 2.039 Å) and the τ torsion angles (these are very large). The sum of these factors causes the relatively small J_1 parameter. Assuming a tetranuclear entity, the J_2 value (–0.85 cm^{-1}) is easily understood by taking into account the long Cu(apical)–N(azido) distance (2.73 Å).

Copper(I) complexes [Cu(SRaaiNR′)(N$_3$)(μ-OHCH$_3$)]$_2$ (**3**) show oxidative responses at approximately 0.4 V. This is quasireversible, as estimated from peak-to-peak separation ($\Delta E_p > 100$ mV) and is assigned to the Cu^{II}/Cu^{I} couple by comparison with literature reports.[11,12,19] Complexes [Cu(SRaaiNR′)$_2$](ClO$_4$) (**4**) show a higher Cu^{II}/Cu^{I} potential, which may be due to the presence of two π-acid-coordinated azoimine functions. Figure 6 shows the cyclic voltammogram (CV) of the complexes in MeOH (Table 4). The CV plots of copper(II) complexes **2** show a reductive response at approximately 0.4 V vs. SCE. On comparing with the CV of Cu(RaaiR′)$_2$X$_2$ (X = N$_3$, NCS),[10] the couple is assigned to a Cu^{II}/Cu^{I} couple. On scanning in the negative direction up to –1.8 V, we observe an irreversible response, E_{pc}, at approximately –0.4 V and a quasireversible one at

–1.0 to –1.2 V ($\Delta E_p > 140$ mV) (Figure 6), which may be assigned to reduction of the azo groups [(–N=N–)/(–N=N–)$^-$] of the chelated ligands. The free ligand does not show any oxidation, but irreversible reductive responses appear at < -1.0 V. The voltammogram also shows a sharp anodic part at approximately –0.2 V, possibly due to the Cu^{I}/Cu^0 couple.[12,33] The reduced Cu^0 is absorbed on the electrode surface, as evidenced by the narrow width of the anodic response with a large peak current.

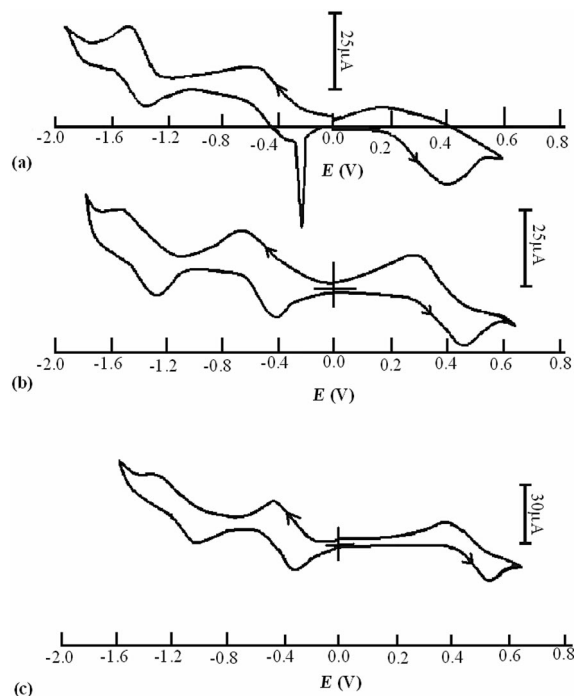Figure 6. Cyclic voltammogram of (a) **2a**, (b) **3a** and (c) **4a** in CH$_2$Cl$_2$.

Table 4. Cyclic voltammetric data.[a]

Complex	Metal redox couple E /V (ΔE_p /mV)		Ligand redox couple E /V (ΔE_p /mV)	
	Cu^{II}/Cu^{I}	Cu^{I}/Cu^0	azo/azo$^-$	azo$^=$/azo$^-$
2a	0.33 (150)	–0.25[b]	–0.48 (160)	–1.40 (170)
2b	0.37 (170)	–0.22[b]	–0.44 (180)	–1.35 (200)
2c	0.38 (160)	–0.22[b]	–0.44 (160)	–1.30 (200)
2d	0.40 (140)	–0.24[b]	–0.48 (180)	–1.38 (180)
3a	0.37 (120)		–0.58 (150)	–1.42 (170)
3b	0.35 (128)		–0.54 (170)	–1.38 (200)
3c	0.30 (130)		–0.56 (180)	–1.42 (200)
3d	0.38 (140)		–0.58 (160)	–1.38 (180)
4a	0.44 (180)		–0.40 (140)	–1.22 (190)
4b	0.42 (180)		–0.47 (160)	–1.24 (200)
4c	0.40 (180)		–0.44 (170)	–1.27 (200)
4d	0.44 (110)		–0.44 (160)	–1.24 (140)

[a] Solvent: MeCN; Pt-disk working electrode, supporting electrolyte: TBAP (0.01 M); reference: SCE; solute concentration: 10^{-3} M; scan rate: 0.05 V s^{-1}; $\Delta E_p = |E_{pa} - E_{pc}|$ mV; E_{pa} = anodic peak potential, E_{pc} = cathodic peak potential in V; $E_{1/2} = 0.5(E_{pa} + E_{pc})$ V. [b] E_{pc}.

DFT calculation has been performed for two different molecules, **2b** and **3b**. The optimised structure of these molecules are developed by using the Gaussian 03 analysis

package. The orbital energies along with contributions from the ligands and metal are given in the Supporting Information. Figure 7 depicts selected occupied and unoccupied frontier orbitals. In Cu^{II} complex **2b**, the highest occupied molecular orbital (MO) is singly occupied, so it is abbreviated as SOMO. The occupied MOs are stabilised, whereas unoccupied MOs are destabilised on going from the Cu^{II} (**2b**) to the Cu^{I} (**3b**) compounds: E_{SOMO}(**2b**) = –4.9 eV and E_{HOMO}(**3b**) = –4.17 eV. This may be due to better electron donation from Cu^{I} (d^{10}) compared to that from Cu^{II} (d^9) toward the π-acidic azoimine function. Solvent polarity stabilises occupied MOs more efficiently than unoccupied MOs. Thus, the energy separation (ΔE) between the SOMO (for **2b**) or HOMO (for **3b**) and the LUMO increases on going from the gas phase to the MeCN phase. The occupied MOs (HOMO-1 and HOMO-2) of **2b** have a significant contribution from Cu (ca. 10%). The bridging azide ($\mu_{1,1}$ and $\mu_{1,3}$-N$_3$) contributes 7% to the HOMO, while the terminal azide contributes 89%. In complex **3b** copper contributes 42% to the HOMO and 13% to the LUMO. Azide contributes to the HOMO

(ca. 39%). The chelating ligand SMeaaiNEt, in general, is the main constituent of unoccupied MOs (**2b**: LUMO to LUMO+10, 99–100% and **3b**: LUMO, 73%; LUMO+1, 95%). The charge-transfer transition in the visible region not observed in the free ligand is assigned to pure MLCT rather than an admixture of dπ(Cu)→π*(azoimine) and π(azide)→π*(azoimine) transitions involving the SOMO→LUMO/LUMO+1/LUMO+2 and HOMO-1/HOMO-2/HOMO-3→LUMO/LUMO+1//LUMO+2 functions. The ILCT π(thioazoimidazole)→π*(azoimine) transitions may appear in the high energy region. In Cu^{I} complex **3b**, the transitions HOMO/HOMO-1/HOMO-3→LUMO/LUMO+1/LUMO+2 have significant dπ(Cu)→π*(thioazoimidazole) contribution.

Cyclic voltammetric behaviour of **3** and **4** are readily rationalised by using the DFT calculation. Because of higher metal (Cu) function in occupied MOs in **3b**, the complexes show metal oxidation. Unoccupied MOs are significantly dominated by the azoimine function, thus reduction may refer to electron addition at the azo-dominated orbital of the ligand.

2b

SOMO   HOMO-1   HOMO-2

LUMO   LUMO+1   LUMO+2

3b

HOMO   HOMO-1   HOMO-2
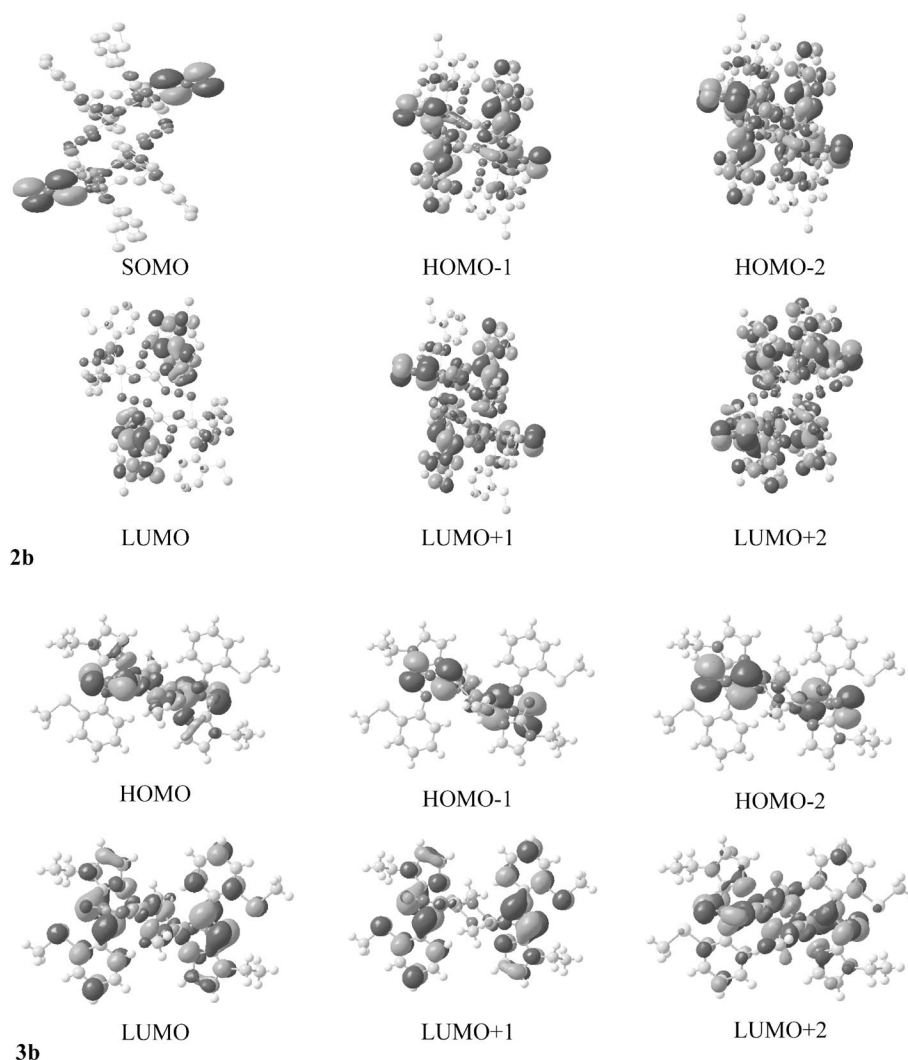
LUMO   LUMO+1   LUMO+2

Figure 7. Selected molecular orbital pictures of **2b** and **3b**.

The spin density calculated for the triplet state from a DFT study determines the exchange coupling between the two metal centres. The degree of delocalisation of the unpaired electron increases if the coordinating atoms of the ligand participate in the singly occupied molecular orbital (SOMO), which leads to the enhancement of the electron density of the donor atoms. Interestingly, the spin density is mainly distributed among the copper $d_{x^2-y^2}$ magnetic orbital and $\mu_{1,1}$-N_3 bridging between two Cu centres [Cu1···Cu2] in the dinuclear entity. It is to be noted that the exchange coupling constant for **2b** calculated by using the crystal coordinates suggests a ferromagnetic interaction (J) of 10.76 cm^{-1}. For the optimised geometry, the calculated (UB3LYP) average Cu-μ-N($\mu_{1,1}$-N_3) bond length is 1.98 Å, which is comparable with the average X-ray value (2.03 Å). The other bond lengths within the coordination sphere deviate marginally from the experimentally observed values. In terms of magnetic properties, the Cu1–μ-N($\mu_{1,1}$-N_3)–Cu2 angle is the most important. According to the Hay model,[33] the antiferromagnetic exchange coupling constant for the binuclear metal complexes, each bearing one unpaired electron, is linearly proportional to the square of the energy difference between the two SOMOs. The overlap between the magnetic orbitals of the copper atoms takes place via the bonding between the $d_{x^2-y^2}$ magnetic orbital of copper and the hybrid orbital of the bridging azido-N. Thus, the spin delocalisation on the bridging group corroborates the antiferromagnetic interaction.

Redox Interconversion Cu^{II} ↔ Cu^{I}

The Cu^{II}–Cu^{I} interconversion experiment was carried out by using a representative compound of the series, [Cu(SMeaaiNMe)(μ-N_3)(N_3)]$_2$ (**2a**). Compound **2a** reacts with ascorbic acid in aqueous methanol in the presence of NaN$_3$ (an excess amount of NaN$_3$ is added to resist dissociation), and a brown-red copper(I) complex precipitates. The identity of the reduced product has been established by matching the spectroscopic and cyclic voltammetric results (Table 2 and Table 4). The compound is diamagnetic. The structure of the coordinated Cu^{I} compound was established by its ^{1}H NMR spectrum and by comparison with the spectrum of directly synthesised [Cu(SMeaaiNMe)(N_3)(μ-OHCH$_3$)]$_2$ (**3a**) (Table 3). Microanalytical data (C,H,N) also confirm the composition of the compound. In a second experiment, to a suspension of [Cu(SMeaaiNMe)(N_3)(μ-OHCH$_3$)]$_2$ (**3a**) in methanol was added chlorine water, and the mixture was stirred in air. Nitrogen gas was bubbled through the solution to remove chlorine followed by the addition of excess NaN$_3$, whereupon the colour of the solution changed to brown-red. A crystalline compound was precipitated by reducing the volume of the solution to half. The compound so obtained was purified by crystallisation from CH$_2$Cl$_2$/MeOH. The spectroscopic (IR and UV/Vis), magnetic and voltammetric identification support the formation of copper(II) complex **2a**, which is supported by microanalytical data and spectral measurements.
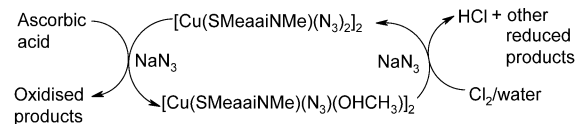
Conclusion

1-Alkyl-2-[(o-thioalkyl)phenylazo](SRaaiNR′) coordinates to Cu^{II} and Cu^{I} in the presence of azide (N_3^-) as a bidentate *N,N′*-chelator. Tetranuclear Cu^{II}-azido-bridged complexes show ferromagnetic and antiferromagnetic coupling. Electrochemistry shows a quasireversible Cu^{II}/Cu^{I} redox couple along with Cu^{I}/Cu^0 response at –0.2 V. The solution spectra show highly intense metal-to-azoimine charge transfer. Cu^{II} (**2**) and Cu^{I} (**3**) complexes undergo redox interconversion; Cu^{II} complex **2b** is reduced by ascorbic acid to a Cu^{I} complex in methanol in the presence of excess NaN$_3$, whilst Cu^{I} complex **3a** is oxidised by chlorine water to Cu^{II} complex (**2**). The spectra, magnetism and redox properties are explained by using DFT computation on optimised geometries.

Experimental Section

Materials: All starting organic compounds were purchased from Aldrich Chemical Co. and used without further purification. CuCl$_2$·2H$_2$O and NaN$_3$ were E. Merck reagent grade. Solvents were distilled from appropriate drying agents under appropriate conditions as per literature in a N$_2$ atmosphere.[34] [Cu(MeCN)$_4$]-(ClO$_4$) was used as copper(I) precursor. All experiments were carried out under N$_2$. The syntheses of the ligands were carried out by following the common procedure[13] of coupling the o-(thioalkyl)-phenyldiazonium ion [obtained by diazotisation of o-(thioalkyl)aniline] with imidazole at pH 7 followed by N1-alkylation using alkyl iodide in the presence of NaH in dry THF under dry and inert conditions.

Caution! Perchlorate salts of metal complexes can be explosive. Although no detonation tendencies have been observed, care is advised and handling of only small quantities recommended.

Physical Measurements: Microanalytical data (C,H,N) were collected with a Perkin–Elmer 2400 CHNS/O elemental analyser. Spectroscopic data were obtained by using the following instruments: Perkin–Elmer model Lambda 25 spectrophotometer (UV/Vis), Perkin–Elmer model RX-1 spectrometer on KBr disks at 4000–450 cm^{-1} (IR), Bruker (AC) 300 MHz FTNMR spectrometer (^{1}H NMR). Electrochemical measurements were performed by using computer-controlled PAR model 250 VersaStat electrochemical instruments with Pt disk electrodes. All measurements were carried out under nitrogen at 298 K with reference to SCE in acetonitrile and by using [*n*Bu$_4$N][ClO$_4$] as supporting electrolyte. The reported potentials are uncorrected for the junction potential. Room temperature (298 K) magnetic susceptibility was measured with a Sherwood Scientific (Cambridge, UK) instrument at 298 K, and data were corrected by subtracting the diamagnetic contribution. The diamagnetic correction was calculated by individually adding the diamagnetic contribution of each atom using Pascal's constants. EPR spectra were recorded in MeCN solution at room temperature (298 K) and liquid nitrogen temperature (77 K) by using a Bruker model EMX 10/12 ESR spectrometer with an X-band ER 4119 HS cylindrical resonator.

Synthesis of Complexes

Copper(II) Complexes. Preparation of [Cu(SMeaaiNMe)(μ-N₃)-(N₃)]₂ (2a):

1-Methyl-2-[*o*-(thiomethyl)phenylazo]imidazole (SMeaaiNMe) (200 mg, 0.86 mmol) in methanol (10 mL) was added dropwise to a methanol solution (10 mL) of $Cu(ClO_4)_2 \cdot 6H_2O$ (330 mg, 0.89 mmol) at 298 K under N_2. The brown-red solution was stirred for 10 min, and a methanol solution of NaN_3 (145 mg, 2.22 mmol) was added. It was then filtered and left undisturbed for a week. Dark brown crystalline compounds were separated. The crystals were filtered, washed with water and cold methanol and dried in vacuo. The yield was 200 mg (61%).

All other complexes were prepared by the same procedure. The yield varied from 60 to 75%. Microanalytical data: found (calcd.) [%] for [Cu(SMeaaiNMe)(μ-N₃)(N₃)]₂ (2a), $(C_{11}H_{12}N_{10}SCu)_2$ (759): C, 34.84 (34.78); H, 3.07 (3.16); N, 36.96 (36.89). [Cu(SMeaaiNEt)(μ-N₃)(N₃)]₂ (2b), $(C_{12}H_{14}N_{10}SCu)_2$ (787): C, 36.55 (36.59); H, 3.47 (3.56); N, 35.65 (35.58). [Cu (SEtaaiNMe)(μ-N₃)(N₃)]₂ (2c), $(C_{12}H_{14}N_{10}SCu)_2$ (787), C, 36.50 (36.59); H, 3.61 (3.56); N, 35.68 (35.58). [Cu(SEtaaiNEt)(μ-N₃)(N₃)]₂ (2d), $(C_{13}H_{16}N_{10}SCu)_2$ (815): C, 38.18 (38.28); H, 3.88 (3.93); N, 34.48 (34.36).

Copper(I) Complexes. Preparation of [Cu(SMeaaiNMe)(N₃)(μ-OHCH₃)]₂ (3a):

To a dry methanol solution of [Cu(MeCN)₄](ClO₄) (133 mg, 0.40 mmol) was added solid sodium azide (5 equiv., 132 mg, 2.03 mmol) whilst stirring at room temperature in an inert atmosphere (N_2). Then a dry methanol solution of SMeaaiNMe (95 mg, 0.41 mmol) was added by a syringe in an inert atmosphere. The resultant deep brown solution was stirred for one hour and then heated under reflux for another one hour. The solution was filtered, and the filtrate was kept undisturbed for crystallisation. After a few days, deep brown crystals appeared, which were separated by filtration. The crystals were washed with dilute methanol (1:1, v/v) and dried with $CaCl_2$ in a desiccator. The complexes were characterised by C,H,N analysis, and spectroscopic data support the composition [Cu(SMeaaiNMe)(N₃)(μ-OHCH₃)]₂ (3a).

All other complexes were prepared by the same procedure. The yield varied from 65 to 75%. Microanalytical data: found (calcd.) [%] for [Cu(SMeaaiNMe)(N₃)(μ-OHCH₃)]₂ (3a), $(C_{12}H_{16}N_7OSCu)_2$ (739): C, 38.88 (38.97); H, 4.26 (4.33); N, 26.56 (26.52). [Cu(SMeaaiNEt)(N₃)(μ-OHCH₃)]₂ (3b), $(C_{13}H_{18}N_7OSCu)_2$ (767):C, 40.59 (40.68); H, 4.72 (4.69); N, 25.48 (25.55). [Cu(SEtaaiNMe)(N₃)(μ-OHCH₃)]₂ (3c), $(C_{13}H_{18}N_7OSCu)_2$ (767): C, 40.62 (40.68); H, 4.64 (4.69); N, 25.50 (25.55). [Cu(SEtaaiNEt)(N₃)(μ-OHCH₃)]₂ (3d), $(C_{14}H_{20}N_7OSCu)_2$ (795): C, 42.17 (42.26); H, 5.00 (5.03); N, 24.58 (24.65).

Preparation of [Cu(SMeaaiNMe)₂](ClO₄) (4a):

The ligand SMeaaiNMe (100 mg, 0.43 mmol) in dry MeOH (25 mL) was added to a methanol solution (20 mL) of [Cu(MeCN)₄][ClO₄] (70 mg, 0.21 mmol) in N_2 at room temperature. The dark-brown solution was stirred for 3 h. The solution was reduced to half of its original volume by bubbling N_2 gas through it, a brown-red crystalline precipitate appeared, which was filtered, washed with methanol/water (1:1, v/v) and dried with $CaCl_2$. The dried compound was purified by column chromatography. A column alumina (neutral) was prepared in benzene. A chloroform solution of the complex was absorbed in the column and eluted first by chloroform. Initially a light yellow band was eluted and rejected. The desired deep brown/red band was collected by elution by using a methanol/chloroform (4:1, v/v) mixture and concentrated slowly in air. The yield was 0.28 g (52%).

All other complexes were prepared by following identical procedures with yields of 55–70%. Microanalytical data: found (calcd.)

[%] for [Cu(SMeaaiNMe)₂](ClO₄) (4a), (C₂₂H₂₄N₈O₄S₂ ClCu) (627): C, 42.04 (42.11); H, 3.88 (3.83); N, 17.92 (17.86). [Cu(SMeaaiNEt)₂](ClO₄) (4b), (C₂₄H₂₈N₈O₄S₂ClCu) (655): C, 43.84 (43.97); H, 4.33 (4.27); N, 17.00 (17.10). [Cu(SEtaaiNMe)₂](ClO₄) (4c), (C₂₄H₂₈N₈O₄S₂ClCu) (655): C, 44.04 (43.97); H, 4.20 (4.27); N, 17.21 (17.10). [Cu(SEtaaiNEt)₂](ClO₄) (4d), (C₂₆H₃₂N₈O₄S₂ClCu) (683): C: 45.63 (45.68); H, 4.75 (4.69); N, 16.32 (16.40).

Copper(II)–Copper(I) Interconversion

[Cu(SMeaaiNMe)(μ-N₃)(N₃)]₂ (2a) → [Cu(SMeaaiNMe)(N₃)(μ-OHCH₃)]₂ (3a): To a suspension (15 mL) of [Cu(SMeaaiNMe)(μ-N₃)(N₃)]₂ (2a) (0.20 g, 0.26 mmol) in methanol was added with stirring under N_2 ascorbic acid (0.09 g, 0.50 mmol) in water (5 mL). The brown suspension quickly changed to deep red-brown, and stirring was continued for 30 min. NaN_3 (0.2 g, excess amount) was added to this solution and stirred. The volume of the solution was reduced by bubbling off N_2 gas, and a precipitate appeared within a short while. The precipitated mass was filtered, washed with water and cold methanol. The residue was dried with $CaCl_2$ and recrystallised by diffusion of CH_2Cl_2 solution to hexane. Brown shining crystals were isolated. The yield of [Cu(SMeaaiNMe)(N₃)(μ-OHCH₃)]₂ (3a) was 0.08 g (42%). Microanalytical data: found (calcd.) [%] for [Cu(SMeaaiNMe)(N₃)(μ-OHCH₃)]₂ (3a), $(C_{12}H_{16}N_7OSCu)_2$ (739): C, 38.92 (38.97); H, 4.36 (4.33); N, 26.45 (26.52).

[Cu(SMeaaiNMe)(N₃)(μ-OHCH₃)]₂ (3a) → [Cu(SMeaaiNMe)(μ₁,₁-N₃)(N₃)]₂ (2a): To a methanol suspension of [Cu(SMeaaiNMe)(N₃)(μ-OHCH₃)]₂ (3a) (0.20 g, 0.27 mmol) methanol saturated with chlorine was added in drops and the mixture was stirred in air. Immediately, the colour changed from red-brown to deep brown. The stirring was continued for 45 min, and then N_2 gas was bubbled for a few minutes with constant stirring. Excess NaN_3 (0.2 g) in water was added, and air was bubbled through the mixture for 30 min and methanol was added from time to time to maintain the volume of the solution at 25 mL. The mixture was filtered and kept in the freezer for 4 h. The brown precipitate was filtered and washed with water and cold methanol. The compound was soluble in the mixture of 2-methoxy ethanol and methanol (1:5, v/v) and was crystallised by concentration in air for a week. The yield of [Cu(SMeaaiNMe)(μ₁,₁-N₃)(N₃)]₂ (2a) was 0.12 g (58%). Microanalytical data: found (calcd.) [%] for [Cu(SMeaaiNMe)(μ₁,₁-N₃)(N₃)]₂ (2a), $(C_{11}H_{12}N_{10}SCu)_2$ (759): C, 34.74 (34.78); H, 3.19 (3.16); N, 36.92 (36.89).

X-ray Crystal Structure Analysis of 2b and 3b: Details of crystal analysis, data collection and structure refinement are given in Table 5. Data for **2b** (blue colour, prism shape, size $0.20 \times 0.20 \times 0.05$ mm) were collected at 93(2) K by using a Rigaku MM007/Mercury CCD diffractometer (Mo-K_α radiation, confocal optics $\lambda = 0.71073$ Å). All refinements were performed by using SHELXTL.[35] Data for **3b** (brown colour, plate shape, size $0.36 \times 0.18 \times 0.10$ mm) were collected with a Bruker SMART CCD area detector using fine-focus sealed tube graphite monochromatised Mo-K_α radiation ($\lambda = 0.71073$ Å) at 293(2) K. Data were corrected for Lorentz polarisation effects and for linear decay. Semiempirical absorption corrections based on ψ-scans were applied. The structure was solved by direct methods using SHELXS-97[35] and successive difference Fourier syntheses.[36] All non-hydrogen atoms were refined anisotropically. The hydrogen atoms were fixed geometrically and refined by using the riding model. In the final difference Fourier map, the residual minima and maxima were –0.315 and 0.455 e/Å³ for **2b** and –0.400 and 0.647 e/Å³ for **3b**. The structures were drawn by using the ORTEP-32[37] and PLATON-99[38] programs.

Table 5. Summary of crystallographic data for **2b** and **3b**.

	2b	**3b**
Empirical formula	$C_{24}H_{28}Cu_2N_{20}S_2$	$C_{26}H_{34}Cu_2N_{14}O_2S_2$
Formula weight	787.86	765.87
Temperature /K	93(2)	293(2)
Crystal system	monoclinic	monoclinic
Space group	$P2_1/n$	$P2_1/c$
Crystal size /mm	$0.20 \times 0.20 \times 0.05$	$0.36 \times 0.18 \times 0.10$
a /Å	14.951(4)	10.8091(19)
b /Å	14.922(3)	13.737(2)
c /Å	15.245(4)	15.4200(19)
β /°	100.474(7)	133.081(7)
V /Å³	3344.6(14)	1672.3(4)
Z	4	2
μ (Mo-K_α) /mm⁻¹	1.448	1.445
θ range /°	2.22–25.35	2.34–25.36
hkl range	$-17 \leq h \leq 18$;	$-13 < h < 13$;
	$-16 \leq k \leq 17$;	$-16 < k < 16$;
	$-18 \leq l \leq 14$	$-18 < l < 18$
D_{calc} /Mgm⁻³	1.565	1.521
Refined parameters	436	211
Total reflections	19901	16956
Unique reflections	5971	3259
R_1[a] [$I > 2\sigma(I)$]	0.0286	0.0529
wR_2[b]	0.0703	0.1607
Goodness of fit	1.025	1.063

[a] $R = \Sigma||F_o| - |F_c||/\Sigma|F_o|$. [b] $wR_2 = [\Sigma w(F_o^2 - F_c^2)^2/\Sigma w(F_o^2)^2]^{1/2}$, $w = 1/[\sigma^2(F_o)^2 + (0.0336P)^2 + (2.7488P)]$ for **2b**; $w = 1/[\sigma^2(F_0)^2 + (0.0942P)^2 + (1.1087P)]$ for **3b** where $P = (F_o^2 + 2F_c^2)/3$.

CCDC-691681 {[Cu(SMeaaiNEt)(μ-N₃)(N₃)]₂ (**2b**)} and -691682 {[Cu(SMeaaiNEt)(N₃)(μ-OHCH₃)]₂ (**3b**)} contain the supplementary crystallographic data for this paper. These data can be obtained free of charge from The Cambridge Crystallographic Data Centre via www.ccdc.cam.ac.uk/data_request/cif.

Computational Methods: All computations were performed by using the Gaussian03 (G03)[39] software package running under Windows. Becke's three-parameter hybrid exchange functional and the Lee–Yang–Parr nonlocal correlation functional[40] (B3LYP) were used throughout. Elements were assigned a 6-31G* basis set in our calculations. For copper, the Los Alamos effective core potential plus double zeta (LanL2DZ)[41,42] basis set was employed. Gas- and solution-phase geometry optimisation were carried out from the geometry obtained from the crystal structure without any symmetry constraints. In all cases, vibrational frequencies were calculated to ensure that optimised geometries represented local minima.

Supporting Information (see also the footnote on the first page of this article): Percentage orbital contribution of **2b** and **3b** in the gas phase, calculated transitions of **3b** with oscillator strength.

Acknowledgments

[1] A. C. Steenabergen, E. Bouwman, R. A. G. de Graft, W. L. Driessen, J. Reedijk, J. P. Zanello, *J. Chem. Soc., Dalton Trans.* **1990**, 3175; R. Bastida, S. Gongalez, T. Rodrignez, A. Sousa, D. E. Fenton, *J. Chem. Soc., Dalton Trans.* **1990**, 3643; M. R. Malachonsk, M. Adams, N. Elia, A. L. Rheingold, R. S. Kelly, *J. Chem. Soc., Dalton Trans.* **1999**, 2177; L. Casella, M. Gullotti, R. Vigato, *Inorg. Chim. Acta* **1986**, *124*, 121; R. A. Allred, S. A. Hufner, K. Rudzka, A. M. Arif, L. M. Berreau, *Dalton Trans.* **2007**, 351–357.

[2] M. E. Hossain, M. N. Alam, M. A. Ali, M. Nazimuddin, E. F. Smith, R. C. Hynes, *Polyhedron* **1996**, *15*, 973.

[3] M. Matzapetakis, D. Ghosh, T. C. Weng, J. E. Penner-Hahn, V. L. Pecoraro, *Biol. Inorg. Chem.* **2006**, *11*, 876–890; M. Oue, A. Ishigahi, K. Kimura, Y. Matsue, T. Shono, *J. PolSci. Polym. Chem.* **1985**, *23*, 2033; T. K. Ronson, H. Adams, L. P. Harding, R. W. Harrington, W. Clegg, M. D. Ward, *Polyhedron* **2007**, *26*, 2000.

[4] E. I. Solomon, R. K. Szilagyi, S. D. George, L. Basumallick, *Chem. Rev.* **2004**, *104*, 419–458; D. B. Rorabacher, *Chem. Rev.* **2004**, *104*, 651; H. W. Yim, L. M. Tran, E. D. Dobbin, D. Rabinovich, L. M. Liablesands, C. D. Incarvito, K.-C. Larn, A. L. Rheingold, *Inorg. Chem.* **1999**, *38*, 2211–2215; P. Ge, B. S. Haggerty, A. L. Rheingold, C. G. Riordan, *J. Am. Chem. Soc.* **1994**, *116*, 8406–8407; A. J. Barton, J. Conolly, W. Levason, A. Mendia-Jalon, S. D. Orchard, G. Reid, *Polyhedron* **2000**, *19*, 1373–1379; P. L. Holland, W. B. Tolman, *J. Am. Chem. Soc.* **2000**, *122*, 6331–6332; J. A. Graden, M. C. Posewitz, J. R. Simon, G. N. George, I. J. Pickering, D. R. Winge, *Biochemistry* **1996**, *35*, 14583–14589.

[5] I. Bertini, H. B. Gray, S. J. Lippard, J. S. Valentine, *Bioinorganic Chemistry*, University Science Books, Mill Valley, CA, **1994**; W. Kaim, B. Schwederski, *Bioinorganic Chemistry: Inorganic Elements in the Chemistry of Life*, J. Wiley & Sons, Chichester-New York-Brisbane-Toronto-Singapore, **1994**, pp. 22 and 196; P. M. Bush, J. P. Whitehead, C. C. Pink, E. C. Gramm, J. L. Eglin, S. P. Watton, L. E. Pence, *Inorg. Chem.* **2001**, *40*, 1871 and references cited therein.

[6] T. Shi, J. Bergulnd, L. I. Elding, *Inorg. Chem.* **1996**, *35*, 3498; S. Choi, S. Mahalingaiah, S. Delaney, N. R. Neale, S. Massod, *Inorg. Chem.* **1999**, *38*, 1800; M. D. Hall, T. W. Hambley, *Coord. Chem. Rev.* **2002**, *232*, 49; E. Bouwman, W. L. Driessen, J. Reedijk, *Coord. Chem. Rev.* **1990**, *104*, 143.

[7] R. Balamurugan, M. Palaniandavar, S. R. Gopalan, G. U. Kulkarni, *Inorg. Chim. Acta* **2004**, *357*, 919–930; M. Vidyanathan, R. Balamurugan, S. Usha, M. Palaniandavar, *J. Chem. Soc., Dalton Trans.* **2001**, 3498 and references cited therein.

[8] B. C. Westerby, K. L. Juntunen, G. H. Leggett, V. B. Pett, M. J. Koenigbauer, M. D. Purgett, M. J. Taschner, L. A. Ochrymowycz, D. B. Rorabacher, *Inorg. Chem.* **1991**, *30*, 2109; K. K. Nanda, A. W. Addison, R. J. Butcher, M. R. McDevitt, T. N. Rao, E. Sinn, *Inorg. Chem.* **1997**, *36*, 134–135.

[9] E. A. Ambundo, L. A. Ochrymowycz, D. B. Rorabacher, *Inorg. Chem.* **2001**, *40*, 5133–5138; L. Q. Hatcher, D.-H. Lee, M. A. Vance, A. E. Milligan, R. Sarangi, K. O. Hodgson, B. Hedman, E. I. Solomon, K. D. Karlin, *Inorg. Chem.* **2006**, *45*, 10055–10057.

[10] U. S. Ray, B. Banerjee, G. Mostafa, T.-H. Lu, C. Sinha, *New J. Chem.* **2004**, *28*, 1432 and references cited therein.

[11] T. K. Misra, D. Das, C. Sinha, *Polyhedron* **1997**, *16*, 4163.

[12] J. Dinda, U. S. Ray, G. Mostafa, T.-H. Lu, A. Usman, I. A. Razak, S. Chantrapromma, H.-K. Fun, C. Sinha, *Polyhedron* **2003**, *22*, 247–255.

[13] B. Banerjee, U. S. Ray, Sk. Jasimuddin, J.-C. Liou, T.-H. Lu, C. Sinha, *Polyhedron* **2006**, *25*, 1299–1306.

[14] S. S. Tandon, L. K. Thompson, M. E. Manuel, J. N. Bridson, *Inorg. Chem.* **1994**, *33*, 5555; G. A. Albada, M. T. Lakin, N. Veldman, A. L. Spek, J. Reedijk, *Inorg. Chem.* **1995**, *34*, 4910; B. Graham, M. T. W. Hearn, P. C. Junk, C. M. Kepert, F. E. Mabbs, B. Moubaraki, K. S. Murray, L. Spiccia, *Inorg. Chem.*

2001, *40*, 1536; P. Manikandan, R. Muthukumaran, K. R. J. Thomas, B. Varghese, G. V. R. Chandramouli, P. T. Manoharan, *Inorg. Chem.* **2001**, *40*, 2378; S. Koner, S. Saha, T. Mallah, K.-I. Okamoto, *Inorg. Chem.* **2004**, *43*, 840; J. D. Woodward, R. V. Backov, K. A. Abboud, D. Dai, H.-J. Koo, M.-H. Whangbo, M. W. Meisel, D. R. Talham, *Inorg. Chem.* **2005**, *44*, 638; Y.-F. Zeng, X. Hu, F.-C. Liu, X.-H. Bu, *Chem. Soc. Rev.* **2009**, *38*, 469; A. Escuer, G. Aromí, *Eur. J. Inorg. Chem.* **2006**, 4721.

[15] D. A. Buckingham, *Coord. Chem. Rev.* **1994**, *587*, 135; A. Escuer, M. A. S. Goher, F. A. Mautner, R. Vicente, *Inorg. Chem.* **2000**, *39*, 2107; M. A. S. Goher, A. Escuer, F. A. Mautner, N. A. Al-Salem, *Polyhedron* **2001**, *20*, 2971; S. Koner, S. Saha, K.-I. Okamoto, J. P. Tuchagues, *Inorg. Chem.* **2003**, *42*, 4668.

[16] U. S. Ray, Sk. Jasimuddin, B. K. Ghosh, M. Monfort, J. Ribas, G. Mostafa, T.-H. Lu, C. Sinha, *Eur. J. Inorg. Chem.* **2004**, 250; U. S. Ray, K. K. Sarker, G. Mostafa, T.-H. Lu, Md. S. El Fallah, C. Sinha, *Polyhedron* **2006**, *25*, 2764.

[17] D. A. Robb in *Copper Proteins and Copper Enzymes* (Ed.: R. Lontie), CRC Press, Inc., Boca Raton, Florida, **1984**, vol. 2, pp. 207; K. D. Karlin, Z. Tyeklar, *Bioinorganic Chemistry of Copper*, Chapman & Hall, New York, **1993**; W. Kaim, B. Schwederski. *Bioinorganic Chemistry: Inorganic Elements in the Chemistry of Life*, J. Wiley & Sons, Chichester-New York-Brisbane-Toronto-Singapore, **1994**, pp. 22 and 196; K. Krylova, C. P. Kulatilleke, M. J. Heeg, C. A. Salhi, L. A. Ochrymowycz, D. B. Rorabacher, *Inorg. Chem.* **1999**, *38*, 4322.

[18] D. Das. Ph. D. Thesis, **1998**, Burdwan University, Burdwan, 713 104, India; P. Bhunia, B. Baruri, U. S. Ray, C. Sinha, S. Das, J. Cheng, T.-H. Lu, *Transition Met. Chem.* **2006**, *31*, 310–315; J. Otsuki, K. Suwa, K. Narutaki, C. Sinha, I. Yoshikawa, K. Araki, *J. Phys. Chem. A* **2005**, *109*, 8064–8069.

[19] D. Datta, A. Chakravorty, *Inorg. Chem.* **1983**, *22*, 1085.

[20] V. Kalsani, M. Schmittel, A. Listori, G. Accorsi, N. Armaroli, *Inorg. Chem.* **2006**, *45*, 2061–2067.

[21] O. Kahn, S. Sikarov, J. Gouteron, S. Jeannin, *Inorg. Chem.* **1983**, *22*, 2877.

[22] P. K. Dhara, S. Pramanik, T.-H. Lu, M. G. B. Drew, P. Chattopadhyay, *Polyhedron* **2004**, *23*, 2457.

[23] S. Torelli, C. Belle, C. Philouze, J.-L. Pierre, W. Rammal, E. Saint-Aman, *Eur. J. Inorg. Chem.* **2003**, 2452–2457; B. Adhikari, C. R. Lucas, *Inorg. Chem.* **1994**, *33*, 1376.

[24] A. B. P. Lever. *Inorganic Electronic Spectroscopy*, Elsevier, Amsterdam, **1984**.

[25] B. Bleaney, K. D. Bowers, *Proc. Roy. Soc. (London) Ser. A* **1952**, *214*, 451.

[26] O. Kahn, *Molecular Magnetism*, VCH Publishers, New York, **1993**.

[27] R. Boca, *Struct. Bonding (Berlin)* **2006**, *117*, 1 and references cited therein.

[28] The series of calculations were made with the computer program CLUMAG, which uses the irreducible tensor operator (ITO) formalism: D. Gatteschi, L. Pardi, *Gazz. Chim. Ital.* **1993**, *123*, 231.

[29] J. Ribas, A. Escuer, M. Monfort, R. Vicente, R. Cortés, L. Lezama, T. Rojo, *Coord. Chem. Rev.* **1999**, *193–195*, 1027 and references cited therein.

[30] E. Ruiz, J. Cano, S. Alvarez, P. Alemany, *J. Am. Chem. Soc.* **1998**, *120*, 11122 and references cited therein.

[31] S. S. Tandon, L. K. Thompson, M. E. Manuel, J. N. Bridson, *Inorg. Chem.* **1994**, *33*, 5555.

[32] P. J. Hay, J. C. Thibeault, R. Hoffmann, *J. Am. Chem. Soc.* **1975**, *97*, 4884.

[33] B. K. Santra, P. A. N. Reddy, A. Chakravarty, *Inorg. Chem.* **2002**, *41*, 1328.

[34] A. I. Vogel, *A Text Book of Practical Organic Chemistry*, 2nd ed., Longman, London, **1959**.

[35] G. M. Sheldrick, *SHELXTL, Crystallographic Software Package, Version 6.10*, Bruker-AXS, Madison, WI, **2002**; G. M. Sheldrick, *SHELXL 97, Program for the Refinement of Crystal Structure*, University of Göttingen, Germany, **1997**.

[36] G. M. Sheldrick, *SHELXS-97, Program for the Solution of Crystal Structure*, University of Göttingen, Germany, **1997**.

[37] ORTEP-3 for Windows, L. J. Farrugia, *J. Appl. Crystallogr.* **1997**, *30*, 565.

[38] A. L. Spek, *PLATON, Molecular Geometry Program*, University of Utrecht, The Netherlands, **1999**.

[39] M. J. Frisch, G. W. Trucks, H. B. Schlegel, P. M. W. Gill, B. G. Johnson, M. A. Robb, J. R. Cheeseman, T. A. Keith, G. A. Petersson, J. A. Montgomery, K. Raghavachari, M. A. Al-Laham, V. G. Zakrzewski, J. V. Ortiz, J. B. Foresman, J. Cioslowski, B. B. Stefanov, A. Nanayakkara, M. Challacombe, C. Y. Peng, P. Y. Ayala, W. Chen, M. W. Wong, J. L. Andres, E. S. Replogle, R. Gomperts, R. L. Martin, D. J. Fox, J. S. Binkley, D. J. Defrees, J. Baker, J. P. Stewart, M. Head-Gordon, C. Gonzalez, J. A. Pople. *Gaussian98*, Gaussian, Inc., PA Pittsburgh, **1998**.

[40] C. Lee, W. Yang, R. G. Parr, *Phys. Rev. B* **1988**, *37*, 785–789.

[41] P. J. Hay, W. R. Wadt, *J. Chem. Phys.* **1985**, *82*, 270.

[42] M. Cossi, V. J. Barone, *J. Chem. Phys.* **2001**, *115*, 4708.

FULL PAPER

Reduction vs. Metathesis in the Reactions of Bismuth Tribromide with a Bulky Lithium Silanide – An Experimental and Theoretical Study

Kirill Yu. Monakhov,[a] Thomas Zessin,[a] and Gerald Linti*[a]

On reaction of $BiBr_3$ with $Li(thf)_3SiPh_2tBu$ (**1**) in the corresponding ratios redox/metathesis reactions were observed, yielding dibismuthane $(tBuPh_2Si)_4Bi_2$ (**2**) and disilylbismuth halide $(tBuPh_2Si)_2BiBr$ (**3**). The latter is a reaction intermediate in the formation of the dark-red **2**. The X-ray crystal structures of **1–3** were determined by low-temperature X-ray diffraction. The $Si_2Bi–BiSi_2$ core of **2** is in the semi-eclipsed conformation. No oligomerization of "nonthermochromic" **2** was observed. Compound **3** is a mixed substituted monomer with a pyramidal environment around the bismuth center. On the basis of quantum chemical calculations, the formation of tertiary bismuthane $(tBuPh_2Si)_3Bi$ is not expected for steric reasons. According to DFT-optimized geometries of the simplified model systems $n[(H_3Si)_2Bi]_2$ ($n = 1–3$), the closed-shell attraction between intermolecular Bi centers in the chain provides a moderate elongation of the intramolecular Bi–Bi

bond in the dibismuthane unit and a shortening of the intermolecular Bi···Bi contacts. According to MP4(SDQ) computations, such oligomerization is carried out by intermolecular interaction of s lone pairs that are bound together and p-type orbitals of the Bi–Bi bonds in the bismuth chain. An increase in the number of $[(H_3Si)_2Bi]_2$ molecules *per* chain results in a decrease in the HOMO–LUMO gap and leads to a bathochromic shift. TD-PBE0 computations suggest that the lowest energy electron transition in **2** is metal–metal charge transfer. In addition, the attractive contributions in the chain $[(H_3A)_2Bi]_2···[Bi(AH_3)_2]_2$ with silyl groups (A = Si) outweigh the repulsion of the Bi···Bi centers, whereas for the alkyl-substituted bismuth chain (A = C) the repulsive van der Waals force dominates. This fact makes the rectangle oligomerization model more preferred for $n[(H_3A)_2Bi]_2$ (A = C; $n = 2$), while for A = Si chain formation is favored in the gas phase.

Introduction

The chemistry of silyl-substituted bismuth compounds is an object of intensive study in the last years, because of the interesting behavior of these compounds in synthetic reactions and the following applications and the ability of these compounds to form interesting structural motifs. Only seventeen examples of such species, whose structures have been determined by X-ray diffraction, are well-known up to now. Primarily, these are homonuclear[1–3] (four examples) and heteronuclear[1,3,5–11] complexes (thirteen examples) containing silyl groups of various steric requirements [$SiMe_3$, $SitBu_3$, $Si(SiMe_3)_3$], which play a stabilizing role here. In these compounds, bismuth displays the oxidation states +1, +2 and +3. Homo- and heteronuclear silyl-substituted bismuth complexes could be obtained by different synthetic strategies: (a) metalation of trisilylbismuthane with alkyllithium,[1] (b) conversion of lithium bis(trisilylbismuthane) with 1,2-dibromoethane,[1] (c) conversion of sodium potassium bismuthide with 1,2-dichlorotetramethyldisilane,[2] (d) reduction of bismuth halides with alkali metal silanides[3] and with silyl-substituted lithium phos-

phanides[4] {the formation of the silyl-substituted bismuth complexes from the reactions of $Ar'BiCl_2$ [$Ar' = 2,6-(2,6-iPr_2-C_6H_3)_2-C_6H_3$] with potassium silanides was not observed},[12] (e) dehydrosilylation of group 13 diorganohydrides with trisilylbismuthane,[5,6,9] (f) heterometallic addition of trisilylbismuthane to group 13 trialkyl compounds,[6–8] (g) conversion of trisilylbismuthane with copper(I) *tert*-butoxide and trialkylphosphanes,[10] and (h) metathesis reaction of a heterometallic aluminum–bismuth adduct with a trialkyl indium–pyridine adduct.[11]

We report here on the redox and metathesis conversions of bismuth tribromide with the lithium silanide $Li(thf)_3-SiPh_2tBu$[13] in various ratios, resulting in a stable silyl-substituted dibismuthane and a disilylbismuth halide. We also use quantum chemical calculations on simplified model compounds of silyl- and alkyl-substituted bismuthanes to obtain an insight into the possibility of forming $(R_3Si)_3Bi$ structures, the stability of the silyl-substituted $(H_3Si)_2E$· radicals against dimerization as well as the instability of $[(H_3Si)_2E]_2$ molecules towards dissociation in the series of pnicogens E = P, As, Sb, Bi. In addition, the oligomerization of $n(H_3A)_2Bi$· radicals (A = C, Si; $n = 2–4$), the bonding and orbital situations as well as the electronic excitations in the dibismuthane and its oligomerized forms were studied with use of density functional (DFT), time-dependent density functional (TD-DFT), and conventional ab ini-

[a] Anorganisch-Chemisches Institut, Universität Heidelberg, Im Neuenheimer Feld 270, 69120 Heidelberg, Germany Fax: +49-6221-546617 E-mail: gerald.linti@aci.uni-heidelberg.de

tio theory to obtain an insight into the nature of Bi–Bi and Bi···Bi interactions, which could be observed in the fluid and crystalline phase.

Results and Discussion

Synthesis

The reactions of $BiBr_3$ with $Li(thf)_3SiPh_2tBu$ (**1**) in the corresponding ratios in the solvent toluene yield the silyl-substituted bismuthanes **2** and **3** (Scheme 1). Thus, the intended salt metathesis reaction of $BiBr_3$ with three equivalents of **1** leads to a redox process under the applied conditions (warming from –78 °C to room temp. during the reaction), resulting in the dibismuthane ($tBuPh_2Si)_4Bi_2$ (**2**) and the disilane ($tBuPh_2Si)_2$. During the reaction the color of the solution changes from green to red-brown. Workup allows isolation of **2** as dark-red crystals soluble in toluene. The ^{29}Si NMR spectrum of the dark-red solution contains two signals: singlets for the silicon atoms of dibismuthane (δ = 15.9 ppm) and disilane (δ = –2.16 ppm).

The formation of ($tBuPh_2Si)_3Bi$ was not observed. This is probably due to steric reasons, which will be discussed later.

Heating of **2** under reflux at 100 °C for 3 h did not lead to disproportionation into elemental bismuth and ($tBuPh_2Si)_3Bi$ or to dissociation of **2** into corresponding radicals. As a result, **2** could be observed in the reaction solution again as a thermodynamically stable compound. This high thermostability may be related to the relatively short Bi–Bi distance in **2**.

The reaction of $BiBr_3$ with **1** in a 1:2 and 1:1 ratio gives the disilylbismuth halide ($tBuPh_2Si)_2BiBr$ (**3**) together with **2**. Here, after workup of the reaction mixture, red crystals of **3** could be isolated from the dark-green hexane solution as well as from the red toluene solution only. The ^{29}Si NMR spectra of the solutions show singlets at δ = –4.19 and –6.10 ppm, respectively. In addition, both solutions contain

2, which forms here predominantly (ratio ca. 2.5:1 according to ^{29}Si NMR signals). Interestingly, the dark-green solution is more stable than that of red color, which decomposes with formation of elemental bismuth after short periods of time at low temperature (–20 °C) or much faster at room temperature. In our opinion, the dark-green oily solution should contain a form of **3** oligomerized via weak Br–Bi···Br intermolecular contacts (like Mes_2BiBr,[14] for example), which are broken on dissolution of the oligomer to give **3**. However, no crystals could be isolated from this solution.

X-ray Crystal Structures

Single crystals of **1**–**3** suitable for X-ray structure determination were isolated from the corresponding solutions at –20 °C.

Tris(tetrahydrofuran)lithium(*tert*-butyldiphenylsilanide)-lithium [$Li(thf)_3SiPh_2tBu$ (**1**)] was synthesized by starting from the reaction of chloro-*tert*-butyldiphenylsilane, $tBuPh_2SiCl$, with lithium granulate in tetrahydrofuran solution according to the literature procedure.[13] The compound was crystallized from a *n*-hexane/thf mixture at –20 °C. Compound **1** crystallizes in the monoclinic crystal system, space group $P2_1/n$ (Table 3). Figure 1 shows the molecular structure of **1** in the solid state. The asymmetric unit contains three independent molecules of **1**. The crystal structure displays monomer silanide units, where the lithium ions are surrounded by three thf molecules and a silicon atom in a tetrahedral geometry. They differ only in the slight disorder of coordinated thf molecules and in the rotational conformation of the $(thf)_3Li$ and the $SiPh_2tBu$ units. For the $C_{Bu}SiLiO$, torsional angle values of 37°, 39°, and 49° are observed. The Si–Li bond lengths in the three independent molecules [266.0(5), 267.5(5), 269.0(5) pm] are fairly similar. This is in the typical range, as compared to other thf adducts of monomeric lithium silanides {262.7 pm in $Li(thf)_3SiPh(NEt_2)_2$,[15] 266.9 pm in Li(thf)$_3$Si-
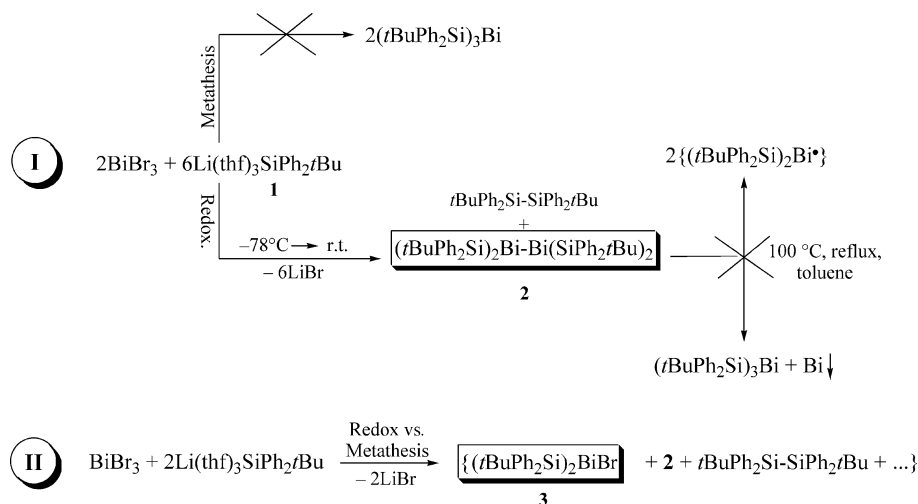
Scheme 1. Reaction pathways I and II leading to the formation of bismuthanes **2** and **3**.

(SiMe$_3$)$_3$,[16] 267.2 pm in Li(thf)$_3$SiPh$_3$,[16] 267.8 and 268.2 pm in Li(thf)$_3$SiPh$_2$(NEt$_2$),[15] 271.7 pm in Li(thf)$_3$-Si*t*Bu$_3$,[17,18] 273.2 pm in Li(thf)$_3$SiPh$_2$(NPh$_2$),[19] and 276.0 pm in Li(thf)$_3$Si(SiMe$_2$SiMe$_3$)$_3$[20]}.
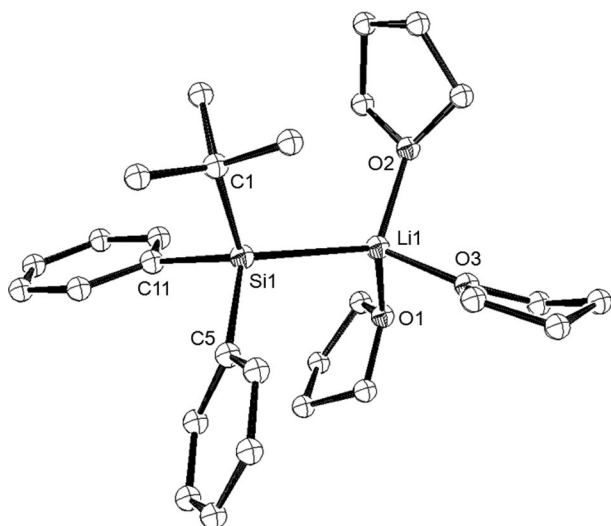

Figure 1. Molecular structure of lithium silanide **1** (crystal; the thermal ellipsoids are given at the 30% probability level; hydrogen atoms are omitted for clarity). Only one of the three independent molecules is shown. Selected bond lengths [pm] and angles [°]: Si1–Li1 267.5(5), Si1–C5 192.0(4), Si1–C11 192.7(4), Si1–C1 195.8(5), O1–Li1 198.1(8), O2–Li1 196.1(8), O3–Li1 192.4(8), C5–Si1–C11 99.8(2), C5–Si1–C1 106.3(2), C11–Si1–C1 102.2(2), O3–Li1–O2 105.1(3), O3–Li1–O1 99.1(4), O2–Li1–O1 106.8(3).

Compound **2** crystallizes in the triclinic crystal system, space group *P*$\bar{1}$, *Z* = 2 (Table 3, Figure 2). The solid-state molecular structure shows a dibismuthane with a Bi–Bi bond length of 300.6 pm. The Si$_2$Bi–BiSi$_2$ core is in the semi-eclipsed conformation, where each bismuth atom is surrounded by two *tert*-butyldiphenylsilyl (*t*BuPh$_2$Si) groups. Two silyl-containing dibismuthanes of similar structural type, but with less bulky silyl (Me$_3$Si) or alkyl [(Me$_3$Si)$_2$-CH] groups, have been reported up to now.[1,21] The Bi–Bi distance in **2** is shorter by 2.9 pm and 4.7 pm than in anti-periplanar molecules (Me$_3$Si)$_4$Bi$_2$ ($d_{Bi–Bi}$ = 303.5 pm)[1] and [(Me$_3$Si)$_2$CH]$_4$Bi$_2$ ($d_{Bi–Bi}$ = 305.3 pm),[21] respectively. Finally, it is 3.4 pm shorter than the sum of the covalent radii ($\Delta\Sigma r_{cov}$ = 304 pm). The Bi–Si bond lengths in **2** are $d_{Bi–Si}$ = 268.6–270.8 pm, which is expected from the covalent radii of bismuth and silicon [r_{cov}(Si) = 0.5$r_{(Si–Si)}$, $r_{(Si–Si)}$ = 238.6 pm in (*t*BuPh$_2$Si)$_2$]. The molecules of **2** can be regarded as isolated ones with a shortest intermolecular Bi⋯Bi distance of 1000 pm. In (Me$_3$Si)$_4$Bi$_2$, aggregation via Bi⋯Bi contacts (380.4 pm) was observed.[1,22] This leads to a moderate elongation of the Bi–Bi bond in the dibismuthane unit. The quantum chemical calculations, which will be discussed later, provide evidence for this.

The space-filling representations of the silyl-substituted molecules **2** and [(Me$_3$Si)$_2$Bi]$_2$ in Figure 3 show that bulky *t*BuPh$_2$Si groups of **2** more effectively surround the reactive
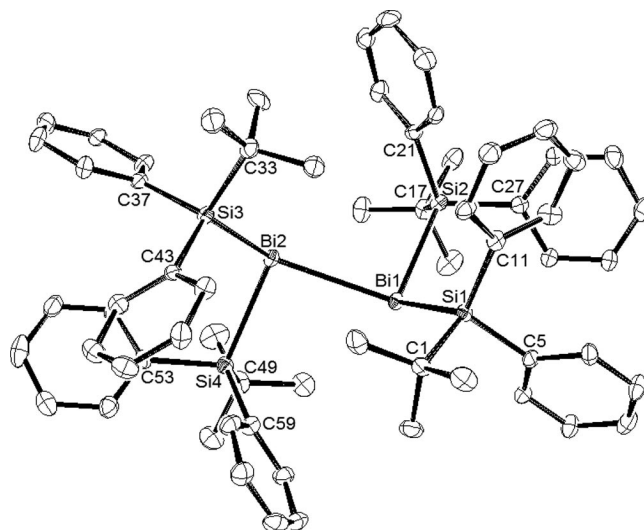

Figure 2. Molecular structure of **2** (crystal; the thermal ellipsoids are given at the 30% probability level; hydrogen atoms are omitted for clarity). Selected bond lengths [pm] and angles [°]: Bi1–Bi2 300.6(8), Bi1–Si2 268.9(2), Bi1–Si1 270.8(2), Bi2–Si4 268.6(3), Bi2–Si3 268.7(3), Si1–C11 187.8(9), Si1–C1 190.2(9), Si1–C5 191.4(9), Si2–C21 186.4(8), Si2–C27 187.1(9), Si2–C17 190.7(8), Si3–C43 187.5(8), Si3–C37 189.6(8), Si3–C33 191.3(10), Si4–C53 187.5(9), Si4–C59 188.3(8), Si4–C49 192.3(9), Si2–Bi1–Si1 101.63(7), Si2–Bi1–Bi2 93.87(6), Si1–Bi1–Bi2 124.58(6), Si4–Bi2–Si3 101.77(8), Si4–Bi2–Bi1 94.98(6), Si3–Bi2–Bi1 124.28(5), C11–Si1–C1 113.6(4), C11–Si1–C5 108.4(4), C1–Si1–C5 106.3(4), C11–Si1–Bi1 118.4(2), C1–Si1–Bi1 107.5(3), C5–Si1–Bi1 101.3(3), C21–Si2–C27 106.5(4), C21–Si2–C17 113.3(4), C27–Si2–C17 106.6(4), C21–Si2–Bi1 115.7(3), C27–Si2–Bi1 107.4(2), C17–Si2–Bi1 106.9(3), C43–Si3–C37 106.9(4), C43–Si3–C33 113.2(4), C37–Si3–C33 106.5(4), C43–Si3–Bi2 117.7(3), C37–Si3–Bi2 102.6(3), C33–Si3–Bi2 108.8(3), C53–Si4–C59 106.9(4), C53–Si4–C49 106.7(4), C59–Si4–C49 113.4(4), C53–Si4–Bi2 107.9(3), C59–Si4–Bi2 115.0(3), C49–Si4–Bi2 106.6(3), Si1–Bi1–Bi2–Si3 4.62(9), Si2–Bi1–Bi2–Si3 –102.36(8), Si1–Bi1–Bi2–Si4 –103.26(8), Si2–Bi1–Bi2–Si4 149.76(8).

Bi–Bi bond. Such effective steric protection of the bismuth centers in **2** can be regarded as one of the main reasons of the stability of this compound.
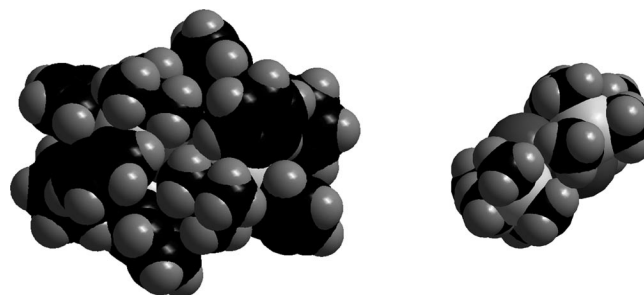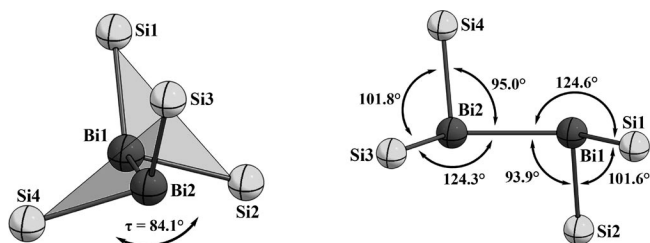

Figure 3. Space-filling models of silyl-substituted dibismuthanes **2** (left) and [(Me$_3$Si)$_2$Bi]$_2$ (right).

The bond angles around bismuth lie in the wide range of 94–125°, resulting in a sum of angles at the bismuth centers (Bi^{sum}) of 320.1° (Bi$_1$) and 321.0° (Bi$_2$). The dihedral angle τ between Si–Bi–Si planes is 84.1° (Figure 4). Thus, all of these angles are evidence of steric strain in **2**.

Figure 4. The core of dibismuthane **2**. Views along the Bi–Bi bond.

Compound **3** crystallizes in the orthorhombic crystal system, space group $P2_12_12_1$. Its solid-state structure (Table 3, Figure 5) is similar to [(Me$_3$Si)$_2$CH]$_2$BiCl,[23] which is described as a mixed-substituted monomeric diorganobismuth halide with a pyramidal environment around the bismuth center. The Bi–Si bond lengths in **3** are 267.8 pm and 269.6 pm, which are similar to the Bi–Si distances in **2**. The Bi–Br distance is 266.7 pm. The Si–Bi–Si angle is 100.22°. As in [(Me$_3$Si)$_2$CH]$_2$BiCl, we observed a slight dissimilarity of the R–Bi–X angles (Si–Bi–Br = 96.97° and 98.70°). Such slight distortions in the Bi–Si bond lengths and Si–Bi–Br angles may be related to steric strain in **3**. In addition, the total sum of angles at the bismuth center (Bi^{sum}) is 295.9°. This is a smaller deviation than that in **2** from the expected structure of R$_3$Bi with bond angles of 90° each.
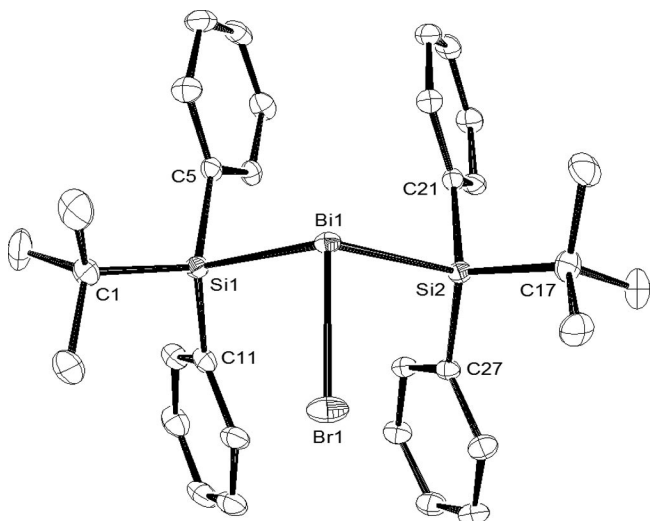

Figure 5. Molecular structure of **3** (crystal; the thermal ellipsoids are given at the 30% probability level; hydrogen atoms are omitted for clarity). Selected bond lengths [pm] and angles [°]: Br1–Bi1 266.7(7), Bi1–Si1 267.8(1), Bi1–Si2 269.6(1), Si1–C11 186.8(5), Si1–C5 187.4(4), Si1–C1 191.0(5), Si2–C27 186.3(4), Si2–C21 186.9(4), Si2–C17 189.8(5), Br1–Bi1–Si1 98.70(3), Br1–Bi1–Si2 96.97(3), Si1–Bi1–Si2 100.22(3), C11–Si1–C5 111.69(2), C11–Si1–C1 107.7(2), C5–Si1–C1 112.9(2), C11–Si1–Bi1 117.2(1), C5–Si1–Bi1 98.4(1), C1–Si1–Bi1 108.8(2), C27–Si2–C21 110.8(2), C27–Si2–C17 113.2(2), C21–Si2–C17 108.0(2), C27–Si2–Bi1 114.4(1), C21–Si2–Bi1 103.1(1), C17–Si2–Bi1 106.7(2).

As can be seen from the space-filling model of **3** (Figure 6), there is a vacant site on the bismuth atom, which is assigned to the lone pair (LP) on the bismuth atom. Through this LP, intermolecular interactions like Br–Bi···Br in the oligomerized form are enabled.
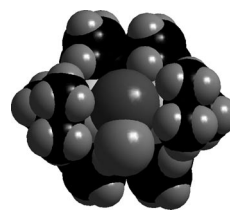
Figure 6. Space-filling models of disilylbismuth bromide **3**.

Quantum Chemical Calculations

Pyramidal (R$_3$Si)$_3$Bi Structures

The possibility of forming (R$_3$Si)$_3$Bi structures may be related to a "hybridization sp valence orbitals effect" of the metal, to the presence of the lone pair on the metal atom and its type, an orientation of the lone pair, and as a consequence the repulsive interactions of the R$_3$Si groups around metal center. Thus, according to the natural localized molecular orbitals (NLMO) analysis at the MP2(full) level on the DFT-optimized geometry of the simplified electrostatic model (H$_3$Si)$_3$Bi, the bismuth atom uses 9.3% s and 90.4% p orbitals for bonding with silyl groups [s$^{8.3\%}$p$^{91.4\%}$ according to the natural bond orbital (NBO)]. The lone pair of electrons on Bi possesses 74.6% s and 25.4% p character (according to the NLMO). As a result, the (H$_3$Si)$_3$Bi structure shows a pyramidal environment around Bi (Figure 7), where the Si–Bi–Si angles are 89°. In NBO evaluations, the Bi–Si bonds are more weakly polarized toward Si atoms (ca. 50.7%). In this manner, the valence sp hybrid orbitals at Bi are adapted for a nucleophilic attack of only moderately bulky alkyl or silyl anions like [(Me$_3$Si$_2$)AH]$^-$ (A = C) or [AMe$_3$]$^-$ (A = Si) to form (R$_3$A)$_3$Bi.[24] Increased steric bulk of substituents leads to an increase in the Bi–Si bond lengths [267.0 pm for (H$_3$Si)$_3$Bi; 267.8 pm for (Me$_3$Si)$_3$Bi; 273.2–275.9 pm for (iPr$_3$Si)$_3$Bi] and the Si–Bi–Si angles [89.0° for (H$_3$Si)$_3$Bi, 96.8° for (Me$_3$Si)$_3$Bi, 107.1–109.7° for (iPr$_3$Si)$_3$Bi], and, consequently, to more steric strain in the molecule. Here, (tBuPh$_2$Si)$_3$Bi is a good example. Thus, according to the DFT-optimized geometry of the tertiary bismuthane (tBuPh$_2$Si)$_3$Bi, the Bi–Si bond lengths and the Si–Bi–Si angles lie between 273.3 and 275.1 pm, and 99.6 and 109.8°, respectively. Such relatively large deviations in the Bi–Si distances and the Si–Bi–Si angles may be related to repulsive interactions of the silyl substituents in (tBuPh$_2$Si)$_3$-Bi. Therefore, three bulky tBuPh$_2$Si ligands may be hardly coordinated to the bismuth centre on the way of experimentally described reactions here, whereas for indium (for example), displaying a planar structural motif in the solid state, this is accessible {see [(tBuPh$_2$Si)$_3$In]}.[25]

89° (R = H)
96.8° (R = Me)
107.1 – 109.7° (R = iPr)
99.6 – 109.8° (R = tBuPh$_2$)
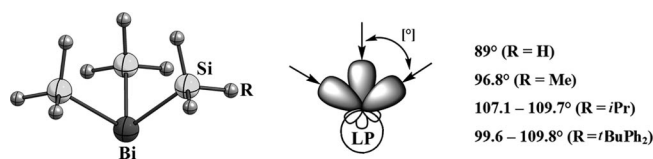
Figure 7. DFT-optimized structure for (R$_3$Si)$_3$Bi (R = H, Me, iPr, tBuPh$_2$) molecules and view of sp valence orbitals of metal.

Pnicogen Radicals (H₃Si)₂E and Their Dimers

Formation of persistent radicals (R′)₂E· (R′ = alkyl or amide) of group 15 elements is well known. Thus, the phosphanyl and arsinyl radicals,[26,27] generated in solution by reaction of the dialkyl- or diamidophosphorus(III) or -arsenic(III) monochlorides with an electron-rich olefin, or under photolytic conditions by melting or vaporizing of the dipnicogens [here, (PR′₂)₂], could be observed in solution as well as in the gas phase and characterized by ESR spectroscopy, gas-phase electron diffraction (GED), and X-ray crystal analysis. In addition, the participation of the group 15 p elements in the formation of the silyl radicals is established. For example, homolysis of tris(triethylsilyl)antimony led to antimony and free triethylsilyl radicals.[28] In case of bismuth, the formation of its (R′)₂Bi· radicals was observed in the gas phase. Thus, the signals for (R′)₂Bi⁺ ions [R′ = (Me₃Si₂)CH or 2,6-(Me₂NCH₂)₂C₆H₃] could be detected by EI mass spectrometry.[21,29] The probable formation of the bismuth radicals in liquid ammonia was reported by Gilman.[30] Di-p-tolylbismuth halide and sodium reacted to yield an intensely green colored solution. The homolytic cleavage of the Bi–Bi single bond should depend on the steric bulk of the ligands. In our case, we could observe a bismuth cation [(tBuPh₂Si)₂Bi]⁺ in toluene solution by LIFDI mass spectrometry, indicating homolytic dissociation of the dibismuthane and subsequent ionization.

Herein, we discuss the stability of the silyl-substituted (H₃Si)₂E· radicals towards dimerization, and thus, the instability of [(H₃Si)₂E]₂ molecules towards dissociation in the series of pnicogens E = P, As, Sb, Bi on the basis of the bond association and dissociation energies, respectively, as well as on the basis of the total charge transfer on the pnicogen atoms during both of these processes.

Upon traveling downward within group E, the bond length E–E in the [(H₃Si)₂E]₂ compounds becomes longer and the natural population analysis (NPA) pnicogen charge becomes more positive (Table 1, Figure 8). This is in line with the increasing covalent radii and decreasing electronegativity of the homologous elements. The relatively small increase in the Bi–Bi bond length compared to that in the Sb–Sb bond length may be related to "relativistic effects", which result in a decrease in the atom sizes and a shortening of the E–E bond. Upon dimerization of the pnicogen radicals, the association energies for [(H₃Si)₂E]₂ decrease within the group (Table 1, Figure 9). In addition, the total intramolecular charge transfer for the lighter elements becomes more negative; this corresponds to a better stabilization of the molecules by the formation of E–E bonds. As a consequence, the instability of the E–E bond increases within the group, which is expressed in a decrease in the bond dissociation energies of [(H₃Si)₂E]₂ molecules. Here, as expected, the longer the bond length, the less is the bond energy. The total charge transfer also indicates that the Bi–Bi bond is the most flexible among the E–E bonds of other pnicogens. The E–E bond strengths for [(H₃Si)₂E]₂ molecules (P–P > As–As > Sb–Sb > Bi–Bi), on the basis of the Wiberg bond indexes (WBIs) and the effective overlapping of orbitals,

Table 1. Intramolecular properties. Computed structural and bond strength parameters, and calculated charges and energies for molecules [(H₃Si)₂E]₂ (E = P, As, Sb, Bi) of C_{2h} symmetry.

Parameter	(H₃Si)₂E–E(SiH₃)₂			
	E = P	E = As	E = Sb	E = Bi
d(E–E)[a]	225.7	247.6	285.6	301.4
Q_{NPA}[b]	–0.3990	–0.2568	+0.0002	+0.0741
ΔQ_{ct}(as)[c]	–0.350	–0.320	–0.283	–0.234
ΔQ_{ct}(dis)[c]	+0.350	+0.320	+0.283	+0.234
WBI[c]	0.995	0.980	0.974	0.970
OOv[d]	0.761	0.722	0.719	0.658
ΔE_{as}[e]	–215.4	–188.8	–155.8	–141.3
ΔE_{dis}[e]	215.4	188.8	155.8	141.3

[a] E–E bond lengths [pm] were computed at the PBE0/BS-I level of theory. [b] The NPA pnicogen charges e were computed at the MP2(full)/BS-II//PBE0/BS-I level. [c] Total charge transfers (ΔQ_{ct}) e upon association (as) and dissociation (dis) and the Wiberg bond index (WBI) for E–E were calculated at the MP2(full)/BS-II//PBE0/BS-I level. [d] Order of overlapping (OOv) of the valence sp orbitals of the pnicogens was computed at the MP2(full)/BS-II//PBE0/BS-I level. [e] E–E bond association (ΔE_{as}) and bond dissociation (ΔE_{dis}) energies [kJ/mol] were calculated at the MP4(SDQ)/BS-II//PBE0/BS-I level.
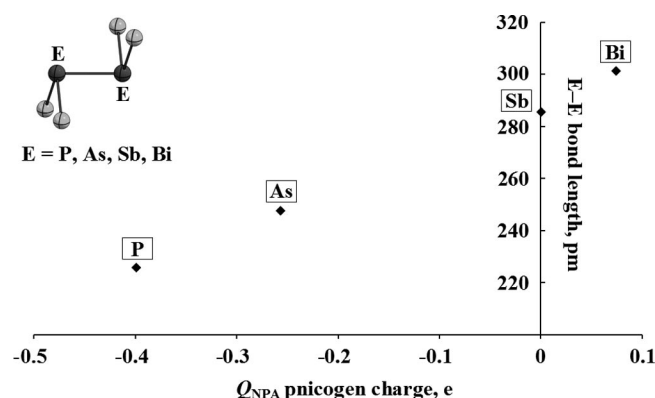

Figure 8. Calculated bond lengths and NPA pnicogen charges for [(H₃Si)₂E]₂ (A = P, As, Sb, Bi).
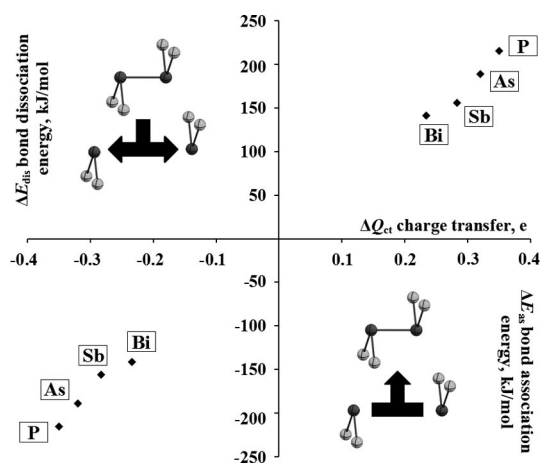
Figure 9. Calculated E–E bond association energies for (H₃Si)₂E· and E–E bond dissociation energies for [(H₃Si)₂E]₂ (E = P, As, Sb, Bi) and corresponding total charge transfers on the pnicogen atoms.

provide evidence for results described above (Table 1). As a result, the $[(H_3Si)_2Bi]_2$ dimers possess the lowest stability among these compounds of pnicogens. An increase in stability of the bismuth species might be achieved by the steric bulk of the silyl substituents. For example, dibismuthanes R_4Bi_2 with little and moderate steric protection [R = Me, Et, $SiMe_3$, $CH(SiMe_3)_2$] are thermolabile and have a tendency toward disproportionation into elemental bismuth and tertiary bismuthanes $(R_3A)_3Bi$. In contrast to this, bismuthane molecules R_yBi_x (x, y = 2–4) with bulky groups [R = Ph, Mes, SitBu, Si(SiMe$_3$)$_3$; in our case R = tBuPh$_2$] are stabilized with respect to thermal decomposition.[1,3,4,31]

N-merization of n(H₃A)₂Bi˙ Radicals and Oligomerization of Dimers

The *n*-merization of $(H_3A)_2Bi\cdot$ radicals into $[(H_3A)_2Bi]_n$ (A = C, Si; *n* = 2–3) and the oligomerization associated with the formation of the systems $n[(H_3A)_2Bi]_2$ (A = C, Si; *n* = 2) via intermolecular Bi⋅⋅⋅Bi contacts here were evaluated by means of structure, charge, and energy calculations (Table 2, Figure 10). According to DFT computations the intramolecular Bi–Bi bond lengths in $n[(H_3A)_2Bi]_2$ elongate upon oligomerization. In $[(H_3A)_2Bi]_3$ a 3c3e bond is to be formulated. The tetramers $n[(H_3A)_2Bi]_2$ (*n* = 2) are a model for the oligomerization observed for R_4Bi_2 compounds in the liquid and crystalline phase. Here, rectangle and chain oligomerization has to be distinguished. Thus, the Bi_2 unit is retained and only weak intermolecular Bi⋅⋅⋅Bi contacts appear. The intermolecular Bi⋅⋅⋅Bi distances in $n[(H_3A)_2-Bi]_2$ are shorter than the sum of van der Waals radii of Bi in the chain oligomerization and longer in case of the distorted rectangle oligomerization. As can be seen, the NPA bismuth charges in the silyl-substituted molecules are much lower than those in the alkyl-substituted molecules. This corresponds to better donor properties of the silyl substituents and leads to a shrinking of the covalent radius of bismuth in the alkyl derivatives. The different electronegativity of C and Si atoms, better polarization of the Bi–C bonds, which are highly polarized toward carbon atoms (ca. 70%)

here, as well as two highly positive charges on neighboring Bi atoms should lead to an elongation of the intermolecular $Bi^{+Q}\cdots^{+Q}Bi$ bond. As a result, the repulsive van der Waals force between two alkyl-substituted dimers (A = C) dominates (Table 2). All in all, this is well expressed for the chain oligomerization. However, the distorted rectangle oligomerization reveals an inverse situation: here, the intermolecular Bi⋅⋅⋅Bi distances between alkyl-substituted dimers are slightly shorter than those between the silyl-substituted dimers. This phenomenon will be discussed later.
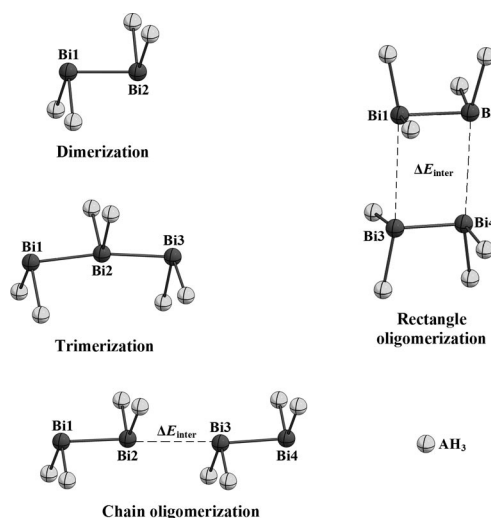

Figure 10. General view of DFT-optimized structures of $[(H_3A)_2-Bi]_n$ (A = C, Si) molecules (hydrogen atoms are omitted for clarity).

The increase in the energy gain (E_n) per radical $(H_3A)_2-Bi\cdot$ unit for $[(H_3A)_2Bi]_n$ and $n[(H_3A)_2Bi]$ (A = C, Si) molecules listed in Table 2 indicates increased stabilization of the corresponding systems. Therefore, the silyl-substituted molecules spend more energy *per* radical unit than alkyl-substituted ones gain. The energies of the intermolecular Bi⋅⋅⋅Bi contacts (ΔE_{inter}) in the tetramers $n[(H_3A)_2Bi]_2$ (*n* = 2) show that for A = C the distorted rectangle oligomerization is more preferred (about 1.4 times more in the exother-

Table 2. Intermolecular properties. Computed structural parameters and calculated charges and energies for molecules $[(H_3A)_2E]_2$ (E = P, As, Sb, Bi; A = C, Si).

| Parameter | $[(H_3A)_2Bi]_n$ | | | | $n[(H_3A)_2Bi]_2$ | | | |
| | *n* = 2 | | *n* = 3 | | *n* = 2 (rectangle) | | *n* = 2 (chain) | |
	A = C	A = Si	A = C	A = Si	A = C	A = Si	A = C	A = Si
Bi1–Bi2[a]	299.9	301.4	319.4	320.2	301.4	302.5	300.8	302.6
Bi2–Bi3	–	–	319.3	319.5	–	–	392.2	379.9
Bi3–Bi4	–	–	–	–	301.4	302.5	300.7	302.5
Bi1–Bi3	–	–	–	–	424.2	429.5	–	–
Bi2–Bi4	–	–	–	–	425.3	431.5	–	–
Q_{NPA}[b]	+0.814	+0.074	+0.849	+0.127	+0.799^{av}	+0.044^{av}	+0.828	+0.099
			+0.773[d]	–0.019[d]	+0.799^{av}	+0.041^{av}	+0.793[e]	+0.028[e]
ΔE_{mer}[c]	–130.5	–141.3	–130.4	–153.2	–277.2	–301.7	–272.4	–303.1
ΔE_{inter}[c]	–	–	–	–	–16.2	–19.1	–11.5	–20.6
E_n[c]	–65.2	–70.6	–43.5	–51.1	–69.3	–75.4	–68.1	–75.8

[a] Bi–Bi bond lengths and intermolecular Bi⋅⋅⋅Bi contacts [pm] were computed at the PBE0/BS-I level of theory. [b] The NPA charges *e* at Bi were computed at the MP2(full)/BS-II//PBE0/BS-I level. [c] Energies of *n*-merization of $(H_3A)_2Bi\cdot$ radicals and energies of intermolecular contacts (ΔE_{mer} and ΔE_{inter}, respectively) [kJ/mol], as well as energy gains per radical unit (E_n) were calculated at the MP4(SDQ)/BS-II//PBE0/BS-I level. [d] NPA charge on the central Bi atom in the trimer. [e] NPA charges on intermolecular interaction centers of bismuth.

mic energy) over chain formation, whilst for A = Si the chain oligomerization is slightly more preferred. As one of the reasons, this inversion barrier at bismuth may be related to better delocalization of two high charges on Bi for A = C via the distorted rectangle, even though the Bi···Bi distances in the rectangle formation are longer than the sum of van der Waals radii of Bi. Such an effect is more weakly expressed for A = Si. An appreciable increase in the exothermic energies ΔE_{inter} with the increase in the number of $n[(H_3A)_2Bi]_2$ molecules *per* chain (n = 3) was not observed. In our opinion, the exchange of H atoms for Me groups in anti-periplanar $[(H_3Si)_2Bi]_2$ should lead to a stronger shift to chain formation on the basis of an increase in the steric strain in the molecule. Thus, the forms of the oligomerization, described above for the gas phase, could be experimentally observed for $(R_2Bi)_2$ [R = Me, SiMe$_3$; R$_2$ = (CMe = CH)$_2$; chain][1,32] and $\{[(Me_3Si)_2CH]_2Bi\}_2$[21] (rectangle). Here, it is necessary to remark that rectangle formation for the $\{[(Me_3Si)_2CH]_2Bi\}_2$ molecule was established in the liquid phase by NMR spectroscopy as a dynamic process of an exchange of the $[(Me_3Si)_2CH]_2Bi$ units between associated molecules, whereas in the crystalline phase, only chain formation for alkyl- and silyl-substituted dibismuthanes is well-known.[1,32] While the results obtained in the gas phase for the silyl-substituted dibismuthane molecules are in line with their experimental behavior in the crystalline phase $\{see\ [(Me_3Si)_2Bi]_2\}$[1]$\}$, the alkyl-substituted derivatives reveal various behavior. In addition, in the gas phase the intramolecular Bi–Bi bond length and the intermolecular Bi···Bi distance in the chained molecule $n[(H_3A)_2Bi]_2$ (A = C; n = 2) are 300.8 and 392.2 pm, respectively, whereas in the crystalline phase experimentally observed Bi–Bi bond length and Bi···Bi distance are 312 and 358 pm, respectively. Interestingly, the lengthening of the intramolecular Bi···Bi distance in the chained R_4Bi_2···Bi_2R_4 (R = H) system to a value of 312 pm (in accordance with experimentally observed Bi–Bi bond lengths for R = Me in the crystalline phase) leads to a shortening in the intermolecular Bi···Bi distance, and as consequence, to an increase of about 11 % in energy of intermolecular contacts.[33] All in all, such a difference in structure and energy behavior in the gas, liquid, and crystalline phases may be related to the temperature factor, phase transitions, as well as to an influence of the solvent molecules. All of these possible reasons demand additional investigations on such factor-dependent systems. In addition, the chain and rectangle oligomerization should strongly depend on steric strain and rigidity of the ligands.

In this manner, an increase in steric strain and rigidity of the substituents on the metal atoms should lead to a moderate shift into chain formation or no oligomerization. As a result, the types of oligomerization represented above are not expected for the molecules with effectively protecting silyl (like tBuPh$_2$Si) or alkyl ligands (see Figure 3, too).

NBO Analysis

The charges (Q_{NPA}) on the bismuth atoms (natural electron configuration 6s$^{1.78}$6p$^{3.13}$) in $[(H_3Si)_2Bi]_2$, obtained by natural population analysis (NPA) at the MP2(full) level, are slightly positive (+0.074 e). The NPA bismuth charge in $(H_3Si)_2BiBr$ is much more positive than in $[(H_3Si)_2Bi]_2$, Q_{NPA} = +0.521 e. The results of the NBO evaluations for $[(H_3Si)_2Bi]_2$ show that the bonding between bismuth centers (Bi–Bi; WBI = 0.97) is mainly carried out by p–p orbital overlap (s$^{5.0\%}$p$^{94.5\%}$d$^{0.5\%}$), (Figure 11). This overlap corresponds to the HOMO, which indicates a σ bond between the bismuth atoms (50 %) (Figure 12). As a result, the $[(H_3Si)_2Bi]_2$ molecule is apolar with a dipole moment of 0 Debye. The hybrid HOMO–1, HOMO–2, HOMO–3, and HOMO–4 contain the main contributions from the Bi–Si interactions, whereas the HOMO–5 and HOMO–6 are metal lone pairs of mainly s character (s$^{78.5\%}$p$^{21.5\%}$; NLMO analysis provides the same result). In the polar molecule $(H_3Si)_2BiBr$ (dipole moment ca. 4 Debye), the lone pair NHO at Bi is of type s (s$^{80.1\%}$p$^{19.9\%}$), too.
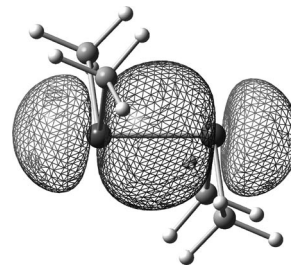

Figure 11. Graphical representation of the NBO hybrid HOMO of the model $(H_3Si)_2Bi–Bi(SiH_3)_2$.

Results from MO Theory

Figure 12 presents the frontier molecular orbitals of $[(H_3Si)_2Bi]_2$ obtained by means of canonical MO theory, which were computed at the MP4(SDQ)/BS-II//PBE0/BS-I level. Thus, according to the atomic orbital population of
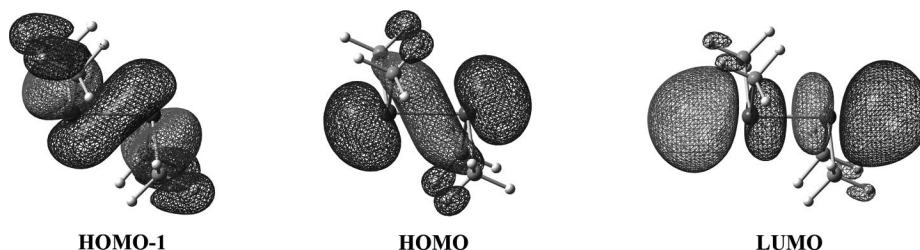

HOMO-1   **HOMO**   **LUMO**

Figure 12. Graphical representation of the frontier canonical molecular orbitals of $(H_3Si)_2Bi–Bi(SiH_3)_2$ ($\pm$ 0.02 isosurface value).

MOs, the components of HOMO–1 and LUMO come mainly from p orbitals of bismuth, while the HOMO contains the large s lone pair orbital parts of bismuth.

According to results of MO theory, the s LPs on Bi in model compound $[(H_3Si)_2Bi]_2$ with non-overloaded silyl substituents correspond to the HOMO. Interactions through these LPs are known and were observed in the reactions of tBu_3M with Bi_2Et_4, resulting in Lewis acid–base adducts $[Et_4Bi_2][MtBu_3]_2$ (where M = Al, Ga).[34] An increase in steric protection of the substituents should lead to a decrease in activity of the s LPs, and accordingly to an increase in stereochemical inert character. Therefore, the stereochemically active role of the LPs of bismuth in **2** is expressed very weakly. The s LP of **3** corresponds to the HOMO, too.

Interestingly, the HOMO–LUMO ΔE gap for $[(H_3Si)_2Bi]_n$ decreases upon oligomerization (Figure 13). Thus, delocalization of p electrons of $(H_3Si)_2Bi^.$ radicals (ΔE = 9.43 eV) in the Bi–Bi bond (the Bi–Bi stretching frequency is 127 cm^{-1}) leads to the reduction of ΔE toward 8.73 eV (n = 2). The Bi–Bi chain-oligomerized forms, $n[(H_3Si)_2Bi]_2$, have gaps of 7.75 eV (n = 2) and 7.24 eV (n = 3), accordingly. The values of the first ionization potentials (IP = E_{HOMO}; on the basis of the Koopman's theorem) and the energy values of the lowest occupied molecular orbitals decrease, accordingly. According to DFT-optimized geometries of the $n[(H_3Si)_2Bi]_2$ systems (n = 1–3), the interaction between intermolecular Bi centers in the chain provides a moderate elongation of the intramolecular Bi–Bi bond in the dibismuthane unit from 301.4 pm for n = 1 through 302.5/302.6 pm for n = 2 toward 302.6/302.7 and 303.9 pm (central unit) for n = 3. In addition, this leads to a shorting of the intermolecular Bi$\cdots$Bi contacts from 379.9 pm for n = 2 toward 378.2 pm (average) for n = 3.
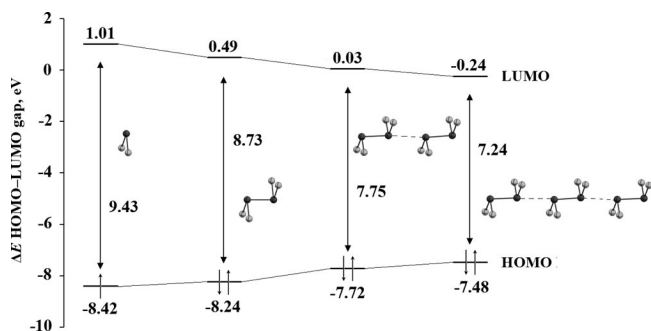

Figure 13. Changes in the HOMO–LUMO energy gap for $n(H_3Si)_2$-Bi$^.$ (n = 1–2) and $n[(H_3Si)_2Bi]_2$ (n = 2–3) systems upon n-merization and chain oligomerization, respectively.

As can be seen in Figure 14, the intermolecular interactions in the chained $[(H_3Si)_2Bi]_2\cdots[Bi(SiH_3)_2]_2$ molecule correspond to the bonding HOMO-1 (s LP orbitals that are bound together) and HOMO-3 (p-type orbitals that are bound together) and the LUMO with overlapping intermolecular p* orbitals, whereas the HOMO and the HOMO-2 are intermolecular antibonding in nature and correspond to the intramolecular interactions in each dimer molecule $[(H_3Si)_2Bi]_2$ (as described in Figure 12). As a result of the

$[(H_3Si)_2Bi]_2\cdots[Bi(SiH_3)_2]_2$ intermolecular interaction, the charges on the bismuth interacting centers are reduced from +0.074 e in dimer $[(H_3Si)_2Bi]_2$ to + 0.028 e in oligomer $[(H_3Si)_2Bi]_2\cdots[Bi(SiH_3)_2]_2$, whereas the charges on the non-interacting bismuth centers become slightly more positive + 0.099 e, accordingly. This induced dipole causes an electrostatic attraction between these two nonpolar molecules. Thus, the dipole moment of $[(H_3Si)_2Bi]_2$ is 0 Debye, whereas that of $[(H_3Si)_2Bi]_2\cdots[Bi(SiH_3)_2]_2$ becomes more positive, 0.46 Debye. In addition, such Bi$\cdots$Bi intermolecular attraction is very weak (0.04) according to the WBI. This fact and the small charges involved here, as well as the absence of other intermolecular contacts, point to the London dispersion force.
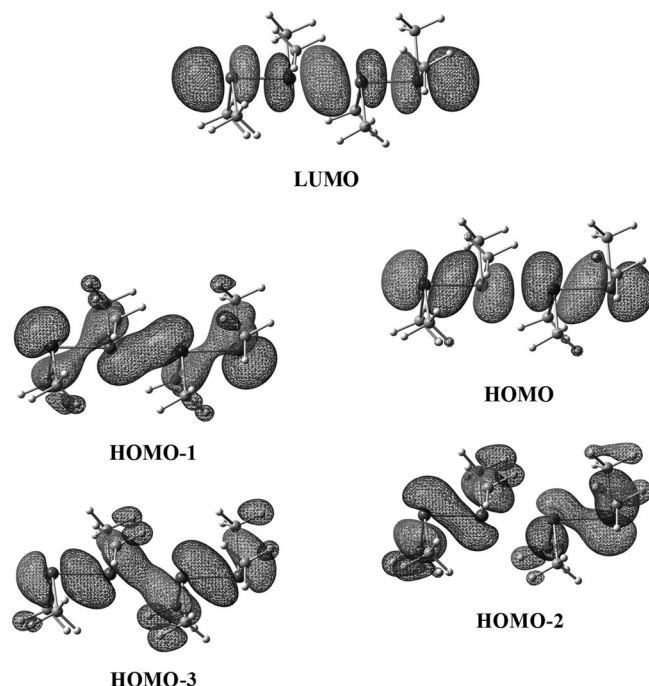

Figure 14. Graphical representation of the frontier canonical molecular orbitals of $[(H_3Si)_2Bi]_2\cdots[Bi(SiH_3)_2]_2$ upon oligomerization ($\pm$ 0.02 isosurface value).

TD-DFT Computations

According to time-dependent (TD) DFT computations of vertical electronic transitions in $[(H_3Si)_2Bi]_2$, the lowest energy $S_0 \rightarrow S_1$ electronic transition corresponds to the HOMO $\rightarrow$ LUMO and HOMO–1 $\rightarrow$ LUMO excitations with a predominantly $n_{Bi(s,p)} \rightarrow n^*_{Bi(p)}$ character. The transitions are in the near UV region (301 nm, 4.12 eV, 33 223 cm^{-1}). Such electron transfer can be described as metal–metal charge transfer (MMCT excitation). Intermolecular interaction of s LPs of the Bi–Bi bond in the bismuth chain-oligomerized form (Figures 13, 14) leads to a bathochromic shift toward lower frequencies. Thus, the lowest energy electronic transitions for $n[(H_3Si)_2Bi]_2$ are 301 (n = 1), 347 (n = 2), and 391 nm (n = 3). This fits well with the results described above (Figure 13). Experimentally, a change in color is observed for $[(Me_3Si)_2Bi]_2$[1] upon transition between the fluid phase {red $[(Me_3Si)_2Bi]_2$} and the crystalline phase

{green n[(Me$_3$Si)$_2$Bi]$_2$, where n is the number of molecules in the Bi chain}. These results are in contrast to those obtained for **2**, which is "nonthermochromic" dibismuthane. In addition, a maximum absorption band for the compounds with more bulky silyl ligands should be shifted to lower energy, too. The absorption spectrum of **2** in toluene provides evidence for this. Thus, the observed lowest energy absorption maximum lies at 465 nm (2.67 eV, 21 505 cm^{-1}) in the visible spectral region and is close to the value of the S$_0$ → S$_1$ electronic transition (the HOMO → LUMO and HOMO–2 → LUMO excitations) determined computationally by using the fixed structure of **2** from X-ray crystallography (418 nm, 2.97 eV, 23 923 cm^{-1}).

Conclusions

By the reactions of BiBr$_3$ with various amounts of the bulky lithium silanide **1**, the formation of Bi–Bi bonded product **2** could be observed. However, **2** was isolated only from the redox reaction in 1:3 ratio, as a main product. The formation of tertiary bismuthane (tBuPh$_2$Si)$_3$Bi was not observed. This is probably due to steric reasons. Accordingly, no oligomerization of **2** is observed. This is in contrast to the observation that Bi$_2$(SiMe$_3$)$_4$ is "thermochromic",[1] where oligomerization via Bi···Bi contacts is observed. In all reactions, both metathesis and redox processes were observed. These led to the formation of Bi–Br bonded product **3** simultaneously with **2**.

The bulky SiPh$_2$$t$Bu ligand is a valuable source, which should promote the radicalization processes in the reactions of trigonal pyramidal structural units (like EX$_3$) of the group 15 elements (E = P, As, Sb, Bi) with alkali metal silanide M(sol)$_n$SiPh$_2$$t$Bu (M = Li, Na, K; n = 0–3) on the basis of the shape of the silyl substituents (steric factor) and "hybridization sp valence orbital effect" of the corresponding element E (electronic factor).

Dibismuthanes such as **2** are potentially useful and important starting reagents for further synthetic applications. On one hand, these may react via the s LPs of Bi as σ-donor, to form Lewis acid–base adducts;[34] on the other hand, the more sterically demanding alkyl or silyl groups (like those in **2**) are, the less stereochemically active these orbitals are. This is due to the increasing protection of the metal center in the molecules. Finally, such compounds with Bi–Bi bonds open a way to ring systems or to bismuth species in its +1 oxidation state, for example.[31b] Sterically protecting ligands should play a key role and determine all probabilities of reaction of the complexes.

Experimental Section

General: All manipulations were carried out with the use of standard Schlenk techniques under an oxygen-free and water-free argon atmosphere and in vacuo. All organic solvents were distilled, dried, and degassed according to standard procedures. Hexane and toluene were dried with sodium/benzophenone and freshly distilled under argon. Li(thf)$_3$SiPh$_2$$t$Bu (**1**), was prepared according to a litera-

ture procedure.[13] Elemental analysis was performed in the microanalytical laboratory of Ruprecht-Karls-University of Heidelberg. ^{1}H, ^{13}C, and ^{29}Si NMR spectra were recorded with a Bruker Advance-400 (399.89, 100.55, and 79.44 MHz for ^{1}H, ^{13}C, and ^{29}Si analyses, respectively) instrument. Chemical shifts are reported in δ units (ppm) and are referenced to an external standard of tetramethylsilane (TMS) SiMe$_4$ (δ = 0.00 ppm) and benzene C$_6$D$_6$ (δ = 7.13 ppm). Electronic spectra were measured at room temp. under an argon atmosphere with a Tidas II J&M spectrophotometer, using toluene as solvent. The LIFDI-MS was recorded with a JEOL JMS-700 operating in the positive ion mode with full scanning in the range 200–1800; compound **2** was supplied as dilute solutions at about 0.2 mg mL^{-1} in toluene.

Crystal Structure Determination: X-ray data for single crystals of **1**–**3** were collected with a STOE IPDS I diffractometer equipped with an image plate area detector, using a graphite monochromator (Mo-K_α) (λ = 71.073 pm). The structure was refined against all F^2 data by full-matrix least-squares techniques (SHELXT 5.01; PC Version, Siemens, Bruker AXS).[35] All non-hydrogen atoms were refined with anisotropic thermal parameters. All H atoms were placed in calculated positions and refined by using a riding model. A summary of crystal data and structure refinements for the compounds are listed in Table 3. CCDC-742475 (**1**), -742476 (**2**·2C$_6$H$_5$Me), -742477 (**3**), and -742909 (tBuPh$_2$Si) contain the supplementary crystallographic data for this paper. These data can be obtained free of charge from The Cambridge Crystallographic Data Centre via www.ccdc.cam.ac.uk/data_request/cif.

Compound 2: A suspension of (2.93 g, 6.34 mmol) Li(thf)$_3$SitBuPh$_2$ (**1**) in toluene (20 mL) was added dropwise to a stirred solution of (0.95 g, 2.11 mmol) BiBr$_3$ in toluene (40 mL) at –78 °C. The dark-colored reaction mixture was stirred for an additional 3 h at low temperature and was then slowly warmed to ambient temperature. Initially, a green solution was observed. After stirring for 16 h, all volatile reaction components were removed with an oil vacuum pump. The residue was extracted with hexane (60 mL) and then with toluene (60 mL). After filtration, dark-red solutions were obtained. The hexane and toluene fractions show similar ^{29}Si NMR signals. The toluene and solutions were reduced to a volume of 15 mL and cooled to –20 °C, resulting in the formation of dark-red crystals of **2**; yield: 1.88 g (64%; with reference to Bi). Compound **2** is soluble in organic solvents and stable in the range –30–100 °C. C$_{64}$H$_{76}$Bi$_2$Si$_4$ (1374.46): calcd. C 55.88, H 5.57; found C 55.69, H 6.05. ^{1}H NMR (400 MHz, C$_6$D$_6$, iTMS): δ = 1.12 (s, CMe_3, 1), 7.58 (m, o-Ph), 7.67 (m, p-Ph), 7.79 (m, m-Ph) ppm. ^{13}C NMR (100.55 MHz, C$_6$D$_6$, iTMS): δ = 26.8 (s, CMe_3), 30.4 (s, CMe_3), 129.7 (m-Ph), 132.6 (p-Ph), 136.0 (o-Ph), 138.2 (i-Ph) ppm. ^{29}Si NMR (79.44 MHz, C$_6$D$_6$, eTMS): δ = 15.9 (s, SiPh$_2$$t$Bu) ppm. UV/Vis (toluene): λ_{max} (ε, L mol^{-1} cm^{-1}) = 465 (2132) nm. LIFDI-MS (toluene): m/z (%) = 1374.6 (100) [M]$^+$, 1135.4 (13) [M$^+$ – SiPh$_2$$t$Bu], 687.3 (18) [($t$BuPh$_2$Si)$_2$Bi]$^+$, 447.3 (5) [($t$BuPh$_2$Si)Bi]$^+$.

Compound 3: A suspension of (3.06 g, 6.63 mmol) (**1**) in toluene (20 mL) was added dropwise to a stirred solution of (1.49 g 3.31 mmol) BiBr$_3$ in toluene (40 mL) at –78 °C. The dark-colored reaction mixture was stirred for an additional 3 h at low temperature and was then slowly warmed to ambient temperature. After stirring for 16 h, all volatile reaction components were removed with an oil vacuum pump, and the residue was extracted first with hexane (60 mL) and then with toluene (60 mL). After filtration of the hexane and toluene fractions, the dark-green (denoted "DGS") and red (denoted "RS") solutions were obtained, respectively. Hexane and toluene solutions were reduced to a volume 15 mL and

Table 3. Crystal data and structure refinement details for **1**–**3**.

	1	**2**·2C₆H₅Me	**3**
Empirical formula	$C_{28}H_{43}LiO_3Si$	$C_{78}H_{92}Bi_2Si_4$	$C_{32}H_{38}BiBrSi_2$
Formula weight [g/mol]	462.32	1559.84	767.69
Temperature [K]	200	200	200
Crystal color	pale green	dark red	red
Crystal size [mm]³	$0.37 \times 0.35 \times 0.24$	$0.3 \times 0.16 \times 0.07$	$0.41 \times 0.14 \times 0.06$
Crystal system	monoclinic	triclinic	orthorhombic
Space group	$P2_1/n$	$P\bar{1}$	$P2_1 2_1 2_1$
a [pm]	1018.6(2)	1368.8(3)	1044.1(2)
b [pm]	1711.3(3)	1421.5(3)	1150.9(2)
c [pm]	4808(1)	1848.0(4)	2526.2(5)
α [°]		96.01(3)	
β [°]	90.08(3)	92.84(3)	
γ [°]		101.42(3)	
V [Å³]	8381(3)	3496(1)	3035(1)
Z	12	2	4
D_{calc} [Mg/m³]	1.099	1.482	1.680
μ (Mo-K_α) [mm⁻¹]	0.109	5.137	7.223
$F(000)$	3020	1564	1504
2θ-range [°]	2.04–26.13	2.52–30.63	2.11–28.15
Abs. corr.	numerical	numerical	numerical
Min/max transm.	0.9618/0.9832	0.255/0.674	0.1945/0.5230
Index ranges	$-12 \leq h \leq 12$	$-19 \leq h \leq 19$	$-13 \leq h \leq 13$
	$-21 \leq k \leq 21$	$-20 \leq k \leq 19$	$-15 \leq k \leq 14$
	$-59 \leq l \leq 59$	$-26 \leq l \leq 26$	$-33 \leq l \leq 33$
Reflections collected	36694	42336	29770
Independent reflections	14556	19419	7354
Observed refl. [$I > 2\sigma(I)$]	6160	9297	6592
Data/restraints/parameters	14556/0/912	19419/0/757	7354/0/326
Goodness-of-fit (S) on F^2	0.842	0.774	0.923
Final R indices [$I > 2\sigma(I)$]	$R1 = 0.0630$	$R1 = 0.0515$,	$R1 = 0.0248$,
	$wR_2 = 0.1291$	$wR_2 = 0.1055$	$wR_2 = 0.0509$
R indices (all data)	$R1 = 0.1463$	$R1 = 0.1249$,	$R1 = 0.0307$,
	$wR_2 = 0.1553$	$wR_2 = 0.1235$	$wR_2 = 0.0521$
Largest diff. peak/hole [e nm⁻³]	214/–192	2578/–3067	1121/–548

cooled to –20 °C, resulting in the formation of only red crystals of **3**. ²⁹Si NMR spectra for both solutions contain the silicon signals of **2** and disilane, too. Yield of DGS: 0.91 g (35.7%; with reference to Bi). Yield of RS: 0.48 g (19.0%; with reference to Bi). After short periods of time at –20 °C or at room temp., both solutions decompose with formation of elemental bismuth. The crystals of **2** (which form predominantly) also were obtained by this reaction in a 1:1 ratio (²⁹Si NMR signals of **2** and disilane were observed, too).

DGS: The signals of **2** and disilane are omitted. ¹H NMR (400 MHz, C₆D₆, iTMS): δ = 7.87 (m, *m*-Ph), 7.71 (m, *p*-Ph), 7.49 (m, *o*-Ph), 1.21 (s, C*Me₃*) ppm. ¹³C NMR (100.55 MHz, C₆D₆, iTMS): δ = 138.5 (*i*-Ph), 137.1 (*o*-Ph), 133.3 (*p*-Ph), 130.0 (*m*-Ph), 31.2 (s, C*Me₃*), 27.0 (s, *C*Me₃) ppm. ²⁹Si NMR (79.44 MHz, C₆D₆, eTMS): δ = –4.2 (s, *Si*Ph₂*t*Bu) ppm.

RS: The signals of **2**, disilane, and DGS are omitted. ¹H NMR (400 MHz, C₆D₆, iTMS): δ = 7.74 (m, *m*-Ph), 7.63 (m, *p*-Ph), 7.29 (m, *o*-Ph), 1.14 (s, C*Me₃*) ppm. ¹³C NMR (100.55 MHz, C₆D₆, iTMS): δ = 138.3 (*i*-Ph), 136.3 (*o*-Ph), 132.7 (*p*-Ph), 129.9 (*m*-Ph), 31.1 (s, C*Me₃*), 27.6 (s, *C*Me₃) ppm. ²⁹Si NMR (79.44 MHz, C₆D₆, eTMS): δ = –6.1 (s, *Si*Ph₂*t*Bu) ppm.

Computational Methods: DFT structure optimizations were performed with the Turbomole program,[36] adopting the multiple "M3" grid size for the density fitting and a SCF convergence criterion of 1×10^{-7} E_h. The initial geometries were fully optimized with the hybrid exchange-correlation functional PBE0.[37] As Gaussian AO basis for all atoms, all-electron split valence SV(P) sets of def2-type[38] were employed (Basis Set System I, which is denoted BS-

I). All other computations were carried out on PBE0 optimized geometries with the Gaussian 03 program package.[39] We used Los Alamos National Laboratory 2 (LANL2) relativistic effective core potentials (RECPs) to describe the core electrons of In, P, As, Sb, Bi, and Br atoms and employed split-valence (double-ζ) quality basis sets to describe their s and p valence electrons. For P, As, Sb, Bi, and Br atoms, the LANL2DZ basis set was augmented by adding one set of polarization and one set of diffuse functions.[40] For Si, C, and H atoms, all-electron split-valence 6-311+G(d,p) basis sets supplemented with a single set of diffuse functions on carbon and silicon atoms were employed.[41] The combination of LANL2DZdp and 6-311+G(d,p) is denoted Basis Set System II (BS-II). The vibrational frequencies were evaluated on all DFT-optimized geometries by using the HF method to verify their status as true local minima on the potential energy surface and to obtain zero-point corrections to the energies (ZPE) without scaling. The nature of the chemical bonding was analyzed by means of the NBO approach with the second-order Møller–Plesset perturbation theory, including all valence electrons in the configuration space [MP2(full)]. The atomic charges were computed within the natural population analysis (NPA). Wiberg indexes were evaluated and used as bond strength indicators. NBO analyses were performed with NBO Version 3.1[42] incorporated in the Gaussian 03 program. To gain insight into the vertical singlet electronic states, time-dependent functional theory[43] (TD-PBE0 method) calculations were performed. Energies reported herein were evaluated by using the fourth-order Møller–Plesset perturbation theory [MP4(SDQ)] in combination with PBE0 parameterization.

Acknowledgments

[1] a) O. Mundt, G. Becker, M. Rössler, C. Witthauer, *Z. Anorg. Allg. Chem.* **1983**, *506*, 42–58; b) G. Becker, O. Mundt in *Unkonventionelle Wechselwirkungen in der Chemie metallischer Elemente*, VCH, Weinheim, **1992**, pp. 199–217.

[2] G. M. Kollegger, H. Siegl, K. Hassler, K. Gruber, *Organometallics* **1996**, *15*, 4337–4338.

[3] a) G. Linti, W. Köstler, *Z. Anorg. Allg. Chem.* **2002**, *628*, 63–66; b) G. Linti, W. Köstler, H. Pritzkow, *Eur. J. Inorg. Chem.* **2002**, 2643–2647.

[4] C. von Hänisch, D. Nikolova, *Eur. J. Inorg. Chem.* **2006**, 4770–4773.

[5] S. Schulz, M. Nieger, *Angew. Chem.* **1999**, *111*, 1020–1021; *Angew. Chem. Int. Ed.* **1999**, *38*, 967–968.

[6] A. Kuczkowski, F. Thomas, S. Schulz, M. Nieger, *Organometallics* **2000**, *19*, 5758–5762.

[7] A. Kuczkowski, S. Schulz, M. Nieger, *Eur. J. Inorg. Chem.* **2001**, 2605–2611.

[8] A. Kuczkowski, S. Schulz, M. Nieger, P. R. Schreiner, *Organometallics* **2002**, *21*, 1408–1419.

[9] F. Thomas, S. Schulz, M. Nieger, *Organometallics* **2002**, *21*, 2793–2795.

[10] D. Fenske, A. Rothenberger, S. Wieber, *Z. Anorg. Allg. Chem.* **2003**, *629*, 929–930.

[11] F. Thomas, S. Schulz, H. Mansikkamäki, M. Nieger, *Angew. Chem.* **2003**, *115*, 5800–5803; *Angew. Chem. Int. Ed.* **2003**, *42*, 5641–5644.

[12] R. Wolf, J. Fischer, R. C. Fischer, J. C. Fettinger, P. P. Power, *Eur. J. Inorg. Chem.* **2008**, 2515–2521.

[13] B. K. Campion, R. H. Heyn, T. D. Tilley, *Organometallics* **1993**, *12*, 2584–2590.

[14] K. H. Ebert, R. E. Schulz, H. J. Breunig, C. Silvestru, I. Haiduc, *J. Organomet. Chem.* **1994**, *470*, 93–98.

[15] C. Strohmann, O. Ulbrich, D. Auer, *Eur. J. Inorg. Chem.* **2001**, 1013–1018.

[16] a) H. V. R. Dias, M. M. Olmstead, K. Ruhlandt-Senge, P. P. Power, *J. Organomet. Chem.* **1993**, *462*, 1–6; b) A. Heine, R. Herbst-Irmer, G. M. Sheldrick, D. Stalke, *Inorg. Chem.* **1993**, *32*, 2694–2698.

[17] N. Wiberg, K. Ameluxen, H.-W. Lerner, H. Schuster, H. Nöth, I. Krossing, M. Schmidt-Ameluxen, T. Seifert, *J. Organomet. Chem.* **1997**, *542*, 1–18.

[18] H.-W. Lerner, I. Sänger, F. Schödel, K. Polborn, M. Bolte, M. Wagner, *Z. Naturforsch., Teil B* **2007**, *62*, 1285–1290.

[19] A. Kawachi, K. Tamao, *J. Am. Chem. Soc.* **2000**, *122*, 1919–1926.

[20] Y. Apeloig, M. Yuzefovich, M. Bendikov, D. Bravo-Zhivotovskii, D. Bläser, R. Boese, *Angew. Chem. Int. Ed.* **2001**, *40*, 3016–3020.

[21] G. Balázs, H. J. Breunig, E. Lork, *Organometallics* **2002**, *21*, 2584–2586.

[22] C. Silvestru, H. J. Breunig, H. Althaus, *Chem. Rev.* **1999**, *99*, 3277–3327.

[23] H. Althaus, H. J. Breunig, R. Rösler, E. Lork, *Organometallics* **1999**, *18*, 328–331.

[24] B. Murray, J. Hvoslef, H. Hope, P. P. Power, *Inorg. Chem.* **1983**, *22*, 3421.

[25] G. Linti, M. Bühler, K. Yu. Monakhov, T. Zessin, *Dalton Trans.* **2009**, 8071–9078.

[26] a) S. L. Hinchley, C. A. Morrison, D. W. H. Rankin, C. L. B. Macdonald, R. J. Wiacek, A. H. Cowley, M. F. Lappert, G. Gundersen, J. A. C. Clyburne, P. P. Power, *Chem. Commun.* **2000**, 2045; b) S. L. Hinchley, C. A. Morrison, D. W. H. Rankin, C. L. B. Macdonald, R. J. Wiacek, A. Voigt, A. H. Cowley, M. F. Lappert, G. Gundersen, J. A. C. Clyburne, P. P. Power, *J. Am. Chem. Soc.* **2001**, *123*, 9045–9053.

[27] a) M. J. S. Gynane, A. Hudson, M. F. Lappert, P. P. Power, H. Goldwhite, *J. Chem. Soc., Dalton Trans.* **1980**, 2428–2433; b) P. P. Power, *Chem. Rev.* **2003**, *103*, 789–809.

[28] N. S. Vyazankin, G. A. Razuvaev, O. A. Kruglaya, G. S. Semchikova, *J. Organomet. Chem.* **1966**, *6*, 474.

[29] L. Balázs, H. J. Breunig, E. Lork, A. Soran, C. Silvestru, *Inorg. Chem.* **2006**, *45*, 2341–2346.

[30] a) H. Gilman, H. L. Yablunky, *J. Am. Chem. Soc.* **1941**, *63*, 212–216; b) H. Gilman, H. L. Yale, *Chem. Rev.* **1942**, *30*, 281–320.

[31] a) A. J. Ashe III, E. G. Ludwig Jr., J. Oleksyszyn, *Organometallics* **1983**, *2*, 1859–1866; b) H. J. Breunig, *Z. Anorg. Allg. Chem.* **2005**, *631*, 621–631.

[32] a) O. Mundt, H. Riffel, G. Becker, A. Simon, *Z. Naturforsch., Teil B* **1988**, *43*, 952; b) A. J. Ashe III, J. W. Kampf, D. B. Puranik, S. M. Al-Taweel, *Organometallics* **1992**, *11*, 2743–2745.

[33] K. W. Klinkhammer, P. Pyykkö, *Inorg. Chem.* **1995**, *34*, 4134–4138.

[34] A. Kuczkowski, S. Schulz, M. Nieger, *Angew. Chem.* **2001**, *113*, 4351–4353; *Angew. Chem. Int. Ed.* **2001**, *40*, 4222–4225.

[35] G. M. Sheldrick, *Acta Crystallogr., Sect. A* **2008**, *64*, 112–122.

[36] R. Ahlrichs, M. Bär, M. Häser, H. Horn, C. Kölmel, *Chem. Phys. Lett.* **1989**, *162*, 165–169.

[37] C. Adamo, V. Barone, *J. Chem. Phys.* **1999**, *110*, 6158.

[38] a) B. Metz, H. Stoll, M. Dolg, *J. Chem. Phys.* **2000**, *113*, 2563–2569; b) F. Weigend, R. Ahlrichs, *Phys. Chem. Chem. Phys.* **2005**, *7/18*, 3297–3305.

[39] M. J. Frisch, G. W. Trucks, H. B. Schlegel, G. E. Scuseria, M. A. Robb, J. R. Cheeseman, J. A. Montgomery Jr., T. Vreven, K. N. Kudin, J. C. Burant, J. M. Millam, S. S. Iyengar, J. Tomasi, V. Barone, B. Mennucci, M. Cossi, G. Scalmani, N. Rega, G. A. Petersson, H. Nakatsuji, M. Hada, M. Ehara, K. Toyota, R. Fukuda, J. Hasegawa, M. Ishida, T. Nakajima, Y. Honda, O. Kitao, H. Nakai, M. Klene, X. Li, J. E. Knox, H. P. Hratchian, J. B. Cross, V. Bakken, C. Adamo, J. Jaramillo, R. Gomperts, R. E. Stratmann, O. Yazyev, A. J. Austin, R. Cammi, C. Pomelli, J. W. Ochterski, P. Y. Ayala, K. Morokuma, G. A. Voth, P. Salvador, J. J. Dannenberg, V. G. Zakrzewski, S. Dapprich, A. D. Daniels, M. C. Strain, O. Farkas, D. K. Malick, A. D. Rabuck, K. Raghavachari, J. B. Foresman, J. V. Ortiz, Q. Cui, A. G. Baboul, S. Clifford, J. Cioslowski, B. B. Stefanov, G. Liu, A. Liashenko, P. Piskorz, I. Komaromi, R. L. Martin, D. J. Fox, T. Keith, M. A. Al-Laham, C. Y. Peng, A. Nanayakkara, M. Challacombe, P. M. W. Gill, B. Johnson, W. Chen, M. W. Wong, C. Gonzalez, and J. A. Pople, *Gaussian 03*, Revision E. 01, Gaussian, Inc., Wallingford CT, **2004**.

[40] a) P. J. Hay, W. R. Wadt, *J. Chem. Phys.* **1985**, *82*, 270; b) P. J. Hay, W. R. Wadt, *J. Chem. Phys.* **1985**, *82*, 284; c) P. J. Hay, W. R. Wadt, *J. Chem. Phys.* **1985**, *82*, 299; d) C. E. Check, T. O. Faust, J. M. Bailey, B. J. Wright, T. M. Gilbert, L. S. Sunderlin, *J. Phys. Chem. A* **2001**, *105*, 8111.

[41] a) R. Krishnan, J. S. Binkley, R. Seeger, J. A. Pople, *J. Chem. Phys.* **1980**, *72*, 650; b) T. Clark, J. Chandrasekhar, P. v. R. Schleyer, *J. Comput. Chem.* **1983**, *4*, 294.

[42] a) E. D. Glendening, A. E. Reed, J. E. Carpenter, F. Weinhold, *NBO program*, vers. 3.1; b) A. E. Reed, L. A. Curtiss, F. Weinhold, *Chem. Rev.* **1988**, *88*, 899.

[43] M. E. Casida, C. Jaorski, K. C. Casida, D. R. Salahub, *J. Chem. Phys.* **1998**, *108*, 4439.